Investigating the Transcriptional and Histological Profile of Pericardial Adipose Tissue

Thesis submitted as requirement for the degree of Doctor of Philosophy

School of Biological Sciences

Alaa Al-Dibouni, BSc (Biomedical Science)

September 2021

Alaa Al - Dibouni

ABSTRACT

Introduction: The nutritional environment encountered *in utero* and during adulthood influences the development of adipose tissue (AT). Brown-like cells residing in AT that often promote a beneficial metabolic profile, may become dysfunctional in metabolic disease. Alterations in AT may increase the risk of developing Cardiovascular Disease and Type 2 Diabetes.

Aim: There is still a lack of knowledge regarding the role of AT associated with the heart, such as pericardial adipose tissue (PAT), in normal and dysregulated metabolism. This thesis aims to provide an insight into the therapeutic potential and adipogenic, inflammatory and thermogenic capacity of PAT, in mice.

Method: The transcriptional and histological profile of PAT, compared to other adipose depots, was assessed in male C57BL/6 mice. Firstly, PAT was harvested from mice fed either a chow or high-fat (HF)-diet, for 7 or 26 weeks. Secondly, PAT was sampled from offspring mice fed a post-weaning diet of either a chow or HF-diet for 26 weeks, from dams fed a chow or HF-diet prior to and during pregnancy and lactation. Finally, PAT was collected from chow and HF-fed mice treated orally with and without Compound 14 (Cpd14) for 10 days and after a 26-day recovery period.

Results: Firstly, there were differences in brown and white adipocyte markers of PAT, depending on the nutritional environment encountered. Secondly, both the maternal and offspring diet influenced the thermogenic potential of PAT. Finally, Cpd14 potentially upregulated the thermogenic capacity of PAT to induce weight loss in obese mice.

Conclusion: Collectively, PAT in mice has a unique transcriptional and histological profile, altered by dietary exposure *in utero* and during adulthood, and upon therapeutic stimulation. The underlying mechanisms involved are still unknown, however there is compelling evidence that PAT as a beige depot is an attractive therapeutic target.

Alaa Al - Dibouni

DECLARATION

I confirm that this is my own work and the use of all material from other sources have been properly and fully acknowledged.

Alaa Al-Dibouni

Alaa Al - Dibouni

ACKNOWLEDGMENTS

PUBLICATIONS AND PRESENTATIONS

Peer-reviewed publications

Some of the results presented in this thesis have been published in peer-reviewed journals.

1. Gaspar, R. S., Unsworth, A. J., **Al-Dibouni, A.,** Bye, A. P., Sage, T., Stewart, M., Wells, S., Cox, R. D., Gibbins, J. M., Sellayah, D., and E Hughes, C. (2021). Maternal and offspring high-fat diet leads to platelet hyperactivation in male mice offspring. *Scientific reports*, *11*(1), 1473

2. **Al-Dibouni, A.,** Gaspar, R., Ige, S., Boateng, S., Cagampang, F. R., Gibbins, J., Cox, R. D., Sellayah, D. (2020). Unique Genetic and Histological Signatures of Mouse Pericardial Adipose Tissue. *Nutrients*, *12*(6), 1855

Abstracts of scientific meetings

Some of the results presented in this thesis have been presented at scientific meetings.

1. **Al-Dibouni, A.**, Tavassoli, A., Cagampang, F., Elumalai, N., Sellayah, D. (2020). Exploring the Effects of a Novel Anti-Diabetes Compound on Adipose Tissue. Abstract published online in Obesity Abstracts. Poster presentation at the Obesity Update 2020, London, United Kingdom.

2. **Al-Dibouni, A.**, Tavassoli, A., Cagampang, F., Elumalai, N., Sellayah, D. (2019). Investigating the Effects of a Novel Anti-Diabetes Compound on Adipose Tissue. Peer-reviewed abstract published online in the Journal of Human Nutrition and Dietetics (JHND). Oral presentation at the British Dietetics Association (BDA) Research Symposium, Birmingham, United Kingdom.

3. **Al-Dibouni, A.** (2019). Investigating the Effects of a Novel Compound on Adipose Tissue. Oral presentation at the School of Biological Sciences Symposium, University of Reading, United Kingdom. *This won the best 2nd year PhD oral presentation in the Biomedical Sciences category at the symposium.*

4. **Al-Dibouni, A**. (2018). The Effects of a Novel Compound on Adipogenesis. Poster presentation at the School of Biological Sciences Symposium, University of Reading, United Kingdom.

Alaa Al - Dibouni

TABLE OF CONTENTS

LIST OF ABBREVIATIONS

2-DG	2-deoxyglucose
4-AAP	4-aminoantipyrine
ACC	Acetyl-CoA carboxylase
ACTA1	Actin alpha 1
AdipoQ	Adiponectin
AdipoR1	Adiponectin Receptor 1
ADP	Adenosine diphosphate
ADRβ3	Adrenergic receptor beta 3
AICAR	5-Aminoimidazole-4-carboxamide ribonucleotide
AICART	5-Aminoimidazole-4-carboxamide ribonucleotide transferase
AMP	Adenosine monophosphate
AMPK	5' adenosine monophosphate-activated protein kinase
APs	Adipocyte precursors
AT	Adipose Tissue
ATGL	Adipose triglyceride lipase
ATIC	Aminoimidazole carboxamide ribonucleotide transformylase/inosine monophosphate cyclohydrolase
ATP	Adenosine triphosphate
BAT	Brown Adipose Tissue
BMI	Body Mass Index
BMP (7)	Bone Morphogenetic Protein (7)
C	Chow
C/C	Chow/Chow
C/EBP(s)	CCAAT (cytosine-cytosine-adenosine-adenosine-thymidine) Enhancer Binding Protein (s)
C/EBPα/β	CCAAT (cytosine-cytosine-adenosine-adenosine-thymidine) Enhancer Binding Protein alpha/beta
C/HF	Chow/High-fat
CAMKK	Calcium/calmodulin-dependent protein kinase kinase

Alaa Al - Dibouni

cAMP	cyclic AMP adenosine 3' 5' monophosphate
C-Cpd14	Chow-Compound 14
cDNA	Complementary Deoxyribose nucleic acid
CHD	Coronary Heart Disease
CIT	Cold-induced thermogenesis
CLS	Crown-like Structures
COX	Cytochrome C Oxidase
COX7A1	Cytochrome C Oxidase Subunit VIIa Polypeptide 1
COX8B	Cytochrome C Oxidase Subunit VIIIb Polypeptide
Cpd14	Compound 14
CRP	C-reactive protein
Ct	Cycle threshold
CV	Cardiovascular
C-V	Chow-Vehicle
CVD	Cardiovascular Disease
ddH_20	Double distilled water
DG	Diacylglycerol
DIO	Diet-induced obesity
DIO2	Type II iodothyronine deiodinase
DIT	Diet-induced thermogenesis
DNA	Deoxyribose nucleic acid
EAT	Epicardial Adipose Tissue
En1	Engrailed 1
ESPA	sodium N-ethyl-N-(3-sulfopropyl)
ETC	Electron Transport Chain
FABP4	Fatty acid binding protein 4
FFA (s)	Free Fatty Acid (s)
FGF21	Fibroblast Growth Factor 21
FGR	Free Glycerol Reagent
G-1-P	Glucose-1-phosphate

Alaa Al - Dibouni

GK	Glycerol kinase
GPO	Glycerol phosphate oxidase
GTT	Glucose tolerant test
gWAT	gonadal White Adipose Tissue
H+	Hydrogen ions
H_2O	Water
HDL	High-density lipoprotein
HF	High-fat
HF/C	High-fat/Chow
HF/HF	High-fat/High-fat
HF-Cpd14	High-fat-Compound 14
HF-V	High-fat-Vehicle
HPM	High Purine Media
HSL	Hormone-sensitive lipase
H-TGL	Hepatic triglyceride lipase
i.p.	Intraperitoneal
iBAT	interscapular Brown Adipose Tissue
IL6	Interleukin 6
ipGTT	Intraperitoneal glucose tolerance test
IRS-1	Insulin receptor substrate-1
iWAT	inguinal White Adipose Tissue
JNK	c-Jun N-terminal Kinase
LDL	Low-density lipoprotein
LKB1	Liver Kinase B1
LPM	Low Purine Media
MCE	Mitotic Clonal Expansion
MCP1	Monocyte Chemoattractant Protein 1
MetS	Metabolic Syndrome
MG	Monoglyceride
MGB	Minor Groove Binder

Alaa Al - Dibouni

MGL	Monoglyceride lipase
MHO	Metabolically Healthy Obesity
MI	Myocardial infarction
miRNA	Micro Ribonucleic Acid
mRNA	Messenger Ribonucleic Acid
MSCs	Mesenchymal stem cells
MUO	Metabolically Unhealthy Obesity
Myf5	Myogenic factor 5
MYH6	Myosin Heavy Chain 6
MYH7	Myosin Heavy Chain 7
NA	Noradrenaline
NFQ	Non-fluorescent quencher
NOX4	Nicotinamide adenine dinucleotide phosphate Oxidase 4
NPPA	Natriuretic Peptide A
NrF2	Nuclear factor erythroid 2-related factor 2
ORO	Oil Red O
PAT	Pericardial Adipose Tissue
Pax7	Paired boxed protein 7
PCR	Polymerase Chain Reaction
PDGFRα	Platelet-derived growth factor receptor alpha
PGC1α	Peroxisome proliferator-activated receptor gamma coactivator 1 alpha
Pi	Inorganic Phosphate
PI3K	Phosphatidylinositol 3-kinase
PKA	Protein Kinase A
PLIN1	Perilipin 1
POD	Peroxidase
PPAR(s)	Peroxisome proliferator-activated receptor(s)
PPARγ	Peroxisome proliferator-activated receptor gamma
PRDM16	PR domain containing 16
PVAT	Perivascular adipose tissue

Alaa Al - Dibouni

R	Fluorescent reporter
RER	Respiratory exchange rate
RNA	Ribonucleic acid
ROS	Reactive oxygen species
RSV	Resveratrol
RT-qPCR	Real time-quantitative polymer chain reaction
SAT	Subcutaneous Adipose Tissue
Ser79	Serine 79
Slit2	Slit homolog 2
SNS	Sympathetic nervous system
SVF	Stromal vascular fraction
T2D	Type 2 Diabetes
T3	Triiodothyronine
T4	Thyroxine 4
TG (s)	Triglyceride (s)
Thr172	Threonine 172
TNFα	Tumour Necrosis Factor α
TR	Triglyceride reagent
TZDs	Thiazolidinediones
UCP1	Uncoupling protein 1
VAT	Visceral Adipose Tissue
WAT	White Adipose Tissue
Wnt	Wingless-related integration site
Wt1	Wilm's tumour gene
Zfp423	Zinc-finger protein transcription factor

LIST OF FIGURES

LIST OF TABLES

PAGE

CHAPTER 1

INTRODUCTION

Alaa Al - Dibouni

1.1. Obesity

Excessive accumulation of energy, stored in the form of triglycerides in adipose tissue (AT) (World Health Organisation, 1995), increases the risk of an individual becoming overweight or obese. Characterised by low-grade inflammation, obesity is often a result of dysregulated secretion of signalling factors released from adipocytes residing in AT (Chait and den Hartigh, 2020). The classification system body mass index (BMI) utilises the height and weight of a person to establish whether an individual is overweight or obese. A BMI between $25kg/m^2$ and $29.9kg/m^2$ is considered as an overweight phenotype and a BMI of $30kg/m^2$ or greater is obese (World Health Organisation, 1995; Baker, 2019). These statistics share a relationship with the rise of incidents in other metabolic disorders such as Type 2 Diabetes (T2D) and Cardiovascular Disease (CVD) (Baker, 2019). Of note, T2D further increases the risk of developing detrimental cardiovascular (CV) events, such as heart attacks (Diabetes UK, 2019; British Heart Foundation, 2020). In England, obese individuals are more likely to be diagnosed with T2D than healthy weighted individuals (Mary et al., 2014; Diabetes UK, 2019), with the prevalence of global diabetes predicted to double from the year 2000 to 2030 (Wild et al., 2004).

1.1.1. Molecular mechanisms involved in metabolic disease

There is a suggestive causal link between the progression of metabolic disorders. Low-grade inflammation, a characteristic of increased adiposity (high BMI), is associated with impaired free fatty acid (FFA) regulation and insulin resistance. These clinical traits are often associated with the development of T2D (Fernández-Real et al., 2003) and atherosclerotic events (Fujita et al., 2006). The exact mechanisms involved in the development of these disorders are still undefined, however experimental research has probed the potential factors that may be involved in metabolic pathogenesis.

1.1.1.1. Adipose tissue distribution

The pathogenesis of obesity is commonly associated with inflammation and insulin resistance (Sung et al., 2018). Abnormally active fat cells (adipocytes) secrete high levels of pro-inflammatory markers, such as Interleukin 6 (IL6) and Tumour Necrosis Factor α (TNFα). In addition, there is a reduction in the secretion of anti-inflammatory markers, such Adiponectin (Bremer et al., 2011). These factors may also be released from macrophages (Cinti et al., 2005) that reside within AT and assist with promoting a state of chronic inflammation in obesity (Weisberg et al., 2003). While the increase in adipocyte size/volume is linked with metabolic complications, such as insulin resistance (Weyer et al., 2000; Weyer et al., 2001), the deposition of AT around the body greatly determines the magnitude in which metabolic alterations may persist (Vague, 1996). In humans, AT accumulation around the central region, compared to the lower body, is highly associated with increased mortality and development of T2D and CVD (Krotkiewski et al., 1983; Lapidus et al., 1984; Ohlson et al., 1985; Donahue et al., 1987; Fujioka et al., 1987; Després et al., 1989b; Després et al., 1989c; Pouliot et al., 1992; Vague, 1996). In particular, large amounts of white visceral adipose tissue (VAT), is linked insulin resistance (Pouliot et al., 1992; Weiss et al., 2003), pro-inflammation (Dahlén et al., 2014) and reduced high-density lipoprotein (HDL) levels (Després et al., 1989a). The latter acts as a risk factor for the development of CVD (Peiris et al., 1989). This demonstrates that AT distribution (Figure 1.1) is an important indicator for pathogenesis, as opposed to only assessing the extent of adiposity (Larsson et al., 1984).
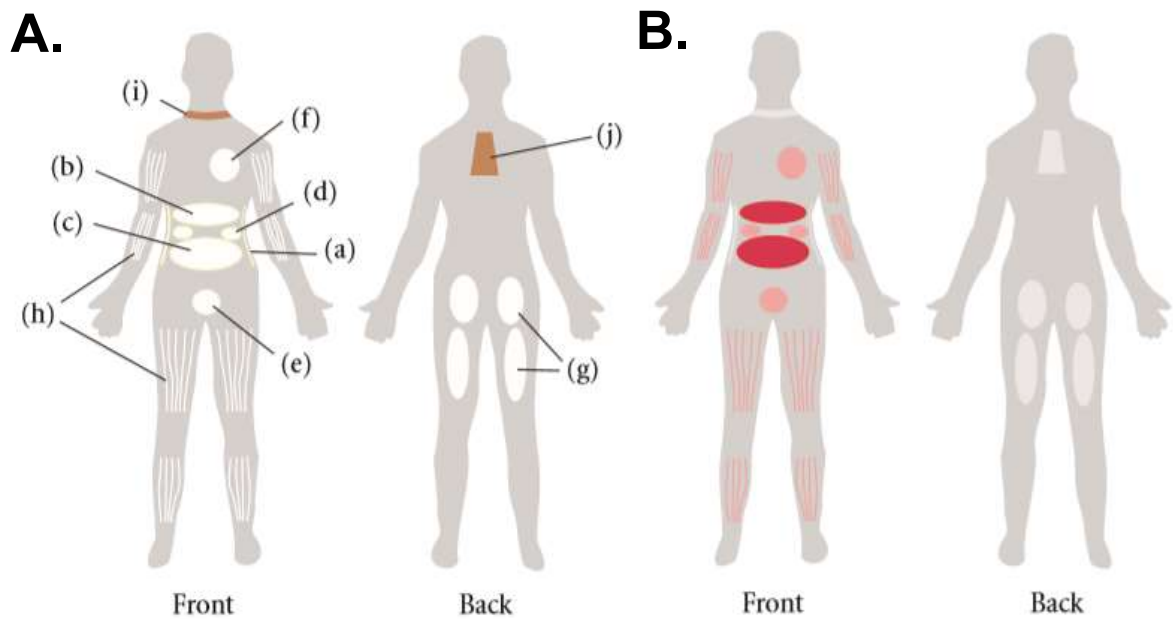
Figure 1.1. Adipose tissue distribution in humans. (A) WAT includes abdominal SAT (a) (gluteofemoral (g) and intramuscular (h)) and VAT which surrounds the internal organs (omental (b), mesenteric (c), retroperitoneal (d), gonadal (e) and pericardial (f)). BAT is located above the clavicle, in the supraclavicular (i) and subscapular (j) regions. **(B)** The areas highlighted in red are the adipose tissue regions which are associated with increased risk of developing obesity and related diseases. Taken from Bjørndal et al., (2011). WAT: White adipose tissue; SAT: Subcutaneous adipose tissue; VAT: Visceral adipose tissue; BAT: Brown adipose tissue.

1.1.1.2. Inflammation

Overexpression of pro-inflammatory markers in AT increases the risk of developing insulin resistance and CV-related events (Hotamisligil et al., 1993; Kern et al., 2001; Bremer et al., 2011). This inflammatory state is partially due to the migration of macrophages that aggregate in clusters, known as Crown-like Structures (CLS) (Bremer et al., 2011). These secrete pro-inflammatory molecules, such as Monocyte Chemoattractant Protein 1 (MCP1) (Kanda et al., 2006). Although macrophage infiltration is a normal trait in lean individuals, during obesity, elevated secretion of MCP1 is associated with increased adiposity (Weisberg et al., 2003). Furthermore, prominent macrophage infiltration in white adipose tissue (WAT) (Cinti et al., 2005) is more deleterious in white visceral fat (Murano et al., 2008), deposited in the abdominal

region (Harman-Boehm et al., 2007), compared to macrophage infiltration in white subcutaneous adipose tissue (SAT) (Cancello et al., 2006; Murano et al., 2008). MCP1 released from macrophages in turn promotes the secretion of other pro-inflammatory molecules from dysfunctional adipocytes (Mohamed-Ali et al., 1999). These include the pro-inflammatory cytokines TNFα (Winkler et al., 2003) and IL6 (Bastard et al., 2000). Elevated levels of these molecules are associated with increased adiposity and characterises low-grade inflammation during obesity. However, the role of IL6 in metabolism is debatable, as studies have demonstrated that IL6-deficient mice acquire obesity (Wallenius et al., 2002). On the contrary, evidence suggests that TNFα is a key pro-inflammatory molecule in the progression of disease. Elevated levels of TNFα inhibits insulin signalling, resulting in insulin resistance (Hotamisligil et al., 1994; Stephens et al., 1997) by disrupting events involved in tyrosine phosphorylation of the insulin receptor and insulin receptor substrate-1 (IRS-1). These events are essential for normal insulin signalling (Feinstein et al., 1993) and disturbing these occurrences contributes to diabetic-related obesity (Xu et al., 2003). In humans, atherosclerotic lesions develop decades prior to manifestation of CVD. However, this plaque formation is more frequent in obese individuals (Manson et al., 1990 ; McGill et al., 2002). As obesity is an inflammatory disease, the pathogenesis of CV-related events is mediated by inflammatory molecules (Henrichot et al., 2005; Takaoka et al., 2010), including TNFα (Lee et al., 2007), and the infiltration of macrophages (Aghamohammadzadeh et al., 2013) in AT in proximity to the heart.

1.1.1.3. Glucose and Lipid metabolism

As a highly plastic depot, AT expands by hypertrophy (increase in cell size) to accommodate for lipid accumulation. In obese individuals, this mechanistic growth of AT is dysfunctional (Klöting et al., 2010). As adipocytes have a limited storage capacity, excess lipid accumulation ('lipotoxicity') may result in 'lipid overflow' into surrounding organs (Krotkiewski et al., 1983; Lönn et al., 2010 Zhou et al., 2019b). Primarily, ectopic deposition of visceral fat and hypertrophy of visceral adipocytes play a role in the development of insulin resistance. High

levels of circulating metabolites inhibit insulin signalling and induce 'lipotoxicitiy' (Moitra et al., 1998; Barak et al., 1999).

Skeletal muscle is the main organ that is involved in glucose metabolism (Rowe et al., 1983). It is highly enriched with mitochondria and relies on oxidative phosphorylation for the production of energy (Kelley et al., 2002). Dysregulated glucose and lipid metabolism in skeletal muscle is implicated in diabetes (Shulman et al., 1990; Kelley and Simoneau, 1994) due to accumulation of FFAs, thus inducing insulin resistance (Boden and Chen, 1995). FFA accumulation upregulates tyrosine phosphorylation of IRS-1 in the insulin signalling pathway. This inhibits activation of phosphatidylinositol 3-kinase (PI3K) (Dresner et al., 1999) and impedes glucose transport (Roden et al., 1996; Dresner et al., 1999; Itani et al., 2002; Yu et al., 2002), uptake (Boden et al., 1991; McQuaid et al., 2011), oxidation (Roden et al., 1996) and glycogen synthesis (Boden et al., 1991; Roden et al., 1996). This insulin resistance is correlated with a reduction of oxidative enzymes within the mitochondria (Simoneau et al., 1999) and accumulation of triglycerides (TGs) (He et al., 2001), of skeletal muscle, in obesity and T2D (Simoneau et al., 1995; Simoneau and Kelley, 1997). Furthermore, a similar mechanism is assumed to suppress glucose production in the liver and establish insulin resistance (Petersen et al., 2002; Seppälä-Lindroos et al., 2002).

Cardiovascular metabolic parameters, such as plasma HDL, are controlled by lipases in the liver, including hepatic triglyceride lipase (H-TGL). During obesity, although the underlying mechanisms are still unknown, dysregulation of hepatic lipases (Després et al., 1989b) causes elevation of HDL levels. This is associated with AT size (Després et al., 1987) and further exacerbated by obesity (Jimenez et al.,1989). The eventual manifestation of these documented processes may result in lipid accumulation ectopically in non-adipose tissue depots and contribute to metabolic disease (Fabbrini et al., 2009).

1.1.1.4. Mitochondrial dysfunction

Mitochondria play a crucial role in biological events including adipocyte differentiation and fatty acid and TG synthesis (lipogenesis) (Tormos et al., 2011). In metabolic diseases, such as diet-

induced obesity (DIO) (Feldmann et al., 2009), the oxidative capacity of mitochondria is reduced. This results in dysregulation of heat production (thermogenesis), upregulation of TG accumulation and a reduction in glucose uptake (Vankoningsloo et al., 2005). In addition to these, an imbalance of adenosine triphosphate (ATP) production and demand (Petersen et al., 2003; Wang et al., 2017) are characteristics of insulin resistance (Petersen et al., 2003) and heart failure (Wang et al., 2017).

Mitochondria residing in cardiomyocytes of the heart, express mitochondrial microRNAs (miRNA) that regulate gene expression associated with oxidative stress (Wang et al., 2017). In a damaged heart, an increase in miRNAs can suppress mitochondrial components, such as Cytochrome C Oxidases (COX), leading to dysfunctional mitochondrial metabolism (Das et al., 2012; Das et al., 2014). This is characterised by an increase in intracellular fatty acid metabolites which may disrupt peripheral insulin signalling (Lowell and Shulman, 2005). This can induce insulin resistance associated with heart endothelial dysfunction, increase the risk of atherosclerosis in obesity (Steinberg et al., 1996) and contribute to acquisition of a diabetic heart (Jagannathan et al., 2015; Shepherd et al., 2017).

Additionally, the hormone Adiponectin controls insulin and glucose metabolism in liver and muscle cells (Yamauchi et al., 2002). Downregulation of Adiponectin Receptor 1 (AdipoR1) expression in turn downregulates the expression of the mitochondrial related gene peroxisome proliferator-activated receptor gamma coactivator 1 alpha (PGC1α), fatty acid oxidation and mitochondrial biogenesis in muscle cells (Iwabu et al., 2010). PGC1α expression is reduced in WAT of obese humans (Semple et al., 2004), muscle of mice (Crunkhorn et al., 2007) and impairs mitochondrial respiration and biogenesis (Uldry et al., 2006). However, therapeutic intervention, at least in diabetic mice, with activators of 5' adenosine monophosphate-activated protein kinase (AMPK), such as thiazolidinediones (TZDs), can increase expression of Adiponectin, AdipoR1 and mitochondrial related genes to improve insulin signalling in skeletal muscle (Coletta et al., 2009).

Furthermore, brown adipose tissue (BAT) has an extensive thermogenic capacity due to the vast number of mitochondria that reside in brown adipocytes. BAT activity is inversely

proportional to BMI, glucose levels and body fat percentage (Cypess, 2009; Saito et al., 2009; Van Marken Lichtenbelt et al., 2009). Although ectopic fat deposition is considered deleterious, skeletal muscle from obesity-resistant mice, compared to obesity-prone mice, have ectopic BAT deposition which expresses higher levels of uncoupling protein 1 (UCP1), a thermogenin housed in mitochondria. A similar observation is observed in humans, suggesting brown adipocyte infiltration in muscles (Crisan et al., 2008). In certain white depots, there are a population of brown-like adipocytes which express UCP1 accompanied by increased mitochondrial biogenesis (Barbatelli et al., 2010) and is upregulated by adrenergic receptor beta 3 (ADRβ3) (Champigny and Ricquier, 1996). Studies in ADRβ3-knockout mice demonstrate a diminished presence of brown-like adipocytes residing within white depots (Jimenez et al., 2003) and in humans, low ADRβ3 activity is associated with increased weight gain (Andersson et al., 2009). This demonstrates a vital role of ADRβ3 action in lipid metabolism in white depots (Krief et al., 1993) and weight management in humans. Although these UCP1-positive (UCP1+) brown-like adipocytes differ from the classical brown adipocytes located in BAT (Jimenez et al., 2003), they present an attractive target for upregulating mitochondrial function to induce thermogenesis and influence the susceptibility of developing obesity (Kontani et al., 2005).

1.1.2. Influences that alter metabolic health

Humans are evolutionary designed to store fat in times of food shortages (Neel, 1999). In modern society, there is an increase in food availability (Spiegelman and Flier, 2001) and this evolutionary trait has become redundant. While eating more and moving less contributes to an increase in BMI, some individuals may have a greater pre-disposition to obesity and related co-morbidities in later life (Reilly and Kelly, 2011; Singh et al., 2008). The geographical location of populations around the world, as well as their genetic background and gender, influence the shift of a lean to obese phenotype in particular individuals (Finucane et al., 2011).

A widely accepted concept considers that the environment of a developing fetus is impacted by maternal influences (Gillman et al., 2010). A mechanism known as plasticity, allows a

developing fetus to alter their physiology and organ development to predict and adapt to the changing maternal environment (West-Eberhard, 2005). Interestingly, a 'U-shaped' relationship defines the association between birthweight and the risk of developing obesity in adulthood (Curhan et al., 1996). The exposure to maternal nutritional intake, such as overnutrition and undernutrition during pregnancy, can increase the risk of metabolic complications in both the mother and offspring in later life (Drehmer et al., 2013).

1.1.2.1. Maternal undernutrition

Exposure to maternal dietary malnourishment during pregnancy (maternal undernutrition) can impact the metabolic health of a developing fetus in later life (Barker et al., 1993). Cohort studies have demonstrated that an increase in mortality of young infants, linked with poor living conditions, is associated with atherosclerosis, a risk factor for CVD (Forsdahl, 1997; Barker and Osmond, 1986). Furthermore, offspring born to mothers who were malnourished during pregnancy had a higher BMI (Ravelli et al., 1999), a higher lipid profile (Roseboom et al., 2000a) and an increased risk of coronary heart disease (CHD) (Roseboom et al., 2000b).

Offspring AT can alter during different stages of pregnancy in response to the maternal nutritional environment encountered *in utero* (Symonds et al., 2007). This can influence the long-term dietary behaviour of a developing offspring (Bellinger et al., 2006). In later life, cardiovascular-related implications (Remacle et al., 2011), lower levels of the 'satiety' hormone Leptin (Jousse et al., 2011) and hyperphagia (Bellinger et al., 2006) are induced by both prenatal and postnatal alterations. In fact, the postnatal overnutrition of an offspring is required to manifest the pathogenesis of metabolic diseases (Bellinger et al., 2006; Jousse et al., 2011). Central endocrine changes that may occur during gestation could lead to such complications. However, the key underlying mechanisms involved in these characteristics are relatively unclear (Ravelli et al., 1999).

1.1.2.2. Maternal overnutrition

As with maternal undernutrition, overnutrition of the mother during pregnancy also influences the health of a developing fetus in later life (Sarker et al., 2019), exacerbated by offspring overnutrition (Cardenas-Perez et al., 2018). As mentioned previously, the demographic of people has an impact on the prevalence of obesity. For instance, offspring exposed to gestational diabetes in mothers of Pima Indians, have higher birthweights and a higher BMI in their adult life (Nelson et al., 1998). Obesity during pregnancy (maternal obesity), induced by maternal overnutrition, causes epigenetic changes in offspring. To illustrate, maternal overnutrition alters DNA methylation of essential developmental genes in offspring, such as upregulating Zinc-finger protein 423 (Zfp423), to progress adipogenesis. This transcription factor in turn induces peroxisome proliferator-activated receptor gamma (PPARγ) expression and commences adipocyte commitment during differentiation (Yang et al., 2013). Additionally, maternal obesity plays a role in the regulation of offspring adipogenesis and development of AT (Borengasser et al., 2013; Liang et al., 2016) via hormonal regulation. Insulin and Leptin hormone levels are elevated in obese mothers. This activates the hormones respective signalling pathways in the placenta and determines the overgrowth potential of a developing fetus (Rosario et al., 2016).

1.1.3. Metabolically Healthy Obesity and Metabolically Unhealthy Obesity

Although BMI is commonly acknowledged as a measure to determine obesity, it does not consider other factors such as muscle mass or body fat composition and distribution (Chait and den Hartigh, 2020). This classification system may falsely define obesity in certain individuals.

Humans can be defined as 'obese' based on the BMI classification system, however, they may not acquire obese-related clinical traits. These individuals are defined to have Metabolically Healthy Obesity (MHO), as opposed to those with co-morbidities, Metabolically Unhealthy Obesity (MUO). In fact, despite excess adiposity (Primeau et al., 2011), MHO is associated with the protection against obesity-related metabolic risks, with the addition of a beneficial

inflammatory profile (Stefan et al., 2009). In humans, obesity is a heterogenous disorder and there is still uncertainty on the definition and limits of parameters used to classify this disease (Liu et al., 2019). Although the mechanisms are not fully understood, factors such as visceral adipose tissue (VAT) accumulation, adipocyte size and differentiation may contribute to the development of a MUO phenotype (Primeau et al., 2011). In addition, anti-inflammatory molecules, such as Adiponectin, are often downregulated in association with fat mass expansion and obesity (Aguilar-Salinas et al., 2008), as well as other factors (Karelis et al., 2004) stated in Table 1.1.

As mentioned earlier, the deposition and distribution of fat around the body is involved in the development of obesity and acts as a predictive risk factor (Vega et al., 2006). For instance, obese men possess thicker amounts of AT around the abdominal region, whereas women are more inclined to deposit fat in the peripheral regions. These differences in metabolic profiles could be due to adipocyte number in depots around the body (Krotkiewski et al., 1983) and contribute to sex-differences involved in metabolic disorders.

Table 1.1. Metabolic characteristics in Metabolically Healthy Obesity (MHO) and Metabolically Unhealthy Obesity (MUO) in humans

	MHO	MUO
VAT content	Low	High
BMI	High	High
Fat mass	High	High
Insulin Sensitivity	High	Low
TG levels	Low	High
HDL Levels	High	Low
LDL levels	Low	High

1.2. Adipose tissue

Adipose tissue (AT) in mammals is distributed around the body. The various depots have their own distinct genetic profile, differing in functional activity depending on its cellular composition and location (Waldén et al., 2012). Stored in the form of TGs, AT is composed of a dynamic collection of adipocytes, amongst other cells including immune and vascular cells. This loose connective tissue provides a cushioning for internal organs and regulates a variety of mammalian homeostatic mechanisms including insulin sensitivity, lipid storage and hormonal control (Nawrocki and Scherer, 2004).

In mammals, AT exists in two compartments: White Adipose Tissue (WAT) and Brown Adipose Tissue (BAT). WAT is further categorised into Subcutaneous Adipose Tissue (SAT), situated under the skin, and Visceral Adipose Tissue (VAT) which surrounds internal organs (Figure 1.1). Furthermore, cells known as 'brown-in-white', abbreviated to 'brite', or 'beige', are a population of non-classical adipocytes that may reside in white depots. Based on their unique morphological (Figure 1.2), functional, and locational aspects, AT is a potential target to regulate obesity.

1.2.1. Development of adipose tissue

Different types of AT develop at specific timings and locations in mammals. In mice, the amount of fat remains relatively constant throughout adulthood (Hemmeryckx et al., 2010; Wang et al., 2013). In humans, there is a tight regulation of adipocyte number throughout adulthood, determined during childhood. Regardless of BMI, adipocytes are renewed every year in adults. This high turnover of fat cells demonstrates a route to therapeutically target obesity (Spalding et al., 2008).

Upon formation, AT responds to a variety of external and hormonal cues to perform specific roles in organisms to maintain homeostasis. Development of AT is regulated by a cascade of transcription factors that control fat production (Suh et al., 2006; Suh et al., 2007). This overlaps with the plastic and sensitive periods of gestation and lactation where maternal influences may manipulate AT expandability in offspring (Liang et al., 2016).

A. B. C.

SAT VAT BAT
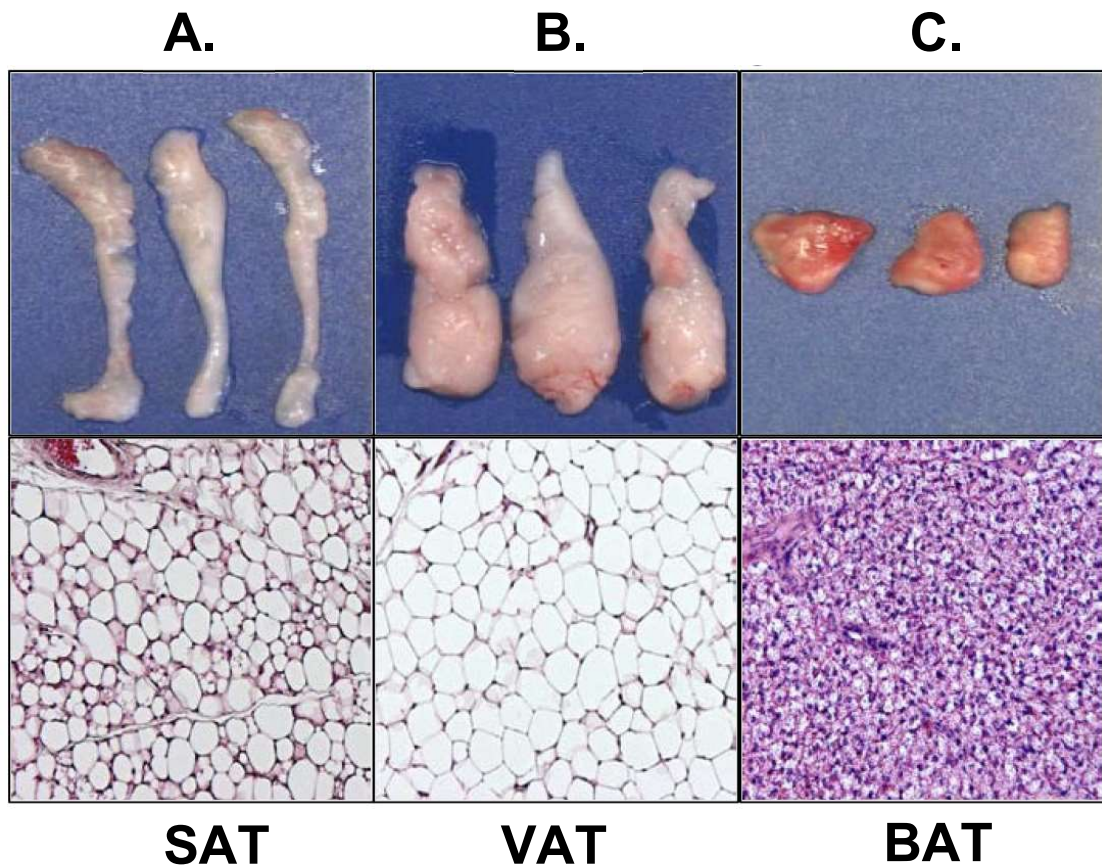
Figure 1.2. Morphology of adipose tissue in mice represented by histological sections stained with Haematoxylin and Eosin. WAT, including SAT and VAT, differ in size and heterogenicity. SAT has a collection of uni-locular and multi-locular adipocytes, whereas VAT is composed more of uni-locular adipocytes. BAT's morphology is distinctively different to WAT as it is uniformly consisted of multi-locular adipocytes. Adapted from Berry et al., (2013). WAT: White adipose tissue; SAT: Subcutaneous adipose tissue; VAT: Visceral adipose tissue; BAT: Brown adipose tissue.

Developmental progenitors are defined for adipose organogenesis, regulated by signalling pathways (Jeffery et al., 2015) and transcription factors (Wang et al., 2015) to generate adipocytes. For example, in mice, inhibition of certain pathways including Wingless-related integration site (Wnt) signalling pathway enables the activation of adipocyte differentiation (Ross et al., 2000), DNA methylation (Lim et al., 2016) and blood vessel formation (angiogenesis) (Billon et al., 2010; Han et al., 2011).

1.2.2. Adipogenesis

Although white and brown adipocytes differ in appearance (Figure 1.3) and the role they play in mammals, they arise via similar transcriptional cascades (Figure 1.4). This process is tightly regulated and results in the formation of mature lipid-laden adipocytes controlled by proteins including peroxisome proliferator-activated receptors (PPARs) and cytosine-cytosine-adenosine-adenosine-thymidine (CCAAT)/enhancer binding proteins (C/EBPs), with C/EBPα being the most abundant C/EBP (Lefterova et al., 2008). PPARγ expression is essential for the development of AT, including white and brown fat (Barak et al., 1999; Rosen et al., 1999). C/EBPα expression, on the other hand, which is required for maintaining insulin sensitivity (Kajimura, Seale and Spiegelman, 2010) and maturation (Lefterova et al., 2008) of mature adipocytes, is only essential for the development of white fat, but not brown fat (Linhart et al., 2001). Homeobox genes are also specific in their expression during white and brown adipocyte differentiation (Cantile et al., 2003). Moreover, fatty acid binding protein 4 (FABP4) is another pro-adipogenic factor needed for the differentiation of adipocytes (Shan et al., 2013; Sim et al., 2017), whilst, other C/EBPs such as C/EBPβ, are important for the initiation and progression of adipogenesis during Mitotic Clonal Expansion (MCE). This works alongside other transcription factors including PPARγ, PGC1α (Huang et al., 2011) and PR domain containing 16 (PRDM16) (Seale et al., 2008).
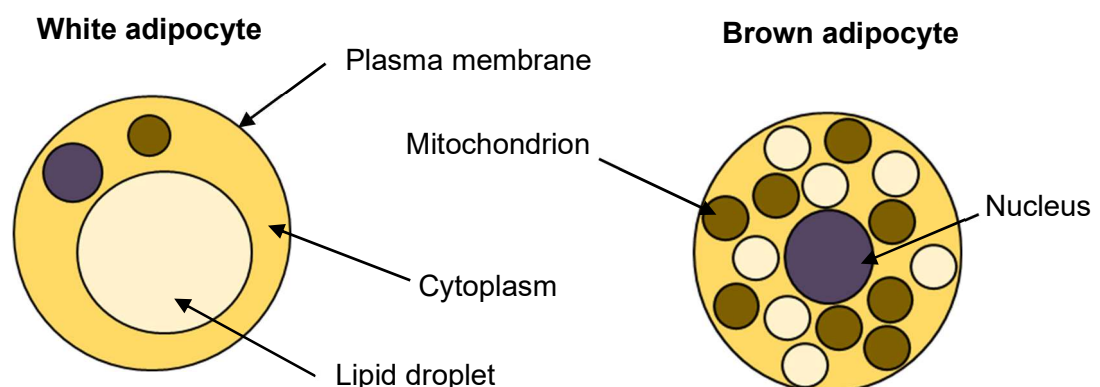
Figure 1.3. Diagrammatic representation of a mature white and brown adipocyte. White adipocytes (left) have a large uni-locular lipid droplet. Brown adipocytes (right) contain considerably more mitochondria than white adipocytes, contributing to the brown colour of the cell.

1.2.3. Mechanisms of growth

Adipose tissue (AT) grows via two mechanisms to store energy in the form of fat. This includes hypertrophy, in which the size of the cell increases, and/or hyperplasia, in which the number of cells increase. Hypertrophy as a growth mechanism in AT occurs in the early stages of AT development (Drolet et al., 2008; Spalding et al., 2008) prior to hyperplastic growth to compensate for the excessive fat storage associated with obesity (Faust et al., 1978).

WAT is heterogenous in both morphology and function. Adipocyte size within the depot plays a role in different homeostatic mechanisms and are correlated with metabolic and phenotypic parameters (Skurk et al., 2007). Abnormal lipid levels are associated with larger visceral adipocytes within VAT, whereas insulin and glucose insensitivity are linked with larger subcutaneous adipocytes within SAT (Hoffstedt et al., 2010).

The dysfunction of AT results from an imbalance between energy intake and expenditure, resulting in both the increase in cell number and volume. If insufficient in regulating lipids, these mechanisms may result in AT dysfunction (Hosogai et al., 2007), excess adiposity (Wang et al., 2013) and upregulated secretion of FFAs and inflammatory molecules in the blood stream (Weisberg et al., 2003). This state of underlying chronic inflammation disrupts physiological mechanisms, such as insulin signalling, and increases the risk of developing obesity accompanied with T2D and CVD (Balagopal et al., 2011).

Angiogenesis is the formation of blood vessels. This is an important process in physiology and is required for adipocyte differentiation (Fukumura et al., 2003). AT mass can be determined through the regulation of the vasculature (Rupnick et al., 2002). Endothelial cell and adipogenic markers increase proportionally during AT development. Studies suggest that the neo-vasculature originates by sprouting from larger, host-derived blood vessels that run parallel to peripheral nerves and a close spatial relationship between angiogenesis and adipogenesis is established (Neels, Thinnes, and Loskutoff, 2004). As angiogenesis is associated with hyperplasia in AT, this mechanism of growth is more desirable during obesity, compared to hypertrophic growth, especially in SAT compared to VAT (Rydén et al., 2014). However, dysregulated AT hypertrophy is associated with a deleterious metabolic profile in

white fat (Rydén et al., 2014; Skurk et al., 2007). This is true more so in visceral fat in individuals suffering from a cluster of risk factors including glucose intolerance and hypertension, known as metabolic syndrome (MetS) (Reaven, 1998; Hoffstedt et al., 2010).

1.3. White adipose tissue

During high-energy demands, FFAs and glycerol are metabolised by surrounding organs, such as the liver (Ahima, 2008) and white adipose tissue (WAT) acts as a storage site to regulate energy. The two subcategories of white fat, subcutaneous and visceral adipose tissue, do not arise from the same developmental origins and thus differ in their functionalities. For example, visceral adipocyte precursor cells express the Wilms' tumour (Wt1) gene, whereas subcutaneous adipocyte precursor cells do not express this gene (Chau et al., 2014). Visceral fat such as gonadal white adipose tissue (gWAT), is limited in its capacity to store lipids and contains substantially more macrophages than subcutaneous fat (Wang et al., 2013). Furthermore, their gene expression profiles are extremely varied. This is suggestive of the underlying differences that these depots play in the role of adiposity. Even between different types of VAT, such as omental and mesenteric, their genetic profile and rates of adipogenesis differ, relating to their contributions to the development of obesity. For instance, mesenteric gene expression is similar to that of SAT and shows its clinical relevance in obesity (Tchkonia et al., 2007). This expression profile and excess accumulation in visceral adipocytes is associated with metabolic dysfunction and obesity-linked complications (Spalding et al., 2008). On the other hand, subcutaneous adipose tissue (SAT), which accounts for almost 80% of AT in the human body, is a beneficial depot as it buffers against lipid accumulation (lipotoxicity) (Spalding et al., 2008) and expansion of this depot counteracts insulin resistance associated with obesity (Kim et al., 2007).

1.3.1. Development of white adipose tissue

In many species, the formation of WAT begins during pregnancy, prior to birth, (Desnoyers et al., 1977; Poissonnet et al., 1983; Poissonnet et al., 1984) and rapidly expands upon exposure

to a high-fat (HF)-diet (Faust et al., 1978; Miller, Faust and Hirsch, 1984). In both humans and rodent models, AT has the ability to expand during later life (Spalding et al., 2008). However, expansion usually ends at adolescence, with humans turning over around 10% of new fat cells each year, whereas mice turnover 0.6% of new adipocytes each day (Rigamonti et al., 2011; Spalding et al., 2008). It is now recognised that new adipocytes can develop from adipocyte precursors throughout life, as demonstrated by differentiating precursor cells to mature adipocytes, *in vitro*, isolated from adult white depots (Hauner et al., 1989).

In mammals, development of AT begins *in utero* and continues throughout life, even during adulthood (Spalding et al., 2008). Current understanding of AT development is still fairly limited as adipocytes are dispersed around the body in various locations. In humans, AT formation occurs in the second trimester of pregnancy (between 14 and 23 weeks). Fetal development is a sensitive period. This period may be prone to nutritional disturbances which could lead to an offspring developing metabolic complications in later life. The formation and proliferation of AT commences between the 14th and 16th week of fetal development, closely associated with angiogenesis. Between the 23rd to 29th week of embryonic development, AT grows mainly by an increase in size (hypertrophy), with the number of cells remaining constant after this period (Poissonnet et al., 1983; Poissonnet et al., 1984).

In rodents, AT development occurs during the final stages of gestation, with an extremely high proliferative phase after birth, for 4 weeks, with markedly less proliferation until puberty (Greenwood and Hirsch, 1974). In mice, a system known as the 'AdipoChaser' has been developed to observe the presence of adipocytes already established and recently formed. This revealed that SAT formation occurs during the early stages of embryogenesis (days 14 to 18). Expression of pro-adipogenic markers including FABP4, PPARγ and C/EBPα in adipocytes occur in the late gestation period to early postnatal period (embryonic day 17.5 to postnatal day 0). Lipid droplets appear on postnatal day 1 (Han et al., 2011) with a unilocular appearance on postnatal day 5 (Birsoy et al., 2011). There is rapid lipid accumulation between day 5 and day 10, postnatally (Kozak et al., 2010), with maturation of white adipocytes occurring primarily in postnatal life, in mice (Han et al., 2011). Visceral adipocytes such as

epididymal adipocytes also develop postnatally (Wang et al., 2013). This concurs with evidence demonstrating that there are no precursor cells in epididymal fat that possess adipogenic capacity until postnatal day 4, in mice (Han et al., 2011).

1.3.2. Endocrine activity

White fat is hormonally active, responds to various stimuli and secretes adipose tissue-specific cytokines, known as adipokines. WAT's role as an endocrine organ is important in the progression of obesity. As an inflammatory disease (Kershaw and Flier, 2004), obesity is characterised by increased hypertrophy and hyperplasia of adipocytes, as well as, infiltration of inflammatory cells and elevation of cytokines in VAT (Samaras et al., 2010; Spranger et al., 2003). This pro-inflammatory state increases the risk of an individual suffering from CV-related and T2D-related events, such as myocardial infarction (MI) (Ridker et al., 2000b) and hyperinsulinemia (Xu et al., 2003), respectively.

1.3.3. Leptin

Leptin, known as the 'satiety' hormone, is secreted from adipocytes, more so from subcutaneous than visceral adipocytes (Van Harmelen et al., 1998). This hormone acts on the hypothalamus to regulate appetite, body weight (Pelleymounter et al., 1995) and insulin sensitivity (Kulkarni et al., 1997) by acting on pancreatic cells via the sympathetic nervous system (SNS) (Park et al., 2010).

Leptin activates the AMPK pathway (Minokoshi et al., 2002). Stimulation regulates glucose metabolism to increase glucose uptake in skeletal muscle and BAT in mice (Kamohara et al., 1997). Leptin gene (ob gene) mutations (Zhang et al., 1995) and dysfunctional Leptin activity causes hyperphagia (irregular increase in eating), insulin resistance and obesity (Friedman, 2011), even on a non-high-fat diet (Rausch et al., 2008) in mice. Elevated Leptin levels from WAT in obese mice (Hosogai et al., 2007) and humans (Considine et al., 1996) are directly proportional with adipocyte size (Skurk et al., 2007) and BMI (Hamilton et al., 1995).
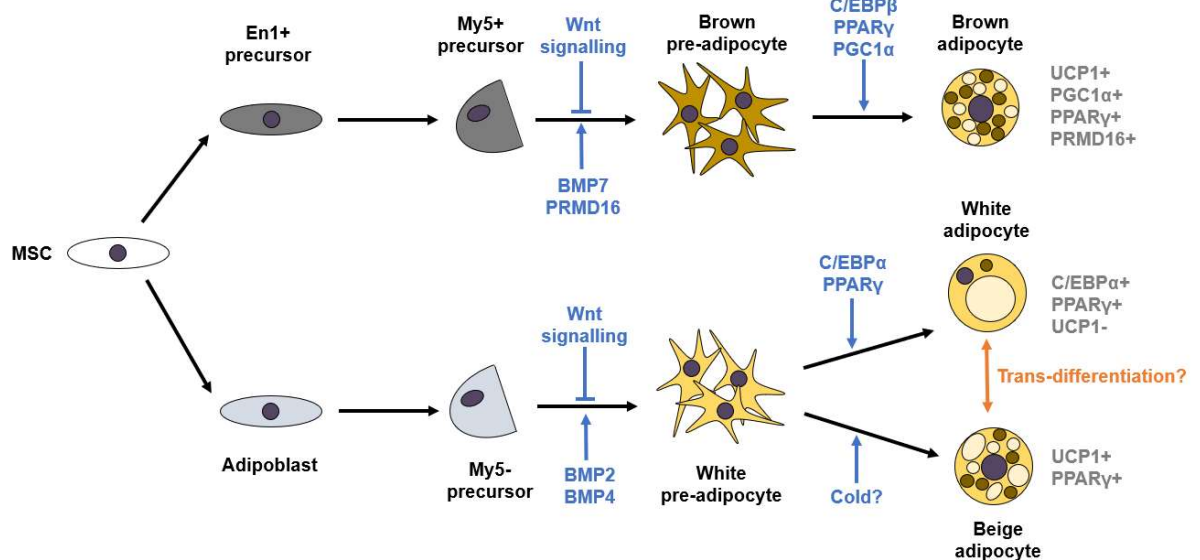
Figure 1.4. **White, brown, and beige adipocyte differentiation.** Adipogenesis is controlled by several positive and negative regulators, some of which are presented in the diagram. White and brown adipocytes, which arise via different developmental origins, share a similar transcriptional cascade of C/EBPs and PPARs for the progression of differentiation. Mesenchymal Stem Cells (MSCs) are either committed to the myogenic cell line from myogenic factor 5 negative (Myf5-) or positive cells (Myf5+). The definitive mechanisms of how beige cells arise are still unclear, but they may acquire certain phenotypic traits from other cells (trans-differentiation) or by stimuli such as cold exposure, beta-adrenergic or PPARγ agonists. The latter stimuli also activates brown adipocytes. +: positive; -: negative; MSC: Mesenchymal Stem Cell; En1: Engrailed 1; Myf5: Myogenic factor 5; Wnt: Wingless-related integration site; BMP: Bone Morphogenetic Protein; C/EBPα/β: CCAAT (cytosine-cytosine-adenosine-adenosine-thymidine) Enhancer Binding Protein alpha/beta; PPARγ: Peroxisome proliferator-activated receptor gamma; PGC1α: Peroxisome proliferator-activated receptor gamma coactivator 1 alpha; PRDM16: PR domain containing 16; UCP1: Uncoupling protein 1. Adapted from Kajimura, Seale and Spiegelman (2010); Park, Kim and Bae (2014); Brestoff and Artis (2015).

This establishes that Leptin plays a vital role in pathogenesis and that obesity in humans is progressed by an imbalance of food intake and energy expenditure (Considine et al., 1996). Weight gained due to the malfunction of Leptin activity can be reversed via Leptin replacement therapy. In humans, therapy increases weight loss, reduces energy intake with a reduction in hyperphagia (Farooqi et al., 2002), improves glycaemic control and reduces TG levels (Oral et al., 2002), with a reversal of an obese phenotype observed in mice (Friedman, 2011).

1.3.4. Adiponectin

As with Leptin, Adiponectin is a true endocrine factor (Chait and den Hartigh, 2020). This hormone encoded by the gene AdipoQ is a potential anti-inflammatory and anti-atherogenic molecule, with levels inversely proportional to insulin resistance (Ouchi and Walsh, 2009). Expression is specific to AT and is reduced in mature adipocytes of obese mice and humans (Hu, Liang and Spiegelman, 1996). Low levels of Adiponectin (hypoadiponectinemia) is associated with adiposity (Kazumi et al., 2004), especially in VAT (Yatagai et al., 2003), and insulin resistance, via a reduction of TG levels in the muscle and liver, in mice (Yamauchi et al., 2001) and humans (Weyer et al., 2001). Adiponectin expression may be manipulated by circulating cytokines including TNFα. This activates the c-Jun N-terminal Kinase (JNK) pathway in adipocytes, causing inhibition of Adiponectin expression (Kim et al., 2005). Adiponectin replacement therapy may provide an insight into treatment of T2D (Yamauchi et al., 2001) to upregulate expression and improve a diabetic phenotype in obesity (Kim et al., 2007).

1.4. Brown adipose tissue

In humans, brown adipose tissue (BAT) is distributed in the supraclavicular and paraspinal regions (Figure 1.1). This is observed by the uptake of positron emitting radiotracer 2-deoxyglucose (2-DG) when an individual is exposed to a cold environment (Saito et al.,2009; Virtanen et al., 2009). Rodents possess similar fat depots topologically to humans, as confirmed by histological (Figure 1.2) and gene expression analysis, especially upon cold

exposure (Zhang et al., 2018). As mentioned previously, white adipocytes are highly active and produce adipokines. Although there is little known about adipokines secreted from brown adipocytes (batokines), there are cases in which they exist. For instance, in BAT, Slit homolog 2 (Slit2) protein is a recently discovered batokine which has been shown to improve glucose homeostasis in mice and is reduced in diabetic humans (Kang et al., 2017a). However, the contribution that batokines play in metabolic health may be insignificant compared to other depots. Regulators of mitochondrial function pose more relevance to BAT activity and act as thermogenic and lipolytic markers. Although recognised as a thermogenic organ, BAT plays a role in regulating glucose homeostasis, reducing fat mass and body weight (Stanford et al., 2013). Recently there has been a shift in research towards the presence of this organ and its therapeutic potential in humans for obesity research (Cypess, 2009; Saito et al., 2009; Virtanen and Al., 2009).

1.4.1. Development of brown adipose tissue

Brown adipocytes arise from the dermomyotome, sharing a developmental lineage to muscle cells (Atit et al., 2006). Engrailed 1 (En1) positive cells (Atit et al., 2006) and Paired boxed protein 7 (Pax7) precursors give rise to brown adipocytes at day 9.5, *in utero* (Lepper and Fan, 2010). Furthermore, morphogens such as bone morphogenetic protein 7 (BMP7) are essential for brown adipocyte differentiation (Tseng et al., 2008) (Figure 1.4).

In humans, BAT deposition happens concurrently within the shoulder and thoracic regions of the fetus, alongside WAT from the 14th week of gestation (Poissonnet et al., 1984). In rodents, interscapular BAT (iBAT) develops during the last stages of embryogenesis at day 15 of gestation. Brown fat becomes more morphologically identifiable at day 17 *in utero* (Nnodim and Lever, 1985) and transcriptionally relevant at day 18 *in utero* until after birth, with an increase in UCP1 expression (Giralt et al., 1990). This expression remains stable (Xue et al., 2007) until stimulation upon cold exposure (Rosenwald et al., 2013).

Similar to rodents, Type II iodothyronine deiodinase (DIO2) activity in iBAT occurs early in human development in neonates (Houstěk et al., 1993). iBAT in humans is situated in the neck

region. This depot shows similarities to that of rodent iBAT with high expression levels of thermogenic and mitochondrial genes including DIO2, UCP1 and PGC1α (Cypess et al., 2015). The functional relevance of brown fat in healthy humans remains unclear, but there seems to be a resemblance of BAT activity in humans and rodents.

1.4.2. Regulators of mitochondrial biogenesis

Type II iodothyronine deiodinase (DIO2) is a thyroid hormone that is stimulated by adrenergic control and cold exposure (Silva and Larsen, 1983) to regulate thermogenesis (De Jesus et al., 2001). DIO2 catalyses the conversion of thyroxine (T4) to triiodothyronine (T3), a more potent and active form of the thyroid hormone. This conversion results in the increase of gene and protein synthesis of uncoupling protein 1 (UCP1) (Bianco and Silva, 1987), a thermogenin housed in brown adipocytes. UCP1 facilitates the proton leakage from the inner mitochondrial membrane to its matrix, allowing the release of energy in the form of heat, known as adaptive thermogenesis, in which uncoupled respiration occurs (Figure 1.5) (Bastías-Pérez et al., 2020).

UCP1 is the main regulator of mitochondrial activity in BAT. However, there are other transcriptional regulators that play vital roles in BAT function and act as potential therapeutic targets. Peroxisome proliferator-activated receptor gamma coactivator 1 alpha (PGC1α) is a transcriptional regulator (Wu et al., 1999). Expression of PGC1α plays an important role in thermogenesis, mitochondrial biogenesis (Uldry et al., 2006) and glucose metabolism (Kleiner et al., 2012) in BAT (Virtanen and Al., 2009). When activated upon cold stimuli, PGC1α initiates other genes such as peroxisome proliferator-activated receptor gamma (PPARγ) and UCP1 in brown fat (Puigserver et al., 1998).

Cytochrome C Oxidase (COX) is the final component in the Electron Transport Chain (ETC) in mitochondria. This catalyses electron movement from reduced cytochrome c to oxygen (Fabrizil et al., 1989; Mitchell, 2011). Upon cold exposure, Cytochrome C Oxidase Subunit VIIa Polypeptide 1 (COX7A1) and Cytochrome C Oxidase Subunit VIIIb Polypeptide (COX8B) are upregulated in BAT and are involved in oxidative phosphorylation (Cummings et al., 2014; Maurer et al., 2015).

1.4.3. Thermogenic activity

In response to external stimuli, the primary role of BAT is to regulate whole-body energy expenditure (Cannon and Nedergaard, 2004) by generating heat (thermogenesis). Thermogenesis is activated to maintain normal body temperature in hibernating and new-born animals (Obregón et al., 1996). This occurs primarily in new-born humans (Cannon and Nedergaard, 2004), rather than in adults, as brown fat regresses throughout adulthood (Lean, 1989). Thermogenesis acts to protect against cold exposure (Lowell and Spiegelman, 2000; Monemdjou, Kozak and Harper, 1999) and is regulated by shivering. However, shivering gradually subsides and non-shivering thermogenesis (adaptive thermogenesis) is initiated (Davis et al., 1960; Davis, 1961).

1.4.3.1. Diet-induced thermogenesis

Diet-induced thermogenesis (DIT) is classified as an increase in energy expenditure over basal fasting levelss and divided by the energy content in food consumed, presented as a percentage (Westerterp, 2004). DIT is defined into two compartments. This includes the obligatory compartment, consisting of heat generated by processes such as absorption and digestion, and the facultative compartment, consisting of heat generated by the dissipation of food energy (Van Marken Lichtenbelt and Schrauwen, 2011).

Diet can influence the facultative component of DIT, by stimulating the SNS, whilst fasting suppresses the SNS (Young and Landsberg, 1977; Young and Landsberg,1997). In humans, DIT during obesity is reduced (Granata and Brandon, 2002), but increased in healthy individuals with high BAT activity (Hibi et al., 2016). On the contrary, results differ based on experimental model and a consensus about DIT in metabolic health has not been achieved (Westerterp, 2004).

1.4.4. Lipolysis

Lipolysis is the breakdown of triglycerides (TGs) into glycerol and free fatty acids (FFAs). TGs are located in adipocyte stores and each lipolytic step in the pathway results in the removal of

a fatty acid (Frühbeck et al., 2014). There are three main mammalian lipases that catalyse this reaction; Adipose TG Lipase (ATGL), Hormone-Sensitive Lipase (HSL) and Monoglyceride Lipase (MGL) (Nielsen et al., 2014) (Figure 1.6).

In white adipocytes, lipolysis is activated to generate FFAs and glycerol to fuel other tissues, whereas, lipolysis in brown adipocytes regulate adaptive thermogenesis (Zhu et al., 2019). In response to cold exposure, brown adipocytes are activated via SNS innervation. β-adrenergic receptors, including ADRβ3 on the surface of brown cells (Bronnikov et al., 1999), are stimulated by the hormone noradrenaline (NA). NA activates adrenergic signalling and induces the breakdown of TGs. This process is known as lipolysis (Figure 1.6). During lipolysis in brown adipocytes, FFAs are released and activate UCP1, acting as an energy source for thermogenesis (Figure 1.5). Following this, UCP1 uncouples the electromotive force from ATP synthesis via ATP synthase and generates heat (Fedorenko, Lishko and Kirichok, 2012; Lidell, Betz and Enerbäck, 2014). Adrenergic mediation in thermogenic events involves the increase of cyclic adenosine 3' 5' monophosphate (cAMP), which stimulates Protein Kinase A (PKA) and phosphorylates perilipin and lipases in the lipolytic pathway (Uldry et al., 2006; Zhao et al., 1997).

1.5. Beige adipocytes

Distributed amongst certain white depots are cells that morphologically and phenotypically resemble both brown and white adipocytes. These are known as brown-in-white ('brite') or beige cells (Figure 1.7). They have thermogenic properties and express brown-like markers when exposed to certain stimuli (Shabalina et al., 2013; Waldén et al., 2012).

Beige adipocytes differ in location and the role they play in metabolic health compared to other classical adipose depots (Chait and den Hartigh, 2020). In rodents, brown-like adipocytes are evident to reside in WAT (Cousin et al., 1992; Zhang et al., 2018) such as SAT including, inguinal white adipose tissue (iWAT). They are multi-locular (Figure 1.7) and express brown adipocyte-related markers such as UCP1, PGC1α (Wu et al., 2012), COX7A1 (Rosenwald et al., 2013) and COX8B (Garcia, Roemmich and Claycombe, 2016). Increased expression of

such markers in WAT of mice may reduce the progression of adverse obesity (Kopecky et al., 1995) and suggests a greater capacity for adipose tissue plasticity between a brown and white phenotype (Cousin et al., 1992).
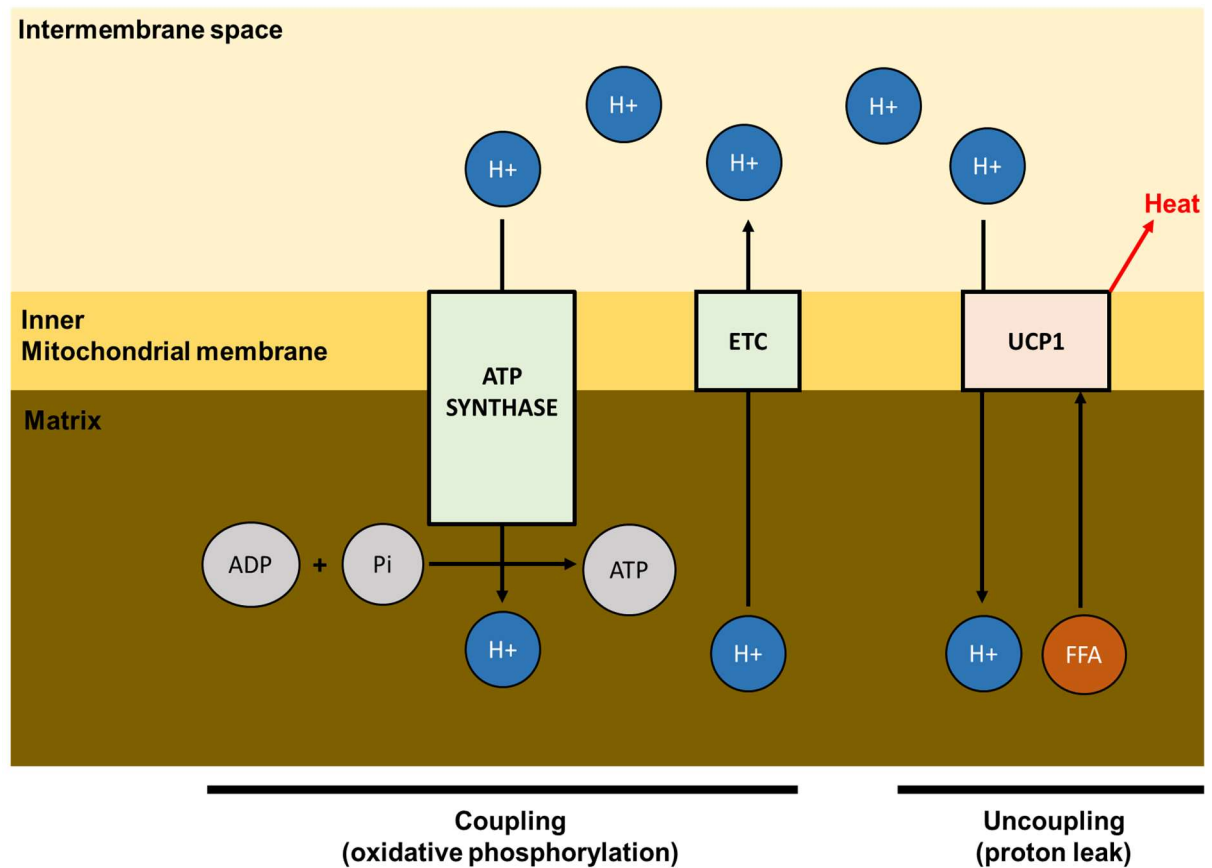
Figure 1.5. Adaptive thermogenesis in mitochondrion of brown adipocytes. Brown adipocytes can generate heat production and increase energy expenditure via uncoupling of oxidative phosphorylation from ATP generation, facilitated by UCP1, acting as a H+ channel. The electrochemical gradient is produced via the ETC (Fedorenko, Lishko and Kirichok, 2012; Lidell, Betz and Enerbäck, 2014). H+: Hydrogen ions; ETC: Electron Transport Chain; UCP1: Uncoupling Protein 1; ADP: Adenosine diphosphate; Pi: Inorganic Phosphate; ATP: Adenosine triphosphate; FFA: Free Fatty Acid.

Under non-stimulatory conditions, these cells resemble white adipocytes, in which they have low levels of basal UCP1 expression. However, beige cells, like brown adipocytes, respond to stimuli such as cAMP (Wu et al., 2012), cold exposure or adrenergic stimulation (Zhang et al.,

2018). They express high levels of UCP1 upon activation (Wu et al., 2012), almost comparable to that observed in brown adipocytes (Zhang et al., 2018) in rodents.

In humans, a population of UCP1+ cells, which resemble recruitable beige adipocytes, are present in the neck region of human adults (Jespersen et al., 2013). These UCP1+ cells resemble those found in mice, rather than classical brown adipocytes. Unlike rodents, visceral white adipocytes in humans are more susceptible to browning than subcutaneous fat (Zuriaga et al., 2017) and suggests the identity of beige-like characterised cells (Shinoda et al., 2015).
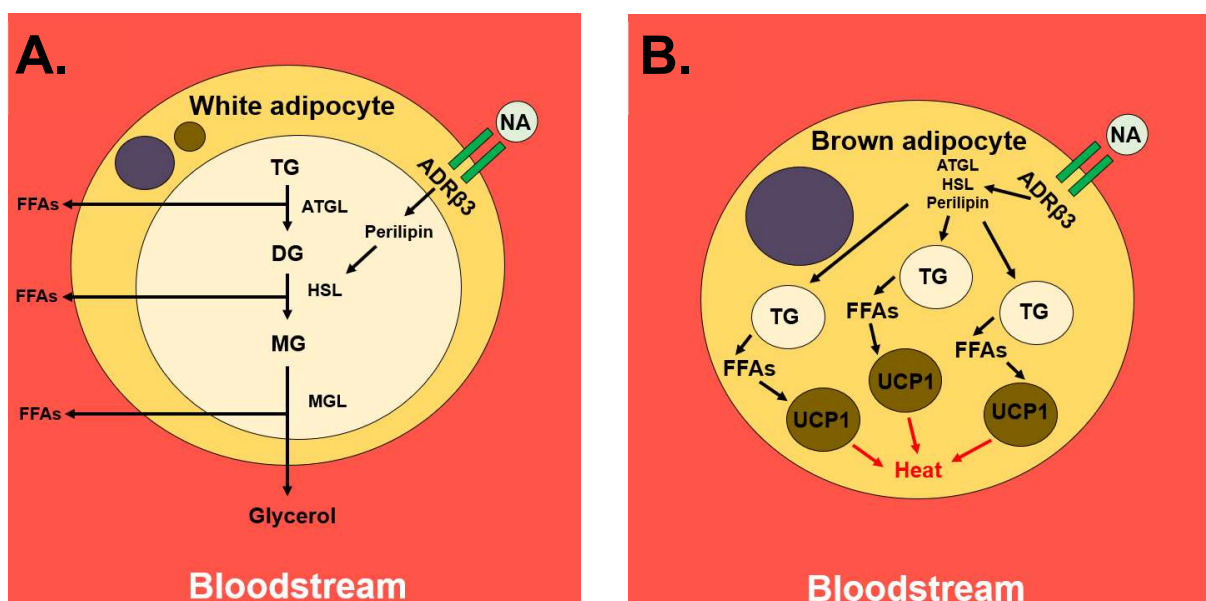
Figure 1.6. **Diagrammatic representation of the lipolytic pathway in white and brown adipocytes by sympathetic innervation.** In white adipocytes **(A)**, sympathetic activation results in a cascade of the lipolytic pathway to convert TGs to FFAs and glycerol as fuel to be utilised by other tissues. In brown adipocytes **(B)**, sympathetic innervation regulates adaptive thermogenesis, including DIT and cold-induced thermogenesis (CIT). UCP1 in mitochondria is activated by FFAs, carried by FABP4 to the mitochondria, released by lipolysis into energy in the form of heat (Zhu et al., 2019). NA: Noradrenaline; ADRβ3: Adrenergic receptor beta 3; TG: Triacylglycerol; DG: Diacylglycerol; MG: Monoglyceride; ATGL: Adipose triglyceride lipase; HSL: Hormone-sensitive lipase; MGL: Monoglyceride lipase; FFAs: Free Fatty Acids; UCP1: Uncoupling Protein 1.
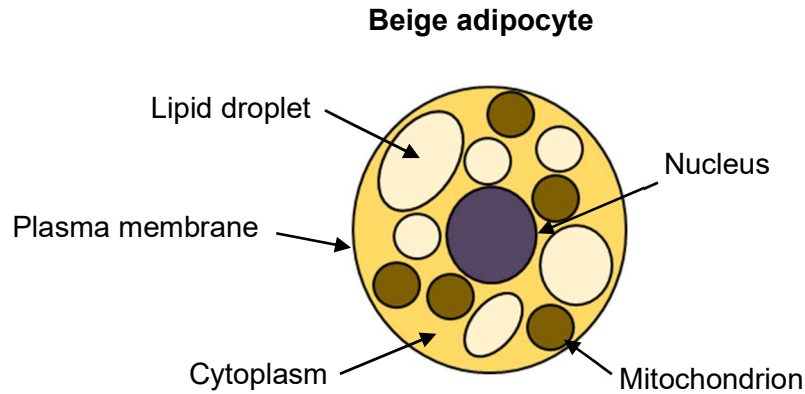
Beige adipocyte

Figure 1.7. Diagrammatic representation of a mature beige adipocyte. Beige adipocytes dispersed within WAT have a combination of smaller and larger lipid droplets and a vast number of mitochondria, contributing to its unique characteristics. WAT: White Adipose Tissue.

1.5.1. Development of beige adipocytes

Brown adipocyte-related markers (Wu et al., 2012; Rosenwald et al., 2013; Garcia, Roemmich and Claycombe, 2016) are optimal for determining the process of 'browning' in white fat (Garcia, Roemmich and Claycombe, 2016). 'Browning' is the process in which white adipocytes acquire a brown-like phenotype and genotype regulated by various cues. In mice, white-like cells express UCP1, appearing between 10 and 30 days of age after birth (Xue et al., 2007). It is still unclear how beige adipocytes arise; however, two processes have been documented to occur. When exposed to cold or adrenergic stimulation, mediated by ADRβ3, beige cells (unilocular in their basal state) undergo 'trans-differentiation' of the phenotype (Wu et al., 2012). This includes the conversion of white adipocytes into mitochondrial-laden, UCP1+ cells (Barbatelli et al., 2010). Managing this shift from a white to beige phenotype may provide an insight into tackling obesity via increased energy expenditure (Rosenwald et al., 2013). On the other hand, beige cells may also arise via '*de novo* differentiation' or 'adipogenesis' from a resident precursor (Wang et al., 2013), resulting in browning of the white depot (Figure 1.4). Previous research demonstrated that Myogenic factor 5 (Myf5) was expressed in precursor cells of the myogenic lineage and that PRDM16 controlled the bidirectional switch between muscle and brown adipocytes (Seale et al., 2008). However, recent studies have reported that white and brown adipocytes may share common progenitor cells. A subgroup of white

adipocytes has been observed to derive from cells expressing Myf5 (Sanchez-Gurmaches et al., 2012) and platelet-derived growth factor receptor alpha (PDGFRα). This is associated with brown adipocytes residing in white depots (Lee et al., 2012). Although WAT browning is considered beneficial in rodents (Seale et al., 2011; Shao et al., 2016), the weight loss results may not be permanent. The effects upon cold stimulation can be rapidly reversed and stimulation by adrenergic effects may promote adverse CV-events (Chait and den Hartigh, 2020).

1.6. Ectopic adipose tissue deposition

The increased prevalence of obesity and associations with CVD have led to a strong interest in understanding 'the obesity paradox.' In some cohort studies, evidence suggests obesity occupies a protective role in individuals who have suffered from detrimental CV-related events (Horwich et al., 2001). However, protection may only protect against short-term mortality risks after a cardiac infarction. The long-term mortality risks are comparable to that of normal-weighted individuals (Nigam et al., 2006). There is a suggestive 'U-shaped' relationship with the association of obesity and risk of CVD (Kapoor and Heidenreich, 2010; Sun et al., 2020; Wang et al., 2020), in which mortality is greatest at both extreme ends of the BMI scale.

Undesirable accumulation of fat in non-adipose tissue organs, such as the heart, may play a role in the initiation of CV-related events in diabetes (Iozzo et al., 2009). Ectopic fat deposition associated with the heart releases significant amounts of fatty acids and pro-inflammatory cytokines. This ectopic fat deposition elicits local effects into the circulatory system of the heart and induces the progression of CVD (Barandier, Montani and Yang, 2005; Henrichot et al., 2005; Yudkin et al., 2005; Kankaanpää et al., 2006; Mahabadi et al., 2009; Hirata et al., 2011; Horckmans et al., 2018) and insulin resistance (Iacobellis and Leonetti, 2005). Furthermore, ectopic AT accumulation associated with the myocardium, somewhat related to VAT adiposity, in animals (Zhou et al., 2000) and humans (Szczepaniak et al., 2007), is associated with myocardium dysfunction. Pericardial adipose tissue (PAT), associated with the heart, has been linked with an increased risk of CVD (Ding et al., 2009; Rosito et al., 2008). Visceral

adiposity appears to be mainly associated with metabolic syndrome (MetS) (Reaven, 1998) and exhibits systemic inflammation (Wu et al., 2016). On the other hand, ectopic AT deposition around the heart has a more local effect and is associated with coronary artery disease (CAD) (Wu et al., 2016), increased atrial size (Fox et al., 2009) and atrial fibrillation (Thanassoulis et al., 2010). The fact that PAT volume is associated with the local effects on the heart, unlike VAT, indicates the importance of AT deposition and the role that PAT may play in CV health.

1.6.1. Adipose tissue in proximity with the heart

There are two distinct adipose depots in proximity to the heart. These are known as pericardial adipose tissue (PAT) and epicardial adipose tissue (EAT) (Figure 1.8), which are linked with metabolic complications in humans.

The distribution and location of EAT relates to its physiology and the role it plays in pathology (Wu et al., 2017). EAT may act to buffer against lipotoxicity as it has a local energy storage capacity for cardiac muscle (Marchington and Pond, 1990). In human disease, EAT accumulation is associated with a higher turnover of FFA release and uptake, compared to other AT (Pezeshkian et al., 2009), and increased risk of atherosclerotic development (Mohammadzadeh et al., 2018).

Although, researchers have previously established that mice do not possess EAT, recent studies have demonstrated a cardiac depot that may resemble EAT in mice, located in the atrial-ventricular groove. As EAT is relatively small, PAT is more abundant and commonly used to study AT in proximity to the heart, for translational studies in human disease (Liu et al., 2014; Yamaguchi et al., 2015). Like visceral white fat, excess PAT accumulation is associated with pro-inflammation (Greif et al., 2009; Ong et al., 2015), low Adiponectin levels (Greif et al., 2009) and increased risk of atherosclerosis (Greif et al., 2009; Rodriguez-Granillo et al., 2018), CVD and obesity (Aslanabadi et al., 2014; Ding et al., 2009; Liu et al., 2010; Mahabadi et al., 2009).

1.7. Pericardial adipose tissue

The pericardium is divided into a parietal and visceral pericardium, with the latter also referred to as the epicardium. Serous fluid within the pericardial cavity, between the parietal and visceral pericardium, protects the heart and acts as a lubricant (Rodriguez and Tan, 2017). PAT resides externally of the parietal pericardium, whereas EAT, is located between the heart muscle (myocardium) and visceral pericardium (Figure 1.8). In this thesis, the following definition stated and referenced by Al-Dibouni et al., (2020), will be used when discussing PAT and EAT.

Studies from rodents (Wu et al., 2012) and humans (Cheung et al., 2013; Guauque-Olarte et al., 2011; Sacks et al., 2013) have identified through gene expression analysis that AT associated with the cardiac and vascular system have both white and brown fat-like features. In adult humans, EAT has the gross appearance of a white-like adipose depot (Sacks et al., 2009) but has histological and genetic patterns that resemble 'beige' cells (Chechi et al., 2019). EAT UCP1 expression levels (Chechi et al., 2019) are correlated with BMI (Sacks et al., 2009) and lipid metabolism (Chechi et al., 2013), yet EAT has a higher inflammatory profile than subcutaneous fat (McAninch et al., 2015). As EAT has both a thermogenic and visceral profile, this demonstrates the possibility of trans-differentiation from brown-to-white adipose tissue and vice versa (Sacks et al., 2013). The trans-differentiation of brown-to-white adipocytes is known as 'whitening.' It is associated with inflammation (McAninch et al., 2015; Kotzbeck et al., 2018), impaired glucose metabolism (Shimizu et al., 2014), inhibited thermogenesis (Miranda et al., 2020) and increased levels of reactive oxygen species (ROS) (Dozio et al., 2014). As 'browning' of white depots is beneficial (Okamatsu-Ogura et al., 2013; Shabalina et al., 2013), targeting brown and beige adipocytes in cardiac depots could induce a beneficial thermogenic profile that is lacking in obesity.

1.7.1. Development of pericardial adipose tissue

The terms pericardial and epicardial fat have been used interchangeably throughout research, due to the complication of dissection for surgery and imaging (Greif et al., 2009). However,

PAT and EAT have different embryonic origins and blood supply systems. PAT originates from ectodermal cells, like SAT, with blood supplied from thoracic vessels. On the other hand, EAT, like VAT, originates from mesodermal cells, with a blood supply from myocardial coronary arteries (Nagy et al., 2017).
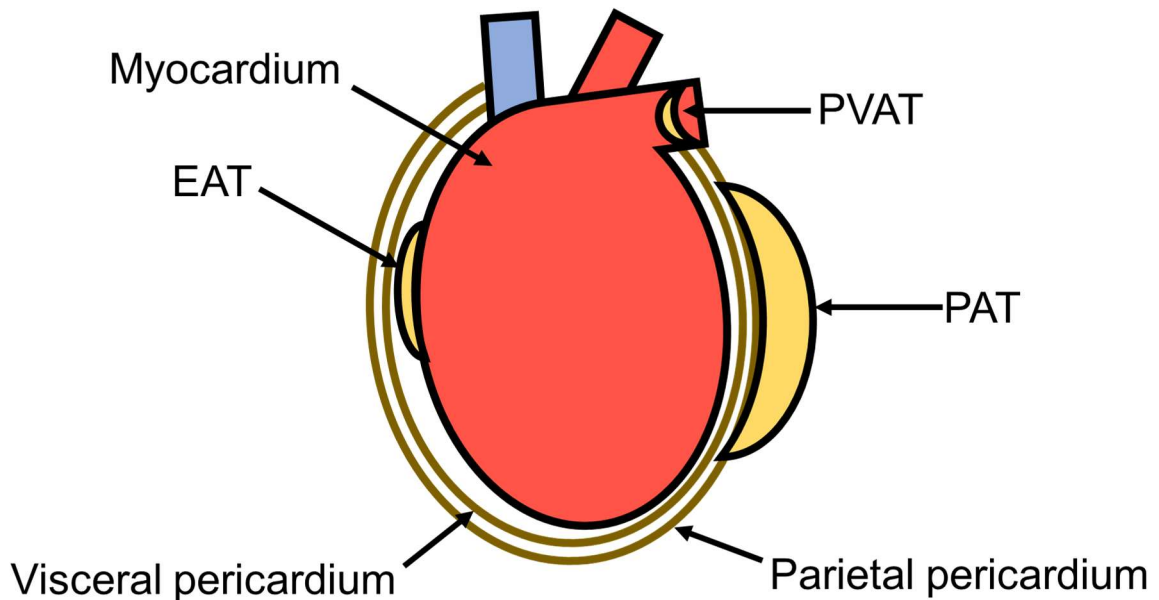
Figure 1.8. Diagrammatic representation of the Heart and associated adipose tissue. EAT is situated between the myocardium and inner layer of the pericardium, whereas PAT is located anterior to the pericardium. EAT is not present in the hearts of rodents but is present in the heart of humans. PVAT: Perivascular adipose tissue; PAT: Pericardial Adipose Tissue; EAT: Epicardial adipose tissue. Adapted from Al-Dibouni *et al.*, (2020).

1.8. Interventions to improve metabolic health

To improve metabolic health in overweight or obese individuals, it is important to lose excess weight (Borges et al., 2019). This may be achieved by managing dietary intake, increasing levels of physical activity, surgery or by therapeutic means (Barrow et al., 2019). During weight loss, chronic inflammation and large dysfunctional cells associated with excess adiposity become reduced (Salans et al., 1968). In addition, insulin sensitivity improves (Ziccardi et al., 2002), TG levels decline (Ryan et al., 2014) and the risk of CVD decreases (Borges et al., 2019), presumably due to reduced macrophage infiltration in AT (Bruun et al., 2006).

Although surgery, such as bariatric surgery, can attenuate macrophage infiltration in AT associated with the heart (Aghamohammadzadeh et al., 2013) and pro-inflammation, diet and exercise are the most desirable forms of managing weight loss. However, for some, these are not viable modes of weight loss action. Alternatively, pharmaceutical compounds are another route that may be taken and are less invasive than surgical interventions. Currently, anti-obesity drugs on the market, such as orlistat, promote weight loss by reducing food intake. However, as with most drugs, beneficial outcomes are accompanied by severe adverse effects, such as gastrointestinal discomfort (Bray and Tartaglia, 2000; Montan et al., 2019). To this end, it is important to investigate potential therapeutic agents that induce weight loss and reduce other health implications, whilst safe for human intake.

1.8.1. Exercise and caloric restriction

Mitochondrial dysfunction is a characteristic in diabetes but can be simply improved by exercise and caloric restriction. In addition to weight loss, exercise improves adiposity and insulin sensitivity via enhanced mitochondrial biogenesis and increased density of mitochondria within skeletal muscles of diabetic individuals (Toledo et al., 2007). Exercise (Jäger et al., 2007) and caloric restriction (Civitarese et al., 2007) is known to activate AMPK, which induces PGC1α phosphorylation and initiates mitochondrial biogenesis (Jäger et al., 2007).

1.8.2. Pharmacological intervention

As obesity is a heterogeneous disorder, many physiological functions may become dysregulated and act as potential therapeutic targets. These include mitochondria, AT and metabolic pathways to counteract obesity and related diseases. Although beneficial, these compounds may be accompanied by side effects such as gastro-intestinal discomfort, have a short half-life and specific doses may give varied outcomes.

1.8.2.1. AMPK pathway

5' adenosine monophosphate-activated protein kinase (AMPK) is the principal energy sensor of the cell and is a promising target for obesity treatment. The compound Resveratrol (RSV) mediates an increase in AMPK and PGC1α activity. RSV can improve mitochondrial function and protect against obesity, insulin resistance and cardiac dysfunction (Baur et al., 2006; Lagouge et al., 2006; Rivera et al., 2009; Thandapilly et al., 2010; Rimbaud et al., 2011). Anti-diabetes drugs also work via the AMPK pathway. Metformin is a first line drug for regulating insulin resistance. This biguanide reduces FFA concentrations and glucose production by reducing gluconeogenesis in diabetic patients (Galuska et al., 1994; Hundal et al., 2000), via an AMPK mediated process (Zhou et al., 2001). Furthermore, Metformin also exerts effects to provide cardio-protection after CV-related events (Sasaki et al., 2009; Yin et al., 2011), potentially by promoting mitochondrial function (Gundewar et al., 2009). Thiazolidinediones (TZDs) or glitazones are anti-diabetic compounds that have a high affinity for PPARγ and work via AMPK-mediated mechanisms (Konrad et al., 2005). These compounds can reduce hypertension and oxidative stress (Dobrian et al., 2004), perhaps by activating PPARγ in macrophages and preventing the release of reactive oxygen species (ROS) (von Knethen and Brüne, 2002) to improve the overall metabolic profile in obesity (Pickavance et al., 1999).

1.8.2.2. Inflammatory response pathway

Obesity is characterised by chronic inflammation. Targeting the inflammatory pathway is another route that may be taken to target this disease. Increased levels of TNFα are associated with obesity and the development of insulin resistance in T2D. Interfering with the TNFα signalling pathway improves insulin sensitivity (Stagakis et al., 2012) and fasting glucose levels (Stanley et al., 2011) in inflammatory-related diseases. TZDs as a therapeutic agent disrupt TNFα from interfering with insulin signalling (Peraldi et al., 1997) and also decreases inflammation (Kolak et al., 2007).

1.8.3. Activity of brown adipose tissue

Obesity and insulin resistance are associated with inactive BAT, downregulation of mitochondrial genes such as PGC1α (Wu et al., 1999; Kleiner et al., 2012; Uldry et al., 2006) and UCP1 (Feldmann et al., 2009) and impaired lipolysis (Tsujita, Morimoto and Okuda, 1995; Arner et al., 2018). These are all targets for improving metabolic health. Transplantation of BAT into the visceral cavity of mice results in an increase in whole-body insulin sensitivity and a reduction in body weight and adiposity (Stanford et al., 2013). Upon cold exposure, detectable BAT activity in humans is accompanied by a higher insulin sensitivity capacity (Yoneshiro et al., 2011), whereas reduced activity is associated with obesity (Orava et al., 2013). Furthermore, In rodent studies, activating BAT by exposure to cold stimuli improves insulin resistance, due to upregulated TG uptake and clearance (Bartelt et al., 2011). The presence of UCP1+ cells (Cypess et al., 2009) and BAT activity (Van Marken Lichtenbelt et al., 2009) are negatively correlated with BMI and percentage body fat in humans exposed to cold stimuli (Saito et al., 2009). They also have an increased rate of thermogenesis (Van Marken Lichtenbelt et al., 2009). In addition to targeting UCP1 expression, ADRβ3 is a potential therapeutic target for obesity (Arch et al., 1984; Collins et al., 1997) with high functional activity associated with weight loss (Andersson et al., 2009). Furthermore, ADRβ3 gene expression levels are negatively correlated with BMI (Cao et al., 2018) and ADRβ3 agonistic action induces thermogenesis in human BAT (Cypess et al., 2015). Furthermore, taking advantage of 'browning' in susceptible white fat may increase energy expenditure and provide protection against obesity in mice (Vegiopoulos et al., 2010; Seale, et al., 2011). This browning process can be induced in brown-like adipocytes differentiating within the white depot by TZDs (Petrovic et al., 2010) and demonstrates a possible route for activating thermogenesis in brown-like cells that reside in humans.

1.9. Mice as an animal model for obesity

Over the last few decades, extensive knowledge of the mouse genome has been acquired which demonstrates the similarities between mice and humans (Guénet, 2005), at the level of the genome. Due to ethical issues, it is not feasible to freely conduct experiments in humans to document obesity, maternal influences or therapeutic intervention. For this reason, smaller studies are conducted in mice to perform such experimental paradigms.

The distribution of AT in mice differs slightly to that of humans. For example, omental WAT does not exist in mice, but SAT characteristics are still comparable between the two species (Zuriaga et al., 2017) and it is becoming increasingly more important to use mice as models for biomedical research.

As a model for obesity, male mice are more prone to developing metabolic diseases, such as T2D (Vitali et al., 2012), when induced by a high-fat (HF)-diet, compared to female mice (Hwang et al., 2010). Inducing obesity by a HF-diet in mice, results in a similar phenotype as in humans (Clegg et al., 2011). In particular, C57BL/6 mice develop obesity resembling that of human obesity, in that a gradual accumulation of AT, metabolic and hormonal changes occurs (Becskei, Lutz and Riediger, 2009; Becskei, Lutz and Riediger, 2010). Furthermore, C57BL/6 mice possess the classical brown and white adipose tissue depots, as well as, brown-like cells populated in inguinal white adipose tissue (Vitali et al., 2012). Mice as animal models are advantageous in that both their gestation and lifespan periods allow the observation of fetal development *in utero*. As developmental programming *in utero* can influence fetal metabolism, inducing a HF-diet in pregnant dams may also effect the developing fetus and offspring in later life (Guo and Jen, 1995; Tamashiro et al., 2009).

1.10. Rationale

The accumulation of fat in non-adipose tissue depots is a common characteristic in obesity. Excess ectopic fat deposition around the heart, such as PAT, has been associated with an increased risk of CV-implications (Greif et al., 2009; Liu et al., 2011; Rosito et al., 2008). As PAT is in close proximity to the heart, it effects local cardiac function, rather than systemically

(Ding et al., 2009; Rosito et al., 2008), and may have a significant impact on metabolic health. Obesity in humans are usually induced by excessive caloric dietary intake. A diet high in sugar (Yi et al., 2020) and fat (Wang et al.,2018) increases the risk of ectopic fat accumulation. However, a healthier lifestyle, exercising and restricting caloric intake aids in the reduction of ectopic fat deposition (Larson-Meyer et al., 2006; Lim et al., 2011). Weight loss is linked to a reduction in ectopic fat associated with the heart (Iacobellis et al., 2008; Snel et al., 2012) and reduced visceral adiposity (Bosy-Westphal et al., 2010).

Studies have suggested that PAT has both a white and brown adipogenic potential, in which it acts as a visceral fat depot with endocrine-like traits (Horckmans et al., 2018; Bale, West and Conover, 2018) and has a thermogenic capacity (Al-Dibouni et al., 2020), respectively. However, these studies have not delved further into how these beige-like signatures identified in pericardial fat are effected by various dietary influences encountered *in utero* and during adulthood, and its response to therapeutic stimulation.

The 'thrifty phenotype hypothesis,' as proposed by Hales and Barker (2001), states that undernutrition at various timepoints in the developmental stages of a fetus is associated with metabolic dysfunction later in life (Barker et al., 1993). There is evidence to suggest that maternal undernutrition effects the state of cardiac AT. PAT from new-born sheep has been identified as a brown depot. The thermogenic capacity, but not adipogenic potential, of pericardial fat is effected by maternal undernutrition in the late gestation period. This is demonstrated by a downregulation of brown adipocyte-related genes including UCP1, DIO2 and ADRβ3 (Ojha et al., 2013). However, maternal undernutrition induced earlier in the gestation period, followed by *ad libitum* feeding in the mothers, upregulated the expression of UCP1 and visceral adipogenic makers such as C/EBPα in PAT of offspring (Ojha et al., 2014). Although the underlying mechanisms of maternal undernutrition are still unclear, it provides a basis that gene expression of pericardial fat may be altered depending on the window of susceptibility in fetal development. This offers an insight into investigating the effects of the other extreme of maternal nutrition (maternal overnutrition) in the development of offspring AT. Maternal obesity models demonstrate gene expression changes in white fat during the fetal

development of rodents (Borengasser et al., 2013; Shankar et al., 2008) and the effects of maternal overnutrition at specific periods throughout lactation and/or pregnancy in rodents (Sarker et al., 2019) and in sheep (Muhlhausler et al., 2007a; Muhlhausler et al., 2007b). Ojha et al., focused on pericardial fat in offspring in the context of maternal undernutrition during pregnancy in sheep (Ojha et al., 2013; Ojha et al., 2014), yet maternal overnutrition was not elucidated. The study conducted in this thesis utilises the evidence that thermogenic and adipogenic gene expression markers are altered under maternal influences in pericardial fat, as demonstrated by Ojha et al. Current knowledge is lacking in how exposure to extreme maternal obesogenic conditions, prior to and during gestation and lactation in mice, followed by an obesogenic post-weaning diet in offspring, effects the thermogenic and adipogenic capacity of pericardial fat.

Given that PAT may have a brown-like phenotype, stimulating the SNS with ADRβ3 mediated action can activate beige adipocytes in animals (Barbatelli et al., 2010). In some human studies, this activation causes only short-term effects such as improved insulin sensitivity (Weyer et al., 1998) and reduced TG levels (Larsen et al., 2002). In other human studies, there have been no differences in thermogenesis demonstrated upon ADRβ3-mediated activation (Buemann et al., 2000; Larsen et al., 2002). This could be due to the efficacy of ADRβ3-mimetics and the dose to ensure no adverse off-target effects are established (Buemann et al., 2000). Although ADRβ3-agonists can increase lipolysis and energy expenditure in obese men (Van Baak et al., 2002) and increase thermogenesis in BAT, side effects such as increased heart rate, may still occur (Cypess et al., 2015). Moreover, activating the AMPK pathway with anti-diabetes compounds could be an alternative route to activate thermogenesis. A recently developed agent known as Compound 14 (Cpd14) activates AMPK *in vitro* (Spurr et al., 2012) and promotes weight loss in obese mice (Asby et al., 2015). However, the mechanistic effects of weight loss and action in AT with Cpd14 treatment is still undetermined. Activation of AMPK may modulate metabolism by regulating the thermogenic capacity of brown-like cells populated in a beige depot like perciardial fat.

1.11. Aims and Objectives

The volume of pericardial fat has been associated with metabolic complications. However, there is little known about the white and/or brown characteristics that pericardial fat may adopt under normal environmental cues and/or changes in the nutritional status of an animal encountered *in utero* and/or during adulthood. The aim of this thesis is to investigate the transcriptional and histological profile of pericardial adipose tissue, in direct comparison to classical white depots, visceral gonadal and subcutaneous inguinal adipose tissue, and brown adipose tissue:

Aim 1: Investigate the effects of an obesogenic diet on pericardial adipose tissue at different timepoints during adulthood.

Objective 1: Determine the histological and adipogenic, inflammatory and thermogenic transcriptional profile of pericardial adipose tissue of 10-week-old male mice and 30-week-old male mice fed a chow or high-fat-diet.

Aim 2: Investigate the effects of an obesogenic maternal diet prior to and during pregnancy and lactation in offspring mice.

Objective 2: Determine the histological and adipogenic, inflammatory and thermogenic transcriptional profile of pericardial adipose tissue of 30-week-old male offspring mice fed a chow or high-fat diet, post-weaning, from dams fed a chow or high-fat-diet.

Aim 3: Investigate the effects of a novel anti-diabetes compound, Cpd14, on pericardial adipose tissue in lean and obese mice.

Objective 3: Determine the histological and adipogenic, inflammatory and thermogenic transcriptional profile of pericardial adipose tissue of 10-week-old male mice fed a chow or high-fat-diet and treated orally with Cpd14 for 10 days and following a 26-day recovery period.

CHAPTER 2

MATERIALS AND METHODS

2.1. Materials and reagents

Cell culture: 3T3-L1 mouse cell line (Catalogue code: 86052701), High glucose Dulbecco's Modified Eagle's Medium (DMEM, Product code: D429), Trypsin-EDTA, phenol red, 0.25% (Product code: T4049), Dimethyl sulfoxide (DMSO, Product code: D4540), 3-isobutyl-1-methylxanthine (IBMX, Product code: I5879), Dexamethasone (Product code: D1756), Insulin solution human (Product code: I9278), Phosphate Buffered Saline (PBS, Product code: D8537), Penicillin-Streptomycin (P/S, Product code: P4333), Collagenase from Clostridium histolyticum (Product code: C0130), LookOut® Mycoplasma Erase Spray (L1420), Freezing container, Nalgene® Mr. Frosty (Product code: C1562), LookOut® Mycoplasma PCR Detection Kit (Product code: MP0035), JumpStart™ Taq DNA Polymerase with $MgCl_2$ (Product code: D9307) were purchased from Sigma-Aldrich, United Kingdom. Gibco™ Fetal Bovine Serum (FBS, Product code: 11573397), Gibco™ Dialyzed Fetal Bovine Serum (FBS, Product code: 11520646), Invitrogen™ Trypan Blue stain (0.4%) (Product code: T10282) and Invitrogen™ Countess™ Reusable Slides (Product code: 15311986) for use with the Countess™ Automated Cell Counter, Gibco™ Collagenase, Type I, powder (Product code:11500536), Thermo Scientific™ Nalgene™ General Long-Term Storage Cryogenic Tubes (Product code: 10731432) were purchased from Fisher Scientific, United Kingdom. 6-well tissue culture treated plate with lid (Item number: 657160), 12-well tissue culture treated plate with lid (Item number: 665180), $75cm^2$ tissue culture treated flask with filter cap (Item number: 658175), were purchased from Greiner Bio-One Limited, United Kingdom. Cell scrapers (Product code: 1173209), were purchased from Camlab, United Kingdom. 2-Propanol (Product code: 20842.330) was purchased from VWR, United Kingdom. CellTiter 96® AQ$_{ueous}$ One Solution Cell Proliferation Assay (MTS) (Product code: G3580) was purchased from Promega. Compound 14 (Cpd14) was provided by the research group at University of Southampton, United Kingdom.

Agarose gel: Invitrogen™ SYBR™ Safe DNA gel stain 10,000X concentrate in DMSO (Product code: 10328162), Invitrogen™ 1 Kb Plus DNA ladder (and 10X BlueJuice Gel Loading Buffer) (Product code: 11578636), Invitrogen™ UltraPure™ Agarose (Product code:

11553277), Boric acid (Product code: 10263370), Ethylenediaminetetraacetic acid (EDTA) 99+% ACS reagent (Product code: 10413551) were purchased from Fisher Scientific, United Kingdom. Tris Base ULTROL® Grade (Product code: 648311), was purchased from Calbiochem, United Kingdom. Sodium hydroxide (Product code: 221465) was purchased from Sigma-Aldrich, United Kingdom.

RNA isolation from cell lysates: RNeasy Mini Kit (Catalogue Number: 74104) was purchased from Qiagen, United Kingdom. Dithiothreitol (DTT, Product code: 10592945), BD™ Microlance™ Stainless Steel Needles 25G 25mm (Product code: 12389169) was purchase from Fisher Scientific, United Kingdom. BD Plastipak Syringe 1ml (Produce code: 1201270) was purchased from Camlab, United Kingdom.

RNA isolation from frozen tissue: Chloroform (Product code: 372978), Invitrogen™ TRI Reagent™ Solution (Product Code: 1131294), 2-Propanol (Product code: 10315720), Ethanol absolute (Product code: 10041814), DNase and RNase free water (Product code: 10295243), MP Biomedicals™ Lysing Matrix D (Product code: 11432420), were purchased from Fisher Scientific. United Kingdom.

cDNA synthesis: Applied Biosystems™ High-Capacity cDNA Reverse Transcription Kit (Product code: 10186954), Invitrogen™ RNaseOUT™ Recombinant Ribonuclease Inhibitor (Product code: 10154652) were purchased from Fisher Scientific, United Kingdom.

RT-qPCR: qPCRBIO Probe Mix No-ROX (Product code: PB20.23-20) was purchased from PCR biosystems, United Kingdom. Sealing tape, optically clear (Product code: 95.1994) was purchased from Sarstedt, United Kingdom. Thermo Scientific™ PCR Plate, 96-well, segmented, semi-skirted, white (Product code: 10058822), Applied Biosystems™ TaqMan™ Gene Expression Assays, FAM-MGB (Product code: 10794597) (Table 2.1) were purchased from Fisher Scientific, United Kingdom. External well factor solution (Product number: 1708794) was purchased from Bio-Rad, United Kingdom.

Triglyceride extraction and quantification from cell lysates: Triton™ X-100 (Product code: T8787), Triglyceride Reagent (TR, Product code: T2449), Free Glycerol Reagent (FGR, Product code: F6428) were purchased from Sigma-Aldrich, United Kingdom. 96-well micro test

plates F-bottom (Product code: 1144689), were purchased from Camlab, United Kingdom. UltraPure™ Glycerol (Product code: 11508746) was purchased from Fisher Scientific, United Kingdom.

Table 2.1. Applied Biosystems™ TaqMan™ Gene Expression Assays for RT-qPCR

Gene	Assay ID
ACTA1	Mm00808218_g1
AdipoQ	Mm00456425_m1
ADRβ3	Mm02601819_g1
C/EBPα	Mm00514283_s1
COX7A1	Mm00438297_g1
COX8B	Mm00432648_m1
DIO2	Mm00515664_m1
FABP4	Mm00445878_m1
GAPDH	Mm99999915_g1
IL6	Mm00446190_m1
Leptin	Mm00434759_m1
MYH6	Mm00440359_m1
MYH7	Mm00600555_m1
NOX4	Mm00479246_m1
NPPA	Mm01255747_g1
PGC1α	Mm01208835_m1
PLIN1	Mm01320554_g1
PPARγ	Mm00440940_m1
PPIA	Mm02342430_g1
TNFα	Mm00443258_m1
UCP1	Mm01244861_m1

Triglyceride extraction and quantification from frozen heart tissue: Nonidet P 40 (NP-40) Substitute conc. (Product code: 11754599001) was purchased from Roche, United Kingdom. Triglyceride quantification colorimetric/fluorometric Kit (Product code: MAK266), was purchased from Sigma-Aldrich, United Kingdom. Nunc™ MicroWell™ 96-Well Microplates (Product code: 10058820) were purchased from Fisher Scientific, United Kingdom.

Protein analysis and Western Blots: Abcam 10X RIPA Buffer (Product code: 15584906), Thermo Scientific™ Pierce™ Protease Inhibitor Mini Tablets (Product code: 15672129) Thermo Scientific™ Pierce™ Phosphatase Inhibitor Mini Tablets (Product code: 15691759), UltraPure™ Glycerol (Product code: 11508746), Thermo Scientific™ Pierce™ BCA Protein Assay Kit (Product code: 10741395), Alfa Aesar™ Acrylamide/Bisacrylamide 37.5:1, 40% soln (Product code: 15433569), Sodium Dodecyl Sulfate (SDS, Product code: 10356463), Thermo Scientific™ PageRuler™ Unstained Broad Range Protein Ladder (Product code: 11892124), Thermo Scientific™ SuperSignal™ West Femto Maximum Sensitivity Substrate (Product code: 11859290), Dithiothreitol (DTT, Product code: 10592945), GE Healthcare Whatman™ Gel Blotting Paper Grade GB003 (Product code: 12415272), Sodium Chloride (Product code: 10092740), Thermo Scientific™ Coomassie Brilliant Blue R-250 Dye (Product code: 11876744) were purchased from Fisher Scientific, United Kingdom. 96-well micro test plates F-bottom (Product code: 1144689), Tris Base ULTROL® Grade (Product code: 648311), was purchased from Calbiochem, United Kingdom. Methanol (Product code: 322415), acetic acid (Product code: 27225-M), N,N,N′,N′-Tetramethylethylenediamine (TEMED, Product code: T9281), Glycine (Product code: G8898), Methanol (Product code: 322415), TWEEN® 20 (Product code: P1379), BSAV-RO Roche Bovine Serum Albumin Fraction V (Product code: 10735086001), Ammonium persulfate (APS) (Product code: A3678), Ponceau S (Product code: P3504), Bromophenol Blue (Product code: 114391), Antibodies (Table 2.2) were purchased from Sigma-Aldrich, United Kingdom. Supported Nitrocellulose Membrane (Product number: 1620094) was purchased from Bio-rad, United Kingdom. Marvel Original Skimmed Milk Powder was purchased from Premier Foods, United Kingdom. Antibodies purchased from Cell signalling, United Kingdom, are listed in Table 2.2.

Cytology: Formalin solution, neutral buffered, 10% (Product code: HT501128)**,** Phosphate Buffered Saline (PBS, Product code: D8537**)** were purchased from Sigma-Aldrich, United Kingdom. Alfa Aesar™ Oil Red O (Product code: 114590300) was purchased from Fisher Scientific, United Kingdom. 2-Propanol (Catalogue number: 20842.330) was purchased from VWR, United Kingdom.

Histology: SuperFrost Plus™ Adhesion slides (Product code: 15438060) and BRAND Coplin Staining Troughs (Produce code: 10315091) and ReadyProbes™ Hydrophobic Barrier Pap Pen (Product code: 16660484), Xylene (Product number: 10385910), Thermo Scientific 1LT lamb DPX mounting medium (Product code: 12658646), BRAND Coplin Staining Troughs 10315091 (Product code: 10315091) and BRAND™ Borosilicate Glass Cover Glasses (Product code: 15212469) were purchased from Fisher Scientific, United Kingdom. Optimal Cutting Temperature (OCT) Compound (Code: AGR1180) was purchased from Agar Scientific, United Kingdom. Hematoxylin Solution, Mayer's (Product number: MHS16), Eosin Y solution, aqueous (Product number: HT110216), Magnesium sulfate (Product number: M2643), Sodium bicarbonate (Product code: S5761), humidity chamber (Product code: H6644), Hydrochloric acid 37% (Product code: 258148) were purchased from Sigma-Aldrich, United Kingdom. Ethanol absolute (Catalogue number: 20821.330) was purchased from VWR, United Kingdom.

Table 2.2. Antibodies for Western blot analysis

Product number	Antibody	Isotype	Molecular Weight (kDa)	Dilution ratio	Blocking buffer	Primary/ Secondary	Purchase details
A2066	Anti-β-Actin	Rabbit	42	1:4000	Milk	Primary	Sigma-Aldrich
A0545	Anti-Rabbit IgG (whole molecule) – Peroxidase	Goat	N/A	1:5000	Milk	Secondary	Sigma-Aldrich
2535	Phospho-AMPKα (Thr172)	Rabbit IgG	62	1:1000	BSA	Primary	Cell signalling
5831	AMPKα	Rabbit	62	1:1000	BSA	Primary	Cell signalling
11818	Phospho-Acetyl CoA Carboxylase (ACC) (Ser79)	Rabbit IgG	280	1:1000	BSA	Primary	Cell signalling
5831	ACC	Rabbit	280	1:1000	BSA	Primary	Cell signalling

2.2. Methods

2.2.1. Cell culture

3T3-L1 mouse pre-adipocytes were used in this study to determine the effects of Compound 14 (Cpd14) on adipocyte differentiation, *in vitro*. Cells were grown in basal media, consisting of High Glucose (HG) Dulbecco's Modified Eagle's Medium (DMEM) supplemented with 10% (v/v) Fetal Bovine Serum (FBS) and 1% Penicillin-Streptomycin (P/S) (10,000 U/ml, 10mg/ml, respectively) and incubated in a humidified atmosphere of 5% CO_2, at 37°C. Before supplementing to the media, FBS was filtered with a 0.45µM filter and syringe to remove any precipitates. Next, basal media was filtered with a 0.22µM filter and syringe to remove any contamination that may have occurred during preparation of media. These were aliquoted and stored at 4°C. Aseptic techniques were carried out by spraying tissue culture laminar flow hood surfaces with 70% ethanol and LookOut® Mycoplasma Erase Spray. The latter eliminates Mycoplasma contamination almost immediately by preventing growth of Mycoplasma which may interfere with cell culture experiments.

2.2.1.1. Counting cells

To determine the cell count and viability of growing cells from 75cm^2 (T75) flasks, after sub-culturing which is a process to enable the propagation of cell lines, 10µl of cell suspension was added to 10µl of trypan blue solution (0.4%) (an exclusion dye). 10µl of sample was pipetted into a plastic, disposable chamber slide and inserted into the Invitrogen Countess™ Automated Cell Counter (Fisher Scientific). 0.4µl of volume is counted which equates to 4 squares (1mm × 1mm) in a standard haemocytometer. After selecting 'count' on the touch-screen of the machine, there is an output of live and dead cell concentrations per ml, total cell concentration per ml and the percentage of live cells to dead cells (cell viability), as well as, displaying an image on the screen of the cell suspension inserted for counting (Figure 2.1). Using an automated cell counter is faster, more accurate and a less subjective way of counting cells and viability than manual counting.
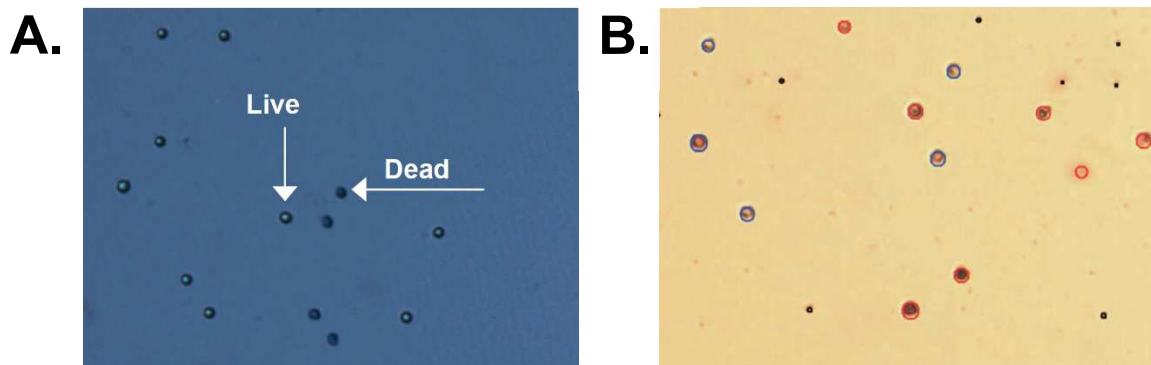
Figure 2.1. Images displayed on Invitrogen Countess™ Automated Cell Counter before and after counting cells of cell suspension inserted into the machine. (A) Before counting cells, live cells have brighter centres and darker edges compared to dead cells which have a consistent blue colour. Trypan blue exclusively labels dead cells by entering through the damaged cell membrane and into the cytoplasm. **(B)** After counting cells, cells circled in blue are considered as 'live' cells, red circled cells are indicated as 'dead' cells and black circled objects are excluded when determining cell count.

2.2.1.2. Sub-culturing and freezing cells

Once the number of cells and viability (between 80 and 100 %) was determined automatically, T75 flasks (surface area of 75 cm^2) were seeded as a 1 in 3 split ratio. Cell suspensions were obtained by passaging/splitting cells grown in 75cm^2 culture flasks and maintained in basal media, incubated in a humidified atmosphere of 5% CO_2, at 37°C. At ~80% confluence, media was removed from cells and washed with PBS. Trypsin-EDTA was added for 1 minute at room temperature to digest the focal adhesions that aid in anchoring cells to the T75 flask and remove the bonds that hold cells together. Trypsin-EDTA was removed and cells were incubated (5% CO_2, at 37°C) for 2 minutes before adding basal media. As the FBS supplemented to basal media contains protease inhibitors, it disables Trypsin-EDTA and prevents further digestions of bonds. T75 flasks were used to grow and maintain cells for future experiments that were seeded in 6-well or 12-well culture plates. The oldest passage used for the experiments was passage 18. Any cells not used for seeding of experiments or

maintenance were centrifuged at 1000rpm for 5 minutes. The supernatant was discarded and the pellet was diluted in freezing media consisting of basal media and 5% DMSO, to prevent ice crystallisation during freezing which could damage cells. Approximately, 0.5 x 10^6 cells/1.5ml to 1 x 10^6 cells/1.5ml, as determined by automatic counting, were transferred to a 2ml cryogenic tube, and placed in the Nalgene® Mr. Frosty Freezing Container (Fisher Scientific), immersed in 2-Propanol. The cells were kept in the -80°C freezer for no longer than 24 hours and transferred to liquid nitrogen, indefinitely. The Nalgene® Mr. Frosty Freezing Container allows the optimal conditions to preserve cells with a cooling rate close to -1°C per minute.

2.2.1.3. Mycoplasma detection

An aliquot of media was collected from 80% confluent cells maintained in T75 flasks before sub-culturing and frozen at -20°C for future use with the assay. Detection of Mycoplasma contamination in growing cells was modified from the manufacturer's instructions for the LookOut® Mycoplasma PCR Detection Kit (Fisher Scientific). Reagents and media were completely thawed before continuing with the kit and kept on ice. 100µl of media was heated at 95°C for 5 minutes to denature samples, using Fisherbrand™ Isotemp™ Digital Dry Bath/Block Heater (Product code: 15387928, Fisher Scientific), then kept on ice.

To prepare the stock reaction mix, 22.5µl of Rehydration buffer and 0.5µl of JumpStart™ Taq DNA Polymerase with MgCl$_2$ (2.5U/µL) (Sigma-Aldrich) was used per sample, including negative and positive controls. JumpStart™ Taq DNA Polymerase with MgCl$_2$ is an inactivated antibody and a hot-start enzyme which has been manufactured to reduce non-specific amplification, whilst maximising product yield. At 70°C, DNA polymerase activity is optimal and the polymerase chain reaction (PCR) result in a higher yield and specificity.

23µl of reaction mix was added, per test reaction tube, to test samples and a negative control. The test reaction tubes are pre-coated with primers, deoxyribonucleotide triphosphates (dNTPs), internal DNA controls and gel loading buffer/dye. Half the number of test reaction tubes were used for the number of samples that were tested. The 23µl sample/negative control

mix was divided into two Eppendorf PCR tubes (11.5µl final volume). 1µl of media was added to the designated tube and 1µl of Nuclease-free water was added to the negative control tube. 25µl of reaction mix was added to the positive control PCR reaction tube, which contains all components as listed above for test reaction tubes, in addition to non-infectious DNA fragments of Mycoplasma orale genome, prepared by PCR. The positive control mix was divided into two Eppendorf PCR tubes (12.5µl final volume). After each reagent was added, reaction tubes were centrifuged to ensure efficient mixing. To perform the PCR on the T100™ Thermal cycler (Catalogue number: 186-1096, Bio-Rad), the following conditions were used in Table 2.3.

Mycoplasma was detected using an 1.5% agarose gel. For preparation of the gel, buffers, running times and gel imaging, see section 2.2.3. Plates seeded from Mycoplasma negative media corresponding to the T75 flasks were used as experimental plates (Figure 2.2).

Table 2.3. Settings for T100™ Thermal cycler to perform PCR

Settings	1 cycle	40 cycles			Cool down
Temperature (°C)	94	94	55	72	4
Time (seconds)	120	30	30	30	∞

2.2.1.4.   Cell viability assay

To determine the cell titre and viability of cells seeded in 12-well plates, the CellTiter 96® AQueous One Solution Cell Proliferation Assay (Promega) was used. This colourimetric solution contains a tetrazolium compound called 3-(4,5-dimethylthiazol-2-yl)-5-(3-carboxymethoxyphenyl)-2-(4-sulfophenyl)-2H-tetrazolium, inner salt) (MTS) and an electron coupling reagent called phenazine ethosulfate (PES). Due to its stability, PES combines with MTS to form a stable compound. The quantity of the formazan product, quantified by 490nm absorbance, is directly proportional to the number of living cells in cultured cells (Figure 2.3).
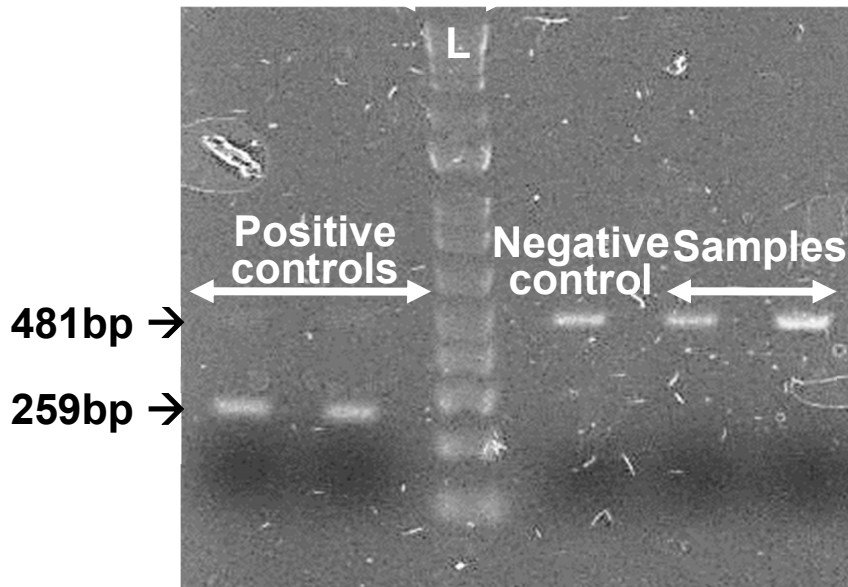
Figure 2.2. Image of an agarose gel from a Mycoplasma detection test. Two positive controls (on the left of the ladder) were run every gel that was prepared, with a band at 259bp and an additional band of the internal control at 481bp. One negative control (on the right of the ladder) was run every gel and showed a band at 481bp. Mycoplasma spp. from 260 ± 8 bp. All samples show bands at 481bp and therefore are a negative sample and Mycoplasma free. L: Ladder; bp: base pair.
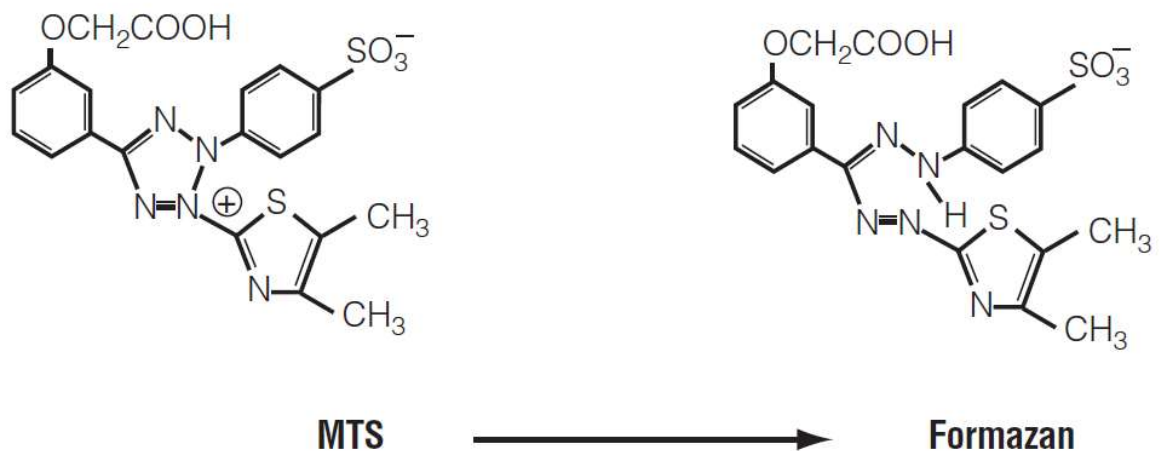
Figure 2.3. The structure of MTS tetrazolium and its formazan product. MTS: 3-(4,5-dimethylthiazol-2-yl)-5-(3-carboxymethoxyphenyl)-2-(4-sulfophenyl)-2H-tetrazolium, inner salt).

Media was discarded from the wells and 500µl of fresh media was added directly to cells per 33µl of CellTiter 96® AQueous One Solution Cell Proliferation Assay. The cell culture plate was incubated at 37ºC, at 5% CO_2, for 40 minutes. The media was collected and 180µl, in duplicates, were pipetted into a 96-well plate and absorbances were read at 490nm using the SPECTRAmax® 190 Microplate Spectrophotometer (Part number: 0112-0085, Molecular Devices Corporation), using SOFTmax PRO software. The readings were corrected to the blank well (containing no cells).

To correct the samples from the blank:

Average Sample Absorbance – Average Blank Absorbance

To normalise cell titre data to the control:

Absorbance of sample – Average absorbance readings of the control group

2.2.2. Animal models

All animal work as stated in sections 2.2.2.1, 2.2.2.2 and 2.2.2.3 was conducted by the technical staff at either the University of Southampton or the Medical Research Council Harwell Institute.

2.2.2.1. Ethical approval

All animal studies were either performed and approved by the University of Southampton or by the Medical Research Council Harwell Institute Animal Welfare and Ethical Review Board. All procedures were carried out within project license restrictions under the UK Animals (Scientific Procedures) Act 1986, issued by the UK Government Home Office.

2.2.2.2. Animal husbandry

All C57BL/6 mice used to carry out experimental procedures were maintained under a 12-hour light/dark cycle and a constant temperature of 22°C ± 2°C, with food and water available *ad libitum*. Mice were fed either a chow diet or high-fat (HF)-diet, to resemble that of a human 'western' diet (Table 2.4.).

Table 2.4. Nutritional composition of chow (C) and high-fat (HF)-diets

% Kcal From	10-week-old mice		30-week-old mice	
	Chow (C) diet	High-fat (HF)- diet	Chow (C) diet	High-fat (HF)- diet
Fat	7	45	10	60
Protein	18	20	20	20
Carbohydrate	75	35	70	20

2.2.2.3. Dissection of adipose tissue

Whole adipose tissue including gonadal white adipose tissue (gWAT), inguinal white adipose tissue (iWAT), interscapular brown adipose tissue (iBAT) and pericardial adipose tissue (PAT), as well as the myocardium of the heart, represented in Figure 2.4 and Figure 2.5, were dissected from mice.
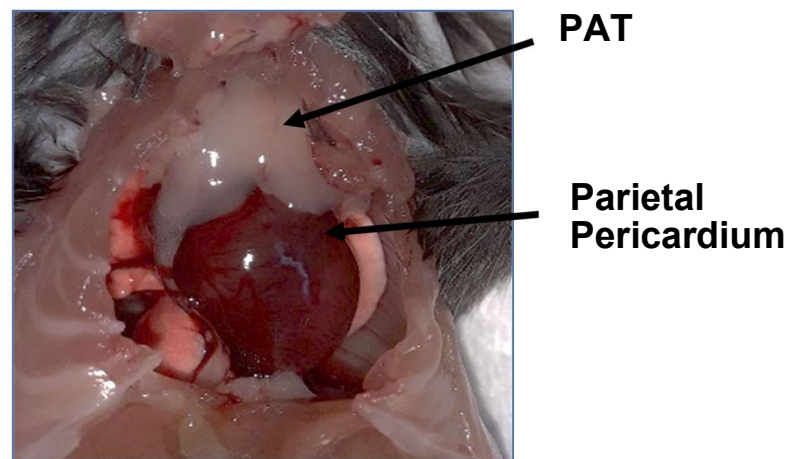
Figure 2.4. Location of PAT in mice. Adapted from Al-Dibouni et al., (2020). PAT: Pericardial Adipose Tissue.
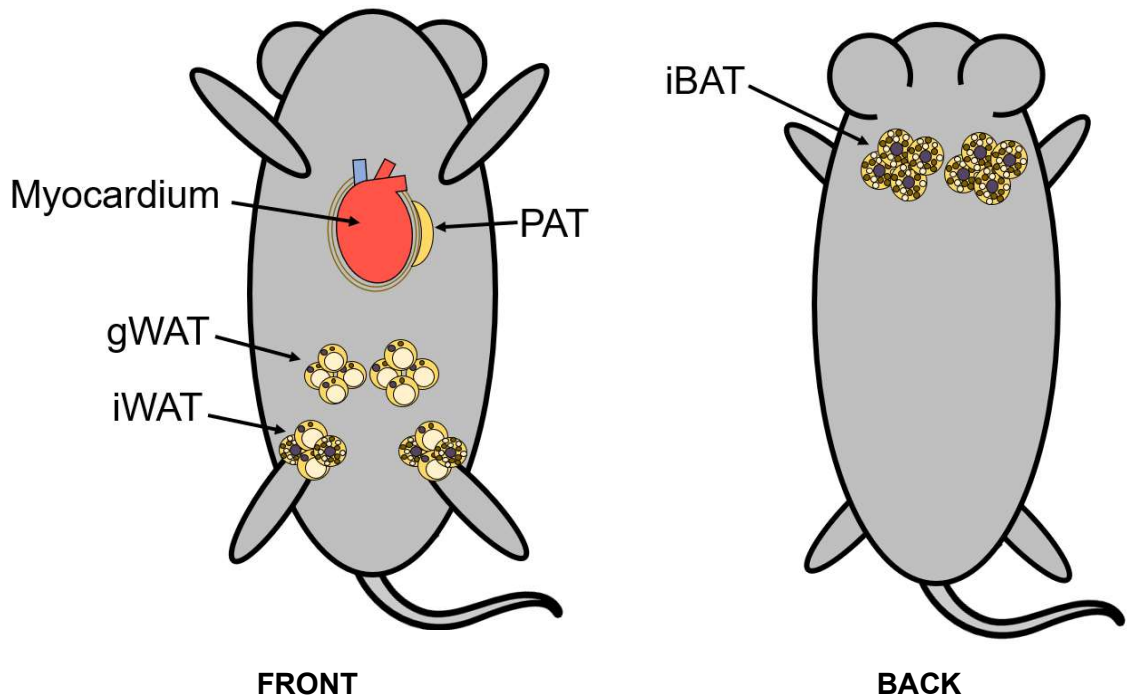
Figure 2.5. Location of gWAT, iWAT, iBAT, PAT and Myocardium of the heart in mice.

gWAT: gonadal White Adipose Tissue; iWAT: inguinal White Adipose Tissue; iBAT: interscapular Brown Adipose Tissue; PAT: Pericardial Adipose Tissue.

2.2.3. Agarose gel

As RNA, like DNA, is negatively charged, the fragments can be separated based on size in response to an electric charge. An agarose gel was used to determine the quality of RNA and for Mycoplasma detection tests. For both procedures, a 1.5% agarose gel was prepared as shown below.

To prepare 100ml of 0.5M Ethylenediaminetetraacetic acid (EDTA) pH 8 for the Tris-Boric Acid-EDTA (TBE) buffer:

- 14.6g of EDTA was added to 75ml of double distilled water (ddH$_2$O) and stirred vigorously on a magnetic stirrer with a magnet

- Sodium hydroxide (NaOH) pellets were added until the EDTA powder had completely dissolved. EDTA will only fully dissolve once the pH reaches ~8

- The pH was determined using the Fisherbrand™ accumet™ AE150 Benchtop pH Meter (Catalogue number: 13-636-AE151, Fisher Scientific). Acid/Alkali solutions were added to adjust the pH to ~8 and ddH$_2$O was added to achieve a final volume of 100ml

To prepare 1 litre of stock solution of 10X TBE buffer, the following were dissolved in 800ml of ddH$_2$O and the volume was adjusted to 1 litre with ddH$_2$O:

- 108g of 89mM Tris Base ULTROL® Grade

- 55g of 89mM Boric acid

- 40ml of 0.5M EDTA

To prepare 1 litre of working solution of 1X TBE buffer:

- 1-part 10X TBE buffer

- 9-parts ddH$_2$O

To prepare 5X BlueJuice Gel Loading Buffer from 10X BlueJuice Gel Loading Buffer, equal parts of 10X BlueJuice Gel Loading Buffer was diluted with ddH$_2$O.

To prepare stock concentration of 0.8mg/ml of Invitrogen™ 1 Kb Plus DNA ladder, 50µl of 5X BlueJuice Gel Loading Buffer was added to the stock solution of 250µg.

To prepare RNA samples for loading, 2µl of RNA sample was diluted with 2µl of 5X BlueJuice Gel Loading Buffer and 6µl of ddH$_2$O, to make a final volume of 10µl.

To prepare 50ml of 1.5% agarose gel, 0.75g of Invitrogen™ UltraPure™ Agarose, which is ideal for separation analysis of RNA and DNA fragments from 500bp to 23,000bp, with no RNAse or DNAse activity, was added to 50ml of 1X TBE in an uncovered glass duran. This was heated in the microwave, in 30 second bursts and swirled each time, until the agarose powder had fully dissolved.

Once the agarose gel solution had cooled, 2µl of Invitrogen™ SYBR™ Safe DNA gel stain was added per 50ml of agarose gel solution (1:25,000 dilution) for visualisation of RNA/DNA in the gel. Invitrogen™ SYBR™ Safe DNA gel stain (Fisher Scientific) binds to nucleic acids

and fluoresces upon excitation. This is suitable for staining both RNA for integrity (Figure 2.6) and DNA for Mycoplasma detection (Figure 2.2) in agarose gels, detected by UV transilluminator systems. It is a safer alternative and offers the same sensitivity of detection as ethidium bromide. The agarose gel solution containing the gel stain was poured into Scie Plas Easigel H1-SET Horizontal Gel Unit (Product code: 15825571, Fisher Scientific), with a 1.5mm 20-well comb and boarders in place. Once the gel had set, the comb and boarders were removed, and 1X TBE buffer was poured over the gel until completely covered and below the 'maximum' line, as indicated by the apparatus. 2µl of the prepared Invitrogen™ 1 Kb Plus DNA ladder (0.5µg/µl) was added for all runs, with 10µl of sample added per lane. All gels were run at constant 80mA for 30 minutes, until the bands migrated 2.5cm down the gel. This was visualised using the Syngene™ G:BOX Chemi XX9 (Product code: 15859922, Fisher Scientific), and software GeneSys with chemiluminescent image capture.
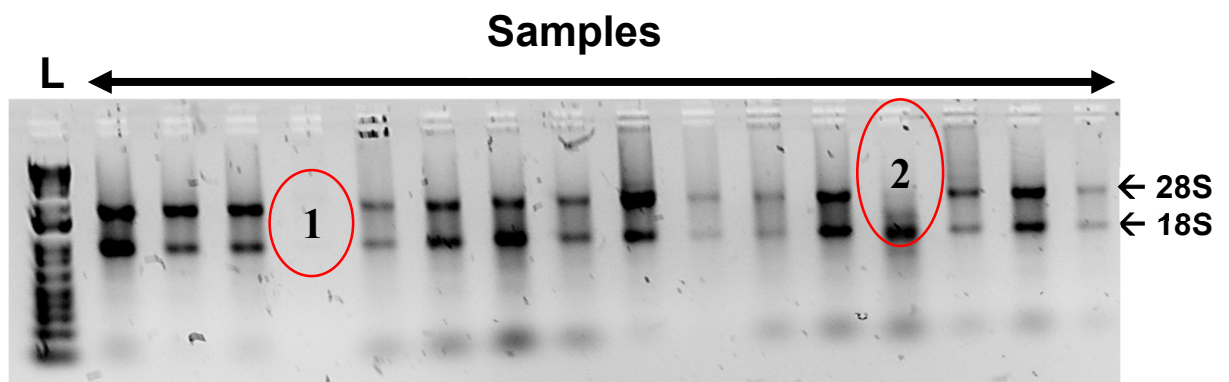
Figure 2.6. Image of a non-denaturing agarose gel to determine the integrity of RNA after extraction from frozen adipose and heart tissue. Non-denaturing agarose gels do not give clear, distinct bands, however, is suitable for visualisation of the 28S rRNA and 18S rRNA bands (2:1 ratio of band width). Samples with visible 28S and 18S bands were considered to have intact total RNA and were used for cDNA synthesis and PCR analysis. Samples which showed almost invisible bands (1 and 2), due to low RNA yield and/or degraded RNA, appear as smears and were re-extracted from the original tissue for RNA. The sample may have been introduced to degradation either before, during or after tissue sampling, as well as, throughout the process of RNA isolation. L: Ladder; RNA: Ribonucleic acid; cDNA: Complementary deoxyribose nucleic acid; PCR: Polymerase chain reaction; 18S: 18 Svedberg; 28S: Svedberg.

2.2.4. RNA isolation

Extracting RNA from cell lysates and tissues allows the study of genes which have been expressed. These genes make cells diverse and relate to how cells respond to a specific stimulus, such as drug treatment. Messenger Ribonucleic Acid (mRNA) detection is essential to investigate gene expression and what specific proteins are synthesised from genes.

To achieve purification of total RNA, it is essential to ensure the disruption of cell walls and membranes. This allows the release of RNA via homogenisation of cells or tissues to shear genomic DNA and other components in the cell. If these steps are not performed fully, this will result in a low yield of RNA.

2.2.4.1. RNA isolation from cell lysates

Isolation and homogenisation were performed using Qiagen's RNeasy mini kit, as suggested by the manufacturer (Qiagen). The maximum amount of RNA that can achieved in this protocol is 100µg as determined by the binding capacity of the RNeasy spin columns. The RNeasy protocol allows RNA isolation and purification by using selective binding technology of silica-based membranes and microspin technologies. Moreover, DNase digestion was not performed in the processing of cell lysates, as the silica membrane of RNeasy Mini spin columns remove the majority of DNA present in the sample after centrifugation. The Buffer RNeasy Lysis (RLT), a reducing agent, and Buffer RW1 have a high salt content, enabling a maximum of 100µl to bind to the membrane. The lysis buffer is stable at room temperature for one month. The presence of RNases, which degrade RNA, need to be inactivated. This is achieved by cell lysis and homogenisation using a denaturing buffer containing guanidine-thiocyanate. If homogenisation is incomplete, this can result in a low yield of RNA isolated from the sample. The addition of ethanol allows efficient binding of samples to the membrane of the RNeasy Mini spin columns, with contaminants being washed away.

To prepare 10ml of 1M Dithiothreitol (DTT) stock solution, 1.54g of DTT was dissolved in 10ml ddH$_2$O by vortexing and was aliquouted in 1ml Eppendorf tubes and kept at -20ºC for storage.

To prepare 10ml of Buffer RLT and 1M DTT:

- 10ml of Buffer RLT

- 400µl of 1M DTT

To prepare Buffer RPE, add 4 volumes of 100% ethanol, as specified depending on size of kit.

6-well plates were used to seed experiments as this provides the optimal number of cells for isolation of RNA and to achieve a sufficient yield. After discarding media, cultured cells were washed with 1ml PBS. Cells were collected with 350µl of RNA lysis buffer (40µl of 1M DTT per 1ml Buffer RNeasy Lysis (RLT)) by pipetting and aspirating multiple times around the well to collect the cells. Cell lysates were collected into an Eppendorf tube and stored at -80°C for future use or kept on ice to continue with the procedure. Cell lysate homogenisation was achieved by using a BD™ Microlance™ Stainless Steel Needles (25G 25mm) attached to a BD Plastipak Syringe (1ml) and passing through the sample 10 times.

350µl of 70% ethanol was added to the homogenised sample and mixed well by pipetting. The supernatant was transferred to a RNeasy Mini spin column in a 2ml Collection Tube and centrifuged at 8,900rpm for 20 seconds at 20°C to 25ºC. The flow-through was discarded and the collection tube was re-used, unless stated otherwise. Any volume that remained in the RNeasy Mini spin column was centrifuged again, as stated earlier. 700µl of Buffer RW1 was added to the column and centrifuged at 8,900rpm for 20 seconds at 20°C to 25ºC. The flow-through was discarded. 500µl of Buffer RPE was added to the column and centrifuged at 8,900rpm for 20 seconds at 20°C to 25ºC. The flow-through was discarded. 500µl of Buffer RPE was added to the column and centrifuged at 8,900rpm for 2 minutes at 20°C to 25ºC. The RNeasy Mini spin column was transferred to a new 2ml Collection Tube and centrifuged at

8,900rpm for 1 minute at 20°C to 25ºC. The RNeasy Mini spin column was transferred to a 1.5ml Eppendorf tube and 30µl of Nuclease-free water was added and centrifuged at 8,900rpm for 1 minute at 20°C to 25ºC. The RNeasy Mini spin column was disposed and the flow-through contained the RNA of the sample.

2.2.4.2. RNA isolation from frozen tissue

Animal tissues are not protected from degradation after harvesting until the tissue sample is flash-frozen or homogenised in reagents that inhibit RNases or denaturing substances. If this does not occur, unwanted gene expression alternations will progress, therefore immediately freezing samples at a low temperature of -80ºC is vital in maintaining RNA integrity and quality. When processing samples for RNA, tissues should be harvested as quickly and efficiently as possible, therefore it is best to estimate the weight of tissue being used, to avoid thawing samples when handling and initially weighing the sample. To preserve tissue integrity, samples were placed on a pre-cooled petri dish, on top of dry ice to ensure low temperatures were maintained, and cut for isolation of RNA, triglycerides, and protein. If the sample thaws too much, this may result in RNA degradation and skewed results when performing RT-qPCR. Homogenisation was achieved with TRI™ Reagent Solution and MP Biomedicals™ Lysing Matrix D tubes, agitated by MP Biomedicals™ FastPrep-24™ 5G Instrument (Product code: 15260488, Fisher Scientific). MP Biomedicals™ Lysing Matrix D tubes (Fisher Scientific) contains 1.4mm ceramic spheres to help disrupt the sample with agitation with TRI™ Reagent Solution, when using a homogenising instrument. Simultaneous disruption and homogenisation of the sample occurs when the spheres hit the cells to shear the tissue. TRI™ Reagent Solution is composed of a mixture of guanidine-thiocynate and phenol to extract and homogenise RNA, DNA and protein from tissue samples, while inhibiting the activity of RNases. This is a reliable technique to isolate RNA from tissue samples larger than ~5 mg. The MP Biomedicals™ FastPrep-24™ 5G Instrument is optimised to disrupt and homogenise cells while colliding Lysing Matrix Beads in contact with the sample to isolate stable RNA by disrupting cells and releasing RNA.

To disrupt and homogenise mouse adipose tissue and heart samples, the MP Biomedicals™ FastPrep-24™ 5G Instrument (Product code: 15260488, Fisher Scientific) was used. 1ml of TRI™ Reagent Solution (Fisher Scientific) was added to samples in a 2ml MP Biomedicals™ Lysing Matrix D tube (Fisher Scientific) on a specific setting stated in Table 2.5. Homogenisation was performed 1 to 3 times or until the tissue had completely homogenised. Tissues such as the heart may have a low yield due to the make-up of this connective tissue.

Table 2.5. Programme settings for the MP Biomedicals™ FastPrep-24™ 5G Instrument to disrupt and homogenise mice tissue

Mouse sample type	Speed (m/s)	Adapter	Time (seconds)	Lysing matrix
Adipose tissue	6.0	QuickPrep	40	D
Heart	6.0	QuickPrep	30	D

The homogenate was transferred to a clean Eppendorf tube. 200µl of chloroform per 1ml of TRI™ Reagent Solution was added to allow the phases to separate after centrifugation. Samples were vortexed vigorously for ~15 seconds (samples should resemble a cloudy pink appearance) and left to stand at room temperature for 5 minutes for nucleoproteins to separate. The sample was centrifuged at 13,000rpm for 15 minutes at 2°C to 8°C. If vortexing is not vigorous enough, the yield of RNA may be low. After centrifugation, the sample separates into 3 layers. The top layer is a clear aqueous phase containing RNA (desired phase for this protocol), the middle layer is the interphase containing DNA and the bottom layer is the organic phase (red phenol-chloroform phase), containing proteins and lipids (Figure 2.7). After centrifugation, if the sample did not separate into 3 distinct layers, or the layers were inverted, the sample was vortexed and was transferred into 2 clean Eppendorf tubes. 500µl TRI™ Reagent Solution were added to each tube and were vortexed and centrifuged as stated before.
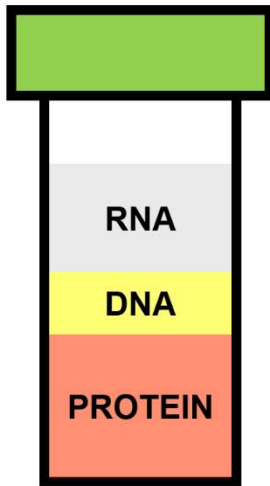
Figure 2.7. The separated layers of RNA, DNA and Protein after centrifugation of homogenised tissue with TRI™ Reagent Solution and chloroform. RNA: Ribonucleic acid; DNA: Deoxyribose nucleic acid.

For RNA isolation, the supernatant was collected into a clean Eppendorf tube. The supernatant was collected carefully without interfering with the interphase layer, as this could lead to a reduction in purity of RNA. 500µl of 2-Propanol per 1ml of TRI™ Reagent Solution was added to the supernatant to precipitate the RNA from the aqueous phase. Samples were inverted gently before centrifuging at 13,000rpm for 10 minutes at 2°C to 8°C. The supernatant was discarded, and the pellet was washed with 1ml 75% ethanol per 1ml of TRI™ Reagent. The solution was washed by vortexing briefly. The sample was then centrifuged at 13,000rpm for 5 minutes at 2°C to 8°C. The supernatant was discarded and the pellet was air-dried for 30 minutes at room temperature before diluting and solubilizing the pellet with Nuclease-free water. Depending on pellet size, the amount of Nuclease-free water used to dissolve the pellet varied between 10µl to 100µl. Dissolving the pellet with Nuclease-free water based on size ensured accurate readings on the Nanodrop ND-1000 spectrophotometer V3.5 (Fisher Scientific) and RNA concentrations were no more that 1500ng/µl, to avoid pipetting extreme small amounts for cDNA synthesis.

2.2.4.3. RNA quantification

To quantify RNA to determine the amount of total RNA for gene expression analysis procedures, the Nanodrop ND-1000 spectrophotometer V3.5 (Fisher Scientific) was used (Figure 2.8). The concentration of RNA (ng/µl) present in a sample was determined by measuring the absorbance between 260nm and 280nm by UV spectroscopy as calculated

using Beer-Lambert's law. An absorbance at 260nm (A260) reading of 1.0 equates to ~40 µg/ml of single-stranded RNA. The A260/A280 ratio is used to determine the purity of RNA, with a ratio of ~2.0, indicating RNA with high purity. If the ratios are lower, this may indicate presence of phenol, protein or other contaminants that may absorb ~280nm. The A260/A230 ratio is another test for purity of RNA. After initialising the instrument, a blank is read. This is 1µl of elution buffer, in this case Nuclease-free water. This reading is a reference and when a sample is measured, the light intensity transmitted through the sample is recorded, using the following calculation, computed by the machine:

Beer-Lambert's law to correlate absorbance with concentration:

Absorbance = -log (Intensity of the sample/Intensity of the blank)

$$A = E * b * c$$

A: absorbance; E: wavelength-dependent molar absorptivity coefficient (litre/mol-cm); b: path length (cm); c: molarity (M)

Figure 2.8. Use of Nanodrop ND-1000 spectrophotometer V3.5. 1µl of sample/blank is pipetted on the receiving fibre of the lower pedestal **(A-B)**. When the sampling arm is lowered with the source fibre and 'measure' is selected on the software on the connected computer, this initiates a spectral measurement with a pulsed xenon lamp providing a source of light. The spectrometer uses a linear charged-couple device to analyse light passing through the sample **(C)**. The detection limit for RNA is between 2ng/µl and 3000ng/µl. RNA: Ribonucleic acid

2.2.5. cDNA synthesis

The Applied Biosystem™ High-Capacity cDNA Reverse Transcription Kit allows the reverse transcription of 2µg of total RNA to be synthesised to single stranded cDNA in a total reaction volume of 20µl, for subsequent qPCR procedures. The random primer method was used to initiate the synthesis of cDNA and to ensure the synthesis of the first strand ensues efficiently. Via reverse transcription, DNA is synthesised from an RNA template to produce cDNA. Complementary DNA (cDNA) is superior to RNA in stability and its resistance to degradation, thus is used to perform a polymerase chain reaction (PCR), being amplified during the process. Reverse transcription uses a short primer, which is complementary to the 3' end of RNA, and an RNA template to directly synthesis the first strand of cDNA. This can be used immediately as a template for PCR. This allows the detection of a low yield of RNA in samples and amplification of cloning gene copies.

To ensure that RNA has no RNase activity, Invitrogen™ RNaseOUT™ Recombinant Ribonuclease Inhibitor (40U/µL) was added to the reaction mix (Table 2.6). This inhibitor is active against RNases A, B and C and protects mRNA, whilst improving the total yield and length of cDNA.

Total RNA was reverse transcribed using the High-Capacity cDNA Reverse Transcription Kit (Fisher Scientific), following the instructions as suggested by the manufacturer. The following conditions in Table 2.7 were used to synthesise 500ng and 1000ng cDNA, using the T100™ Thermal cycler (Catalogue number: 186-1096, Bio-Rad). Samples and controls were prepared in PCR tubes, using the master mix stated in Table 2.6, and the volume of Nuclease-free water was adjusted depending on the concentration of RNA. A negative template control (NTC) was prepared by adding the master mix and Nuclease-free water, to act as a general control for nucleic acid contamination. A no reverse transcriptase control (NRT) was prepared by adding master mix, without the MultiScribe™ Reverse Transcriptase, plus an RNA sample. This control determines if there is any DNA contamination which may have occurred during RNA isolation.

Table 2.6. Preparation for 1X Reverse Transcription (RT) master mix

Component	Volume (µl)
10X RT Buffer	2.0
25X dNTP Mix (100mM)	0.8
10X RT Random Primers	2.0
MultiScribe™ Reverse Transcriptase (50U/µl)	1.0
Invitrogen™ RNaseOUT™ Recombinant Ribonuclease Inhibitor (40U/µl)	0.5
Nuclease-free water	8.0
Total volume	14.3

Table 2.7. Settings for T100™ Thermal cycler to perform cDNA synthesis

Settings	Step 1	Step 2	Step 3	Step 4
Temperature (°C)	25	37	85	4
Time (minutes)	10	120	5	∞

To prepare a total volume of 500ng of cDNA in 20µl:

500(ng)/RNA concentration (ng/µl). For example, 500(ng)/800(ng/µl) = 1.2µl of RNA needed.

In a PCR tube, add 14.3µl of master mix, plus 1.2µl of RNA and adjust volume with Nuclease-free water to 20µl, in this case, 4.5µl.

2.2.6. RT-qPCR

Real Time quantitative Polymerase Chain Reaction (RT-qPCR) is used to study the changes in gene expression of cDNA in samples. The genes expressed document the static event that has happened in the cell and is associated with mRNA level changes.

A two-step RT-qPCR was performed for gene expression analysis (Figure 2.9). This involved a multitude of DNA denaturation cycles at certain temperatures to increase the number of gene copies. In RT-qPCR, fluorescent reporters monitor the PCR product, with the amount of fluorescence emitted from the fluorophore proportional to the amount of amplicon.

The Applied Biosystems™ TaqMan™ Gene Expression Assays (Table 2.8) used in PCR contain a reporter dye, in this case FAM™. This is linked to a non-fluorescent quencher (NFQ), at the 5' end. A minor groove binder (MGB) is located at the 3' end of the probe and is attached to the NFQ (Figure 2.10).

In PCR, there are three phases that occur, including exponential, linear and plateau. The exponential phase provides the most accurate quantitative data output. During this phase, the MyiQ™ Single-Colour Real-Time PCR Detection System (Catalogue number: 170-9740, Bio-Rad) detects the fluorescence and calculates the threshold. The threshold is the detection level that achieves a fluorescent intensity above the background. When the sample reaches this threshold, this is termed the cycle threshold (Ct). As soon as the exponential phase is reached, the threshold is drawn manually of accuracy for each sample (Figure 2.11). The filter-based optical design of PCR allows the optimum light wavelength for excitation and emission, allowing optimal discrimination between fluorophores.
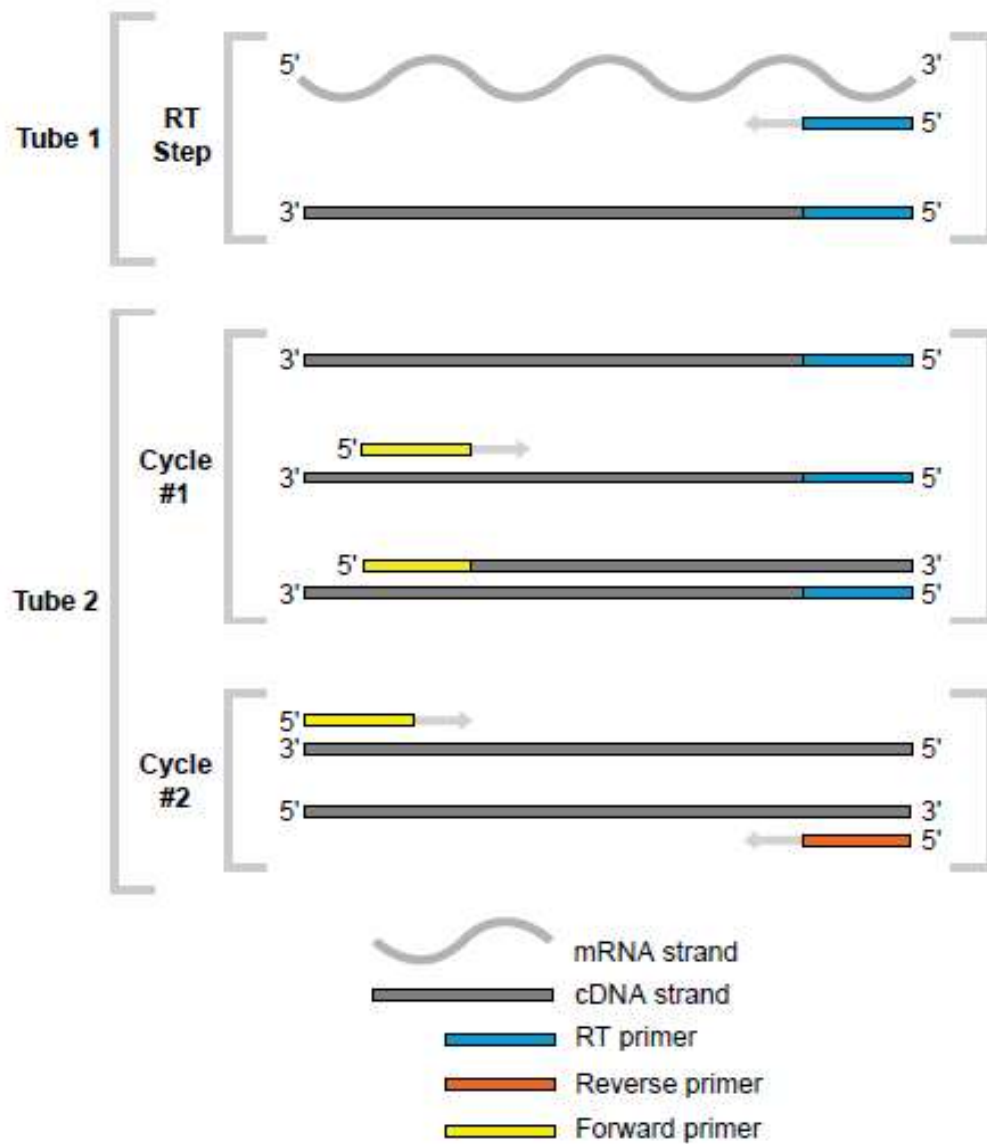
Figure 2.9. Two-step RT-qPCR. Reverse transcription and PCR amplification steps are performed in separate reactions. This is a useful process for detecting a variety of gene transcripts from a sample. The reverse transcription is initially primed with random primers, which bind across the length of mRNA, resulting in RNA being transcribed. RT: Real Time; q: quantitative; PCR: Polymerase Chain Reaction; (m)RNA: (messenger) ribonucleic acid.

Step 1. Polymerization: A fluorescent reporter (R) dye and a quencher (NFQ) are attached to the 5' and 3' ends of a TaqMan® probe, respectively.
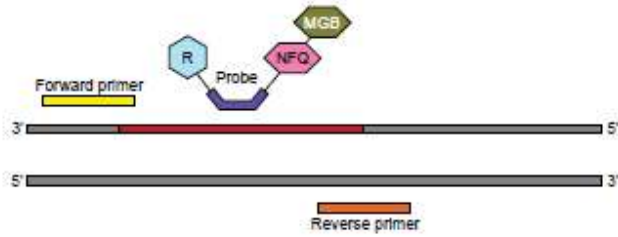
Step 2. Strand displacement: When the probe is intact, the reporter dye emission is quenched.
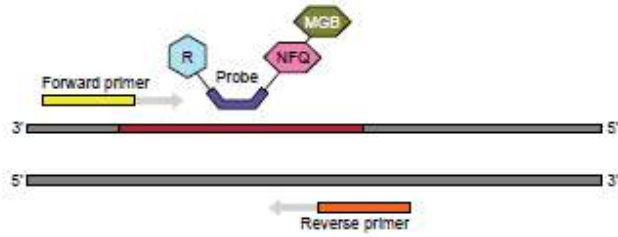
Step 3. Cleavage: During each extension cycle, the DNA polymerase cleaves the reporter dye from the probe.
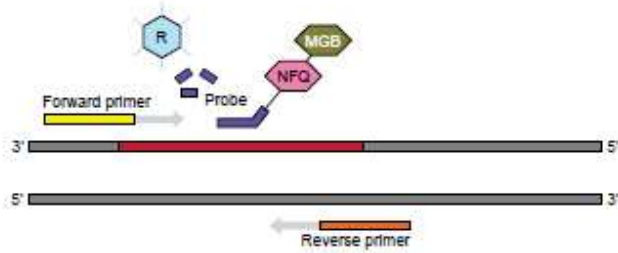
Step 4. Polymerization completed: After separation from the quencher, the reporter dye fluoresces.
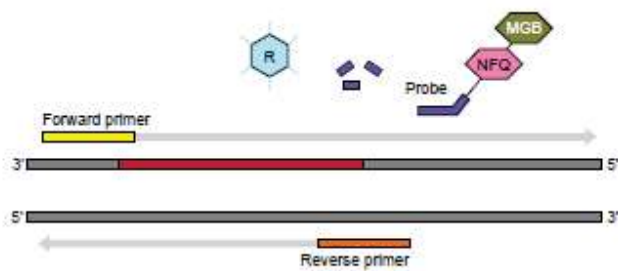
Figure 2.10. The chemistry behind TaqMan probe-based assays. R: Fluorescent reporter;

NFQ: Non-fluorescent quencher; MGB: Minor groove binder
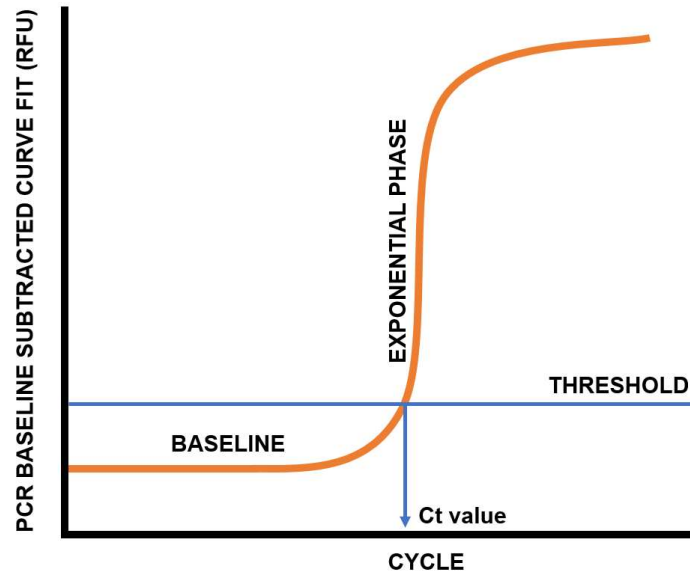
Figure 2.11. RT-qPCR amplification output graph. RT-qPCR: Real time-quantitative Polymerase Chain Reaction; RFU: Relative Fluorescence Units; Ct: Cycle threshold

Table 2.8. Concentration of Applied Biosystems™ TaqMan™ Gene Expression Assay FAM-MBG

Concentration					
Forward primer		**Reverse primer**		**Probe**	
1X	**20X**	**1X**	**20X**	**1X**	**20X**
900nM	18µM	900nM	18µM	250nM	5µM

To prepare cDNA for PCR:

For example, to prepare 30ng of cDNA (6ng/ul) from 500ng/20µl

C: concentration; V: volume

C1V1 = C2V2

500ng x 5µl = 30ng x V2

(500ng x 5µ) / 30ng = V2

83.3µl = V2 final volume

83.3µl - 20µl = 63µl of Nuclease-free water needed to dilute sample

Each well of a Thermo Scientific™ PCR Plate (96-wells) contained 5µl of diluted cDNA and 15µl of the master mix, as stated in Table 2.9. Plates were sealed with sealing tape and centrifuged for 2 minutes at 1200rpm. Any bubbles after centrifugation were removed, as these disturb results, by flicking the bottom of the wells. Plates prepared throughout the day were kept in the fridge for later use. qPCR Probe Mix No-ROX (PCR biosystems) was used to determine the expression of genes of 30ng cDNA on the MyiQ™ Single-Colour Real-Time PCR Detection System (Catalogue number: 170-9740, Bio-Rad) with the following conditions stated in Table 2.10. The fold change in mRNA was calculated by the comparative method ($2^{-\Delta\Delta}$ Ct method) (Pfaffl, 2001) and using a housekeeping gene to normalise the data for all samples. Readings were prepared in duplicates (20µl per reaction).

$2^{-\Delta\Delta}$ Ct method is as follows:

1) To determine ΔCt: Mean Ct of target gene – Mean Ct of housekeeping gene

2) To determine ΔΔCt: ΔCt of sample – Mean ΔCt of control group

3) To determine $2^{-\Delta\Delta}$Ct (fold change in mRNA expression): 2^-ΔΔCt

Table 2.9. Preparation for cDNA synthesis mix

Reagent	Per reaction (µl)
Template cDNA (~30ng)	5
Applied Biosystems™ TaqMan™ Gene Expression Assay FAM-MBG	0.8
2x qPCRBIO Probe Mix	10
Nuclease-free water	4.2
Final volume	20

Table 2.10. Settings for MyiQ™ Single-Colour Real-Time PCR Detection System to perform RT-qPCR

Settings	1 cycle	40 cycles	40 cycles
Temperature (°C)	95	95	60
Time (seconds)	120	5	25

2.2.7. Triglyceride extraction

Triglycerides (TGs) are esters which are derived from a chain of three fatty acids and one glycerol molecule. They are the main components of vegetable oils, adipose tissue in animals and cholesterol, playing a vital role in energy metabolism. Elevated levels of TGs are associated with metabolic diseases such as cardiovascular disease.

2.2.7.1. Triglyceride extraction from cell lysates

Experiments were seeded in a 6-well plate for TG extraction to provide an optimal number of cells for sufficient TG yield. Media was discarded and cells were washed with 1ml PBS. 90μl of a non-ionic emulsifier and surfactant to solubilize proteins, 5% Triton™ X-100, was added to the wells. Cell lysates were harvested by scrapping the cells with a cell scraper.

TG content was determined using Triglyceride Reagent (TR) and Free Glycerol Reagent (FGR) (Table 2.11), using the protocol as recommended by Sigma's Serum Triglyceride Determination Kit (Catalogue number: TR0100). This kit quantitatively measures the amount of TGs at an absorbance of 540nm. As TGs do not occur freely, but are bound to surface proteins, this method involves enzymatic activity to determine TG quantification as demonstrated in Figure 2.12. TR includes lipases to hydrolyse TG to glycerol and FGR uses coupled enzyme reactions which cause an increase in absorbance, directly proportional to glycerol concentration. This is essential to detect hydrolysed TGs by colourimetric assessment.

To perform the Serum Triglyceride Determination Assay:

FGR is reconstituted with 40ml of ddH$_2$O and TR is reconstituted with 10ml of ddH$_2$O and mixed by inversion. These reagents, as well as the UltraPure™ Glycerol stock solution, are stored at 4°C, but must equilibrate to room temperature before performing the assay,

To prepare 1ml of 5% Triton™ X-100. The solution was vortexed until Triton™ X-100 was fully dissolved:

- 50µl of Triton™ X-100

- 950µl of ddH$_2$O

Triglycerides $\xrightarrow{\text{Lipoprotein Lipase}}$ Glycerol + Fatty acids

Glycerol + ATP $\xrightarrow{\text{GK}}$ G-1-P + ADP

G-1-P + O$_2$ $\xrightarrow{\text{GPO}}$ DAP + H$_2$O$_2$

H$_2$O$_2$ + 4-AAP + ESPA $\xrightarrow{\text{POD}}$ Quinoneimine dye + H$_2$O
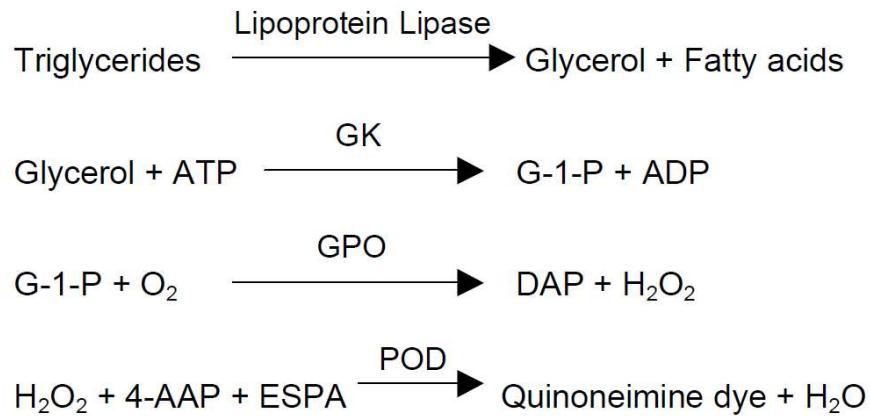
Figure 2.12. Triglyceride Assay Enzymatic Reaction. ATP: Adenosine triphosphate; GK: Glycerol kinase; G-1-P: Glucose-1-phosphate; ADP: Adenosine diphosphate; O$_2$: Oxygen; GPO: Glycerol phosphate oxidase; DAP: dihydroxyacetone phosphate; H$_2$O$_2$: Hydrogen peroxide; 4-AAP: 4-aminoantipyrine; ESPA: sodium N-ethyl-N-(3-sulfopropyl); POD: Peroxidase; H$_2$O: water.

To prepare UltraPure™ Glycerol (density of 1.26 g/ml) stock concentration of 136.8mM (12.6mg/ml) (1:100 dilution), dilute 0.5ml of UltraPure™ Glycerol in 49.5ml of ddH$_2$O.

To prepare UltraPure™ Glycerol working concentration of 2.85mM (0.26mg/ml) (1:50 dilution), dilute 0.1ml of 136.8mM UltraPure™ Glycerol stock solution in 4.7ml of ddH$_2$O.

Table 2.11. Preparation of reagents for Triglyceride extraction from cell lysates

Volume (µl) per sample	Triacylglycerol Working Reagent (TWR)	Triacylglycerol Reagent Blank (TRB)
FGR	320	320
TR	80	N/A
ddH$_2$O	N/A	80

Cell lysate homogenisation was achieved by using BD™ Microlance™ Stainless Steel Needles (25G 25mm) attached to a BD Plastipak Syringe (1ml) and passing through the sample 10 times. The homogenised solution was heated to 95°C for 5 minutes to denature samples and vortexed for 2 seconds and heated again for 10 minutes at 95°C using Fisherbrand™ Isotemp™ Digital Dry Bath/Block Heater (Product code: 15387928, Fisher Scientific). This was repeated once more. The samples were then centrifuged for 5 minutes at 14,000rpm and the supernatant was collected. 400µl of TWR and 4µl of ddH$_2$O (blank), standard or samples were prepared in Eppendorf tubes. 400µl of TRB and 4µl of ddH$_2$O (blank), standard or samples were prepared in Eppendorf tubes. This was incubated for 5 minutes at 37ºC in an incubator. 180µl from each Eppendorf tube was pipetted into a 96-well micro test plates (F-bottom) in duplicates and absorbances were read at 540nm on SPECTRAmax® 190 Microplate Spectrophotometer (Part number: 0112-0085, Molecular Devices Corporation), using SOFTmax PRO software. All values were corrected to the blank absorbance and TG concentration was normalised to total cellular protein concentration, as determined by bicinchoninic acid (BCA) method (see section 2.2.9).

To determine all readings, the average absorbance for each blank, standard and sample were calculated. To correct the readings, the average absorbance reading of the blank was subtracted from the average absorbance reading for standards and samples.

Calculations to determine TG content:

Total TG concentration (equivalent triolein concentration):

((Average Sample Absorbance – Average Blank Absorbance) * 2.5 mg/ml triolein)) /

(Average Standard Absorbance – Average Blank Absorbance)

Glycerol concentration (equivalent triolein concentration):

((Average Sample Absorbance – Average Blank Absorbance) * 2.5 mg/ml triolein)) /

(Average Standard Absorbance – Average Blank Absorbance)

To determine the true TG concentration:

Total TG concentration (mg/ml) - Glycerol concentration (mg/ml)

To convert equivalent triolein concentration from mg/ml to mM, the concentration (mg/ml) is multiplied by 1.13.

To normalise TG concentration to protein, the determined protein concentration (µg/µl) was multiplied by 100 (µg) and TG (mM) was divided by protein (µg). These values should be lower than 10mg/ml as the Triglyceride Reagent is linear.

2.2.7.2. Triglyceride extraction from frozen heart tissue

Triglyceride concentrations from frozen heart tissue was determined (colourimetric detection) using the Triglyceride Quantification Kit (Sigma-Aldrich). TGs are converted to free fatty acids and glycerol, which is then oxidised to produce a colourimetric product, to detect between the range of 2mM and 10,000mM TGs. Before use, vials were centrifuged briefly, and the Triglyceride Assay Buffer was equilibrated at room temperature. The Triglyceride Probe was warmed at 37ºC for 5 minutes to melt the solution, prior to use. The Triglyceride Enzyme Mix was reconstituted with 220µl of Triglyceride Assay Buffer. The lipase solution was reconstituted in 220µl of Triglyceride Assay Buffer.

The Triglyceride Standard solution vial was placed in the Fisherbrand™ Isotemp™ Digital Dry Bath/Block Heater (Product code: 15387928, Fisher Scientific), at 100ºC for 1 minute. The

solution turned cloudy in appearance. This was vortexed for 30 seconds until the solution became clear. The heating and vortexing steps were repeated once more. The values obtained from the Triglyceride standard, as prepared in Table 2.12, was used to plot a standard curve (Figure 2.13). The amount of the TG present in the samples and blanks (Table 2.13), in duplicates, was determined from the curve.

To prepare 5% Nonidet P-40 (NP-40) Substitute conc:

0.5ml of NP-40 was added to 9.5ml of ddH_2O and vortexed.

To prepare 500µl 0.2mM standard solution in Eppendorf tubes from Triglyceride standard stock (1mM):

- 100µl of Triglyceride standard
- 400µl of Triglyceride Assay Buffer

Frozen heart tissue extracts of ~20mg were sectioned and transferred to a MP Biomedicals™ Lysing Matrix D tube in a solution of 200µl 5% Nonidet P-40 (NP-40) Substitute conc, used to solubilise membrane proteins. This was homogenised using the MP Biomedicals™ FastPrep-24™ 5G Instrument (Product code: 15260488, Fisher Scientific) and settings stated in Table 2.5. The homogenised sample was transferred to a clean Eppendorf tube, heated to 90°C for 5 minutes, using Fisherbrand™ Isotemp™ Digital Dry Bath/Block Heater (Product code: 15387928, Fisher Scientific) until the NP-40 substitute became cloudy. Samples were cooled to room temperature for 5 minutes. The heating process was repeated once more to solubilize triglycerides. Samples were centrifuged for 2 minutes at 14,000rpm and supernatants containing the triglycerides were collected and diluted 10-fold.

The Nunc™ MicroWell™ 96-Well Microplate was incubated for 60 minutes at room temperature, protected from light and absorbances were read at 570nm on the SPECTRAmax® 190 Microplate Spectrophotometer (Part number: 0112-0085, Molecular Devices Corporation) using SOFTmax PRO software. Readings were performed in duplicates.

Table 2.12. Preparation of Triglyceride standard curve from 0.2mM standard solution

Nmole/well	0.2mM standard solution (µl)	Triglyceride Assay Buffer (µl)	Final volume added to wells (µl)
0	0	150	50
2	30	120	50
4	60	90	50
6	90	60	50
8	120	30	50
10	150	0	50

To prepare 50µl of Master Reaction Mix per reaction:

- 46µl of Triglyceride Assay Buffer
- 2µl of Triglyceride Probe
- 2µl of Triglyceride Enzyme Mix

All values were corrected to the blank absorbance and TG concentration was normalised to the depot weight.

Table 2.13. Preparation of blank and samples for Triglyceride quantification

	Volume per sample (µl)	Triglyceride Assay Buffer (µl)	Lipase (µl)	Final volume (µl)
Blank (5% NP-40)	10	42	0	52
Sample (1:10)	10	40	2	52

Calculations to determine TG content:

To determine all readings, the average absorbance for each blank, standard and sample were calculated.

To correct the samples from the blank:

Average Sample Absorbance – Average Blank Absorbance

To determine amount of TG (nmole) in samples determined from standard curve:

Corrected Absorbance / Slope of line

To determine concentration of TG (nmole/µl):

Amount of TG in sample (nmole) from standard curve / Sample volume added into wells

This value is then multiplied by the dilution factor, i.e. 10. To convert equivalent triolein concentration from nmole/µl to ng/µl, the concentration (nmole/µl) is multiplied by the TG (triolein) molecular weight, 885.4g/mole. TG concentration (ng/µl) was divided by depot weight (~20mg).

Figure 2.13. Triglyceride standard curve for colourimetric detection. The standard curve was prepared by plotting the value of the average blank minus the corrected 570nm read-out for each Triglyceride standard versus concentration (nmole/well). The standard curve was used to determine the Triglyceride concentration of each unknown sample.

2.2.8. Protein extraction from frozen gonadal white adipose tissue

Genes contain the material and information to produce proteins with specific structures to carry out functions in the cell. Unlike research into gene expression analysis, protein analysis is more complex due to the diversity of proteins' structure.

To prepare 10X Protease/Phosphatase Inhibitors (4°C), stored at -20°C when diluted:

- 1 tablet in 1ml ddH$_2$O

To prepare 1X RIPA lysis buffer, stable for 1 month at 4°C:

- 100µl of 10X RIPA buffer (4°C)

- 100µl of 10X Thermo Scientific™ Pierce™ Protease Inhibitor Mini Tablet

- 100µl of 10X Thermo Scientific™ Pierce™ Phosphatase Inhibitor Mini Tablet

- Adjust volume to 1ml with ddH$_2$O

To lyse tissues for the extraction of protein, 5µl of cold 1X Radioimmunoprecipitation assay (RIPA) buffer, containing Thermo Scientific™ Pierce™ Protease Inhibitor Mini Tablets and Thermo Scientific™ Pierce™ Phosphatase Inhibitor Mini Tablets, to prevent proteolysis and maintain the phosphorylation status of proteins, per 1mg of gonadal white adipose tissue (gWAT) was used. Samples were vortexed, embedded in ice and sonicated at 60% amplitude, 10 seconds on and 10 seconds off for 1 minute on ice using Sonics Vibra-Cell Autotune series high intensity ultrasonic processor (Model CV18, Serial Number 9733, Sonics). This process was repeated two more times (or until full homogenisation) and vortexed between sonication cycles. Samples were centrifuged between 2°C to 8°C at 13000rpm for 30 minutes. The supernatant was collected for protein quantification using Thermo Scientific™ Pierce™ BCA Protein Assay Kit, read at 562nm, using the SPECTRAmax® 190 Microplate Spectrophotometer (Part number: 0112-0085, Molecular Devices Corporation) and SOFTmax PRO software.

2.2.9. Protein quantification

The concentration of protein levels in a sample were determined using the Thermo Scientific™ Pierce™ BCA Protein Assay Kit by colourimetric product. This kit combines the reduction of Cu^{2+} to Cu^{1+} protons and the colourimetric detection of cuprous cation (Cu^{1+}) by bicinchoninic acid (BCA). Firstly, the biuret reaction is achieved by peptides in proteins forming a coloured complex with cupric ions in an alkaline environment. Secondly, BCA reacts with the reduced cation (Cu^{1+}) to form a purple/blue coloured reaction. This displays a strong positive linear absorbance at 562nm.

Preparation of blanks, samples and albumin standards (ratio to working reagent (WR) of 1:8) were prepared as stated in Table 2.14 and Table 2.15. Protein concentration of samples were determined using a standard curve (Figure 2.14). Tubes were mixed well by inversion and incubated for 30 minutes at 37ºC. After incubation, 180µl of blank, standards and samples were pipetted in duplicates in a 96-well plate. The plate was read at 562nm with the SPECTRAmax® 190 Microplate Spectrophotometer (Part number: 0112-0085, Molecular Devices Corporation), using SOFTmax PRO software.

Calculations to determine protein concentration:

To correct the samples from the blank:

Average Sample Absorbance – Average Blank Absorbance

To determine amount of protein (µg/µl) in samples determined from standard curve:

(Corrected Absorbance /Slope of line)/volume of blank or sample (2.5µl))

To prepare the working reagent (WR), mix 50 parts of Reagent A with 1 part of Reagent B (1:50)

Table 2.14.   Preparation of Bovine Serum Albumin (BSA) standards from 2mg/ml Albumin Standard

Concentration (µg/ml)	ddH$_2$O (µl)	2mg/ml Albumin Standard (µl)	Concentration (µg) in 2.5µl
0	80.00	0.00	0.00
20	79.20	0.80	0.50
50	78.00	2.00	1.25
100	76.00	4.00	2.50
200	72.00	8.00	5.00
400	64.00	16.00	10.00
800	48.00	32.00	20.00
1000	40.00	40.00	25.00
1200	32.00	48.00	30.00

Table 2.15. Preparation of blanks, samples and standards for protein quantification

	Volume (µl)	Working reagent (µl)	ddH$_2$O (µl)
Blank (lysis buffer)	5	400	45
Standard	50	400	0
Sample	5	400	45

Protein standard curve
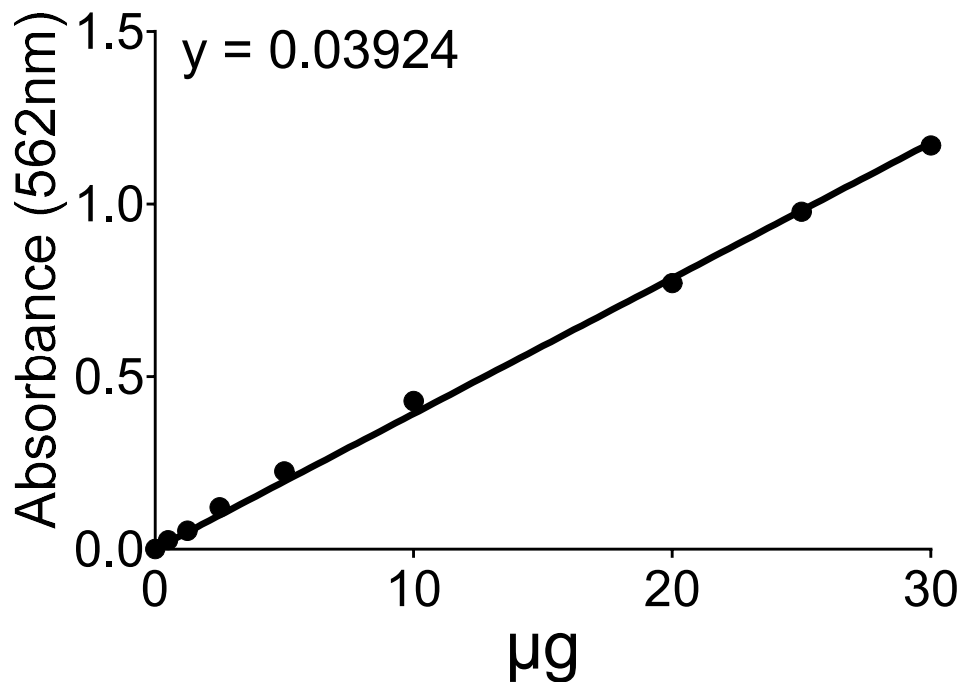
Figure 2.14. Protein standard curve for colourimetric detection. A standard curve was prepared by plotting the value of the average blank minus the corrected 562nm read-out for each albumin standard versus the concentration (μg). The standard curve was used to determine the protein concentration of each unknown sample.

2.2.10. Western blot

Western blots (Burnette, 1981) are used to detect the abundance of desired proteins by sodium dodecyl sulphate-polyacrylamide gel electrophoresis (SDS-PAGE). Smaller proteins migrate at a faster rate than larger proteins, with polyacrylamide acting as a mesh for this separation to occur. SDS binds to proteins and with the help of reducing agents, such as DTT, disulphide bonds are cleaved to result in an unfolded, linear negatively charged protein. Once this occurs, the polypeptides are transferred to a nitrocellulose membrane via immunoblotting and an electric current. Next, the membrane is blocked to prevent non-specific binding of antibodies in the following antibody incubation stages.

To prepare 10% running gel (per gel):

- 2ml of ddH$_2$O

- 1ml of Alfa Aesar™ Acrylamide/Bisacrylamide 37.5:1, 40% soln

- 1ml of 1.5M Tris (pH 8.8)

- 40µl of 10% SDS

- 20µl of 10% APS

- 6.7µl of TEMED

To prepare the stacking gel (stored at 4°C):

- 6ml of Alfa Aesar™ Acrylamide/Bisacrylamide 37.5:1, 40% soln

- 6.25ml of 1M Tris (pH 6.8)

- 250µl of 20% SDS

- Adjust volume to 50ml with ddH$_2$O

To prepare the working stacking gel, 2ml of refrigerated stacking gel was used with the addition of APS and TEMED (same volume as the running gel).

To prepare 1X Running Buffer:

- 6g of Tris base (final concentration of 0.005M)

- 28.8ml of Glycine (final concentration of 0.04M)

- 10ml of 10% SDS (final concentration of 1%)

- Adjust volume to 1L with ddH$_2$O

To prepare 5X Loading Buffer (stored at -20°C):

- 3.2ml of Tris 1M (pH 6.8) (final concentration of 320mM)

- 1g of SDS (final concentration of 10%)

- 5ml of Glycerol (final concentration of 50%)

- 25mg of Bromophenol blue (final concentration of 0.25%)

- Adjust volume to 10ml with ddH$_2$O

Add 100µl of 1M DTT per 1ml 5X Loading Buffer

To prepare 1X Transfer/Blotting Buffer:

- 3g of Tris base (final concentration of 0.012M)

- 14.4g of Glycine (final concentration of 0.10M)

- 10ml of 10% SDS (final concentration of 0.1%)

- 200ml of Methanol (final concentration of 10%)

- Adjust volume to 1L with ddH$_2$O

To prepare 10X Tris-Buffered-Salines (TBS) (pH 7.6)

- 2.42g of Tris base

- 8g of Sodium Chloride (NaCl)

- Adjust pH to 7.6 with hydrochloric acid (HCL)

- Adjust volume to 100ml with ddH$_2$O

To prepare Washing Buffer (1X TBS-T):

- 10ml of 10X TBS

- 500µl of 20% TWEEN® 20

- Adjust volume to 100ml with ddH$_2$O

To prepare Milk Blocking Buffer:

- 5ml of 10X TBS (final concentration of 1X TBS)

- 250µl of 20% Tween-20 (final concentration of 0.1%)

- 2.5g of non-fat (skimmed) dry milk (final concentration of 5%)

- Adjust volume to 50ml with ddH$_2$O

To prepare BSA Blocking Buffer:

- 5ml of 10X TBS (final concentration of 1X TBS)

- 250µl of 20% Tween-20 (final concentration of 0.1%)

- 2.5g of Bovine Serum Albumin (BSA) (final concentration of 5%)

- Adjust volume to 50ml with ddH$_2$O

To ensure complete dissolution of solution, leave at 4°C for BSA to dissolve without agitation

To prepare protein samples, protein samples were vortexed and 20µg of sample was prepared with 5X Loading buffer, containing 1M DTT, and lysis buffer. The samples were heated at 100°C for 5 minutes using Fisherbrand™ Isotemp™ Digital Dry Bath/Block Heater (Product code: 15387928, Fisher Scientific) and centrifuged briefly.

To prepare Coomassie stain:

- 1g of Coomassie (final concentration 0.25%)

- 250ml of methanol (final concentration 50%)

- 50ml of acetic acid (final concentration 10%)

- Adjust volume to 500ml with ddH$_2$O

To prepare Coomassie de-stain:

- 40ml of methanol

- 10ml of acetic acid

- 50ml of ddH$_2$O

Sodium dodecyl sulphate-polyacrylamide gel electrophoresis (SDS-PAGE)

Firstly, the 0.75mm glass plates were cleaned with 75% ethanol and wiped dry with a tissue. They were placed in the supports and fixed with the green supporter clips. A buffer dam was used if only one gel was being run. The running gel was prepared as stated, with APS and TEMED added only prior to pouring the gel in a 15ml tube. The gel was mixed well and 4ml was poured in between the plates. Some solution was left in the tube to check polymerisation. 1ml ddH$_2$O was added on top of the setting running gel to prevent contact of the gel with air, as this inhibits polymerisation. Once the running gel had polymerised, ddH$_2$O was retired and excess water was dried between the plates with a paper towel to ensure all ddH$_2$O was removed. The stacking gel was prepared, mixed well and immediately added to the top of the running gel and the comb was placed. When polymerised, the comb was retired and the formed wells were washed with distilled water. The plates with the set gels were placed in the supports inside the Mini Trans-Blot® Electrophoretic Transfer Cell (Catalogue numbers: 170-3930, Bio-Rad). Running buffer was used to fill the cell/tank and inside the support/gels, as well as washing the formed wells.

20µl of samples and 10µl of Thermo Scientific™ PageRuler™ Unstained Broad Range Protein Ladder was loaded. The inside of the cassette was topped up with running buffer. Cables were placed and the gel was run at fixed 120V for 1 hour.

Coomassie staining (optional)

To check the integrity of the protein extraction, the gel was stained with Coomassie for 30 minutes to 1 hour, on agitation. To de-stain, Coomassie de-stain was added for 30 minutes to 1 hour or overnight, until the bands were visible. The gel was imaged using the Syngene™ G:BOX Chemi XX9 (Product code: 15859922, Fisher Scientific), using the software GeneSys with chemiluminescent image capture (Figure 2.15). If protein quality/integrity was not being assessed, this stage was omitted and the blotting step was performed after electrophoresis.
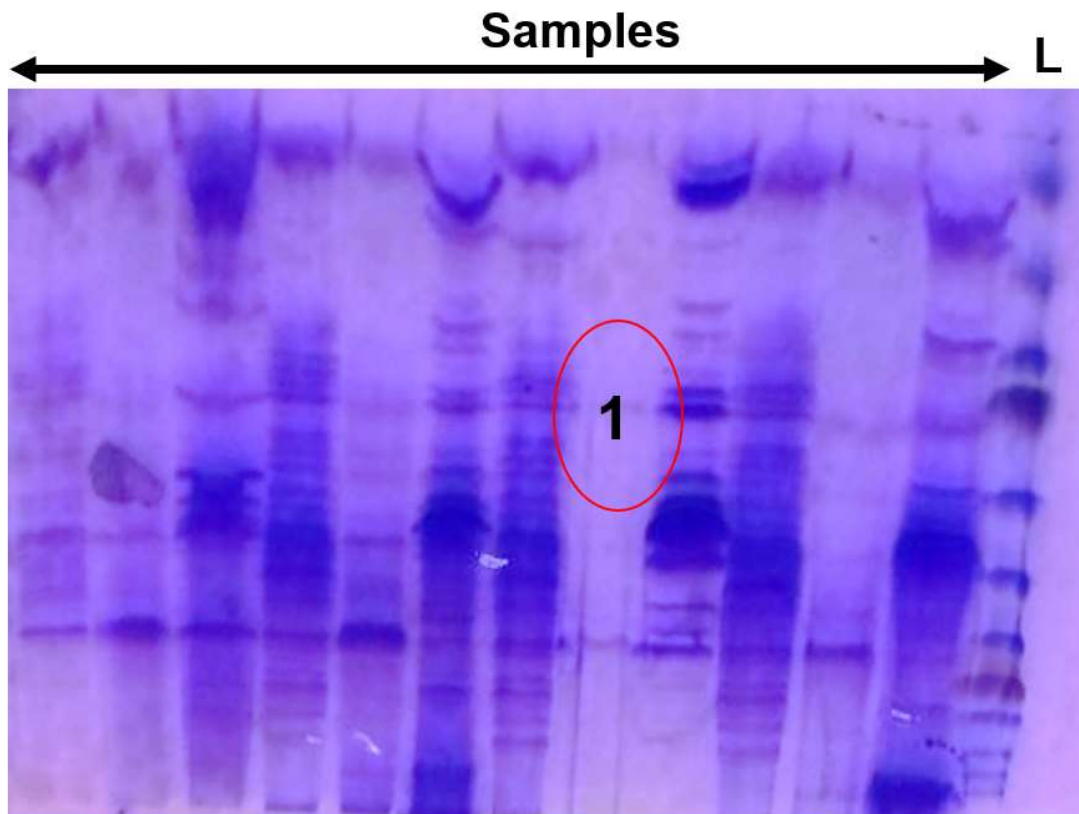
Figure 2.15. Coomassie stain. The integrity of proteins extracted from tissue was determined by staining SDS-PAGE gels with Coomassie dye. This binds to basic amino acids in proteins. Samples with visible bands were used for Western blots, however, samples with almost invisible bands (1) were considered as 'degraded' and re-extracted for protein from the original tissue. SDS-PAGE: Sodium dodecyl sulphate-polyacrylamide gel electrophoresis; L: Ladder.

Blotting: Transferring the protein from gel to the membrane

The blotting procedure was performed under wet conditions. The GE Healthcare Whatman™ Gel Blotting Paper Grade GB003 was cut to 7.5cm x 9.5cm and the Supported Nitrocellulose Membrane was cut to 7cm x 9cm and soaked in cold transfer buffer. After electrophoresis, the gel was removed from the glass plates using a spatula and the wells were cut off. The top left corner of the membrane was notched to indicate orientation. The sandwich (Figure 2.16) was prepared in transfer buffer. The cassette was locked and placed in the transfer apparatus, on top of a magnetic stirrer. Transfer buffer was added, and an ice pack was placed inside the apparatus to prevent heat build-up. The transfer was run at fixed 350mA for 1 hour.
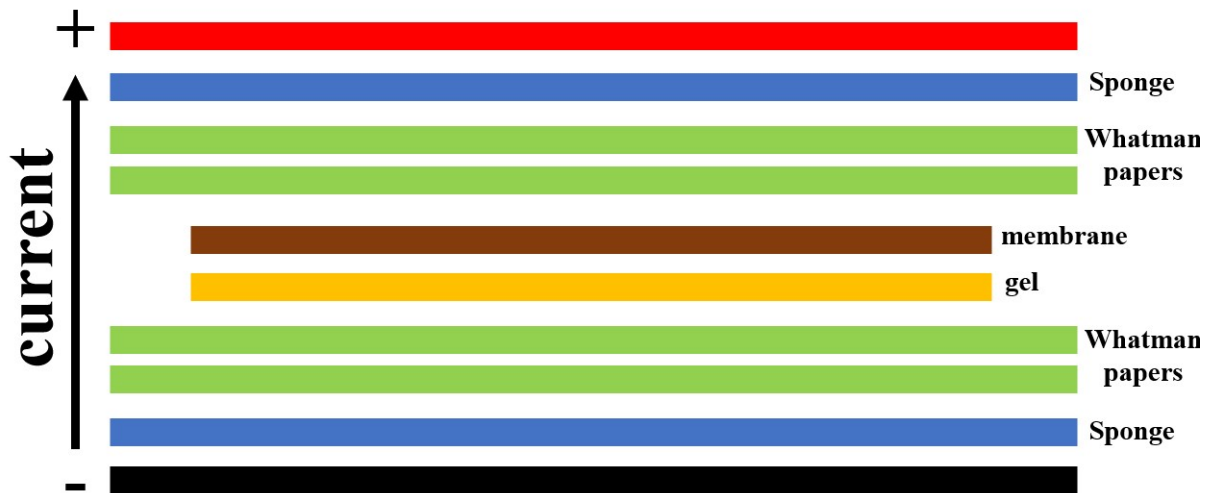
Figure 2.16. Preparation of sandwich for electrophoresis.

Ponceau staining

After the transfer, all layers were removed from the membrane. This was carried out in transfer buffer. As the membrane was removed, it was noted that the proteins have been transferred from the gel to the membrane, with no proteins left on the gel. To determine successful transfer of proteins from gel to membrane, the reversible stain Ponceau was used by binding to positively charged amino acids. The membrane was washed with 1X TBS-T for 5 minutes on agitation and then stained with Ponceau, in agitation, for 5 minutes. Afterwards, the membrane was rinsed with 1X TBS-T until the protein bands were visible to indicate successful protein transfer. The membrane was washed again with 1X TBS-T until Ponceau was no longer visible and the ladder was drawn on with a pencil.

Blocking

The membrane was immersed in blocking solution for 1 hour at room temperature, with agitation, to prevent non-specific binding from occurring in later stages of the Western blot.

Antibody incubation

The blocking buffer was discarded, and the membrane was incubated with primary antibody overnight, in agitation, at 2°C to 8°C. The following day, the antibody solution was discarded, and the membrane was washed with 1X TBS-T thrice for 10 minutes, on agitation. The

secondary antibody (horseradish peroxidase (HRP)-conjugated) was added to the membrane for 1 hour at room temperature. The antibody solution was discarded, and the membrane was washed with 1X TBS-T thrice for 10 minutes, on agitation.

Detection

The developing solution was prepared by adding equal amounts (1:1) of luminol and peroxide buffers. The Thermo Scientific™ SuperSignal™ West Femto Maximum Sensitivity Substrate Kit is a sensitive chemiluminescent substrate system. It has HRP enzymes and allows the detection of low amounts of proteins on membranes probed with antibodies. The solution was added over the whole membrane and left for 5 minutes, without agitation. Excess liquid was removed by dabbing the corner on tissue. The membrane was placed in between two plastic sheets and care was taken to ensure the protein side was dry. Visualisation of membranes were achieved by Syngene™ G:BOX Chemi XX9 (Product code: 15859922,Fisher Scientific), using the software GeneSys with chemiluminescent image capture with selection of the 'visible marker.' Different membranes were imaged separately as signals differ between detected antibodies.

2.2.11. Cytology

2.2.11.1. Oil Red O staining

Oil Red O is a lysochrome dye used to detect lipids present in cells by staining neutral TGs, lipids and cholesterol. To perform Oil Red O staining, Alfa Aesar™ Oil Red O was dissolved in 2-Propanol (0.5% in 2-Propanol) and left overnight, on agitation, to dissolve. The next day, the solution was filtered with a 0.45μM filter and syringe. A working concentration (3mg/ml) of the stain was prepared by diluting the stock solution with ddH$_2$O (3:2 ratio) and filtered again with a 0.45μM filter. Both the stock and working solutions were filtered before each use. Media was removed from cells seeded in a 12-well plate and washed with 1ml PBS for 5 minutes before fixing with 1ml formalin solution (neutral buffered,10%) for 30 minutes. The fixed 3T3-L1 cells were washed with 1ml PBS for 5 minutes thrice after removing formalin, on agitation. 500μl of

3mg/ml Oil Red O was added to the cells for 1 hour at room temperature, on agitation. After discarding the stain, cells were washed with 1ml PBS for 5 minutes thrice and wells were covered with 1ml PBS to prevent cells from drying out. Images were taken with the Nikon TE200 Brightfield Inverted Microscope, at 10x object lens.

2.2.11.2. Oil Red O extraction

To determine the amount of Oil Red O absorbed by the cells, PBS was discarded and cells were air-dried for 5 minutes. Images were taken before eluting the stain. 450µl 2-Propanol was added to each well, on agitation, for 5 minutes. 180µl of elution was read, in duplicates, at 560nm using the SPECTRAmax® 190 Microplate Spectrophotometer (Part number: 0112-0085, Molecular Devices Corporation) and SOFTmax PRO software.

Calculations to determine Oil Red O stain:

The blank used in these experiments were undifferentiated 3T3-L1 cells.

To correct the samples from the blank:

Average Sample Absorbance – Average Blank Absorbance

To normalise Oil Red O data to the control:

Absorbance of sample – Average absorbance readings of control group

To normalise data to cell titre as determined in 2.2.1.4:

Oil Red O data normalised to the control / Cell titre data normalised to the control

2.2.12. Histology

To preserve cells and tissues for histological analysis, gonadal, inguinal and pericardial fat were fixed with 10% neutral buffered formalin. The adipose tissue depots were embedded in Optimal Cutting Temperature (OCT) compound and sectioned between 10µM and 15µM using a Bright 5040 Cryostat (Bright Instruments Limited). Sections were stained with Haematoxylin

and Eosin (H&E) and imaged with a Nikon TE200 Brightfield Inverted Microscope, at x40 objective lens.

Settings for the cryostat:

- Specimen temperature : - 30°C

- Chamber temperature: - 35°C

- 'Continuous' cold temperature

- Motor switches set to 'off' and 'single'

- Blade holder angel at 2.5º

2.2.12.1 Haematoxylin and Eosin

As adipocyte size/volume is altered during normal and obesogenic environments, the general morphology of adipose tissue from mice and presence of brown-like cells within susceptible white depots were observed. Haematoxylin and Eosin (H&E) staining protocol is commonly used as it is quick, inexpensive and simple to perform. Haematoxylin with a combination of metal cations, such as aluminium, is a basic dye that stains acidic structures purple/blue, such as the nuclei of cells. Eosin is acidic and stains basic structures red/pink, such as the cytoplasm and extracellular matrix.

To prepare 1% acid alcohol:

- 49.5ml of 70% Ethanol

- 0.5ml of 37% Hydrochloric Acid (HCl)

To prepare working solution of Scott's tap water:

- 20g of Magnesium Sulphate

- 2g of Sodium Bicarbonate

- Adjust volume to 1 litre with ddH_20

To prepare 1% Eosin from Eosin Y (5w):

- 20ml of Eosin Y

- 80ml of ddH$_2$0

Tissue sections were placed on SuperFrost Plus™ Adhesion slides and air-dried for 10 to 30 minutes before staining with the H&E procedure. Incubations took place in BRAND Coplin Staining Troughs, unless stated otherwise. The backs of slides were rinsed under running tap water for 20 seconds. Slides were incubated with ddH$_2$O for 2 minutes. Drops of Haematoxylin were added to tissue sections for 5 minutes. The backs of slides were rinsed under running tap water for 20 seconds. The tissue sections were differentiated in 1% acid alcohol (8 to 12 dips). Next, bluing of Haematoxylin was achieved by incubating slides in Scott's tap water, which helps minimise the loss of tissues from slides, for 2 minutes. Slides were stained with a few drops of 1% Eosin for 2 minutes. The backs of slides were rinsed under running tap water for 20 seconds. Slides were dehydrated through changes of 70% ethanol for 20 seconds, 90% ethanol for 20 seconds and 100% ethanol for 20 seconds. Next, slides were cleared in 2 changes of xylene, 5 minutes each, to clarify the samples. Slides were air-dried for 10 to 30 minutes and drops of Thermo Scientific 1LT lamb DPX mounting medium was added and coverslips were placed.

To perform analysis with Image-J on captured images (Figure 2.17):

1. File → Open →Select 'Image'

2. Image → Adjust → Brightness/Contrast → Auto

3. Analyze → Set measurements→ Select 'Area' and 'Overlay'

4. Circle the adipocytes and click 'control-M' to measure the area

5. Save area values on the 'results' window to excel

Assuming the shape of adipocytes are spherically, to calculate adipocyte volume, Image-J software was used to determine adipocyte area, as stated below and described by Al-Dibouni et al., (2020).

To determine adipocyte volume from adipocyte area:

$$Radius = \sqrt{(Area/3.14)}$$

$$Radius^3 = Radius\text{^}3$$

$$Volume \ of \ a \ sphere = (4/3)*(3.14*Radius^3)$$

To determine percentage change in adipocyte volume:

$$(Adipocyte \ volume \ / \ Average \ adipocyte \ volume \ of \ control \ group) * 100$$

To assess adipocyte size distribution, raw values of the adipocyte volumes derived from Image-J analysis were used. This was achieved by using the frequency function as an array formula in excel and calculating the percentage of cells present within each cell volume category, also known as a bin, across the adipocyte size spectrum (presented as arbitrary units (a.u.)).

To determine % cells:

$$(Value \ of \ frequency \ / \ frequency \ total) * 100$$

For certain studies, depot weight was measured as it is an indication of the capacity of adipose tissue expandability and associated with metabolic dysfunction. Depot weights were used to determine adipocyte number. This was calculated from the adipocyte volume (presented as arbitrary units) determined using the following equation previously described by Merkestein et al., (2015):

$$Depot \ weight \ (g) \ / \ ((adipose \ tissue \ density \ 0.915 \ g/cm^{-3}) * mean \ adipocyte \ volume \ (a.u.))$$
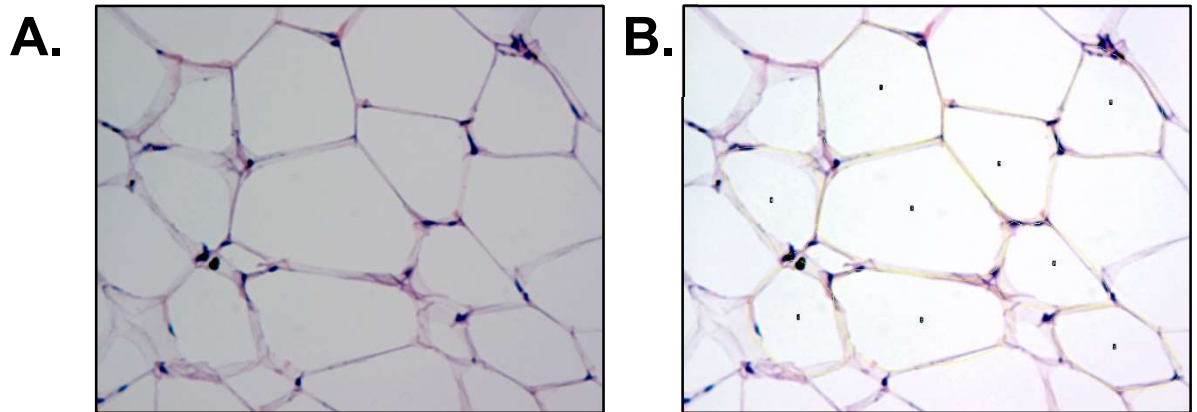
Figure 2.17. Image-J analysis. Image taken with Nikon TE200 Brightfield Inverted Microscope, at x40 objective lens, of iWAT before **(A)** and after **(B)** processing and analysing on Image-J. iWAT: inguinal White Adipose Tissue.

2.2.13. Statistical analysis

For all experimental procedures documented, samples were run in technical duplicates. For cell culture experiments, three biological replicates were used and for animal studies a minimum of four and maximum of 17 biological replicates were used. In all cases, N refers to the number of mice in each group or number of wells seeded containing 3T3-L1 cells.

To determine the statistical significance between the means of two independent groups, an unpaired, parametric, two-tailed t-test was performed. This test assumes that random samples are approximately normally distributed and the means of the two groups are equal.

A one-way analysis of variance (ANOVA) was used to determine the relationship between the sample means of three or more independent groups, assuming normal distribution, to determine if any groups were statistically significant against each other. This test allows each group to be compared against each other instead of individual t-tests. A one-way ANOVA considers one independent variable effecting a dependant variable. For example, the effect of dietary feeding in mice on gene expression in different adipose depots (Al-Dibouni et al., 2020). A two-way ANOVA considers two independent variables to determine their relevance in the context of the data presented. For example, the effects of two independent dietary feedings, such as a chow and a high-fat (HF)-diet given to animal dams, and the effect it has on their offspring (Gaspar et al., 2021) and differences amongst groups with therapeutic intervention

(Sheen et al., 2018). This test aids in determining the importance of one treatment versus the other. The outcome from a two-way ANOVA will result in a main and an interaction effect. The main effect is not dissimilar to a standard one-way ANOVA, in which each group's effect is considered on an individual basis. However, all factors are considered simultaneously with the interaction effect (Krantz, 2019). The aim is to determine the extent of the effect of the intervention within the categories of each subgroup (Ferreira and Patino, 2017). In this thesis, the two-way ANOVA models were considered additive if no interactions were detected (Fujikoshi, 1993).

In some cases, such as body weight changes over a certain period, a repeated measures ANOVA was conducted in which all representatives of a sample group were measured at different timepoints/conditions.

To establish which groups were statistically significant against each other, a post-hoc test (Tukey's multiple comparison) was conducted following an ANOVA, under the assumption that there was homogeneity of the variances.

Biochemical and metabolic parameters, the inflammatory and thermogenic capacity and adipocyte size are dysfunctional in diseases such as obesity. The association of these markers were correlated for analysis. To determine if two independent quantitative variables were significantly related to each other, a simple linear regression was performed. This allows an estimate of the strength and direction of the two variables, regarding linear relationship. Pearson's correlation coefficient (r) values range between -1 and 1. The closer to an r value of 1, the stronger the relationship is between the two parameters and vice versa. The negative or positive sign before the r value, determines the relationship between the two variables. If the r value is equal to -/+1, this shows that the variables can be explained by linearity. This test provides an inference between the variables as correlation does not equal causation.

The software GraphPad Prism versions 6.00 to 9.00 (GraphPad Software, California, United States of America) were used to produce all statistical analysis and graphs. Data are presented as mean $\pm$ standard error of the mean (SEM). Standard error (SE) is the deviation of a sample population from the mean. In statistical analysis, sample means can deviate from the true mean of a population.

This deviation is the SEM and measures the distance away from the sample mean and includes inference based on the distribution of samples. The confidence level for all analysis was 95%. A p value is a probability measure to indicate evidence against the null hypothesis or in favour of the alternative hypothesis. A value of $p<0.05$ was deemed as statistically significant with * $p<0.05$, ** $p<0.01$, *** $p<0.001$ and **** $p<0.0001$.

.

CHAPTER 3

INVESTIGATING THE EFFECTS OF DIETARTY INTAKE ON PERICARDIAL ADIPOSE TISSUE IN MICE

3.1. INTRODUCTION

Excessive food consumption in the human population contributes to the rise in obesity incidence (Vandevijvere et al., 2015). In humans, excessive food intake induces weight gain, fat mass and heart complications (Bouchard et al.,1990). Overfeeding is also accompanied by metabolic dysfunction, such as insulin resistance, due to enlargement of adipocytes and their limited capacity to accommodate for excess lipid accumulation (Cotillard et al., 2014). The impact of the latter is dependent on the degree of adiposity (Arner et al., 2010) and distiburtion of adipocytes around the body. Hypertrophy of abdominal visceral adipocytes are associated more with higher levels of circulating triglycerides (TGs), compared to hyperplastic enlargement in subcutaneous depots (Veilleux et al., 2011).

Obesity is a heterogenic disorder in humans and metabolic complications acquired differ due to the influence of uncontrollable factors such as genetics and environmental cues. Scientists have benefited from the use of animals, in particular rodents, to study obesity pathogenesis. In rodents, diet-induced obesity (DIO) can be displayed by feeding animals with commercially available diets, with a caloric fat intake of 45% or 60%. The former fat caloric intake is sufficient to induce obesity in rodents, but 60% kcal fat diet produces a more extreme case of obesity. The latter enables the observation of metabolic dysfunction manifesting in a quicker timeframe. Obesity induced by a high-fat (HF)-diet in rodents results in an increase in caloric intake (Yang et al., 2014), when food is provided *ad libitum* (Licholai et al., 2018), and an increase in weight gain (Yang et al., 2014). Although DIO in mice does not directly mimic human obesity, the aim is to monitor and understand the physiological alterations that may occur in human obesity.

During early adulthood, adipocyte number is mainly determined via the regulation of adipocyte survival and death, to ensure numbers are unchanged (Spalding et al., 2008). Any differences that occur in adipocyte number are established during the childhood of lean and obese individuals (Knittle et al., 1979). For instance, overfeeding in rodents results in the generation of newly formed adipocytes (Faust et al., 1978) but number remains constant during adulthood (Spalding et al., 2008). Under chow conditions, WAT adipogenesis in adult mice is relatively low (Wang et al.,2013). Adult progenitors are specified before developmental progenitors,

which characterises the extensive plasticity of AT during child and adult obesity (Jiang et al.,2014). During DIO, pre-existing and newly formed visceral adipocytes are primarily influenced by hypertrophy in the first month of post-weaning feeding. After a prolonged HF-feeding plan, there is an increase in adipocyte number (hyperplasia) in visceral fat (Wang et al., 2013). Subcutaneous fat number remains relatively low during the prenatal stages and differentiation is completed before birth (Wang et al.,2013). Due to the different developmental stages of white fat, their adipogenic potential in adult development varies (Wang et al.,2013) and plays different roles in pathogenesis. Under obesogenic conditions, due to the limited capacity of visceral adipocytes, hyperplasia of subcutaneous fat persists. This suggests a regulatory role of the latter when exposed to induced excess caloric intake (Wang et al.,2013). Reduced expandability of visceral fat is reflected by the weight of adipose depot pads and is linked with metabolic disease when induced by excessive feeding (Van Beek et al., 2015). As visceral hypertrophy is a determinant of a deleterious phenotype (Laforest et al., 2015), increased adipocyte size due to TG accumulation during obesogenic conditions (Spalding et al., 2008) is linked with a pro-inflammatory response characterised in obesity. This influences the risk of developing insulin resistance and CVD (Drolet et al., 2008; Skurk et al., 2007; Kabir et al., 2011).

Laboratory animals are well established models for studying the progression of obesity induced by a HF-diet. Overfeeding in mice causes excessive energy storage and increases adipocyte size (hypertrophy). Adipocyte capacity is limited and enlargement of classical visceral depots are associated with increased metabolic risk, under obesogenic conditions. Given that cardiac adipose tissue is associated with the heart and obesogenic complications in disease, there is still little known about the role of pericardial fat in metabolic dysfunction in comparison to other classical adipose depots.

3.1.1. Aims

The aim is to document how the genetic and morphological signatures of PAT compares to other adipose depots under short-term and pro-longed obesogenic environments. The transcriptional and histological profile of pericardial adipose tissue (PAT) was compared to gonadal (gWAT), inguinal (iWAT) and interscapular brown (iBAT) adipose tissue harvested from **(1)** 10-week-old male mice fed a chow-diet of 7% kcal fat (control) or a high-fat-diet of 45% kcal fat for 7 weeks to induce obesity and **(2)** 30-week-old male mice fed a chow-diet of 10% kcal diet (control) or a high-fat diet of 60% kcal fat for 26 weeks to induce morbid obesity.

3.2. METHODS

3.2.1. Animal and experimental design

10-week-old mice: All animal work was conducted by the technical staff at the University of Southampton. Research was performed in accordance with the UK Animals (Scientific Procedures) Act 1986 and with Home Office licences held at the University of Southampton. Maintained under a 12-hour light/dark cycle and a constant temperature of 22°C ± 2°C, C57BL/6J male mice were used in this study, with food and water available *ad libitum.* At the age of 3 weeks old, mice were randomly allocated to either a chow (C) (7% kcal fat) or a high-fat (HF) (45% kcal fat) diet, for 7 weeks. Death of mice by carbon dioxide euthanasia and neck dislocation was confirmed by cessation of the circulation. Dissection of gonadal white adipose tissue (gWAT), inguinal white adipose tissue (iWAT), interscapular brown adipose tissue (iBAT) and pericardial adipose tissue (PAT) for gene expression (samples stored at -80°C until further analysis) and histological analysis (samples stored at 4°C until further analysis) were performed at the end of the experimental procedure (10 weeks of age) (Figure 3.1).
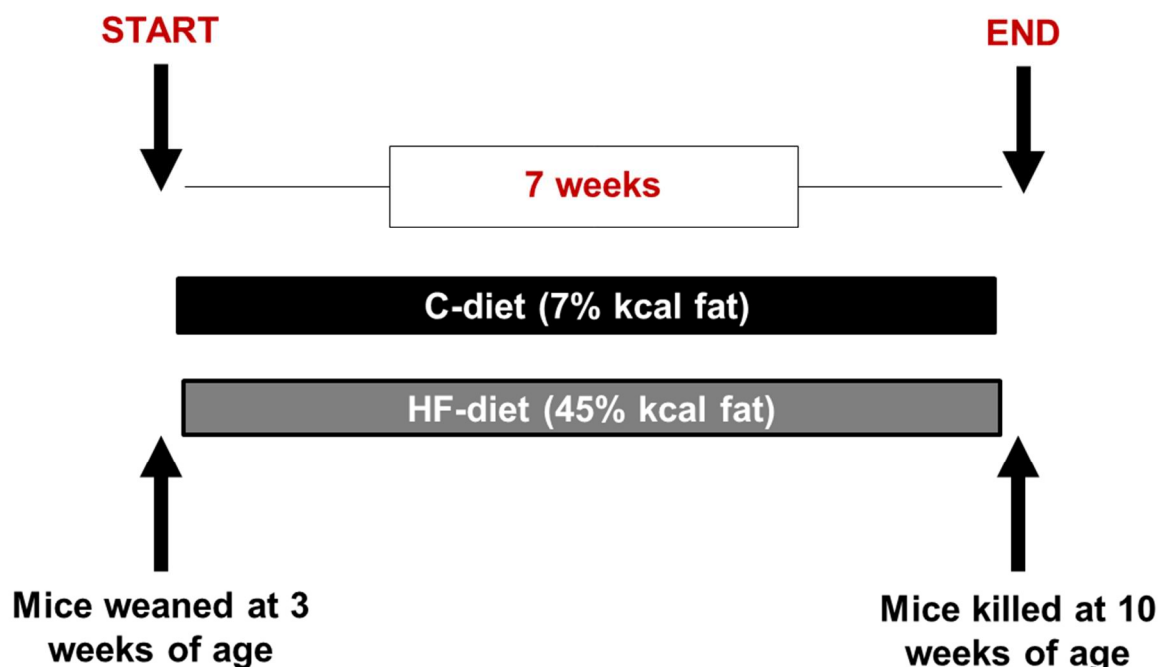
Figure 3.1. Experimental design of male mice fed a C-diet or HF-diet for 7 weeks. C-diet: Chow-diet; HF-diet: High-fat-diet.

30-week-old mice: All animal work was conducted by the technical staff at the Medical Research Council Harwell Institute. Research was approved by the Medical Research Council (MRC) Harwell Institute Animal Welfare and Ethical Review Board. All procedures were carried out within project license restrictions (PPL 30/3146) under the UK Animals (Scientific Procedures) Act 1986, issued by the UK Government Home Office. Maintained under a 12-hour light/dark cycle and a constant temperature of 22°C ± 2°C, C57BL/6N male mice were used in this study, with food and water available *ad libitum*. At the age of 4 weeks old, male mice were assigned to a chow (C) (10% kcal fat) or a high-fat (HF) (60% kcal fat) diet, for 26 weeks. Throughout the dietary intervention, mice were weighed weekly, metabolic cage analysis was performed at 22 weeks using TSE PhenoMaster *in vivo* calorimetry system, whilst body composition and intraperitoneal glucose tolerance test (ipGTT) were measured at 26 weeks of age. Body composition was measured by nuclear magnetic resonance (EchoMRI™, Zinsser Analytic GmbH, Eschborn, Germany) which determined total body fat, lean mass and free fluid in grams. The percentage of each component was then calculated based on the total body weight of the animal. Percentage body fat was calculated by dividing fat by weight and multiplying by 100. ipGTT was performed following an 8-hour fast and the area under the curve (AUC) was determined, with baseline values were subtracted. 2g/kg glucose was intraperitoneally administered to fasted mice and blood was taken from the tail vein, under local anaesthetic (EMLA cream, AstraZeneca, United Kingdom) at 0 (baseline), 15, 30, 60 and 120 minutes, post glucose injection. Whole blood glucose was measured using an AlphaTRAK meter and test strips (Abbott Animal Health, United Kingdom). Blood was collected by a cardiac puncture under terminal anesthetic, in mice at the age of 30 weeks. For serological analysis, the blood was left to clot and centrifuged at 3000xg for 3 minutes. Sera was frozen at -80°C until further analysis. All samples for biochemistry analysis of serum, including free fatty acids, triglycerides and cholesterol, were performed using AU680 Clinical Chemistry Analyser (Beckman Coulter, High Wycombe, United Kingdom), by the Clinical Chemistry core facility, MRC Harwell Institute (Oxfordshire, United Kingdom) using commercially-available kits and performed according to manufacturer instructions. Death of mice was confirmed by cessation

of the circulation and neck dislocation. Dissection of gonadal white adipose tissue (gWAT), inguinal white adipose tissue (iWAT), interscapular brown adipose tissue (iBAT) and pericardial adipose tissue (PAT) for gene expression (samples stored at -80°C until further analysis) and histological analysis (samples stored at 4°C until further analysis) were performed at the end of the experimental procedure (30 weeks of age) (Figure 3.2).
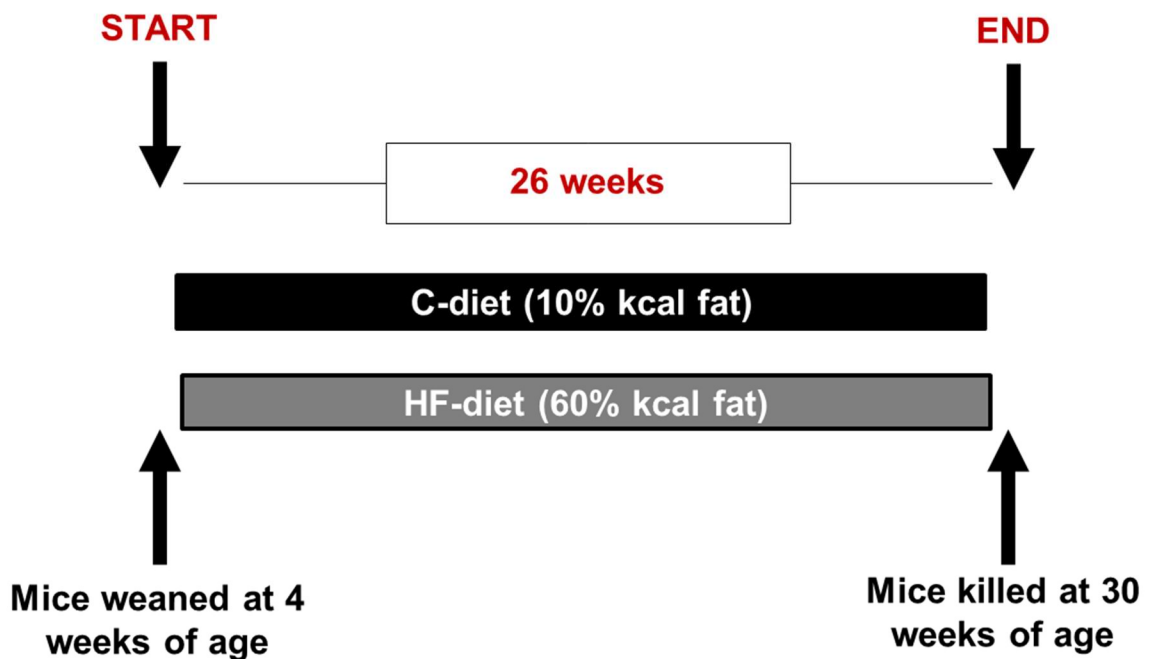
Figure 3.2. Experimental design of male mice fed a C-diet or HF-diet for 26 weeks. C-diet: Chow-diet; HF-diet: High-fat-diet.

3.2.2. RNA isolation

1ml Invitrogen™ TRI Reagent™ Solution per 50mg to 100mg of gWAT, iWAT, iBAT and PAT was transferred to a MP Biomedicals™ Lysing Matrix D tube. Lysing tubes were placed in the MP Biomedicals™ FastPrep-24™ 5G Instrument, with the QuickPrep Adaptor (Fisher Scientific) and homogenised at a speed of 6.0m/s, for 40 seconds. Isolation of RNA was performed as recommended by the manufactures of Invitrogen™ TRI Reagent™ Solution (Fisher Scientific). RNA was quantified and quality was checked as stated in section 2.2.3 and section 2.2.4.3. RNA samples were stored at -80°C until further analysis.

3.2.3. cDNA synthesis and RT-qPCR

Total RNA was reverse transcribed using the Applied Biosystems™ High-Capacity cDNA Reverse Transcription Kit (Fisher Scientific) and Invitrogen™ RNaseOUT™ Recombinant Ribonuclease Inhibitor (Fisher Scientific), following the instructions as recommended by the manufacturer to synthesise cDNA, performed using the T100™ Thermal cycler (Bio-Rad). 500ng to 1000ng of cDNA was synthesised as stated in the section 2.2.5. The gene expression of 30ng cDNA was determined using qPCRBIO Probe Mix No-ROX (PCR Biosystems), performed on the MyiQ™ Single-Colour Real-Time PCR Detection System (Bio-Rad). Samples were measured in duplicates and the fold change in gene expression levels were determined using the comparative threshold cycle (Ct) method, also referred to as the $2^{-\Delta\Delta}$ Ct method (section 2.2.6). The target genes as listed in Table 3.1 were relative to the housekeeping gene, peptidylprolyl isomerase A (PPIA). All Applied Biosystems™ TaqMan™ Gene Expression Assays (FAM-MGB) were purchased from Fisher Scientific (Table 3.1). cDNA was stored at -20°C until further analysis.

Table 3.1. Applied Biosystems™ TaqMan™ Gene Expression Assays for RT-qPCR

Gene	Assay ID
AdipoQ	Mm00456425_m1
ADRβ3	Mm02601819_g1
C/EBPα	Mm00514283_s1
COX7A1	Mm00438297_g1
COX8B	Mm00432648_m1
DIO2	Mm00515664_m1
FABP4	Mm00445878_m1
IL6	Mm00446190_m1
Leptin	Mm00434759_m1
PGC1α	Mm01208835_m1
PPARγ	Mm00440940_m1
PPIA	Mm02342430_g1
TNFα	Mm00443258_m1
UCP1	Mm01244861_m1

3.2.4. Histology

Formalin fixed gWAT, iWAT and PAT embedded in Optimal Cutting Temperature (OCT) compound were sectioned between 10μM and 15μM using a Bright 5040 Cryostat (Bright Instruments Limited). Sections were stained with Haematoxylin and Eosin (H&E) and imaged with a Nikon TE200 Brightfield Inverted Microscope, at x40 objective lens. Assuming the shape of adipocytes are spherical, to calculate adipocyte volume, Image-J software was used to determine adipocyte area and volume distribution as stated in section 2.2.12.1. The percentage change in volume was determined by normalising adipocyte volume to the chow (C)-fed mice, unless stated otherwise, and multiplying by 100. H&E stained slides were stored at room temperature until further analysis.

3.2.5. Statistical analysis

GraphPad Prism was used to perform statistical analysis of one-way ANOVA, repeated measures ANOVA, unpaired t-test or Pearson's correlation coefficient. ANOVAs were performed with post-hoc Tukey's multiple comparison. All values were relative to their respective depots from chow (C)-fed mice, unless stated otherwise. Graphs are expressed as mean $\pm$ standard error of the mean (s.e.m), unless stated otherwise. A value of $p<0.05$ was deemed as statistically significant with * $p<0.05$, ** $p<0.01$, *** $p<0.001$ and **** $p<0.0001$.

3.3. RESULTS

3.3.1. Biochemical and metabolic parameters

30-week-old male mice fed a high-fat (HF)-diet over 26 weeks, were heavier (Figure 3.3A), had a reduced percentage lean weight (Figure 3.3B) ($p < 0.001$), increased percentage fat weight (Figure 3.3C) ($p < 0.001$), glucose intolerant demonstrated by an ipGTT (Figure 3.3D) and analysis of area under the curve (AUC) (Figure 3.3E) and a lower respiratory exchange rate (RER) (Figure 3.3L and Figure 3.3M), compared to 30-week-old male mice fed a chow diet. Levels of fasting glucose (Figure 3.3F) ($p < 0.0001$), free fatty acids (FFAs) (Figure 3.3H) ($p < 0.01$), total cholesterol (Figure 3.3I) ($p < 0.001$), HDL (Figure 3.3J) ($p < 0.001$) and LDL (Figure 3.3K) ($p < 0.01$), were higher in HF-fed mice compared to C-fed mice. There were no differences between the depot weights of pericardial fat between chow and HF-fed mice (Figure 3.3N).
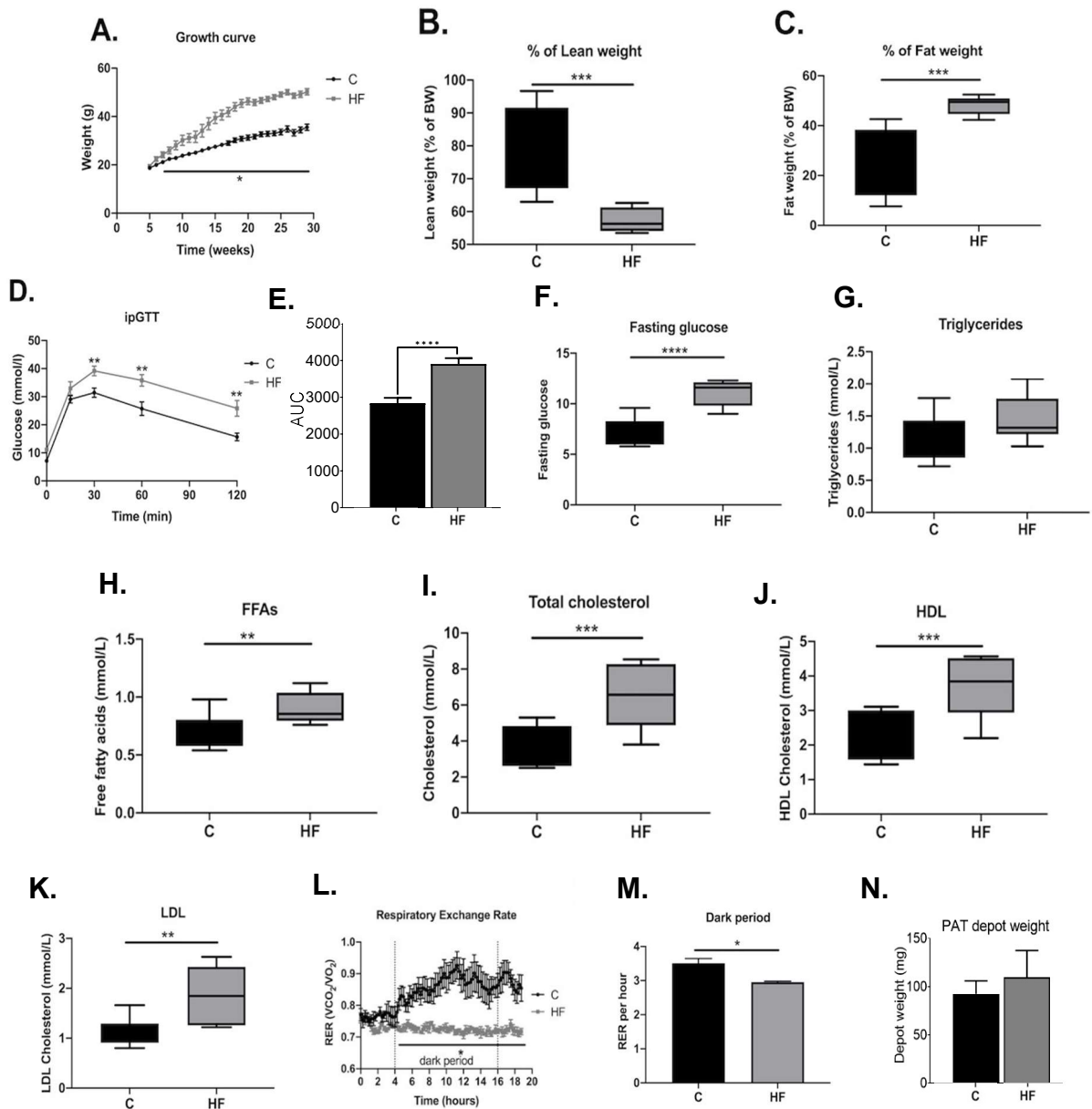
Figure 3.3. Metabolic effects of chow-fed and high-fat-fed 30-week-old male mice. Growth curve with weekly weight measurements **(A),** % lean mass **(B),** % fat mass **(C)**, intraperitoneal glucose tolerance test (ipGTT) with glucose measured at 0, 15, 30, 60 and 120 minutes after glucose injection **(D),** area under the curve (AUC) of blood glucose levels **(E)**, fasting glucose **(F),** serum triglycerides **(G),** serum free fatty acids (FFAs) **(H),** serum total cholesterol **(I),** serum HDL **(J),** serum LDL **(K),** Respiratory Exchange Rate (RER) **(L)** during the dark period **(M),** PAT depot weight **(N)** in chow (C) and high-fat (HF)-fed 30-week-old male mice. Graphs represent mean $\pm$ s.e.m **(A,D,E,L-N)** and minimum to maximum values of boxplots **(B,C,E,F,G,H,I,J).** Data analysed by an unpaired t-test **(B,C,E-K,M,N)** and by repeated measures ANOVA with Tukey's multiple correction **(A,D,L).** N = 8-17 for **A-M,** N = 3-10. * $p<0.05$, ** $p<0.01$, *** $p<0.001$ and **** $p<0.0001$.

3.3.2. Adipose tissue gene expression differences at baseline in chow-fed mice

All gene expression levels were relative to C-gWAT (Figure 3.4 and Figure 3.5).

Adipogenic markers: In 10-week-old mice, PPARγ (Figure 3.4B) and C/EBPα (Figure 3.4C) expression was lower in PAT compared to gWAT ($p<0.01$ and $p<0.0001$, respectively), iWAT ($p<0.001$ and $p<0.0001$, respectively) and iBAT ($p<0.001$ and $p<0.001$, respectively). In 10-week-old and 30-week-old mice, PAT FABP4 (Figure 3.4A and Figure 3.5A) expression was lower compared to gWAT ($p<0.0001$ and $p<0.05$, respectively) and iWAT ($p<0.0001$ and $p<0.05$).

Inflammatory markers: In 10-week-old mice, PAT TNFα expression (Figure 3.4E) was significantly higher compared to gWAT ($p<0.05$) and in 30-week-old mice, PAT TNFα expression (Figure 3.5E) was significantly higher compared to iBAT ($p<0.01$). In 10-week-old mice, Leptin (Figure 3.4F) and AdipoQ (Figure 3.4G) expression was lower in PAT compared to gWAT ($p<0.0001$ and $p<0.0001$, respectively) and iWAT ($p<0.05$ and $p<0.05$, respectively). In 30-week-old mice, PAT Leptin expression (Figure 3.5F) was significantly lower compared to gWAT ($p<0.05$) and PAT AdipoQ expression (Figure 3.5G) was lower compared to iWAT ($p<0.01$) and gWAT ($p<0.0001$).

Thermogenic markers: In 10-week-old mice, UCP1 (Figure 3.4H) and DIO2 (Figure 3.4J) expression in PAT was significantly lower compared to iBAT ($p<0.0001$ and $p<0.0001$, respectively). PAT ADRβ3 expression (Figure 3.4I) was lower than gWAT ($p<0.0001$) and iWAT ($p<0.01$). In 30-week-old mice, PAT UCP1 (Figure 3.5H) levels were lower than iBAT and higher than gWAT ($p<0.01$) and iWAT ($p<0.01$). PAT ADRβ3 levels (Figure 3.5I) were lower than gWAT ($p<0.01$). PAT DIO2 expression (Figure 3.5J) was higher than iWAT ($p<0.01$) and gWAT ($p<0.01$).

Mitochondrial markers: In 10-week-old mice, COX7A1 (Figure 3.4L), COX8B (Figure 3.4M) and PGC1α (Figure 3.4K) levels were significantly lower compared to iBAT ($p<0.0001$, $p<0.0001$ and $p<0.01$, respectively). In 30-week-old mice, PAT PGC1α (Figure 3.5K) was significantly lower compared to iBAT ($p<0.05$). PAT COX7A1 (Figure 3.5L) and COX8B (Figure 3.5M) levels were significantly lower than iBAT ($p<0.0001$ and $p<0.0001$, respectively) and higher compared to gWAT ($p<0.01$ and $p<0.01$, respectively) and iWAT ($p<0.01$ and $p<0.01$, respectively).
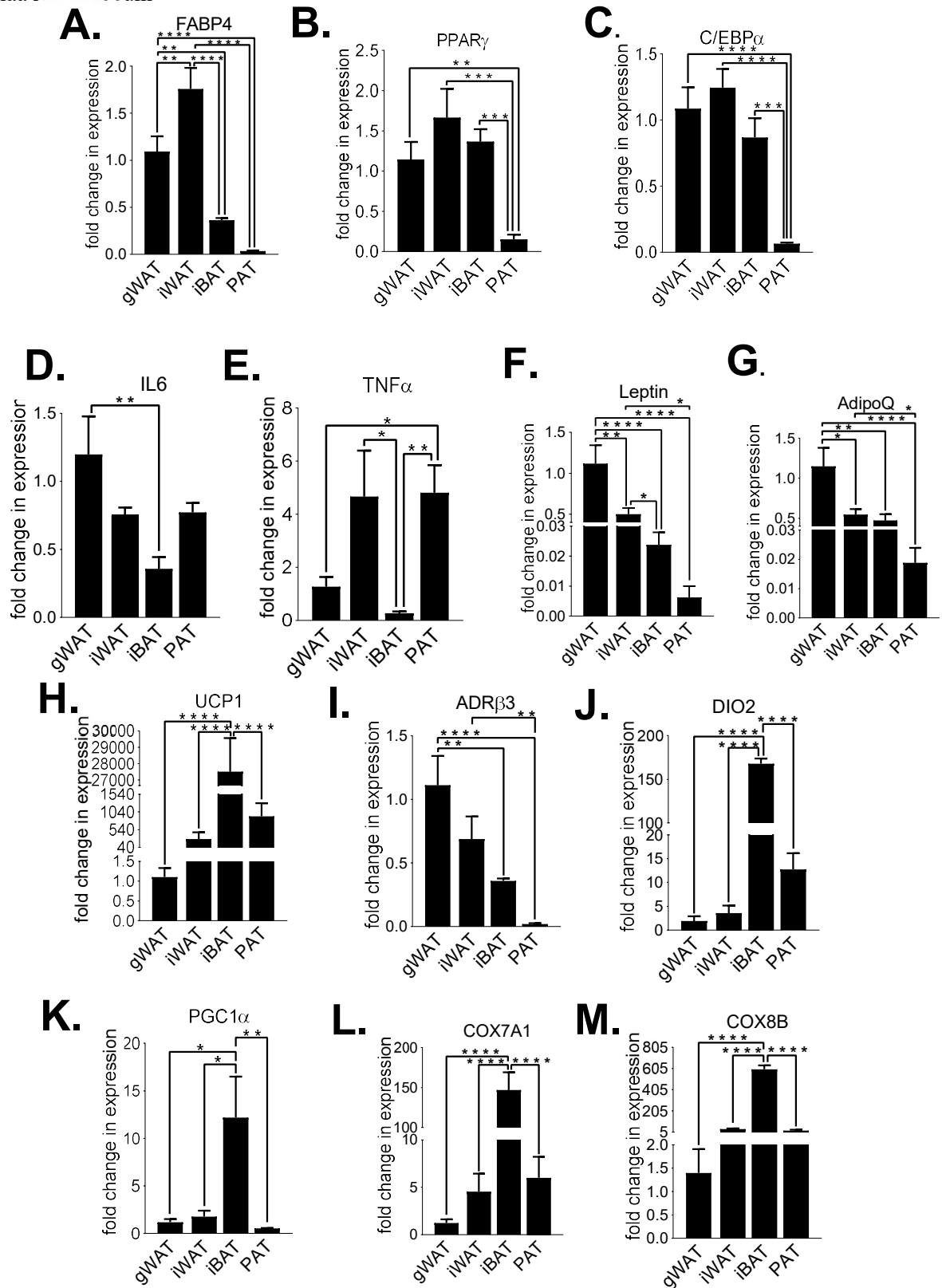
Figure 3.4. FABP4 **(A)**, PPARγ **(B)**, C/EBPα **(C)**, IL6 **(D)**, TNFα **(E)**, Leptin **(F)**, AdipoQ **(G)**, UCP1 **(H)**, ADRβ3 **(I)**, DIO2 **(J)**, PGC1α **(K)**, COX7A1 **(L)** and COX8B **(M)** fold change in mRNA expression in **gWAT**, **iWAT**, **iBAT** and **PAT** of chow (C)-fed **10-week-old male mice**, relative to C-gWAT. Graphs represent mean + s.e.m. Data analysed by one-way ANOVA and Tukey's multiple comparison test. N = 6-8. * p < 0.05, ** p < 0.01, *** p < 0.001 and **** p < 0.0001.
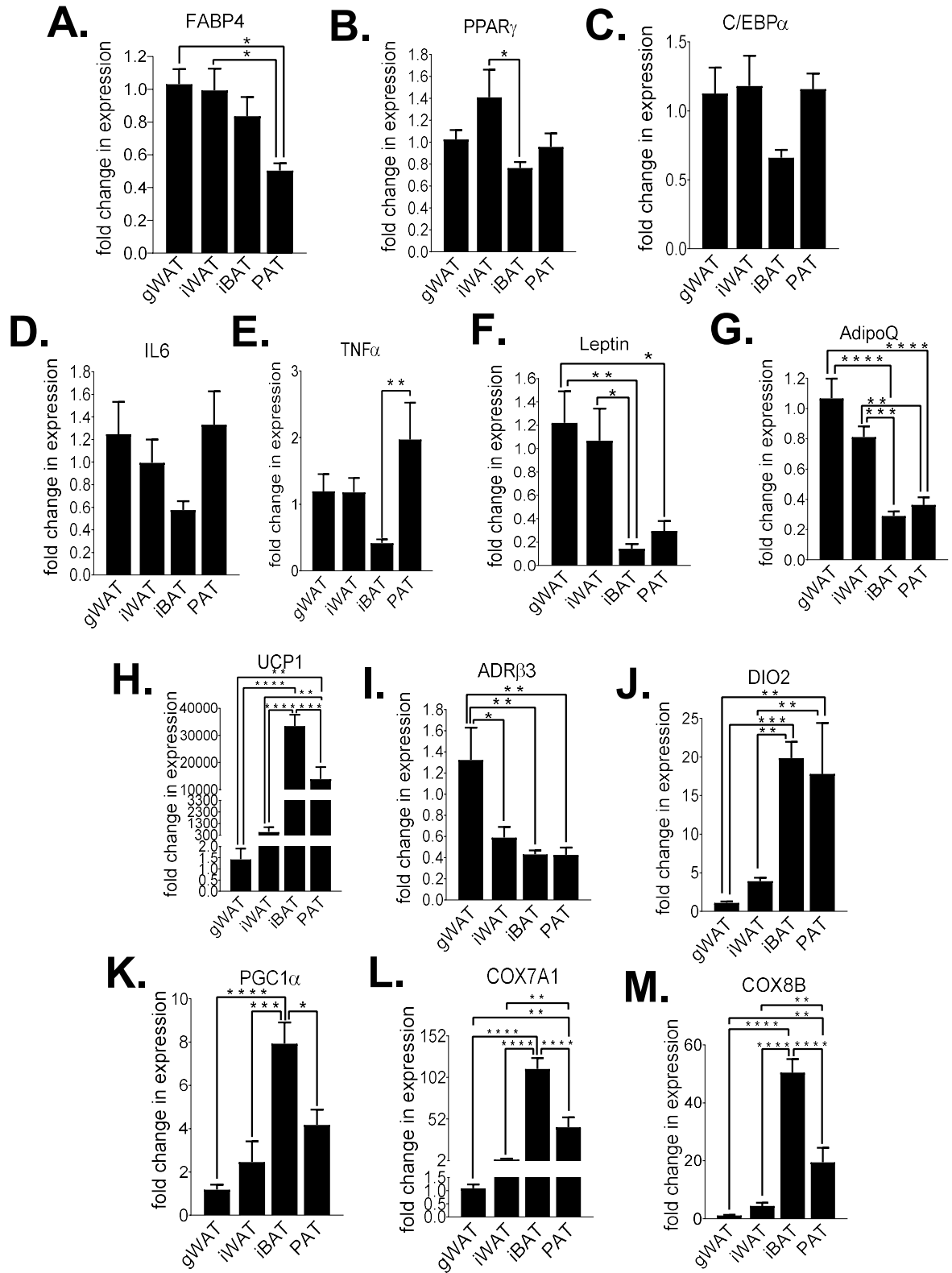
Figure 3.5. FABP4 **(A)**, PPARγ **(B)**, C/EBPα **(C)**, IL6 **(D)**, TNFα **(E)**, Leptin **(F)**, AdipoQ **(G)**, UCP1 **(H)**, ADRβ3 **(I)**, DIO2 **(J)**, PGC1α **(K)**, COX7A1 **(L)** and COX8B **(M)** fold change in mRNA expression of **gWAT**, **iWAT**, **iBAT** and **PAT** of chow (C)-fed **30-week-old male mice**, relative to C-gWAT. Graphs represents mean ± s.e.m. Data analysed by one-way ANOVA and Tukey's multiple comparison test. N = 8-12. * $p<0.05$, ** $p<0.01$, *** $p<0.001$ and **** $p<0.0001$.

3.3.3. Adipose tissue gene expression differences in HF-fed mice

All gene expression levels were relative to HF-gWAT (Figure 3.6 and Figure 3.7).

Adipogenic markers: In 10-week-old mice, PAT FABP4 expression (Figure 3.6A) was lower than gWAT ($p<0.001$) and iWAT ($p<0.001$). For PPARγ (Figure 3.6B), PAT expression was significantly lower compared to gWAT ($p<0.05$) and iBAT ($p<0.01$). For C/EBPα (Figure 3.6C), PAT expression was significantly lower compared to gWAT ($p<0.0001$) and iWAT ($p<0.0001$). 30-week-old PAT FABP4 expression (Figure 3.7A) was significantly lower expression in PAT compared to gWAT ($p<0.01$), iWAT ($p<0.01$) and iBAT ($p<0.05$), and PPARγ (Figure 3.7B) showed a significantly lower expression in PAT compared to iBAT ($p<0.05$).

Inflammatory markers: In 10-week-old mice, PAT Leptin expression (Figure 3.6F) was lower compared to gWAT and iWAT ($p<0.001$ and $p<0.01$) and AdipoQ expression (Figure 3.6G) in gWAT ($p<0.0001$), iWAT ($p<0.01$) and iBAT ($p<0.01$). In 30-week-old mice, IL6 (Figure 3.7D) and TNFα (Figure 3.7E) expression was higher in in PAT compared to iBAT ($p<0.001$ and $p<0.001$, respectively) and iWAT ($p<0.0001$ and $p<0.01$, respectively). PAT Leptin levels (Figure 3.7F) were significantly lower compared to gWAT ($p<0.01$) and iWAT ($p<0.001$). PAT AdipoQ levels (Figure 3.7G) were significantly lower compared to gWAT ($p<0.05$) and iWAT ($p<0.001$).

Thermogenic markers: In 10-week-old mice and 30-week-old mice, PAT expression was significantly lower in UCP1 (Figure 3.6H, $p<0.0001$ and Figure 3.7H, $p<0.0001$), ADRβ3 (Figure 3.6I, $p<0.0001$ and Figure 3.7I, $p<0.0001$) and DIO2 (Figure 3.6J, $p<0.0001$ and Figure 3.7J, $p<0.0001$) compared to iBAT. In 10-week-old mice only, PAT ADRβ3 expression (Figure 3.6I, $p<0.01$) was significantly lower than gWAT.

Mitochondrial markers: In 10-week-old and 30-week-old mice, PAT expression was significantly lower in COX7A1 (Figure 3.6L, $p<0.0001$ and Figure 3.7L, $p<0.0001$) and COX8B (Figure 3.6M, $p<0.0001$ and Figure 3.7M, $p<0.0001$) compared to iBAT. In 10-week-old mice only, PAT PGC1α expression (Figure 3.6K, $p<0.001$) was lower than iBAT.
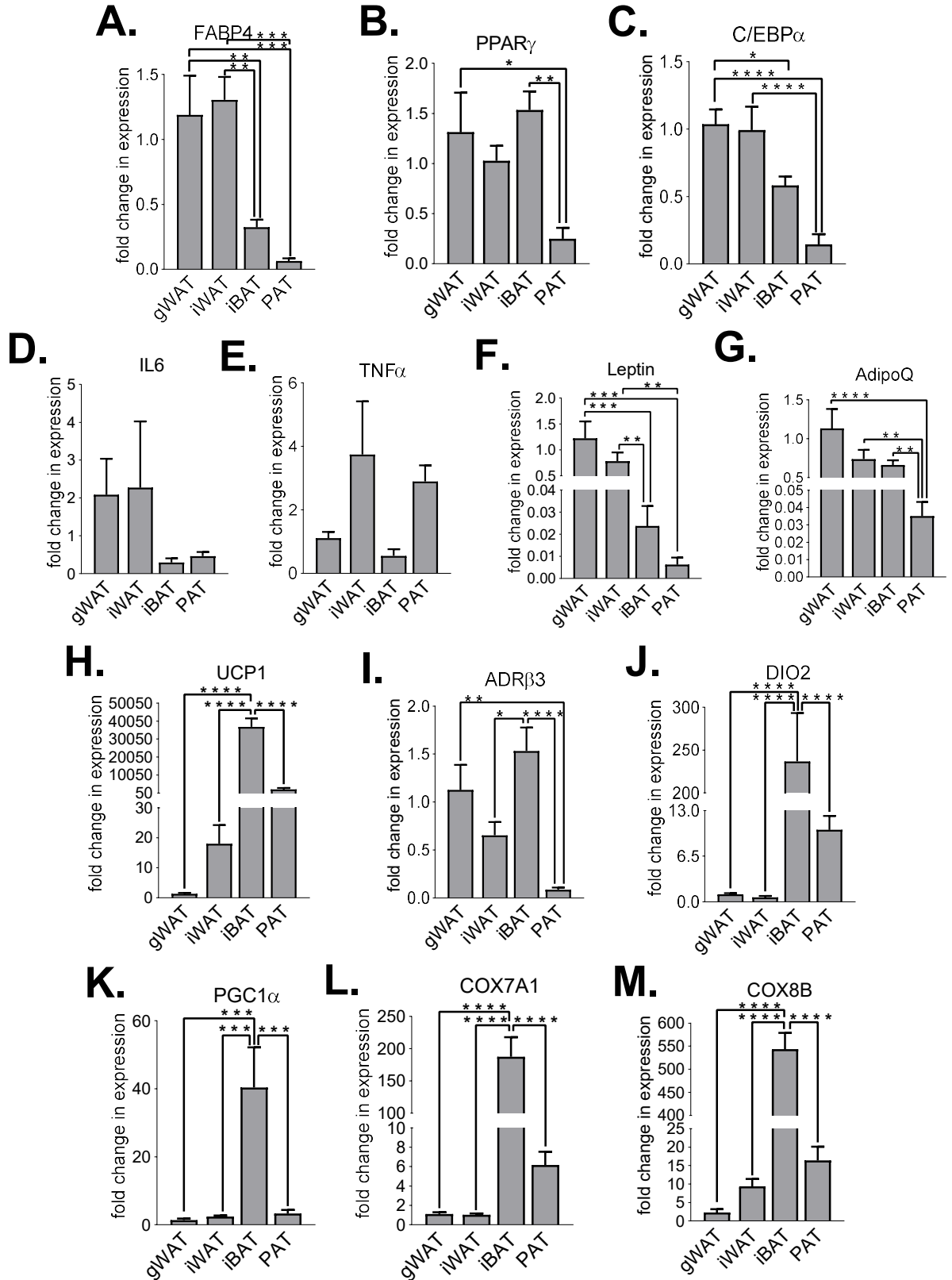
Figure 3.6. FABP4 **(A)**, PPARγ **(B)**, C/EBPα **(C)**, IL6 **(D)**, TNFα **(E)**, Leptin **(F)**, AdipoQ **(G)**, UCP1 **(H)**, ADRβ3 **(I)**, DIO2 **(J)**, PGC1α **(K)**, COX7A1 **(L)** and COX8B **(M)** fold change in mRNA expression in **gWAT**, **iWAT**, **iBAT** and **PAT** of high-fat (HF)-fed **10-week-old male mice**, relative to HF-gWAT. Graphs represent mean + s.e.m. Data analysed by one-way ANOVA and Tukey's multiple comparison test. N = 6-8. * p<0.05, ** p<0.01, *** p<0.001 and **** p<0.0001.
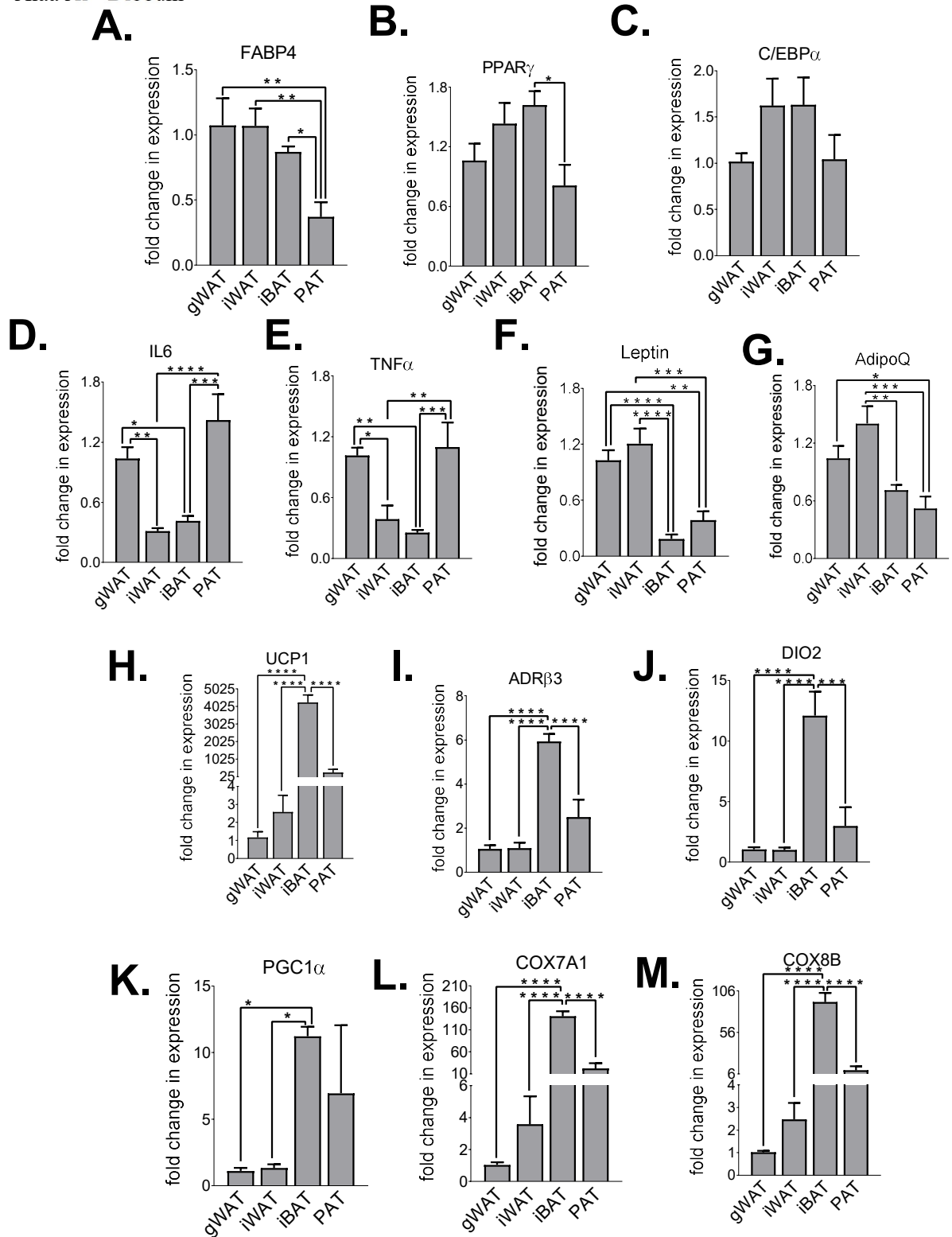
Figure 3.7. FABP4 **(A)**, PPARγ **(B)**, C/EBPα **(C)**, IL6 **(D)**, TNFα **(E)**, Leptin **(F)**, AdipoQ **(G)**, UCP1 **(H)**, ADRβ3 **(I)**, DIO2 **(J)**, PGC1α **(K)**, COX7A1 **(L)** and COX8B **(M)** fold change in mRNA expression in **gWAT**, **iWAT**, **iBAT** and **PAT** of high-fat (HF)-fed **30-week-old male mice**, relative to HF-gWAT. Graphs represent mean $\pm$ s.e.m. Data analysed by one-way ANOVA and Tukey's multiple comparison test. N = 8-12. * $p<0.05$, ** $p<0.01$, *** $p<0.001$ and **** $p<0.0001$.

3.3.4. Adipose tissue gene expression differences in chow-fed and HF-fed mice

Adipogenic markers: In 30-week-old mice, PAT HF-fed mice exhibited significantly lower expression levels of PPARγ (Figure 3.14B, $p<0.05$) and a trend towards lower expression ($p=0.0515$) compared to chow-fed animals.

Inflammatory markers: In 30-week-old mice, PAT TNFα expression (Figure 3.11B, $p<0.05$) and Leptin (Figure 3.13A, $p<0.05$) was significantly higher in HF-fed mice compared to chow-fed mice.

Thermogenic markers: In 10-week-old mice, HF-PAT ADRβ3 expression (Figure 3.14B, $p<0.05$) was higher compared to C-PAT.

Mitochondrial markers: There were no statistically significant differences in mitochondrial markers of PAT.
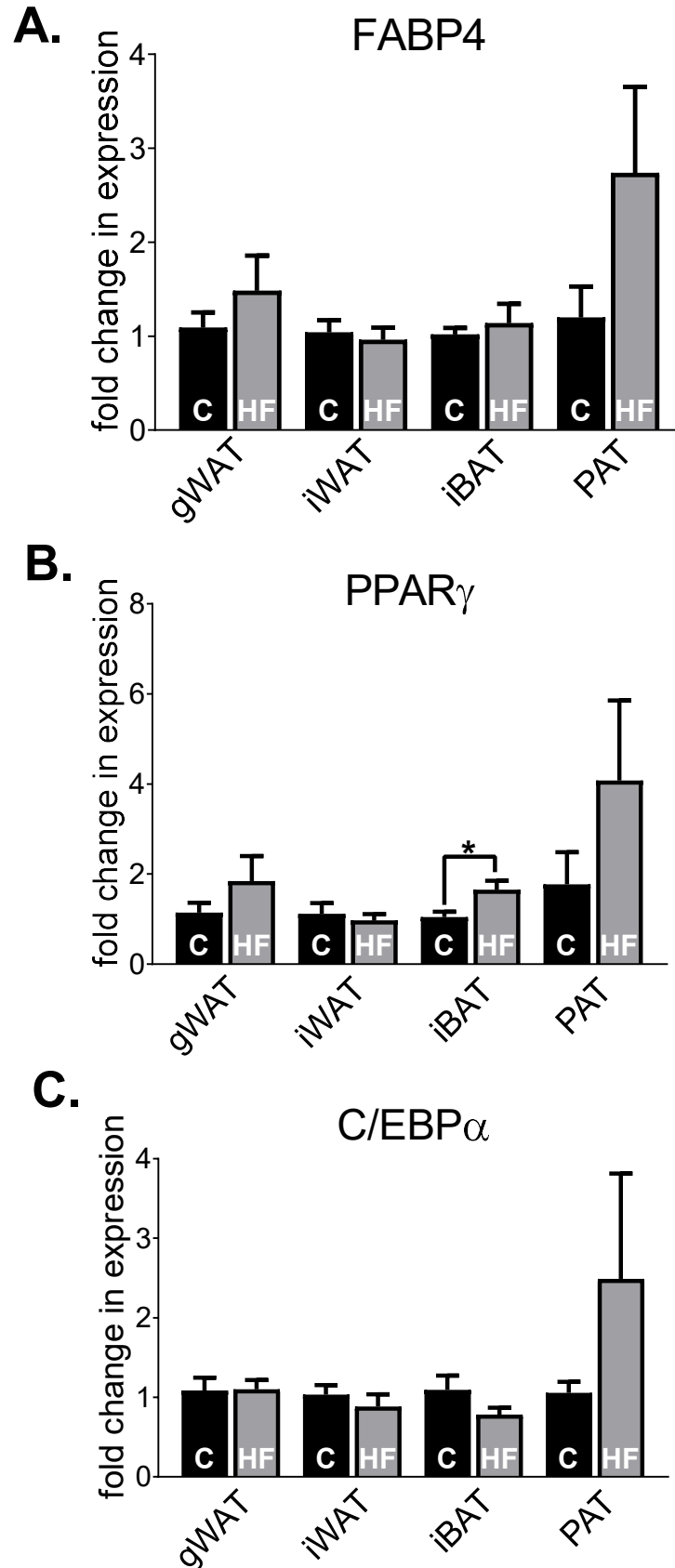
Figure 3.8. FABP4 **(A)**, PPARγ **(B)** and C/EBPα **(C)** fold change in mRNA expression in **gWAT**, **iWAT**, **iBAT** and **PAT** of chow (C) or high-fat (HF)-fed **10-week-old male mice**, relative to their respective C. Graphs represent mean + s.e.m. Data analysed by an unpaired t-test between C and HF of each depot. N = 6-8. * $p<0.05$, ** $p<0.01$, *** $p<0.001$ and **** $p<0.0001$.
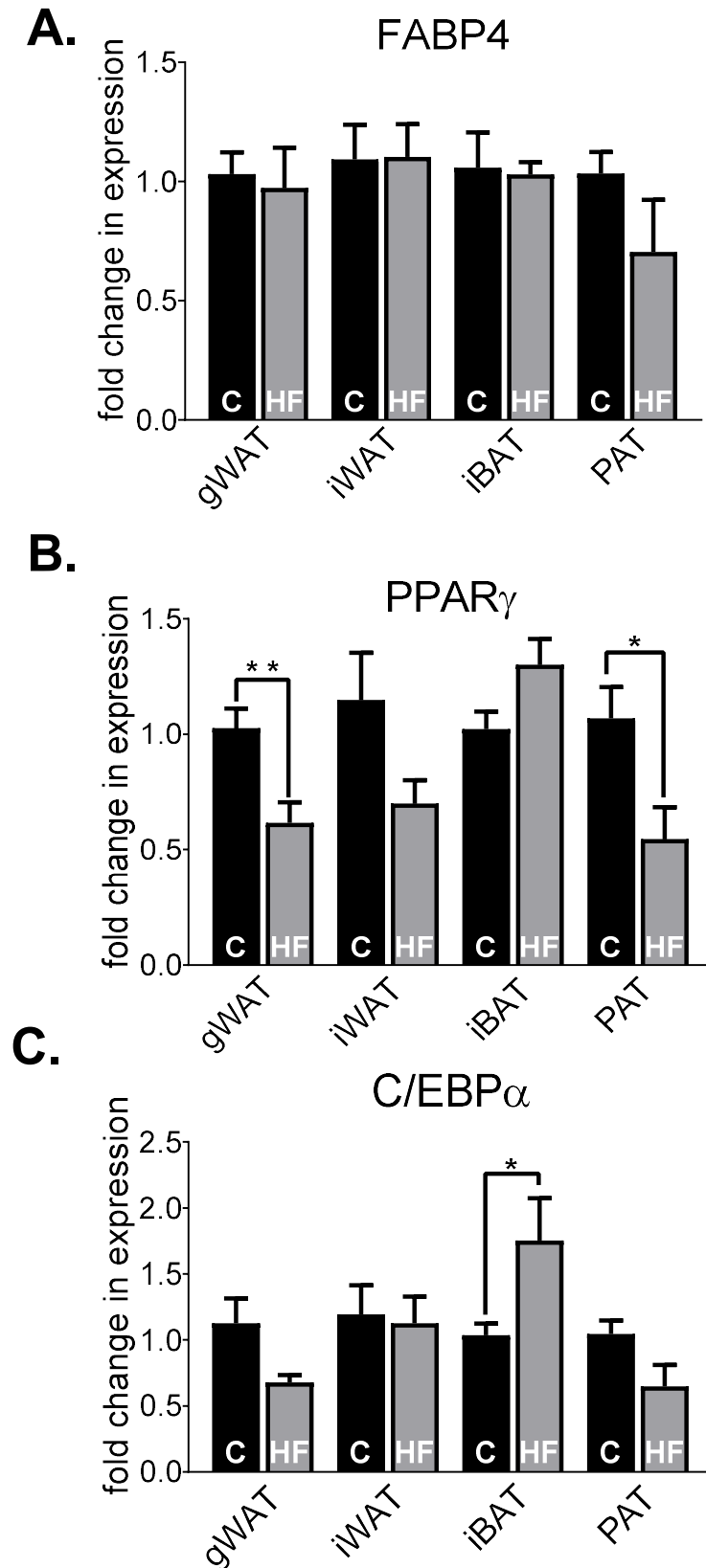
Figure 3.9. FABP4 **(A)**, PPARγ **(B)** and C/EBPα **(C)** fold change in mRNA expression in **gWAT**, **iWAT**, **iBAT** and **PAT** of chow (C) or high-fat (HF)-fed **30-week-old male mice**, relative to their respective C. Graphs represent mean ± s.e.m. Data analysed by an unpaired t-test between C and HF of each depot. N = 6-12. * $p<0.05$, ** $p<0.01$, *** $p<0.001$ and **** $p<0.0001$.

A.

B.
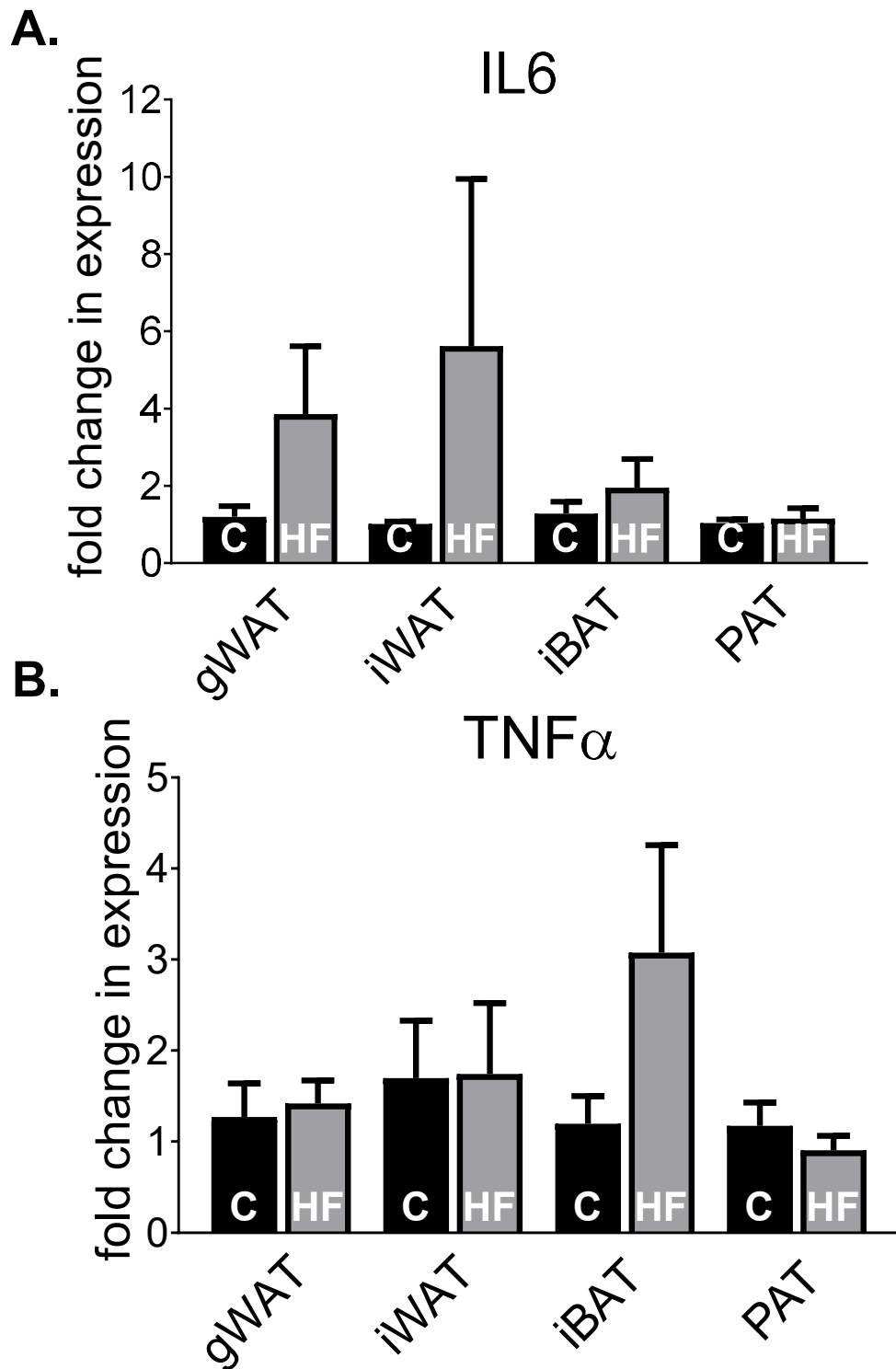
Figure 3.10. IL6 **(A)** and TNFα **(B)** fold change in mRNA expression in **gWAT**, **iWAT**, **iBAT** and **PAT** of chow (C) or high-fat (HF)-fed **10-week-old male mice**, relative to their respective C. Graphs represents mean + s.e.m. Data analysed by an unpaired t-test between C and HF of each depot. N = 6-8. * $p < 0.05$, ** $p < 0.01$, *** $p < 0.001$ and **** $p < 0.0001$.

Figure 3.11. IL6 (**A**) and TNFα (**B**) fold change in mRNA expression in **gWAT**, **iWAT**, **iBAT** and **PAT** of chow (C) or high-fat (HF)-fed **30-week-old male mice**, relative to their respective C. Graphs represent mean ± s.e.m. Data analysed by an unpaired t-test between C and HF of each depot. N = 6-12. * $p<0.05$, ** $p<0.01$, *** $p<0.001$ and **** $p<0.0001$.
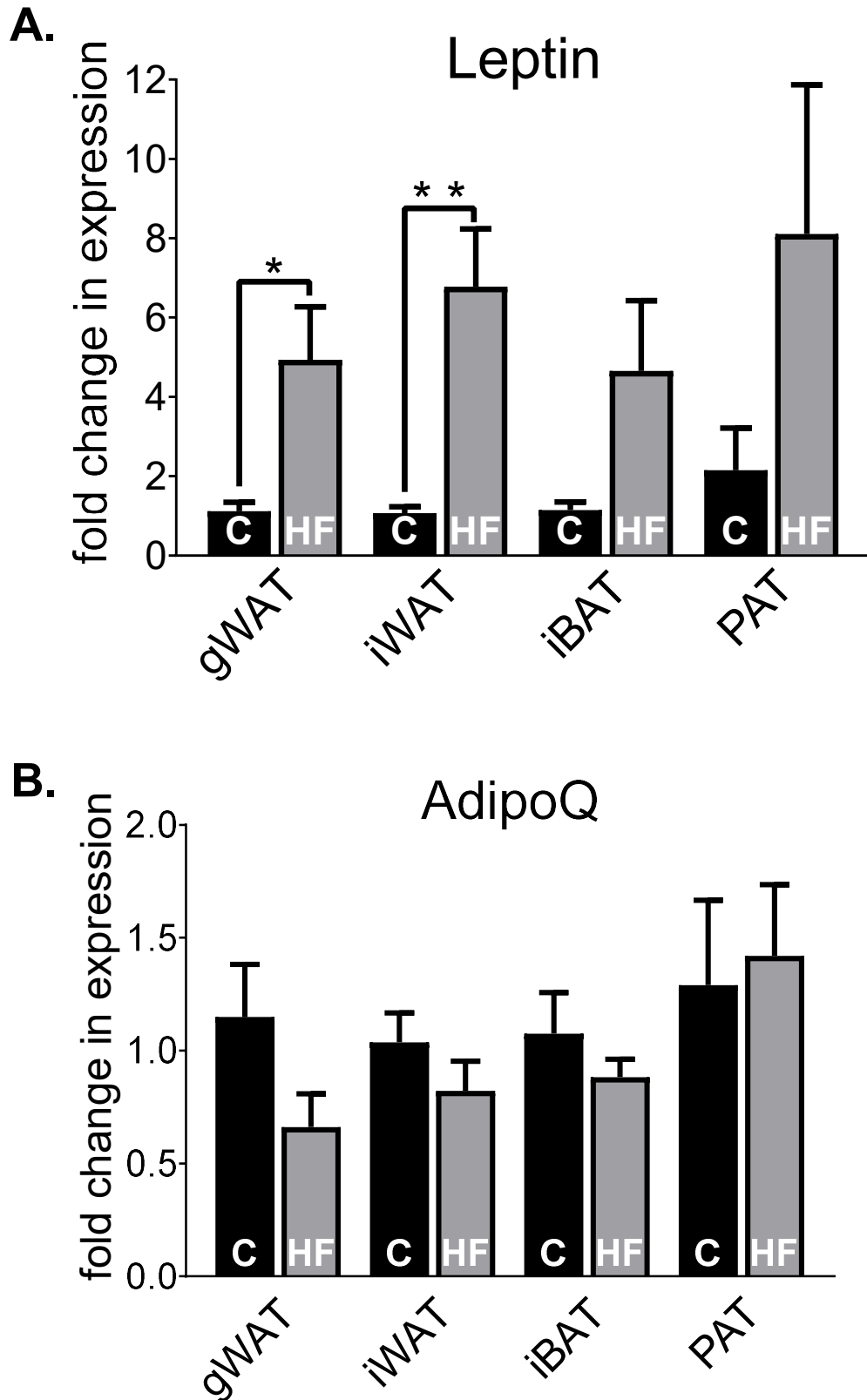
Figure 3.12. Leptin **(A)** and AdipoQ **(B)** fold change in mRNA expression in **gWAT**, **iWAT**, **iBAT** and **PAT** of chow (C) or high-fat (HF)-fed **10-week-old male mice**, relative to their respective C. Graphs represent mean + s.e.m. Data analysed by an unpaired t-test between C and HF of each depot. N = 6-8. * $p < 0.05$, ** $p < 0.01$, *** $p < 0.001$ and **** $p < 0.0001$.

A.

B.
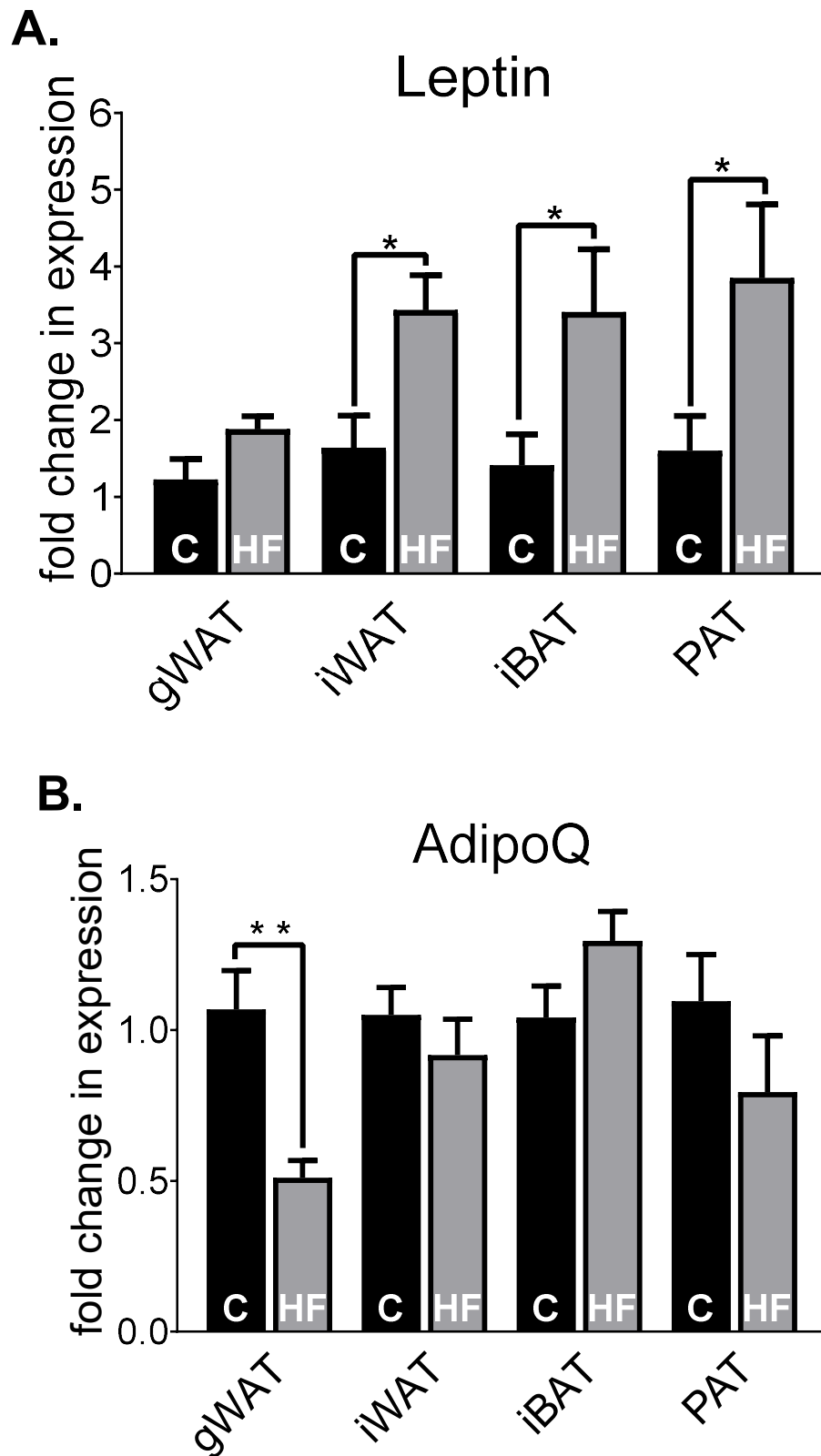
Figure 3.13. Leptin **(A)** and AdipoQ **(B)** fold change in mRNA expression in **gWAT**, **iWAT**, **iBAT** and **PAT** of chow (C) or high-fat (HF)-fed **30-week-old male mice**, relative to their respective C. Graphs represent mean $\pm$ s.e.m. Data analysed by an unpaired t-test between C and HF of each depot. N = 6-12. * p<0.05, ** p<0.01, *** p<0.001 and **** p<0.0001.

Figure 3.14. UCP1 **(A)**, ADRβ3 **(B)** and DIO2 **(C)** fold change in mRNA expression in **gWAT**, **iWAT**, **iBAT** and **PAT** of chow (C) or high-fat (HF)-fed **10-week-old male mice**, relative to their respective C. Graphs represent mean + s.e.m. Data analysed by an unpaired t-test between C and HF of each depot. N = 6-8. * $p<0.05$, ** $p<0.01$, *** $p<0.001$ and **** $p<0.0001$.

A.

B.

C.
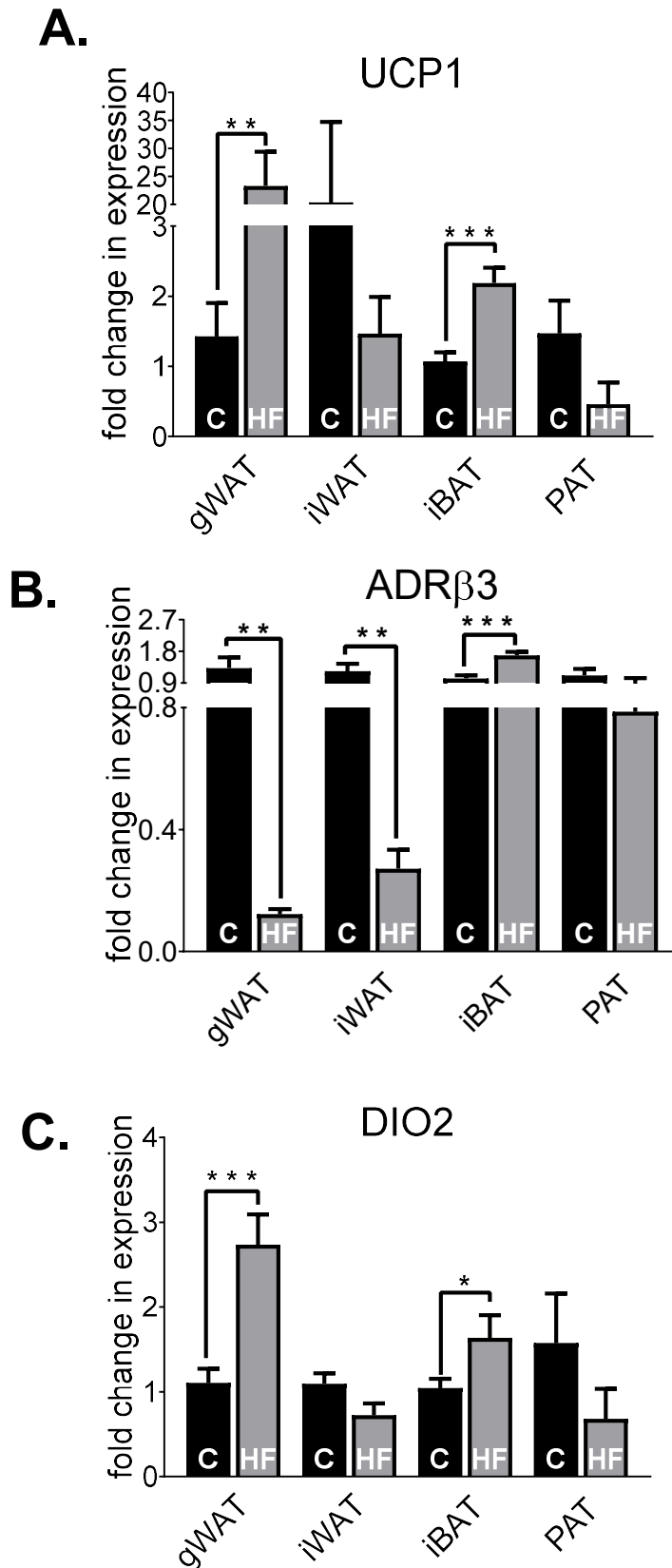
Figure 3.15. UCP1 **(A),** ADRβ3 **(B)** and DIO2 **(C)** fold change in mRNA expression in **gWAT**, **iWAT**, **iBAT** and **PAT** of chow (C) or high-fat (HF)-fed **30-week-old male mice**, relative to their respective C. Graphs represent mean ± s.e.m. Data analysed by an unpaired t-test between C and HF of each depot. N = 6-12. * $p<0.05$, ** $p<0.01$, *** $p<0.001$ and **** $p<0.0001$.

Figure 3.16. PGC1α **(A)**, COX7A1 **(B)** and COX8B **(C)** fold change in mRNA expression in

gWAT, **iWAT**, **iBAT** and **PAT** of chow (C) or high-fat (HF)-fed **10-week-old male mice**,

relative to their respective C. Graphs represent mean + s.e.m. Data analysed by an unpaired

t-test between C and HF of each depot. N = 6-8. * $p<0.05$, ** $p<0.01$, *** $p<0.001$ and ****

$p<0.0001$.

A.

B.

C.

Figure 3.17. PGC1α **(A)**, COX7A1 **(B)** and COX8B **(C)** fold change in mRNA expression in

gWAT, **iWAT**, **iBAT** and **PAT** of chow (C) or high-fat (HF)-fed **30-week-old male mice**,

relative to their respective C. Graphs represent mean ± s.e.m. Data analysed by an unpaired

t-test between C and HF of each depot. N = 6-12. * p<0.05, ** p<0.01, *** p<0.001 and ****

p<0.0001.

3.3.5. Adipose tissue histological differences in chow-fed and HF-fed mice

Percentage change in cell volume: Under chow conditions in 10-week-old mice (Figure 3.18A), C-PAT had significantly smaller cells compared C-gWAT and iWAT ($p<0.01$ and $p<0.0001$, respectively). Under HF conditions (Figure 3.18C), HF-PAT had significantly smaller cells compared to HF-gWAT ($p<0.001$). When all depots are compared to C-gWAT (Figure 3.18E), HF-gWAT had significantly larger cells compared to C-PAT and HF-PAT ($p<0.0001$ and $p<0.0001$, respectively). In addition, HF-iWAT, had significantly larger cells compared to C-PAT and HF-PAT ($p<0.001$ and $p<0.05$, respectively). In 30-week-old mice, when relative to C-gWAT (Figure 3.19E), C-PAT had significantly smaller cells compared to HF-gWAT ($p<0.01$) and HF-iWAT ($p<0.01$).

Adipose tissue morphology: In 10-week-old and 30-week-old mice, HF-PAT (Figure 3.24A, $p<0.01$ and Figure 3.25A, $p<0.001$) had larger cells compared to C-PAT. In 10-week-old and 30-week-old mice, the morphological presence of multi-locular brown-like cells was observed C-PAT (Figure 3.24C and Figure 3.25C), but only in 10-week-old mice were these cells present in HF-PAT as well (Figure 3.24C).

Cell volume distribution: For full post-hoc analysis of 10-week-old male mice demonstrated in Figure 3.18B, Figure 3.18D and Figure 3.18F, refer to Appendix Table 3.1 and Appendix Table 3.2. For full post-hoc analysis of 30-week-old male mice demonstrated in Figure 3.18B, Figure 3.19D and Figure 3.19F, refer to Appendix Table 3.3 and Appendix Table 3.4. In general, pericardial adipocytes have a higher prevalence of smaller cells within the depot in both chow and HF-fed mice.

For PAT cell volume distribution of 10-week-old mice (Figure 3.24D), there was a higher occurrence of smaller cells in C-PAT compared to HF-PAT in the 1×10^6 to 5×10^6 bin and 5×10^6 to 1×10^7 bin ($p<0.05$ and $p<0.01$, respectively).

In 30-week-old chow-fed mice (Figure 3.18B), in the 5×10^5 to 1×10^6 bin, C-PAT had a higher frequency of smaller cells compared to C-iWAT ($p<0.01$), and C-PAT had fewer larger cells compared to C-iWAT ($p<0.05$), in the 5×10^6 to 1×10^7 bin. In Figure 3.18F, in the 5×10^5 to 1×10^6 bin, C-PAT had a higher prevalence of smaller cells compared to C-iWAT ($p<0.01$) and HF-iWAT ($p<0.01$). In the 5×10^6 to 1×10^7 bin, C-PAT had significantly fewer larger adipocytes compared to C-iWAT ($p<0.05$). Furthermore, within the bin containing the largest cell size ($>1 \times 10^7$), C-PAT had a lower frequency of larger cells compared to HF-gWAT ($p<0.001$) and HF-iWAT ($p<0.01$). The distribution of chow-fed adipocyte size (Figure 3.19B) and combination of both dietary groups (Figure 3.19F) seem to have a normal distribution, compared to adipocyte size of HF-fed mice presented with a negatively skewed distribution, suggesting a higher prevalence of medium sized cells.

Regarding the distribution of adipocyte size in chow and HF-fed mice in 30-week-old mice, PAT (Figure 3.24D, $p<0.001$) had significantly more larger cells in HF-fed mice compared to C-fed mice, in the $>1 \times 10^7$ bin, the largest cell size bin. In PAT (Figure 3.25D), in the 5×10^5 to 1×10^6 bin ($p<0.05$) and 1×10^6 to 5×10^6 bin ($p<0.05$), there were significantly fewer smaller cells in HF-fed mice compared to C-fed mice. In the 5×10^6 to 1×10^7 bin, there were significantly more larger cells in HF-fed mice compared to C-fed mice ($p<0.05$). Both gWAT and iWAT cell volume distribution graphs resemble a negatively skewed distribution, compared to a normal distribution in PAT, suggesting that these depots have a higher prevalence of having larger adipocytes.

The overall graph of pericardial adipocyte size resembles a positively skewed distribution, compared to gWAT and iWAT, suggesting smaller sized cells are more prevalent in pericardial fat.

Alaa Al - Dibouni
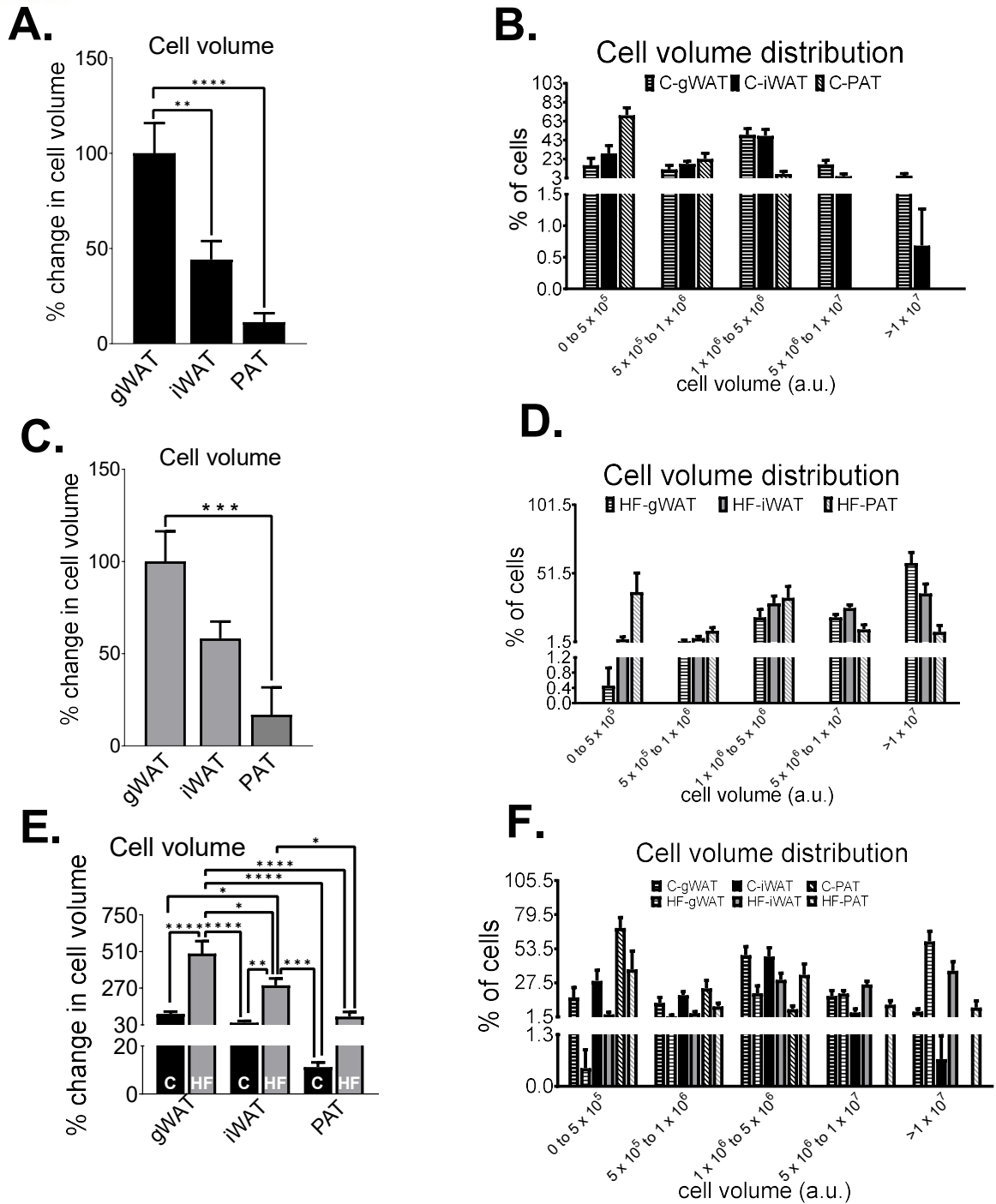
Figure 3.18. The percentage change in cell volume normalised to c-gWAT **(A)** and cell volume distribution **(B)** of **gWAT**, **iWAT** and **PAT** of chow (C)-fed **10-week-old male mice**. The percentage change in cell volume normalised to HF-gWAT **(C)** and cell volume distribution **(D)** of **gWAT**, **iWAT** and **PAT** of high-fat (HF)-fed **10-week-old male mice**. The percentage change in cell volume normalised to C-gWAT **(E)** and cell volume distribution **(F)** of **gWAT**, **iWAT** and **PAT** of chow (C) or high-fat (HF)-fed **10-week-old male mice**. Graphs represent mean ± s.e.m. Data analysed by one-way ANOVA (post-hoc Tukey correction) between depots **(A,C,E)** and cell volume (a.u.) groups **(B,D,F).** N = 6-7. * p<0.05, ** p<0.01, *** p<0.001 and **** p<0.0001.
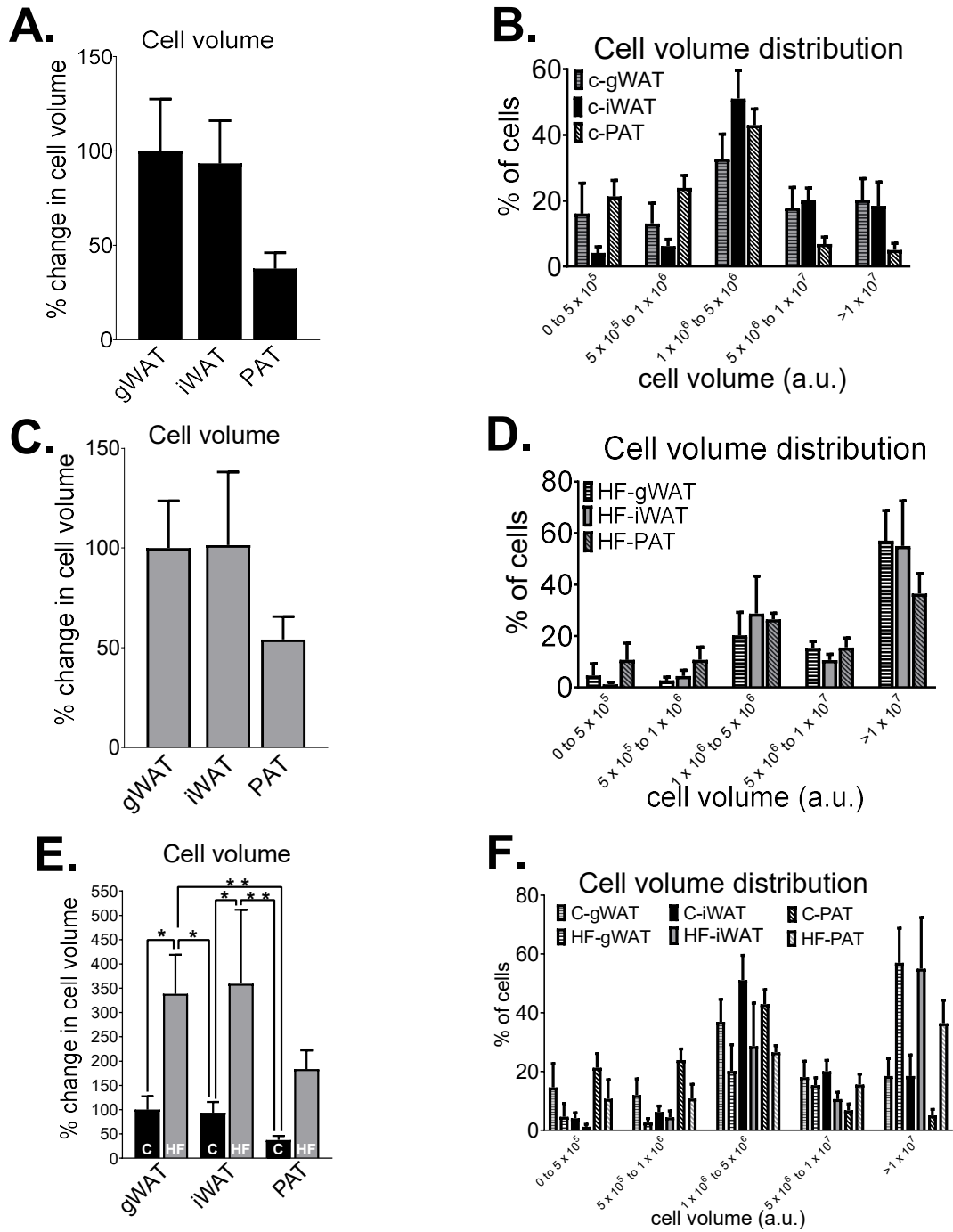
Figure 3.19. The percentage change in cell volume normalised to c-gWAT **(A)** and cell volume distribution **(B)** of gWAT, iWAT and PAT of chow (C)-fed **30-week-old male mice**. The percentage change in cell volume normalised to HF-gWAT **(C)** and cell volume distribution **(D)** of gWAT, iWAT and PAT of high-fat (HF)-fed **30-week-old male mice**. The percentage change in cell volume normalised to C-gWAT **(E)** and cell volume distribution **(F)** of gWAT, iWAT and PAT of chow (C) or high-fat (HF)-fed **30-week-old male mice**. Graphs represent mean $\pm$ s.e.m. Data analysed by one-way ANOVA (post-hoc Tukey correction) between depots **(A,C,E)** and cell volume (a.u.) groups **(B,D,F).** N = 6-11. * $p<0.05$, ** $p<0.01$, *** $p<0.001$ and **** $p<0.0001$.

A.

Cell volume

B.

C.

Cell volume distribution
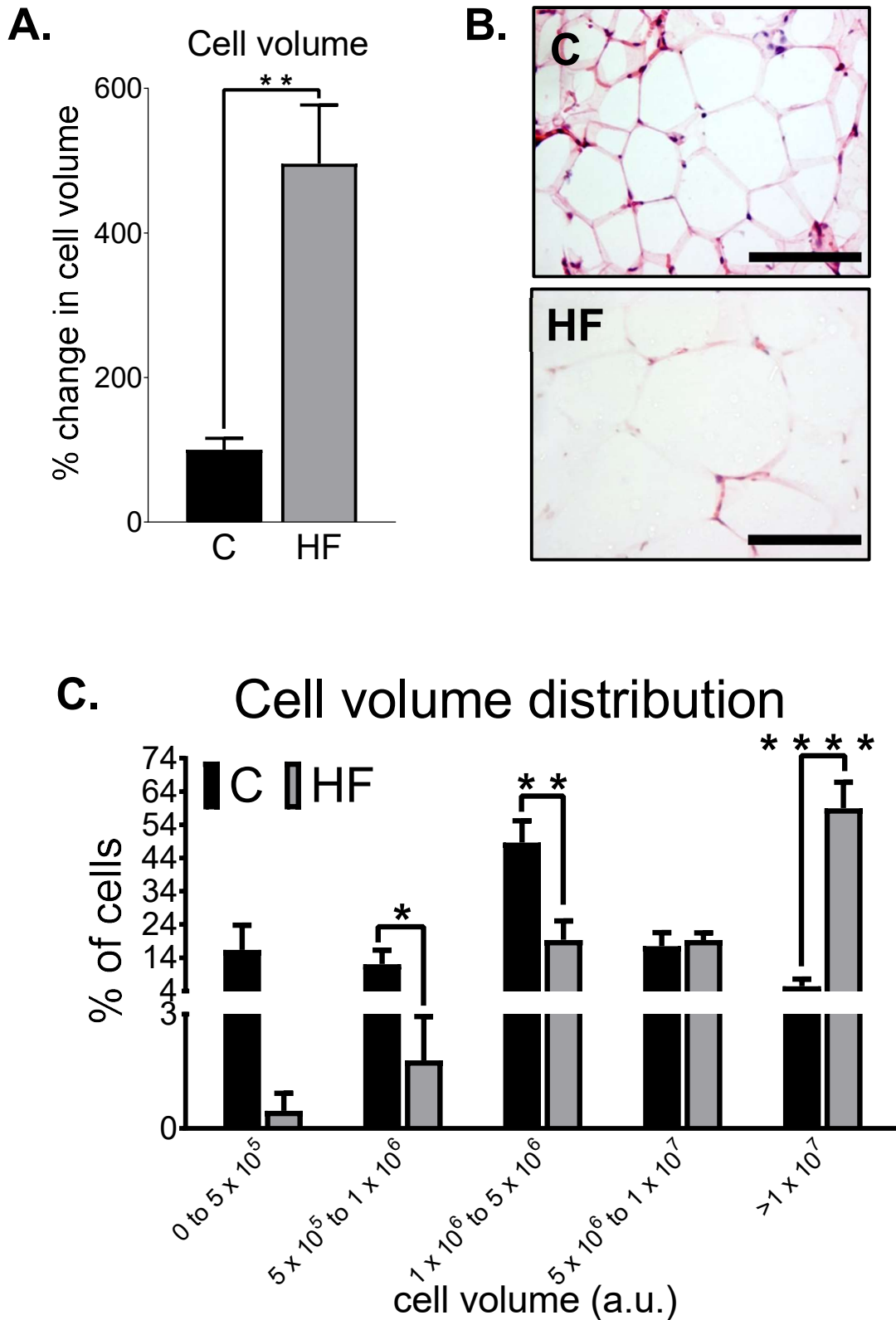
cell volume (a.u.)

Figure 3.20. The percentage change in cell volume normalised to C **(A)**, H&E representative images of cell size **(B)** and cell volume distribution of **gWAT** from chow (C) or high-fat (HF)-fed **10-week-old male mice**. All scale bars represent 100μM and imaged at x40 optical lens with Nikon TE200 brightfield inverted microscope. Graphs represent mean $\pm$ s.e.m. Data analysed by an unpaired t-test between C and HF **(A)** and cell volume (a.u.) groups **(C).** N = 6-7. * $p<0.05$, ** $p<0.01$, *** $p<0.001$ and **** $p<0.0001$.

A.

Cell volume

B.

C.

Cell volume distribution
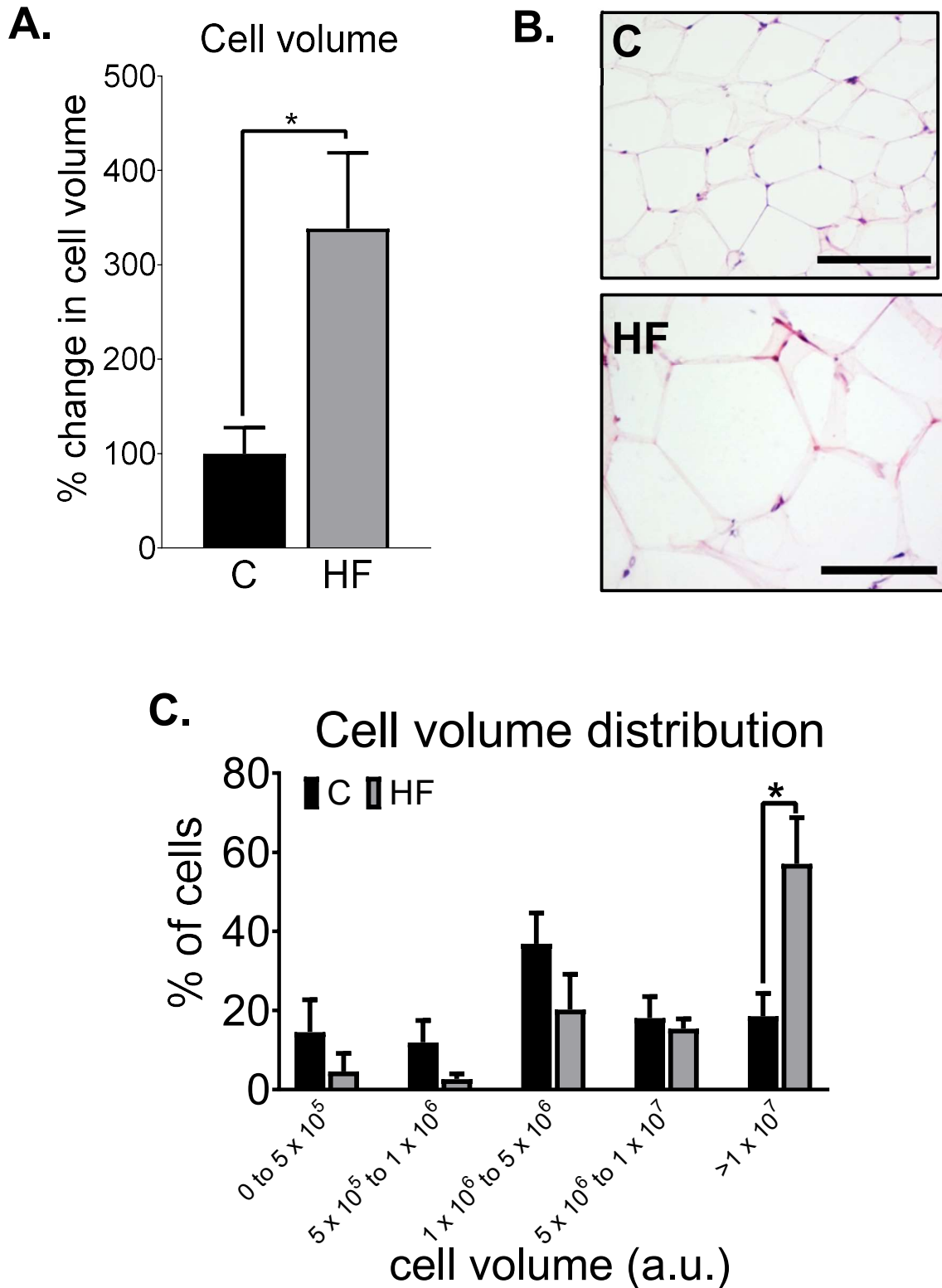
cell volume (a.u.)

Figure 3.21. The percentage change in cell volume normalised to C **(A)**, H&E representative images of cell size **(B)** and cell volume distribution **(C)** of **gWAT** from chow (C) or high-fat (HF)-fed **30-week-old male mice**. All scale bars represent 100μM and imaged at x40 optical lens with Nikon TE200 brightfield inverted microscope. Graphs represents mean ± s.e.m. Data analysed by an unpaired t-test between C and HF **(A)** and cell volume (a.u.) groups **(C). N =** 8. * $p<0.05$, ** $p<0.01$, *** $p<0.001$ and **** $p<0.0001$.
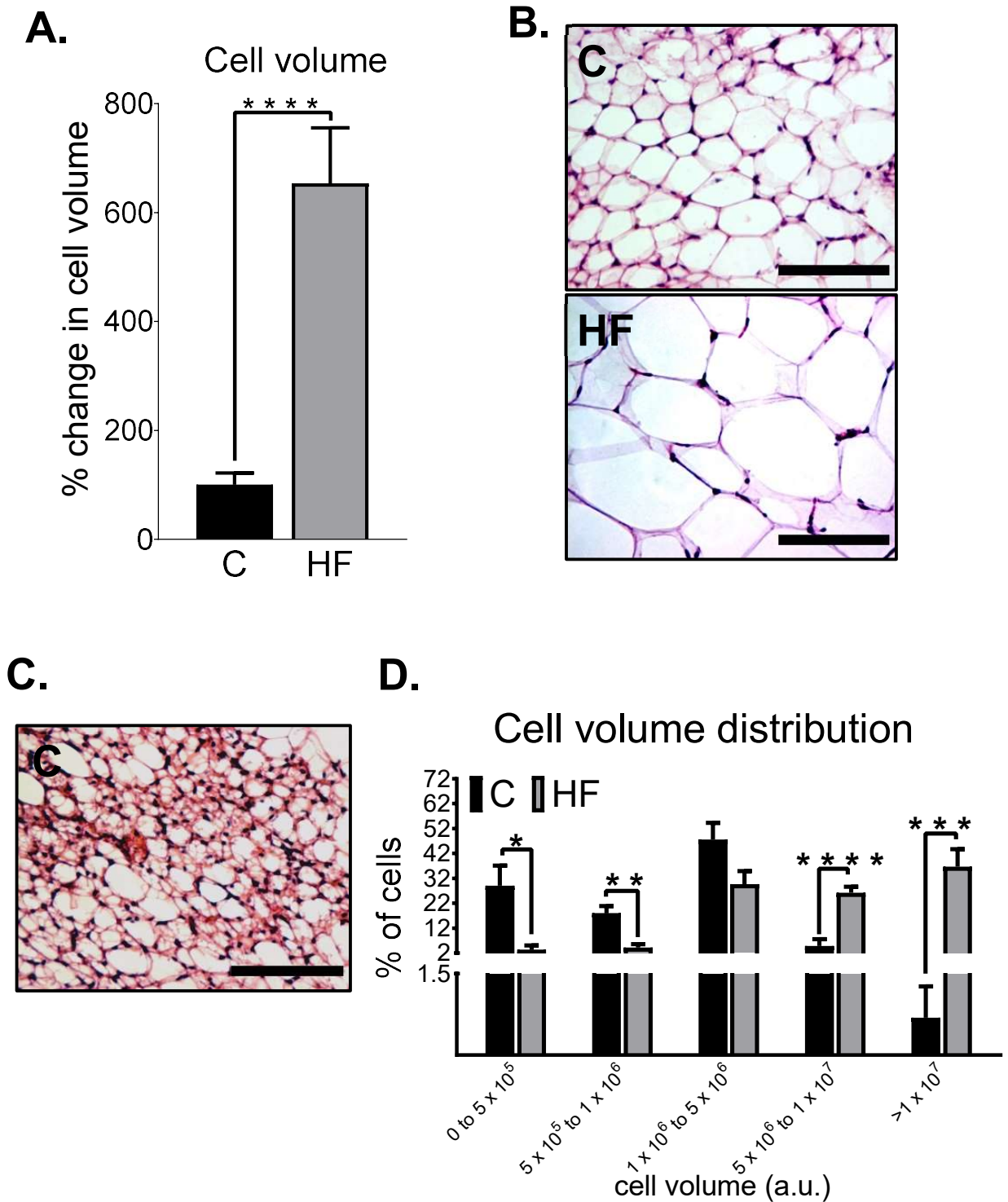
Figure 3.22. The percentage change in cell volume normalised to C **(A)**, H&E representative images of cell size **(B)**, multi-locular cells **(C)** and cell volume distribution **(D)** of **iWAT** from chow (C) or high-fat (HF)-fed **10-week-old male mice**. All scale bars represent 100µM and imaged at x40 optical lens with Nikon TE200 brightfield inverted microscope. Graphs represent mean $\pm$ s.e.m. Data analysed by an unpaired t-test between C and HF **(A)** and cell volume (a.u.) groups **(D)**. N = 6-7. * $p<0.05$, ** $p<0.01$, *** $p<0.001$ and **** $p<0.0001$.

A.

Cell volume

B.

C.

D.
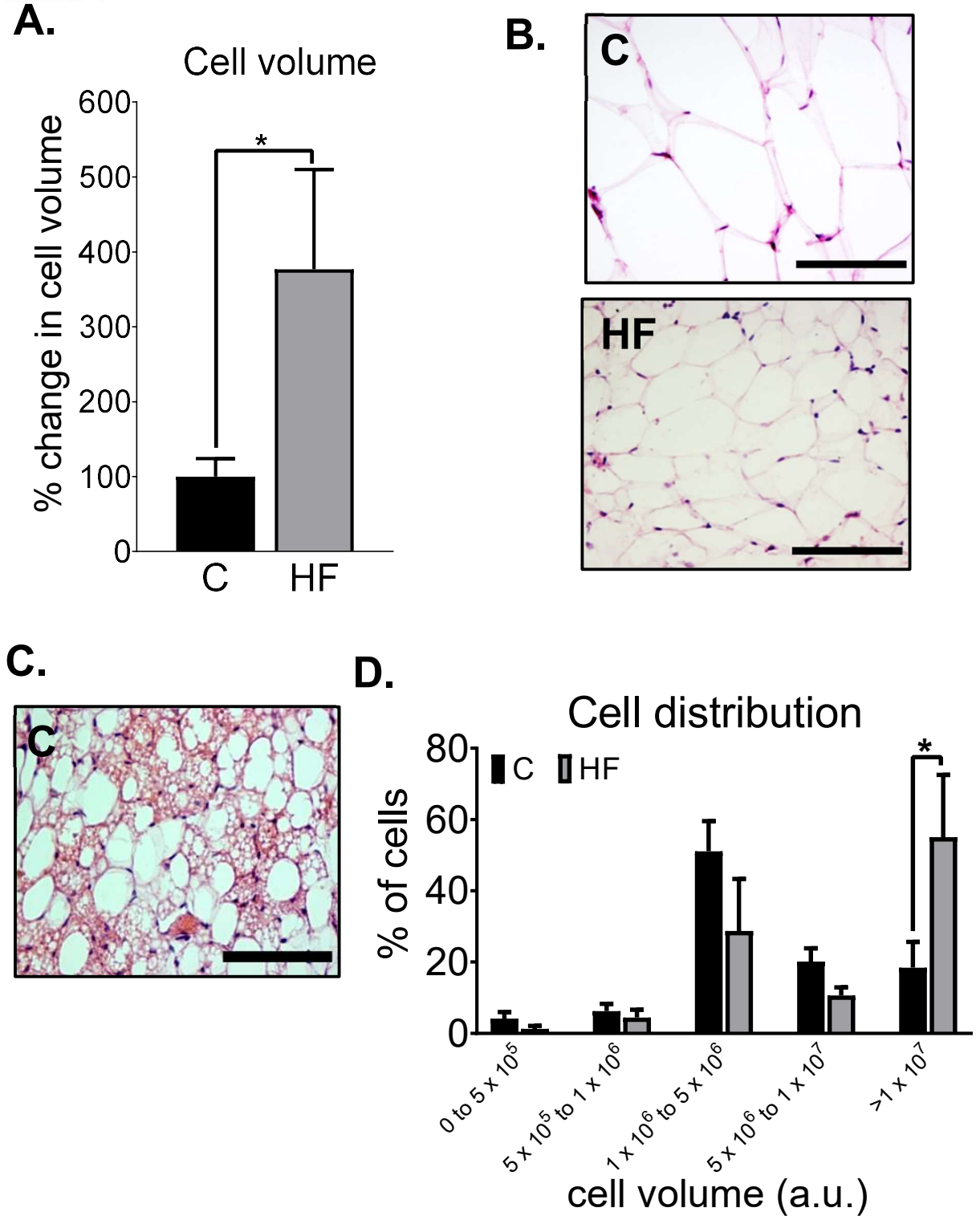
Cell distribution

Figure 3.23. The percentage change in cell volume normalised to C **(A)**, H&E representative images of cell size **(B)**, multi-locular cells **(C)** and cell volume distribution **(D)** of **iWAT** from chow (C) or high-fat (HF)-fed **30-week-old male mice**. All scale bars represent 100μM and imaged at x40 optical lens with Nikon TE200 brightfield inverted microscope. Graphs represents mean ± s.e.m. Data analysed by an unpaired t-test between C and HF **(A)** and cell volume (a.u.) groups **(D)**. N = 6-9. * $p<0.05$, ** $p<0.01$, *** $p<0.001$ and **** $p<0.0001$.

A.

B.

C.

D.
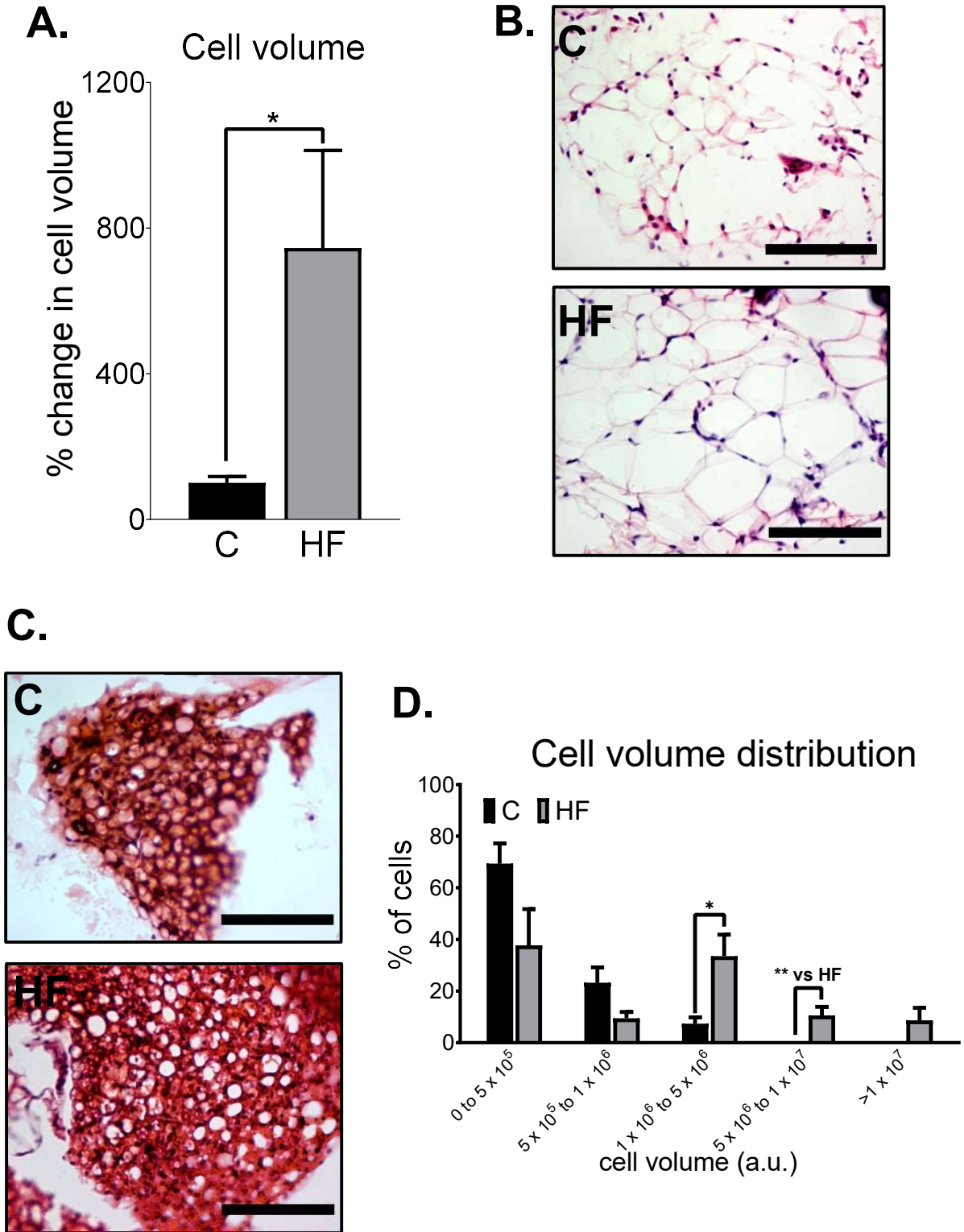
Figure 3.24. The percentage change in cell volume normalised to C **(A)**, H&E representative images of cell size **(B)**, multi-locular cells **(C)** and cell volume distribution **(D)** of **PAT** from chow (C) or high-fat (HF)-fed **10-week-old male mice**. All scale bars represent 100μM and imaged at x40 optical lens with Nikon TE200 brightfield inverted microscope. Graphs represent mean ± s.e.m. Data analysed by an unpaired t-test between C and HF **(A)** and cell volume (a.u.) groups **(D)**. N = 6. * $p<0.05$, ** $p<0.01$, *** $p<0.001$ and **** $p<0.0001$.
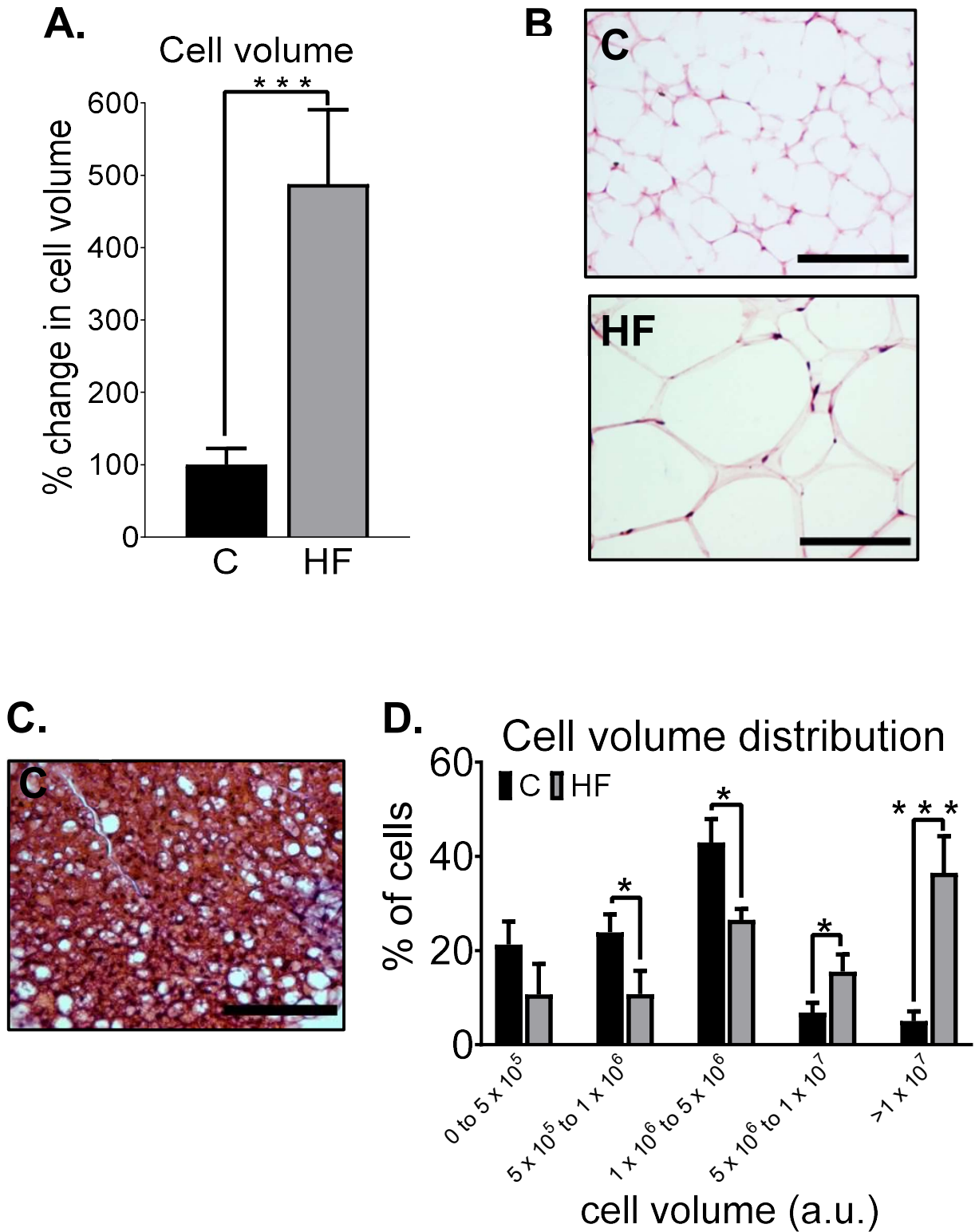
Figure 3.25. The percentage change in cell volume normalised to C **(A)**, H&E representative images of cell size **(B)**, multi-locular cells **(C)** and cell volume distribution **(D)** of **PAT** from chow (C) or high-fat (HF)-fed **30-week-old male mice**. All scale bars represent 100µM and imaged at x40 optical lens with Nikon TE200 brightfield inverted microscope. Graphs represents mean ± s.e.m. Data analysed by an unpaired t-test between C and HF **(A)** and cell volume (a.u.) groups **(D)**. N = 6-11. * $p<0.05$, ** $p<0.01$, *** $p<0.001$ and **** $p<0.0001$.

3.3.6. The relationship between biochemical and metabolic parameters, gene expression levels and percentage change in cell volume in adipose tissue of chow-fed and HF-fed mice

Inflammatory markers vs serum metabolite levels: In 30-week-old mice, there was a positive correlation in PAT IL6 (Appendix Figure 4.3C) (p<0.01) and TNFα (Appendix Figure 4.3F) (p<0.05) compared to percentage change in cell volume. In PAT, there was a positive relationship between TNFα expression and serum total cholesterol (Appendix Figure 4.6D, p=0.001), serum HDL (Appendix Figure 4.6H, p<0.001) and serum LDL (Appendix Figure 4.6L, p<0.01).

Inflammatory markers vs phenotypic data: In 30-week-old mice, IL6 mRNA levels were positively correlated in PAT compared to body fat content (Appendix Figure 4.5H, p<0.01), body weight (Appendix Figure 4.5L p<0.05), percentage body fat (Appendix Figure 4.5P, p<0.01), fasting blood glucose levels (Appendix Figure 4.5D) (p<0.05). There was a positive relationship between PAT TNFα expression and body fat content (Appendix Figure 4.7H, p<0.01), body weight (Appendix Figure 4.7L, p<0.05) and percentage body fat (Appendix Figure 4.7P, p<0.05). There was a negative trend between PAT UCP1 expression and percentage change in cell volume (Appendix Figure 4.3I, p<0.05), serum total cholesterol (Appendix Figure 4.8D, p<0.05), serum HDL (Appendix Figure 4.8H, p<0.05), body fat content (Appendix Figure 4.9H, p<0.01), body weight (Appendix Figure 4.9L, p<0.05) and percentage body fat (Appendix Figure 4.9P, p<0.01) and a negative trend towards significance in serum LDL levels (Appendix Figure 4.8L, p=0.0529).

Percentage change in volume vs serum metabolite levels: In 30-week-old mice, the relationship between the percentage change in cell volume in PAT, showed a positive trend between serum total cholesterol (Appendix Figure 4.10C, p<0.01), serum HDL (Appendix Figure 4.10F, p<0.01), serum LDL (Appendix Figure 4.10I, p<0.01).

Percentage change in volume vs phenotypic data: In 30-week-old mice, the relationship between the percentage change in cell volume PAT, showed a positive trend between body fat content (Appendix Figure 4.11F, p<0.0001), body weight (Appendix Figure 4.11I,

p<0.0001), percentage body fat (Appendix Figure 4.11L, p<0.001) and fasting blood glucose (Appendix Figure 4.11C, p=0.01).

Inflammatory markers vs percentage change in cell volume: In 30-week-old mice, PAT Leptin levels were associated with percentage change in cell volume (Appendix Figure 4.12C, p<0.05).

30-week Inflammatory markers vs phenotypic data: In 30-week-old mice, PAT Leptin levels were positively correlated with body weight (Appendix Figure 4.13G, p<0.01) and PAT AdipoQ levels were negatively correlated with PAT depot weight (Appendix Figure 4.14F, p<0.01).

3.4. DISCUSSION

Pericardial fat in both 10-week-old and 30-week-old male mice demonstrated a unique transcriptional and histological profile under chow (7% kcal fat diet and 10% kcal fat diet, respectively) and HF-conditions (45% kcal fat diet and 60% kcal fat diet, respectively). The distinctive signatures were demonstrated by a **(1)** thermogenic and/or **(2)** visceral profile of pericardial fat under baseline and obesogenic conditions. This was further supported by the morphological resemblance of **(3)** uni-locular white-like cells and/or **(4)** multi-locular brown-like cells residing within pericardial fat.

The classification of pericardial fat in mice as either a white or brown depot under normal physiological conditions during development is unclear. Depending on the need to upregulate thermogenesis or act as a storage site, 'beige' depots like perirenal fat adopt either brown-like or white-like characteristics (Clarke et al., 1997b). In fact, white depots have the capacity to recruit thermogenic cells, characterised by higher levels of UCP1 mRNA expression (Shabalina et al., 2013). In 10-week-old male mice under baseline conditions (chow-fed state), the expression of UCP1 was second only to that of brown fat. This response was further potentiated in older chow-fed mice (30-week-old) in which PAT UCP1 mRNA expression levels were significantly higher than inguinal subcutaneous fat. These UCP1 levels were negatively correlated with cell volume, body fat content, percentage body fat and serum levels of total cholesterol and HDL. Although relationships were not significant in iWAT, this resembles a similar correlative relationship as subcutaneous inguinal fat.

Given that subcutaneous fat resembles a 'beige' depot under cold exposure with elevated levels of UCP1 expression (Waldén et al., 2012), the results suggest that under chow conditions, pericardial fat in mice resembles a 'beige' depot. This is further supported by DIO2 expression levels which is associated with upregulated thermogenesis (Christoffolete et al., 2004). The expression profile of DIO2 in 10-week-old and 30-week-old chow-fed male mice were similar to that of UCP1 expression levels in pericardial fat. In 30-week-old chow-fed male mice, DIO2 expression levels in PAT where higher than that of gonadal and inguinal white fat. Under chow conditions, DIO2 mRNA levels in pericardial fat were comparable to that of brown

fat in 30-week-old chow-fed male mice. However, in 10-week-old chow-fed male mice, pericardial DIO2 expression levels were significantly lower than brown fat. Indeed, this was true for the expression of mitochondrial-related genes PGC1α, COX7A1 and COX8B in 10-week-old chow-fed male mice. Interestingly, the same transcriptional profile was observed in PGC1α in 30-week-old chow-fed male mice, however COX7A1 and COX8B expression levels were significantly higher compared to the white depots. This data suggests that under basal (chow) conditions, the thermogenic capacity of pericardial fat is upregulated in 30-week-old male mice, in comparison to 10-week-old male mice. This demonstrates the thermogenic changes that occur in pericardial fat during postnatal development.

In 10-week-old chow-fed male mice, all pro-adipogenic markers were lower in pericardial fat compared to all depots. However, expression of FABP4, a mature adipocyte marker (Shan et al., 2013; Sim et al., 2017), did not differ between brown and pericardial fat. In 30-week-old chow-fed male mice, only FABP4 expression was lower than gonadal and inguinal fat.

C/EBPα and PPARγ expression is essential for the maintenance of mature adipocytes (Christy et al., 1991; Christy et al., 1989; Imai et al., 2004) and C/EBPα expression is vital for white fat development, *in vivo* (Linhart et al., 2001). Moreover, in 30-week-old and 10-week-old male mice, TNFα levels in PAT were higher compared to brown fat, and further elevated compared to white fat, respectively. Perhaps high expression levels of this cytokine in pericardial fat, compared to white and brown fat, is linked with lower levels of pro-adipogenic markers, as TNFα suppresses adipocyte differentiation (Kurebayashi et al., 2001), therefore reducing lipid accumulation and adipocyte size. This is further supported by a relationship between pericardial adipocyte volume and TNFα mRNA expression levels in 30-week-old male mice. This suggests that pericardial adipocytes resemble an adipogenic profile that is dissimilar to white fat, further exaggerated in older 30-week-old male mice, than in 10-week-old male mice. Indeed, a reduction in pro-adipogenic markers are associated with smaller, multi-locular cells (Aziz et al., 2017; Sudhakar et al., 2020). Furthermore, adipokines Adiponectin (AdipoQ) (Musovic and Olofsson, 2019) and Leptin (Cinti et al., 1997) are primarily secreted by white adipocytes. The expression of the latter is associated with adipocyte size and UCP1 mRNA

levels, under reciprocal control in brown fat (Cancello et al., 1998; Kim et al., 2003). AdipoQ and Leptin expression levels were significantly reduced in pericardial fat compared to gWAT in 30-week-old male mice and further reduced compared to iWAT in 10-week-old male mice. This is reflected by a population of brown-like cells in chow-fed 10-week-old and 30-week-old male mice. However, unlike 30-week-old chow-fed male mice, only pericardial adipocyte size from 10-week-old chow-fed male mice indicated a reduction in cell size compared to the white depots. In fact, this profile was true for pericardial fat of HF-fed mice too. This is suggestive of an upregulated hypertrophic mechanism in growth as pericardial adipocyte size was increased in older mice (30-week-old), with no significant differences between pericardial fat and white depots.

The presence and activity of brown adipocytes are associated with an improvement in body weight, whole-body insulin sensitivity (Stanford et al., 2013; Yoneshiro et al., 2011) and thermogenic capacity (Van Marken Lichtenbelt et al., 2009). With this view, these positive effects of brown cell activity are reduced in obesity (Orava et al., 2013) and can be dysregulated by HF-feeding. The metabolic profile was determined of 30-week-old male mice fed an extreme obesogenic 60% kcal fat diet, over a 26-week period, compared to a 10% kcal fat diet. The chronic HF-fed diet induced obesity, compared to chow-fed mice, characterised by an increase in body weight, a reduction in percentage lean weight, increase in percentage fat weight and reduced energy expenditure, demonstrated by reduced respiratory exchange rate (RER). Furthermore, this feeding plan induced glucose intolerance, demonstrated after an ipGTT and elevated fasting blood glucose levels and serum levels of FFAs, total cholesterol, HDL, and LDL. In pericardial fat of 30-week-old male mice, there were no observable sub-populations of multi-locular brown-like cells in mice fed a HF-diet (60% kcal fat diet), unlike in chow-fed mice (10% kcal fat diet). However, in 10-week-old male mice, brown-like cells were present, regardless of a 7-week dietary intake of a chow (7% kcal fat) or HF-diet (45% kcal fat). A pro-longed HF-diet may induce the trans-differentiation of brown-to-white cells in pericardial fat of 30-week-old HF-fed male mice. AT development is altered due to nutritional changes during adulthood. Perhaps an extreme obesogenic environment induces the

'whitening' (Dobner et al., 2017; Kuipers et al., 2019) of pericardial fat. This may impair the thermogenic capacity of pericardial adipocytes to reduce energy expenditure and promote obesity and metabolic dysfunction in 30-week-old HF-fed male mice.

High levels of thermogenic markers in brown fat are often associated with a leaner phenotype in humans (Cypess, 2009). Interestingly, the thermogenic and mitochondrial-related genes are elevated in brown fat, followed by pericardial fat. Of note, ADRβ3 expression is downregulated in obesity (Kurylowicz et al., 2015), yet there were elevated levels of ADRβ3 expression in pericardial fat of 10-week-old HF-fed male mice, compared to chow-fed mice. This may be due to diet-induced thermogenesis (DIT) upon HF-feeding. The facultative component of DIT is influenced by diet to stimulate the SNS (Young and Landsberg, 1977), mediated by UCP1 activation (Feldmann et al., 2009; Hibi et al., 2016). In fact, it would be expected that ADRβ3 expression would be elevated in brown fat. However, in pericardial fat, expression of ADRβ3 is lower than gonadal fat in 30-week-old chow-fed male mice, and a further reduction compared to inguinal fat in 10-week-old chow-fed male mice. Perhaps there is a thermogenic response in these white depots as well, independent of UCP1 expression (Granneman et al., 2003), which is greater in adrenergic output compared to brown and pericardial fat to promote improved metabolic health in chow-fed mice.

Under an obesogenic environment, a similar profile of pro-adipogenic markers in pericardial fat of chow-fed mice was demonstrated. However, unlike in 10-week-old HF-fed male mice, the pro-inflammatory markers of IL6 and TNFα in pericardial fat of 30-week-old HF-fed male mice, were elevated compared to inguinal and brown fat. In fact, levels were almost comparable to that of gonadal fat, a visceral depot, and IL6 and TNFα levels were only elevated in 30-week-old HF-fed male mice, compared to chow-fed male mice. These inflammatory levels were positively correlated with body fat content, body weight and adiposity. Moreover, IL6 mRNA levels of pericardial fat were positively linked with fasting blood glucose levels, and TNFα expression was positively correlated with serum total cholesterol, HDL and LDL levels. This suggests that an extreme HF-fed diet may be potentiating a deleterious pro-inflammatory visceral status in pericardial fat.

Moreover, hypertrophy of visceral fat is associated with a pro-inflammatory state in metabolic and CV pathogenesis (Drolet et al., 2008; Elie et al., 2016; Horckmans et al., 2018; Kang et al., 2017b). Pericardial adipocyte cell volume was elevated in HF-fed 10-week-old and 30-week-old male mice. In 30-week-old male mice, these levels were positively associated with IL6 and Leptin mRNA levels, body weight, adiposity and blood levels of fasting glucose, total cholesterol, HDL and LDL. Although there were no differences between pericardial depot weights in 30-week-old male mice, regardless of diet, this may be due to the small sample size (N = 3) in the HF-fed group, as capacity of adipose depots are reflected by their depot weight (Van Beek et al., 2015). With this said, depot weight was negatively correlated with the expression of the anti-inflammatory gene AdipoQ, which is often downregulated in obesity (Hu, Liang and Spiegelman, 1996).

Additionally, Leptin mRNA expression levels were elevated in HF-fed 30-week-old male mice compared to chow-fed male mice in pericardial fat. As elevated levels of Leptin are associated with BMI (Hamilton et al., 1995), Leptin mRNA expression of 30-week-old male mice was positively correlated with body weight. Given that hypertrophy is associated with metabolic dysfunction (Laforest et al., 2015), in both 10-week-old and 30-week-old HF-fed male mice, pericardial adipocyte size was increased in comparison to their respective chow groups. The hypertrophic and pro-inflammatory status of pericardial fat under a HF-diet demonstrates a similar trend to that of visceral gonadal fat, in this and previous studies (Drolet et al., 2008; Kang et al., 2017b). This along with correlation analysis represents the visceral-like qualities of pericardial fat, more so under extreme obesogenic conditions (30-week-old HF-fed male mice), to potentiate metabolic dysfunction.

3.4.1. Conclusion

This study has demonstrated that pericardial fat adopts a 'beige' signature to adapt to various nutritional environments. Further studies are required to directly analyse the thermogenic capacity of pericardial fat demonstrated by transcriptional and histological analysis. However, the results presented demonstrate that under baseline conditions, pericardial fat has thermogenic properties which are somewhat dysregulated upon HF-feeding, further exaggerated by an extreme obesogenic environment.

CHAPTER 4

INVESTIGATING THE EFFECTS OF MATERNAL OVERNUTRITION ON PERICARDIAL ADIPOSE TISSUE IN OFFSPRING MICE

4.1. INTRODUCTION

Around 20% of women are either overweight or obese during the early stages of pregnancy (Public Health England, 2018). Obesity during pregnancy, known as maternal obesity, increases the risk of developing insulin resistance, elevated levels of circulating FFAs (Boyle et al., 2017), hypertension and gestational diabetes (Khan et al., 2017), in the pregnant mother. Not only does maternal obesity pose detrimental health effects on the mother, but also impacts the normal development of a growing fetus. This could lead to negative outcomes, such as epigenetic alterations (Zhang et al., 2009) or even neonatal death (Zhou et al., 2019a).

The concept that the maternal environment during pregnancy influences the metabolic health and organ programming *in utero* in offspring was originally introduced by Professor David Barker (Barker and Osmond, 1986). Epidemiological studies revealed convincing evidence that low infant birthweight, suggestive of undernutrition *in utero*, was highly correlated with an increased risk of developing CVD in later life (Barker et al., 1993; Osmond et al., 1993). These observations introduced the 'thrifty phenotype hypothesis.' This hypothesis proposes that undernutrition *in utero,* at various timepoints or 'windows of susceptibility' during the developmental stages of a fetus, are associated with the increased risk of metabolic complications of an offspring during adulthood (Barker et al., 1993; Hales and Barker, 2001).

Furthermore, as AT development is a sensitive period primarily regulated during the perinatal stages of gestation, in particular the early postnatal period (Greenwood and Hirsch, 1974), maternal undernutrition may effect AT growth, contributing to health complications in offspring in later life. This has been demonstrated in the altered capacity of thermogenesis in non-classical adipose depots, which have both white and brown-like qualities, in offspring exposed to maternal undernutrition during different developmental timepoints.

Perirenal adipose tissue, associated with the kidneys, is a brown depot that resembles white adipose tissue characteristics postnatally in sheep. Clarke et al., demonstrated that in the early stages of postnatal life, high UCP1 gene expression levels were correlated with the thyroid hormone T3, resembling a brown-like depot. However, as a lamb increases with age, UCP1 gene expression levels decline, accompanied by increased lipid accumuation in adipocytes,

resembling a white-like depot (Clarke et al., 1997b). Interestingly, maternal undernutrition during the periconception period or late gestational period results in either an increase or decrease in UCP1 gene expression, respectively. This is observed in fetal perirenal adipose tissue of sheep, prior to birth (Budge et al., 2004). As expression levels decline after birth (Finn et al.,1998), the initial increase in UCP1 expression of fetal perirenal fat may act as a mechanism to induce thermogenesis in a fetus (Clarke et al., 1997a) to regulate body temperature nearing the time of birth.

As with sheep, rodent offspring AT development is also effected by exposure to maternal undernutrition, *in utero*. Under normal developmental conditions, gonadal white fat is characterised largely by white adipocytes. However, exposure to maternal undernutrition during the final stages of gestation and lactation results in an increase of UCP1 expression. This is suggestive of a 'browning' effect in offspring white fat induced by maternal undernutrition, to promote thermogenesis for survival purposes (Delahaye et al., 2010), as demonstrated in perirenal fat of offspring ewes (Budge et al., 2004).

The effects of maternal undernutrition in offspring perirenal fat are similar to that of pericardial fat which also possesses brown and white adipose depot characteristics. In pericardial fat of offspring sheep, exposure to maternal undernutrition during the early or late stages of gestation results in an increase (Ojha et al., 2014) or decrease (Ojha et al., 2013) in UCP1 gene expression levels, respectively. Regardless of the stage at which maternal undernutrition is induced, white adipogenic markers are increased in pericardial fat of offspring (Ojha et al., 2013; Ojha et al., 2014). Moreover, the origins of excess pericardial adiposity may stem from offspring exposure to maternal undernutrition *in utero.* This could contribute to metabolic complications in the offspring in adulthood (Ojha et al., 2014).

It is clear that exposure to maternal undernutrition during certain periods of fetal development effects the thermogenic capacity of offspring AT. This entices a premise that perhaps even maternal overnutrition may also effect offspring AT development. Obesogenic pregnancies may exacerbate chronic inflammation and lead to an inflammatory environment *in utero.* This could influence the metabolic health of an offspring later in life (Challier et al., 2008), including

an increased risk of weight gain (Boney et al., 2005; Oken et al.,2008), growth (Desai et al., 2014), adiposity, insulin resistance (Catalano et al., 2009), obesity (National Health Service, 2019) and CVD (Samuelsson et al., 2008).

Using maternal obesity animal models may provide an insight into the mechanisms involved in which human maternal obesity effects offspring AT development. Whilst it is unclear whether genetic variations (Yang et al., 2013) are passed on from mother to offspring *in utero*, there is evidence to suggest that rodent neonates fed a high-fat (HF)-diet are more susceptible to increased adipocyte differentiation (Boyle et al., 2016). This is further exacerbated by a maternal HF-diet (Borengasser et al., 2013). The maternal HF-diet predisposes an offspring to share an affinity to food with a high fat content (Bayol et al., 2007) and is associated with increased weight gain, fat mass and development of MetS in offspring (Borengasser et al., 2013). This increased hyperphagic response could be due to dysregulated Leptin signalling, a pathway that is essential for regulating appetite (Segovia et al., 2018). In perirenal fat of offspring sheep, exposure to maternal overnutrition during the late gestational period, causes an upregulation of pro-adipogenic white markers including Leptin and PPARγ (Muhlhausler et al., 2007a; Muhlhausler et al., 2007b).

Additionally, rodent studies have demonstrated that a combination of exposure with maternal overnutrition and offspring HF-diet post-weaning, further exaggerates the effects of maternal obesity on AT development (Sheen et al., 2018). Maternal obesity often induces negative effects on offspring, including larger visceral white fat (Guberman et al., 2013; Lecoutre et al., 2016; Sellayah et al., 2019), disrupted brown fat activity, further promoting dysregulated thermogenesis (Gaspar et al., 2021) and increased cardiac fat mass associated with CV impairment (Fernandez-twinn et al., 2012). This may contribute to an increased risk of metabolic dysfunction acquired in offspring.

There is sound knowledge that obesity in adulthood may originate from the environment encountered *in utero.* Maternal undernutrition models have demonstrated that UCP1 gene expression of pericardial fat is altered depending on the timepoint of exposure and impedes normal development of AT.

Despite this, there is a lack of knowledge establishing to what extent pericardial fat is effected by maternal overnutrition in animals and the following health implications involved in offspring.

4.1.1. Aims

The aim is to document how the genetic and morphological signatures of PAT compares to other adipose depots under a standard maternal diet and maternal overnutrition. In this study, the transcriptional and histological profile of pericardial adipose tissue (PAT) was compared to gonadal (gWAT), inguinal (iWAT) and interscapular brown (iBAT) adipose tissue harvested from **(1)** 30-week-old male mice fed a chow-diet of 10% kcal fat or a high-fat-diet of 60% kcal fat, post-weaning, for 26 weeks from dams fed either a chow-diet or high-fat-diet prior to and during pregnancy and lactation.

4.2. METHODS

4.2.1. Animal and experimental design

All animal work was conducted by the technical staff at the Medical Research Council (MRC) Harwell Institute. Research was approved by the Medical Research Council Harwell Institute Animal Welfare and Ethical Review Board. All procedures were carried out within project license restrictions (PPL 30/3146) under the UK Animals (Scientific Procedures) Act 1986, issued by the UK Government Home Office. Maintained under a 12-hour light/dark cycle and a constant temperature of 22°C ± 2°C, C57BL/6N mice were used in this study, with food and water available *ad libitum*. At 8 weeks old, female C57BL/6N mice (dams) were randomly assigned either a chow (C) (10% kcal fat) or a high-fat (HF) (60% kcal fat) diet for 6 weeks prior to pregnancy. At 14 weeks of age, the female mice were mated with chow-fed C57BL/6N male mice and maintained on their respective diets during gestation (3 weeks) and lactation (4 weeks). In total, the dietary intervention from dams lasted 13 weeks. The presence of a vaginal plug confirmed pregnancy in dams and was deemed as day 0.5 of pregnancy. Weaning of male C57BL/6N offspring mice occurred at 4 weeks of age. These mice were randomly assigned either a chow (C) (10% kcal fat) or a high-fat (HF) (60% kcal fat) diet for 26 weeks. This resulted in four experimental offspring groups: C/C, C/HF, HF/C and HF/HF – the letters before the forward slash refer to the maternal diet and the letters after the forward slash refer to the offspring's diet post-weaning (Table 4.1). The two maternal dietary groups generated 11 C-fed-diet litters and 11 HF-fed-diet litters which were randomly assigned to the two offspring dietary groups. This included offspring from C-fed dams to C/C or C/HF and offspring from HF-fed dams to HF/C or HF/HF. These new groups constituted from different litters, some originated from C litters and others from HF litters. From this, the littermates were randomised across different C or HF-fed groups to avoid littermate bias. One litter was often used in more than one group. Out of the 11 litters from C-fed dams and 11 litters from HF-fed dams, there 7 litters for C/C, 6 litters for C/HF, 9 litters for HF/C and 7 litters for HF/HF. Body weight and fat pads from dams were analysed before mating to confirm induction of obesity using nuclear magnetic resonance. Throughout the dietary intervention, mice were weighed weekly,

metabolic cage analysis was performed at 22 weeks using TSE PhenoMaster *in vivo* calorimetry system, whilst body composition and intraperitoneal glucose tolerance test (ipGTT) were measured at 26 weeks of age. Body composition was measured by nuclear magnetic resonance (EchoMRI™, Zinsser Analytic GmbH, Eschborn, Germany) which determined total body fat, lean mass and free fluid in grams. The percentage of each component was then calculated based on the total body weight of the animal. Percentage body fat was calculated by dividing fat by weight and multiplying by 100. ipGTT was performed following an 8-hour fast and the area under the curve (AUC) was determined, with baseline values were subtracted. 2g/kg glucose was intraperitoneally administered to fasted mice and blood was taken from the tail vein, under local anaesthetic (EMLA cream, AstraZeneca, United Kingdom) at 0 (baseline), 15, 30, 60 and 120 minutes, post glucose injection. Whole blood glucose was measured using an AlphaTRAK meter and test strips (Abbott Animal Health, United Kingdom). Blood was collected by a cardiac puncture under terminal anesthetic in mice at the age of 30 weeks. For serological analysis, the blood was left to clot and centrifuged at 3000xg for 3 minutes. Sera was frozen at -80°C until further analysis. All samples for biochemistry analysis of serum, including fatty acids, triglycerides and cholesterol, were performed using AU680 Clinical Chemistry Analyser (Beckman Coulter, High Wycombe, United Kingdom), by the Clinical Chemistry core facility, MRC Harwell Institute (Oxfordshire, United Kingdom) using commercially-available kits and performed according to manufacturer instructions. Death of mice by carbon dioxide euthanasia and neck dislocation was confirmed by cessation of the circulation. Dissection of gonadal white adipose tissue (gWAT), inguinal white adipose tissue (iWAT), interscapular brown adipose tissue (iBAT), pericardial adipose tissue (PAT) and myocardium of the heart for gene expression (samples stored at -80°C until further analysis) and histological analysis (samples stored at 4°C until further analysis) were performed at the end of the experimental procedure (30 weeks of age) (Figure 4.1).

Table 4.1. Experimental offspring groups fed either a chow (C) or high-fat (HF)-diet post-weaning

Abbreviation	Feeding plan
C/C	Offspring fed a C-diet post-weaning and born from C-fed mothers/dams
C/HF	Offspring fed a HF-diet post-weaning and born from C-fed mothers/dams
HF/C	Offspring fed a C-diet post-weaning and born from HF-fed mothers/dams
HF/HF	Offspring fed a HF-diet post-weaning and born from HF-fed mothers/dams

4.2.2. RNA isolation

1ml of Invitrogen™ TRI Reagent™ Solution per 50mg to 100mg of gWAT, iWAT, iBAT, PAT and heart was transferred to a MP Biomedicals[TM] Lysing Matrix D tube. Lysing tubes were placed in the MP Biomedicals™ FastPrep-24™ 5G Instrument, with the QuickPrep Adaptor (Fisher Scientific). Adipose tissue was homogenised at a speed of 6.0m/s, for 40 seconds and heart tissue was homogenised at a speed of 6.0m/s, for 30 seconds. Isolation of RNA was performed as recommended by the manufactures of Invitrogen™ TRI Reagent™ Solution (Fisher Scientific). RNA was quantified and quality was checked as stated in section 2.2.3 and section 2.2.4.3. RNA samples were stored at -80°C until further analysis.

4.2.3. cDNA synthesis and RT-qPCR

Total RNA was reverse transcribed using the Applied Biosystems™ High-Capacity cDNA Reverse Transcription Kit (Fisher Scientific) and Invitrogen™ RNaseOUT™ Recombinant Ribonuclease Inhibitor (Fisher Scientific), following the instructions as recommended by the manufacturer to synthesise cDNA, performed using the T100™ Thermal cycler (Bio-Rad). 500ng to 1000ng of cDNA was synthesised as stated in section 2.2.5. The gene expression of 30ng cDNA was determined using qPCRBIO Probe Mix No-ROX (PCR Biosystems), performed on the MyiQ™ Single-Colour Real-Time PCR Detection System (Bio-Rad). Samples were measured in duplicates and the fold change in gene expression levels were

determined using the comparative threshold cycle (Ct) method, also referred to as the $2^{-\Delta\Delta}$ Ct method (section 2.2.6). The target genes as listed in Table 4.2 were relative to the housekeeping gene, peptidylprolyl isomerase A (PPIA) for adipose tissue and Glyceraldehyde 3-phosphate dehydrogenase (GAPDH) for heart tissue. All Applied Biosystems™ TaqMan™ Gene Expression Assays (FAM-MGB) were purchased from Fisher Scientific. cDNA was stored at -20°C until further analysis.

4.2.4. Histology

Formalin fixed gWAT, iWAT and PAT embedded in Optimal Cutting Temperature (OCT) compound were sectioned between 10μM and 15μM using a Bright 5040 Cryostat (Bright Instruments Limited). Sections were stained with Haematoxylin and Eosin (H&E) and imaged with a Nikon TE200 Brightfield Inverted Microscope, at x40 objective lens. Assuming the shape of adipocytes are spherical, to calculate adipocyte volume, Image-J software was used to determine adipocyte area and volume distribution as stated in section 2.2.12.1. The percentage change in volume was determined by normalising adipocyte volume to the C-fed mice, unless stated otherwise, and multiplying by 100. Adipocyte number was determined in PAT as stated in section 2.2.12.1. H&E stained slides were stored at room temperature until further analysis.
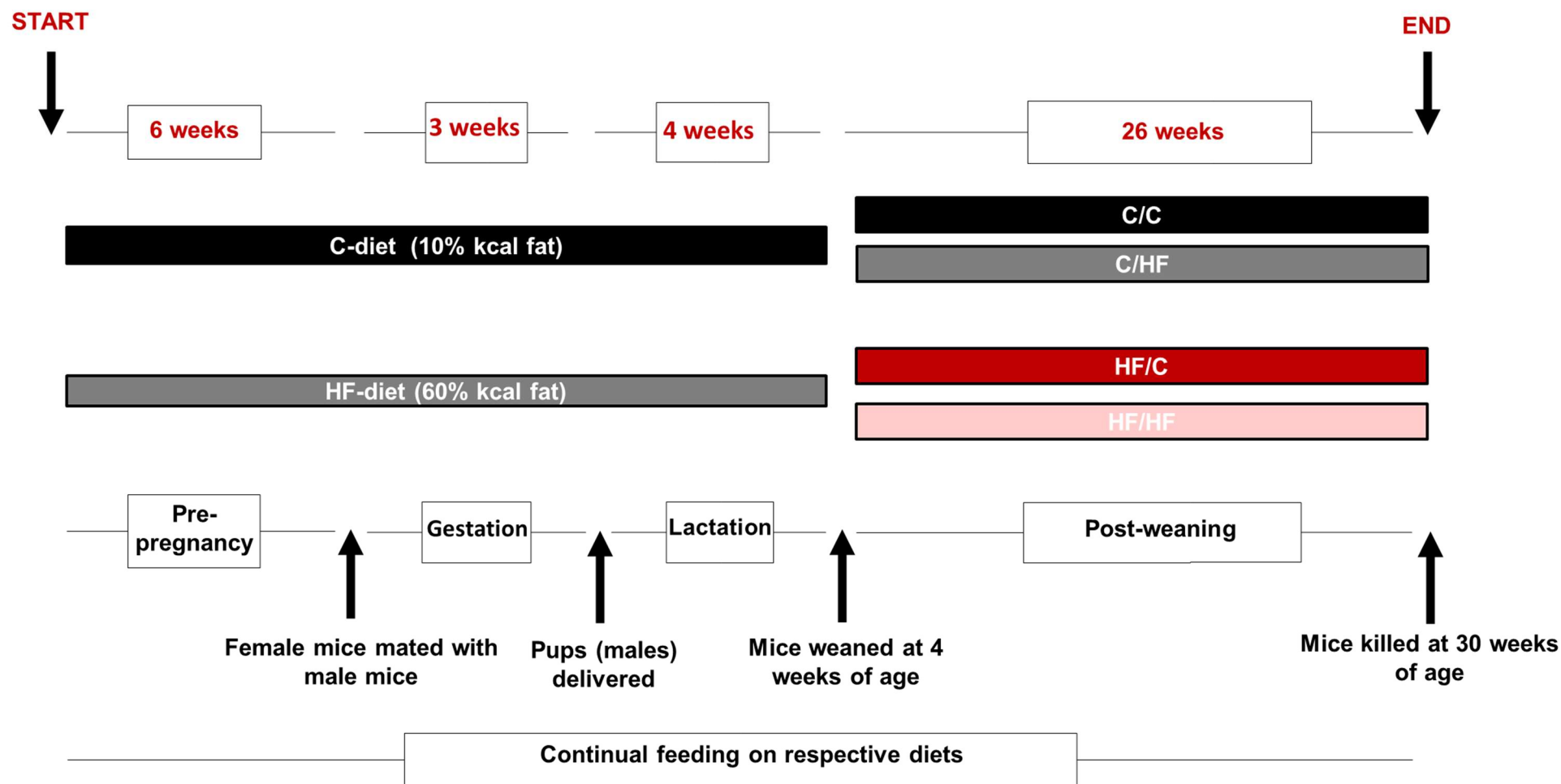
Figure 4.1. Experimental design of female dams and male mice offspring fed a C-diet or HF-diet for 26 weeks. Four experimental offspring groups:

C/C, C/HF, HF/C and HF/HF – the letters before the forward slash refer to the maternal diet and the letters after the forward slash refer to the offspring's

diet post-weaning i.e. maternal diet/offspring diet. C-diet: Chow-diet; HF-diet: High-fat-diet.

Table 4.2. Applied Biosystems™ TaqMan™ Gene Expression Assays for RT-qPCR

Gene	Assay ID
ACTA1	Mm00808218_g1
AdipoQ	Mm00456425_m1
ADRβ3	Mm02601819_g1
C/EBPα	Mm00514283_s1
COX7A1	Mm00438297_g1
COX8B	Mm00432648_m1
DIO2	Mm00515664_m1
FABP4	Mm00445878_m1
GAPDH	Mm99999915_g1
IL6	Mm00446190_m1
Leptin	Mm00434759_m1
MYH6	Mm00440359_m1
MYH7	Mm00600555_m1
NOX4	Mm00479246_m1
NPPA	Mm01255747_g1
PGC1α	Mm01208835_m1
PLIN1	Mm01320554_g1
PPARγ	Mm00440940_m1
PPIA	Mm02342430_g1
TNFα	Mm00443258_m1
UCP1	Mm01244861_m1

4.2.5. Triglyceride extraction and quantification from frozen heart tissue

200µl of 5% NP-40 Substitute Conc. per 20mg of frozen heart tissue was transferred to a MP Biomedicals™ Lysing Matrix D tube. Lysing tubes were placed in the MP Biomedicals™ FastPrep-24™ 5G Instrument, with the QuickPrep Adaptor (Fisher Scientific) and homogenised at a speed of 6.0m/s, for 30 seconds. Duplicates were performed in Nunc™ MicroWell™ 96-Well Microplates and extraction of triglycerides was performed as recommended by the manufacturers of the Triglyceride quantification kit (Sigma-Aldrich) as stated in section 2.2.7.2. Absorbance levels were measured at 570nm on the SPECTRAmax® 190 Microplate Spectrophotometer (Molecular Devices Corporation), using SOFTmax PRO

software. All values were corrected to the blank absorbance and TG concentration was normalised to the heart depot weight. Triglyceride extracts were stored at -80°C until further analysis.

4.2.6. Statistical analysis

GraphPad Prism was used to perform statistical analysis of one-way ANOVA, two-way ANOVA, repeated measures ANOVA, unpaired t-test or Pearson's correlation coefficient. ANOVAs were performed with post-hoc Tukey's multiple comparison. All values were relative to their respective depots from chow (C)-fed mice, unless stated otherwise. Graphs are expressed as mean $\pm$ standard error of the mean (s.e.m), unless stated otherwise. A value of $p < 0.05$ was deemed as statistically significant with * $p < 0.05$, ** $p < 0.01$, *** $p < 0.001$ and **** $p < 0.0001$. The overall effects of maternal and offspring diet are expressed on the graph if the interactions are significant.

4.3. RESULTS

4.3.1. Biochemical and metabolic parameters from 30-week-old offspring mice fed a chow and HF-diet from chow and HF-fed dams

The biochemical and metabolic effects of maternal and offspring diet were assessed in Appendix Table 1.1. For metabolic analysis (Figure 4.2), N = 10–17 mice from 7–9 litters per group (Figure 4.2A-C). For Figure D–O, N = 4 mice from 3 litters for C/C, N = 3 mice from 3 litters for C/HF, N = 8 mice from 4 litters for HF/C and N = 8 mice from 4 litters for HF/HF. HF/HF offspring were significantly heavier in comparison to C/C ($p<0.01$), from 7 weeks of age, whereas differences compared to C/HF occurred at 8 weeks of age. Interestingly, in the final 4 weeks of the experimental procedure, HF/C mice were lighter than C/C (Figure 4.2A). C/HF and HF/HF offspring were significantly glucose intolerant as determined by an ipGTT (Figure 4.2B) compared to C/C ($p<0.001$ and $p<0.05$, respectively) and HF/C ($p<0.0001$ and $p<0.0001$, respectively) in Figure 4.2C. HF offspring groups exhibited lower respiratory exchange rates (RER), with a reduction in energy expenditure (Figure 4.2D-F). For fasting blood glucose levels (Figure 4.2J), C/HF had significantly higher levels compared to C/C ($p<0.001$), HF/C ($p<0.0001$) and HF/HF ($p<0.001$). The serum levels of triglycerides (Figure 4.2K) and free fatty acids (FFAs) (Figure 4.2L) were significantly elevated in HF/HF offspring compared to C/C ($p<0.01$ and $p<0.001$, respectively) and HF/C ($p<0.01$ and $p<0.05$, respectively). In total fat mass (Figure 4.2H), total adiposity (Figure 4.2I), serum levels of total cholesterol (Figure 4.2M), HDL (Figure 4.2N) and LDL (Figure 4.2O) were elevated in C/HF compared to C/C ($p<0.0001$, $p<0.0001$, $p<0.001$, $p<0.001$ and $p<0.01$, respectively) and HF/C ($p<0.0001$, $p<0.0001$, $p<0.0001$, $p<0.0001$ and $p<0.0001$, respectively). HF/HF levels of these five parameters were higher compared to C/C ($p<0.0001$, $p<0.0001$, $p<0.0001$, $p<0.001$ and $p<0.001$, respectively). HF/HF pericardial depot weight was significantly heavier than HF/C ($p<0.001$), with the latter having significantly lighter weights compared to C/C ($p<0.05$), C/HF ($p<0.05$) and HF/HF ($p<0.001$).
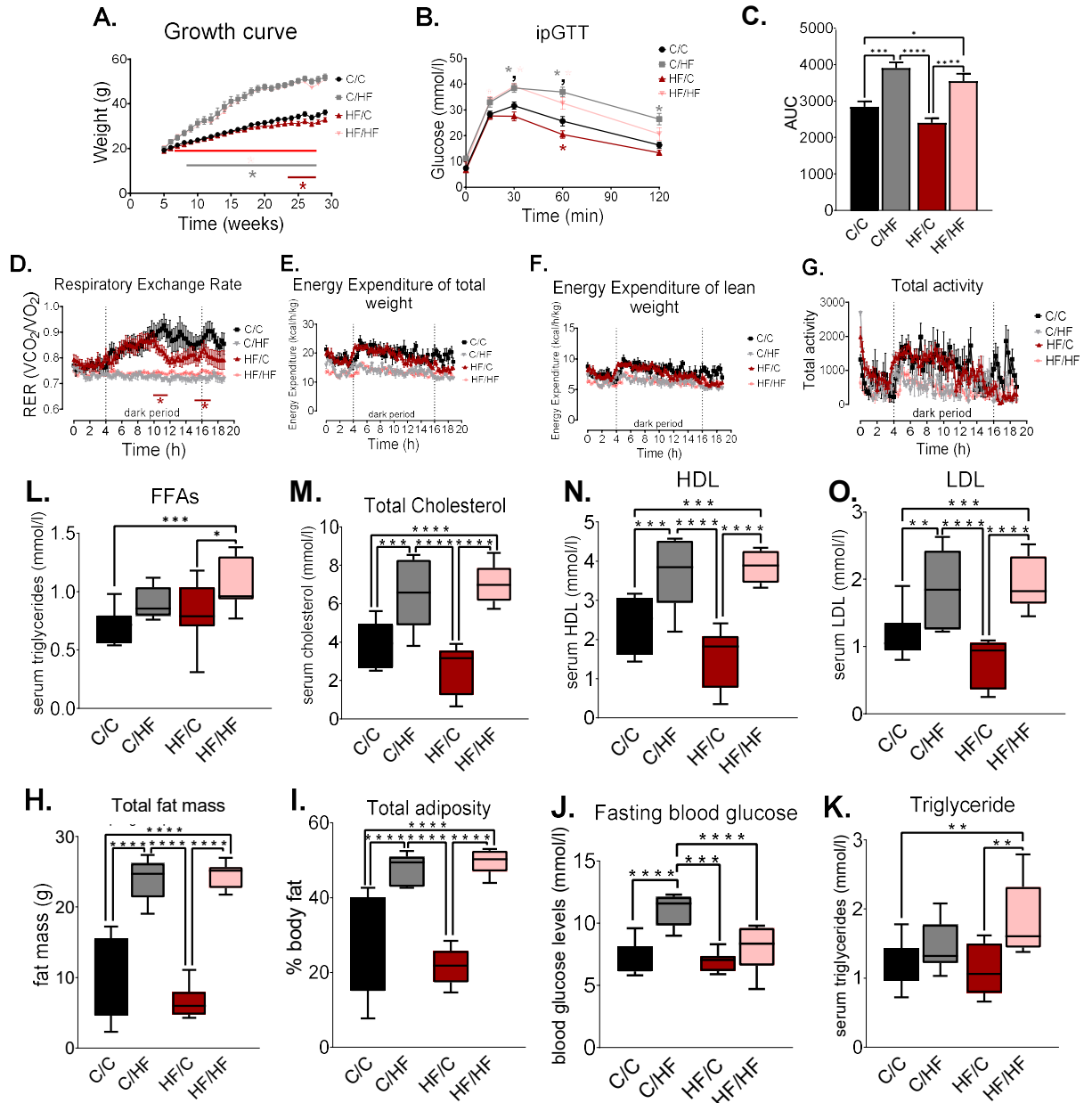
Figure 4.2. Metabolic effects of maternal overnutrition on 30-week-old male offspring mice. Growth curve with weekly weight measurements **(A)**, intraperitoneal glucose tolerance test (ipGTT) with glucose measured at 0, 15, 30, 60 and 120 minutes after glucose injection **(B)**, area under the curve (AUC) of blood glucose levels **(C)**, Respiratory Exchange Rate (RER) **(D)**, Energy expenditure of total weight **(E)** and lean weight **(F)**, Total ambulatory activity **(G)**, Total fat mass **(H)**, Total adiposity **(I)**, Fasting blood glucose **(J)**, Triglycerides **(K)**, Free fatty acids (FFAs) **(L)**, Total cholesterol **(M)**, HDL **(N)**, LDL **(O)** were measured in chow (C) or high-fat (HF)-fed 30-week-old male offspring mice from dams fed a chow (C) or (HF)-diet. Graphs represent mean ± s.e.m **(A-F)** and minimum to maximum values of boxplots **(H-O)**. Data analysed by repeated measures ANOVA **(A,B,D-G)** and two-way ANOVA **(C,H-O)** with Tukey's multiple comparisons test. N = 8-17.
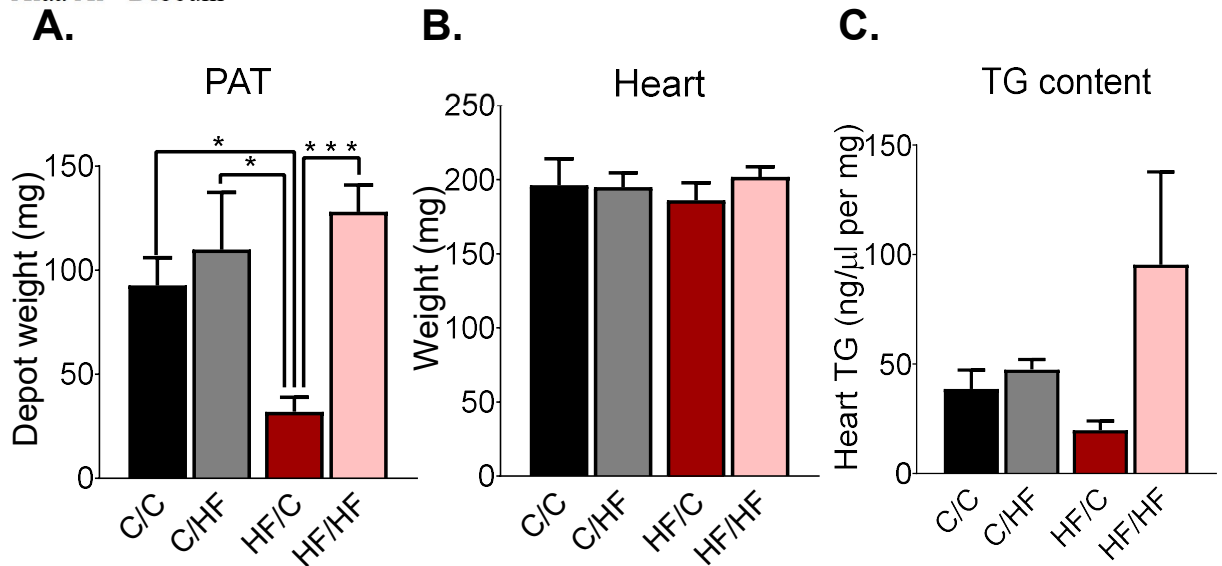
Figure 4.3. PAT depot weight **(A),** Heart weight **(B)** and Triglyceride (TG) content of Heart **(C)** from chow (C) or high-fat (HF)-fed 30-week-old male offspring mice from dams fed a chow (C) or (HF)-diet. Graphs represent means ± s.e.m. Data was analysed by two-way ANOVA and Tukey's multiple comparison test. For **A,** N=3, For **B** and **C**, N= 6 – 10.

4.3.2. Adipose and heart tissue gene expression differences in 30-week-old offspring mice fed a chow and HF-diet from chow and HF-fed dams

The effects of maternal and offspring diet of gene expression of adipogenic, inflammatory, thermogenic and mitochondrial-related markers were assessed in Appendix Table 2.1.

gWAT (Figure 4.4): For adipogenic expression markers, FABP4 expression (Figure 4.4A) was significantly lower in the HF/HF offspring group compared to C/C (p<0.01), C/HF (p<0.01) and HF/C (p<0.01). PPARγ expression (Figure 4.4B) was significantly lower expression in HF/HF compared to C/C (p<0.0001) and HF/C (p<0.0001), lower expression in C/HF compared to C/C (p<0.01) and a trend towards significance with higher expression in C/HF compared to HF/HF (p=0.0573). HF/C had significantly higher expression in C/EBPα expression (Figure 4.4C) compared to C/HF (p<0.05) and HF/HF (p<0.05). AdipoQ expression (Figure 4.4G) was elevated in C/C compared to C/HF (p<0.01), HF/C (p<0.0001) and HF/HF (p<0.01). Although there were no significant differences in Leptin expression (Figure 4.4F), there was a trend towards a higher expression in C/HF compared to HF/C (p=0.056).

iWAT (Figure 4.5): ADRβ3 expression (Figure 4.5B) was lower in HF/HF compared to C/C (p<0.01) and HF/C (p<0.05). In addition, C/HF had lower expression compared to C/C (p<0.05) and HF/C (p<0.05).

iBAT (Figure 4.6): UCP1 levels (Figure 4.6A) were elevated in C/HF compared to C/C (p<0.05) and HF/C (p<0.05). ADRβ3 expression (Figure 4.6B) was lower in C/C compared to C/HF (p<0.01) and HF/C (p<0.05). PGC1α expression (Figure 4.6D) and COX8B expression (Figure 4.6F) were elevated in C/HF (p<0.01 and p<0.05, respectively). COX7A1 levels (Figure 4.6E) were significantly higher in HF/HF compared to C/C (p<0.05) and HF/C (p<0.05).

PAT (Figure 4.7): HF/HF C/EBPα expression was significantly lower expression compared to C/C (p<0.05) and there was a trend towards lower expression in FABP4 (p=0.0528) and PPARγ (p=0.0567). IL6 mRNA levels (Figure 4.7D) in C/HF were significantly higher compared to C/C (p<0.01), HF/C (p<0.0001) and HF/HF (p<0.0001). TNFα expression (Figure 4.7E) was higher in HF/HF compared to C/C (p<0.0001) and C/HF (p<0.001), with HF/C expression being higher than C/C (p<0.05). Leptin expression levels (Figure 4.7F) were lower in HF/C compared to C/HF (p<0.01) and HF/HF (p<0.05).

Heart (Figure 4.8): There were no significant differences between the groups in any of the genes assessed.
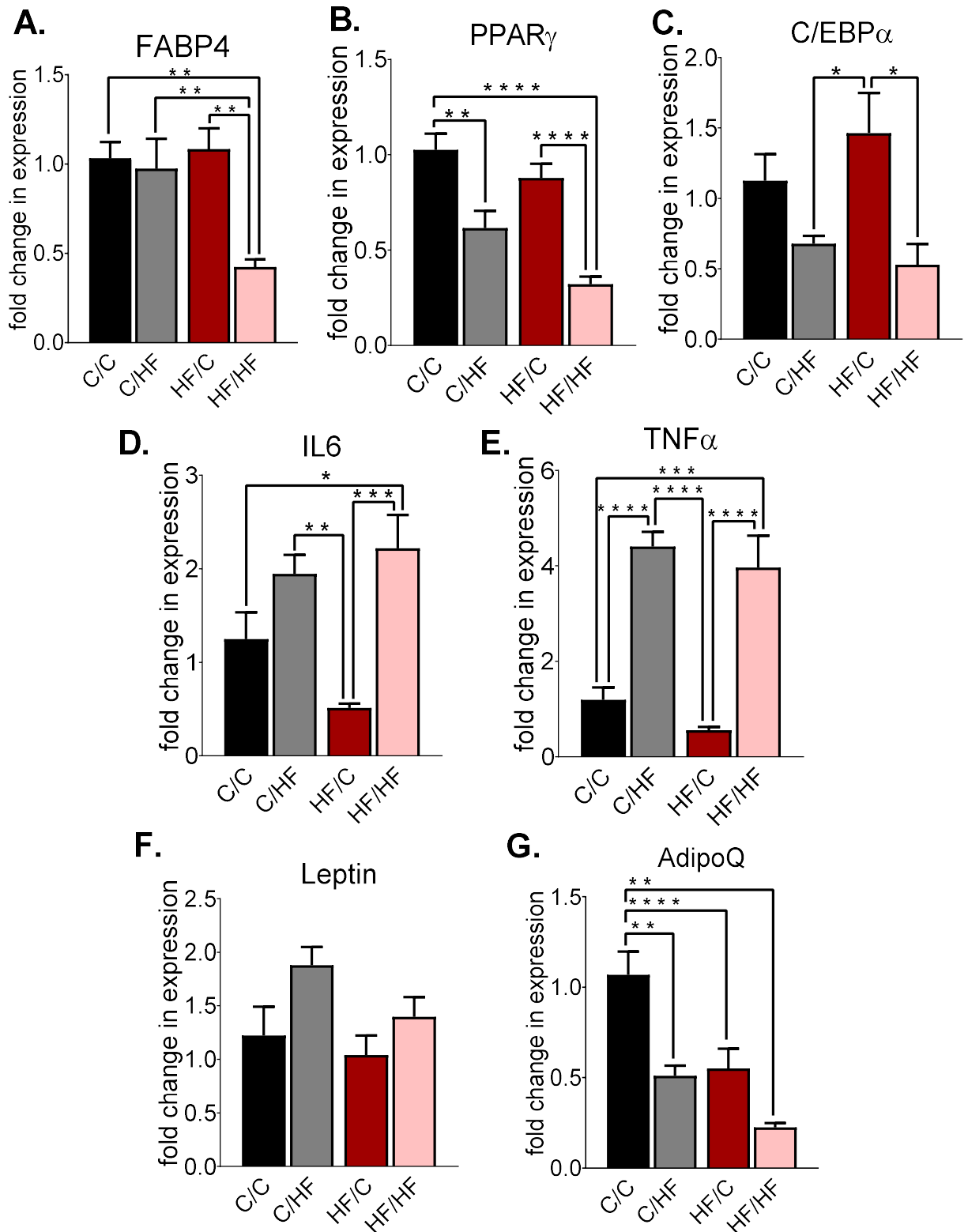
Figure 4.4. FABP4 **(A)**, PPARγ **(B),** C/EBPα **(C)**, IL6 **(D),** TNFα **(E),** Leptin **(F)** and AdipoQ **(G)** fold change in mRNA expression of **gWAT** of chow (C) or high-fat (HF)-fed 30-week-old male offspring mice from dams fed a chow (C) or (HF)-diet, normalised to C/C. Graphs represent mean ± s.e.m. Data analysed by two-way ANOVA and Tukey's multiple comparison test. N = 7-9. * p<0.05, ** p<0.01, *** p<0.001 and **** p<0.0001.
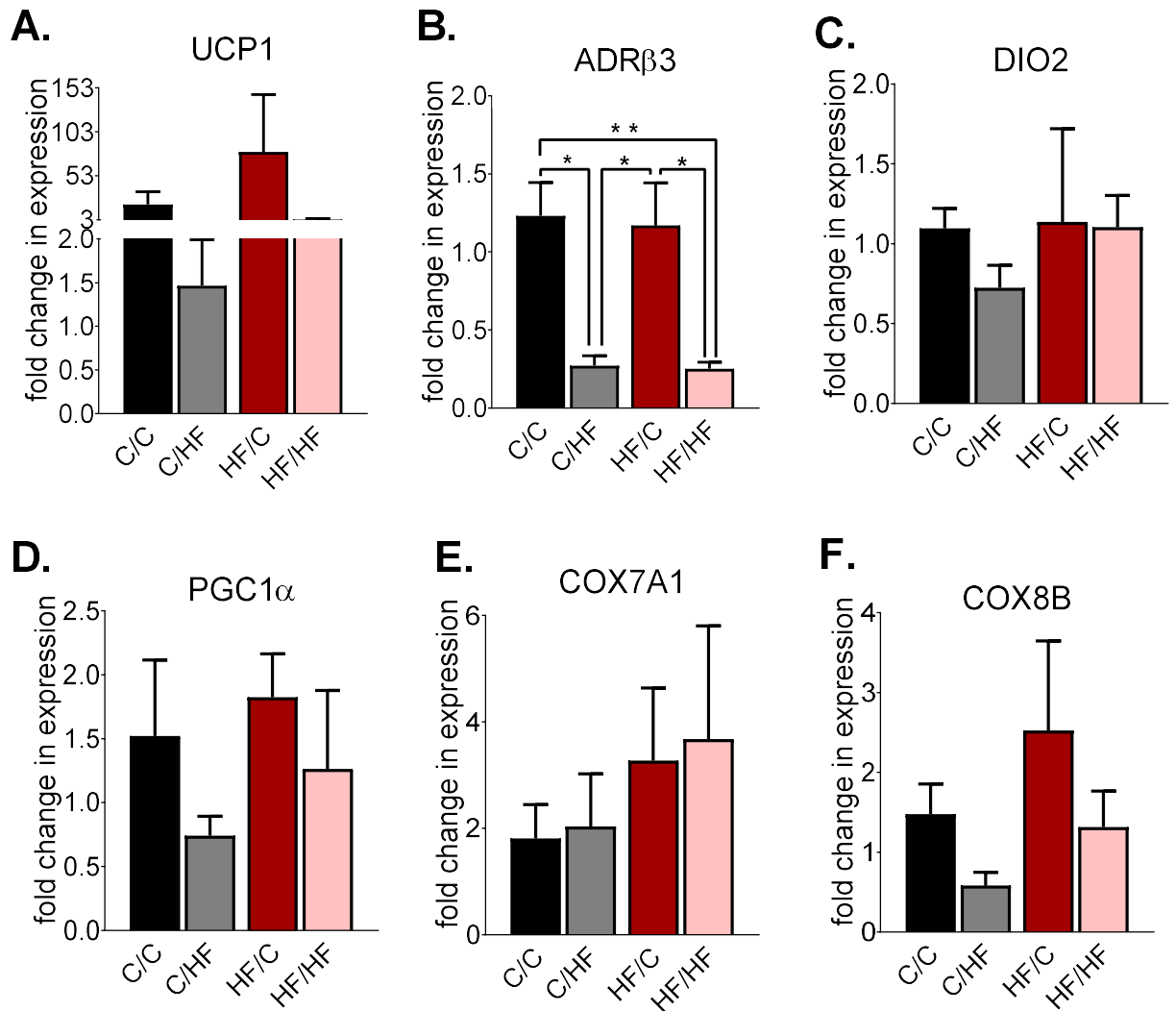
Figure 4.5. UCP1 **(A)**, ADRβ3 **(B)**, DIO2 **(C)**, PGC1α **(D),** COX7A1 **(E)** and COX8B **(F)** fold change in mRNA expression of **iWAT** of chow (C) or high-fat (HF)-fed 30-week-old male offspring mice from dams fed a chow (C) or (HF)-diet, relative to C/C. Graphs represent mean ± s.e.m. Data analysed by two-way ANOVA and Tukey's multiple comparison test. N = 6-12. * p<0.05, ** p<0.01, *** p<0.001 and **** p<0.0001.
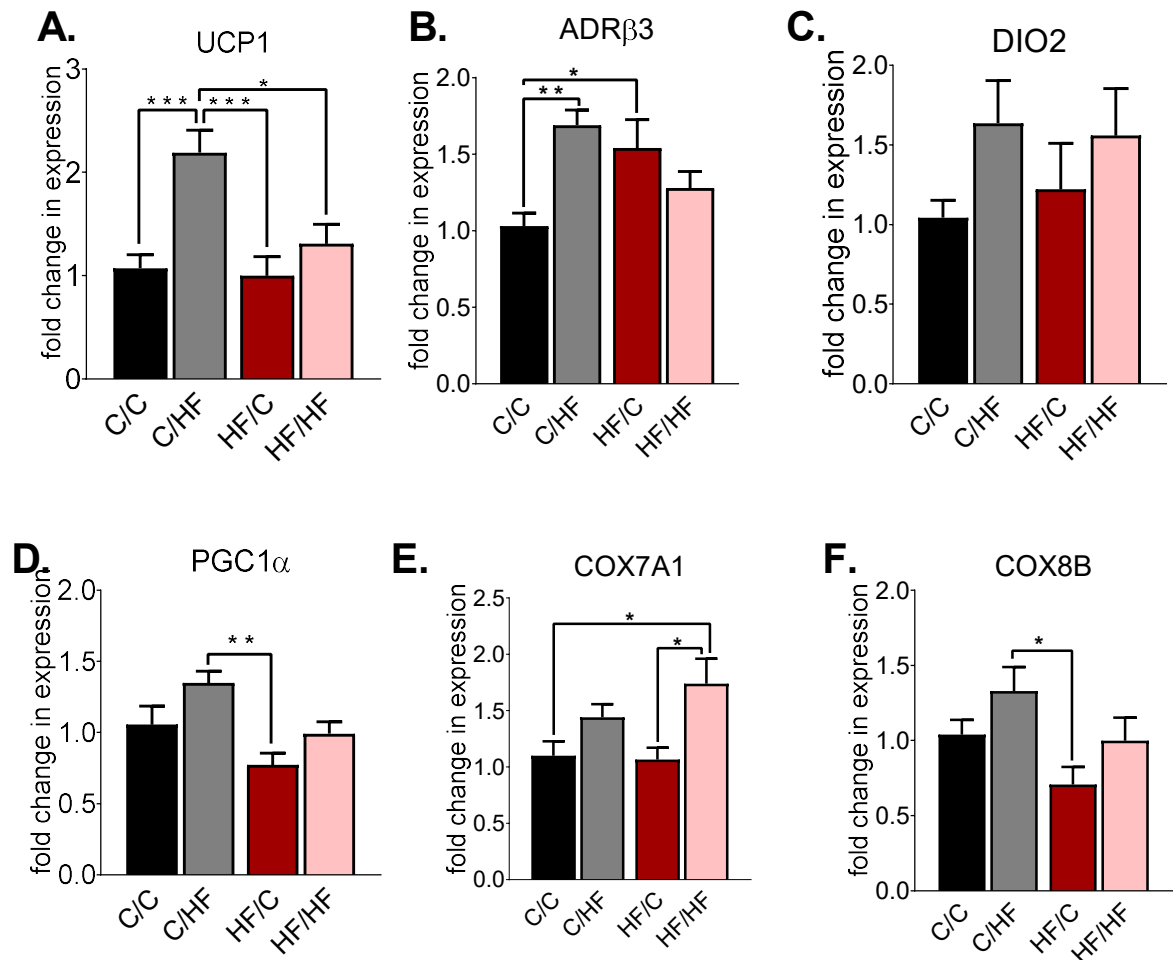
Figure 4.6. UCP1 **(A)**, ADRβ3 **(B)**, DIO2 **(C)**, PGC1α **(D),** COX7A1 **(E)** and COX8B **(F)** fold change in mRNA expression of **iBAT** of chow (C) or high-fat (HF)-fed 30-week-old male offspring mice from dams fed a chow (C) or (HF)-diet, normalised to C/C. Graphs represent mean ± s.e.m. Data analysed by two-way ANOVA and Tukey's multiple comparison test. N = 6-12. * $p < 0.05$, ** $p < 0.01$, *** $p < 0.001$ and **** $p < 0.0001$.
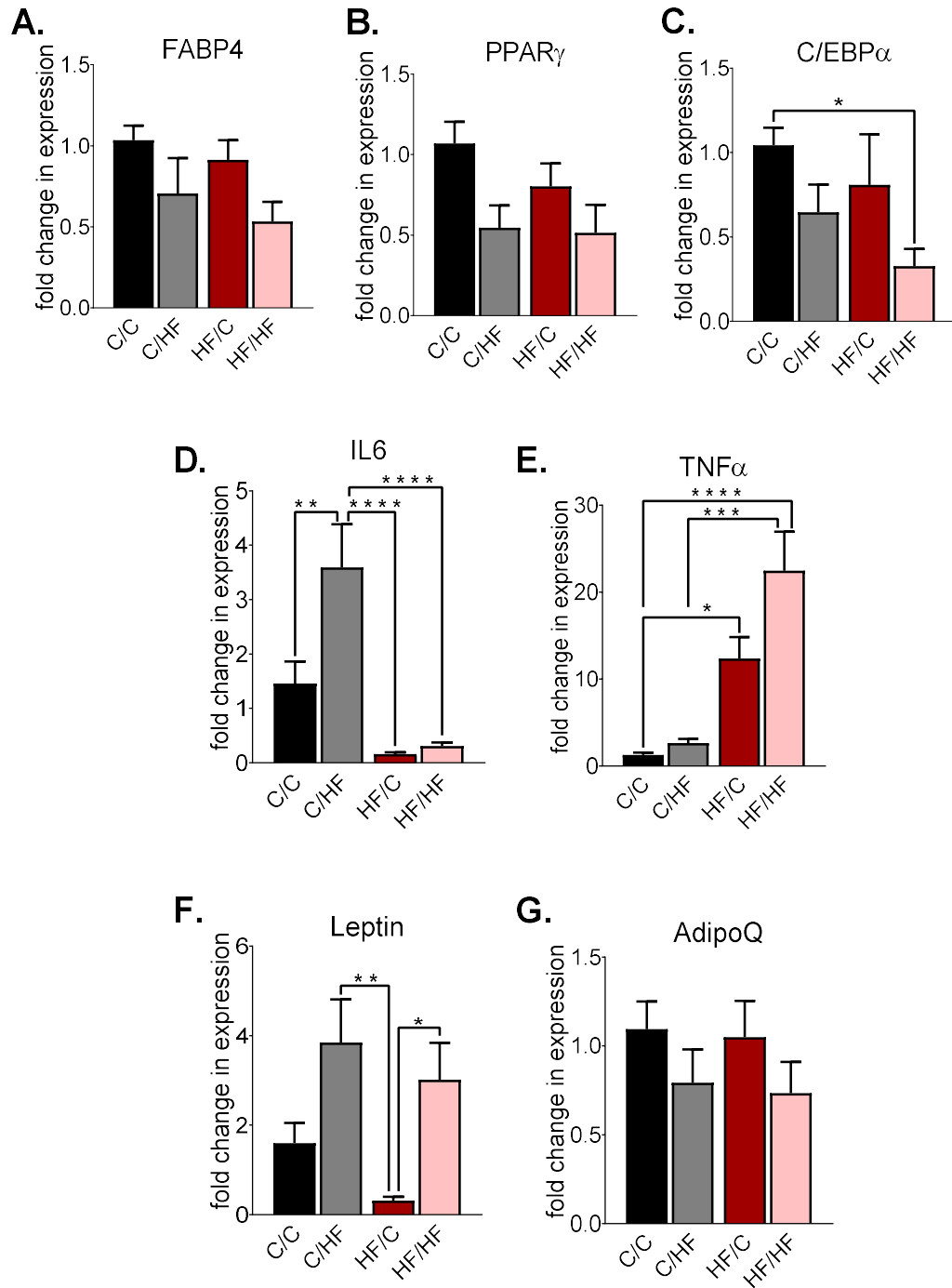
Figure 4.7. FABP4 **(A)**, PPARγ **(B),** C/EBPα **(C)**, IL6 **(D),** TNFα **(E),** Leptin **(F)** and AdipoQ **(G)** fold change in mRNA expression of **PAT** of chow (C) or high-fat (HF)-fed 30-week-old male offspring mice from dams fed a chow (C) or (HF)-diet, normalised to C/C. Graphs represent mean ± s.e.m. Data analysed by two-way ANOVA and Tukey's multiple comparison test. N = 7-9. * p<0.05, ** p<0.01, *** p<0.001 and **** p<0.0001.
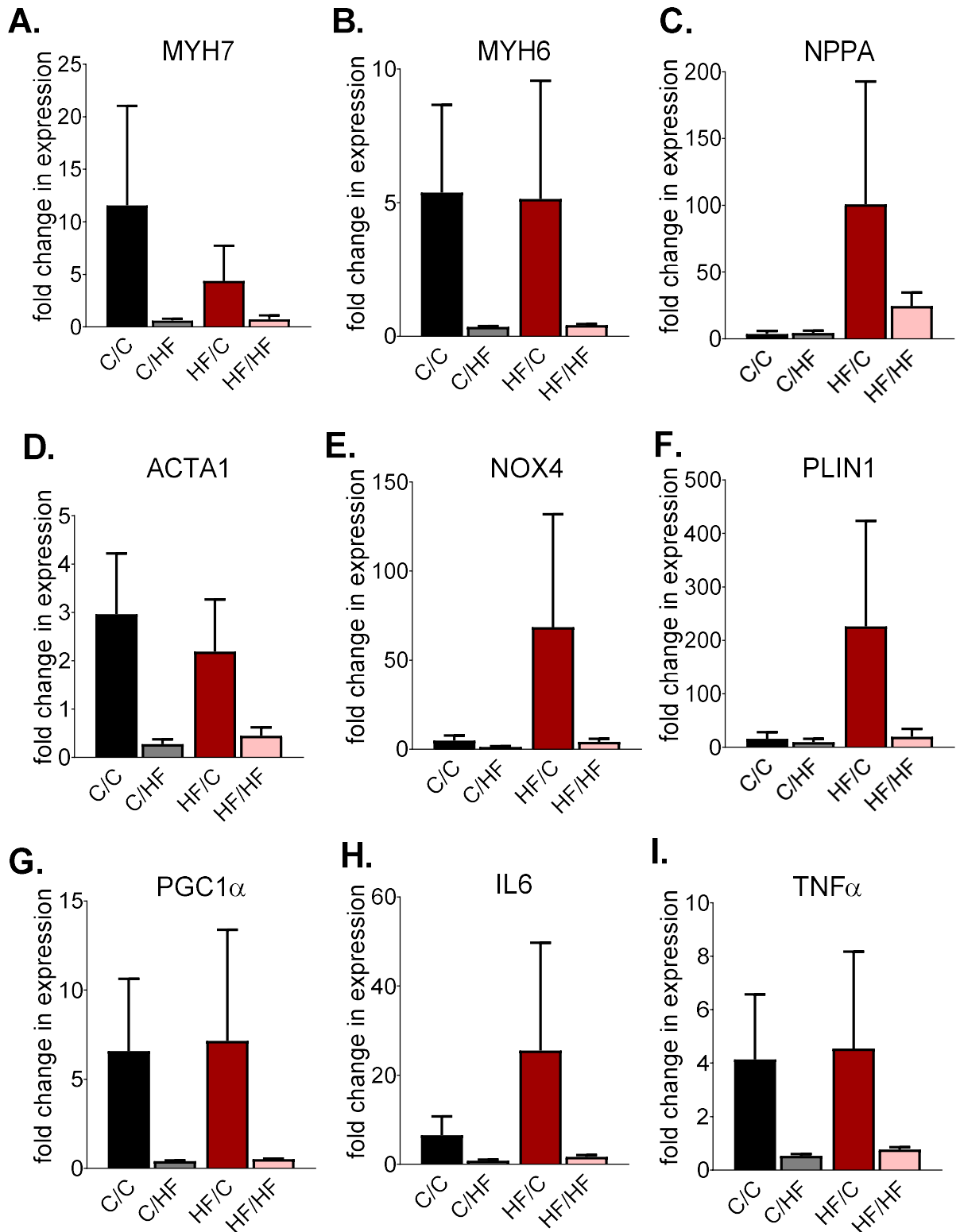
Figure 4.8. MYH7 **(A)**, MYH6 **(B)**, NPPA **(C)**, ACTA1 **(D)**, NOX4 **(E)**, PLIN **(F)**, PGC1α **(G)**, IL6 **(H)** and TNFα **(I)** fold change in mRNA expression of **Heart** of chow (C) or high-fat (HF)-fed 30-week-old male offspring mice from dams fed a chow (C) or (HF)-diet, relative to C/C. Graphs represent mean ± s.e.m. Data analysed by two-way ANOVA and Tukey's multiple comparison test. N = 5-8. * $p<0.05$, ** $p<0.01$, *** $p<0.001$ and **** $p<0.0001$.

4.3.3. Adipose tissue histological differences in 30-week-old offspring mice fed a chow and HF-diet from chow and HF-fed dams

Percentage change in cell volume: The effects of maternal and offspring diet cell volume and number were assessed in Appendix Table 3.5 and Appendix Table 3.6. In all depots, HF/HF cell volume was drastically elevated compared to the other offspring groups, which was presented morphological by stained images. HF/HF of gWAT had a significantly larger volume compared to C/C ($p < 0.0001$), C/HF ($p < 0.01$) and HF/C ($p < 0.001$), when normalised to C/C (Figure 4.9A). There was a trend towards larger cells in C/HF compared to C/C ($p = 0.0514$). iWAT C/C offspring group having significantly smaller cells compared to C/HF ($p < 0.05$) and HF/HF ($p < 0.0001$), and C/HF had significantly smaller cells compared to HF/HF ($p < 0.01$) (Figure 4.10A). PAT C/C had significantly smaller cells compared to C/HF ($p < 0.05$) and HF/HF ($p < 0.0001$) (Figure 4.11A). C/HF had larger cells compared to HF/C ($p < 0.05$), and HF/HF had significantly larger cells compared to C/HF ($p < 0.05$) and HF/C ($p < 0.0001$). Adipocyte number of PAT (Figure 4.11B) was significantly elevated in HF/C compared HF/HF.

Adipose tissue morphology: Histological analysis was mirrored by morphological observation of cell size of H&E stained gWAT (Figure 4.9B), iWAT (Figure 4.10B) and PAT (Figure 4.11C), with the largest cells in HF/HF. Furthermore, a population of multi-locular brown-like cells were observed in chow-fed offspring (C/C and HF/C), regardless of maternal diet, in iWAT (Figure 4.10C) and PAT (Figure 4.11D).

Cell volume distribution: For statistical significance between groups and effects of maternal and offspring diet, refer to Appendix Table 3.7 and Appendix Table 3.8. In general, both gWAT (Figure 4.9C) and iWAT (Figure 4.10D), compared to PAT (Figure 4.11E), resemble negatively skewed distributions of cell volumes, suggesting cells in these depots have a higher frequency of being larger.
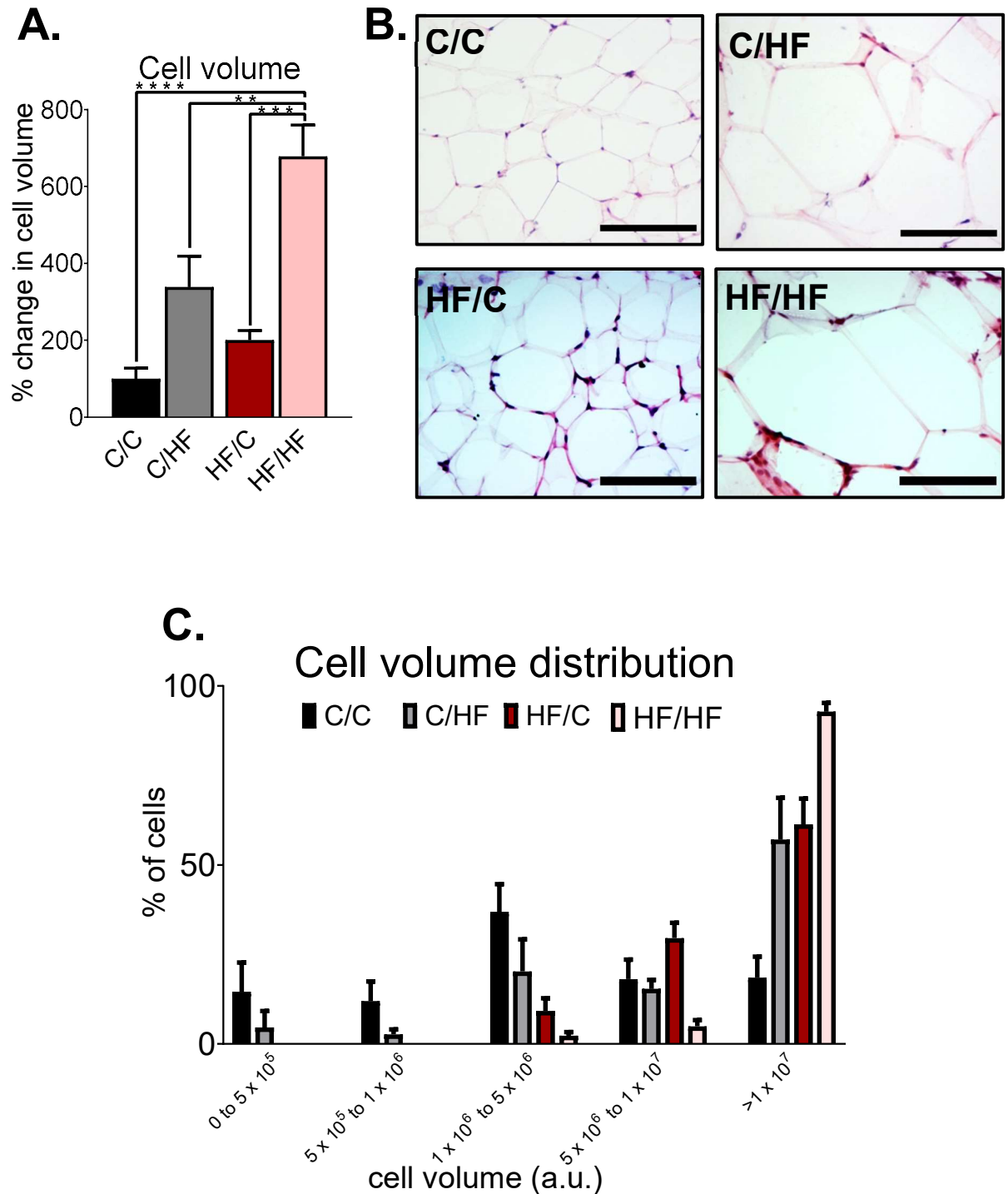
Figure 4.9. The percentage change in cell volume normalised to C/C **(A)**, H&E representative images of cell size **(B)** and cell volume distribution **(C)** of **gWAT** of chow (C) or high-fat (HF)-fed 30-week-old male offspring mice from dams fed a chow (C) or (HF)-diet. All scale bars represent 100μM and imaged at x40 optical lens with Nikon TE200 brightfield inverted microscope. Graphs represent mean $\pm$ s.e.m. Data analysed by two-way ANOVA and Tukey's multiple comparison test between C/C, C/HF, HF/C and HF/HF **(A)** and cell volume (a.u.) groups **(C)**. N = 6-8. * $p<0.05$, ** $p<0.01$, *** $p<0.001$ and **** $p<0.0001$.
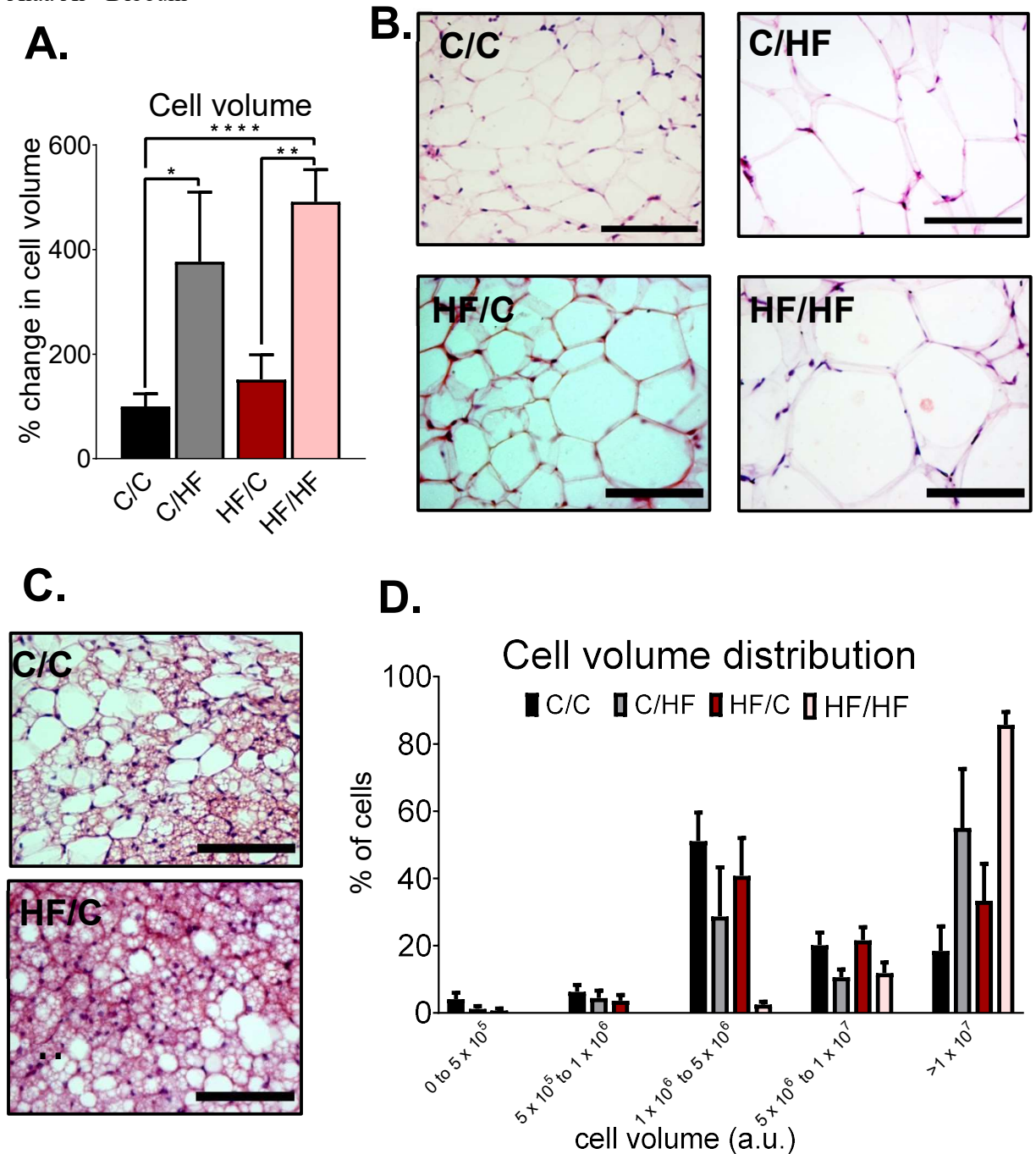
Figure 4.10. The percentage change in cell volume normalised to C/C **(A)**, H&E representative images of cell size **(B)**, multi-locular cells **(C)** and cell volume distribution **(D)** of **iWAT** of chow (C) or high-fat (HF)-fed 30-week-old male offspring mice from dams fed a chow (C) or (HF)-diet. All scale bars represent 100μM and imaged at x40 optical lens with Nikon TE200 brightfield inverted microscope. Graphs represent mean $\pm$ s.e.m Data analysed by two-way ANOVA and Tukey's multiple comparison test between C/C, C/HF, HF/C and HF/HF **(A)** and cell volume (a.u.) groups **(D)**. N = 6-8. * $p<0.05$, ** $p<0.01$, *** $p<0.001$ and **** $p<0.0001$.
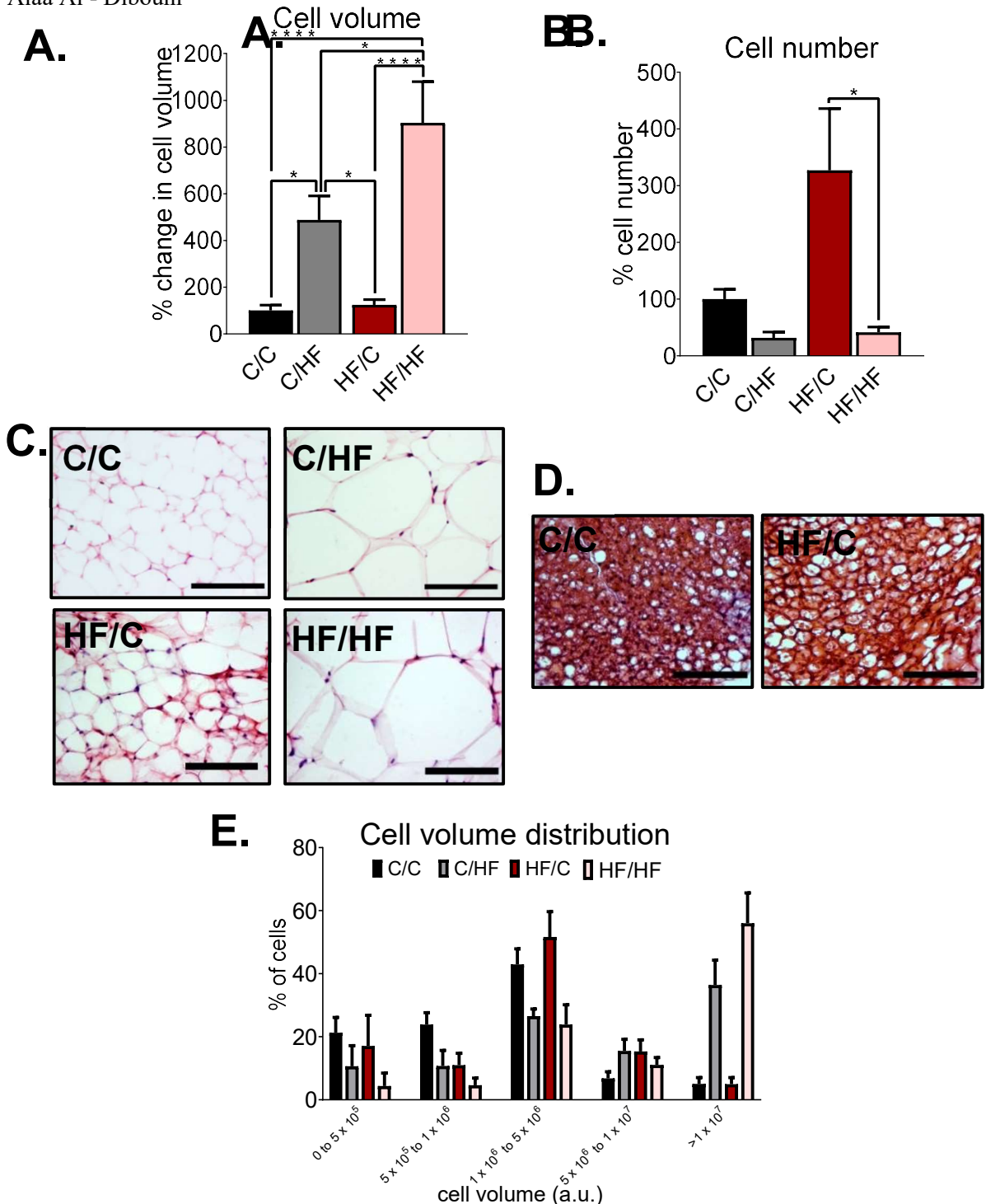
Figure 4.11. The percentage change in cell volume **(A)** and cell number **(B)** normalised to C/C, H&E representative images of cell size **(C)**, multi-locular cells **(D)** and cell volume distribution **(E)** of **PAT** of chow (C) or high-fat (HF)-fed 30-week-old male offspring mice from dams fed a chow (C) or (HF)-diet, normalised to C/C. All scale bars represent 100µM and imaged at x40 optical lens with Nikon TE200 brightfield inverted microscope. Graphs represent mean ± s.e.m Data analysed by two-way ANOVA and Tukey's multiple comparison test between C/C, C/HF, HF/C and HF/HF **(A,B)** and cell volume (a.u.) groups **(E).** For **B,** N = 3, For **A, C-E,** N= 8-10. * p<0.05, ** p<0.01, *** p<0.001 and **** p<0.0001.

4.3.4. The relationship between biochemical and metabolic parameters, gene expression levels and percentage change in cell volume in adipose tissue of 30-week-old offspring mice fed a chow and HF-diet from chow and HF-fed dams

Inflammatory markers vs serum metabolite levels: IL6 mRNA levels were positively correlated in gWAT (Appendix Figure 4.15A) ($p<0.01$) and PAT (Appendix Figure 4.15B) ($p<0.05$), and TNFα levels were positively correlated in gWAT (Appendix Figure 4.15C) ($p<0.01$). Furthermore, there was a positive correlation in gWAT and PAT IL6 levels compared with serum total cholesterol (Appendix Figure 4.16A, $p<0.0001$ and Figure 4.16B, $p<0.05$, respectively). In gWAT, there was a positive correlation between IL6 and serum HDL (Figure 4.16C) ($p<0.0001$) and serum LDL (Appendix Figure 4.16E) ($p<0.001$), body fat content (Appendix Figure 4.17C) ($p<0.0001$). PAT IL6 levels were positively correlated with triglyceride levels (Appendix Figure 4.16H) ($p<0.01$).TNFα mRNA gene expression levels were positively associated in gWAT compared to serum total cholesterol (Appendix Figure 4.18A) ($p<0.0001$), serum HDL (Appendix Figure 4.18C) ($p<0.0001$), serum LDL (Appendix Figure 4.18E) ($p<0.0001$) and serum triglycerides (Appendix Figure 4.18G) ($p<0.05$).

Inflammatory markers vs phenotypic data: In gWAT, there was a positive correlation between IL6 and body weight (Appendix Figure 4.17E) ($p<0.0001$) and percentage body fat (Figure 4.17G) ($p<0.0001$). TNFα mRNA gene expression levels were positively associated in gWAT compared and fasting blood glucose levels (Appendix Figure 4.19A) ($p<0.001$), body fat content (Appendix Figure 4.19C) ($p<0.0001$), body weight (Appendix Figure 4.19E) ($p<0.0001$) and percentage body fat (Appendix Figure 4.19G) ($p<0.0001$). TNFα mRNA gene expression levels in PAT were positively correlated with fasting blood glucose levels (Appendix Figure 4.19B) ($p<0.01$).

UCP1 vs serum metabolite levels: UCP1 mRNA expression in iWAT was negatively correlated with serum total cholesterol (Appendix Figure 4.20A) ($p<0.01$) and free fatty acids (Appendix Figure 4.20I) ($p<0.01$), whereas in iBAT, serum total cholesterol (Appendix Figure 4.20B) ($p<0.01$), serum HDL (Appendix Figure 4.20D) ($p<0.01$) and serum LDL (Appendix Figure 4.20F) ($p<0.001$) were positively correlated with UCP1 expression.

UCP1 vs phenotypic data: UCP1 mRNA expression in iWAT was negatively correlated with percentage body fat (Appendix Figure 4.21G) ($p<0.05$). In iBAT, UCP1 levels were positively correlated with body fat content (Appendix Figure 4.21D) ($p<0.001$), body weight (Appendix Figure 4.21F) ($p<0.001$) and percentage body fat (Appendix Figure 4.21H) ($p<0.01$).

Percentage change in cell volume vs serum metabolite levels: The percentage change in cell volume in gWAT, iWAT and PAT was positively correlated with serum total cholesterol (Appendix Figure 4.22A, $p<0.0001$, Appendix Figure 4.22B, $p<0.001$ and Appendix Figure 4.22C, $p<0.0001$, respectively), serum HDL (Appendix Figure 4.22D, $p<0.0001$, Appendix Figure 4.22E, $p<0.001$ and Appendix Figure 4.22F, $p<0.0001$, respectively), serum LDL (Appendix Figure 4.22G, $p<0.001$, Appendix Figure 4.22H, $p<0.001$ and Appendix Figure 4.22I, $p<0.0001$, respectively), serum triglycerides (Appendix Figure 4.22J, $p<0.01$, Appendix Figure 4.22K, $p<0.0001$ and Appendix Figure 4.22L, $p<0.001$, respectively) and serum free fatty acids (Appendix Figure 4.22M, $p<0.001$, Appendix Figure 4.22N, $p<0.01$ and Appendix Figure 4.22O, $p<0.05$).

Percentage change in cell volume vs phenotypic data: The percentage change in cell volume in gWAT, iWAT and PAT was positively correlated with body fat content (Appendix Figure 4.23D, $p<0.001$, Appendix Figure 4.23E, $p<0.001$ and Appendix Figure 4.23F, $p<0.0001$, respectively), body weight (Appendix Figure 4.23G, $p<0.001$, Appendix Figure 4.23H, $p<0.001$ and Appendix Figure 4.23I, $p<0.0001$, respectively) and percentage body fat (Appendix Figure 4.23J, $p<0.001$, Appendix Figure 4.23K, $p<0.001$ and Appendix Figure 4.23L, $p<0.0001$, respectively). iWAT percentage change in cell volume was positively correlated with fasting blood glucose levels (Appendix Figure 4.23B) ($p<0.05$). PAT depot weight was positively related to the percentage change in cell volume (Appendix Figure 4.26A) ($p<0.05$).

Inflammatory markers vs percentage change in cell volume: gWAT AdipoQ expression was negatively correlated with the percentage change in cell volume (Appendix Figure 4.24C) ($p<0.001$),

Inflammatory markers vs phenotypic data: gWAT AdipoQ expression was negatively correlated with body weight (Appendix Figure 4.25E, $p<0.001$) and total fat mass (Appendix Figure 4.25G, $p<0.001$). gWAT and PAT Leptin gene expression levels were positively associated with body weight (Appendix Figure 4.25A, $p<0.01$ and Appendix Figure 4.25B $p<0.0001$, respectively) and total fat mass (Appendix Figure 4.25C, $p<0.01$ and Appendix Figure 4.25D $p<0.001$, respectively). PAT depot weight was positively correlated with Leptin gene expression levels (Appendix Figure 4.26D) ($p<0.05$) and negatively correlated with AdipoQ expression levels (Appendix Figure 4.26E) ($p<0.05$).

4.4. DISCUSSION

Maternal overnutrition prior to and during pregnancy and lactation **(1)** increased hypertrophy and **(2)** reduced hyperplastic growth of pericardial fat, **(3)** promoted 'whitening' of pericardial adipocytes and **(4)** increased pericardial depot weights of 30-week-old male offspring mice fed a HF-diet post-weaning (HF/HF). Interestingly, the effects of a chow-diet post-weaning demonstrated a contrary effect in which maternal overnutrition **(5)** reduced hypertrophy and **(6)** increased hyperplastic growth of pericardial fat, **(7)** promoted 'browning' of pericardial adipocytes and **(8)** reduced pericardial depot weight in 30-week-old male offspring mice (HF/C).

Obesogenic adipogenesis in visceral fat is a key mechanism in which AT expands induced by a HF-diet (Sellayah et al., 2019). Leptin expression is often associated with that of white fat, rather than brown fat (Cinti et al., 1997), and is positively regulated by C/EBPα expression (de la Brousse, Shan and Chen, 1996; He et al.,1995; Hwang et al., 1996). With this view, it would be suggested that expression levels of both these genes would resemble each other under normal conditions. Maternal obesity has been reported to induce adipocyte differentiation as demonstrated by an upregulation of PPARγ (Borengasser et al., 2013; Desai et al., 2015; Samuelsson et al., 2008) and Leptin mRNA expression levels (Borengasser et al., 2013; Lecoutre et al., 2016). This is observed in rodent HF/C offspring compared to C/C offspring of visceral fat (Borengasser et al., 2013; Desai et al., 2015; Lecoutre et al., 2016) and inguinal fat (Samuelsson et al., 2008). On the other hand, other studies have shown that the mRNA expression levels of the pro-adipogenic markers PPARγ (Lecoutre et al., 2016) and C/EBPα (Desai et al., 2015) are reduced in visceral fat of HF/C compared to C/C offspring. The discrepancies observed in these studies compared to the study presented in this chapter, could be due to several influencing factors. This may include the time and length of exposure to maternal overnutrition, species variability, the age of the animals at the end of experimentation and depot specificity. Indeed, in pericardial fat, C/EBPα expression levels were significantly lower in HF/HF mice, whereas, Leptin mRNA expression levels were significantly higher in HF/HF, as well as in C/HF, compared to HF/C. The decrease in pro-adipogenic markers in

HF/HF may represent an adaptive mechanism in offspring to reduce lipid accumulation in pericardial adipocytes in response to the excess nutritional status exposed to *in utero* (Lecoutre et al., 2016; Lukaszewski et al., 2011; Ortega et al., 2010). In fact, diet-induced obesity (DIO) results in a sparse distribution of adipocytes (Jo et al., 2009). The proposed adaptive mechanistic effect may explain as to why pericardial adipocytes of HF-fed offspring varied in size, as represented by cell volume distribution analysis.

Exposure to maternal overnutrition in offspring fed a HF-diet post-weaning (HF/HF) results in elevated levels of plasma Leptin (Samuelsson et al., 2008). Interestingly, Leptin mRNA expression levels in pericardial fat were highest in C/HF, followed by HF/HF, and lowest in HF/C in 30-week-old male offspring mice. Perhaps exposure to an extreme form of maternal overnutrition prior to and during pregnancy and lactation positively effects HF/C offspring to compensate for the nutritional abundance exposed to *in utero*. The 'thrifty phenotype hypothesis' proposes that the *in utero* environment prepares the offspring for a pre-expected postnatal environment. This is demonstrated by a reduced weight gain in HF-fed offspring (C/HF and HF/HF), regardless of maternal overnutrition in rats (Peric Kacarevic et al., 2016; Šnajder et al., 2019). On the contrary, in this chapter, C/HF and HF/HF offspring had an increase in weight gain over a 26-week feeding period and were presented with the highest levels of total fat mass and adiposity. The contradictory results between these studies may be due to species variability. However, it is more likely because maternal obesity in rat dams was not induced as food and water was not available *ad libitum* for either dams or offspring (Peric Kacarevic et al., 2016; Šnajder et al., 2019). Unlike in this chapter, in which a rigorous form of maternal obesity was induced to effect offspring metabolic health. In accordance to the results in this chapter, Bruce et al., demonstrated that 30-week-old female C/HF and HF/HF offspring mice had the highest body weights, total fat mass and total cholesterol plasma levels. Maternal overnutrition promoted a more deleterious phenotype in HF/HF compared to C/HF female offspring (Bruce et al., 2009). On the other hand, in this chapter, metabolic dysfunction was more prominent in C/HF than HF/HF offspring. This was demonstrated by the reduced ability to clear glucose after an ipGTT and higher levels of circulating metabolic markers, compared

to the other offspring groups. Perchance sex-differences influence the favourability of metabolic dysfunction in C/HF and HF/HF offspring. On the other hand, perhaps a more obesogenic feeding plan of 60% kcal fat diet in this study, compared to the 45% kcal fat diet utilised by Bruce et al., effects metabolic function in offspring differently.

In well-fed offspring ewes after prenatal maternal overnutrition, Leptin mRNA levels in perirenal fat are significantly higher than standard-fed offspring (Muhlhausler et al., 2007b). In addition, Leptin plasma levels are associated with infant adiposity (Cetin et al., 2000; Tapanainen et al., 2001) and body weight, especially in diet-induced obesity (DIO) (Frederich et al., 1995). In this study, Leptin mRNA expression levels in pericardial fat were significantly higher in HF-fed offspring (C/HF and HF/HF), regardless of maternal diet. This was positively correlated with body weight and total fat mass levels. This could be due to the increase in lipid accumulation of pericardial adipocytes, as demonstrated by an increase in cell volume via histological analysis. This suggests that Leptin gene expression in pericardial fat is increased in response to a HF-diet post-weaning, rather than exposure to maternal overnutrition.

Moreover, pericardial depot weight of 30-week-old male offspring mice was extremely elevated in HF-fed offspring (C/HF and HF/HF), compared to chow-fed offspring exposed to maternal overnutrition (HF/C). Moreover, there was a positive relationship between depot weight compared to pericardial Leptin mRNA levels and adipocyte size. Studies have demonstrated that visceral depots are heaviest in HF/HF compared to C/HF in mice (Sellayah et al., 2019) and that pericardial fat is increased in new-born sheep exposed to maternal overnutrition during gestation (Long et al., 2012). However, in this study, the PAT depot weights and an increase in body weight between C/HF and HF/HF, over the 26-week feeding plan, were comparable. This is in line with previous research documenting weight gain in a maternal obesity model (Loche et al., 2018). This could be due to a more obeseogenic adult environment of 60% kcal fat diet to promote heavier and comparable depot and body weights, compared to the 45% kcal fat diet in the study conducted by Sellayah et al.

The total fat mass and adiposity of offspring mice was reflected in the depot weight of PAT. C/HF and HF/HF exhibited an increase in depot weight compared to HF/C. The results suggest

that adipocyte hypertrophy in pericardial adipocytes (increase in cell volume) is responsible for the increase in PAT depot weight. This demonstrates the lipid storage capacity of 30-week-old male offspring mice fed a HF-diet, regardless of maternal overnutrition. In fact, PAT depot weight was negatively associated with AdipoQ mRNA expression levels, suggestive of excess visceral fat accumulation (Yatagai et al., 2003).

During AT development, visceral fat switches its expansion mechanisms from an increase of cell volume (hypertrophy) to cell number (hyperplasia) (Wang et al., 2013). Sellayah et al., demonstrated that the cell number of visceral fat from C/HF was higher than that of C/C, yet the increase in cell number between HF/HF compared to C/HF was considerably higher. The limited capacity of visceral depots is reflected by their depot weight (Van Beek et al., 2015) and hypertrophy is associated with metabolic dysfunction (Laforest et al., 2015). This includes an increase in FFA turnover (Pezeshkian et al., 2009), elevated Leptin levels and an increased pro-inflammatory response (Murano et al., 2008). Interestingly, chow-fed offspring exposed to maternal overnutrition (HF/C), demonstrated an increase in cell number in pericardial adipocytes, compared to HF/HF. This is suggestive of hyperplastic growth in 30-week-old male offspring, as cell number was significantly higher in HF/C compared to HF/HF. This implies that under a chow environment post-weaning, exposure to maternal overnutrition may not implicate a negative effect on lipid accumulation and storage capacity of pericardial fat in chow-fed 30-week-old male offspring.

Over the 26-week feeding period, 30-week-old HF/C male offspring mice increased less weight and had improved glucose homeostasis as demonstrated after an ipGTT, compared to C/C. HF/C offspring exhibited lower levels of circulating TGs, FFAs, total cholesterol, HDL and LDL compared to HF/HF. Furthermore, these levels were also lower compared to C/HF, except for TG and FFAs levels. This suggests that a combination of maternal and offspring diet is needed to induce elevating levels of serum TG and FFAs. The biochemical and metabolic effects observed in C/HF and HF/HF were opposite to that of the effects demostrated in C/C and HF/C, in which the former two offspring groups presented with metabolic dysfunction. Maternal overnutrition during gestation promotes adipocyte hypertrophy via upregulation of glucose

uptake and lipid biosynthesis (Lecoutre et al., 2016; Long et al., 2012). The effects of maternal overnutrition may potentiate an increase in pericardial adipocyte hypertrophy of HF/HF, often associated with dysfunctional adipocytes and a deleterious metabolic profile (Rydén et al., 2014). This is further characterised by a positive relationship between pericardial adipocyte volume and levels of TGs, FFAs, total cholesterol, HDL, LDL, body fat content, body weight and percentage body fat. This is suggestive of a link between pericardial adipocyte size and metabolic dysfunction.

In mice fed a HF-diet, visceral fat often expands via hypertrophy, whereas subcutaneous fat grows via hyperplasia (Joe et al., 2009). Visceral fat that preferentially expands via hypertrophy in obesity increases the risk of insulin resistance (McLaughlin et al., 2011; Miyazaki and DeFronzo, 2009) compared to the expansion of subcutaneous fat which provides protection against DIO (Kim et al., 2007). As hyperplastic growth is associated with a beneficial metabolic profile, perhaps a HF-diet encountered *in utero* in mice fed a chow-fed diet post-weaning (HF/C), leads to an expansion of adipocytes via an increase in cell number (hyperplasia) at 30-weeks of age in pericardial fat. Pericardial fat may adopt the characteristics of subcutaneous fat upon exposure to a chow-diet post-weaning (C/C and HF/C). On the contrary, under an obesogenic environment post-weaning (C/HF and HF/HF), pericardial fat may resemble a visceral depot in offspring. This demonstrates the importance of an offspring diet post-weaning, regardless of exposure to maternal nutrition *in utero,* in adapting pericardial adipose tissue plasticity to regulate metabolic function in offspring.

The role of subcutaneous fat is associated with improved metabolic health, as expansion counteracts insulin resistance in obesity (Kim et al., 2007). This subcutaneous profile in pericardial fat is reflected in the improved glucose homeostasis levels of HF/C, compared to all offspring groups, after an ipGTT. Additionally, brown fat plays a role in improving lipid and glucose metabolism, with activity associated with improved insulin resistance (Bartelt et al., 2011), increased thermogenesis (Van Marken Lichtenbelt et al., 2009) and reduced body weight (Saito et al., 2009). Pericardial fat may resemble both a subcutaneous and brown-like profile upon a chow-fed diet in 30-week-old male offspring mice (HF/C), to counteract the

environment of nutritional excess encountered *in utero*.

This previous statement is reinforced by the presence of multi-locular cells in C/C and HF/C of pericardial fat, suggestive of brown-like cells that positively influence metabolism. Leptin is predominantly secreted by white adipocytes (Cinti et al., 1997). However, the expression levels of C/EBPα in pericardial fat cannot be accounted solely by Leptin expression levels, as C/EBPα in brown fat is upregulated under adrenergic control (Manchado et al., 1994; Rehnmark et al,.1993). C/EBPα mRNA expression levels are significantly higher in C/C compared to HF/HF, further confirming the suspected presence of brown-like cells. This may preserve normal metabolic function in C/C offspring compared to HF/HF offspring. In addition, expression levels of Leptin are significantly higher in C/HF and HF/HF, compared to HF/C. The HF-fed post-weaning offspring groups do not possess a sub-population of multi-locular cells. This suggests that a HF-diet post-weaning may induce a trans-differentiation of brown-to-white cells ('whitening') in pericardial fat characterised as either a subcutaneous (Dobner et al., 2017) or brown (Miranda et al., 2020) depot. The 'whitening' of cells is associated with impaired metabolism (Shimizu et al., 2014) and dysregulated thermogenesis (Miranda et al., 2020), as observed in C/HF and HF/HF offspring in this study. This is demonstrated by impaired glucose clearance following an ipGTT and a reduced respiratory exchange rate (RER). The opposite is true for C/C and HF/C offspring mice in which brown-like cells are present in the pericardial depots. This may contribute to better metabolic health via improved glucose clearance and an upregulated thermogenic capacity in pericardial fat to reduce weight gain.

As mentioned earlier, perhaps exposure to maternal overnutrition results in an offspring predicting an environment high in fat. This may program pericardial fat to upregulate the thermogenic capacity of pericardial adipocytes to counteract a potential obesogenic environment in adulthood. This resembles a 'predictive adaptive response' (Bateson, Gluckman and Hanson, 2014) in which a developing fetus predicts the nutritional environment that may be encountered postnatally. In this case, predicting an obesogenic environment has conferred an advantageous metabolic phenotype in HF/C. This is reflected by a reduction in pericardial adipocyte and depot size, body weight and improved glucose tolerance. This is in

line with previous research indicating that an increased thermogenic capacity of brown fat, potentially via adrenergic output, may lead to a beneficial metabolic profile in HF/C offspring mice (Gaspar et al., 2021).

Obesity induced by a HF-diet is characterised by low-grade inflammation. Offspring exposed to maternal overnutrition *in utero* (HF/C and HF/HF) have elevated levels of TNFα mRNA expression in pericardial fat. As TNFα is elevated in white fat of obese mice (Hotamisligil et al., 1995), perhaps high expression levels in HF/HF are linked with a reduction in the pro-adipogenic marker C/EBPα of pericardial fat. This pro-inflammatory cytokine is known to suppress adipocyte differentiation (Kurebayashi et al., 2001) and mediate insulin resistance (Hotamisligil et al., 1993). This was demonstrated by a relationship between TNFα expression levels in pericardial fat and fasting blood glucose levels. TNFα mRNA levels were significantly elevated in HF/C and HF/HF of pericardial fat. This is in line with significantly lower fasting blood glucose levels of these animals, almost comparable to that of C/C, compared to C/HF. It is still unclear how TNFα adipose tissue expression effects insulin resistance, however human studies have reported that plasma levels of IL6, but not TNFα, are elevated in T2D (Carey et al., 2004).

Of interest, IL6 mRNA expression levels in pericardial fat were only elevated in HF-fed offspring exposed to a maternal chow-diet (C/HF). Studies have suggested that IL6 is a regulator of lipid metabolism and that plasma IL6, but not TNFα, stimulates lipid accumulation, albeit in trophoblasts (Lager et al., 2011). As pericardial fat IL6 mRNA levels are positively associated with adipocyte size and serum TG levels, it is possible that these levels may contribute to the deleterious phenotype demonstrated in C/HF.

Although both IL6 and TNFα are expressed in adipose tissue, IL6 is abundantly expressed (Kern et al., 2001). HF/C presented both the lowest depot weight and IL6 mRNA expression levels in PAT, whilst C/HF and HF/HF had the highest levels of IL6 and TNFα expression, respectively, with comparable depot weights. Although pericardial depot weight was not significantly correlated with cytokine mRNA levels, the results still provide an insight into how maternal overnutrition may promote a pro-inflammatory state in pericardial fat, further

exaggerated by the post-weaning diet of an offspring.

Furthermore, IL6 mRNA expression in skeletal muscle is greater in that of insulin-resistant rats compared to healthy rats, after stimulation with insulin (Carey et al., 2003). C/HF offspring mice presented with the greatest insensitivity to glucose after an ipGTT and had elevated levels of fasting blood glucose, compared to all the other offspring groups. Altered insulin metabolism may sensitise IL6 mRNA levels in pericardial fat, with an interactive effect between maternal and offspring diet mediating this response.

4.4.1. Conclusion

Exposure to maternal overnutrition prior to and during pregnancy and lactation induces varying effects in 30-week-old male offspring mice. This is dependent on the dietary conditions encountered post-weaning. Further gene and protein analysis of thermogenic and mitochondrial markers is required to confirm the that pericardial fat adapts postnatally in response to maternal overnutrition encountered *in utero*. However, this study documents critical effects are due primarily to postnatal diet, rather than exposure to a prenatal maternal diet. This induces either a trans-differentiation of white-to-brown or brown-to-white cells in pericardial fat of chow-fed offspring (C/C and HF/C) or HF-fed offspring (C/HF and HF/HF), respectively. This either confers a beneficial or deleterious metabolic profile in 30-week-old male offspring mice, such as upregulating or impeding the thermogenic capacity of pericardial adipocytes.

CHAPTER 5

INVESTIGATING THE EFFECTS OF CPD14 ON

PERICARDIAL ADIPOSE TISSUE IN MICE

5.1. INTRODUCTION

5' adenosine monophosphate-activated protein kinase (AMPK) is a serine/threonine heterotrimeric enzyme, known as the 'master regulator of metabolism', which controls acetyl-CoA carboxylase (ACC) (Carlson and Kim, 1973). AMPK contains catalytic α subunits and non-catalytic subunits, including β and γ (Stapleton et al., 1997) and is activated by changes in intracellular AMP:ATP ratio, or other stimuli including glucose starvation, exercise or hormone stimulation, such as Leptin (Shaw et al., 2004). Biological activators including Liver Kinase B1 (LKB1) can activate AMPK by phosphorylating the Threonine 172 (Thr172) residue on the catalytic AMPKα subunit, *in vitro* (Shaw et al., 2004). Other activators include Calcium/calmodulin-dependent protein kinase kinase (CAMKK) (Hawley et al., 1995) and AMP, the 'true' regulator that allosterically promotes AMPK phosphorylation via LKB1 mediation (Gowans et al., 2013). AMPK activation by upstream molecules inhibits ATP utilisation in large amounts, therefore activates catabolism to equilibrate cellular homeostasis (Chen et al., 2017). Manipulating this pathway holds the potential to therapeutically target AMPK to provide protection against metabolic diseases.

Despite the role of AMPK activators as anti-diabetic agents, they also pose beneficial effects on adipose tissue to target obesity. *In vitro* experiments have demonstrated that in 3T3-L1 adipocytes, treatment of AMPK activators such as AICAR (Lee et al., 2011), Metformin (Chen et al., 2018; Chen et al., 2017) and dietary compounds (Ono and Fujimori, 2011) inhibit adipogenesis. This is documented by a reduction in gene expression levels of pro-adipogenic markers including FABP4, PPARγ and C/EPBα. This suppression is associated with AMPK activation and promotion of brown adipocyte differentiation, demonstrated in human fetal pre-adipocytes (Wu et al., 2019).

In vitro studies demonstrate an insight into targeting dysregulated adipogenesis that occurs in obesity. However, cell culture experiments do not represent the true effects that occur in physiology and thus *in vivo* studies are conducted. In addition to inducing weight loss and improving insulin sensitivity in obese (Yuan et al., 2019) and diabetic mice (Alfaras et al., 2017), AMPK activators improve endoplasmic reticulum stress in fat from obese (Yuan et al.,

2019) and diabetic mice (Li et al., 2016). In addition, AMPK activation improves fatty acid metabolism in white and brown fat (Yuan et al., 2019) and has anti-inflammatory properties that target white fat (Jing et al., 2018).

Previous research has extensively demonstrated the effect of AMPK activators on adipogenesis *in vitro*, yet their role in inducing 'browning' remains to be elucidated. This being said, there is evidence to suggest that AMPK activators enhance thermogenesis in brown fat of obese mice (Wu et al., 2019) and promotes 'browning' in subcutaneous white fat (Qi et al., 2019). This may provide protection against metabolic dysfunction in obesity (Wu et al., 2018).

Whilst AMPK activators elicit beneficial results, undesirable side effects including gastrointestinal discomfort (Dujic et al., 2015), lactic acidosis (Zhang et al., 2019) and intoxication (Sánchez-Díaz et al., 2017) may persist. To this end, there is evidence to suggest that AMPK activators may induce 'browning' and upregulate thermogenesis in brown-like cells, providing an insight into pericardial fat as a potential target.

Developed by Tavassoli and Benkovic, derivatives of small molecules were studied to determine their potential as inhibitors of 5-Aminoimidazole-4-carboxamide ribonucleotide transferase (AICART), for the suppression of tumorigenesis via AMPK activation. The study demonstrated that the most potent inhibitor of AICART activity in cancer cells was Compound 14 (Cpd14) (Tavassoli and Benkovic, 2005). Cpd14 acts by selectively blocking the final two steps of *de novo* purine biosynthesis by inhibiting AICART activity via the disruption of aminoimidazole carboxamide ribonucleotide transformylase/inosine monophosphate cyclohydrolase (ATIC) homodimerization. This increases endogenous levels of 5-Aminoimidazole-4-carboxamide ribonucleotide (AICAR), which acts in a similar manner to AMP, to activate AMPK (Spurr et al., 2012). Asby et al., further demonstrated that Cpd14 phosphorylates AMPKα Thr172 and ACC Serine 79 (Ser79), a vital and direct event of AMPK activation, respectively, in cancer cells (Asby et al., 2015).

As AMPK function is a promising therapeutic target for a variety of metabolic diseases, the effects of Cpd14 *in vivo* were further probed using mice as an obesity model. A daily treatment of Cpd14 (0.05mg/g) for 7 days by intraperitoneal (i.p.) administration in obese mice resulted

sin a marked reduction in body weight, despite continual feeding on a high-fat (HF)-diet. This was accompanied by improved insulin sensitivity (Asby et al., 2015). Although the effects of Cpd14 on adipose tissue (AT) and further mechanistic effects are still unknown, the improved metabolic profile demonstrated in Cpd14-treated obese mice holds promise for this compound to regulate metabolic disorders.

It is evident that Cpd14 has the therapeutic potential for weight gain and insulin resistance in mice, perhaps by activating AMPK, as demonstrated in cancer cells (Asby et al., 2015). Despite this, the way in which Cpd14 elicits its action *in vivo* is still unknown and whether AT is targeted during treatment. In AT, AMPK increases UCP1 expression and thermogenesis (Vila-Bedmar et al., 2010). As pericardial fat has a thermogenic capacity (Al-Dibouni et al., 2020), perhaps Cpd14 treatment acts as an AMPK agonist on pericardial adipose tissue (PAT) to regulate metabolism in disease. Furthermore, in humans, weight loss is associated with a reduced metabolic risk accompanied with better profiles of an inflammatory response and insulin levels. However, after weight loss, individuals are prone to weight re-gain accompanied by an underlying inflammatory signature.

5.1.1. Aims

The aim is to demonstrate how the genetic and morphological signatures of 3T3-L1 cells and PAT compares to other adipose depots upon therapeutic intervention. In this study, transcriptional and cytological/histological analysis was performed to determine the effect of Cpd14 treatment **(1)** on adipocyte differentiation in 3T3-L1 cells, treated for 72 hours, and on pericardial adipose tissue (PAT), compared with gonadal (gWAT), inguinal (iWAT) and interscapular brown (iBAT) adipose tissue harvested from **(2)** 10-week-old male mice fed a chow-diet of 7% kcal fat or a high-fat (HF)-diet of 45% kcal fat for 7 weeks and treated orally with Cpd14 for 10 days and **(3)** following a 26-day recovery period from Cpd14 treatment in ~15-week-old male mice fed a high-fat-diet of 45% kcal fat.

5.2. METHODS

5.2.1. Synthesis of Cpd14

The synthesis of Cpd14 is detailed extensively by Spurr et al., and was carried out by the technical staff at the University of Southampton. Synthesis consists of multiple steps to synthesise Boc-Phe(4-NO2)-diethylamide, fmoc-Arg(Pbf)-CONH-Phe(4-NO2)-L-Diethylamide, Amino-Arg(Pbf)-CONH-Phe(4-NO2)-L-Diethylamide, Acetyl-Arg(Pbf)-CONH-Phe(4-NO2)-L-Diethylamide and finally, Cpd14 (Acetyl-Arg-CONH-Phe(4-NO2)-L-Diethylamide), with a molecular weight of 464g/mol, with the chemical structure $C_{21}H_{33}N_7O_5$. The final stage of Cpd14 synthesis includes Thin Layer Chromatography (TLC) to monitor the reaction, extracting the solvent *in vacuo* to produce a viscous yellow liquid, which is then evaporated, dried, and filtered to produce a white precipitate (263mg, 100% crude yield). This crude product is purified by reverse phase High Performance Liquid Chromatography (HPLC) and lyophilised to attain a white solid product (125mg, 50% yield) of Cpd14 (Figure 5.1).
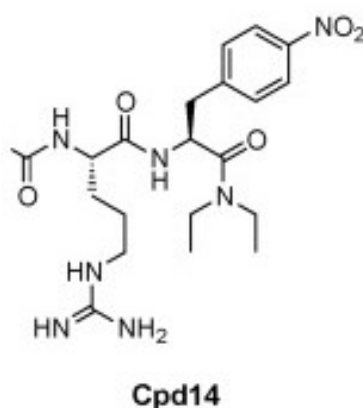
Cpd14

Figure 5.1. Chemical structure of Cpd14. Adapted from Asby et al., (2015). Cpd14: Compound 14.

5.2.2. Cell culture studies

3T3-L1 mammalian cells are originally subcloned from embryonic fibroblasts (Green and Meuth, 1974) and are routinely used for *in vitro* therapeutic research. Upon appropriate stimuli, the fibroblast-like cells undergo several rounds of mitotic clonal expansion (MCE) over 48 hours, once cell division has halted after reaching confluencey (Bernlohr et al., 1985). When MCE diminishes and cells attain cell growth arrest, elevated expression of proteins is achieved

and gives rise to an adipocyte phenotype, *in vitro.* These lipid-laden mature adipocytes resemble adipocytes located *in vivo* (Novikoff et al., 1980; Mikkelsen et al., 2010). This process is highly regulated by a strict control of genes and signalling pathways. The accumulation of triglycerides (TGs) to document the progression of adipocyte differentiation (adipogenesis) can be determined by staining cells with Oil Red O (ORO) and quantification of stain uptake, and TG levels can indicate potential alterations in lipid metabolism upon treatment.

AMPK activators inhibit adipocyte differentiation *in vitro* and act as potential therapeutic agents for regulating dysregulated adipogenesis characterised in obesity (Lee et al., 2011; Chen et al., 2018). In cancer cells, if Cpd14 activates AMPK, cells must be actively producing purines via the *de novo* purine biosynthetic pathway (low purine environment) rather than the salvage pathway (high purine environment) (Asby et al., 2015). To encourage this mode of action in 3T3-L1 cells, cells were cultured in Low Purine Media (LPM) upon Cpd14 treatment. LPM contains dialysed FBS that does not contain small-weighted molecules that may interfere with the treatment process or normal growth of cells. In this *in vitro* study*,* 3T3-L1 cells were acutely stimulated with LPM or HPM supplemented with Cpd14 at the early stages of adipogenesis (Figure 5.2). As the effects of Cpd14 in adipocyte differentiation are unknown, the highest concentration of 1mM as documented by Asby et al., was administered to 3T3-L1 cells. The transcriptional and cytological analysis of differences with Cpd14 compared with Vehicle were performed at the end of adipogenesis (Day 7) to determine the effects of Cpd14 on adipocyte differentiation.

Terminology: Basal media is indicated as high purine basal media (HPBM) and is defined as high glucose DMEM, 10% FBS and 1% P/S. Low purine basal media (LPBM) is defined as high glucose DMEM, 10% purine-free dialyzed FBS (depleted of small molecules i.e. amino acids) and 1% P/S. High/Low purine adipogenic media (HPAM/LPAM) is defined as HPBM/LPBM containing 1µM dexamethasone, 0.5mM IBMX and 1µg/ml insulin. High/low purine insulin media (HPIM/LPIM) is defined as HPBM/LPBM containing 1µg/ml insulin.

Sub-culturing 3T3-L1 cells: 3T3-L1 cells were re-suspended in HPBM supplemented with 5% DMSO and stored in liquid nitrogen for future use. Cells were cultured in 75cm^2 culture

flasks (T75) and maintained in HPBM, incubated in a humidified atmosphere of 5% CO_2, at 37°C. At ~80% confluence, media was removed from cells and washed with PBS. Trypsin-EDTA was added for 1 minute at room temperature. Trypsin-EDTA was removed and cells were incubated for 2 minutes before adding HPBM. Trypan Blue solution (0.4%) was added to an aliquot of cell suspension to determine the cell number by using the Countess™ Automated Cell Counter (Fisher Scientific).

Differentiation of 3T3-L1 cells: 3T3-L1 mouse pre-adipocytes were obtained from Sigma-Aldrich. Cells were seeded in HPBM in either 12-well plates, for Oil Red O staining, or 6-well plates, for cell lysate extraction for RNA and TGs, and incubated in a humidified atmosphere of 5% CO_2 at 37°C. 2 days post-confluent (designated as Day 0, unless stated otherwise), cells were induced with adipogenic media for 48 hours (from Day 0 to Day 2). The culture media was changed to insulin media for 48 hours (Day 2 to Day 4). From Day 4 onwards, media was refreshed every 2 days until the end of adipocyte differentiation (Day 7). To determine the effects on differentiation, Cpd14 (dissolved in ddH_2O) at 1mM or Vehicle (ddH_2O), was added to the medium (HPBM/LPBM) 24 hours prior to differentiation and supplemented to the adipogenic media (HPAM/LPAM) for 48 hours. 3T3-L1 cells were treated for a total of 72 hours (Figure 5.2).

Mycoplasma detection: An aliquot of media was collected from 80% confluent cells maintained in flasks before sub-culturing. Detection of Mycoplasma contamination in growing cells was performed as recommended by the manufacturer's instructions for the LookOut® Mycoplasma PCR Detection Kit (Sigma-Aldrich). Mycoplasma was detected using an 1.5% agarose gel with SYBR Safe™ DNA gel stain (Fisher Scientific) visualised using the Syngene™ G:BOX Chemi XX9. Plates seeded from Mycoplasma negative media corresponding to the T75 flasks were used as experimental plates. Aliquots of media were stored at -20°C until further analysis.

RNA isolation: Before discarding media from cells, cells were imaged with the Evos Fl Microscope, at x10 objective lens. After removing media, cultured cells were washed once with PBS and cells were collected with RNA lysis buffer (40µl of 1M DTT per 1ml Buffer RNeasy

Lysis (RLT)). Cell lysates were homogenised by passing the sample through a 25G needle and RNA isolation was performed as described by the Qiagen's RNeasy mini kit's protocol (Qiagen). RNA was quantified as stated in section 2.2.4.3. RNA extracts were stored at -80°C until further analysis.

cDNA synthesis and RT-qPCR: Total RNA was reverse transcribed using the Applied Biosystems™ High-Capacity cDNA Reverse Transcription Kit (Fisher Scientific) and Invitrogen™ RNaseOUT™ Recombinant Ribonuclease Inhibitor (Fisher Scientific), following the instructions as recommended by the manufacturer to synthesise cDNA, performed using the T100™ Thermal cycler (Bio-Rad). 500ng of cDNA was synthesised as stated in section 2.2.5. The gene expression of 30ng cDNA was determined using qPCRBIO Probe Mix No-ROX (PCR Biosystems), performed on the MyiQ™ Single-Colour Real-Time PCR Detection System (Bio-Rad). Samples were measured in duplicates and the fold change in gene expression levels were determined using the comparative threshold cycle (Ct) method, also referred to as the $2^{-\Delta\Delta}$ Ct method (section 2.2.6). The target genes listed in Table 5.1 were relative to the housekeeping gene, peptidylprolyl isomerase A (PPIA). All Applied Biosystems™ TaqMan™ Gene Expression Assays (FAM-MGB) were purchased from Fisher Scientific. cDNA was stored at -20°C until further analysis.

Table 5.1. Applied Biosystems™ TaqMan™ Gene Expression Assays for RT-qPCR

Gene	Assay ID
C/EBPα	Mm00514283_s1
FABP4	Mm00445878_m1
PPARγ	Mm00440940_m1
PPIA	Mm02342430_g1

Triglyceride extraction and quantification: Media was discarded and cells were washed with PBS. 5% Triton-X 100 was added and cell lysates were harvested by scrapping the cells off the wells. Cell lysates were heated to 95°C for 5 minutes and vortexed briefly and heated again for 10 minutes at 95°C. This was repeated once more. The samples were then centrifuged for 5 minutes at 14,000rpm and the supernatant was collected. Triglyceride (TG) content was determined by using the Triacylglycerol Determination Kit (Sigma-Aldrich) as suggested by the manufacturer. All values were corrected to the blank absorbance and TG concentration was normalised to total cellular protein concentration as determined by bicinchoninic acid (BCA) method (section 2.2.9). Absorbances were measured at 540nm on the SPECTRAmax® 190 Microplate Spectrophotometer (Molecular Devices Corporation), using SOFTmax PRO software. Triglyceride extracts were stored at -80°C until further analysis.

Cell titre: The number of cells (viability) was determined using the CellTiter 96® AQueous One Solution Cell Proliferation Assay, as stated in section 2.2.1.4.

Cytology: Media was removed from cells and washed with PBS for 5 minutes before fixing with formalin solution (neutral buffered, 10%) for 30 minutes. The fixed cells were washed with PBS for 5 minutes thrice after removing formalin, on agitation. 3mg/ml Oil Red O stain, an indicator of lipid accumulation, was added to the cells for 1 hour at room temperature, on agitation. After removing Oil Red O, cells were washed with PBS for 5 minutes thrice and images were taken of the wells. After imaging with Nikon TE200 brightfield inverted microscope (x10 objective lens) and before eluting the stain, cells were air-dried and images were taken once again of the well. The stain was eluted with 100% 2-Propanol and absorbances were read at 560nm on the SPECTRAmax® 190 Microplate Spectrophotometer (Molecular Devices Corporation), using SOFTmax PRO software. Analysis was performed as documented in section 2.2.11.2.
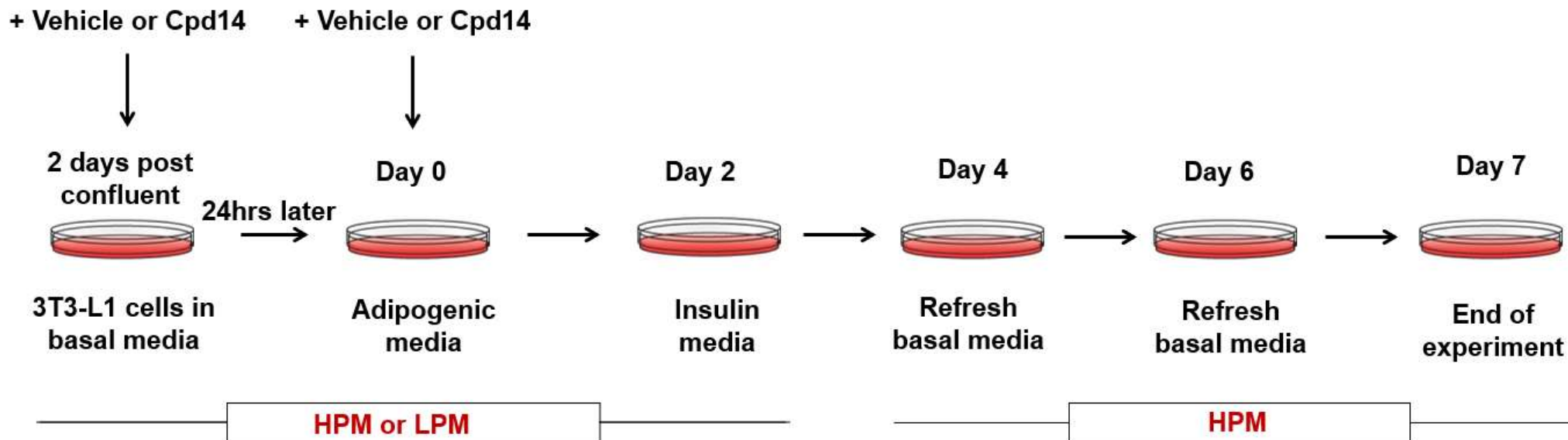
Figure 5.2. Experimental design of 3T3-L1 cells treated with Vehicle or Cpd14. 3T3-L1 cells were treated with Vehicle or Cpd14 for 72 hours, maintained in HPM or LPM. From Day 0 to Day 2, cells were maintained in either HPAM or LPAM. From Day 2 to Day 4, cells were maintained in either HPIM or LPIM. From Day 4 to Day 7, all 3T3-L1 cells were maintained in HPM. HPM: High Purine Media; LPM: Low Purine Media; HPIM: High Purine Insulin Media; LPAM: Low Purine Insulin Media; HPAM: High Purine Adipogenic Media; LPAM: Low Purine Adipogenic Media; Cpd14: Compound 14.

5.2.3. Animal studies

Animal and experimental procedure: All animal work was conducted by the technical staff at the University of Southampton. Research was performed in accordance with the UK Animals (Scientific Procedures) Act 1986 and with Home Office licences held at the University of Southampton. Maintained under a 12-hour light/dark cycle and a constant temperature of 22°C ± 2°C, C57BL/6J male mice were used in this study, with food and water available *ad libitum*. At the age of 3 weeks old, mice were randomly allocated to either a chow (C)-diet (7% kcal fat) or a high-fat (HF)-diet (45% kcal fat). At the end of the experimental procedure, death of mice by carbon dioxide euthanasia and neck dislocation was confirmed by cessation of the circulation.

10-day treatment period: In one study, animals were fed a C or HF-diet for 7 weeks and at 10 weeks of age were treated orally with Vehicle (physiological saline) or Cpd14 (dissolved in 0.9% saline [w/v]) at a dose of 0.1 mg/g mouse body weight. Fasting blood glucose concentrations were measured from whole blood obtained from the tail vein after 10 days of oral administration of Vehicle or Cpd14. There are four experimental groups: C-V, C-Cpd14, HF-V and HF-Cpd14 – The letters before the '-' indicates the dietary intake and the letters after the '-' indicate whether Vehicle (V) or Cpd14 was administered. The body weights were measured daily during this period. After 10 days of treatment, mice were fasted overnight and injected intraperitoneally with D-glucose (2g/kg mouse body weight) for a 3-hour glucose tolerance test (GTT) and the area under the curve (AUC) was determined, with baseline values were subtracted. Blood glucose concentration was then assayed using an Aviva Accu-Chek glucometer (Roche Diagnostics Ltd, United Kingdom) at 0 (baseline), 15, 30, 60, 90, 120, and 180 minutes. Food intake was measured by weighing the remaining food each day and topping them up thereafter. At the end of the experimental procedure, ~11.5-week-old male mice were euthanised and gonadal white adipose tissue (gWAT), inguinal white adipose tissue (iWAT), interscapular brown adipose tissue (iBAT), pericardial adipose tissue (PAT) and the stromal vascular fraction (SVF) from gWAT were harvested for gene expression (stored at -80°C until further analysis) and histological analysis (stored at 4°C until further analysis) (Figure 5.3).

Stromal Vascular Fraction isolation from gonadal white adipose tissue: In white adipose tissue (WAT) resides a population of adipocytes in the stromal vascular fraction (SVF) (Hagberg et al., 2018). These adipocytes demonstrate a possible origin of adipocyte stem cells which proliferate, differentiate and contribute to the stem cell pool population (Rodeheffer, Birsoy and Friedman, 2008; Tang et al., 2008). For research purposes, the adipocytes residing in the SVF can be isolated and cultured *ex vivo* (Hollenberg and Vost, 1968). As obesity alters the cellular content of the SVF (Silva et al., 2015), perhaps Cpd14 could target the adipogenic potential of adipocytes in obese mice. In this study, SVF was extracted from chow and HF-fed mice treated with Vehicle or Cpd14 orally for 10 days and cultured *ex vivo*. The Stromal Vascular Fraction (SVF) was isolated by mincing gonadal white adipose tissue (gWAT) from 6 mice per treatment. This was transferred to 15ml tubes and incubated in 0.2% collagenase solution in DMEM at 37°C. To aid digestion, tissue samples were vigorously vortexed every 10 minutes then centrifuged at 350xg for 5 minutes. The pellets were re-suspended in basal media and passed through a 40µM strainer into a 6cm dish and incubated at 37°C, 5% CO_2. For adipocyte differentiation from pre-adipocytes to mature adipocytes, gWAT SVF cells of 2 mice per group were pooled together. 2 days post-confluent, adipogenesis was induced with an adipogenic cocktail consisting of basal media supplemented with 1µM dexamethasone, 0.5mM IBMX and 0.5µg/ml insulin for 48 hours. After 48 hours, adipogenic media was replaced with basal media supplement with 0.5µg/ml insulin until Day 7, when RNA was isolated. RNA was stored at -80°C until further analysis. This was conducted by the technical staff at the University of Southampton.

26-day recovery period: In another study, animals were fed a HF-diet for 7 weeks. At 10 weeks of age, mice were treated orally with Vehicle (physiological saline) or Cpd14 (dissolved in 0.9% saline [w/v]) at a dose of 0.1 mg/g mouse body weight. After the 10-day treatment experimental paradigm as stated previously, mice were continually fed on a HF-diet (total of 12 weeks), without Vehicle or Cpd14 administration for a further 26 days. There are two experimental groups: HF-V and HF-Cpd14 – The letters before the '-' indicates the dietary intake and the letters after the '-' indicate whether Vehicle (V) or Cpd14 was administered.

Body weights, fasting glucose concentrations and an ipGTT was performed as described in the methodology of the 10-day treatment period. At the end of the experimental procedure, ~15-week-old male mice were euthanised and gonadal white adipose tissue (gWAT), inguinal white adipose tissue (iWAT), interscapular brown adipose tissue (iBAT) and pericardial adipose tissue (PAT) were harvested for gene expression (stored at -80°C until further analysis) and histological analysis (stored at 4°C until further analysis) (Figure 5.3).

RNA isolation from frozen adipose tissue: 1ml Invitrogen™ TRI Reagent™ Solution per 50mg to 100mg of gWAT, iWAT, iBAT and PAT was transferred to a MP Biomedicals™ Lysing Matrix D tube. Lysing tubes were placed in the MP Biomedicals™ FastPrep-24™ 5G Instrument, with the QuickPrep Adaptor (Fisher Scientific) and homogenised at a speed of 6.0m/s, for 40 seconds. Isolation of RNA was performed as recommended by the manufactures of Invitrogen™ TRI Reagent™ Solution (Fisher Scientific). RNA was quantified and quality was checked as stated in section 2.2.3 and 2.2.4.3. RNA samples were stored at -80°C until further analysis.

RNA isolation from gWAT SVF: RNA lysis buffer (40µl of 1M DTT per 1ml Buffer RNeasy Lysis (RLT)) was added to cells and collected. Cell lysates were homogenised by passing the sample through a 25G needle and RNA isolation was performed as described by the Qiagen's RNeasy mini kit's protocol (Qiagen). RNA was quantified as stated in section 2.2.4.3. RNA extracts were stored at -80°C until further analysis.

cDNA synthesis and RT-qPCR: Total RNA was reverse transcribed using the Applied Biosystems™ High-Capacity cDNA Reverse Transcription Kit (Fisher Scientific) and Invitrogen™ RNaseOUT™ Recombinant Ribonuclease Inhibitor (Fisher Scientific), following the instructions as recommended by the manufacturer to synthesise cDNA, performed using the T100™ Thermal cycler (Bio-Rad). 500ng to 1000ng of cDNA was synthesised as stated in section 2.2.5.The gene expression of 30ng cDNA was determined using qPCRBIO Probe Mix No-ROX (PCR Biosystems), performed on the MyiQ™ Single-Colour Real-Time PCR Detection System (Bio-Rad). Samples were measured in duplicates and the fold change in gene expression levels were determined using the comparative threshold cycle (Ct) method,

also referred to as the $2^{-\Delta\Delta}$ Ct method (section 2.2.6). The target genes as stated in Table 5.2 were relative to the housekeeping gene, peptidylprolyl isomerase A (PPIA). All Applied Biosystems™ TaqMan™ Gene Expression Assays (FAM-MGB) were purchased from Fisher Scientific. cDNA was stored at -20°C until further analysis.

Histology: Formalin fixed gWAT, iWAT and PAT embedded in Optimal Cutting Temperature (OCT) compound were sectioned between 10μM and 15μM using a Bright 5040 Cryostat (Bright Instruments Limited). Sections were stained with Haematoxylin and Eosin (H&E) and imaged with a Nikon TE200 Brightfield Inverted Microscope, at x40 objective lens. Assuming the shape of adipocytes are spherical, to calculate adipocyte volume, Image-J software was used to determine adipocyte area and volume distribution as stated in section 2.2.12.1. The percentage change in volume was determined by normalising adipocyte volume to the C-fed mice, unless stated otherwise, and multiplying by 100. Adipocyte number was determined in gWAT as stated in section 2.2.12.1. H&E stained slides were stored at room temperature until further analysis.

Protein analysis of gonadal white adipose tissue: Protein was extracted from gWAT using the RIPA buffer method as stated in section 2.2.8. Protein was quantified using the BCA method as stated in section 2.2.9 and absorbances were measured at 560nm on the SPECTRAmax® 190 Microplate Spectrophotometer (Molecular Devices Corporation), using SOFTmax PRO software. To determine changes in AMPK and ACC levels in Vehicle and Cpd14-treated mice, the antibodies stated in Table 2.2 were used to perform a Western Blot, as stated in section 2.2.10. The quality of protein was examined with Coomassie stain to visualise protein bands. Protein extracts were stored at -80°C until further analysis.

Table 5.2. Applied Biosystems™ TaqMan™ Gene Expression Assays for RT-qPCR

Gene	Assay ID
AdipoQ	Mm00456425_m1
ADRβ3	Mm02601819_g1
C/EBPα	Mm00514283_s1
COX7A1	Mm00438297_g1
COX8B	Mm00432648_m1
DIO2	Mm00515664_m1
FABP4	Mm00445878_m1
IL6	Mm00446190_m1
Leptin	Mm00434759_m1
PGC1α	Mm01208835_m1
PPARγ	Mm00440940_m1
PPIA	Mm02342430_g1
TNFα	Mm00443258_m1
UCP1	Mm01244861_m1

5.2.4. Statistical analysis

GraphPad Prism was used to perform statistical analysis of one-way ANOVA, two-way ANOVA, repeated measures ANOVA, unpaired t-test or Pearson's correlation coefficient. ANOVAs were performed with post-hoc Tukey's multiple comparison. All values were relative to their respective depots from chow (C)-fed mice, unless stated otherwise. Graphs are expressed as mean $\pm$ standard error of the mean (s.e.m), unless stated otherwise. A value of $p<0.05$ was deemed as statistically significant with * $p<0.05$, ** $p<0.01$, *** $p<0.001$ and **** $p<0.0001$. The overall effects of treatment and diet are expressed on the graph if the interactions are significant.

Figure 5.3. Experimental design of the 10-day treatment period and 26-day recovery period in chow-fed and high-fat-fed mice treated with Vehicle or Cpd14. There are four experimental groups: C-V, C-Cpd14, HF-Cpd14 and HF-V – The letters before the '-' indicates the dietary intake and the letters after the '-' indicate whether Cpd14 or Vehicle (V) was administered. C: Chow-diet; HF: High-fat-diet; Cpd14: Compound 14; V: Vehicle; BW: Body weight; GTT: Glucose Tolerance Test.

5.3. RESULTS

5.3.1. Cell culture

5.3.1.1. Adipocyte gene expression differences in Day 7 3T3-L1 cells treated with Vehicle or Cpd14

High Purine Media (HPM) is the suggested basal media for differentiating 3T3-L1 cells successfully *in vitro*. This study was interested in observing the optimum conditions for Cpd14 action in 3T3-L1 cells, therefore HPM and LPM were supplemented with Cpd14 for 72 hours and grown until Day 7 in normal basal media (HPM) (Figure 5.2). Under both experimental conditions of HPM and LPM, there were no significant differences observed in morphological observations (Figure 5.4A and Figure 5.5A, respectively), lipid accumulation by ORO (Figure 5.4B and Figure 5.5B, respectively) and TG content analysis (Figure 5.4C and Figure 5.5C, respectively), cell viability (Figure 5.4D and Figure 5.5D, respectively) and gene expression differences of pro-adipogenic markers FABP4, PPARγ and C/EBPα (Figure 5.4E and Figure 5.5E, respectively), regardless of Cpd14 treatment.
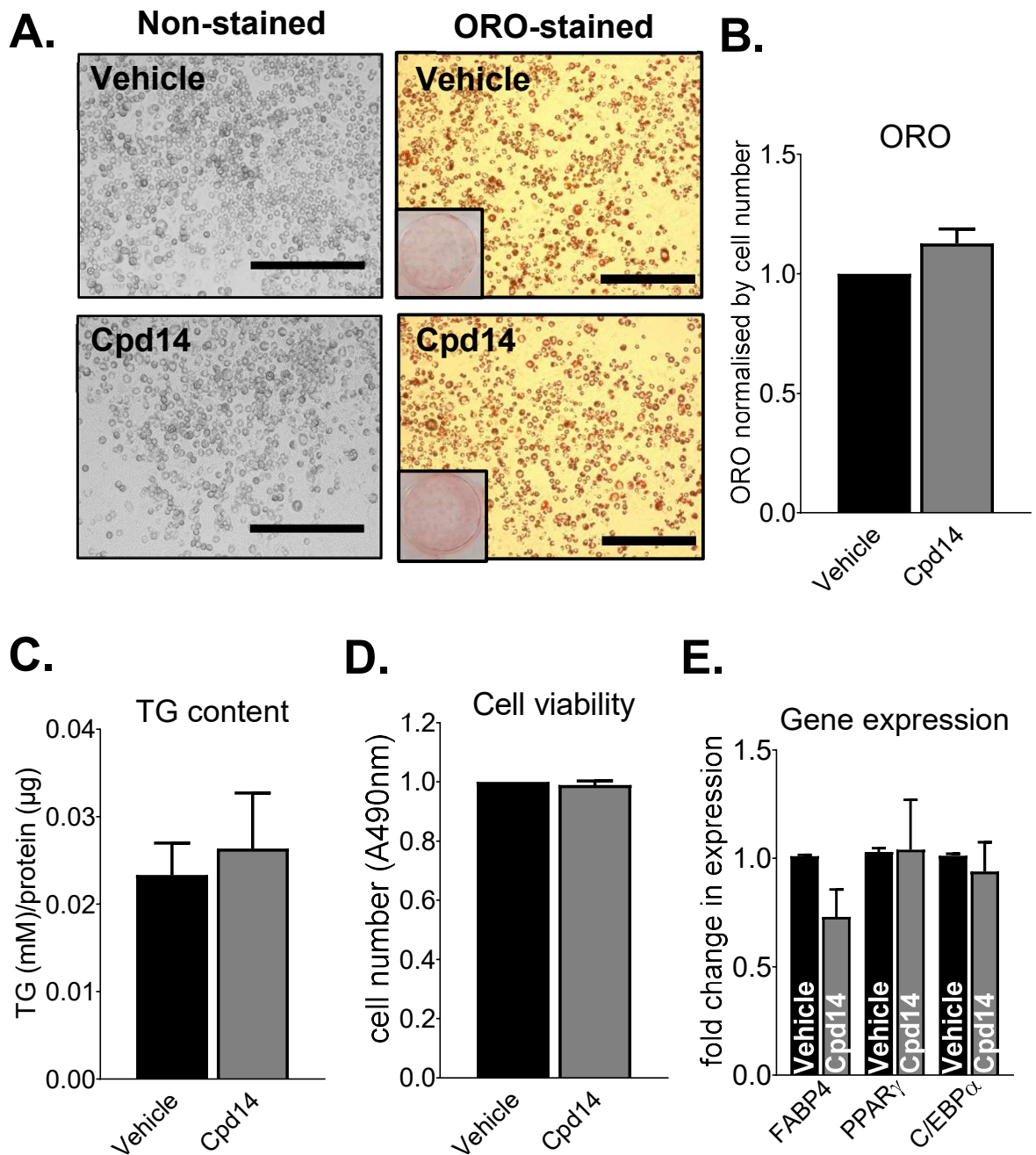
Figure 5.4. Day 7 3T3-L1 cells treated with Vehicle or Cpd14 for 72 hours in HPM. Representative images of cells unstained/stained with ORO, and wells of ORO-stained cells before elution **(A)**. All scale bars represent 400µM and imaged at x10 optical lens with Evos Fl Microscope **(left)** and Nikon TE200 Brightfield Inverted Microscope **(right).** ORO absorbance normalised to the cell titre **(B)**, TG content normalised to protein levels **(C)**, cell viability normalised to Vehicle **(D)** and FABP4, PPARγ and C/EBPα fold change in mRNA expression relative to their respective Vehicle **(E)**. Graphs represent mean ± s.e.m. Data analysed by an unpaired t-test. N = 3. * p<0.05, ** p<0.01, *** p<0.001 and **** p<0.0001.

Figure 5.5. Day 7 3T3-L1 cells treated with Vehicle or Cpd14 for 72 hours in LPM. Representative images of cells unstained/stained with ORO, and wells of ORO-stained cells before elution **(A)**. All scale bars represent 400µM and imaged at x10 optical lens with Evos FI Microscope **(left)** and Nikon TE200 Brightfield Inverted Microscope **(right).** ORO absorbance normalised to the cell titre **(B)**, TG content normalised to protein levels **(C)**, cell viability normalised to Vehicle **(D)** and FABP4, PPARγ and C/EBPα fold change in mRNA expression relative to their respective Vehicle **(E)**. Graphs represent mean ± s.e.m . Data analysed by an unpaired t-test. N = 3. * $p<0.05$, ** $p<0.01$, *** $p<0.001$ and **** $p<0.0001$.

5.3.2. Animal studies

5.3.2.1. 10-day treatment period in chow-fed and HF-fed mice

5.3.2.1.1. Metabolic parameters from chow-fed and HF-fed 10-week-old mice treated with Vehicle or Cpd14

Treatment of therapeutic compounds are often linked with improved metabolic parameters including body weight and insulin sensitivity. Over the 10-day treatment period of orally administered Cpd14, non-fasting (Figure 5.6B) and fasting blood glucose levels (Figure 5.6C) after an ipGTT (Figure 5.6D and Figure 5.6E, $p<0.0001$), body weight (Figure 5.6G) and gWAT depot weight (Figure 5.6H, $p<0.0001$) were markedly lower in HF-Cpd14 mice compared to HF-V. Interestingly, in Cpd14-treated chow-fed mice (C-Cpd14), the blood glucose levels (Figure 5.6A) increased until Day 7, then decreased until the end of the treatment period (Day 10), with body weight remaining unchanged throughout (Figure 5.6F). Furthermore, fasting blood glucose levels (Figure 5.6C), after an ipGTT (Figure 5.6E) and gWAT depot weight (Figure 5.6H) in HF-V mice were significantly higher than C-V ($p<0.0001$, $p<0.0001$ and $p<0.0001$, respectively) and C-Cpd14 ($p<0.0001$, $p<0.0001$ and $p<0.0001$, respectively). In addition, caloric intake (Figure 5.6I) was higher in HF-V compared to C-V ($p<0.05$).
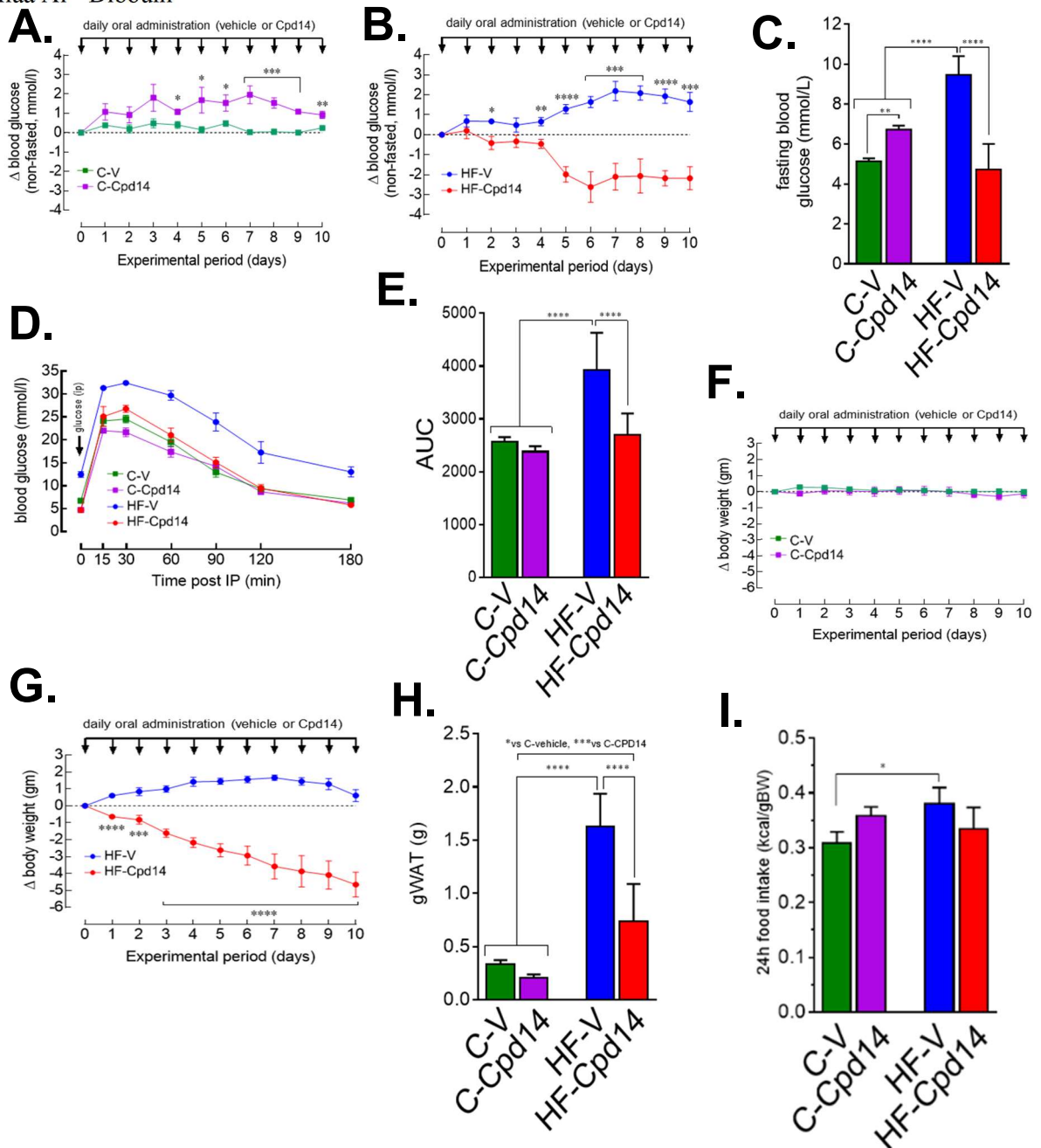
Figure 5.6. Metabolic effects of Vehicle and Cpd14 treatment in chow-fed and high-fat fed mice. Daily non-fasting blood glucose levels expressed as change (Δ) in glucose levels **(A-B)**, fasting blood glucose levels **(C),** intraperitoneal glucose tolerance test (ipGTT) with glucose measured at 0, 15, 30, 60, 90, 120 and 180 minutes after glucose injection **(D)** and area under the curve (AUC) of blood glucose levels **(E)**, the change (Δ) in body weight **(F-G)**, gWAT depot weight **(H)** and caloric intake relative to body weight **(I)** from chow (C) and high-fat (HF)-fed male mice treated orally with Vehicle (V) or Cpd14 for 10 days. Graphs represent mean $\pm$ s.e.m. Data analysed by ANOVA **(C,E,H,I)** and by repeated measures ANOVA **(A,B,D,F,G)** with Tukey's multiple correction test. N = 5-8. * $p < 0.05$, ** $p < 0.01$, *** $p < 0.001$ and **** $p < 0.0001$ and grey-coloured stars indicate significance of the group against V.

5.3.2.1.2. Gonadal white adipose tissue gene expression differences from cells of the stromal vascular fraction in chow-fed and HF-fed 10-week-old mice treated with Vehicle or Cpd14

For the effects of treatment and diet in Vehicle and Cpd14-treated mice, refer to Appendix Table 2.2. Cell lysates were collected for RNA at Day 7 of adipogenesis (end of the experimental procedure) to examine differences in gene expression levels of pro-adipogenic markers FABP4 (Figure 5.7A), PPARγ (Figure 5.7B) and C/EBPα (Figure 5.7C). HF-Cpd14 exhibited lower levels of FABP4 (Figure 5.7A) compared to HF-V and PPARγ expression was lower in HF-Cpd14 mice (Figure 5.7B) compared to C-Cpd14. FABP4 levels were higher in HF-V compared C-V ($p < 0.001$) and C-Cpd14 ($p < 0.01$).
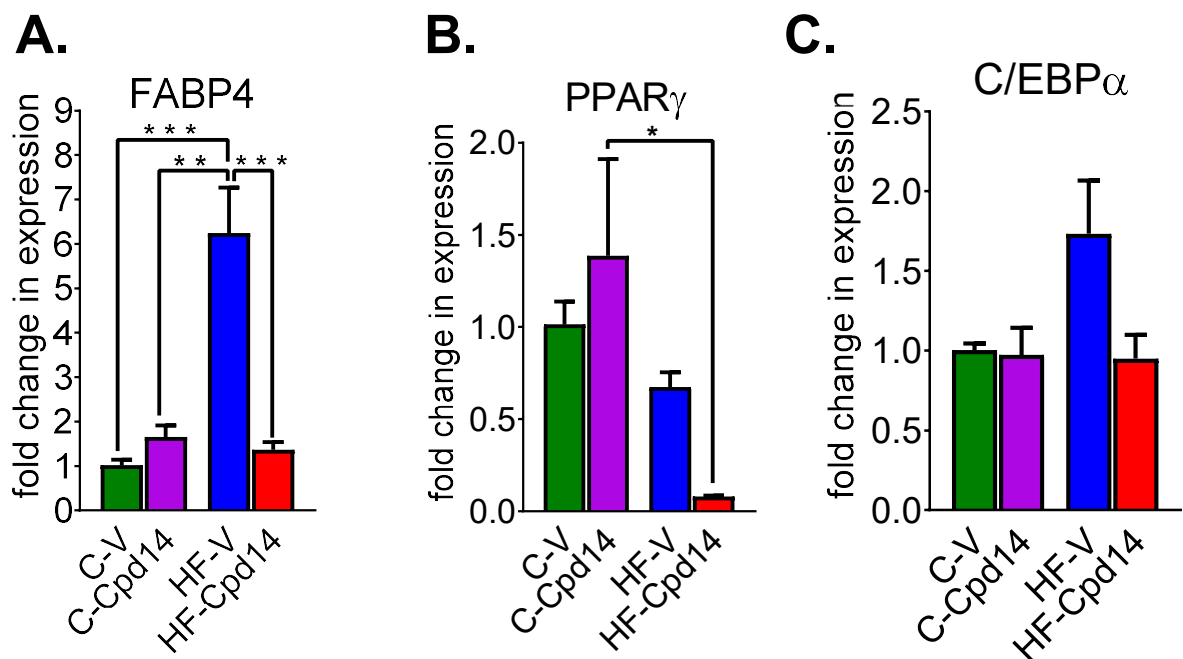
Figure 5.7. FABP4 **(A)**, PPARγ **(B)** and C/EBPα **(C)** fold change in mRNA expression from pre-adipocytes isolated from **gWAT SVF** differentiated *ex vivo* until Day 7 of adipogenesis of chow (C) and high-fat (HF)-fed male mice treated orally with Vehicle (V) or Cpd14 for 10 days, normalised to C-V. Graphs represent mean ± s.e.m. Data analysed by two-way ANOVA, post-hoc Tukey correction. N = 3. * $p < 0.05$, ** $p < 0.01$, *** $p < 0.001$ and **** $p < 0.0001$.

5.3.2.1.3. Adipose tissue gene expression differences in chow-fed and HF-fed 10-week-old mice treated with Vehicle or Cpd14

For the effects of treatment and diet in Vehicle and Cpd14-treated mice, refer to Appendix Table 2.3.

gWAT (Figure 5.8A): There were significantly higher levels of PPARγ (Figure 5.8B) and C/EBPα (Figure 5.8C) in C-Cpd14 mice compared to C-V mice ($p<0.05$ and $p<0.01$, respectively) and HF-Cpd14 mice ($p<0.05$ and $p<0.001$, respectively). Furthermore, there were significantly higher levels of C/EBPα expression in C-Cpd14 mice compared to HF-V mice ($p<0.05$) (Figure 5.8C). Leptin levels (Figure 5.8F) were higher in HF-V mice compared to C-V mice ($p<0.01$), C-Cpd14 ($p<0.01$) and HF-Cpd14 ($p<0.05$).

iWAT (Figure 5.9): UCP1 (Figure 5.9A) and DIO2 (Figure 5.9C) were significantly higher in C-Cpd14 mice compared to HF-V ($p<0.0001$ and $p<0.05$, respectively) and HF-Cpd14 mice ($p<0.0001$ and $p<0.05$, respectively), with UCP1 (Figure 5.9A) expression in C-Cpd14 mice also having higher expression compared to C-V mice ($p<0.001$). COX7A1 (Figure 5.9E) and COX8B (Figure 5.9F) expression levels were higher in C-Cpd14 mice compared to HF-V mice ($p<0.01$ and $p<0.01$, respectively), with COX8B C-Cpd14 expression also higher than that of HF-Cpd14 ($p<0.05$).

iBAT (Figure 5.10): UCP1 levels (Figure 5.10A) were significantly lower in C-Cpd14 mice compared to HF-V ($p<0.01$) and HF-Cpd14 mice ($p<0.05$). In ADRβ3 (Figure 5.10B) and COX8B (Figure 5.10F), levels were lower in C-V ($p<0.05$ and $p<0.05$, respectively) and C-Cpd14 mice ($p<0.001$ and $p<0.0001$), compared with HF-V mice, and higher in HF-Cpd14 ($p<0.05$ and $p<0.05$, respectively) compared with C-Cpd14 mice. DIO2 mRNA levels (Figure 5.10C) were lower expression in C-Cpd14 ($p<0.01$) and HF-Cpd14 mice ($p<0.05$), compared with HF-V. There were significantly higher levels in HF-Cpd14 mice compared to C-Cpd14 ($p<0.05$), in COX7A1 expression (Figure 5.10E).

PAT (Figure 5.11): Gene expression levels were unaltered with treatment with Cpd14 in chow or HF-fed mice of pericardial adipose tissue.
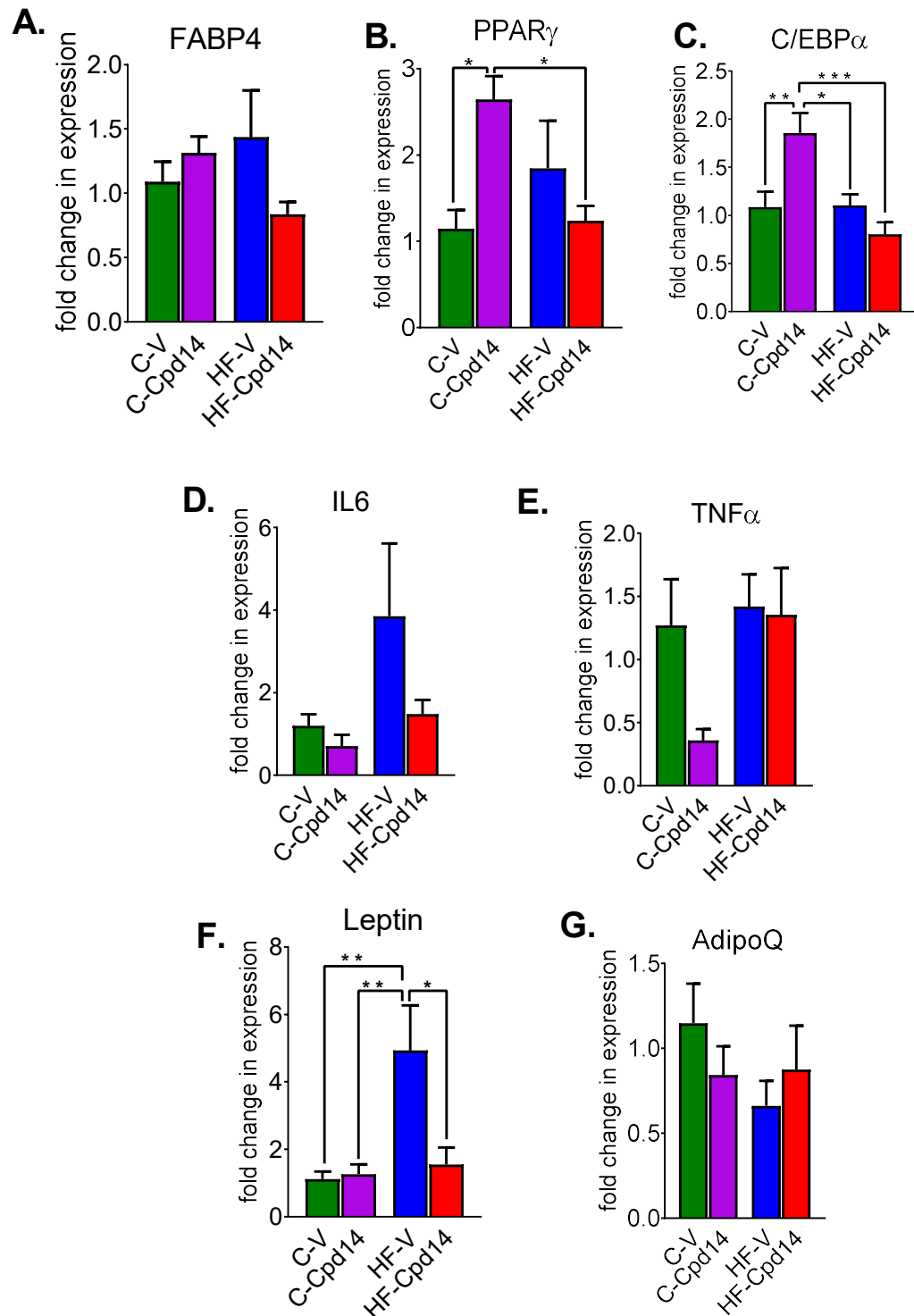
Figure 5.8. FABP4 **(A)**, PPARγ **(B)**, C/EBPα **(C)**, IL6 **(D)**, TNFα **(E),** Leptin **(F)** and AdipoQ **(G)** fold change in mRNA expression of **gWAT** of chow (C) and high-fat (HF)-fed male mice treated orally with Vehicle (V) or Cpd14 for 10 days, normalised to C-V. Graphs represent mean $\pm$ s.e.m. Data analysed by two-way ANOVA and Tukey's multiple comparison test. N = 6-7. * p<0.05, ** p<0.01, *** p<0.001 and **** p<0.0001.
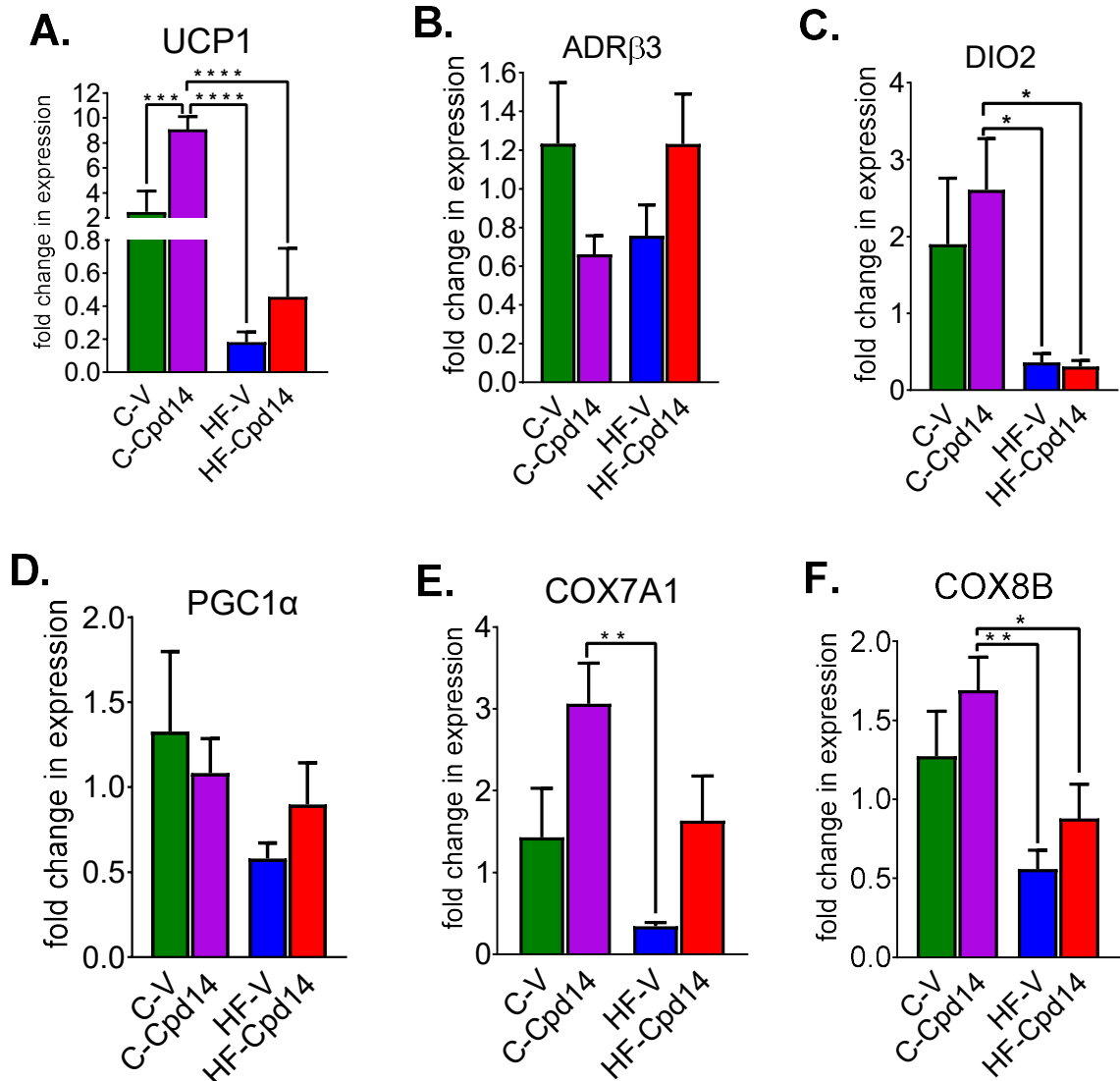
Figure 5.9. UCP1 **(A)**, ADRβ3 **(B)**, DIO2 **(C)**, PGC1α **(D)**, COX7A1 **(E)** and COX8B **(F)** fold

change in mRNA expression of **iWAT** of chow (C) and high-fat (HF)-fed male mice treated

orally with Vehicle (V) or Cpd14 for 10 days, normalised to C-V. Graphs represent mean $\pm$

s.e.m. Data analysed by two-way ANOVA and Tukey's multiple comparison test. N = 7-8. The

overall effects of treatment and diet are expressed on the graph if reported as significant. *

p<0.05, ** p<0.01, *** p<0.001 and **** p<0.0001.
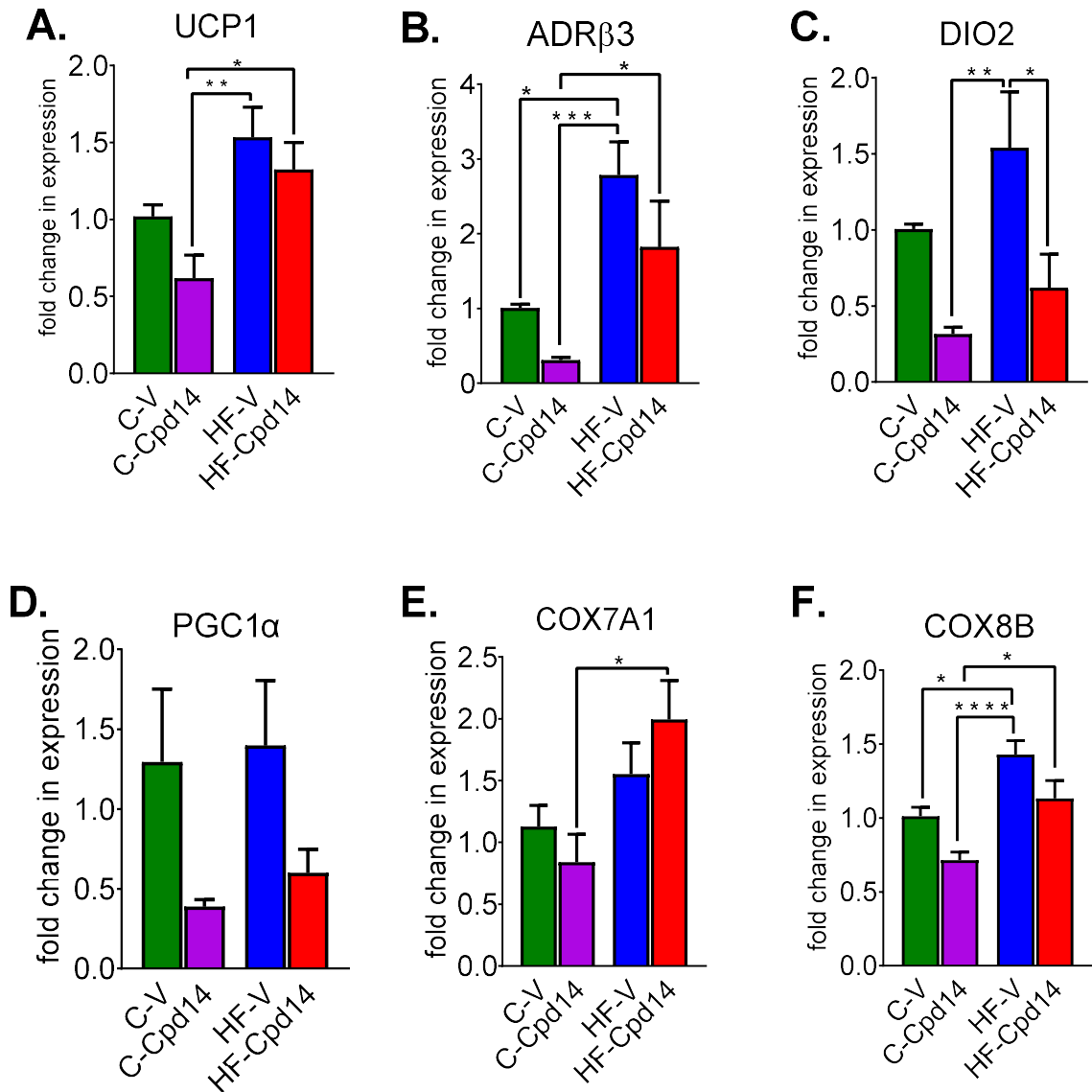
Figure 5.10. UCP1 **(A)**, ADRβ3 **(B)**, DIO2 **(C)**, PGC1α **(D)**, COX7A1 **(E)** and COX8B **(F)** fold change in mRNA expression of **iBAT** of chow (C) and high-fat (HF)-fed male mice treated orally with Vehicle (V) or Cpd14 for 10 days, normalised to C-V. Graphs represent mean $\pm$ s.e.m. Data analysed by two-way ANOVA and Tukey's multiple comparison test. N = 8. The overall effects of treatment and diet are expressed on the graph if reported as significant. * $p<0.05$, ** $p<0.01$, *** $p<0.001$ and **** $p<0.0001$.
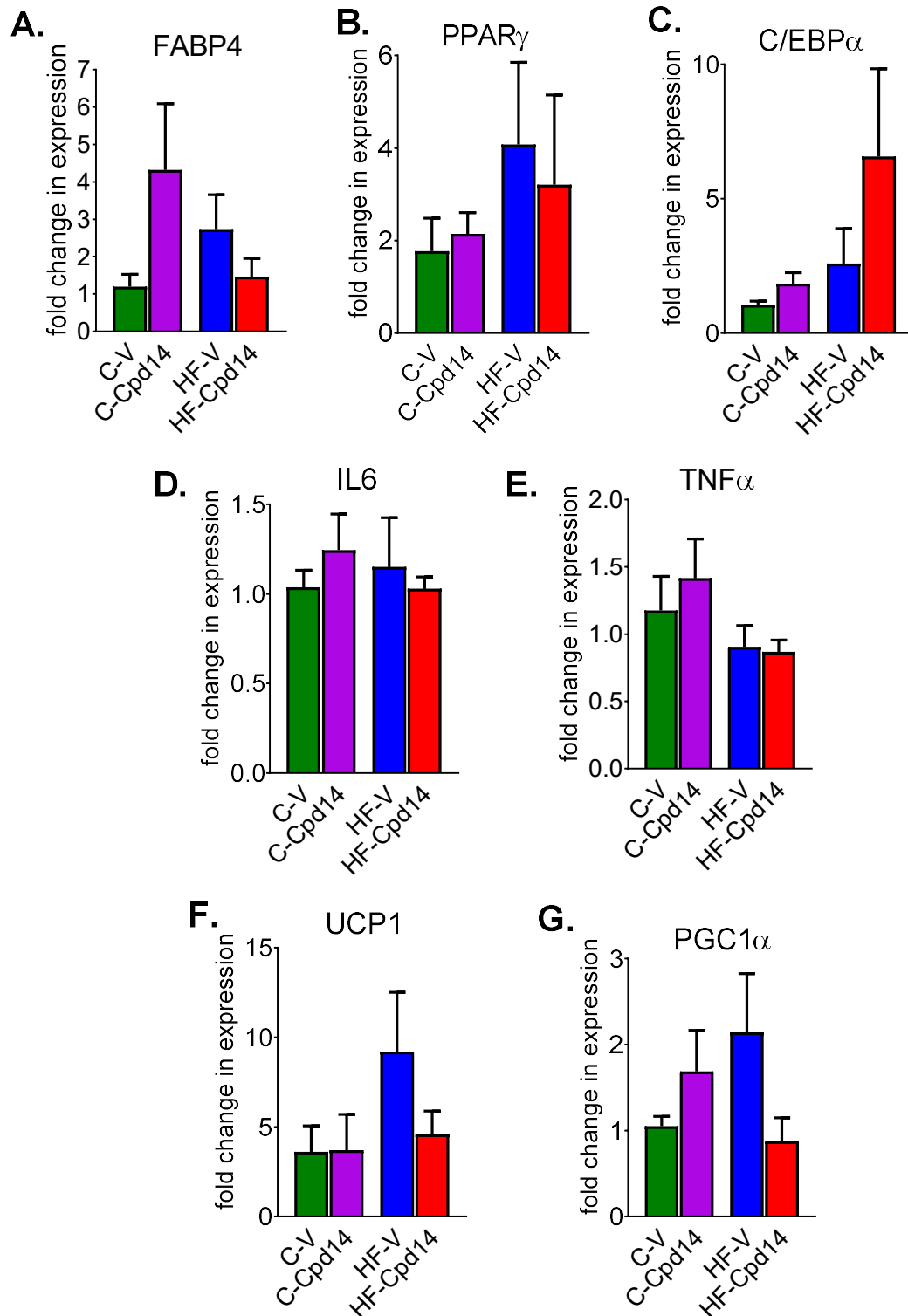
Figure 5.11. FABP4 **(A)**, PPARγ **(B)**, C/EBPα **(C)**, IL6 **(D)**, TNFα **(E)**, UCP1 **(F)** and PGC1α **(G)** fold change in mRNA expression of **PAT** of chow (C) and high-fat (HF)-fed male mice treated orally with Vehicle (V) or Cpd14 for 10 days, normalised to C-V. Graphs represent mean ± s.e.m. Data analysed by two-way ANOVA and Tukey's multiple comparison test. N = 6-7... * p<0.05, ** p<0.01, *** p<0.001 and **** p<0.0001.

5.3.2.1.4. Gonadal white adipose tissue protein level differences in chow-fed and HF-fed 10-week-old mice treated with Vehicle or Cpd14

A Western blot was performed to determine AMPK activation observing any visible changes in protein levels of AMPK and ACC, using phospho- and unphospho-specific antibodies, with β-Actin as a reference (Figure 5.12), as stated by Asby et al. There is a visible increase in total AMPK levels (Figure 5.12A) in C-Cpd14 mice, but no other visible differences were observed in total levels of ACC or phosphorylated ACC (p-ACC) (Figure 5.12B) or AMPK (p-AMPK) (Figure 5.12A) in either C-fed or HF-fed treated mice with Vehicle or Cpd14.

A.

B.
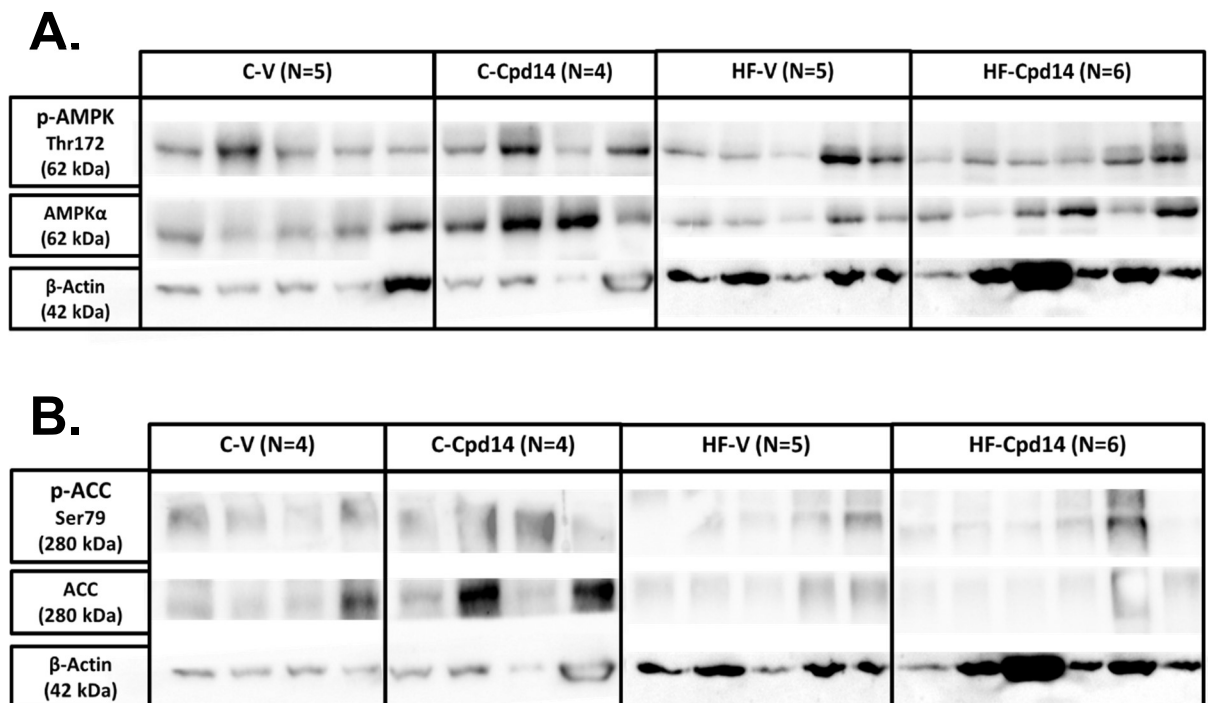
Figure 5.12. p-AMPK/AMPK **(A)** and p-ACC/ACC **(B)** protein levels of **gWAT** of chow (C) and high-fat (HF)-fed male mice treated orally with Vehicle (V) or Cpd14 for 10 days. β-Actin used as a reference. N = 4-6. (p)-AMPK Thr172: (phospho)-5' adenosine monophosphate-activated protein kinase Threonine 172; (p)-ACC Ser79: (phospho)-Acetyl-CoA carboxylase Serine 79: β-Actin; beta-Actin: kDa: kilodaltons.

5.3.2.1.5. Adipose tissue histological differences in chow-fed and HF-fed 10-week-old mice treated with Vehicle or Cpd14

Percentage change in cell volume: For the effects of treatment and diet in Vehicle and Cpd14-treated mice in cell volume, refer to Appendix Table 3.9. In gWAT (Figure 5.13A), iWAT (Figure 5.14A) and PAT (Figure 5.15A), there were lower adipocyte volumes in C-V ($p < 0.0001$, $p < 0.0001$ and $p < 0.01$, respectively), C-Cpd14 ($p < 0.0001$, $p < 0.0001$ and $p < 0.01$, respectively) and HF-Cpd14 mice ($p < 0.05$, $p < 0.001$ and $p < 0.05$, respectively), compared to HF-V mice. Furthermore, in gWAT, HF-Cpd14 cell volume was higher than C-Cpd14 mice ($p < 0.05$) (Figure 5.13A).

Adipose tissue morphology: Histological analysis of larger cells in HF-V mice was mirrored by morphological observations of gWAT (Figure 5.13B), iWAT (Figure 5.14B) and PAT (Figure 5.15B). Furthermore, the presence of multi-locular brown-like cells were observed in C-Cpd14 and HF-Cpd14 mice of iWAT (Figure 5.14C) and PAT (Figure 5.15C), with further observations in C-V and HF-V mice of PAT (Figure 5.15C).

Cell volume distribution: For statistical analysis and the effects of treatment and diet in Vehicle and Cpd14-treated mice, refer to Appendix Table 3.10 and Appendix Table 3.11. Overall, the cell volume distribution graph resembled a positively skewed distribution in pericardial fat (Figure 5.15D), compared to gWAT (Figure 5.13D) and iWAT (Figure 5.14D), suggesting cells in this depot have a higher prevalence of being smaller.
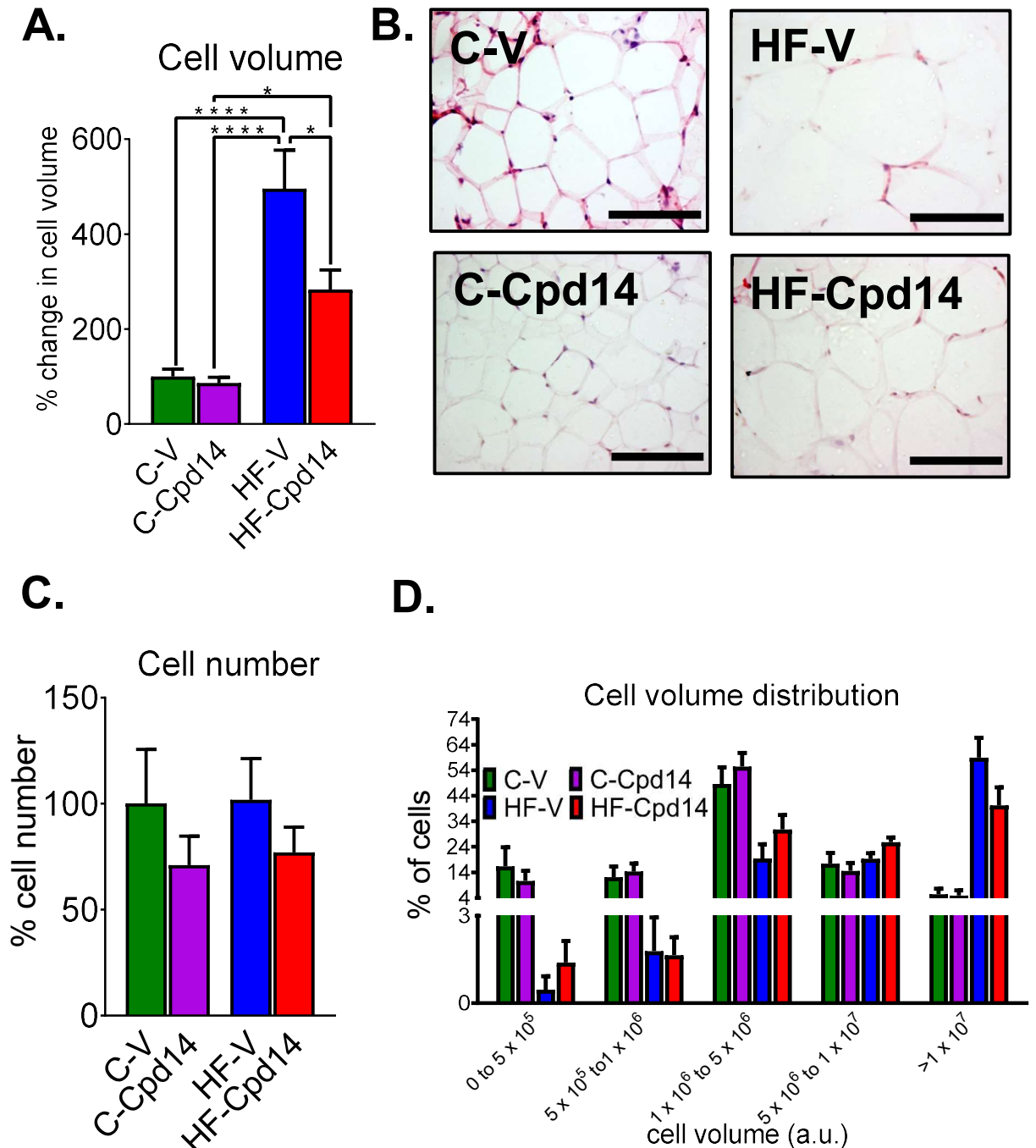
Figure 5.13. The percentage change in cell volume normalised to C-V **(A)**, H&E representative images of cell size **(B)**, cell number normalised to C-V **(C)** and cell volume distribution **(D)** of **gWAT** from chow (C) and high-fat (HF)-fed male mice treated orally with Vehicle (V) or Cpd14 for 10 days. All scale bars represent 100µM and imaged at x40 optical lens with Nikon TE200 brightfield inverted microscope. Graphs represent mean $\pm$ s.e.m. Data analysed by two-way ANOVA and Tukey's multiple comparison test between C-V, C-Cpd14, HF-V and HF-Cpd14 **(A,C)** and cell volume (a.u.) groups **(D)**. N = 6-8.
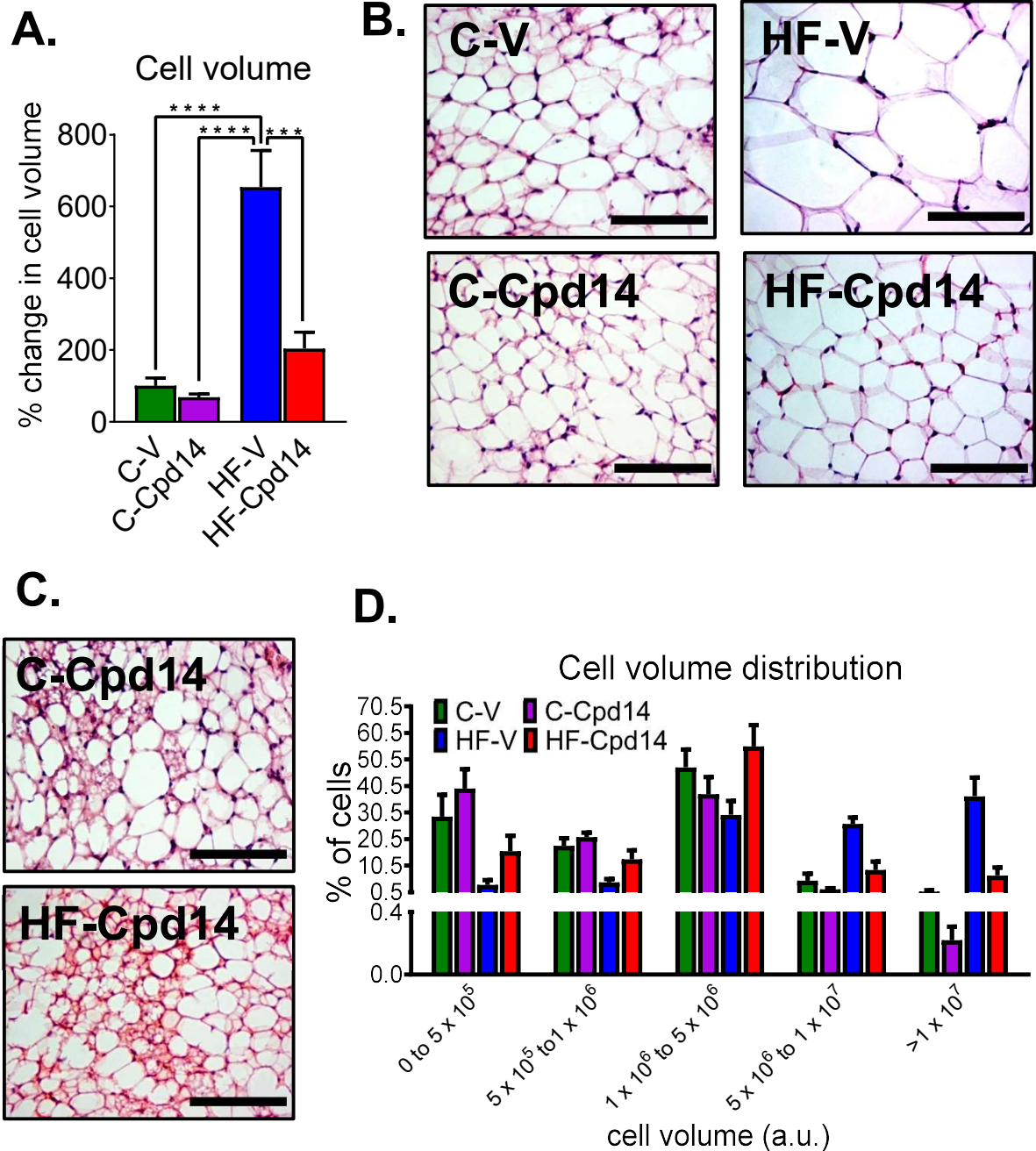
Figure 5.14 The percentage change in cell volume normalised to C-V **(A)**, H&E representative images of cell size (B), multi-locular cells **(C)** and cell volume distribution **(D)** of **iWAT** from chow (C) and high-fat (HF)-fed male mice treated orally with Vehicle (V) or Cpd14 for 10 days. All scale bars represent 100μM and imaged at x40 optical lens with Nikon TE200 brightfield inverted microscope. Graphs represent mean $\pm$ s.e.m. Data analysed by two-way ANOVA and Tukey's multiple comparison test between C-V, C-Cpd14, HF-V and HF-Cpd14 **(A)** and cell volume (a.u.) groups **(D)**. N = 5-8.
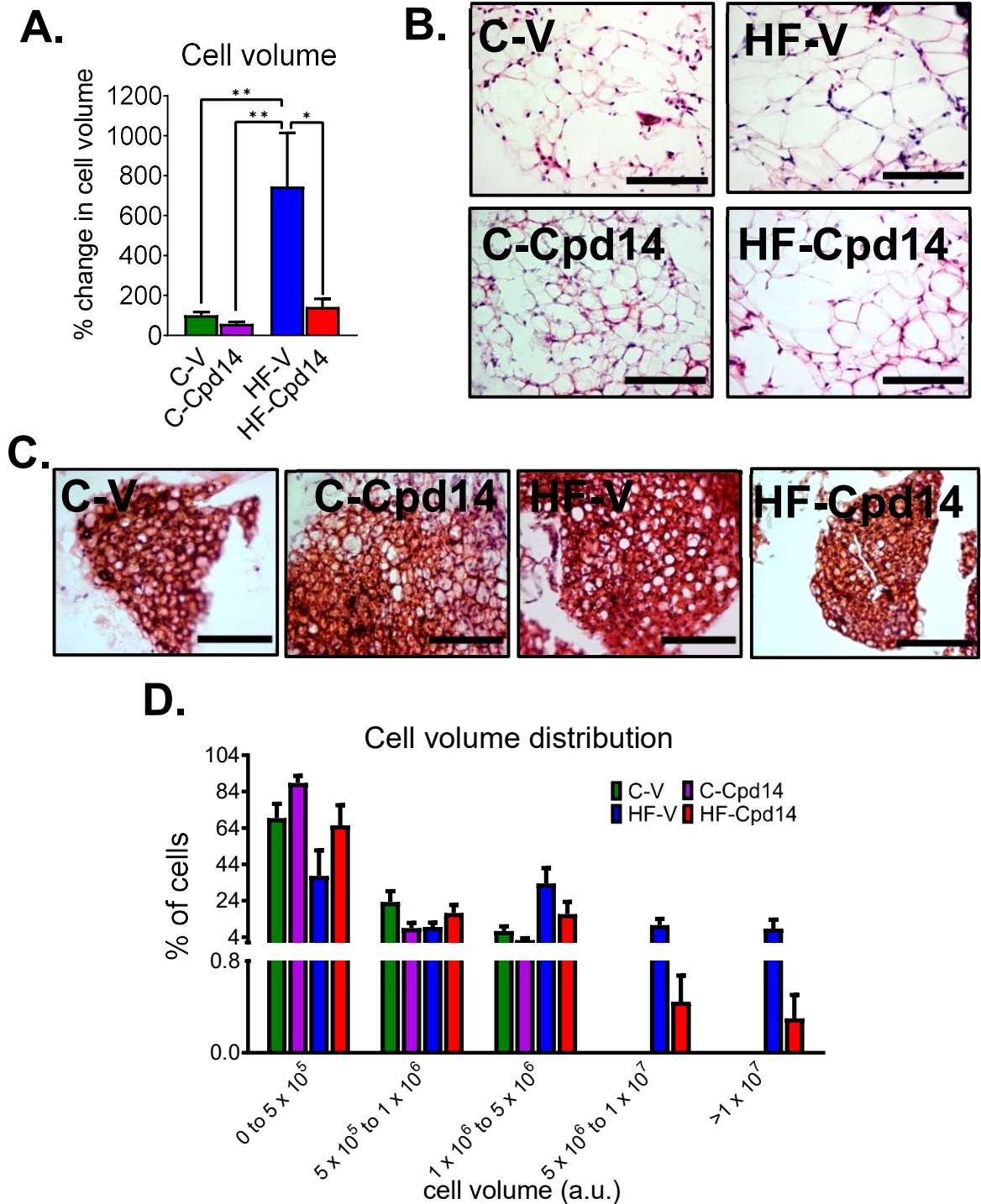
Figure 5.15. The percentage change in cell volume normalised to C-V **(A)**, H&E representative images of cell size **(B)**, multi-locular cells **(C)** and cell volume distribution **(D)** of **PAT** from chow (C) and high-fat (HF)-fed male mice treated orally with Vehicle (V) or Cpd14 for 10 days. All scale bars represent 100µM and imaged at x40 optical lens with Nikon TE200 brightfield inverted microscope. Graphs represent mean $\pm$ s.e.m. Data analysed by two-way ANOVA and Tukey's multiple comparison test between C-V, C-Cpd14, HF-V and HF-Cpd14 **(A)** and cell volume (a.u.) groups **(D)**. N = 5-8.

5.3.2.1.6. The relationship between biochemical and metabolic parameters, gene expression levels and percentage change in cell volume in adipose tissue of chow-fed and HF-fed 10-week-old mice treated with Vehicle or Cpd14

Percentage change in cell volume vs inflammatory markers: Percentage change in cell volume of PAT (Appendix Figure 4.27B) was positively correlated with IL6 mRNA levels ($p < 0.05$), gWAT percentage change in cell volume levels (Appendix Figure 4.27E) were positively associated with Leptin mRNA levels ($p < 0.0001$)

Percentage change in cell volume vs UCP1: iWAT percentage change in cell volume levels (Appendix Figure 4.27G) were negatively associated with UCP1 mRNA levels ($p < 0.01$).

Depot weight vs inflammatory markers: gWAT depot weight was positively associated with the percentage change in cell volume (Appendix Figure 4.28A) ($p < 0.0001$) and mRNA levels of IL6 (Appendix Figure 4.28B) ($p < 0.01$), TNFα (Appendix Figure 4.28C) ($p < 0.01$) and Leptin (Appendix Figure 4.28D) ($p < 0.0001$).

5.3.3. 26-day recovery period in HF-fed mice

5.3.3.1. Metabolic parameters in HF-fed 10-week-old mice treated with Vehicle or Cpd14, following a recovery period

Non-fasting blood glucose levels initially increased within the first 10 days of the recovery period but remained relatively constant during the last 6 days in HF-Cpd14 mice (Figure 5.18A). During the recovery period, there was an increase in weight gain of HF-Cpd14 mice, reaching similar levels to before Cpd14 treatment (Figure 5.18E). No other changes in fasting blood glucose (Figure 5.18B) or glucose levels during an ipGTT (Figure 5.18C and Figure 5.18D) were observed.

5.3.3.2. Adipose tissue gene expression differences in HF-fed 10-week-old mice treated with Vehicle or Cpd14, following a recovery period

In gWAT (Figure 5.19), there was a trend towards lower Leptin mRNA expression levels (Figure 5.19F) (p=0.0565) in HF-Cpd14 mice compared to HF-V mice. COX7A1 expression (Figure 5.20E) (p<0.05) was lower in HF-Cpd14 mice compared to HF-V mice of iWAT.

5.3.3.3. Adipose tissue histological differences in HF-fed 10-week-old mice treated with Vehicle or Cpd14, following a recovery period

Histological analysis of gWAT, iWAT and PAT did not document any significant differences in cell volume (Figure 5.23A, Figure 5.24A and Figure 5.25A, respectively) or distribution (Figure 5.23C, Figure 5.24C and Figure 5.25C, respectively). Interestingly, distribution of cell volume in PAT showed a normal distribution (Figure 5.25C), suggesting many of these adipocytes are medium sized, whereas gWAT cell volume resembled a negatively skewed distribution (Figure 5.23C), compared to iWAT (Figure 5.24C), suggesting gonadal cells have a higher frequency of being larger.
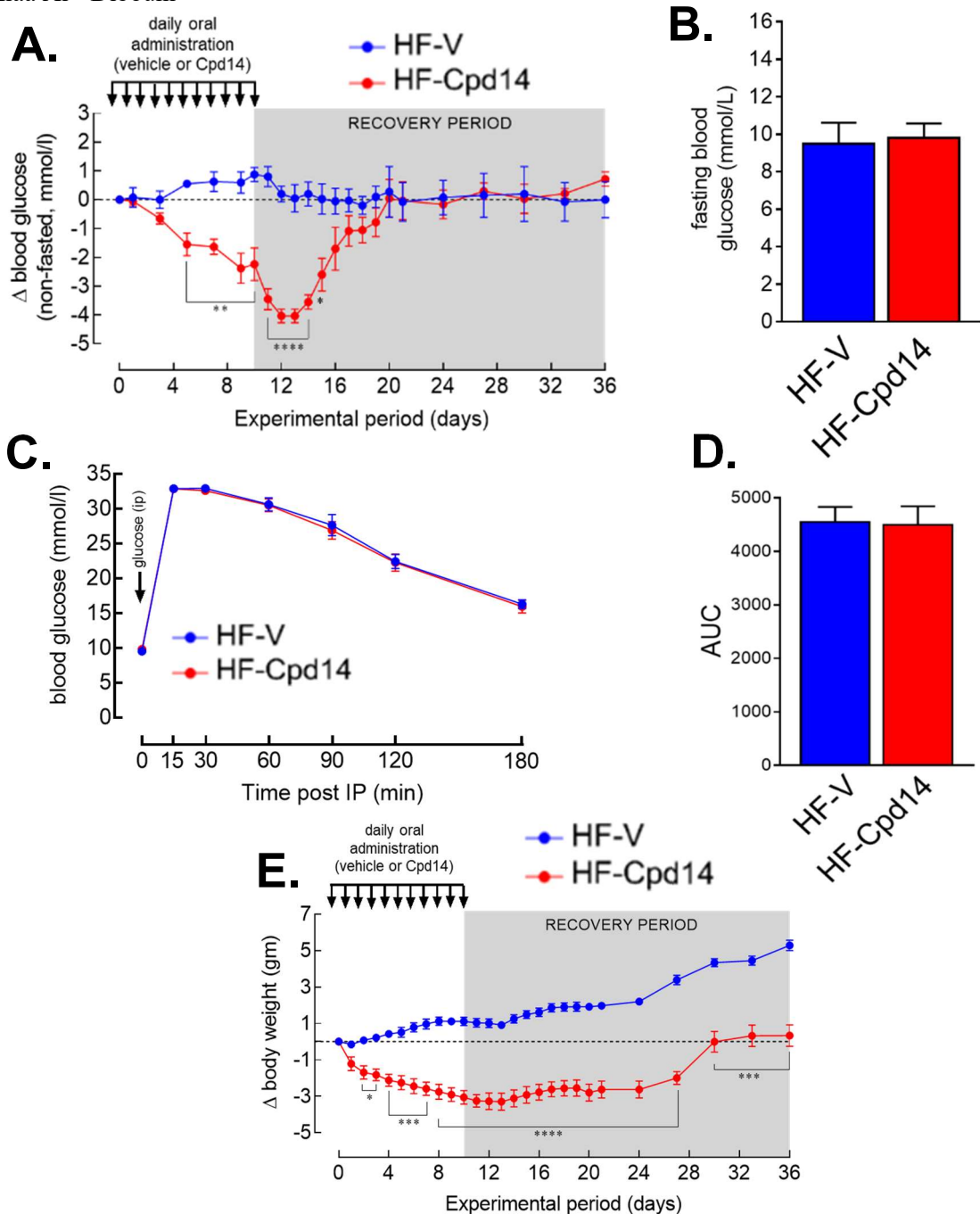
Figure 5.18. Metabolic effects of Vehicle and Cpd14 in high-fat-fed mice. Daily non-fasting blood glucose levels expressed as change (Δ) in glucose levels **(A)**, fasting blood glucose levels **(B),** intraperitoneal glucose tolerance test (ipGTT) with glucose measured at 0, 15, 30, 60, 90, 120 and 180 minutes after glucose injection **(C)** and area under the curve (AUC) of blood glucose levels **(D)**, the change (Δ) in body weight **(E)** from high-fat (HF)-fed mice treated orally with Vehicle or Cpd14 for 10 days, following a 26-day recovery period without treatment. Graphs represent mean $\pm$ s.e.m. Data analysed by an unpaired t-test **(B,D)** and by repeated measures ANOVA with Tukey's multiple correction test **(A,C,E)**. N = 4-6. * $p<0.05$, ** $p<0.01$, *** $p<0.001$ and **** $p<0.0001$ and grey-coloured stars indicate significance of the group against HF-V.
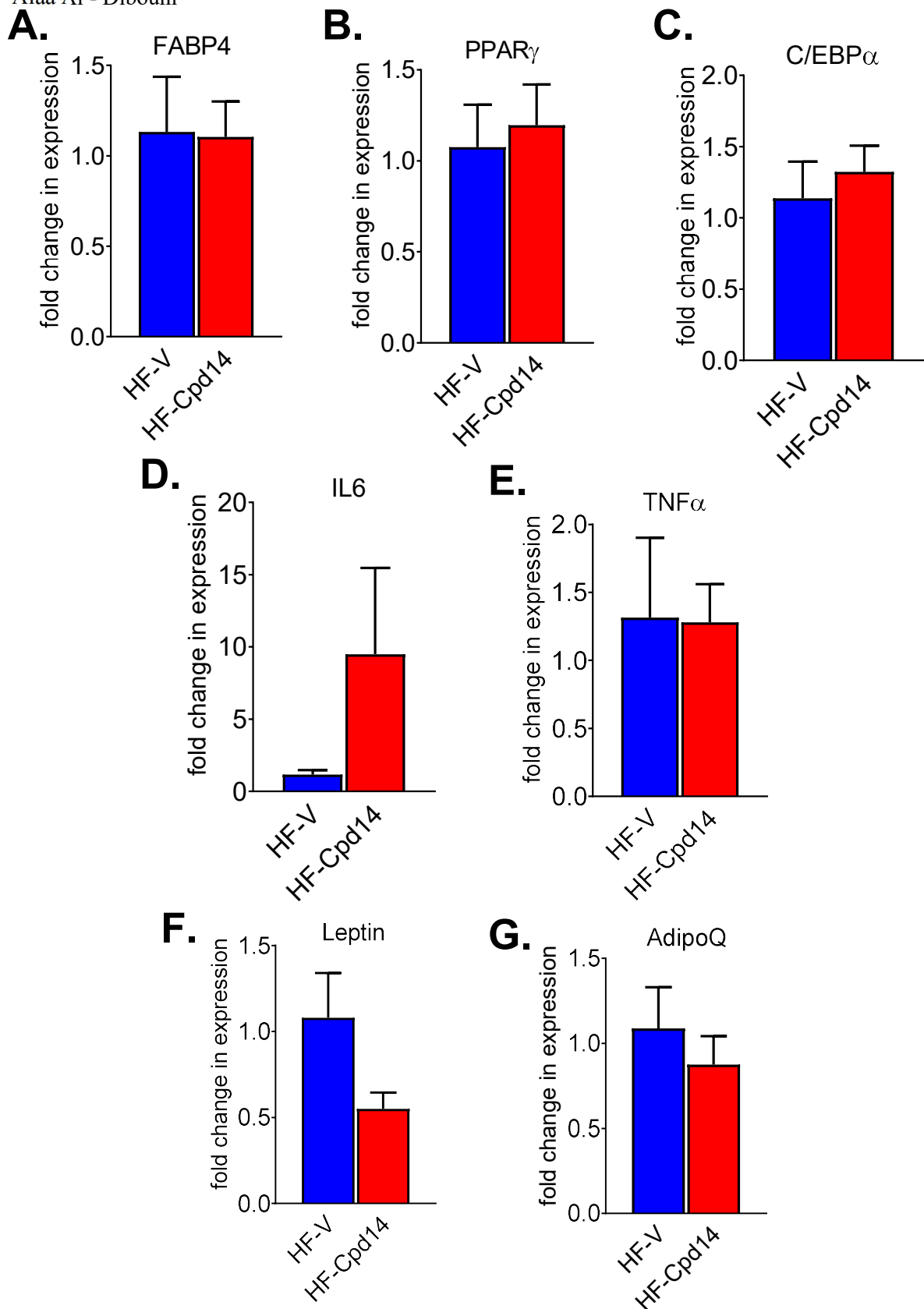
Figure 5.19. FABP4 **(A)**, PPARγ **(B)**, C/EBPα **(C)**, IL6 **(D)**, TNFα **(E)**, Leptin **(F)** and AdipoQ **(G)** fold change in mRNA expression of **gWAT** of high-fat (HF)-fed male mice treated orally with Vehicle (V) or Cpd14 for 10 days, following a 26-day recovery period without treatment, relative to HF-V. Graphs represent mean $\pm$ s.e.m. Data analysed by an unpaired t-test. N = 4-6. * p<0.05, ** p<0.01, *** p<0.001 and **** p<0.0001.
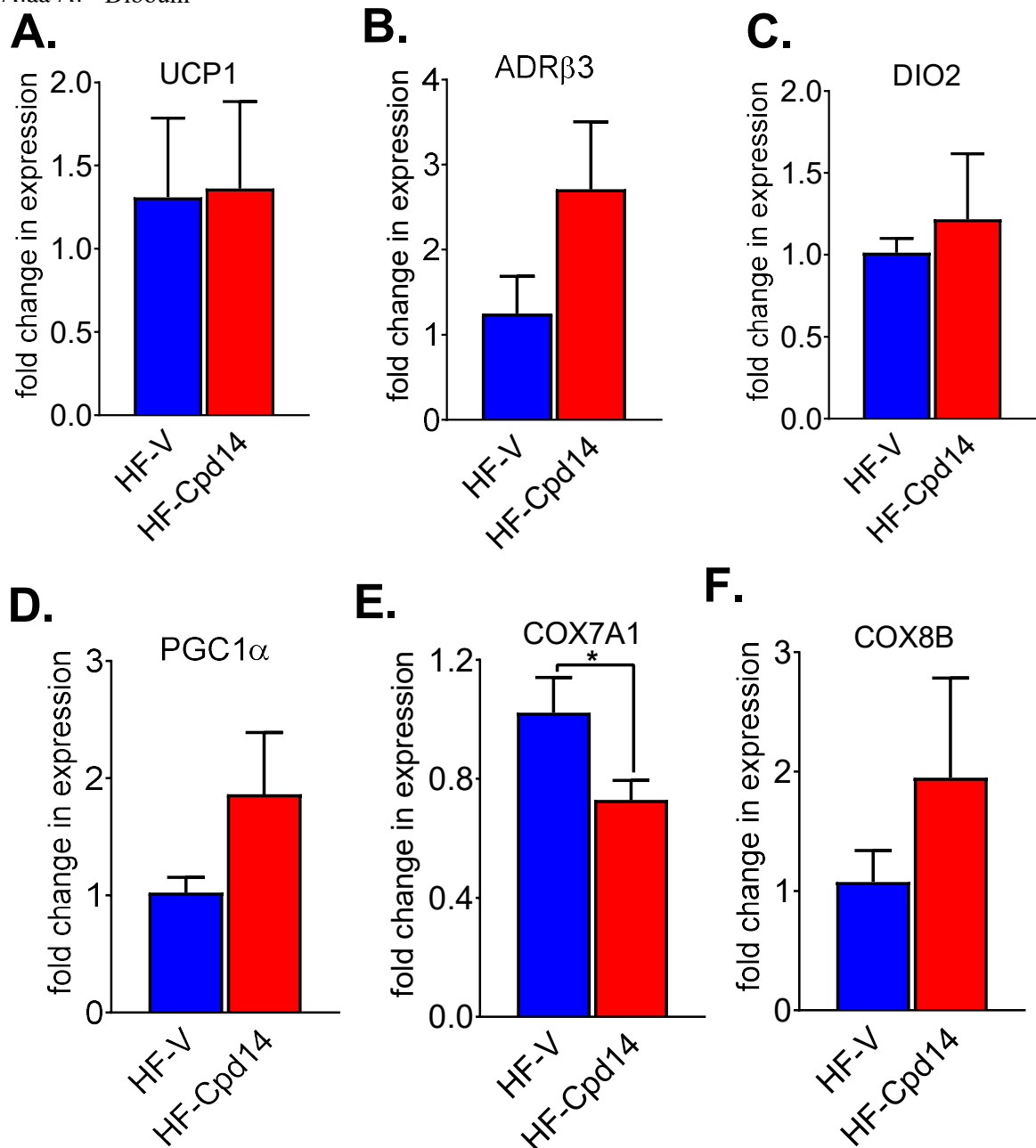
Figure 5.20. UCP1 **(A)**, ADRβ3 **(B)**, DIO2 **(C)**, PGC1α **(D)**, COX7A1 **(E)** and COX8B **(F)** fold change in mRNA expression of **iWAT** of high-fat (HF)-fed male mice treated orally with Vehicle (V) or Cpd14 for 10 days, following a 26-day recovery period without treatment, relative to HF-V. Graphs represent mean ± s.e.m. Data analysed by an unpaired t-test. N = 4-6. * p<0.05, ** p<0.01, *** p<0.001 and **** p<0.0001.
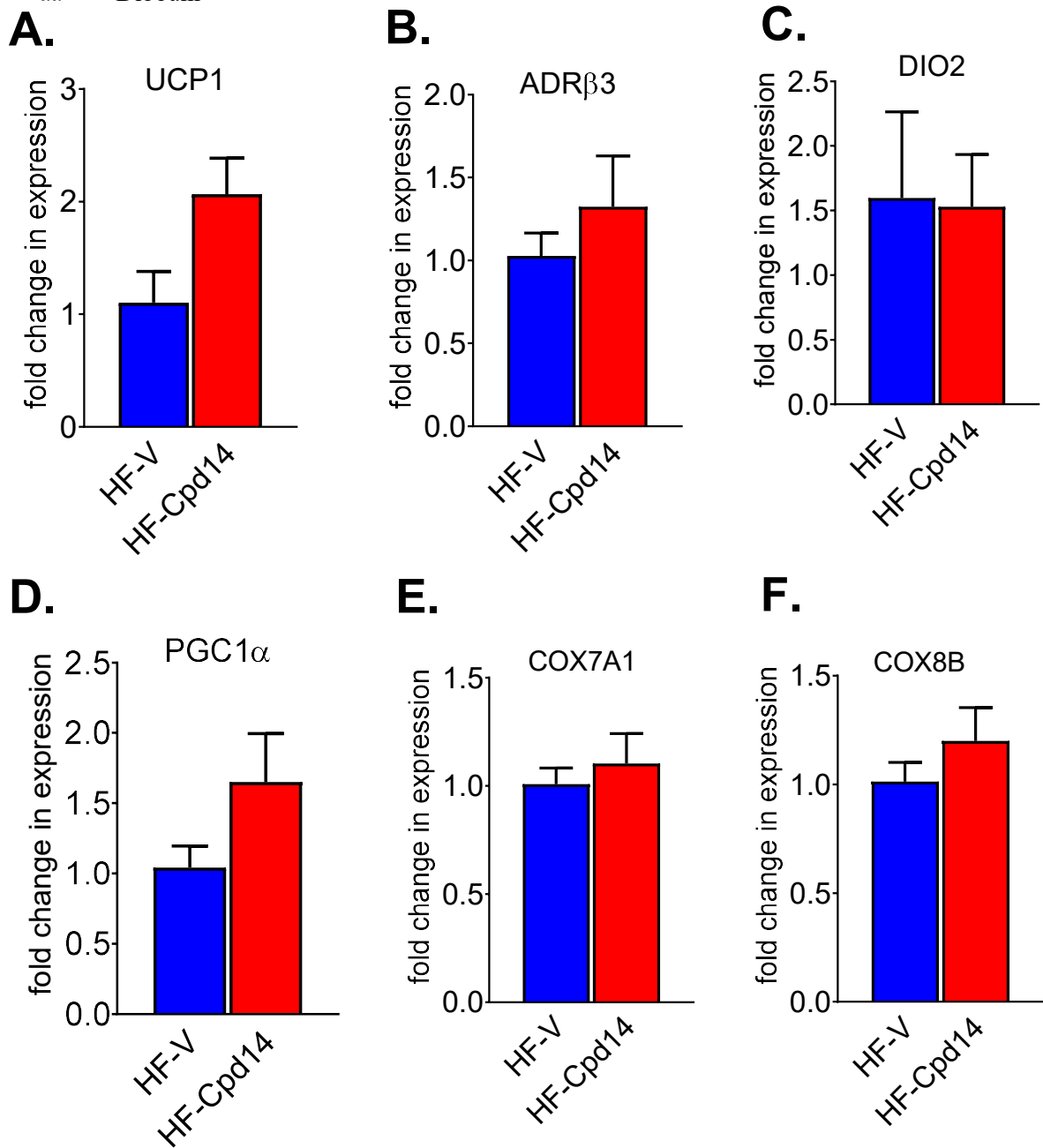
Figure 5.21. UCP1 **(A)**, ADRβ3 **(B)**, DIO2 **(C)**, PGC1α **(D)**, COX7A1 **(E)** and COX8B **(F)** fold change in mRNA expression of **iBAT** of high-fat (HF)-fed male mice treated orally with Vehicle (V) or Cpd14 for 10 days, following a 26-day recovery period without treatment, relative to HF-V. Graphs represent mean ± s.e.m. Data analysed by an unpaired t-test. N = 4-6. * $p < 0.05$, ** $p < 0.01$, *** $p < 0.001$ and **** $p < 0.0001$.
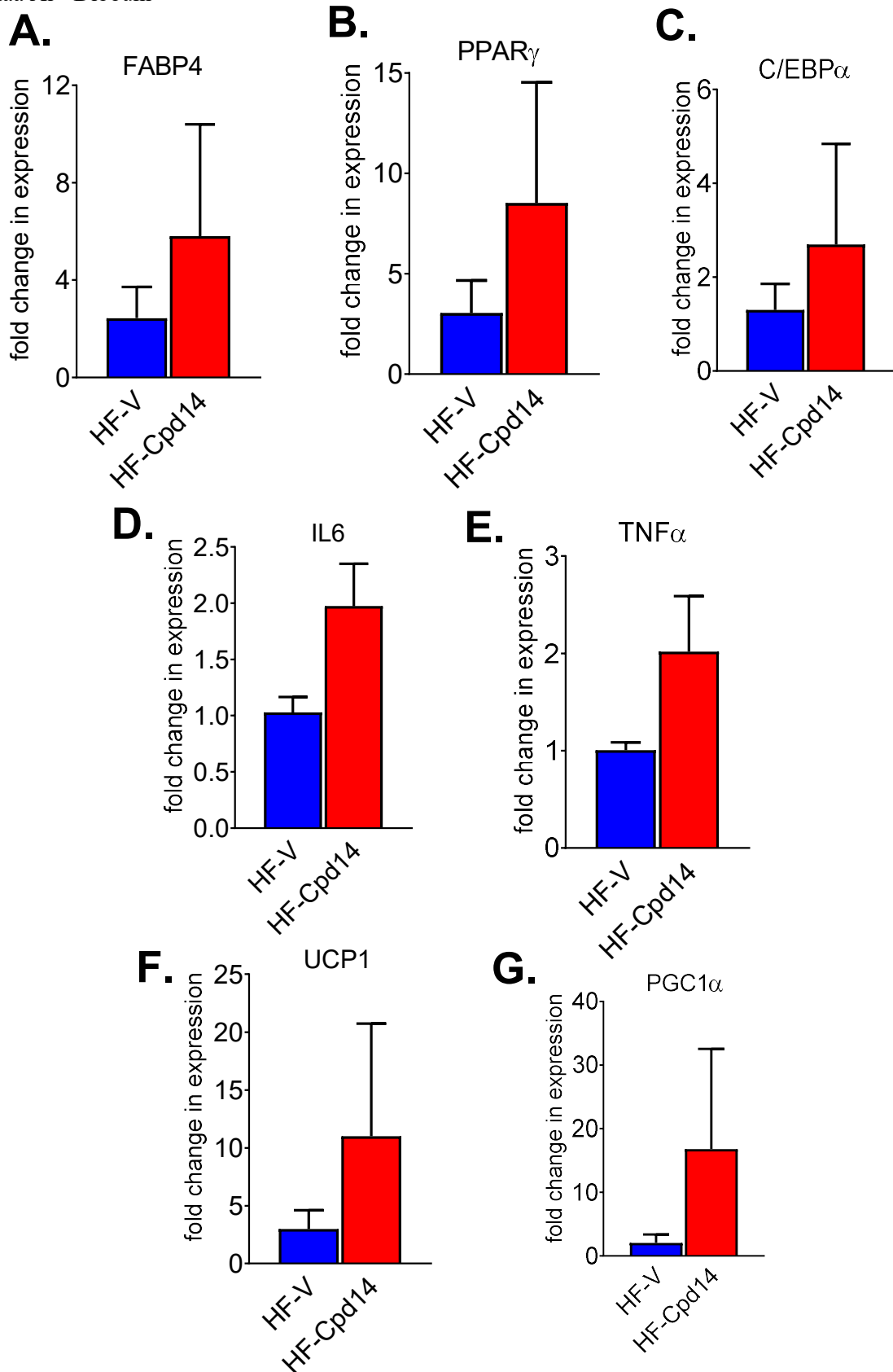
Figure 5.22. FABP4 **(A)**, PPARγ **(B)**, C/EBPα **(C)**, IL6 **(D)**, TNFα **(E)**, UCP1 **(F)** and PGC1α **(G)** fold change in mRNA expression of **PAT** of high-fat (HF)-fed male mice treated orally with Vehicle (V) or Cpd14 for 10 days, following a 26-day recovery period without treatment, relative to HF-V. Graphs represent mean ± s.e.m. Data analysed by an unpaired t-test. N = 4-6. * p<0.05, ** p<0.01, *** p<0.001 and **** p<0.0001.

A.

Cell volume

B.

C.

Cell volume distribution
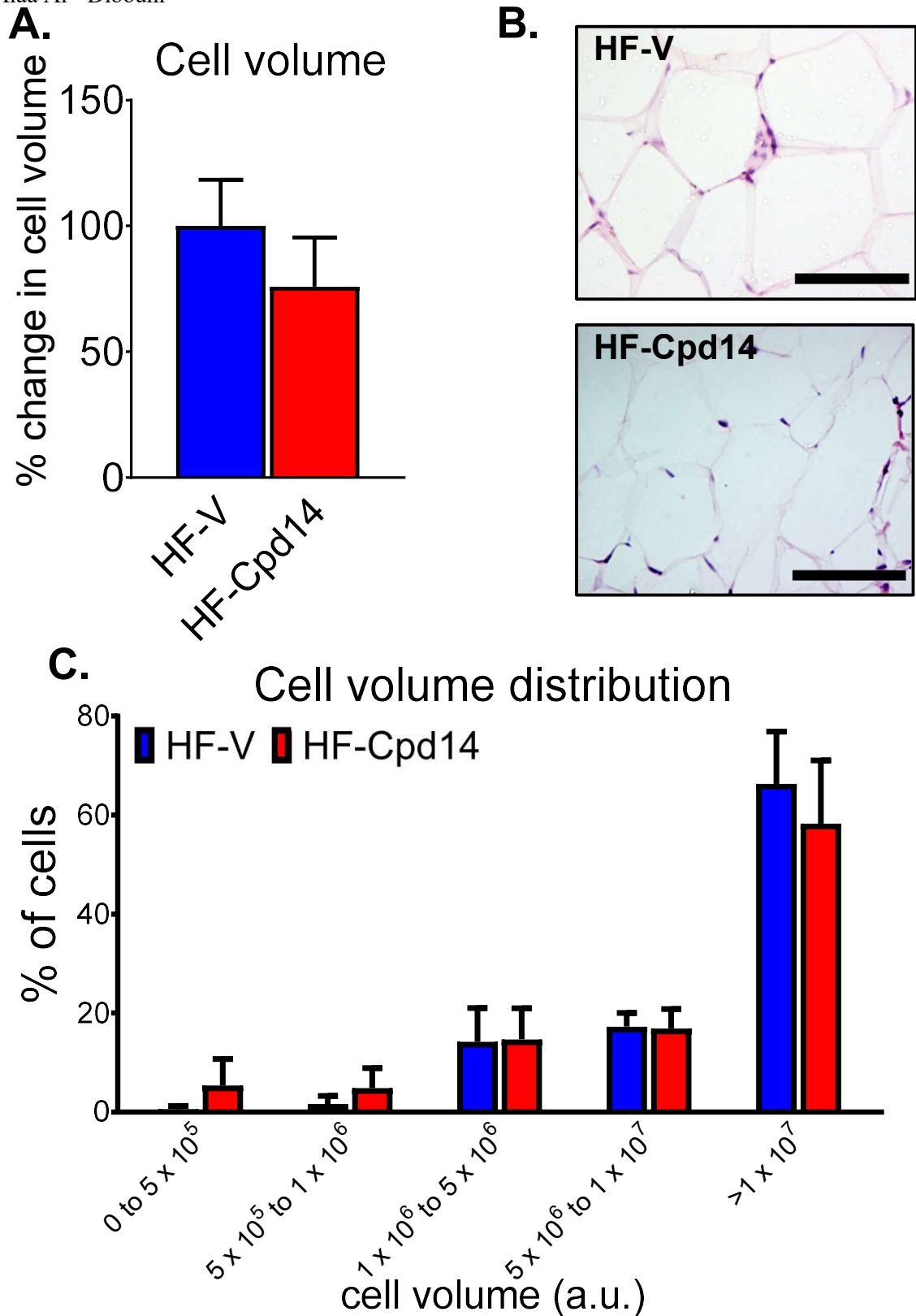
Figure 5.23. The percentage change in cell volume normalised to HF-V **(A)**, H&E representative images of cell size **(B)** and cell volume distribution **(C)** of **gWAT** of high-fat (HF)-fed male mice treated orally with Vehicle (V) or Cpd14 for 10 days, following a 26-day recovery period without treatment. All scale bars represent 100μM and imaged at x40 optical lens with Nikon TE200 brightfield inverted microscope. Graphs represent mean $\pm$ s.e.m. Data analysed by an unpaired t-test. N = 4-6. * $p<0.05$, ** $p<0.01$, *** $p<0.001$ and **** $p<0.0001$.

A.

Cell volume

B.

HF-V

HF-Cpd14

C.

Cell volume distribution
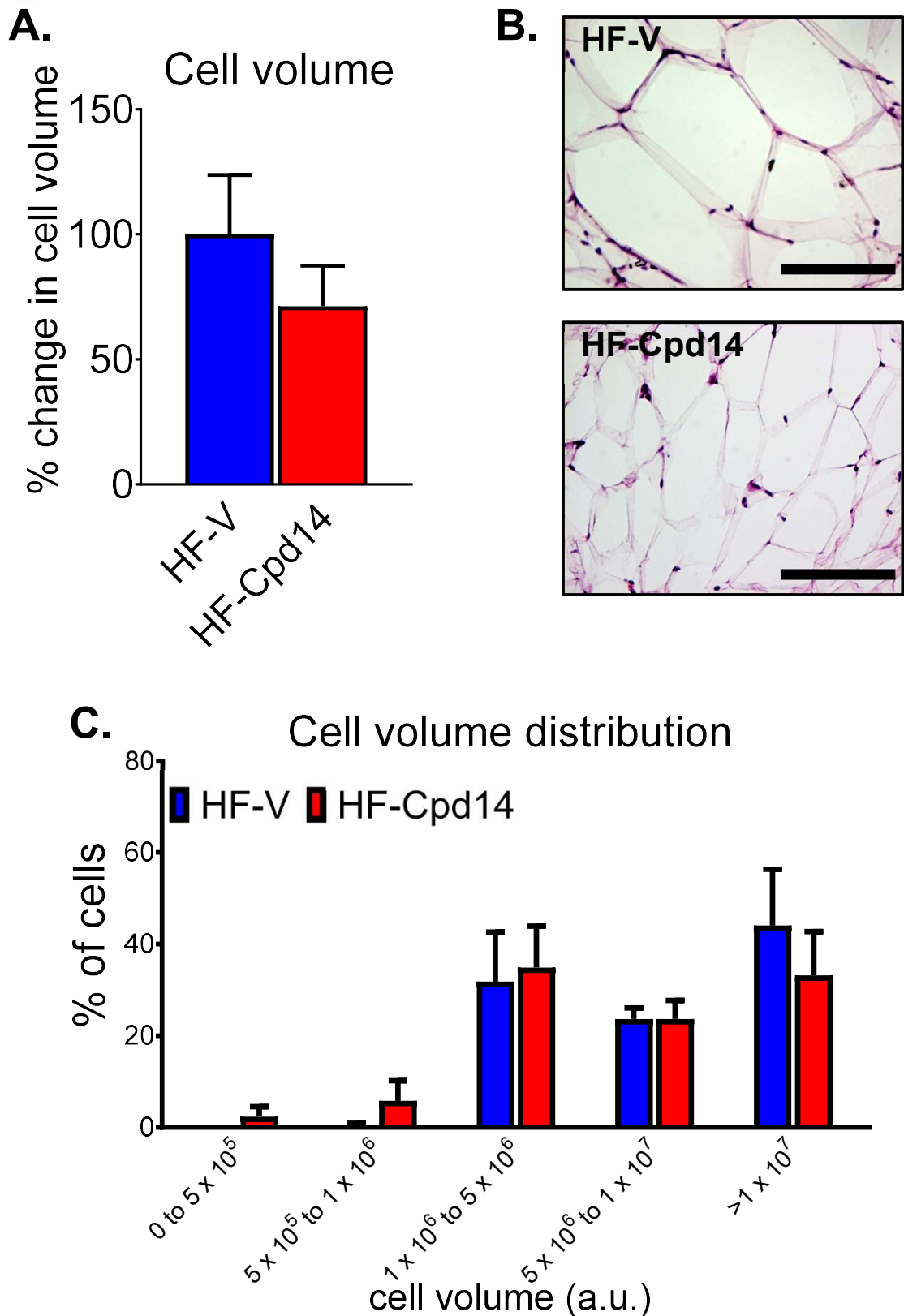
Figure 5.24. The percentage change in cell volume normalised to HF-V **(A)**, H&E representative images of cell size **(B)** and cell volume distribution **(C)** of **iWAT** of high-fat (HF)-fed male mice treated orally with Vehicle (V) or Cpd14 for 10 days, following a 26-day recovery period without treatment. All scale bars represent 100μM and imaged at x40 optical lens with Nikon TE200 brightfield inverted microscope. Graphs represent mean $\pm$ s.e.m. Data analysed by an unpaired t-test. N = 4-6. * $p<0.05$, ** $p<0.01$, *** $p<0.001$ and **** $p<0.0001$.

A.

B.

C.
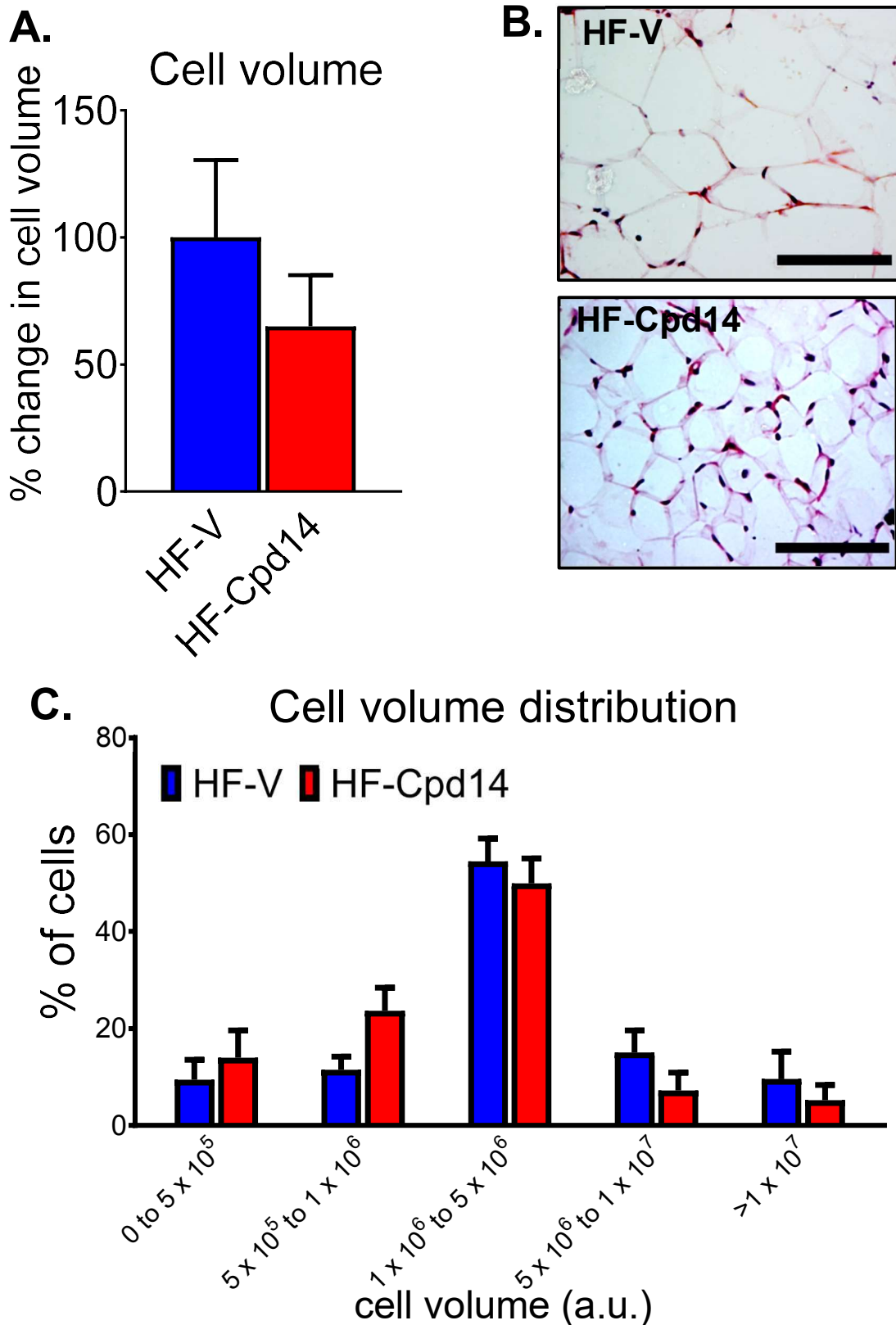
Figure 5.25. The percentage change in cell volume normalised to HF-V **(A)**, H&E representative images of cell size **(B)** and cell volume distribution **(C)** of **PAT** of high-fat (HF)-fed male mice treated orally with Vehicle (V) or Cpd14 for 10 days, following a 26-day recovery period without treatment. All scale bars represent 100µM and imaged at x40 optical lens with Nikon TE200 brightfield inverted microscope. Graphs represent mean ± s.e.m. Data analysed by an unpaired t-test. N = 4-6. * $p < 0.05$, ** $p < 0.01$, *** $p < 0.001$ and **** $p < 0.0001$.

5.4. DISCUSSION

Treatment with 1mM Cpd14 for 72 hours, in high and low purine conditions, **(1)** did not inhibit adipocyte differentiation or **(2)** induce 'browning' of 3T3-L1 cells, *in vitro.* 10 daily doses of oral 0.1mg/g Cpd14 administered in chow-fed and HF-fed mice **(3)** reduced the cell volume of pericardial adipocytes but **(4)** did not alter the transcriptional levels of adipogenic, inflammatory, thermogenic, or mitochondrial function-related markers in pericardial fat. Following a 26-day recovery period after Cpd14 treatment, **(5)** there were no changes in pericardial adipocyte volume, **(6)** no transcriptional alterations in adipogenic, inflammatory, thermogenic, or mitochondrial function-related markers, but there was **(7)** an induction of 'whitening' in pericardial fat of HF-fed mice.

5.4.1. Cell culture studies

3T3-L1 cells are a widely used murine cell line to study cellular alterations upon treatment *in vitro* and helps understand the physiological processes occurring *in vivo.* Obesity is characterised by excessive TG accumulation in AT and dysregulated adipocyte differentiation. Therapeutic agents may target transcriptional cascades involved in adipogenesis (Lin and Lane, 1992) to inhibit adipocyte differentiation, therefore downregulating TG accumulation in adipocytes to improve metabolism. C/EBPα and PPARγ expression is essential for the progression and maintenance of lipid-laden fat cells (Christy et al., 1991; Christy et al., 1989; Imai et al., 2004). FABP4 expression acts as an additional marker for the presence of mature adipocytes (Shan et al., 2013; Sim et al., 2017). AMPK activators such as AICAR (Lee et al.,2011) and Metformin (Chen et al., 2018) inhibit adipocyte differentiation in 3T3-L1 cells by downregulating these pro-adipogenic markers. Regardless of high (HPM) or low purine media (LPM) conditions, treatment of 1mM Cpd14 for 72 hours *in vitro*, did not effect positive regulators of adipogenesis or lipid accumulation. This suggests that Cpd14 does not inhibit adipocyte differentiation, under these conditions. Furthermore, Asby et al., demonstrated that 1mM Cpd14 does not effect the viability of cells, suggesting that reduced profileration in cancer cells was due to a cytostatic effect on cells, rather than a cytotoxic effect. In 3T3-L1 cells, there

were no differences in cell titre levels. This indicates that Cpd14 does not induce toxic effects on the viability of adipocytes, *in vitro.*

In metabolism, there are two significant pathways that are utilised by cells. These include the *de novo* purine biosynthetic pathway and the salvage pathway. Under HPM conditions, there is inhibition of *de novo* purine synthesis (Henderson and Khoo, 1965), whilst the salvage pathway persists (Murray, 1971). In cancer cells, Cpd14 is only active under conditions that favour the *de novo* biosynthetic pathway. This is demonstrated by AMPK activation under LPM conditions, as cells are actively producing purines (Asby et al., 2015). As a potential AMPK activator, Cpd14 did not elicit an inhibitory effect on adipogenesis in 3T3-L1 cells under LPM conditions. As the salvage pathway persists in normal functional cells (like 3T3-L1 cells), possibly Cpd14 at 1mM is not active. Rapidly dividing and proliferating cells like cancer cells, predominately produce purines via the *de novo* purine biosynthetic pathway, rather than the salvage pathway (Spurr et al., 2012). This suggests a rationale for no observable effects of Cpd14 on adipogenesis in 3T3-L1 cells, under LPM conditions.

Treatment for 48 hours with higher concentrations of Metformin, inhibits adipogenesis mediated via AMPK activation in 3T3-L1 cells. This results in cytotoxic effects, whereas lower doses induce adipogenesis, independently of AMPK activity (Chen et al., 2018). Cpd14 treatment did not effect adipocyte differentiation under this experimental paradigm, in either HPM or LPM. However, an effect may be observed with a wider range of concentrations administered at certain timepoints during adipocyte development, *in vitro.* This is required to provide a clearer understanding into the potential of Cpd14 as an AMPK activator to inhibit adipocyte differentiation.

The trans-differentiation of white-to-brown adipocytes, also known as 'browning,' provides protection against obesity. Promoting white adipocytes to adopt a 'beige' phenotype via pharmacological stimulation could improve metabolic dysfunction in human obesity. The 'browning' process is demonstrated by the action of AMPK activators in 3T3-L1 cells. As well as inhibiting adipocyte differentiation (Zhang et al., 2017), there is an upregulation of brown adipocyte-associated genes including UCP1, PGC1α and DIO2 (Bae and Kim, 2020; Kim et

al., 2020; Sudhakar et al., 2020), and increased mitochondrial biogenesis (Bae and Kim, 2020). White 3T3-L1 cells morphologically resemble brown-like cells in which there is a transition from uni-locular adipocytes to multi-locular adipocytes (Aziz et al., 2017; Sudhakar et al., 2020). As an AMPK agonist in cancer cells (Asby et al., 2015), there were no significant differences in morphological observations or lipid accumulation between Vehicle and Cpd14-treated 3T3-L1 cells, grown in HPM or LPM. This suggests that acute stimulation with Cpd14 does not induce 'browning' of 3T3-L1 cells. Once again, this may be due to the experimental design. Chronic stimulation, higher concentrations, or treatment of Cpd14 at Day 7 in mature adipocytes, may induce 'browning' in 3T3-L1 adipocytes. However, analysis of brown-like markers such as UCP1 and PGC1α are required to confirm these results.

5.4.2. Animal studies

Asby et al., reported the effects of Cpd14 as a potential therapeutic agent to target metabolic dysfunction in mice. This was demonstrated in mice treated with a 7-day intraperitoneal adminstration of 0.05mg/g Cpd14. Both chow and HF-fed mice had improved glucose tolerance and lost weight over the treatment period, with a larger response seen in HF-fed mice (HF-Cpd14) (Asby et al.,2015). In this study, after a 10-day oral treatment of Cpd14, the body weights between C-V and C-Cpd14 mice were comparable. However, a marked decrease in weight gain was observed in HF-Cpd14 mice compared to HF-V, in accordance with the previous study.

Diet-induced obesity (DIO) dysregulates normal physiological pathways in the body and often leads to metabolic complications. These include a reduced thermogenic capacity, impaired lipolysis (Tsujita, Morimoto and Okuda,1995) and an imbalance between ATP production and demand, resulting in insulin resistance (Petersen et al., 2003). After an ipGTT, 10-day Cpd14-treated mice, regardless of diet, presented an increased glucose clearance rate, over 2-hours. This suggests improved glucose homeostasis in Cpd14-treated mice, compared to glucose intolerance observed in HF-V mice. AMPK activators target AT of obese mice (Wu et al., 2018) to improve glucose homeostasis (Foretz et al., 2010; Horakova et al., 2019) and counteract

metabolic dysfunction. Although further analysis is required, with this view, it is possible that Cpd14 upregulates the AMPK pathway via ACC phosphorylation, as demonstrated by *in vitro* studies (Asby et al.,2015). As glucose intolerance is induced in HF-fed mice but not chow-fed mice, this suggests a possible route for Cpd14 to control glucose homeostasis (O'Neill et al., 2014), in HF-fed mice.

Interestingly, non-fasting and fasting blood glucose levels over the 10-day treatment period were elevated in C-Cpd14 mice compared to C-V mice. The opposite effect was demonstrated in HF-Cpd14 mice, in which levels decreased compared to HF-V. As Asby et al., administered Cpd14 via an intraperitoneal (i.p.) injection, perhaps this acts directly on the AT and has a local effect to induce beneficial effects on weight and glucose levels in chow-fed mice. In this study, chow-fed mice reacted negatively to oral Cpd14 administration and this route may have induced more systemic effects in chow-fed mice, at the level of the organism. Although i.p. injections have similar pharmacokinetic effects to oral administration (Lukas, Brinle and Greengard, 1971), the latter is more relevant and less invasive than i.p. injections. As oral administration produces a slower drug dissolution (Becker, 2006), perhaps a longer period of Cpd14 treatment in chow-fed mice would regulate levels to that observed in C-V mice. This is possible as non-fasting blood glucose levels in C-Cpd14 mice reduced in the final days of the experimental procedure.

Given that a HF-diet increases adipocyte size which is reflected by an increase in caloric intake (Jo et al., 2009), there were no differences in caloric intake in the 10-day Cpd14-treated mice. Furthermore, AMPK activators reduce adipocyte size upon treatment in HF-fed mice, accompanied by a reduction in weight gain and glucose levels (Jing et al., 2018; Wu et al., 2018).Pericardial adipocyte size was reduced in Cpd14-treated mice compared to HF-V mice. This suggests that the weight loss effects in HF-fed mice may have been induced by action of Cpd14 treatment, rather than due to a lack of appetite.

Anti-diabetic compounds induce a process known as 'browning' in white depots (Petrovic et al., 2010) to induce a trans-differentiation of white-to-brown adipocytes. These cells are associated with increased thermogenesis when activated by AMPK compounds (Qi et al.,

2019; Wu et al., 2018; Wu et al.,2019). They provide protection against obesity by upregulating UCP1 expression (Vila-Bedmar et al., 2010), a hallmark of brown adipocytes. In pericardial fat, a sub-population of multi-locular brown-like cells were present in pericardial fat of 10-day treated mice, regardless of Cpd14 treatment or diet. In fact, there were no differences in UCP1 mRNA gene expression levels, in chow or HF-fed mice. This is suggestive of the comparable adoption of brown-like cells in pericardial fat of all mice. Pollard et al., demonstrated that AMPK activity is independent of UCP1 expression in brown-like cells in HF-fed mice, yet mice were still protected against obesity. Although further metabolic analysis is required via indirect calorimetry to determine respiratory exchange rate (RER) (Alfaras et al., 2017; Pollard et al., 2019), perhaps AMPK activation via Cpd14 treatment increases energy expenditure, without effecting UCP1 expression. Cpd14 may target thermogenic active adipocytes in pericardial fat to increase adrenergic output in HF-fed mice to promote weight loss.

Of note, after a 26-day recovery period, there were no differences in glucose homeostasis or body weight between HF-fed mice treated with (HF-Cpd14) or without Cpd14 (HF-V). In fact, HF-Cpd14 mice gradually re-gained body weight over this period. This said, HF-V mice were still significantly heavier than HF-Cpd14 mice, after the 26-day recovery period. Weight re-gain after weight loss in obesity may be associated with hyperphagia, as documented by an increase in caloric intake (Schmitz et al., 2016). Caloric intake of HF-Cpd14 mice was not recorded after the 26-day recovery period. It cannot be concluded whether the weight re-gain in HF-Cpd14 mice was due to increased appetite or that Cpd14 does provide protection against a chronic HF-feeding after the 10-day treatment.

After substantial weight loss, a history of an obese phenotype resonates an inflammatory fingerprint in visceral fat, along with chronic hypertrophy, and promotes weight re-gain. However, in brown fat, there are no differences in thermogenic capacity after weight loss (Fischer et al., 2018). In this study, after the 26-day recovery period, there were no significant differences in UCP1 mRNA expression, adipocyte size or the presence of a sub-population of multi-locular cells that were once observed after the 10-day treatment in pericardial fat. It is possible that the pro-longed HF-diet induced a trans-differentiation of brown-to-white

adipocytes. The 'whitening' of brown cells is accompanied by impaired whole-body glucose metabolism (Shimizu et al., 2014). This is consistent with the comparable glucose intolerance observations in HF-V and HF-Cpd14 mice, after an ipGTT. Chronic hypertrophy or a persistent inflammatory signature, demonstrated by histological and transcriptional analysis, was not observed. Perhaps Cpd14 provides a certain protection against DIO after treatment, during the recovery period.

5.4.3. Conclusion

It is still unclear whether Cpd14 effects adipogenesis *in vitro.* However, *in vivo* studies have demonstrated that Cpd14 may target brown-like cells residing in pericardial fat. This may increase thermogenesis to upregulate energy expenditure to induce weight loss and regulate glucose homeostasis, possibly via AMPK mediation, in HF-fed mice. Whilst further functional research is necessary to further confirm the agonistic effect of Cpd14 on AMPK, the current evidence suggests a promising role for Cpd14 as a therapeutic agent to regulate metabolic dysfunction.

CHAPTER 6

GENERAL DISCUSSION

Ectopic fat deposition and dysregulated adipose tissue function may increase the risk of an individual ascertaining metabolic health complications. Obesity research has often focused on the physiological function of classical adipose depots, including white and brown fat, that encompass most of the fat stores in humans. However, limited knowledge is known about the pathophysiology of fat that is in proximity to the heart. In particular, accumulation of pericardial adipose tissue (PAT), which resides externally of the parietal pericardium in both humans and mice, has been associated with obesity and CV-related events. On the other hand, the role of pericardial fat in metabolic function under normal physiological conditions and disease is still unclear. In this thesis, the transcriptional and histological profile of pericardial fat was determined to provide a wider insight into the signatures of this depot under chow and high-fat conditions, in mice. This is to emulate normal conditions and metabolic dysfunction that may occur in human physiology to understand the capacity of pericardial fat in response to these circumstances.

Under normal physiological conditions, fat deposited around the heart acts as a protective cushioning and buffers against lipotoxicity (Marchington and Pond, 1990). Whether pericardial fat in mice adopts either white or brown features under these conditions is still unknown. Under chow (normal) conditions in 10-week-old and 30-week-old male mice, the gene expression of thermogenic and mitochondrial-related genes was extremely elevated compared to the white depots studied, only second to that of brown fat. In fact, white depots have the capacity to recruit thermogenic cells, characterised by higher levels of UCP1 mRNA expression (Shabalina et al., 2013). UCP1 expression of pericardial fat was associated with a beneficial metabolic profile in mice and is suggestive of holding a 'beige' signature, as that of white subcutaneous fat (Waldén et al., 2012). With this said, expression of AdipoQ (Musovic and Olofsson, 2019) and Leptin (Cinti et al., 1997), associated with white adipocytes, was reduced in pericardial fat compared to white depots. In addition, a sub-population of multi-locular cells resembling brown-like cells were observed in chow-fed mice, regardless of age, and in offspring fed a post-weaning chow-diet, regardless of maternal obesity. Interestingly, the expression of brown-like markers of pericardial fat, demonstrated by transcriptional analysis,

was further exaggerated in mature mice of 30-weeks old, compared to younger 10-week-old mice. Pericardial fat may regulate adipocyte thermogenic capacity, depending on the metabolic requirement of mice *in utero* and adulthood, as demonstrated in the 'beige' depot of perirenal fat (Clarke et al., 1997a; Clarke et al., 1997b).

The 'beige' signature of pericardial fat under normal conditions may be altered by changes in the nutritional environment and impact the metabolic health of an animal. This is demonstrated by the susceptibility of brown-like cells to undergo trans-differentiation to white-like cells, known as 'whitening', under obesogenic conditions. In 30-week-old male mice, compared to 10-week-old male mice, fed a HF-diet, a sub-population of brown-like cells which are visible under chow conditions, are no longer observable. In addition, pericardial adipocytes increased in cell volume via hypertrophic mechanisms, often associated with visceral pathogenesis. The 'whitening' and expansion of pericardial cells was also implemented in male offspring fed a HF-diet post-weaning, regardless of maternal obesity. As these animals were presented with an obese phenotype due to induced offspring overnutrition, the thermogenic capacity of pericardial fat was hindered and may act to promote metabolic dysfunction in mice.

The normal functionality of brown-like cells is associated with a beneficial metabolic profile, under chow conditions. Therapeutic intervention may act on white cells in adipose tissue to promote 'browning' and therefore upregulate thermogenesis and provide protection against obesity. This is suggested in previous research in which AMPK activation promotes metabolic health (Vila-Bedmar et al., 2010; Wu et al., 2018). Although the trans-differentiation of white-to-brown adipocytes was not microscopically observed in cell culture experiments, a 10-day treatment with Cpd14 *in vivo* resulted in weight loss and reduced pericardial adipocyte size of obese mice. This is suggestive of increased energy expenditure. Furthermore, Cpd14 may act on brown-like cells present within pericardial fat to induce a protection against diet-induced obesity (DIO), even after a 26-day recovery period without Cpd14 treatment.

6.1. CONCLUSION

Together, these results demonstrate that pericardial fat may have a thermogenic capacity that is disrupted upon overnutrition during fetal development (maternal obesity) and/or during adulthood (adult obesity). This depot resembles a white and brown-like signature which may be targeted by pharmacological stimulation, via AMPK, to increase energy expenditure in mice. Further research is required to confirm the functionality and underlying mechanisms involved to confirm the genomic and histological analysis stated. However, this study has provided compelling evidence into the distinctive profile of pericardial adipose tissue in mice as a 'beige' depot. This warrants further attention into metabolic studies as a therapeutic target.

6.2. STRENGTHS OF THE STUDY

According to wider knowledge, this is the first time that pericardial fat in mice has been presented as an adipose depot that holds both brown-like and white-like capabilities, as demonstrated by transcriptional and histological analysis. Collectively, it has been demonstrated that pericardial fat is sensitive to changes in normal nutritional and physiological conditions, which may promote either a beneficial or deleterious phenotype in mice. From this, pericardial adipose tissue is an attractive therapeutic target to induce 'browning' in white-like cells and promote thermogenesis of brown-like cells to increase energy expenditure and promote metabolic health.

6.3. LIMITATIONS OF THE STUDY

One of the primary limitations of this study is the absence of analysis of UCP1 expression at a transcriptional level, across certain studies. This will aid in understanding how the thermogenic capacity of pericardial fat is effected in offspring mice exposed to maternal overnutrition prior to and during the gestation and lactation period. With this said, the addition of UCP1 gene expression analysis in cell culture experiments with Cpd14 treatment would be beneficial in determining the 'browning' effects of this compound on white adipocytes. This will aid further into the understanding of Cpd14 as a therapeutic agent for obesity.

Another limitation of the research conducted in this thesis is the lack of functional studies. This analysis would aid in determining whether the gene expression changes in brown adipocyte-related genes, such as upregulation of UCP1 in pericardial fat, translates into a functional increase in metabolic activity. This can be achieved using the XF Flux Analyzer (Seahorse Bioscience) to provide real-time output of whole tissues to quantify mitochondrial biogenesis in fat. Studies have demonstrated that in brown fat, basal oxygen consumption is largely due to proton leakage, higher than that of white fat (Calderon-Dominguez et al., 2017), and that low-thermogenic capacity in brown adipocytes results in reduced basal mitochondrial respiration (Song et al., 2020). This technology provides a greater and wider understanding into the respiratory state of tissues, rather than culturing cells or isolating mitochondria for respiratory experiments (Calderon-Dominguez et al., 2017). Furthermore, studies using 3T3-L1 adipocytes have demonstrated that treatment with Fibroblast Growth Factor 21 (FGF21) increases basal respiration, oxidative consumption (Chau et al., 2010) and induces UCP1 expression with similar oxidative outcomes in adipocyte precursors (APs) of the SVF of cervical fat (beige fat) in humans (Lee et al., 2014). A similar effect was observed in liver cells treated with Metformin (Wang et al., 2019). This provides an insight into studies that could be conducted with Cpd14 to identify if the weight loss in obese mice was due to an increase in energy expenditure. As pericardial fat has brown-like qualities, the Seahorse Technology could be a viable route for determining metabolic activity in pericardial adipocytes from all experiments performed in this thesis.

Furthermore, the studies conducted only use male mice and not female mice for transcriptional and histological analysis. In particular, maternal obesity models have demonstrated that maternal nutrition programs adiposity of offspring in a sex-dependent manner (Lecoutre et al., 2016). Often there are discrepancies between genders such as weight gain, with sex differences becoming apparent in older mice (Desai et al., 2014) and increased adiposity in female offspring compared to male offspring in mice (Sellayah et al., 2019). Although the response to obesity is associated with sex-differences, there is evidence to suggest that metabolic alterations are sex-specific. This includes elevated levels of cardiovascular-related

inflammatory markers, such as C-reactive protein (CRP), in female HF/HF offspring, compared to male offspring in mice (Elahi et al., 2009). This increased sensitivity to a HF-diet in female offspring could be explained in part due to female sex hormones, as supported by human obesity studies in which women have higher levels of CRP than men (Ridker et al., 2000a; Visser et al., 1999). Documenting CRP levels provides a potential mechanistic association between CVD and metabolic dysfunction. Furthermore, these sex-differences are further observed in men and women treated with AMPK activators such as Metformin (Lyons et al., 2013). For instance, diabetic women taking Metformin have a higher survival rate of colorectal cancer, when compared with men (Park et al., 2017). Oestrogen hormones may play a role in this significant result, yet it is still undefined. Therefore, it would be interesting to observe whether Cpd14 effects are further exaggerated in female mice, as observed in male mice.

6.4. FUTURE RESEARCH

From gene expression and histologically analysis, it plausible to comment that PAT has both white and brown-like qualities, which are altered by dietary feeding exposed during *in utero* and adulthood. Undoubtedly, further functionality experimentation is necessary to confirm the presence of brown-like cells and the mechanistic effects of Cpd14 as a therapeutic agent to target pericardial fat.

Immunohistochemistry for UCP1: To confirm the presence of brown-like cells dispersed amongst pericardial fat, the abundance of UCP1, an essential brown adipose tissue marker, can be targeted by immunohistochemistry (IHC). This can be performed by using Abcam's Rabbit specific HRP/DAB Detection IHC Detection Kit - Micro-polymer (Product code: ab236469).

Throughout IHC, all steps must be performed in a humidity chamber (Product code: H6644, Sigma-Aldrich), with limited light exposure to prevent photobleaching. A positive control such as iBAT and a negative control such as gWAT or tissues not stained with the primary antibody should be used. All buffers and solutions must be equilibrated at room temperature, with Anti-UCP1 antibody (Product code: ab10983, Abcam) kept on ice. Air-dry slides for 30 minutes to

prevent sections from falling off during antibody incubations. Rehydrate slides 3 times in PBS for 5 minutes in BRAND Coplin Staining Troughs (Fisher Scientific). Surround tissue sections in a hydrophobic barrier with ReadyProbes™ Hydrophobic Barrier Pap Pen (Product code: 16660484, Fisher Scientific). Add enough drops of Hydrogen Peroxide Block to cover the sections. Incubate for 10 minutes. Wash slides 2 times in PBS for 5 minutes in Coplin staining troughs. Apply Protein Block to slides and incubate for 10 minutes at room temperature. Wash slides 1 time in PBS for 5 minutes. Apply primary antibody (1:1000) and incubate overnight at 2ºC to 8ºC. Wash slides 3 times in PBS for 5 minutes. Apply HRP-conjugate to slides and incubate for 15 minutes. Wash slides 4 times in PBS for 5 minutes. Prepare the required volume for DAB staining using 1µl DAB chromogen per 50µl DAB substrate. Incubate slides for 1 to 10 minutes, until desired colour is reached. Rinse slides 4 times in PBS for 5 minutes in Coplin staining troughs. Counterstain slides for better visualisation with a few drops of 25% Haematoxylin for a few seconds and immediately wash in ddH_20 for 5 minutes. Clear Haematoxylin-stained slides with 90% ethanol for 10 seconds, twice, then in 100% ethanol for 10 seconds, twice and finally twice with Xylene for 10 seconds each. A few drops of Mounting Media for IHC (Product code: ab64230, Abcam) is added to stained slides and a coverslip is placed on top. Image slides with brightfield microscopy and once stained, store in a dark slide box or book between -20°C and 4°C.

Developmental adipogenesis: *In vivo*, adipogenesis occurs at distinct timepoints in mammals, during development and adulthood, in response to a HF-diet. To determine whether maternal overnutrition impacts pericardial fat earlier on in offspring development, PAT can be harvested from mice at 4 weeks of age, as this is when gWAT is fully developed in mice and developmental adipogenesis is complete (Wang et al., 2013). It is unclear whether maternal overnutrition/obesity effects developmental or obesogenic adipogenesis in pericardial fat from offspring. Both histological analysis and gene expression, as presented throughout this thesis, can be conducted in PAT of mice at 4 weeks of age to observe these differences in chow and HF-fed offspring from chow and HF-fed dams, as demonstrated by Sellayah et al., (2019) in gWAT.

AMPK activation: AMPK activators are suggested to improve metabolic dysregulation by acting on adipose tissue, *in vivo* (Boyle et al., 2011). As protein phosphorylation is a transient and dynamic event (Lin et al., 2010), harvesting 3T3-L1 cell lysates and pericardial adipocytes from animals, respectively, treated with Cpd14 a few hours after administration will aid in observing a more distinct change in protein levels of AMPKα Thr172 and ACC Ser79. Chen et al., (2018) suggests that AMPK activity must remain at a certain threshold required for adipogenesis, with further activation resulting in the inhibition of adipocyte differentiation. To determine the mechanistic action of Cpd14 *in vitro*, cell lysates can be extracted for protein to perform a Western blot. This will determine differences in AMPKα Thr172 and ACC Ser76, using phospho- and unphospho-specific antibodies, after stimulation with Cpd14 at different concentrations in cells maintained in HPM and LPM, with β-actin as a reference. A time-dependent experiment can be set up to determine the levels of phosphorylation at certain points, for example, at 0 (baseline), 2, 4, 6, 12 and 24 hours after induction with Cpd14, *in vitro*. 1X RIPA Buffer, containing Protease Inhibitor Mini Tablets and Phosphatase Inhibitor Mini Tablets, will act as a lysis buffer to harvest protein from 3T3-L1 cells and pericardial fat. ddH_2O can be used as a negative control and Metformin as a positive control (Chen et al., 2018). In addition, a specific AMPK inhibitor, such as Compound C can be used as it is potent enough to suppress Metformin phosphorylating AMPK and prevent inhibition of adipogenesis. If Cpd14 acts by upregulating AMPK in 3T3-L1 cells, Cpd14 combined with Compound C treated in cells should not have a signal at the molecular weight associated with AMPK on a Western blot.

Mitochondrial biogenesis: Studies have demonstrated that increased oxidative stress is associated with obesity (Furukawa et al., 2004). AMPK activation by Metformin improves mitochondrial biogenesis and upregulates thermogenesis in brown fat (Karise et al., 2019). This can be demonstrated by the MitoTracker Red CMXRos stain that measures the mitochondrial contents in cells. In addition, chronic stimulation with AMPK activators results in the increase of mitochondrial oxygen consumption rate (OCR), as measured by XF Flux Analyzer (Seahorse Bioscience) and further confirmed by analysing the oxidative

phosphorylation complexes in the mitochondria by Western blots (Karnewar et al., 2018). Using the methods stated above could help elucidate the mechanistic effects of Cpd14 and confirm the thermogenic capacity in pericardial fat upon a HF-feeding in obesity. The exact methodology to conduct experiments in adipocytes and adipose tissue using the XF Flux Analyzer (Seahorse Bioscience) are documented by Bugge, Dib and Collins (2014), with extensive methodology in brown adipocytes recorded by Mahdaviani, Benador and Shiribai (2015).

Adipocyte differentiation: In this thesis, cell culture studies focused on the acute stimulation with Cpd14 on adipogenesis in 3T3-L1 cells. As described by Shen et al., (2018), mature adipocytes act as an energy reservoir in a process known as lipogenesis. Fatty acids are taken up from the diet and are converted into TGs for long-term storage. Studies have shown that compounds can activate AMPK activity. This improves insulin sensitivity in mature adipocytes by suppressing lipid accumulation, inducing lipolysis via AMPK activation and upregulation of UCP1 and PGC1α expression (Shen et al., 2019). Although Cpd14 did not effect adipocyte differentiation in the experimental paradigm presented in this thesis, perhaps Cpd14 administration in mature adipocytes *in vitro* could help elucidate its mode of action. On the other hand, Cpd14 may have an effect early on in adipogenesis. The gene expression changes that regulate mitotic clonal expansion (MCE), including C/EBPβ, could be assessed. Furthermore, labelling cells with 5-bromodeoxyuridine (BrdU), which incorporates into replicating DNA, could be used to assess MCE and cell proliferation in Cpd14-treated cells, as described by Merkestein et al., (2015).

Organismal toxicity: Asby et al., reported that a dose-dependent decline in cell viability in cancer cells with Cpd14 was most likely due to cytostatic effects rather than cytotoxic effects. In this thesis, 1mM Cpd14 in 3T3-L1 cells did not alter cell viability, however, the toxicology of Cpd14 *in vivo* has not been determined. This can be achieved by measuring biomarkers in the blood to predict organismal toxicity such as lactic acid to measure lactic acidosis (Hess et al., 2018) and serum levels of metabolic markers and adipokines such as Leptin (Salomäki et al., 2014), observed in treatment with Metformin in animal studies.

REFERENCES

Aghamohammadzadeh, R., Greenstein, A. S., Yadav, R., Jeziorska, M., Hama, S., Soltani, F., Pemberton, P. W., Ammori, B., Malik, R. A., Soran, H., and Heagerty, A. M. (2013). Effects of bariatric surgery on human small artery function: Evidence for reduction in perivascular adipocyte inflammation, and the restoration of normal anticontractile activity despite persistent obesity. Journal of the American College of Cardiology, 62(2), 128–135.

Aguilar-Salinas, C. A., García, E., Robles, L., Riaño, D., Ruiz-Gomez, D. G., García-Ulloa, A. C., Melgarejo, M. A., Zamora, M., Guillen-Pineda, L. E., Mehta, R., Canizales-Quinteros, S., Luna, M. T. T., and Gómez-Pérez, F. J. (2008). High adiponectin concentrations are associated with the metabolically healthy obese phenotype. Journal of Clinical Endocrinology and Metabolism, 93(10), 4075–4079.

Ahima, R. S. (2014). Adipose Tissue as an Endocrine Organ. Cellular Endocrinology in Health and Disease, 14(August), 229–237.

Al-Dibouni, A., Gaspar, R., Ige, S., Boateng, S., Cagampang, F. R., Gibbins, J., Cox, R. D., and Sellayah, D. (2020). Unique genetic and histological signatures of mouse pericardial adipose tissue. Nutrients, 12(6), 1–17.

Alfaras, I., Mitchell, S. J., Mora, H., Lugo, D. R., Warren, A., Navas-Enamorado, I., Hoffmann, V., Hine, C., Mitchell, J. R., Le Couteur, D. G., Cogger, V. C., Bernier, M., and de Cabo, R. (2017). Health benefits of late-onset metformin treatment every other week in mice. Npj Aging and Mechanisms of Disease, 3(1).

Andersson, D., Wahrenberg, H., and Löfgren, P. (2009). B3-Adrenoceptor function and long-term changes in body weight. International Journal of Obesity, 33(6), 662–668.

Arch, J. R. S., Ainsworth, A. T., Cawthorne, M. A., Piercy, V., Sennitt, M. V., Thody, V. E., Wilson, C., and Wilson, S. (1984). Atypical β-adrenoceptor on brown adipocytes as target for anti-obesity drugs. Nature, 309(5964), 163–165.

Arner, E., Westermark, P. O., Spalding, K. L., Britton, T., Rydén, M., Frisén, J., Bernard, S., and Arner, P. (2010). Adipocyte turnover: relevance to human adipose tissue morphology. Diabetes, 59(1), 105–109.

Arner, P., Andersson, D. P., Bäckdahl, J., Dahlman, I., and Rydén, M. (2018). Weight Gain and Impaired Glucose Metabolism in Women Are Predicted by Inefficient Subcutaneous Fat Cell Lipolysis. Cell metabolism, 28(1), 45–54.e3.

Asby, D. J., Cuda, F., Beyaert, M., Houghton, F. D., Cagampang, F. R., and Tavassoli, A. (2015). AMPK Activation via Modulation of De Novo Purine Biosynthesis with an Inhibitor of ATIC Homodimerization. Chemistry and Biology, 22(7), 838–848.

Aslanabadi, N., Salehi, R., Javadrashid, A., Tarzamani, M., Khodadad, B., Enamzadeh, E., and Montazerghaem, H. (2014). Epicardial and Pericardial Fat Volume Correlate with the Severity of Coronary Artery Stenosis. Journal of Cardiovascular and Thoracic Research, 6(4), 235–239.

Atit, R., Sgaier, S. K., Mohamed, O. A., Taketo, M. M., Dufort, D., Joyner, A. L., Niswander, L., and Conlon, R. A. (2006). B-Catenin Activation Is Necessary and Sufficient To Specify the Dorsal Dermal Fate in the Mouse. Developmental Biology, 296(1), 164–176.

Aziz, S. A., Wakeling, L. A., Miwa, S., Alberdi, G., Hesketh, J. E., and Ford, D. (2017). Metabolic programming of a beige adipocyte phenotype by genistein. Molecular nutrition and food research, 61(2), 1600574.

Bae, I. S., and Kim, S. H. (2020). Sinapic Acid Promotes Browning of 3T3-L1 Adipocytes via p38 MAPK/CREB Pathway. BioMed research international, 2020, 5753623.

Baker, C. (2019). Obesity Statistics. Obesity Statistics (Briefing Paper, Number 3336), 3336, 1–18.

Balagopal, P., De Ferranti, S. D., Cook, S., Daniels, S. R., Gidding, S. S., Hayman, L. L., McCrindle, B. W., Mietus-Snyder, M. L., and Steinberger, J. (2011). Nontraditional risk factors

and biomarkers for cardiovascular disease: Mechanistic, research, and clinical considerations for youth: A scientific statement from the american heart association. Circulation, 123(23), 2749–2769.

Bale, L. K., West, S. A., and Conover, C. A. (2018). Characterization of mouse pericardial fat: regulation by PAPP-A. Growth hormone and IGF research: official journal of the Growth Hormone Research Society and the International IGF Research Society, 42-43, 1–7.

Barak, Y., Nelson, M. C., Ong, E. S., Jones, Y. Z., Ruiz-Lozano, P., Chien, K. R., Koder, A., and Evans, R. M. (1999). PPARγ is required for placental, cardiac, and adipose tissue development. Molecular Cell, 4(4), 585–595.

Barandier, C., Montani, J. P., and Yang, Z. (2005). Mature adipocytes and perivascular adipose tissue stimulate vascular smooth muscle cell proliferation: Effects of aging and obesity. American Journal of Physiology - Heart and Circulatory Physiology, 289(5 58-5), 1807–1813.

Barbatelli, G., Murano, I., Madsen, L., Hao, Q., Jimenez, M., Kristiansen, K., Giacobino, J. P., De Matteis, R., and Cinti, S. (2010). The emergence of cold-induced brown adipocytes in mouse white fat depots is determined predominantly by white to brown adipocyte transdifferentiation. American Journal of Physiology - Endocrinology and Metabolism, 298(6), 1244–1253.

Barker, D. J., and Osmond, C. (1986). Infant mortality, childhood nutrition, and ischaemic heart disease in England and Wales. Lancet (London, England), 1(8489), 1077–1081.

Barker, D. J., Gluckman, P. D., Godfrey, K. M., Harding, J. E., Owens, J. A., and Robinson, J. S. (1993). Fetal nutrition and cardiovascular disease in adult life. Lancet (London, England), 341(8850), 938–941.

Barrow, D. R., Abbate, L. M., Paquette, M. R., Driban, J. B., Vincent, H. K., Newman, C., Messier, S. P., Ambrose, K. R., and Shultz, S. P. (2019). Exercise prescription for weight

management in obese adults at risk for osteoarthritis: Synthesis from a systematic review. BMC Musculoskeletal Disorders, 20(1), 1–9.

Bartelt, A., Bruns, O. T., Reimer, R., Hohenberg, H., Ittrich, H., Peldschus, K., Kaul, M. G., Tromsdorf, U. I., Weller, H., Waurisch, C., Eychmüller, A., Gordts, P. L. S. M., Rinninger, F., Bruegelmann, K., Freund, B., Nielsen, P., Merkel, M., and Heeren, J. (2011). Brown adipose tissue activity controls triglyceride clearance. Nature Medicine, 17(2), 200–206.

Bastard, J. P., Jardel, C., Bruckert, E., Blondy, P., Capeau, J., Laville, M., Vidal, H., and Hainque, B. (2000). Elevated levels of interleukin 6 are reduced in serum and subcutaneous adipose tissue of obese women after weight loss. Journal of Clinical Endocrinology and Metabolism, 85(9), 3338–3342.

Bastías-Pérez, M., Zagmutt, S., Soler-Vázquez, M. C., Serra, D., Mera, P., and Herrero, L. (2020). Impact of Adaptive Thermogenesis in Mice on the Treatment of Obesity. Cells, 9(2), 316.

Bateson, P., Gluckman, P., and Hanson, M. (2014). The biology of developmental plasticity and the Predictive Adaptive Response hypothesis. The Journal of physiology, 592(11), 2357–2368.

Baur, J. A., Pearson, K. J., Price, N. L., Jamieson, H. A., Lerin, C., Kalra, A., Prabhu, V. V., Allard, J. S., Lopez-Lluch, G., Lewis, K., Pistell, P. J., Poosala, S., Becker, K. G., Boss, O., Gwinn, D., Wang, M., Ramaswamy, S., Fishbein, K. W., Spencer, R. G., Lakatta, E. G., … Sinclair, D. A. (2006). Resveratrol improves health and survival of mice on a high-calorie diet. Nature, 444(7117), 337–342.

Bayol, S. A., Farrington, S. J., and Stickland, N. C. (2007). A maternal "junk food" diet in pregnancy and lactation promotes an exacerbated taste for "junk food" and a greater propensity for obesity in rat offspring. British Journal of Nutrition, 98(4), 843–851.

Becker D. E. (2006). Drug therapy in dental practice: general principles. Part 1 - Pharmacokinetic considerations. Anesthesia progress, 53(4), 140–146.

Becskei, C., Lutz, T. A., and Riediger, T. (2009). Blunted fasting-induced hypothalamic activation and refeeding hyperphagia in late-onset obesity. Neuroendocrinology, 90(4), 371–382.

Becskei, C., Lutz, T. A., and Riediger, T. (2010). Reduced fasting-induced activation of hypothalamic arcuate neurons is associated with hyperleptinemia and increased leptin sensitivity in obese mice. American Journal of Physiology - Regulatory Integrative and Comparative Physiology, 299(2), 632–641.

Bellinger, L., Sculley, D. V., and Langley-Evans, S. C. (2006). Exposure to undernutrition in fetal life determines fat distribution, locomotor activity and food intake in ageing rats. International Journal of Obesity, 30(5), 729–738.

Bernlohr, D. A., Bolanowski, M. A., Kelly, T. J., and Lane, M. D. (1985). Evidence for an increase in transcription of specific mRNAs during differentiation of 3T3-L1 preadipocytes. Journal of Biological Chemistry, 260(9), 5563–5567.

Berry, D. C., Stenesen, D., Zeve, D., and Graff, J. M. (2013). The developmental origins of adipose tissue. Development (Cambridge), 140(19), 3939–3949.

Bianco, A. C., and Silva, J. E. (1987). Intracellular conversion of thyroxine to triiodothyronine is required for the optimal thermogenic funciton of brown adipose tissue. Journal of Clinical Investigation, 79(1), 295–300.

Billon, N., Kolde, R., Reimand, J., Monteiro, M. C., Kull, M., Peterson, H., Tretyakov, K., Adler, P., Wdziekonski, B., Vilo, J., and Dani, C. (2010). Comprehensive transcriptome analysis of mouse embryonic stem cell adipogenesis unravels new processes of adipocyte development. Genome Biology, 11(8).

Birsoy, K., Berry, R., Wang, T., Ceyhan, O., Tavazoie, S., Friedman, J. M., and Rodeheffer, M. S. (2011). Analysis of gene networks in white adipose tissue development reveals a role for ETS2 in adipogenesis. Development, 138(21), 4709–4719.

Bjørndal, B., Burri, L., Staalesen, V., Skorve, J., and Berge, R. K. (2011). Different adipose depots: Their role in the development of metabolic syndrome and mitochondrial response to hypolipidemic agents. Journal of Obesity, 2011, 490650.

Boden, G., Jadali, F., White, J., Liang, Y., Mozzoli, M., Chen, X., Coleman, E., and Smith, C. (1991). Effects of fat on insulin-stimulated carbohydrate metabolism in normal men. Journal of Clinical Investigation, 88(3), 960–966.

Boden, G., and Chen, X. (1995). Effects of fat on glucose uptake and utilization in patients with non-insulin-dependent diabetes. Journal of Clinical Investigation, 96(3), 1261–1268.

Boney, C. M., Verma, A., Tucker, R., and Vohr, B. R. (2005). Metabolic syndrome in childhood: Association with birth weight, maternal obesity, and gestational diabetes mellitus. Pediatrics, 115(3), e290–e296.

Borengasser, S. J., Zhong, Y., Kang, P., Lindsey, F., Ronis, M. J. J., Badger, T. M., Gomez-Acevedo, H., and Shankar, K. (2013). Maternal obesity enhances white adipose tissue differentiation and alters genome-scale DNA methylation in male rat offspring. Endocrinology, 154(11), 4113–4125.

Borges, J. H., Carter, S. J., Bryan, D. R., and Hunter, G. R. (2019). Exercise training and/or diet on reduction of intra-abdominal adipose tissue and risk factors for cardiovascular disease. European Journal of Clinical Nutrition, 73(7), 1063–1068.

Bosy-Westphal, A., Kossel, E., Goele, K., Blöcker, T., Lagerpusch, M., Later, W., Heller, M., Glüer, C. C., and Müller, M. J. (2010). Association of pericardial fat with liver fat and insulin sensitivity after diet-induced weight loss in overweight women. Obesity, 18(11), 2111–2117.

Bouchard, C., Tremblay, A., Després, J. P., Nadeau, A., Lupien, P. J., Thériault, G., Dussault, J., Moorjani, S., Pinault, S., and Fournier, G. (1990). The response to long-term overfeeding in identical twins. The New England journal of medicine, 322(21), 1477–1482.

Boyle, J. G., Logan, P. J., Jones, G. C., Small, M., Sattar, N., Connell, J. M. C., Cleland, S. J., and Salt, I. P. (2011). AMP-activated protein kinase is activated in adipose tissue of individuals with type 2 diabetes treated with metformin: A randomised glycaemia-controlled crossover study. Diabetologia, 54(7), 1799–1809.

Boyle, K. E., Patinkin, Z. W., Shapiro, A. L. B., Bader, C., Vanderlinden, L., Kechris, K., Janssen, R. C., Ford, R. J., Smith, B. K., Steinberg, G. R., Davidson, E. J., Yang, I. V., Dabelea, D., and Friedman, J. E. (2017). Maternal obesity alters fatty acid oxidation, AMPK activity, and associated DNA methylation in mesenchymal stem cells from human infants. Molecular Metabolism, 6(11), 1503–1516.

Boyle, K. E., Patinkin, Z. W., Shapiro, A. L. B., Baker, P. R., Dabelea, D., and Friedman, J. E. (2016). Mesenchymal stem cells from infants born to obese mothers exhibit greater potential for adipogenesis: The healthy start babybump project. Diabetes, 65(3), 647–659.

Bray, G. A., and Tartaglia, L. A. (2000). Medicinal strategies in the treatment of obesity. Nature, 404(6778), 672–677.

Bremer, A. A., Devaraj, S., Afify, A., and Jialal, I. (2011). Adipose tissue dysregulation in patients with metabolic syndrome. Journal of Clinical Endocrinology and Metabolism, 96(11), 1782–1788.

Brestoff, J. R., and Artis, D. (2015). Immune regulation of metabolic homeostasis in health and disease. Cell, 161(1), 146–160.

British Heart Foundation. (2020). UK Factsheet. British Heart Foundation, January, 1–21.

Bronnikov, G., Bengtsson, T., Kramarova, L., Golozoubova, V., Cannon, B., and Nedergaard, J. (1999). β1 to β3 Switch in control of cyclic adenosine monophosphate during brown

adipocyte development explains distinct β-adrenoceptor subtype mediation of proliferation and differentiation. Endocrinology, 140(9), 4185–4197.

Bruce, K. D., Cagampang, F. R., Argenton, M., Zhang, J., Ethirajan, P. L., Burdge, G. C., Bateman, A. C., Clough, G. F., Poston, L., Hanson, M. A., McConnell, J. M., and Byrne, C. D. (2009). Maternal high-fat feeding primes steatohepatitis in adult mice offspring, involving mitochondrial dysfunction and altered lipogenesis gene expression. Hepatology, 50(6), 1796–1808.

Bruun, J. M., Helge, J. W., Richelsen, B., and Stallknecht, B. (2006). Diet and exercise reduce low-grade inflammation and macrophage infiltration in adipose tissue but not in skeletal muscle in severely obese subjects. American Journal of Physiology - Endocrinology and Metabolism, 290(5), 961–967.

Budge, H., Edwards, L. J., McMillen, I. C., Bryce, A., Warnes, K., Pearce, S., Stephenson, T., and Symonds, M. E. (2004). Nutritional manipulation of fetal adipose tissue deposition and uncoupling protein 1 messenger RNA abundance in the sheep: Differential effects of timing and duration. Biology of Reproduction, 71(1), 359–365.

Buemann, B., Toubro, S., and Astrup, A. (2000). Effects of the two β3-agonists, ZD7114 and ZD2079 on 24 hour energy expenditure and respiratory quotient in obese subjects. International Journal of Obesity, 24(12), 1553–1560.

Bugge, A., Dib, L., and Collins, S. (2014). Measuring respiratory activity of adipocytes and adipose tissues in real time. Methods in Enzymology, 538(February), 233–247.

Burnette W. N. (1981). "Western blotting": electrophoretic transfer of proteins from sodium dodecyl sulfate--polyacrylamide gels to unmodified nitrocellulose and radiographic detection with antibody and radioiodinated protein A. Analytical biochemistry, 112(2), 195–203.

Calderon-Dominguez, M., Alcalá, M., Sebastián, D., Zorzano, A., Viana, M., Serra, D., and Herrero, L. (2017). Brown Adipose Tissue Bioenergetics: A New Methodological Approach. Advanced Science, 4(4).

Cancello, R., Tordjman, J., Poitou, C., Guilhem, G., Bouillot, J. L., Hugol, D., Coussieu, C., Basdevant, A., Hen, A. B., Bedossa, P., Guerre-Millo, M., and Clément, K. (2006). Increased infiltration of macrophages in omental adipose tissue is associated with marked hepatic lesions in morbid human obesity. Diabetes, 55(6), 1554–1561.

Cancello, R., Zingaretti, M. C., Sarzani, R., Ricquier, D., and Cinti, S. (1998). Leptin and UCP1 genes are reciprocally regulated in brown adipose tissue. Endocrinology, 139(11), 4747–4750.

Cannon, B., and Nedergaard, J. (2004). Brown Adipose Tissue: Function and Physiological Significance. Physiological Reviews, 84(1), 277–359.

Cantile, M., Procino, A., D'Armiento, M., Cindolo, L., and Cillo, C. (2003). HOX gene network is involved in the transcriptional regulation of in vivo human adipogenesis. Journal of Cellular Physiology, 194(2), 225–236.

Cao, W. Y., Liu, Z., Guo, F., Yu, J., Li, H., and Yin, X. (2018). Adipocyte ADRB3 Down-Regulated in Chinese Overweight Individuals Adipocyte ADRB3 in Overweight. Obesity Facts, 11(6), 524–533.

Cardenas-Perez, R. E., Fuentes-Mera, L., De La Garza, A. L., Torre-Villalvazo, I., Reyes-Castro, L. A., Rodriguez-Rocha, H., Garcia-Garcia, A., Corona-Castillo, J. C., Tovar, A. R., Zambrano, E., Ortiz-Lopez, R., Saville, J., Fuller, M., and Camacho, A. (2018). Maternal overnutrition by hypercaloric diets programs hypothalamic mitochondrial fusion and metabolic dysfunction in rat male offspring. Nutrition and Metabolism, 15(1), 1–16.

Carey, A. L., Lamont, B., Andrikopoulos, S., Koukoulas, I., Proietto, J., and Febbraio, M. A. (2003). Interleukin-6 gene expression is increased in insulin-resistant rat skeletal muscle following insulin stimulation. Biochemical and biophysical research communications, 302(4), 837–840.

Carey, A. L., Bruce, C. R., Sacchetti, M., Anderson, M. J., Olsen, D. B., Saltin, B., Hawley, J. A., and Febbraio, M. A. (2004). Interleukin-6 and tumor necrosis factor-alpha are not increased

in patients with Type 2 diabetes: evidence that plasma interleukin-6 is related to fat mass and not insulin responsiveness. Diabetologia, 47(6), 1029–1037.

Carlson, C. A., and Kim, K. H. (1973). Regulation of hepatic acetyl coenzyme A carboxylase by phosphorylation and dephosphorylation. The Journal of biological chemistry, 248(1), 378–380.

Catalano, P. M., Presley, L., Minium, J., and Mouzon, S. H. De. (2009). Fetuses of obese mothers develop insulin resistance in utero. Diabetes Care, 32(6), 1076–1080.

Cetin, I., Morpurgo, P. S., Radaelli, T., Taricco, E., Cortelazzi, D., Bellotti, M., Pardi, G., and Beck-Peccoz, P. (2000). Fetal plasma leptin concentrations: relationship with different intrauterine growth patterns from 19 weeks to term. Pediatric research, 48(5), 646–651.

Chait, A., and den Hartigh, L. J. (2020). Adipose Tissue Distribution, Inflammation and Its Metabolic Consequences, Including Diabetes and Cardiovascular Disease. Frontiers in Cardiovascular Medicine, 7(February), 1–41.

Challier, J. C., Basu, S., Bintein, T., Minium, J., Hotmire, K., Catalano, P. M., and Hauguel-de Mouzon, S. (2008). Obesity in pregnancy stimulates macrophage accumulation and inflammation in the placenta. Placenta, 29(3), 274–281.

Champigny, O., and Ricquier, D. (1996). Evidence from in vitro differentiating cells that adrenoceptor agonists can increase uncoupling protein mRNA level in adipocytes of adult humans: An RT-PCR study. Journal of Lipid Research, 37(9), 1907–1914.

Chau, M. D. L., Gao, J., Yang, Q., Wu, Z., and Gromada, J. (2010). Fibroblast growth factor 21 regulates energy metabolism by activating the AMPK-SIRT1-PGC-1α pathway. Proceedings of the National Academy of Sciences of the United States of America, 107(28), 12553–12558.

Chau, Y. Y., Bandiera, R., Serrels, A., Martínez-Estrada, O. M., Qing, W., Lee, M., Slight, J., Thornburn, A., Berry, R., Mchaffie, S., Stimson, R. H., Walker, B. R., Chapuli, R. M., Schedl,

A., and Hastie, N. (2014). Visceral and subcutaneous fat have different origins and evidence supports a mesothelial source. Nature Cell Biology, 16(4), 367–375.

Chechi, K., Blanchard, P. G., Mathieu, P., Deshaies, Y., and Richard, D. (2013). Brown fat like gene expression in the epicardial fat depot correlates with circulating HDL-cholesterol and triglycerides in patients with coronary artery disease. International journal of cardiology, 167(5), 2264–2270.

Chechi, K., Vijay, J., Voisine, P., Mathieu, P., Bossé, Y., Tchernof, A., Grundberg, E., and Richard, D. (2019). UCP1 expression–associated gene signatures of human epicardial adipose tissue. JCI Insight, 4(8), 1–14.

Chen, D., Wang, Y., Wu, K., and Wang, X. (2018). Dual effects of metformin on adipogenic differentiation of 3T3-L1 preadipocyte in AMPK-dependent and independent manners. International Journal of Molecular Sciences, 19(6).

Chen, S. C., Brooks, R., Houskeeper, J., Bremner, S. K., Dunlop, J., Viollet, B., Logan, P. J., Salt, I. P., Ahmed, S. F., and Yarwood, S. J. (2017). Metformin suppresses adipogenesis through both AMP-activated protein kinase (AMPK)-dependent and AMPK-independent mechanisms. Molecular and Cellular Endocrinology, 440, 57–68.

Cheung, L., Gertow, J., Werngren, O., Folkersen, L., Petrovic, N., Nedergaard, J., Franco-Cereceda, A., Eriksson, P., and Fisher, R. M. (2013). Human mediastinal adipose tissue displays certain characteristics of brown fat. Nutrition and Diabetes, 3(May), e66.

Christoffolete, M. A., Linardi, C. C., de Jesus, L., Ebina, K. N., Carvalho, S. D., Ribeiro, M. O., Rabelo, R., Curcio, C., Martins, L., Kimura, E. T., and Bianco, A. C. (2004). Mice with targeted disruption of the Dio2 gene have cold-induced overexpression of the uncoupling protein 1 gene but fail to increase brown adipose tissue lipogenesis and adaptive thermogenesis. Diabetes, 53(3), 577–584.

Christy, R. J., Kaestner, K. H., Geiman, D. E., and Lane, M. D. (1991). CCAAT/enhancer binding protein gene promoter: binding of nuclear factors during differentiation of 3T3-L1 preadipocytes. Proceedings of the National Academy of Sciences of the United States of America, 88(6), 2593–2597.

Christy, R. J., Yang, V. W., Ntambi, J. M., Geiman, D. E., Landschulz, W. H., Friedman, A. D., Nakabeppu, Y., Kelly, T. J., and Lane, M. D. (1989). Differentiation-induced gene expression in 3T3-L1 preadipocytes: CCAAT/enhancer binding protein interacts with and activates the promoters of two adipocyte-specific genes. Genes and Development, 3(9), 1323–1335.

Cinti, S., Frederich, R. C., Zingaretti, M. C., De Matteis, R., Flier, J. S., and Lowell, B. B. (1997). Immunohistochemical localization of leptin and uncoupling protein in white and brown adipose tissue. Endocrinology, 138(2), 797–804.

Cinti, S., Mitchell, G., Barbatelli, G., Murano, I., Ceresi, E., Faloia, E., Wang, S., Fortier, M., Greenberg, A. S., and Obin, M. S. (2005). Adipocyte death defines macrophage localization and function in adipose tissue of obese mice and humans. Journal of Lipid Research, 46(11), 2347–2355.

Civitarese, A. E., Carling, S., Heilbronn, L. K., Hulver, M. H., Ukropcova, B., Deutsch, W. A., Smith, S. R., and Ravussin, E. (2007). Calorie restriction increases muscle mitochondrial biogenesis in healthy humans. PLoS Medicine, 4(3), 485–494.

Clarke, L., Bryant, M. J., Lomax, M. A., and Symonds, M. E. (1997a). Maternal manipulation of brown adipose tissue and liver development in the ovine fetus during late gestation. British Journal of Nutrition, 77(6), 871–883.

Clarke, L., Buss, D. S., Juniper, D. T., Lomax, M. A., and Symonds, M. E. (1997b). Adipose tissue development during early postnatal life in ewe-reared lambs. Experimental physiology, 82(6), 1015–1027.

Clegg, D. J., Gotoh, K., Kemp, C., Wortman, M. D., Benoit, S. C., Brown, L. M., D'Alessio, D., Tso, P., Seeley, R. J., and Woods, S. C. (2011). Consumption of a high-fat diet induces central insulin resistance independent of adiposity. Physiology and Behavior, 103(1), 10–16.

Coletta, D. K., Sriwijitkamol, A., Wajcberg, E., Tantiwong, P., Li, M., Prentki, M., Madiraju, M., Jenkinson, C. P., Cersosimo, E., Musi, N., and DeFronzo, R. A. (2009). Pioglitazone stimulates AMP-activated protein kinase signalling and increases the expression of genes involved in adiponectin signalling, mitochondrial function and fat oxidation in human skeletal muscle in vivo: A randomised trial. Diabetologia, 52(4), 723–732.

Collins, S., Daniel, K. W., Petro, A. E., and Surwit, R. S. (1997). Strain-specific response to β3-adrenergic receptor agonist treatment of diet-induced obesity in mice. Endocrinology, 138(1), 405–413.

Considine, R. V., Sinha, M. K., Heiman, M. L., Kriauciunas, A., Stephens, T. W., Nyce, M. R., Ohannesian, J. P., Marco, C. C., Mckee, L. J., Bauer, T. L., and Caro, J. F. (1996). Serum immunoreactive-leptin concentrations in normal-weight and obese humans. New England Journal of Medicine, 334(5), 292–295.

Cotillard, A., Poitou, C., Torcivia, A., Bouillot, J. L., Dietrich, A., Klöting, N., Grégoire, C., Lolmede, K., Blüher, M., and Clément, K. (2014). Adipocyte size threshold matters: Link with risk of type 2 diabetes and improved insulin resistance after gastric bypass. Journal of Clinical Endocrinology and Metabolism, 99(8), 1466–1470.

Cousin, B., Cinti, S., Morroni, M., Raimbault, S., Ricquier, D., Penicaud, L., and Casteilla, L. (1992). Occurrence of brown adipocytes in rat white adipose tissue: Molecular and morphological characterization. Journal of Cell Science, 103(4), 931–942.

Crisan, M., Casteilla, L., Lehr, L., Carmona, M., Paoloni-Giacobino, A., Yap, S., Sun, B., Léger, B., Logar, A., Pénicaud, L., Schrauwen, P., Cameron-Smith, D., Russell, A. P., Péault, B., and Giacobino, J.-P. (2008). A Reservoir of Brown Adipocyte Progenitors in Human Skeletal Muscle. Stem Cells, 26(9), 2425–2433.

Crunkhorn, S., Dearie, F., Mantzoros, C., Gami, H., Da Silva, W. S., Espinoza, D., Faucette, R., Barry, K., Bianco, A. C., and Patti, M. E. (2007). Peroxisome proliferator activator receptor γ coactivator-1 expression is reduced in obesity: Potential pathogenic role of saturated fatty acids and p38 mitogen-activated protein kinase activation. Journal of Biological Chemistry, 282(21), 15439–15450.

Cummings, B. P., Bettaieb, A., Graham, J. L., Stanhope, K., Haj, F. G., and Havel, P. J. (2014). Administration of pioglitazone alone or with alogliptin delays diabetes onset in UCD-T2DM rats. Journal of Endocrinology, 221(1), 133–144.

Curhan, G. C., Chertow, G. M., Willett, W. C., Spiegelman, D., Colditz, G. A., Manson, J. E., Speizer, F. E., and Stampfer, M. J. (1996). Birth weight and adult hypertension and obesity in women. Circulation, 94(6), 1310–1315.

Cypess. (2009). Identification and Importance of Brown Adipose Tissue in Adult Humans. Clinical Lymphoma Myeloma, 360(15), 1509–1517.

Cypess, A. M., Weiner, L. S., Roberts-toler, C., Elía, E. F., Kessler, H., Kahn, P. A., English, J., Chatman, K., Trauger, S. A., Doria, A., and Kolodny, G. M. (2015). Activation of Human Brown Adipose Tissue by a β3-Adrenergic Receptor Agonist. 21(1), 33–38.

Dahlén, E. M., Tengblad, A., Länne, T., Clinchy, B., and Ernerudh, J. (2014). Abdominal obesity and low-grade systemic inflammation as markers of subclinical organ damage in type 2 diabetes. 40, 76–81.

Das, S., Bedja, D., Campbell, N., Dunkerly, B., Chenna, V., Maitra, A., and Steenbergen, C. (2014). miR-181c regulates the mitochondrial genome, bioenergetics, and propensity for heart failure in vivo. PLoS ONE, 9(5), 1–9.

Das, S., Ferlito, M., Kent, O. A., Fox-Talbot, K., Wang, R., Liu, D., Raghavachari, N., Yang, Y., Wheelan, S. J., Murphy, E., and Steenbergen, C. (2012). Nuclear miRNA regulates the mitochondrial genome in the heart. Circulation research, 110(12), 1596–1603.

Davis, T. R. (1961). Chamber cold acclimatization in man. Journal of Applied Physiology, 9(May 1961), 1011–1015.

Davis, T. R., Johnston, D. R., Bell, F. C., and Cremer, B. J. (1960). Regulation of shivering and non-shivering heat production during acclimation of rats. The American Journal of Physiology, 198(9), 471–475.

De Jesus, L. A., Carvalho, S. D., Ribeiro, M. O., Schneider, M., Kim, S. W., Harney, J. W., Larsen, P. R., and Bianco, A. C. (2001). The type 2 iodothyronine deiodinase is essential for adaptive thermogenesis in brown adipose tissue. Journal of Clinical Investigation, 108(9), 1379–1385.

de la Brousse, F. C., Shan, B., and Chen, J. L. (1996). Identification of the promoter of the mouse obese gene. Proceedings of the National Academy of Sciences of the United States of America, 93(9), 4096–4101.

Delahaye, F., Lukaszewski, M. A., Wattez, J. S., Cisse, O., Dutriez-Casteloot, I., Fajardy, I., Montel, V., Dickes-Coopman, A., Laborie, C., Lesage, J., Breton, C., and Vieau, D. (2010). Maternal perinatal undernutrition programs a "brown-like" phenotype of gonadal white fat in male rat at weaning. American Journal of Physiology - Regulatory Integrative and Comparative Physiology, 299(1), 101–110.

Desai, M., Jellyman, J. K., Han, G., Beall, M., Lane, R. H., and Ross, M. G. (2014). Maternal obesity and high-fat diet program offspring metabolic syndrome. American journal of obstetrics and gynecology, 211(3), 237.e1–237.e13.

Desai, M., Jellyman, J. K., Han, G., Lane, R. H., and Ross, M. G. (2015). Programmed regulation of rat offspring adipogenic transcription factor (PPARγ) by maternal nutrition. Journal of developmental origins of health and disease, 6(6), 530–538.

Desnoyers, F., Vodovar, N., Delpal, S., and Paillard, G. (1977). Etude structurale et ultrastructurale du tissu adipeux périrénal au stade de sa formation chez le porc. Annales de Biologie Animale Biochimie Biophysique, 17(3A), 269–282.

Després, J. P., Ferland, M., Moorjani, S., Nadeau, A., Tremblay, A., Lupien, P. J., Theriault, G., and Bouchard, C. (1989a). Role of hepatic-triglyceride lipase activity in the association between intra-abdominal fat and plasma HDL cholesterol in obese women. Arteriosclerosis, 9(4), 485–492.

Després, J. P., Fong, B. S., Julien, P., Jimenez, J., and Angel, A. (1987). Regional variation in HDL metabolism in human fat cells: effect of cell size. The American journal of physiology, 252(5 Pt 1), E654–E659.

Després, J. P., Moorjani, S., Ferland, M., Tremblay, A., Lupien, P. J., Nadeau, A., Pinault, S., Theriault, G., and Bouchard, C. (1989b). Adipose tissue distribution and plasma lipoprotein levels in obese women. Importance of intra-abdominal fat. Arteriosclerosis, 9(2), 203–210.

Després, J. P., Nadeau, A., Tremblay, A., Ferland, M., Moorjani, S., Lupien, P. J., Thériault, G., Pinault, S., and Bouchard, C. (1989c). Role of deep abdominal fat in the association between regional adipose tissue distribution and glucose tolerance in obese women. Diabetes, 38(3), 304–309.

Diabetes UK. (2019). Diabetes UK Facts and Figures 2019. Diabetes UK, 1–48. Retrieved on 30/03/2021 from www.diabetes.org.uk

Ding, J., Hsu, F. C., Harris, T. B., Liu, Y., Kritchevsky, S. B., Szklo, M., Ouyang, P., Espeland, M. A., Lohman, K. K., Criqui, M. H., Allison, M., Bluemke, D. A., and Carr, J. J. (2009). The association of pericardial fat with incident coronary heart disease: The Multi-Ethnic Study of Atherosclerosis (MESA). American Journal of Clinical Nutrition, 90(3), 499–504.

Dobner, J., Ress, C., Rufinatscha, K., Salzmann, K., Salvenmoser, W., Folie, S., Wieser, V., Moser, P., Weiss, G., Goebel, G., Tilg, H., and Kaser, S. (2017). Fat-enriched rather than high-fructose diets promote whitening of adipose tissue in a sex-dependent manner. Journal of Nutritional Biochemistry, 49, 22–29.

Dobrian, A. D., Schriver, S. D., Khraibi, A. A., and Prewitt, R. L. (2004). Pioglitazone Prevents Hypertension and Reduces Oxidative Stress in Diet-Induced Obesity. Hypertension, 43(1), 48–56.

Donahue, R. P., and Abbott, R. D. (1987). Central obesity and coronary heart disease in men. Lancet (London, England), 2(8569), 1215.

Dozio, E., Vianello, E., Briganti, S., Fink, B., Malavazos, A. E., Scognamiglio, E. T., Dogliotti, G., Sigrüener, A., Schmitz, G., and Corsi Romanelli, M. M. (2014). Increased reactive oxygen species production in epicardial adipose tissues from coronary artery disease patients is associated with brown-to-white adipocyte trans-differentiation. International Journal of Cardiology, 174(2), 413–414.

Drehmer, M., Duncan, B. B., Kac, G., and Schmidt, M. I. (2013). Association of Second and Third Trimester Weight Gain in Pregnancy with Maternal and Fetal Outcomes. PLoS ONE, 8(1).

Dresner, A., Laurent, D., Marcucci, M., Griffin, M. E., Dufour, S., Cline, G. W., Slezak, L. A., Andersen, D. K., Hundal, R. S., Rothman, D. L., Petersen, K. F., and Shulman, G. I. (1999). Effects of free fatty acids on glucose transport and IRS-1-associated phosphatidylinositol 3-kinase activity. Journal of Clinical Investigation, 103(2), 253–259.

Drolet, R., Richard, C., Sniderman, A. D., Mailloux, J., Fortier, M., Huot, C., Rhéaume, C., and Tchernof, A. (2008). Hypertrophy and hyperplasia of abdominal adipose tissues in women. International Journal of Obesity, 32(2), 283–291.

Dujic, T., Zhou, K., Donnelly, L. A., Tavendale, R., Palmer, C. N. A., and Pearson, E. R. (2015). Association of organic cation transporter 1 with intolerance to metformin in type 2 diabetes: A GoDARTS study. Diabetes, 64(5), 1786–1793.

Elahi, M. M., Cagampang, F. R., Mukhtar, D., Anthony, F. W., Ohri, S. K., and Hanson, M. A. (2009). Long-term maternal high-fat feeding from weaning through pregnancy and lactation

predisposes offspring to hypertension, raised plasma lipids and fatty liver in mice. British Journal of Nutrition, 102(4), 514–519.

Elie, A. G. I. M., Jensen, P. S., Nissen, K. D., Geraets, I. M. E., Xu, A., Song, E., Hansen, M. L., Irmukhamedov, A., Rasmussen, L. M., Wang, Y., and De Mey, J. G. R. (2016). Adipokine imbalance in the pericardial cavity of cardiac and vascular disease patients. PLoS ONE, 11(5), 1–14.

Fabbrini, E., Magkos, F., Mohammed, B. S., Pietka, T., Abumrad, N. A., Patterson, B. W., Okunade, A., and Klein, S. (2009). Intrahepatic fat , not visceral fat , is linked with metabolic complications of obesity. Proc Natl Acad Sci U S A., 106(36), 15430–5.

Fabrizil, G. M., Rizzuto, R., Nakasel, H., Mital, S., Lomax, M. I., Grossmano, L. I., and Schonl, E. A. (1989). Sequence of a cDNA specifying subunit VIIa of human cytochrome c oxidase. Nucleic Acids Research, 17(17), 7107.

Farooqi, I. S., Depaoli, A. M., Rahilly, S. O., Farooqi, I. S., Matarese, G., Lord, G. M., Keogh, J. M., Lawrence, E., Agwu, C., Sanna, V., Jebb, S. A., Perna, F., Fontana, S., Lechler, R. I., Depaoli, A. M., and Rahilly, S. O. (2002). Beneficial effects of leptin on obesity. The Journal of Clinical Investigation, 110(8), 1093–1103.

Faust, I. M., Johnson, P. R., Stern, J. S., and Hirsch, J. (1978). Diet-induced adipocyte number increase in adult rats: A new model of obesity. American Journal of Physiology Endocrinology Metabolism and Gastrointestinal Physiology, 4(3).

Fedorenko, A., Lishko, P. V., and Kirichok, Y. (2012). Mechanism of fatty-acid-dependent UCP1 uncoupling in brown fat mitochondria. Cell, 151(2), 400–413.

Feinstein, R., Kanety, H., Papa, M. Z., Lunenfeld, B., and Karasik, A. (1993). Tumor necrosis factor-α suppresses insulin-induced tyrosine phosphorylation of insulin receptor and its substrates. Journal of Biological Chemistry, 268(35), 26055–26058.

Feldmann, H. M., Golozoubova, V., Cannon, B., and Nedergaard, J. (2009). UCP1 Ablation Induces Obesity and Abolishes Diet-Induced Thermogenesis in Mice Exempt from Thermal Stress by Living at Thermoneutrality. Cell Metabolism, 9(2), 203–209.

Fernández-Real, J. M., Broch, M., Vendrell, J., and Ricart, W. (2003). Insulin resistance, inflammation, and serum fatty acid composition. Diabetes Care, 26(5), 1362–1368.

Fernandez-Twinn, D. S., Blackmore, H. L., Siggens, L., Giussani, D. A., Cross, C. M., Foo, R., and Ozanne, S. E. (2012). The programming of cardiac hypertrophy in the offspring by maternal obesity is associated with hyperinsulinemia, AKT, ERK, and mTOR activation. Endocrinology, 153(12), 5961–5971.

Ferreira, J. C., and Patino, C. M. (2017). Subgroup analysis and interaction tests: Why they are important and how to avoid common mistakes. Jornal Brasileiro de Pneumologia, 43(3), 162.

Finn, D., M. A. Lomax and P. Trayhurn (1998). An immunohistochemical and in situ hybridisation study of the postnatal development of uncoupling protein-1 and uncoupling protein-1 mRNA in lamb perirenal adipose tissue. Cell and Tissue Research, 294(3): 461-466.

Finucane, M. M., Stevens, G. A., Cowan, M., Lin, J. K., Paciorek, C. J., Singh, G. M., Gutierrez, H. R., Lu, Y., Bahalim, A. N., and Farzadfar, F. (2011). National, regional, and global trends in body mass index since 1980: Systematic analysis of health examination surveys and epidemiological studies with 960 country-years and 9.1 million participants. The Lancet, 377(9765), 557–567.

Fischer, I. P., Irmler, M., Meyer, C. W., Sachs, S. J., Neff, F., Hrabě de Angelis, M., Beckers, J., Tschöp, M. H., Hofmann, S. M., and Ussar, S. (2018). A history of obesity leaves an inflammatory fingerprint in liver and adipose tissue. International journal of obesity (2005), 42(3), 507–517.

Foretz, M., Hébrard, S., Leclerc, J., Zarrinpashneh, E., Soty, M., Mithieux, G., Sakamoto, K., Andreelli, F., and Viollet, B. (2010). Metformin inhibits hepatic gluconeogenesis in mice independently of the LKB1/AMPK pathway via a decrease in hepatic energy state. The Journal of clinical investigation, 120(7), 2355–2369.

Forsdahl, A. (1997). Are poor living conditions in childhood and adolescence an important risk factor for arteriosclerotic heart disease? British Journal OfPreventive and Social Medicine, 31(2), 91–95.

Fox, C. S., Gona, P., Hoffmann, U., Porter, S. A., Salton, C. J., Massaro, J. M., Levy, D., Larson, M. G., Agostino, R. B. D., Donnell, C. J. O., and Manning, W. J. (2009). Pericardial Fat, Intra-thoracic Fat, and Measures of Left Ventricular Structure and Function: The Framingham Heart Study. 119(12), 1586–1591.

Frederich, R. C., Hamann, A., Anderson, S., Löllmann, B., Lowell, B. B., and Flier, J. S. (1995). Leptin levels reflect body lipid content in mice: evidence for diet-induced resistance to leptin action. Nature medicine, 1(12), 1311–1314.

Friedman, J. M. (2011). Leptin and the Regulation of Body Weight. Keio Journal of Medicine, 60(1), 1–9.

Frühbeck, G., Méndez-Giménez, L., Fernández-Formoso, J. A., Fernández, S., and Rodríguez, A. (2014). Regulation of adipocyte lipolysis. In Nutrition Research Reviews, 27 (1). 63–93.

Fujikoshi, Y. (1993). Two-way ANOVA models with unbalanced data. Discrete Mathematics, 116(1–3), 315–334.

Fujioka, S., Matsuzawa, Y., Tokunaga, K., and Tarui, S. (1987). Contribution of intra-abdominal fat accumulation to the impairment of glucose and lipid metabolism in human obesity. Metabolism: clinical and experimental, 36(1), 54–59.

Fujita, K., Nishizawa, H., Funahashi, T., Shimomura, I., and Shimabukuro, M. (2006). Systemic oxidative stress is associated with visceral fat accumulation and the metabolic syndrome. Circulation Journal, 70(11), 1437–1442.

Fukumura, D., Ushiyama, A., Duda, D. G., Xu, L., Tam, J., Krishna, V., Chatterjee, K., Garkavtsev, I., and Jain, R. K. (2003). Paracrine regulation of angiogenesis and adipocyte differentiation during in vivo adipogenesis. Circulation research, 93(9), e88–e97.

Furukawa, S., Fujita, T., Shimabukuro, M., Iwaki, M., Yamada, Y., Nakajima, Y., Nakayama, O., Makishima, M., Matsuda, M., and Shimomura, I. (2004). Increased oxidative stress in obesity and its impact on metabolic syndrome. The Journal of clinical investigation, 114(12), 1752–1761.

Galuska, D., Nolte, L. A., Zierath, J. R., and Hospital, K. (1994). Effect of metformin on insulin-stimulated glucose transport in isolated skeletal muslce obtained from patients with NIDDM. Diabetologia, 37, 826–832.

Garcia, R. A., Roemmich, J. N., and Claycombe, K. J. (2016). Evaluation of markers of beige adipocytes in white adipose tissue of the mouse. Nutrition and Metabolism, 13(1), 1–14.

Gaspar, R. S., Unsworth, A. J., Al-Dibouni, A., Bye, A. P., Sage, T., Stewart, M., Wells, S., Cox, R. D., Gibbins, J. M., Sellayah, D., and E. Hughes, C. (2021). Maternal and offspring high-fat diet leads to platelet hyperactivation in male mice offspring. Scientific Reports, 11(1), 1–13.

Gillman, M. W., Oakey, H., Baghurst, P. A., Volkmer, R. E., Robinson, J. S., and Crowther, C. A. (2010). Effect of treatment of gestational diabetes mellitus on obesity in the next generation. Diabetes Care, 33(5), 964–968.

Giralt, M., Martin, I., Iglesias, R., Vinas, O., Villarroya, F., and Mampel, T. (1990). Ontogeny and perinatal modulation of gene expression in rat brown adipose tissue: Unaltered iodothyronine 5′-deiodinase activity is necessary for the response to environmental temperature at birth. European Journal of Biochemistry, 193(1), 297–302.

Gowans, G. J., Hawley, S. A., Ross, F. A., and Hardie, D. G. (2013). AMP is a true physiological regulator of amp-activated protein kinase by both allosteric activation and enhancing net phosphorylation. Cell Metabolism, 18(4), 556–566.

Granata, G. P., and Brandon, L. J. (2002). The thermic effect of food and obesity: Discrepant results and methodological variations. Nutrition Reviews, 60(8), 223–233.

Granneman, J. G., Burnazi, M., Zhu, Z., and Schwamb, L. A. (2003). White adipose tissue contributes to UCP1-independent thermogenesis. American journal of physiology. Endocrinology and metabolism, 285(6), E1230–E1236.

Green, H., and Meuth, M. (1974). An established pre-adipose cell line and its differentiation in culture. Cell, 3(2), 127–133.

Greenwood, M. R. C., and Hirsch, J. (1974). Postnatal development of adipocyte cellularity in the normal rat. Journal of Lipid Research, 15(5), 474–483.

Greif, M., Becker, A., Von Ziegler, F., Lebherz, C., Lehrke, M., Broedl, U. C., Tittus, J., Parhofer, K., Becker, C., Reiser, M., Knez, A., and Leber, A. W. (2009). Pericardial Adipose Tissue Determined by Dual Source CT Is a Risk Factor for Coronary Atherosclerosis. Arteriosclerosis, Thrombosis, and Vascular Biology, 29(5), 781–786.

Guauque-Olarte, S., Gaudreault, N., Piché, M. È., Fournier, D., Mauriège, P., Mathieu, P., and Bossé, Y. (2011). The transcriptome of human epicardial, mediastinal and subcutaneous adipose tissues in men with coronary artery disease. PLoS ONE, 6(5), e19908

Guberman, C., Jellyman, J. K., Han, G., Ross, M. G., and Desai, M. (2013). Maternal high-fat diet programs rat offspring hypertension and activates the adipose renin-angiotensin system. American Journal of Obstetrics and Gynecology, 209(3), 262.e1-262.e8.

Guénet J. L. (2005). The mouse genome. Genome research, 15(12), 1729–1740.

Gundewar, S., Calvert, J. W., Jha, S., Toedt-Pingel, I., Ji, S. Y., Nunez, D., Ramachandran, A., Anaya-Cisneros, M., Tian, R., and Lefer, D. J. (2009). Activation of AMP-activated protein kinase by metformin improves left ventricular function and survival in heart failure. Circulation research, 104(3), 403–411.

Guo, F., and Jen, K. L. C. (1995). High-fat feeding during pregnancy and lactation effects offspring metabolism in rats. Physiology and Behavior, 57(4), 681–686.

Hagberg, C. E., Li, Q., Kutschke, M., Bhowmick, D., Kiss, E., Shabalina, I. G., Harms, M. J., Shilkova, O., Kozina, V., Nedergaard, J., Boucher, J., Thorell, A., and Spalding, K. L. (2018). Flow Cytometry of Mouse and Human Adipocytes for the Analysis of Browning and Cellular Heterogeneity. Cell reports, 24(10), 2746–2756.e5.

Hales, C. N., and Barker, D. J. (2001). The thrifty phenotype hypothesis. British medical bulletin, 60, 5–20.

Hamilton, B. S., Paglia, D., Kwan, A. Y., and Deitel, M. (1995). Increased obese mRNA expression in omental fat cells from massively obese humans. Nature medicine, 1(9), 953–956.

Han, J., Lee, J. E., Jin, J., Lim, J. S., Oh, N., Kim, K., Chang, S. I., Shibuya, M., Kim, H., and Koh, G. Y. (2011). The spatiotemporal development of adipose tissue. Development, 138(22), 5027–5037.

Harman-Boehm, I., Blüher, M., Redel, H., Sion-Vardy, N., Ovadia, S., Avinoach, E., Shai, I., Klöting, N., Stumvoll, M., Bashan, N., and Rudich, A. (2007). Macrophage infiltration into omental versus subcutaneous fat across different populations: Effect of regional adiposity and the comorbidities of obesity. Journal of Clinical Endocrinology and Metabolism, 92(6), 2240–2247.

Hauner, H., Entenmann, G., Wabitsch, M., Gaillard, D., Ailhaud, G., Negrel, R., and Pfeiffer, E. F. (1989). Promoting effect of glucocorticoids on the differentiation of human adipocyte

precursor cells cultured in a chemically defined medium. Journal of Clinical Investigation, 84(5), 1663–1670.

Hawley, S. A., Selbert, M. A., Goldstein, E. G., Edelman, A. M., Carling, D., and Hardie, D. G. (1995). 5'-AMP activates the AMP-activated protein kinase cascade, and Ca2+/calmodulin activates the calmodulin-dependent protein kinase I cascade, via three independent mechanisms. Journal of Biological Chemistry, 270(45), 27186–27191.

He, J., Watkins, S., and Kelley, D. E. (2001). Skeletal muscle lipid content and oxidative enzyme activity in relation to muscle fiber type in type 2 diabetes and obesity. Diabetes, 50(4), 817–823.

He, Y., Chen, H., Quon, M. J., and Reitman, M. (1995). The mouse obese gene. Genomic organization, promoter activity, and activation by CCAAT/enhancer-binding protein alpha. The Journal of biological chemistry, 270(48), 28887–28891.

Hemmeryckx, B., Loeckx, D., Dresselaers, T., Himmelreich, U., Hoylaerts, M. F., and Roger Lijnen, H. (2010). Age-associated adaptations in murine adipose tissues. Endocrine Journal, 57(10), 925–930.

Henderson, J. F., and Khoo, K. Y. (1965). On the Mechanism of Feedback Inhibition of Purine Biosynthesis De Novo. The Journal of Biological Chemistry, 240(7), 3104–3109.

Henrichot, E., Juge-Aubry, C. E., Pernin, A., Pache, J. C., Velebit, V., Dayer, J. M., Meda, P., Chizzolini, C., and Meier, C. A. (2005). Production of chemokines by perivascular adipose tissue: A role in the pathogenesis of atherosclerosis? Arteriosclerosis, Thrombosis, and Vascular Biology, 25(12), 2594–2599.

Hess, C., Unger, M., Madea, B., Stratmann, B., and Tschoepe, D. (2018). Range of therapeutic metformin concentrations in clinical blood samples and comparison to a forensic case with death due to lactic acidosis. Forensic science international, 286, 106–112.

Hibi, M., Oishi, S., Matsushita, M., Yoneshiro, T., Yamaguchi, T., Usui, C., Yasunaga, K., Katsuragi, Y., Kubota, K., Tanaka, S., and Saito, M. (2016). Brown adipose tissue is involved in diet-induced thermogenesis and whole-body fat utilization in healthy humans. International Journal of Obesity, 40(11), 1655–1661.

Hirata, Y., Tabata, M., Kurobe, H., Motoki, T., Akaike, M., Nishio, C., Higashida, M., Mikasa, H., Nakaya, Y., Takanashi, S., Igarashi, T., Kitagawa, T., and Sata, M. (2011). Coronary atherosclerosis is associated with macrophage polarization in epicardial adipose tissue. Journal of the American College of Cardiology, 58(3), 248–255.

Hoffstedt, J., Arner, E., Wahrenberg, H., Andersson, D. P., Qvisth, V., Löfgren, P., Rydén, M., Thörne, A., Wirén, M., Palmér, M., Thorell, A., Toft, E., and Arner, P. (2010). Regional impact of adipose tissue morphology on the metabolic profile in morbid obesity. Diabetologia, 53(12), 2496–2503.

Hollenberg, C. H., and Vost, A. (1968). Regulation of DNA synthesis in fat cells and stromal elements from rat adipose tissue. The Journal of Clinical Investigation, 47(11), 2485–2498.

Horakova, O., Kroupova, P., Bardova, K., Buresova, J., Janovska, P., Kopecky, J., and Rossmeisl, M. (2019). Metformin acutely lowers blood glucose levels by inhibition of intestinal glucose transport. Scientific reports, 9(1), 6156.

Horckmans, M., Bianchini, M., Santovito, D., Megens, R. T. A., Springael, J. Y., Negri, I., Vacca, M., Di Eusanio, M., Moschetta, A., Weber, C., Duchene, J., and Steffens, S. (2018). Pericardial adipose tissue regulates granulopoiesis, fibrosis, and cardiac function after myocardial infarction. Circulation, 137(9), 948–960.

Horwich, T. B., Fonarow, G. C., Hamilton, M. A., MacLellan, W. R., Woo, M. A., and Tillisch, J. H. (2001). The relationship between obesity and mortality in patients with heart failure. Journal of the American College of Cardiology, 38(3), 789–795.

Hosogai, N., Fukuhara, A., Oshima, K., Miyata, Y., Tanaka, S., Segawa, K., Furukawa, S., Tochino, Y., Komuro, R., Matsuda, M., and Shimomura, I. (2007). Adipose tissue hypoxia in obesity and its impact on adipocytokine dysregulation. Diabetes, 56(4), 901–911.

Hotamisligil, G. S., Arner, P., Caro, J. F., Atkinson, R. L., and Spiegelman, B. M. (1995). Increased adipose tissue expression of tumor necrosis factor-alpha in human obesity and insulin resistance. The Journal of clinical investigation, 95(5), 2409–2415.

Hotamisligil, G. S., Murray, D. L., Choy, L. N., Spiegelman, B. M., and Kirschner, M. W. (1994). Tumor necrosis factor a inhibits signaling from the insulin receptor. Proceedings of the National Academy of Sciences of the United States of America, 91(May), 4854–4858.

Hotamisligil, G. S., Shargill, N. S., and Spiegelman, B. M. (1993). Adipose expression of tumor necrosis factor-alpha: direct role in obesity-linked insulin resistance. Science (New York, N.Y.), 259(5091), 87–91.

Houstěk, J., Vízek, K., Pavelka, S., Kopecký, J., Krejcová, E., Hermanská, J., and Cermáková, M. (1993). Type II iodothyronine 5'-deiodinase and uncoupling protein in brown adipose tissue of human newborns. The Journal of clinical endocrinology and metabolism, 77(2), 382–387.

Hu, E., Liang, P., and Spiegelman, B. M. (1996). AdipoQ is a novel adipose-specific gene dysregulated in obesity. Journal of Biological Chemistry, 271(18), 10697–10703.

Huang, P. L., Chen, Y. C., Chen, L. H., Juan, C. C., Ku, H. H., Wang, S. T., Chiou, S. H., Chiou, G. Y., Chi, C. W., Hsu, C. C., Lee, H. C., Chen, L. K., and Kao, C. L. (2011). PGC-1α mediates differentiation of mesenchymal stem cells to brown adipose cells. Journal of Atherosclerosis and Thrombosis, 18(11), 966–980.

Hundal, R. S., Krssak, M., Dufour, S., Laurent, D., Lebon, V., Chandramouli, V., Inzucchi, S. E., Schumann, W. C., Petersen, K. F., Landau, B. R., and Shulman, G. I. (2000). Mechanism by Which Metformin Reduces Glucose Production in Type 2 Diabetes. Diabetes, 49(12), 2063–2069.

Hwang, C. S., Mandrup, S., MacDougald, O. A., Geiman, D. E., and Lane, M. D. (1996). Transcriptional activation of the mouse obese (ob) gene by CCAAT/enhancer binding protein alpha. Proceedings of the National Academy of Sciences of the United States of America, 93(2), 873–877.

Hwang, L. L., Wang, C. H., Li, T. L., Chang, S. D., Lin, L. C., Chen, C. P., Chen, C. T., Liang, K. C., Ho, I. K., Yang, W. S., and Chiou, L. C. (2010). Sex differences in high-fat diet-induced obesity, metabolic alterations and learning, and synaptic plasticity deficits in mice. Obesity (Silver Spring, Md.), 18(3), 463–469.

Iacobellis, G., and Leonetti, F. (2005). Epicardial adipose tissue and insulin resistance in obese subjects. Journal of Clinical Endocrinology and Metabolism, 90(11), 6300–6302.

Iacobellis, G., Singh, N., Wharton, S., and Sharma, A. M. (2008). Substantial changes in epicardial fat thickness after weight loss in severely obese subjects. Obesity, 16(7), 1693–1697.

Imai, T., Takakuwa, R., Marchand, S., Dentz, E., Bornert, J. M., Messaddeq, N., Wendling, O., Mark, M., Desvergne, B., Wahli, W., Chambon, P., and Metzger, D. (2004). Peroxisome proliferator-activated receptor gamma is required in mature white and brown adipocytes for their survival in the mouse. Proceedings of the National Academy of Sciences of the United States of America, 101(13), 4543–4547.

Iozzo, P., Lautamaki, R., Borra, R., Lehto, H. R., Bucci, M., Viljanen, A., Parkka, J., Lepomaki, V., Maggio, R., Parkkola, R., Knuuti, J., and Nuutila, P. (2009). Contribution of glucose tolerance and gender to cardiac adiposity. Journal of Clinical Endocrinology and Metabolism, 94(11), 4472–4482.

Itani, S. I., Ruderman, N. B., Schmieder, F., and Boden, G. (2002). Lipid-induced insulin resistance in human muscle is associated with changes in diacylglycerol, protein kinase C, and IκB-α. Diabetes, 51(7), 2005–2011.

Iwabu, M., Yamauchi, T., Okada-Iwabu, M., Sato, K., Nakagawa, T., Funata, M., Yamaguchi, M., Namiki, S., Nakayama, R., Tabata, M., Ogata, H., Kubota, N., Takamoto, I., Hayashi, Y. K., Yamauchi, N., Waki, H., Fukayama, M., Nishino, I., Tokuyama, K., Kadowaki, T. (2010). Adiponectin and AdipoR1 regulate PGC-1α and mitochondria by Ca 2+ and AMPK/SIRT1. Nature, 464(7293), 1313–1319.

Jagannathan, R., Thapa, D., Nichols, C. E., Shepherd, D. L., Stricker, J. C., Croston, T. L., Baseler, W. A., Lewis, S. E., Martinez, I., and Hollander, J. M. (2015). Translational Regulation of the Mitochondrial Genome Following Redistribution of Mitochondrial MicroRNA in the Diabetic Heart. Circulation. Cardiovascular genetics, 8(6), 785–802.

Jäger, S., Handschin, C., St-Pierre, J., and Spiegelman, B. M. (2007). AMP-activated protein kinase (AMPK) action in skeletal muscle via direct phosphorylation of PGC-1α. Proceedings of the National Academy of Sciences of the United States of America, 104(29), 12017–12022.

Jeffery, E., Church, C. D., Holtrup, B., Colman, L., and Matthew, S. (2015). Rapid Depot-Specific Activation of Adipocyte Precursor Cells at the Onset of Obesity. Nature Cell Biology, 17(4), 376–385.

Jespersen, N. Z., Larsen, T. J., Peijs, L., Daugaard, S., Homøe, P., Loft, A., De Jong, J., Mathur, N., Cannon, B., Nedergaard, J., Pedersen, B. K., Møller, K., and Scheele, C. (2013). A classical brown adipose tissue mrna signature partly overlaps with brite in the supraclavicular region of adult humans. Cell Metabolism, 17(5), 798–805.

Jiang, Y., Berry, D. C., Tang, W., and Graff, J. M. (2014). Independent stem cell lineages regulate adipose organogenesis and adipose homeostasis. Cell reports, 9(3), 1007–1022.

Jimenez, J. G., Fong, B., Julien, P., Després J. P., Rotstein, L., and Angel, A. (1989). Effect of massive obesity on low and high density lipoprotein binding to human adipocyte plasma membranes. International journal of obesity, 13(5), 699–709.

Jimenez, M., Barbatelli, G., Allevi, R., Cinti, S., Seydoux, J., Giacobino, J. P., Muzzin, P., and Preitner, F. (2003). β3-adrenoceptor knockout in C57BL/6J mice depresses the occurrence of brown adipocytes in white fat. European Journal of Biochemistry, 270(4), 699–705.

Jing, Y., Wu, F., Li, D., Yang, L., Li, Q., and Li, R. (2018). Metformin improves obesity-associated inflammation by altering macrophages polarization. Molecular and Cellular Endocrinology, 461(1), 256–264.

Jo, J., Gavrilova, O., Pack, S., Jou, W., Mullen, S., Sumner, A. E., Cushman, S. W., and Periwal, V. (2009). Hypertrophy and/or Hyperplasia: Dynamics of Adipose Tissue Growth. PLoS computational biology, 5(3), e1000324.

Joe, A. W., Yi, L., Even, Y., Vogl, A. W., and Rossi, F. M. (2009). Depot-specific differences in adipogenic progenitor abundance and proliferative response to high-fat diet. Stem cells (Dayton, Ohio), 27(10), 2563–2570.

Jousse, C., Parry, L., Lambert-Langlais, S., Maurin, A., Averous, J., Bruhat, A., Carraro, V., Tost, J., Letteron, P., Chen, P., Jockers, R., Launay, J., Mallet, J., and Fafournoux, P. (2011). Perinatal undernutrition effects the methylation and expression of the leptin gene in adults: implication for the understanding of metabolic syndrome. The FASEB Journal, 25(9), 3271–3278.

Kabir, M., Stefanovski, D., Hsu, I. R., Iyer, M., Woolcott, O. O., Zheng, D., Catalano, K. J., Chiu, J. D., Kim, S. P., Harrison, L. N., Ionut, V., Lottati, M., Bergman, R. N., and Richey, J. M. (2011). Large size cells in the visceral adipose depot predict insulin resistance in the canine model. Obesity (Silver Spring, Md.), 19(11), 2121–2129.

Kajimura, S., Seale, P., and Spiegelman, B. M. (2010). Transcriptional Control of Brown Fat Development. Cell Metabolism, 11(4), 257–262.

Kamohara, S., Burcelin, R., Halaas, J. L., Friedman, J. M., and Charron, M. J. (1997). Acute stimulation of glucose metabolism in mice by leptin treatment. Nature, 389(6649), 374–377.

Kanda, H., Tateya, S., Tamori, Y., Kotani, K., Hiasa, K., Kitazawa, R., Kitazawa, S., Miyachi, H., Maeda, S., Egashira, K., and others. (2006). MCP-1 contributes to macrophage infiltration into adipose tissue, insulin resistance, and hepatic steatosis in obesity. Journal of Clinical Investigation, 116(6), 1494.

Kang, Y. E., Choung, S., Lee, J. H., Kim, H. J., and Ku, B. J. (2017a). The role of circulating slit2, the one of the newly batokines, in human diabetes mellitus. Endocrinology and Metabolism, 32(3), 383–388.

Kang, Y. M., Jung, C. H., Cho, Y. K., Jang, J. E., Hwang, J. Y., Kim, E. H., Lee, W. J., Park, J. Y., and Kim, H. K. (2017b). Visceral adiposity index predicts the conversion of metabolically healthy obesity to an unhealthy phenotype. PLoS ONE, 12(6), 1–14.

Kankaanpää, M., Lehto, H. R., Pärkkä, J. P., Komu, M., Viljanen, A., Ferrannini, E., Knuuti, J., Nuutila, P., Parkkola, R., and Iozzo, P. (2006). Myocardial triglyceride content and epicardial fat mass in human obesity: relationship to left ventricular function and serum free fatty acid levels. The Journal of clinical endocrinology and metabolism, 91(11), 4689–4695.

Kapoor, J. R., and Heidenreich, P. A. (2010). Obesity and survival in patients with heart failure and preserved systolic function: A U-shaped relationship. American Heart Journal, 159(1), 75–80.

Karelis, A. D., St-Pierre, D. H., Conus, F., Rabasa-Lhoret, R., and Poehlman, E. T. (2004). Metabolic and body composition factors in subgroups of obesity: What do we know? Journal of Clinical Endocrinology and Metabolism, 89(6), 2569–2575.

Karise, I., Bargut, T. C., del Sol, M., Aguila, M. B., and Mandarim-de-Lacerda, C. A. (2019). Metformin enhances mitochondrial biogenesis and thermogenesis in brown adipocytes of mice. Biomedicine and Pharmacotherapy, 111(October 2018), 1156–1165.

Karnewar, S., Neeli, P. K., Panuganti, D., Kotagiri, S., Mallappa, S., Jain, N., Jerald, M. K., and Kotamraju, S. (2018). Metformin regulates mitochondrial biogenesis and senescence through

AMPK mediated H3K79 methylation: Relevance in age-associated vascular dysfunction. Biochimica et biophysica acta. Molecular basis of disease, 1864(4 Pt A), 1115–1128.

Kazumi, T., Kawaguchi, A., Hirano, T., and Yoshino, G. (2004). Serum Adiponectin Is Associated with High-Density Lipoprotein Cholesterol, Triglycerides, and Low-Density Lipoprotein Particle Size in Young Healthy Men. Metabolism: Clinical and Experimental, 53(5), 589–593.

Kelley, D. E., and Simoneau, J. A. (1994). Impaired free fatty acid utilization by skeletal muscle in non-insulin- dependent diabetes mellitus. Journal of Clinical Investigation, 94(6), 2349–2356.

Kelley, D. E., He, J., Menshikova, E. V., and Ritov, V. B. (2002). Dysfunction of mitochondria in human skeletal muscle in type 2 diabetes. Diabetes, 51(10), 2944–2950.

Kern, P. A., Ranganathan, S., Li, C., Wood, L., and Ranganathan, G. (2001). Adipose tissue tumor necrosis factor and interleukin-6 expression in human obesity and insulin resistance. American journal of physiology. Endocrinology and metabolism, 280(5), E745–E751.

Kershaw, E. E., and Flier, J. S. (2004). Adipose tissue as an endocrine organ. Journal of Clinical Endocrinology and Metabolism, 89(6), 2548–2556.

Khan, M. N., Rahman, M. M., Shariff, A. A., Rahman, M. M., Rahman, M. S., and Rahman, M. A. (2017). Maternal undernutrition and excessive body weight and risk of birth and health outcomes. Archives of Public Health, 75(1), 1–10.

Kim, D. W., Kim, B. S., Kwon, H. S., Kim, C. G., Lee, H. W., Choi, W. H., and Kim, C. G. (2003). Atrophy of brown adipocytes in the adult mouse causes transformation into white adipocyte-like cells. Experimental and Molecular Medicine, 35(6), 518–526.

Kim, J. Y., Van De Wall, E., Laplante, M., Azzara, A., Trujillo, M. E., Hofmann, S. M., Schraw, T., Durand, J. L., Li, H., Li, G., Jelicks, L. A., Mehler, M. F., Hui, D. Y., Deshaies, Y., Shulman, G. I., Schwartz, G. J., and Scherer, P. E. (2007). Obesity-associated improvements in

metabolic profile through expansion of adipose tissue. Journal of Clinical Investigation, 117(9), 2621–2637.

Kim, K., Nam, K. H., Yi, S. A., Park, J. W., Han, J. W., and Lee, J. (2020). Ginsenoside Rg3 induces browning of 3T3-L1 adipocytes by activating AMPK signaling. Nutrients, 12(2), 1–11.

Kim, K. Y., Kim, J. K., Jeon, J. H., Yoon, S. R., Choi, I., and Yang, Y. (2005). c-Jun N-terminal kinase is involved in the suppression of adiponectin expression by TNF-α in 3T3-L1 adipocytes. Biochemical and Biophysical Research Communications, 327(2), 460–467.

Kleiner, S., Mepani, R. J., Laznik, D., Ye, L., Jurczak, M. J., Jornayvaz, F. R., Estall, J. L., Bhowmick, D. C., Shulman, G. I., and Spiegelman, B. M. (2012). Development of insulin resistance in mice lacking PGC-1α in adipose tissues. Proceedings of the National Academy of Sciences of the United States of America, 109(24), 9635–9640.

Klöting, N., Fasshauer, M., Dietrich, A., Kovacs, P., Schön, M. R., Kern, M., Stumvoll, M., and Blüher, M. (2010). Insulin-sensitive obesity. American Journal of Physiology - Endocrinology and Metabolism, 299(3), 506–515.

Knittle, J. L., Timmers, K., Ginsberg-Fellner, F., Brown, R. E., and Katz, D. P. (1979). The growth of adipose tissue in children and adolescents. Cross-sectional and longitudinal studies of adipose cell number and size. Journal of Clinical Investigation, 63(2), 239–246.

Kolak, M., Yki-Järvinen, H., Kannisto, K., Tiikkainen, M., Hamsten, A., Eriksson, P., and Fisher, R. M. (2007). Effects of chronic rosiglitazone therapy on gene expression in human adipose tissue in vivo in patients with type 2 diabetes. Journal of Clinical Endocrinology and Metabolism, 92(2), 720–724.

Konrad, D., Rudich, A., Bilan, P. J., Patel, N., Richardson, C., Witters, L. A., and Klip, A. (2005). Troglitazone causes acute mitochondrial membrane depolarisation and an AMPK-mediated increase in glucose phosphorylation in muscle cells. Diabetologia, 48(5), 954–966.

Kontani, Y., Wang, Y., Kimura, K., Inokuma, K. I., Saito, M., Suzuki-Miura, T., Wang, Z., Sato, Y., Mori, N., and Yamashita, H. (2005). UCP1 deficiency increases susceptibility to diet-induced obesity with age. Aging Cell, 4(3), 147–155.

Kopecky, J., Clarke, G., Enerbäck, S., Spiegelman, B., and Kozak, L. P. (1995). Expression of the mitochondrial uncoupling protein gene from the aP2 gene promoter prevents genetic obesity. Journal of Clinical Investigation, 96(6), 2914–2923.

Kotzbeck, P., Giordano, A., Mondini, E., Murano, I., Severi, I., Venema, W., Cecchini, M. P., Kershaw, E. E., Barbatelli, G., Haemmerle, G., Zechner, R., and Cinti, S. (2018). Brown adipose tissue whitening leads to brown adipocyte death and adipose tissue inflammation. Journal of Lipid Research, 59(5), 784–794.

Kozak, L. P., Newman, S., Chao, P. M., Mendoza, T., and Koza, R. A. (2010). The early nutritional environment of mice determines the capacity for adipose tissue expansion by modulating genes of caveolae structure. PLoS ONE, 5(6).

Krantz. (2019). Main Effects and Interactions.

Krief, S., Ltnnqvist, F., Raimbault, S., Baude, B., Spronsen, A. Van, Amer, P., Strosberg, A. D., Ricquier, D., and Emorine, L. J. (1993). Tissue Distribution of B3-adrenergic Receptor mRNA in Man. Journal of Clinical Investigation, 91(January), 344–349.

Krotkiewski, M., Bjorntorp, P., Sjostrom, L., and Smith, U. (1983). Impact of obesity on metabolism in men and women. Importance of regional adipose tissue distribution. Journal of Clinical Investigation, 72(3), 1150–1162.

Kuipers, E. N., Held, N. M., In Het Panhuis, W., Modder, M., Ruppert, P. M. M., Kersten, S., Kooijman, S., Guigas, B., Houtkooper, R. H., Rensen, P. C. N., and Boon, M. R. (2019). A single day of high-fat diet feeding induces lipid accumulation and insulin resistance in brown adipose tissue in mice. American Journal of Physiology. Endocrinology and Metabolism, 317(5), E820–E830.

Kulkarni, R. N., Wang, Z. L., Wang, R. M., Hurley, J. D., Smith, D. M., Ghatei, M. A., Withers, D. J., Gardiner, J. V., Bailey, C. J., and Bloom, S. R. (1997). Leptin rapidly suppresses insulin release from insulinoma cells, rat and human islets and, in vivo, in mice. Journal of Clinical Investigation, 100(11), 2729–2736.

Kurebayashi, S., Sumitani, S., Kasayama, S., Jetten, A. M., and Hirose, T. (2001). TNF-alpha inhibits 3T3-L1 adipocyte differentiation without downregulating the expression of C/EBPbeta and delta. Endocrine journal, 48(2), 249–253.

Kurylowicz, A., Jonas, M., Lisik, W., Jonas, M., Wicik, Z. A., Wierzbicki, Z., Chmura, A., and Puzianowska-Kuznicka, M. (2015). Obesity is associated with a decrease in expression but not with the hypermethylation of thermogenesis-related genes in adipose tissues. Journal of translational medicine, 13, 31.

Laforest, S., Labrecque, J., Michaud, A., Cianflone, K., and Tchernof, A. (2015). Adipocyte size as a determinant of metabolic disease and adipose tissue dysfunction. Critical Reviews in Clinical Laboratory Sciences, 52(6), 301–313.

Lager, S., Jansson, N., Olsson, A. L., Wennergren, M., Jansson, T., and Powell, T. L. (2011). Effect of IL-6 and TNF-α on fatty acid uptake in cultured human primary trophoblast cells. Placenta, 32(2), 121–127.

Lagouge, M., Argmann, C., Gerhart-Hines, Z., Meziane, H., Lerin, C., Daussin, F., Messadeq, N., Milne, J., Lambert, P., Elliott, P., Geny, B., Laakso, M., Puigserver, P., and Auwerx, J. (2006). Resveratrol Improves Mitochondrial Function and Protects against Metabolic Disease by Activating SIRT1 and PGC-1α. Cell, 127(6), 1109–1122.

Lapidus, L., Bengtsson, C., Larsson, B., Pennert, K., Rybo, E., and Sjöström, L. (1984). Distribution of adipose tissue and risk of cardiovascular disease and death: A 12 year follow up of participants in the population study of women in Gothenburg, Sweden. British Medical Journal, 289(6454), 1257–1261.

Larsen, T. M., Toubro, S., Van Baak, M. A., Gottesdiener, K. M., Larson, P., Saris, W. H. M., and Astrup, A. (2002). Effect of a 28-d treatment with L-796568, a novel β3-adrenergic receptor agonist, on energy expenditure and body composition in obese men. American Journal of Clinical Nutrition, 76(4), 780–788.

Larson-Meyer, D. E., Heilbronn, L. K., Redman, L. M., Newcomer, B. R., Frisard, M. I., Anton, S., Smith, S. R., Alfonso, A., and Ravussin, E. (2006). Effect of calorie restriction with or without exercise on insulin sensitivity, beta-cell function, fat cell size, and ectopic lipid in overweight subjects. Diabetes care, 29(6), 1337–1344.

Larsson, B., Svärdsudd, K., Welin, L., Wilhelmsen, L., Björntorp, P., and Tibblin, G. (1984). Abdominal adipose tissue distribution, obesity, and risk of cardiovascular disease and death: 13 year follow up of participants in the study of men born in 1913. British medical journal (Clinical research ed.), 288(6428), 1401–1404.

Lean M. E. (1989). Brown adipose tissue in humans. The Proceedings of the Nutrition Society, 48(2), 243–256.

Lecoutre, S., Deracinois, B., Laborie, C., Eberlé, D., Guinez, C., Panchenko, P. E., Lesage, J., Vieau, D., Junien, C., Gabory, A., and Breton, C. (2016). Depot- and sex-specific effects of maternal obesity in offspring's adipose tissue. Journal of Endocrinology, 230(1), 39–53.

Lee, H., Kang, R., Bae, S., and Yoon, Y. (2011). AICAR, an activator of AMPK, inhibits adipogenesis via the WNT/β-catenin pathway in 3T3-L1 adipocytes. International journal of molecular medicine, 28(1), 65–71.

Lee, P., Werner, C. D., Kebebew, E., and Celi, F. S. (2014). Functional thermogenic beige adipogenesis is inducible in human neck fat. International Journal of Obesity, 38(2), 170–176.

Lee, S. H., Chen, Y. C., Chen, Y. J., Chang, S. L., Tai, C. T., Wongcharoen, W., Yeh, H. I., Lin, C. I., and Chen, S. A. (2007). Tumor necrosis factor-α alters calcium handling and increases arrhythmogenesis of pulmonary vein cardiomyocytes. Life Sciences, 80(19), 1806–1815.

Lee, Y. H., Petkova, A. P., Mottillo, E. P., and Granneman, J. G. (2012). In vivo identification of bipotential adipocyte progenitors recruited by β3-adrenoceptor activation and high-fat feeding. Cell metabolism, 15(4), 480–491.

Lefterova, M. I., Zhang, Y., Steger, D. J., Schupp, M., Schug, J., Cristancho, A., Feng, D., Zhuo, D., Stoeckert, C. J., Liu, X. S., and Lazar, M. A. (2008). PPARγ and C/EBP factors orchestrate adipocyte biology via adjacent binding on a genome-wide scale. Genes and Development, 22(21), 2941–2952.

Lepper, C., and Fan, C. M. (2010). Inducible lineage tracing of Pax7-descendant cells reveals embryonic origin of adult satellite cells. Genesis (New York, N.Y. : 2000), 48(7), 424–436.

Li, A., Zhang, S., Li, J., Liu, K., Huang, F., and Liu, B. (2016). Metformin and resveratrol inhibit Drp1-mediated mitochondrial fission and prevent ER stress-associated NLRP3 inflammasome activation in the adipose tissue of diabetic mice. Molecular and Cellular Endocrinology, 434, 36–47.

Liang, X., Yang, Q., Fu, X., Rogers, C. J., Wang, B., Pan, H., Zhu, M. J., Nathanielsz, P. W., and Du, M. (2016a). Maternal obesity epigenetically alters visceral fat progenitor cell properties in male offspring mice. Journal of Physiology, 594(15), 4453–4466.

Liang, X., Yang, Q., Zhang, L., Maricelli, J. W., Rodgers, B. D., Zhu, M. J., and Du, M. (2016). Maternal high-fat diet during lactation impairs thermogenic function of brown adipose tissue in offspring mice. Scientific Reports, 6(May), 1–12.

Licholai, J. A., Nguyen, K. P., Fobbs, W. C., Schuster, C. J., Ali, M. A., and Kravitz, A. V. (2018). Why Do Mice Overeat High-Fat Diets? How High-Fat Diet Alters the Regulation of Daily Caloric Intake in Mice. Obesity (Silver Spring, Md.), 26(6), 1026–1033.

Lidell, M. E., Betz, M. J., and Enerbäck, S. (2014). Brown adipose tissue and its therapeutic potential. Journal of Internal Medicine, 276(4), 364–377.

Lim, E. L., Hollingsworth, K. G., Aribisala, B. S., Chen, M. J., Mathers, J. C., and Taylor, R. (2011). Reversal of type 2 diabetes: Normalisation of beta cell function in association with decreased pancreas and liver triacylglycerol. Diabetologia, 54(10), 2506–2514.

Lim, Y. C., Chia, S. Y., Jin, S., Han, W., Ding, C., and Sun, L. (2016). Dynamic DNA methylation landscape defines brown and white cell specificity during adipogenesis. Molecular Metabolism, 5(10), 1033–1041.

Lin, F. T., and Lane, M. D. (1992). Antisense CCAAT/enhancer-binding protein RNA suppresses coordinate gene expression and triglyceride accumulation during differentiation of 3T3-L1 preadipocytes. Genes and Development, 6(4), 533–544.

Lin, J., Xie, Z., Zhu, H., and Qian, J. (2010). Understanding protein phosphorylation on a systems level. Briefings in Functional Genomics and Proteomics, 9(1), 32–42.

Linhart, H. G., Ishimura-Oka, K., Demayo, F., Kibe, T., Repka, D., Poindexter, B., Bick, R. J., and Darlington, G. J. (2001). C/EBPα is required for differentiation of white but not brown adipose tissue. Proceedings of the National Academy of Sciences of the United States of America, 98(22), 12532–12537.

Liu, C., Wang, C., Guan, S., Liu, H., Wu, X., Zhang, Z., Gu, X., Zhang, Y., Zhao, Y., Tse, L. A., and Fang, X. (2019). The Prevalence of Metabolically Healthy and Unhealthy Obesity according to Different Criteria. Obesity Facts, 12(1), 78–90.

Liu, J., Fox, C. S., Hickson, D. M. A., May, W. L., Ding, J., Carr, J. J., and Taylor, H. A. (2011). Pericardial fat and echocardiographic measures of cardiac abnormalities: The jackson heart study. Diabetes Care, 34(2), 341–346.

Liu, J., Fox, C. S., Hickson, D. M., Sarpong, D., Ekunwe, L., May, W. D., Hundley, G. W., Carr, J. J., and Taylor, H. A. (2010). Pericardial adipose tissue, atherosclerosis, and cardiovascular disease risk factors: The Jackson heart study. Diabetes Care, 33(7), 1635–1639.

Liu, Q., Huang, X., Oh, J. H., Lin, R. Z., Duan, S., Yu, Y., Yang, R., Qiu, J., Melero-Martin, J. M., Pu, W. T., and Zhou, B. (2014). Epicardium-to-fat transition in injured heart. Cell Research, 24(11), 1367–1369.

Loche, E., Blackmore, H. L., Carpenter, A. A., Beeson, J. H., Pinnock, A., Ashmore, T. J., Aiken, C. E., de Almeida-Faria, J., Schoonejans, J. M., Giussani, D. A., Fernandez-Twinn, D. S., and Ozanne, S. E. (2018). Maternal diet-induced obesity programmes cardiac dysfunction in male mice independently of post-weaning diet. Cardiovascular research, 114(10), 1372–1384.

Long, N. M., Rule, D. C., Zhu, M. J., Nathanielsz, P. W., and Ford, S. P. (2012). Maternal obesity upregulates fatty acid and glucose transporters and increases expression of enzymes mediating fatty acid biosynthesis in fetal adipose tissue depots. Journal of Animal Science, 90(7), 2201–2210.

Lönn, M., Mehlig, K., Bengtsson, C., and Lissner, L. (2010). Adipocyte size predicts incidence of type 2 diabetes in women. FASEB journal: official publication of the Federation of American Societies for Experimental Biology, 24(1), 326–331.

Lowell, B. B., and Shulman, G. I. (2005). Mitochondrial dysfunction and type 2 diabetes. Science, 307(5708), 384–387.

Lowell, B. B., and Spiegelman, B. M. (2000). Towards a molecular understanding of adaptive thermogenesis. Nature, 404(6778), 652–660.

Lukas, G., Brindle, S. D., and Greengard, P. (1971). The route of absorption of intraperitoneally administered compounds. The Journal of pharmacology and experimental therapeutics, 178(3), 562–564.

Lukaszewski, M. A., Mayeur, S., Fajardy, I., Delahaye, F., Dutriez-Casteloot, I., Montel, V., Dickes-Coopman, A., Laborie, C., Lesage, J., Vieau, D., and Breton, C. (2011). Maternal prenatal undernutrition programs adipose tissue gene expression in adult male rat offspring

under high-fat diet. American journal of physiology. Endocrinology and metabolism, 301(3), E548–E559.

Lyons, M. R., Peterson, L. R., McGill, J. B., Herrero, P., Coggan, A. R., Saeed, I. M., Recklein, C., Schechtman, K. B., and Gropler, R. J. (2013). Impact of sex on the heart's metabolic and functional responses to diabetic therapies. American Journal of Physiology - Heart and Circulatory Physiology, 305(11).

Mahabadi, A. A., Massaro, J. M., Rosito, G. A., Levy, D., Murabito, J. M., Wolf, P. A., O'Donnell, C. J., Fox, C. S., and Hoffmann, U. (2009). Association of pericardial fat, intrathoracic fat, and visceral abdominal fat with cardiovascular disease burden: The Framingham Heart Study. European Heart Journal, 30(7), 850–856.

Mahdaviani, K., Benador, I., and Shirihai, O. (2015). Assessment of Brown Adipocyte Thermogenic Function by High-throughput Respirometry. Bio-protocol, 5(21), e1641.

Manchado, C., Yubero, P., Viñas, O., Iglesias, R., Villarroya, F., Mampel, T., and Giralt, M. (1994). CCAAT/enhancer-binding proteins alpha and beta in brown adipose tissue: evidence for a tissue-specific pattern of expression during development. The Biochemical journal, 302 (Pt 3)(Pt 3), 695–700.

Manson, J. E., Colditz, G. A., Stampfer, M. J., Willett, W. C., Rosner, B., Monson, R. R., Speizer, F. E., and Hennekens, C. H. (1990). A prospective study of obesity and risk of coronary heart disease in women. The New England journal of medicine, 322(13), 882–889.

Marchington, J. M., and Pond, C. M. (1990). Site-specific properties of pericardial and epicardial adipose tissue: the effects of insulin and high-fat feeding on lipogenesis and the incorporation of fatty acids in vitro. International journal of obesity, 14(12), 1013–1022.

Mary, G. Hancock, C., Holman, N., Outwaite, H., Oldridge, L., Anna, C., Ells, L. (2014). Adult Obesity and Type 2 Diabetes. Public Health England, 1–39.

Maurer, S. F., Fromme, T., Grossman, L. I., Hüttemann, M., and Klingenspor, M. (2015). The brown and brite adipocyte marker Cox7a1 is not required for non-shivering thermogenesis in mice. Scientific reports, 5, 17704.

McAninch, E. A., Fonseca, T. L., Poggioli, R., Panos, A. L., Salerno, T. A., Deng, Y., Li, Y., Bianco, A. C., and Iacobellis, G. (2015). Epicardial adipose tissue has a unique transcriptome modified in severe coronary artery disease. Obesity, 23(6), 1267–1278.

McGill, H. C., McMahan, C. A., Herderick, E. E., Zieske, A. W., Malcom, G. T., Tracy, R. E., and Strong, J. P. (2002). Obesity accelerates the progression of coronary atherosclerosis in young men. Circulation, 105(23), 2712–2718.

McLaughlin, T., Lamendola, C., Liu, A., and Abbasi, F. (2011). Preferential fat deposition in subcutaneous versus visceral depots is associated with insulin sensitivity. The Journal of clinical endocrinology and metabolism, 96(11), E1756–E1760.

McQuaid, S. E., Hodson, L., Neville, M. J., Dennis, A. L., Cheeseman, J., Humphreys, S. M., Ruge, T., Gilbert, M., Fielding, B. A., Frayn, K. N., & Karpe, F. (2011). Downregulation of adipose tissue fatty acid trafficking in obesity: a driver for ectopic fat deposition?. Diabetes, 60(1), 47–55.

Merkestein, M., Laber, S., McMurray, F., Andrew, D., Sachse, G., Sanderson, J., Li, M., Usher, S., Sellayah, D., Ashcroft, F. M., and Cox, R. D. (2015). FTO influences adipogenesis by regulating mitotic clonal expansion. Nature Communications, 6, 1–9.

Mikkelsen, T. S., Xu, Z., Zhang, X., Wang, L., Gimble, J. M., Lander, E. S., and Rosen, E. D. (2010). Comparative epigenomic analysis of murine and human adipogenesis. Cell, 143(1), 156–169.

Miller, W. H., Faust, I. M., and Hirsch, J. (1984). Demonstration of de novo production of adipocytes in adult rats by biochemical and radioautographic techniques. Journal of Lipid Research, 25(4), 336–347.

Minokoshi, Y., Kim, Y. B., Peroni, O. D., Fryer, L. G. D., Müller, C., Carling, D., and Kahn, B. B. (2002). Leptin stimulates fatty-acid oxidation by activating AMP-activated protein kinase. Nature, 415(6869), 339–343.

Miranda, C. S., Silva-Veiga, F., Martins, F. F., Rachid, T. L., Mandarim-De-Lacerda, C. A., and Souza-Mello, V. (2020). PPAR-α activation counters brown adipose tissue whitening: a comparative study between high-fat– and high-fructose–fed mice. Nutrition, 78, 110791.

Mitchell, P. (2011). Chemiosmotic coupling in oxidative and photosynthetic phosphorylation. Biochimica et Biophysica Acta - Bioenergetics, 1807(12), 1507–1538.

Miyazaki, Y., and DeFronzo, R. A. (2009). Visceral fat dominant distribution in male type 2 diabetic patients is closely related to hepatic insulin resistance, irrespective of body type. Cardiovascular diabetology, 8, 44.

Mohamed-Ali, V., Goodrick, S., Bulmer, K., Holly, J. M. P., Yudkin, J. S., and Coppack, S. W. (1999). Production of soluble tumor necrosis factor receptors by human subcutaneous adipose tissue in vivo. American Journal of Physiology - Endocrinology and Metabolism, 277(6 40-6), 971–975.

Mohammadzadeh, M., Mohammadzadeh, V., Shakiba, M., Motevalli, M., Abedini, A., Kadivar, S., Entezari, P., and Mohammadzadeh, A. (2018). Assessing the Relation of Epicardial Fat Thickness and Volume, Quantified by 256-Slice Computed Tomography Scan, With Coronary Artery Disease and Cardiovascular Risk Factors. Archives of Iranian Medicine, 21(3), 95–100.

Moitra, J., Mason, M. M., Olive, M., Krylov, D., Gavrilova, O., Marcus-Samuels, B., Feigenbaum, L., Lee, E., Aoyama, T., Eckhaus, M., Reitman, M. L., and Vinson, C. (1998). Life without white fat: a transgenic mouse. Genes and development, 12(20), 3168–3181.

Monemdjou, S., Kozak, L. P., and Harper, M. E. (1999). Mitochondrial proton leak in brown adipose tissue mitochondria of Ucp1- deficient mice is GDP insensitive. American Journal of Physiology - Endocrinology and Metabolism, 276(6), E1073-82.

Montan, P. D., Sourlas, A., Olivero, J., Silverio, D., Guzman, E., and Kosmas, C. E. (2019). Pharmacologic therapy of obesity: mechanisms of action and cardiometabolic effects. Annals of Translational Medicine, 7(16), 393–393.

Muhlhausler, B. S., Duffield, J. A., and McMillen, I. C. (2007a). Increased maternal nutrition stimulates peroxisome proliferator activated receptor-γ, adiponectin, and leptin messenger ribonucleic acid expression in adipose tissue before birth. Endocrinology, 148(2), 878–885.

Muhlhausler, Beverly S., Duffield, J. A., and McMillen, I. C. (2007b). Increased maternal nutrition increases leptin expression in perirenal and subcutaneous adipose tissue in the postnatal lamb. Endocrinology, 148(12), 6157–6163.

Murano, I., Barbatelli, G., Parisani, V., Latini, C., Muzzonigro, G., Castellucci, M., and Cinti, S. (2008). Dead adipocytes, detected as crown-like structures, are prevalent in visceral fat depots of genetically obese mice. Journal of Lipid Research, 49(7), 1562–1568.

Murray, A. W. (1971). The Biological Significance of Purine Salvage. Annual Review of Biochemistry, 40(1), 811–826.

Musovic, S., and Olofsson, C. S. (2019). Adrenergic stimulation of adiponectin secretion in visceral mouse adipocytes is blunted in high-fat diet induced obesity. Scientific Reports, 9(1), 1–12.

Nagy, E., Jermendy, A. L., Merkely, B., and Maurovich-Horvat, P. (2017). Clinical importance of epicardial adipose tissue. Archives of medical science : AMS, 13(4), 864–874.

Nawrocki, A. R., and Scherer, P. E. (2004). The delicate balance between fat and muscle: Adipokines in metabolic disease and musculoskeletal inflammation. Current Opinion in Pharmacology, 4(3), 281–289.

Neel J. V. (1999). The "thrifty genotype" in 1998. Nutrition reviews, 57(5 Pt 2), S2–S9.

Neels, J. G., Thinnes, T., and Loskutoff, D. J. (2004). Angiogenesis in an in vivo model of adipose tissue development. The FASEB Journal, 18(9), 983–985.

Neill, H. M., Lally, J. S., Galic, S., Thomas, M., Azizi, P. D., Fullerton, M. D., Smith, B. K., Pulinilkunnil, T., Chen, Z., Samaan, M. C., Jorgensen, S. B., Dyck, J. R., Holloway, G. P., Hawke, T. J., van Denderen, B. J., Kemp, B. E., and Steinberg, G. R. (2014). AMPK phosphorylation of ACC2 is required for skeletal muscle fatty acid oxidation and insulin sensitivity in mice. Diabetologia, 57(8), 1693–1702.

Nelson, R. G., Morgenstern, H., and Bennett, P. H. (1998). Birth weight and renal disease in Pima Indians with type 2 diabetes mellitus. American Journal of Epidemiology, 148(7), 650–656.

National Health Service (NHS). (2019). National Child Measurement Programme , England 2018 / 19 School Year Key Facts. September, 1–20.

Nielsen, T. S., Jessen, N., Jørgensen, J. O. L., Møller, N., and Lund, S. (2014). Dissecting adipose tissue lipolysis: Molecular regulation and implications for metabolic disease. Journal of Molecular Endocrinology, 52(3), 199–222.

Nigam, A., Wright, R. S., Allison, T. G., Williams, B. A., Kopecky, S. L., Reeder, G. S., Murphy, J. G., and Jaffe, A. S. (2006). Excess weight at time of presentation of myocardial infarction is associated with lower initial mortality risks but higher long-term risks including recurrent re-infarction and cardiac death. International journal of cardiology, 110(2), 153–159.

Nnodim, J. O., and Lever, J. D. (1985). The pre- and postnatal development and ageing of interscapular brown adipose tissue in the rat. Anatomy and embryology, 173(2), 215–223.

Novikoff, A. B., Novikoff, P. M., Rosen, O. M., and Rubin, C. S. (1980). Organelle relationships in cultured 3T3-L1 preadipocytes. The Journal of cell biology, 87(1), 180–196.

Obregón, M. J., Calvo, R., Hernández, A., Escobar del Rey, F., and Morreale de Escobar, G. (1996). Regulation of uncoupling protein messenger ribonucleic acid and 5'-deiodinase activity by thyroid hormones in fetal brown adipose tissue. Endocrinology, 137(11), 4721–4729.

Ohlson, L. O., Larsson, B., Svärdsudd, K., Welin, L., Eriksson, H., Wilhelmsen, L., Björntorp, P., and Tibblin, G. (1985). The influence of body fat distribution on the incidence of diabetes mellitus. 13.5 years of follow-up of the participants in the study of men born in 1913. Diabetes, 34(10), 1055–1058.

Ojha, S., Robinson, L., Yazdani, M., Symonds, M. E., and Budge, H. (2013). Brown adipose tissue genes in pericardial adipose tissue of newborn sheep are downregulated by maternal nutrient restriction in late gestation. Pediatric Research, 74(3), 246–251.

Ojha, S., Symonds, M. E., and Budge, H. (2014). Suboptimal maternal nutrition during early-to-mid gestation in the sheep enhances pericardial adiposity in the near-term fetus. Reproduction, Fertility and Development, 27(8), 1205–1212.

Okamatsu-Ogura, Y., Fukano, K., Tsubota, A., Uozumi, A., Terao, A., Kimura, K., and Saito, M. (2013). Thermogenic ability of uncoupling protein 1 in beige adipocytes in mice. PLoS ONE, 8(12), 1–10.

Oken, E., Rifas-Shiman, S. L., Field, A. E., Frazier, A. L., and Gillman, M. W. (2008). Maternal gestational weight gain and offspring weight in adolescence. Obstetrics and gynecology, 112(5), 999–1006.

Ong, K. L., Ding, J., McClelland, R. L., Cheung, B. M. Y., Criqui, M. H., Barter, P. J., Rye, K. A., and Allison, M. A. (2015). Relationship of pericardial fat with biomarkers of inflammation and hemostasis, and cardiovascular disease: The Multi-Ethnic Study of Atherosclerosis. Atherosclerosis, 239(2), 386–392.

Ono, M., and Fujimori, K. (2011). Antiadipogenic effect of dietary apigenin through activation of AMPK in 3T3-L1 cells. Journal of Agricultural and Food Chemistry, 59(24), 13346–13352.

Oral, E. A., Simha, V., Ruiz, E., Andewelt, A., Premkumar, A., Snell, P., Wagner, A. J., DePaoli, A. M., Reitman, M. L., Taylor, S. I., Gorden, P., and Garg, A. (2002). Leptin-replacement therapy for lipodystrophy. The New England journal of medicine, 346(8), 570–578.

Orava, J., Nuutila, P., Noponen, T., Parkkola, R., Viljanen, T., Enerbäck, S., Rissanen, A., Pietiläinen, K. H., and Virtanen, K. A. (2013). Blunted metabolic responses to cold and insulin stimulation in brown adipose tissue of obese humans. Obesity, 21(11), 2279–2287.

Ortega, F. J., Mayas, D., Moreno-Navarrete, J. M., Catalán, V., Gómez-Ambrosi, J., Esteve, E., Rodriguez-Hermosa, J. I., Ruiz, B., Ricart, W., Peral, B., Fruhbeck, G., Tinahones, F. J., and Fernández-Real, J. M. (2010). The gene expression of the main lipogenic enzymes is downregulated in visceral adipose tissue of obese subjects. Obesity (Silver Spring, Md.), 18(1), 13–20.

Osmond, C., Barker, D. J. P., Winter, P. D., Fall, C. H. D., and Simmonds, S. J. (1993). Early growth and death from cardiovascular disease in women. British Medical Journal, 307(6918), 1519–1524.

Ouchi, N., and Walsh, K. (2009). Adiponectin anti inflammation. Clinica Chimica Acta, 380(1–2), 24–30.

Park, A., Kim, W. K., and Bae, K. H. (2014). Distinction of white, beige and brown adipocytes derived from mesenchymal stem cells. World journal of stem cells, 6(1), 33–42

Park, J. W., Lee, J. H., Park, Y. H., Park, S. J., Cheon, J. H., Kim, W. H., and Kim, T. Il. (2017). Sex-dependent Difference in the effect of metformin on colorectal cancer-specific mortality of Diabetic colorectal cancer patients. World Journal of Gastroenterology, 23(28), 5196–5205.

Park, S., Ahn, I. S., and Kim, D. S. (2010). Central infusion of leptin improves insulin resistance and suppresses β-cell function, but not β-cell mass, primarily through the sympathetic nervous system in a type 2 diabetic rat model. Life Sciences, 86(23–24), 854–862.

Peiris, A. N., Sothmann, M. S., Hoffmann, R. G., Hennes, M. I., Wilson, C. R., Gustafson, A. B., and Kissebah, A. H. (1989). Adiposity, fat distribution, and cardiovascular risk. Annals of internal medicine, 110(11), 867–872.

Pelleymounter, M. A., Cullen, M. J., Baker, M. B., Hecht, R., Winters, D., Boone, T., and Collins, F. (1995). Effects of the obese gene product on body weight regulation in ob/ob mice. Science (New York, N.Y.), 269(5223), 540–543.

Peraldi, P., Xu, M., and Spiegelman, B. M. (1997). Thiazolidinediones block tumor necrosis factor-α-induced inhibition of insulin signaling. Journal of Clinical Investigation, 100(7), 1863–1869.

Peric Kacarevic, Z., Snajder, D., Maric, A., Bijelic, N., Cvijanovic, O., Domitrovic, R., and Radic, R. (2016). High-fat diet induced changes in lumbar vertebra of the male rat offsprings. Acta histochemica, 118(7), 711–721.

Petersen, K. F., Befroy, D., Dufour, S., Dziura, J., Rothman, D. L., Dipietro, L., Cline, G. W., and Gerald, I. (2003). Mitochondrial Dysfunction in the Elderly: Possible Role in Insulin Resistance. Science, 300(5622), 1140–1142.

Petersen, K. F., Oral, E. A., Dufour, S., Befroy, D., Ariyan, C., Yu, C., Cline, G. W., DePaoli, A. M., Taylor, S. I., Gorden, P., and Shulman, G. I. (2002). Leptin reverses insulin resistance and hepatic steatosis in patients with severe lipodystrophy. Journal of Clinical Investigation, 109(10), 1345–1350.

Petrovic, N., Walden, T. B., Shabalina, I. G., Timmons, J. A., Cannon, B., and Nedergaard, J. (2010). Chronic peroxisome proliferator-activated receptor γ (PPARγ) activation of epididymally derived white adipocyte cultures reveals a population of thermogenically competent, UCP1-containing adipocytes molecularly distinct from classic brown adipocytes. Journal of Biological Chemistry, 285(10), 7153–7164.

Pezeshkian, M., Noori, M., Najjarpour-Jabbari, H., Abolfathi, A., Darabi, M., Darabi, M., Shaaker, M., and Shahmohammadi, G. (2009). Fatty acid composition of epicardial and subcutaneous human adipose tissue. Metabolic syndrome and related disorders, 7(2), 125–131.

Pfaffl M. W. (2001). A new mathematical model for relative quantification in real-time RT-PCR. Nucleic acids research, 29(9), e45.

Pickavance, L. C., Tadayyon, M., Widdowson, P. S., Buckingham, R. E., and Wilding, J. P. H. (1999). Therapeutic index for rosiglitazone in dietary obese rats: Separation of efficacy and haemodilution. British Journal of Pharmacology, 128(7), 1570–1576.

Poissonnet, C. M., Burdi, A. R., and Bookstein, F. L. (1983). Growth and development of human adipose tissue during early gestation. Early Human Development, 8(1), 1–11.

Poissonnet, C.M., Burdi, A. R., and Garn, S. M. (1984). The chronology of adipose tissue appearance and distribution in the human fetus. Early Human Development, 10(1–2), 1–11.

Pollard, A. E., Martins, L., Muckett, P. J., Khadayate, S., Bornot, A., Clausen, M., Admyre, T., Bjursell, M., Fiadeiro, R., Wilson, L., Whilding, C., Kotiadis, V. N., Duchen, M. R., Sutton, D., Penfold, L., Sardini, A., Bohlooly-Y, M., Smith, D. M., Read, J. A., … Carling, D. (2019). AMPK activation protects against diet-induced obesity through Ucp1-independent thermogenesis in subcutaneous white adipose tissue. Nature Metabolism, 1(3), 340–349.

Pouliot, M. C., Després, J. P., Nadeau, A., Moorjani, S., Prud'Homme, D., Lupien, P. J., Tremblay, A., and Bouchard, C. (1992). Visceral obesity in men. Associations with glucose tolerance, plasma insulin, and lipoprotein levels. Diabetes, 41(7), 826–834.

Primeau, V., Coderre, L., Karelis, A. D., Brochu, M., Lavoie, M. E., Messier, V., Sladek, R., and Rabasa-Lhoret, R. (2011). Characterizing the profile of obese patients who are metabolically healthy. International Journal of Obesity, 35(7), 971–981.

Public Health England. (2018). Health of women before and during pregnancy : health behaviours , risk factors and inequalities An initial analysis of the Maternity Services Dataset antenatal booking data About Public Health England. 1–66.

Puigserver, P., Wu, Z., Park, C. W., Graves, R., Wright, M., and Spiegelman, B. M. (1998). A cold-inducible coactivator of nuclear receptors linked to adaptive thermogenesis. Cell, 92(6), 829–839.

Qi, G., Zhou, Y., Zhang, X., Yu, J., Li, X., Cao, X., Wu, C., and Guo, P. (2019). Cordycepin promotes browning of white adipose tissue through an AMP-activated protein kinase (AMPK)-dependent pathway. Acta Pharmaceutica Sinica B, 9(1), 135–143.

Rausch, M. E., Weisberg, S., Vardhana, P., and Tortoriello, D. V. (2008). Obesity in C57BL/6J mice is characterized by adipose tissue hypoxia and cytotoxic T-cell infiltration. International Journal of Obesity, 32(3), 451–463.

Ravelli, A. C. J., Van Der Meulen, J. H. P., Osmond, C., Barker, D. J. P., and Bleker, O. P. (1999). Obesity at the age of 50 y in men and women exposed to famine prenatally. American Journal of Clinical Nutrition, 70(5), 811–816.

Reaven, G.M., (1988). Role of insulin resistance in human disease. Diabetes 37, 1595–1607.

Rehnmark, S., Antonson, P., Xanthopoulos, K. G., and Jacobsson, A. (1993). Differential adrenergic regulation of C/EBP alpha and C/EBP beta in brown adipose tissue. FEBS letters, 318(3), 235–241.

Reilly, J. J., and Kelly, J. (2011). Long-term impact of overweight and obesity in childhood and adolescence on morbidity and premature mortality in adulthood: Systematic review. International Journal of Obesity, 35(7), 891–898.

Remacle, C., Bieswal, F., Bol, V., and Reusens, B. (2011). Developmental programming of adult obesity and cardiovascular disease in rodents by maternal nutrition imbalance. American Journal of Clinical Nutrition, 94(6), 1846–1852.

Ridker, P. M., Hennekens, C. H., Buring, J. E., and Rifai, N. (2000a). C-reactive protein and other markers of inflammation in the prediction of cardiovascular disease in women. The New England journal of medicine, 342(12), 836–843.

Ridker, P. M., Rifai, N., Stampfer, M. J., and Hennekens, C. H. (2000b). Plasma concentration of interleukin-6 and the risk of future myocardial infarction among apparently healthy men. Circulation, 101(15), 1767–1772.

Rigamonti, A., Brennand, K., Lau, F., and Cowan, C. A. (2011). Rapid cellular turnover in adipose tissue. PLoS ONE, 6(3).

Rimbaud, S., Ruiz, M., Piquereau, J., Mateo, P., Fortin, D., Veksler, V., Garnier, A., and Ventura-Clapier, R. (2011). Resveratrol improves survival, hemodynamics and energetics in a rat model of hypertension leading to heart failure. PloS one, 6(10), e26391.

Rivera, L., Morón, R., Zarzuelo, A., and Galisteo, M. (2009). Long-term resveratrol administration reduces metabolic disturbances and lowers blood pressure in obese Zucker rats. Biochemical Pharmacology, 77(6), 1053–1063.

Rodeheffer, M. S., Birsoy, K., and Friedman, J. M. (2008). Identification of White Adipocyte Progenitor Cells In Vivo. Cell, 135(2), 240–249.

Roden, M., Price, T. B., Perseghin, G., Petersen, K. F., Rothman, D. L., Cline, G. W., and Shulman, G. I. (1996). Mechanism of free fatty acid-induced insulin resistance in humans. Journal of Clinical Investigation, 97(12), 2859–2865.

Rodriguez-Granillo, G. A., Reynoso, E., Capunay, C., Carpio, J., and Carrascosa, P. (2018). Pericardial and visceral, but not total body fat, are related to global coronary and extra-coronary atherosclerotic plaque burden. International Journal of Cardiology, 260, 204–210.

Rodriguez, E. R., and Tan, C. D. (2017). Structure and Anatomy of the Human Pericardium. Progress in Cardiovascular Diseases, 59(4), 327–340.

Rosario, F. J., Powell, T. L., and Jansson, T. (2016). Activation of placental insulin and mTOR signaling in a mouse model of maternal obesity associated with fetal overgrowth. American Journal of Physiology - Regulatory Integrative and Comparative Physiology, 310(1), R87–R93.

Roseboom, T. J., Van der Meulen, J. H. P., Osmond, C., Barker, D. J. P., Ravelli, A. C. J., and Bleker, O. P. (2000a). Plasma lipid profiles in adults after prenatal exposure to the Dutch famine. American Journal of Clinical Nutrition, 72(5), 1101–1106.

Roseboom, T. J., Van der Meulen, J. H. P., Osmond, C., Barker, D. J. P., Ravelli, A. C. J., Schroeder-Tanka, J. M., Van Montfrans, G. A., Michels, R. P. J., and Bleker, O. P. (2000b). Coronary heart disease after prenatal exposure to the Dutch famine, 1944-45. Heart, 84(6), 595–598.

Rosen, E. D., Sarraf, P., Troy, A. E., Bradwin, G., Moore, K., Milstone, D. S., Spiegelman, B. M., and Mortensen, R. M. (1999). PPARγ is required for the differentiation of adipose tissue in vivo and in vitro. Molecular Cell, 4(4), 611–617.

Rosenwald, M., Perdikari, A., Rülicke, T., and Wolfrum, C. (2013). Bi-directional interconversion of brite and white adipocytes. Nature Cell Biology, 15(6), 659–667.

Rosito, G. A., Massaro, J. M., Hoffmann, U., Ruberg, F. L., Mahabadi, A. A., Vasan, R. S., O'Donnell, C. J., and Fox, C. S. (2008). Pericardial fat, visceral abdominal fat, cardiovascular disease risk factors, and vascular calcification in a community-based sample the framingham heart study. Circulation, 117(5), 605–613.

Ross, S. E., Hemati, N., Longo, K. A., Bennett, C. N., Lucas, P. C., Erickson, R. L., and MacDougald, O. A. (2000). Inhibition of adipogenesis by Wnt signaling. Science, 289(5481), 950–953.

Rowe, J. W., Minaker, K. L., Pallotta, J. A., and Flier, J. S. (1983). Characterization of the insulin resistance of aging. Journal of Clinical Investigation, 71(6), 1581–1587.

Rupnick, M. A., Panigrahy, D., Zhang, C. Y., Dallabrida, S. M., Lowell, B. B., Langer, R., and Folkman, M. J. (2002). Adipose tissue mass can be regulated through the vasculature. Proceedings of the National Academy of Sciences of the United States of America, 99(16), 10730–10735.

Ryan, A. S., Ge, S., Blumenthal, J. B., Serra, M. C., Prior, S. J., and Goldberg, A. P. (2014). Aerobic exercise and weight loss reduce vascular markers of inflammation and improve insulin sensitivity in obese women. Journal of the American Geriatrics Society, 62(4), 607–614.

Rydén, M., Andersson, D. P., Bergström, I. B., and Arner, P. (2014). Adipose tissue and metabolic alterations: Regional differences in fat cell size and number matter, but differently: A cross-sectional study. Journal of Clinical Endocrinology and Metabolism, 99(10), E1870–E1876.

Sacks, H. S., Fain, J. N., Bahouth, S. W., Ojha, S., Frontini, A., Budge, H., Cinti, S., and Symonds, M. E. (2013). Adult epicardial fat exhibits beige features. Journal of Clinical Endocrinology and Metabolism, 98(9), 1448–1455.

Sacks, H. S., Fain, J. N., Holman, B., Cheema, P., Chary, A., Parks, F., Karas, J., Optican, R., Bahouth, S. W., Garrett, E., Wolf, R. Y., Carter, R. A., Robbins, T., Wolford, D., and Samaha, J. (2009). Uncoupling protein-1 and related messenger ribonucleic acids in human epicardial and other adipose tissues: Epicardial fat functioning as brown fat. Journal of Clinical Endocrinology and Metabolism, 94(9), 3611–3615.

Saito, M., Okamatsu-Ogura, Y., Matsushita, M., Watanabe, K., Yoneshiro, T., Nio-Kobayashi, J., Iwanaga, T., Miyagawa, M., Kameya, T., Nakada, K., Kawai, Y., and Tsujisaki, M. (2009). High incidence of metabolically active brown adipose tissue in healthy adult humans: Effects of cold exposure and adiposity. Diabetes, 58(7), 1526–1531.

Salans, L. B., Knittle, J. L., and Hirsch, J. (1968). The role of adipose cell size and adipose tissue insulin sensitivity in the carbohydrate intolerance of human obesity. Journal of Clinical Investigation, 47(1), 153–165.

Salomäki, H., Heinäniemi, M., Vähätalo, L. H., Ailanen, L., Eerola, K., Ruohonen, S. T., Pesonen, U., and Koulu, M. (2014). Prenatal metformin exposure in a maternal high fat diet mouse model alters the transcriptome and modifies the metabolic responses of the offspring. PLoS ONE, 9(12), 1–22.

Samaras, K., Botelho, N. K., Chisholm, D. J., and Lord, R. V. (2010). Subcutaneous and visceral adipose tissue gene expression of serum adipokines that predict type 2 diabetes. Obesity, 18(5), 884–889.

Samuelsson, A. M., Matthews, P. A., Argenton, M., Christie, M. R., McConnell, J. M., Jansen, E. H. J. M., Piersma, A. H., Ozanne, S. E., Twinn, D. F., Remacle, C., Rowlerson, A., Poston, L., and Taylor, P. D. (2008). Diet-induced obesity in female mice leads to offspring hyperphagia, adiposity, hypertension, and insulin resistance: A novel murine model of developmental programming. Hypertension, 51(2), 383–392.

Sánchez-Díaz, J. S., Monares-Zepeda, E., Martínez-Rodríguez, E. A., Cortés-Román, J. S., Torres-Aguilar, O., Peniche-Moguel, K. G., Díaz-Gutiérrez, S. P., Pin-Gutiérrez, E., Rivera-Solís, G., García-Méndez, R. C., Huanca-Pacaje, J. M., and Calyeca-Sánchez, M. V. (2017). Metformin-related lactic acidosis: Case report. Colombian Journal of Anesthesiology, 45(4), 353–359.

Sanchez-Gurmaches, J., Hung, C. M., Sparks, C. A., Tang, Y., Li, H., and Guertin, D. A. (2012). PTEN loss in the Myf5 lineage redistributes body fat and reveals subsets of white adipocytes that arise from Myf5 precursors. Cell metabolism, 16(3), 348–362.

Sarker, G., Litwan, K., Kastli, R., and Peleg-Raibstein, D. (2019). Maternal overnutrition during critical developmental periods leads to different health adversities in the offspring: relevance of obesity, addiction and schizophrenia. Scientific Reports, 9(1), 1–17.

Sasaki, H., Asanuma, H., Fujita, M., Takahama, H., Wakeno, M., Ito, S., Ogai, A., Asakura, M., Kim, J., Minamino, T., Takashima, S., Sanada, S., Sugimachi, M., Komamura, K.,

Mochizuki, N., and Kitakaze, M. (2009). Metformin prevents progression of heart failure in dogs: role of AMP-activated protein kinase. Circulation, 119(19), 2568–2577.

Schmitz, J., Evers, N., Awazawa, M., Nicholls, H. T., Brönneke, H. S., Dietrich, A., Mauer, J., Blüher, M., and Brüning, J. C. (2016). Obesogenic memory can confer long-term increases in

adipose tissue but not liver inflammation and insulin resistance after weight loss. Molecular Metabolism, 5(5), 328–339.

Seale, P., Bjork, B., Yang, W., Kajimura, S., Chin, S., Kuang, S., Scimè, A., Devarakonda, S., Conroe, H. M., Erdjument-Bromage, H., Tempst, P., Rudnicki, M. A., Beier, D. R., and Spiegelman, B. M. (2008). PRDM16 controls a brown fat/skeletal muscle switch. Nature, 454(7207), 961–967.

Seale, P., Conroe, H. M., Estall, J., Kajimura, S., Frontini, A., Ishibashi, J., Cohen, P., Cinti, S., and Spiegelman, B. M. (2011). Prdm16 determines the thermogenic program of subcutaneous white adipose tissue in mice. J Clin Invest, 121(1), 53–56.

Segovia, S. A., Vickers, M. H., Harrison, C. J., Patel, R., Gray, C., and Reynolds, C. M. (2018). Maternal High-Fat and High-Salt Diets Have Differential Programming Effects on Metabolism in Adult Male Rat Offspring. Frontiers in Nutrition, 5(March), 1–13.

Sellayah, D., Thomas, H., Lanham, S. A., and Cagampang, F. R. (2019). Maternal obesity during pregnancy and lactation influences offspring obesogenic adipogenesis but not developmental adipogenesis in mice. Nutrients, 11(3).

Semple, R. K., Crowley, V. C., Sewter, C. P., Laudes, M., Christodoulides, C., Considine, R. V., Vidal-Puig, A., and O'Rahilly, S. (2004). Expression of the thermogenic nuclear hormone receptor coactivator PGC-1α is reduced in the adipose tissue of morbidly obese subjects. International Journal of Obesity, 28(1), 176–179.

Seppälä-Lindroos, A., Vehkavaara, S., Häkkinen, A. M., Goto, T., Westerbacka, J., Sovijärvi, A., Halavaara, J., and Yki-Järvinen, H. (2002). Fat accumulation in the liver is associated with defects in insulin suppression of glucose production and serum free fatty acids independent of obesity in normal men. Journal of Clinical Endocrinology and Metabolism, 87(7), 3023–3028.

Shabalina, I. G., Petrovic, N., deJong, J. M. A., Kalinovich, A. V., Cannon, B., and Nedergaard, J. (2013). UCP1 in Brite/Beige adipose tissue mitochondria is functionally thermogenic. Cell Reports, 5(5), 1196–1203.

Shan, T., Liu, W., and Kuang, S. (2013). Fatty acid binding protein 4 expression marks a population of adipocyte progenitors in white and brown adipose tissues. FASEB Journal, 27(1), 277–287.

Shankar, K., Harrell, A., Liu, X., Gilchrist, J. M., Ronis, M. J. J., and Badger, T. M. (2008). Maternal obesity at conception programs obesity in the offspring. American Journal of Physiology - Regulatory Integrative and Comparative Physiology, 294(2), 528–538.

Shao, M., Ishibashi, J., Kusminski, C. M., Wang, Q. A., Hepler, C., Vishvanath, L., MacPherson, K. A., Spurgin, S. B., Sun, K., Holland, W. L., Seale, P., and Gupta, R. K. (2016). Zfp423 Maintains White Adipocyte Identity through Suppression of the Beige Cell Thermogenic Gene Program. Cell metabolism, 23(6), 1167–1184.

Shaw, R. J., Kosmatka, M., Bardeesy, N., Hurley, R. L., Witters, L. A., DePinho, R. A., and Cantley, L. C. (2004). The tumor suppressor LKB1 kinase directly activates AMP-activated kinase and regulates apoptosis in response to energy stress. Proceedings of the National Academy of Sciences of the United States of America, 101(10), 3329–3335.

Sheen, J. M., Yu, H. R., Tain, Y. L., Tsai, W. L., Tiao, M. M., Lin, I. C., Tsai, C. C., Lin, Y. J., and Huang, L. T. (2018). Combined maternal and postnatal high-fat diet leads to metabolic syndrome and is effectively reversed by resveratrol: A multiple-organ study. Scientific Reports, 8(1), 1–12.

Shen, S., Liao, Q., Feng, Y., Liu, J., Pan, R., Lee, S. M., and Lin, L. (2019). Myricanol mitigates lipid accumulation in 3T3-L1 adipocytes and high fat diet-fed zebrafish via activating AMP-activated protein kinase. Food chemistry, 270, 305–314.

Shepherd, D. L., Hathaway, Q. A., Pinti, M. V, Nichols, C. E., Durr, J., Sreekumar, S., Hughes, K. M., Stine, S. M., Martinez, I., Hollander, J. M., States, U., Group, B. W., States, U., Biology, C., and States, U. (2017). Exploring the mitochondrial microRNA import pathway through Polynucleotide Phosphorylase (PNPase). Journal of Molecular and Cellular Cardiology, 110, 15–25.

Shimizu, I., Aprahamian, T., Kikuchi, R., Shimizu, A., Papanicolaou, K. N., MacLauchlan, S., Maruyama, S., and Walsh, K. (2014). Vascular rarefaction mediates whitening of brown fat in obesity. Journal of Clinical Investigation, 124(5), 2099–2112.

Shinoda, K., Luijten, I. H., Hasegawa, Y., Hong, H., Sonne, S. B., Kim, M., Xue, R., Chondronikola, M., Cypess, A. M., Tseng, Y. H., Nedergaard, J., Sidossis, L. S., and Kajimura, S. (2015). Genetic and functional characterization of clonally derived adult human brown adipocytes. Nature medicine, 21(4), 389–394.

Shulman, G. I., Rothman, D. L., Jue, T., Stein, P., DeFronzo, R. A., and Shulman, R. G. (1990). Quantitation of muscle glycogen synthesis in normal subjects and subjects with non-insulin-dependent diabetes by 13C nuclear magnetic resonance spectroscopy. The New England journal of medicine, 322(4), 223–228.

Silva, J. E., and Larsen, P. R. (1983). Adrenergic activation of triiodothyronine production in brown adipose tissue. Nature, 305(5936), 712–713.

Silva, K. R., Liechocki, S., Carneiro, J. R., Claudio-Da-Silva, C., Maya-Monteiro, C. M., Borojevic, R., and Baptista, L. S. (2015). Stromal-vascular fraction content and adipose stem cell behavior are altered in morbid obese and post bariatric surgery ex-obese women. Stem Cell Research and Therapy, 6(1), 1–13.

Sim, C. K., Kim, S. Y., Brunmeir, R., Zhang, Q., Li, H., Dharmasegaran, D., Leong, C., Lim, Y. Y., Han, W., and Xu, F. (2017). Regulation of white and brown adipocyte differentiation by RhoGAP DLC1. PLoS ONE, 12(3), 1–19.

Simoneau, J. A., and Kelley, D. E. (1997). Altered glycolytic and oxidative capacities of skeletal muscle contribute to insulin resistance in NIDDM. Journal of Applied Physiology, 83(1), 166–171.

Simoneau, J.A., Colberg, S. R., Thaete, F. L., and Kelley, D. E. (1995). Skeletal muscle glycolytic and oxidative enzyme capacities are determinants of insulin sensitivity and muscle composition in obese women. The FASEB Journal, 9(2), 273–278.

Simoneau, J.A., Veerkamp, J. H., Turcotte, L. P., and Kelley, D. E. (1999). Markers of capacity to utilize fatty acids in human skeletal muscle: relation to insulin resistance and obesity and effects of weight loss. The FASEB Journal, 13(14), 2051–2060.

Singh, A. S., Mulder, C., Twisk, J. W. R., Van Mechelen, W., and Chinapaw, M. J. M. (2008). Tracking of childhood overweight into adulthood: A systematic review of the literature. Obesity Reviews, 9(5), 474–488.

Skurk, T., Alberti-Huber, C., Herder, C., and Hauner, H. (2007). Relationship between adipocyte size and adipokine expression and secretion. Journal of Clinical Endocrinology and Metabolism, 92(3), 1023–1033.

Šnajder, D., Perić Kačarević, Ž., Grgić, A., Bijelić, N., Fenrich, M., Belovari, T., and Radić, R. (2019). Effect of different combination of maternal and postnatal diet on adipose tissue morphology in male rat offspring. Journal of Maternal-Fetal and Neonatal Medicine, 32(11), 1838–1846.

Snel, M., Jonker, J. T., Hammer, S., Kerpershoek, G., Lamb, H. J., Edo Meinders, A., Pijl, H., De Roos, A., Romijn, J. A., Smit, J. W. A., and Jazet, I. M. (2012). Long-term beneficial effect of a 16-week very low calorie diet on pericardial fat in obese type 2 diabetes mellitus patients. Obesity, 20(8), 1572–1576.

Song, A., Dai, W., Jang, M. J., Medrano, L., Li, Z., Zhao, H., Shao, M., Tan, J., Li, A., Ning, T., Miller, M. M., Armstrong, B., Huss, J. M., Zhu, Y., Liu, Y., Gradinaru, V., Wu, X., Jiang, L., Scherer, P. E., and Wang, Q. A. (2020). Low- And high-thermogenic brown adipocyte

subpopulations coexist in murine adipose tissue. Journal of Clinical Investigation, 130(1), 247–257.

Spalding, K. L., Arner, E., Westermark, P. O., Bernard, S., Buchholz, B. A., Bergmann, O., Blomqvist, L., Hoffstedt, J., Näslund, E., Britton, T., Concha, H., Hassan, M., Rydén, M., Frisén, J., and Arner, P. (2008). Dynamics of fat cell turnover in humans. Nature, 453(7196), 783–787.

Spiegelman, B. M., and Flier, J. S. (2001). Obesity and the Regulation Review of Energy Balance total fast of approximately 150 days! This impressive energy reserve is due both to the high energy content of triglycerides versus polysaccharides, and the fact. Cell, 104, 531–543.

Spranger, J., Kroke, A., Mo, M., Hoffmann, K., and Bergmann, M. M. (2003). Inflammatory Cytokines and the Risk to Develop Type 2 Diabetes. Diabetes, 52(March), 812–817.

Spurr, I. B., Birts, C. N., Cuda, F., Benkovic, S. J., Blaydes, J. P., and Tavassoli, A. (2012). Targeting tumour proliferation with a small-molecule inhibitor of AICAR transformylase homodimerization. Chembiochem: a European journal of chemical biology, 13(11), 1628–1634.

Stagakis, I., Bertsias, G., Karvounaris, S., Kavousanaki, M., Virla, D., Raptopoulou, A., Kardassis, D., Boumpas, D. T., and Sidiropoulos, P. I. (2012). Anti-tumor necrosis factor therapy improves insulin resistance, beta cell function and insulin signaling in active rheumatoid arthritis patients with high insulin resistance. Arthritis Research and Therapy, 14(3), R141.

Stanford, K. I., Middelbeek, R. J. W., Townsend, K. L., An, D., Nygaard, E. B., Hitchcox, K. M., Markan, K. R., Nakano, K., Hirshman, M. F., Tseng, Y. H., and Goodyear, L. J. (2013). Brown adipose tissue regulates glucose homeostasis and insulin sensitivity. Journal of Clinical Investigation, 123(1), 215–223.

Stanley, T. L., Zanni, M. V., Johnsen, S., Rasheed, S., Makimura, H., Lee, H., Khor, V. K., Ahima, R. S., and Grinspoon, S. K. (2011). TNF-α antagonism with etanercept decreases glucose and increases the proportion of high molecular weight adiponectin in obese subjects with features of the metabolic syndrome. Journal of Clinical Endocrinology and Metabolism, 96(1).

Stapleton, D., Woollatt, E., Mitchelhill, K. I., Nicholl, J. K., Fernandez, C. S., Michell, B. J., Witters, L. A., Power, D. A., Sutherland, G. R., and Kemp, B. E. (1997). AMP-activated protein kinase isoenzyme family: Subunit structure and chromosomal location. FEBS Letters, 409(3), 452–456.

Stefan, N., Kantartzis, K., Machann, J., Schick, F., Thamer, C., Rittig, K., Balletshofer, B., Machicao, F., Fritsche, A., and Häring, H. U. (2009). Identification and characterization of metabolically benign obesity in humans. Obstetrical and Gynecological Survey, 64(1), 30–31.

Steinberg, H. O., Chaker, H., Leaming, R., Johnson, A., Brechtel, G., and Baron, A. D. (1996). Obesity/insulin resistance is associated with endothelial dysfunction: Implications for the syndrome of insulin resistance. Journal of Clinical Investigation, 97(11), 2601–2610.

Stephens, J. M., Lee, J., and Pilch, P. F. (1997). Tumor necrosis factor-α-induced insulin resistance in 3T3-L1 adipocytes is accompanied by a loss of insulin receptor substrate-1 and GLUT4 expression without a loss of insulin receptor-mediated signal transduction. Journal of Biological Chemistry, 272(2), 971–976.

Sudhakar, M., Sasikumar, S. J., Silambanan, S., Natarajan, D., Ramakrishnan, R., Nair, A. J., and Kiran, M. S. (2020). Chlorogenic acid promotes development of brown adipocyte-like phenotype in 3T3-L1 adipocytes. Journal of Functional Foods, 74(July 2019), 104161.

Suh, J. M., Gao, X., McKay, J., McKay, R., Salo, Z., and Graff, J. M. (2006). Hedgehog signaling plays a conserved role in inhibiting fat formation. Cell Metabolism, 3(1), 25–34.

Suh, J. M., Zeve, D., McKay, R., Seo, J., Salo, Z., Li, R., Wang, M., and Graff, J. M. (2007). Adipose is a conserved dosage-sensitive antiobesity gene. Cell metabolism, 6(3), 195–207.

Sun, D., Li, W., Zhang, H., Li, Y., and Zhang, Q. (2020). Inverted U-shaped relationship between body mass index and multivessel lesions in Chinese patients with myocardial infarction: a cross-sectional study. Journal of International Medical Research, 48(7).

Sung, K., Yeon, M., Kim, Y., Huh, J.-H., Kim, J., Wild, S. H., and Byrne, C. D. (2018). Obesity and incidence of diabetes : Effect of absence of metabolic syndrome , insulin resistance , in fl ammation and fatty liver. Atherosclerosis, 275, 50–57.

Symonds, M. E., Stephenson, T., Gardner, D. S., and Budge, H. (2007). Long-term effects of nutritional programming of the embryo and fetus: Mechanisms and critical windows. Reproduction, Fertility and Development, 19(1), 53–63.

Szczepaniak, L. S., Victor, R. G., Orci, L., and Unger, R. H. (2007). Forgotten but not gone: The rediscovery of fatty heart, the most common unrecognized disease in America. Circulation Research, 101(8), 759–767.

Takaoka, M., Suzuki, H., Shioda, S., Sekikawa, K., Saito, Y., Nagai, R., and Sata, M. (2010). Endovascular injury induces rapid phenotypic changes in perivascular adipose tissue. Arteriosclerosis, Thrombosis, and Vascular Biology, 30(8), 1576–1582.

Tamashiro, K. L. K., Terrillion, C. E., Hyun, J., Koenig, J. I., and Moran, T. H. (2009). Prenatal stress or high-fat diet increases susceptibility to diet-induced obesity in rat offspring. Diabetes, 58(5), 1116–1125.

Tang, W., Zeve, D., Suh, J. M., Bosnakovski, D., Kyba, M., Hammer, R. E., Tallquist, M. D., and Graff, J. M. (2008). White fat progenitor cells reside in the adipose vasculature. Science, 322(5901), 583–586.

Tapanainen, P., Leinonen, E., Ruokonen, A., and Knip, M. (2001). Leptin concentrations are elevated in newborn infants of diabetic mothers. Hormone research, 55(4), 185–190.

Tavassoli, A., and Benkovic, S. J. (2005). Genetically selected cyclic-peptide inhibitors of AICAR transformylase homodimerization. Angewandte Chemie - International Edition, 44(18), 2760–2763.

Tchkonia, T., Lenburg, M., Thomou, T., Giorgadze, N., Frampton, G., Pirtskhalava, T., Cartwright, A., Cartwright, M., Flanagan, J., Karagiannides, I., Gerry, N., Forse, R. A., Tchoukalova, Y., Jensen, M. D., Pothoulakis, C., and Kirkland, J. L. (2007). Identification of depot-specific human fat cell progenitors through distinct expression profiles and developmental gene patterns. American Journal of Physiology - Endocrinology and Metabolism, 292(1), 298–307.

Thanassoulis, G., Massaro, J. M., O'Donnell, C. J., Hoffmann, U., Levy, D., Ellinor, P. T., Wang, T. J., Schnabel, R. B., Vasan, R. S., Fox, C. S., and Benjamin, E. J. (2010). Pericardial fat is associated with prevalent atrial fibrillation: the Framingham Heart Study. Circulation. Arrhythmia and electrophysiology, 3(4), 345–350.

Thandapilly, S. J., Wojciechowski, P., Behbahani, J., Louis, X. L., Yu, L., Juric, D., Kopilas, M. A., Anderson, H. D., and Netticadan, T. (2010). Resveratrol prevents the development of pathological cardiac hypertrophy and contractile dysfunction in the SHR without lowering blood pressure. American journal of hypertension, 23(2), 192–196.

Toledo, F. G. S., Menshikova, E. V., Ritov, V. B., Azuma, K., Radikova, Z., DeLany, J., and Kelley, D. E. (2007). Effects of physical activity and weight loss on skeletal muscle mitochondria and relationship with glucose control in type 2 diabetes. Diabetes, 56(8), 2142–2147.

Tormos, K. V., Anso, E., Hamanaka, R. B., Eisenbart, J., Joseph, J., Kalyanaraman, B., and Chandel, N. S. (2011). Mitochondrial complex III ROS regulate adipocyte differentiation. Cell metabolism, 14(4), 537–544.

Tseng, Y. H., Kokkotou, E., Schulz, T. J., Huang, T. L., Winnay, J. N., Taniguchi, C. M., Tran, T. T., Suzuki, R., Espinoza, D. O., Yamamoto, Y., Ahrens, M. J., Dudley, A. T., Norris, A. W.,

Kulkarni, R. N., and Kahn, C. R. (2008). New role of bone morphogenetic protein 7 in brown adipogenesis and energy expenditure. Nature, 454(7207), 1000–1004.

Tsujita, T., Morimoto, C., and Okuda, H. (1995). Mechanism of increase in basal lipolysis of enlarged adipocytes in obese animals. Obesity research, 3 Suppl 5, 633S–636S.

Uldry, M., Yang, W., St-Pierre, J., Lin, J., Seale, P., and Spiegelman, B. M. (2006). Complementary action of the PGC-1 coactivators in mitochondrial biogenesis and brown fat differentiation. Cell Metabolism, 3(5), 333–341.

Vague, J. (1996). A determinant factor of the forms of obesity. Obesity Research, 4(2), 201–203.

Van Baak, M. A., Hul, G. B. J., Toubro, S., Astrup, A., Gottesdiener, K. M., DeSmet, M., and Saris, W. H. M. (2002). Acute effect of L-796568, a novel β3-adrenergic receptor agonist, on energy expenditure in obese men. Clinical Pharmacology and Therapeutics, 71(4), 272–279.

Van Beek, L., van Klinken, J. B., Pronk, A. C. M., van Dam, A. D., Dirven, E., Rensen, P. C. N., Koning, F., Willems van Dijk, K., and van Harmelen, V. (2015). The limited storage capacity of gonadal adipose tissue directs the development of metabolic disorders in male C57Bl/6J mice. Diabetologia, 58(7), 1601–1609.

Van Harmelen, V., Reynisdottir, S., Eriksson, P., Thörne, A., Hoffstedt, J., Lönnqvist, F., and Arner, P. (1998). Leptin secretion from subcutaneous and visceral adipose tissue in women. Diabetes, 47(6), 913–917.

Van Marken Lichtenbelt, W. D., and Schrauwen, P. (2011). Implications of nonshivering thermogenesis for energy balance regulation in humans. American Journal of Physiology - Regulatory Integrative and Comparative Physiology, 301(2), 285–296.

Van Marken Lichtenbelt, W. D., Vanhommerig, J. W., Smulders, N. M., Drossaerts, J. M. A. F. L., Kemerink, G. J., Bouvy, N. D., Schrauwen, P., and Teule, G. J. J. (2009). Cold-activated brown adipose tissue in healthy men. New England Journal of Medicine, 360(15), 1500–1508.

Vandevijvere, S., Chow, C. C., Hall, K. D., Umali, E., and Swinburn, B. A. (2015). Increased food energy supply as a major driver of the obesity epidemic: a global analysis. Bulletin of the World Health Organization, 93(7), 446–456.

Vankoningsloo, S., Piens, M., Lecocq, C., Gilson, A., De Pauw, A., Renard, P., Demazy, C., Houbion, A., Raes, M., and Arnould, T. (2005). Mitochondrial dysfunction induces triglyceride accumulation in 3T3-L1 cells: Role of fatty acid β-oxidation and glucose. Journal of Lipid Research, 46(6), 1133–1149.

Vega, G. L., Adams-Huet, B., Peshock, R., Willett, D., Shah, B., and Grundy, S. M. (2006). Influence of body fat content and distribution on variation in metabolic risk. Journal of Clinical Endocrinology and Metabolism, 91(11), 4459–4466.

Vegiopoulos, A., Müller-Decker, K., Strzoda, D., Schmitt, I., Chichelnitskiy, E., Ostertag, A., Diaz, M. B., Rozman, J., De Angelis, M. H., Nüsing, R. M., Meyer, C. W., Wahli, W., Klingenspor, M., and Herzig, S. (2010). Cyclooxygenase-2 controls energy homeostasis in mice by de novo recruitment of brown adipocytes. Science, 328(5982), 1158–1161.

Veilleux, A., Caron-Jobin, M., Noël, S., Laberge, P. Y., and Tchernof, A. (2011). Visceral adipocyte hypertrophy is associated with dyslipidemia independent of body composition and fat distribution in women. Diabetes, 60(5), 1504–1511.

Vila-Bedmar, R., Lorenzo, M., and Fernández-Veledo, S. (2010). Adenosine 5′-monophosphate-activated protein kinase-mammalian target of rapamycin cross talk regulates brown adipocyte differentiation. Endocrinology, 151(3), 980–992.

Virtanen, K. A., and Al., E. (2009). Functional Brown Adipose Tissue in Healthy Adults. The New England Journal of Medicine.

Virtanen, K. A., Lidell, M. E., Orava, J., Heglind, M., Westergren, R., Niemi, T., Taittonen, M., Laine, J., Savisto, N. J., Enerbäck, S., and Nuutila, P. (2009). Functional brown adipose tissue in healthy adults. The New England journal of medicine, 360(15), 1518–1525.

Visser, M., Bouter, L. M., McQuillan, G. M., Wener, M. H., and Harris, T. B. (1999). Elevated C-reactive protein levels in overweight and obese adults. Journal of the American Medical Association, 282(22), 2131–2135.

Vitali, A., Murano, I., Zingaretti, M. C., Frontini, A., Ricquier, D., and Cinti, S. (2012). The adipose organ of obesity-prone C57BL/6J mice is composed of mixed white and brown adipocytes. Journal of Lipid Research, 53(4), 619–629.

von Knethen, A., and Brüne, B. (2002). Activation of Peroxisome Proliferator-Activated Receptor γ by Nitric Oxide in Monocytes/Macrophages Down-Regulates p47 phox and Attenuates the Respiratory Burst . The Journal of Immunology, 169(5), 2619–2626.

Waldén, T. B., Hansen, I. R., Timmons, J. A., Cannon, B., and Nedergaard, J. (2012). Recruited vs. nonrecruited molecular signatures of brown, "brite," and white adipose tissues. American Journal of Physiology - Endocrinology and Metabolism, 302(1), 19–31.

Wallenius, V., Wallenius, K., Ahrén, B., Rudling, M., Carlsten, H., Dickson, S. L., Ohlsson, C., and Jansson, J. O. (2002). Interleukin-6-deficient mice develop mature-onset obesity. Nature medicine, 8(1), 75–79.

Wang, L. J., Liu, M. J., Zhai, T. S., Zhu, H. J., Gong, F. Y., Yang, H. B., Yan, K. M., Pan, H., and Zeng, Y. (2020). Identification of U-shaped curve relation between proneurotensin and risk of coronary artery disease (CAD) in patients with premature CAD. Nutrition, Metabolism and Cardiovascular Diseases, 30(3), 483–491.

Wang, Q. A., Tao, C., Gupta, R. K., and Scherer, P. E. (2013). Tracking adipogenesis during white adipose tissue development, expansion and regeneration. Nature Medicine, 19(10), 1338–1344.

Wang, Q. A., Tao, C., Jiang, L., Shao, M., Ye, R., Zhu, Y., Gordillo, R., Ali, A., Lian, Y., Holland, W. L., Gupta, R. K., and Scherer, P. E. (2015). Distinct regulatory mechanisms governing embryonic versus adult adipocyte maturation. Nature Cell Biology, 17(9), 1099–1111.

Wang, X., Song, C., Zhou, X., Han, X., Li, J., Wang, Z., Shang, H., Liu, Y., and Cao, H. (2017). Mitochondria Associated MicroRNA Expression Profiling of Heart Failure. BioMed Research International, 2017.

Wang, Y., An, H., Liu, T., Qin, C., Sesaki, H., Guo, S., Radovick, S., Hussain, M., Maheshwari, A., Wondisford, F. E., O'Rourke, B., and He, L. (2019). Metformin Improves Mitochondrial Respiratory Activity through Activation of AMPK. Cell Reports, 29(6), 1511-1523.e5.

Weisberg, S. P., Leibel, R. L., Anthony, W., Jr, F., Weisberg, S. P., Mccann, D., Desai, M., Rosenbaum, M., Leibel, R. L., and Ferrante, A. W. (2003). Obesity is associated with macrophage accumulation in adipose tissue Find the latest version : Obesity is associated with. J Clin Invest., 112(12), 1796–1808.

Weiss, R., Dufour, S., Taksali, S. E., Tambortlane, W. V, Petersen, K. F., Bonadonna, R. C., Boselli, L., Barbetta, G., Alle, K., Rife, F., Dziura, J., Sherwin, R., Shulman, G. I., and Caprio, S. (2003). Prediabetes in obese youth: a syndrome of impaired glucose tolerance, severe insulin resistance, and altered myocellular and abdominal fat partitioning. 362(9388), 951–957.

West-Eberhard M. J. (2005). Developmental plasticity and the origin of species differences. Proceedings of the National Academy of Sciences of the United States of America, 102 Suppl 1(Suppl 1), 6543–6549.

Westerterp, K. R. (2004). Diet induced thermogenesis. Nutrition and Metabolism, 1, 1–5.

Weyer, C., Foley, J. E., Bogardus, C., Tataranni, P. A., and Pratley, R. E. (2000). Enlarged subcutaneous abdominal adipocyte size , but not obesity itself , predicts Type II diabetes independent of insulin resistance. Diabetologia, 43(12),1498–1506.

Weyer, C., Funahashi, T., Tanaka, S., Hotta, K., Matsuzawa, Y., Pratley, R. E., and Tataranni, P. A. (2001). Hypoadiponectinemia in obesity and type 2 diabetes: Close association with insulin resistance and hyperinsulinemia. Journal of Clinical Endocrinology and Metabolism, 86(5), 1930–1935.

Weyer, C., Tataranni, P. A., Snitker, S., Danforth, E., and Ravussin, E. (1998). Increase in insulin action and fat oxidation after treatment with CL 316,243, a highly selective β3-adrenoceptor agonist in humans. Diabetes, 47(10), 1555–1561.

Weyer, C., Wolford, J. K., Hanson, R. L., Foley, J. E., Tataranni, P. A., Bogardus, C., and Pratley, R. E. (2001). Subcutaneous Abdominal Adipocyte Size , a Predictor of Type 2 Diabetes , Is Linked to Chromosome 1q21 – q23 and Is Associated with a Common Polymorphism in LMNA in Pima Indians. Molecular Genetics and Metabolism 72, 238, 231– 238.

Wild, S., Roglic, G., Green, A., Sicree, R., and King, H. (2004). Global prevalence of diabetes: estimates for the year 2000 and projections for 2030. Diabetes care, 27(5), 1047–1053.

Winkler, G., Kiss, S., Keszthelyi, L., Sápi, Z., Ory, I., Salamon, F., Kovács, M., Vargha, P., Szekeres, O., Speer, G., Karádi, I., Sikter, M., Kaszás, E., Dworak, O., Gerö, G., and Cseh, K. (2003). Expression of tumor necrosis factor (TNF)-alpha protein in the subcutaneous and visceral adipose tissue in correlation with adipocyte cell volume, serum TNF-alpha, soluble serum TNF-receptor-2 concentrations and C-peptide level. European journal of endocrinology, 149(2), 129–135.

World Health Organisation (WHO). 1995. Physical Status: The Use and Interpretation of Anthropometry, WHO Technical Report 854.

Wu, F. Z., Wu, C. C., Kuo, P. L., and Wu, M. T. (2016). Differential impacts of cardiac and abdominal ectopic fat deposits on cardiometabolic risk stratification. BMC Cardiovascular Disorders, 16(1), 1–9.

Wu, J., Boström, P., Sparks, L. M., Ye, L., Choi, J. H., Giang, A. H., Khandekar, M., Virtanen, K. A., Nuutila, P., Schaart, G., Huang, K., Tu, H., van Marken Lichtenbelt, W. D., Hoeks, J., Enerbäck, S., Schrauwen, P., and Spiegelman, B. M. (2012). Beige adipocytes are a distinct type of thermogenic fat cell in mouse and human. Cell, 150(2), 366–376.

Wu, L., Xia, M., Duan, Y., Zhang, L., Jiang, H., Hu, X., Yan, H., Zhang, Y., Gu, Y., Shi, H., Li, J., Gao, X., and Li, J. (2019). Berberine promotes the recruitment and activation of brown adipose tissue in mice and humans. Cell Death and Disease, 10(6).

Wu, L., Zhang, L., Li, B., Jiang, H., Duan, Y., Xie, Z., Shuai, L., Li, J., and Li, J. (2018). AMP-Activated Protein Kinase (AMPK) regulates energy metabolism through modulating thermogenesis in adipose tissue. Frontiers in Physiology, 9(FEB), 1–23.

Wu, Y., Zhang, A., Hamilton, D. J., and Deng, T. (2017). Epicardial Fat in the Maintenance of Cardiovascular Health. Methodist DeBakey Cardiovascular Journal, 13(1), 20–24.

Wu, Z., Puigserver, P., Andersson, U., Zhang, C., Adelmant, G., Mootha, V., Troy, A., Cinti, S., Lowell, B., Scarpulla, R. C., and Spiegelman, B. M. (1999). Mechanisms controlling mitochondrial biogenesis and respiration through the thermogenic coactivator PGC-1. Cell, 98(1), 115–124.

Xu, H., Barnes, G. T., Yang, Q., Tan, G., Yang, D., Chou, C. J., Sole, J., Nichols, A., Ross, J. S., Tartaglia, L. A., and Chen, H. (2003). Chronic inflammation in fat plays a crucial role in the development of obesity-related insulin resistance. The Journal of clinical investigation, 112(12), 1821–1830.

Xue, B., Rim, J. S., Hogan, J. C., Coulter, A. A., Koza, R. A., and Kozak, L. P. (2007). Genetic variability effects the development of brown adipocytes in white fat but not in interscapular brown fat. Journal of Lipid Research, 48(1), 41–51.

Yamaguchi, Y., Cavallero, S., Patterson, M., Shen, H., Xu, J., Kumar, S. R., and Sucov, H. M. (2015). Adipogenesis and epicardial adipose tissue: A novel fate of the epicardium induced by mesenchymal transformation and PPARγ activation. Proceedings of the National Academy of Sciences of the United States of America, 112(7), 2070–2075.

Yamauchi, T., Kamon, J., Minokoshi, Y., Ito, Y., Waki, H., Uchida, S., Yamashita, S., Noda, M., Kita, S., Ueki, K., Eto, K., Akanuma, Y., Froguel, P., Foufelle, F., Ferre, P., Carling, D., Kimura, S., Nagai, R., Kahn, B. B., and Kadowaki, T. (2002). Adiponectin stimulates glucose utilization and fatty-acid oxidation by activating AMP-activated protein kinase. Nature Medicine, 8(11), 1288–1295.

Yamauchi, T., Kamon, J., Waki, H., Terauchi, Y., Kubota, N., Hara, K., Mori, Y., Ide, T., Murakami, K., Tsuboyama-Kasaoka, N., Ezaki, O., Akanuma, Y., Gavrilova, O., Vinson, C., Reitman, M. L., Kagechika, H., Shudo, K., Yoda, M., Nakano, Y., Kadowaki, T. (2001). The fat-derived hormone adiponectin reverses insulin resistance associated with both lipoatrophy and obesity. Nature Medicine, 7(8), 941–946.

Yang, Q. Y., Liang, J. F., Rogers, C. J., Zhao, J. X., Zhu, M. J., and Du, M. (2013). Maternal obesity induces epigenetic modifications to facilitate Zfp423 expression and enhance adipogenic differentiation in fetal mice. Diabetes, 62(11), 3727–3735.

Yang, Y., Smith, D. L., Jr, Keating, K. D., Allison, D. B., and Nagy, T. R. (2014). Variations in body weight, food intake and body composition after long-term high-fat diet feeding in C57BL/6J mice. Obesity (Silver Spring, Md.), 22(10), 2147–2155.

Yatagai, T., Nagasaka, S., Taniguchi, A., Fukushima, M., Nakamura, T., Kuroe, A., Nakai, Y., and Ishibashi, S. (2003). Hypoadiponectinemia is associated with visceral fat accumulation and insulin resistance in Japanese men with type 2 diabetes mellitus. Metabolism: clinical and experimental, 52(10), 1274–1278.

Yi, S. Y., Steffen, L. M., Terry, J. G., R Jacobs, D., Duprez, D., Steffen, B. T., Zhou, X., Shikany, J. M., Harnack, L., and J Carr, J. (2020). Added sugar intake is associated with pericardial adipose tissue volume. European Journal of Preventive Cardiology, 27(18), 2016–2023.

Yin, M., van der Horst, I. C. C., van Melle, J. P., Qian, C., van Gilst, W. H., Silljé, H. H. W., and de Boer, R. A. (2011). Metformin improves cardiac function in a nondiabetic rat model of post-MI heart failure. American Journal of Physiology - Heart and Circulatory Physiology, 301(2), 459–468.

Yoneshiro, T., Aita, S., Matsushita, M., Okamatsu-Ogura, Y., Kameya, T., Kawai, Y., Miyagawa, M., Tsujisaki, M., and Saito, M. (2011). Age-related decrease in cold-activated

brown adipose tissue and accumulation of body fat in healthy humans. Obesity, 19(9), 1755–1760.

Young, J. B., and Landsberg, L. (1977). Stimulation of the sympathetic nervous system during sucrose feeding. Nature, 269(5629), 615–617.

Young, J. B., and Landsberg, L. (1997). Suppression of sympathetic nervous system during fasting. Obesity Research, 5(6), 646–649.

Yu, C., Chen, Y., Cline, G. W., Zhang, D., Zong, H., Wang, Y., Bergeron, R., Kim, J. K., Cushman, S. W., Cooney, G. J., Atcheson, B., White, M. F., Kraegen, E. W., and Shulman, G. I. (2002). Mechanism by which fatty acids inhibit insulin activation of insulin receptor substrate-1 (IRS-1)-associated phosphatidylinositol 3-kinase activity in muscle. Journal of Biological Chemistry, 277(52), 50230–50236.

Yuan, T., Li, J., Zhao, W. G., Sun, W., Liu, S. N., Liu, Q., Fu, Y., and Shen, Z. F. (2019). Effects of metformin on metabolism of white and brown adipose tissue in obese C57BL/6J mice. Diabetology and Metabolic Syndrome, 11(1), 1–10.

Yudkin, J. S., Eringa, E., and Stehouwer, C. D. (2005). "Vasocrine" signalling from perivascular fat: a mechanism linking insulin resistance to vascular disease. Lancet (London, England), 365(9473), 1817–1820.

Zhang, F., Hao, G., Shao, M., Nham, K., An, Y., Wang, Q., Zhu, Y., Kusminski, C. M., Hassan, G., Gupta, R. K., Zhai, Q., Sun, X., Scherer, P. E., and Oz, O. K. (2018). An Adipose Tissue Atlas: An Image-Guided Identification of Human-like BAT and Beige Depots in Rodents. Cell metabolism, 27(1), 252–262.e3.

Zhang, J., Zhang, F., Didelot, X., Bruce, K. D., Cagampang, F. R., Vatish, M., Hanson, M., Lehnert, H., Ceriello, A., and Byrne, C. D. (2009). Maternal high fat diet during pregnancy and lactation alters hepatic expression of insulin like growth factor-2 and key microRNAs in the adult offspring. BMC Genomics, 10(June 2014), 478.

Zhang, L., Zhang, L., Wang, X., and Si, H. (2017). Anti-adipogenic effects and mechanisms of ginsenoside Rg3 in pre-adipocytes and obese mice. Frontiers in Pharmacology, 8(MAR), 1–10.

Zhang, Q. C., Hastings, C., Johnson, K., and Slaven, E. (2019). Metformin-Associated Lactic Acidosis Presenting Like Acute Mesenteric Ischemia. Journal of Emergency Medicine, 57(5), 720–722.

Zhang, Y., Proenca, R., Maffei, M., Barone, M., Leopold, L., and Friedman, J. M. (1995). Positional cloning of the mouse obese gene and its human homologue. Nature, 374(6521), 479.

Zhao, J., Cannon, B., and Nedergaard, J. (1997). α1-Adrenergic stimulation potentiates the thermogenic action of β3- adrenoreceptor-generated cAMP in brown fat cells. Journal of Biological Chemistry, 272(52), 32847–32856.

Zhou, G., Myers, R., Li, Y., Chen, Y., Shen, X., Fenyk-Melody, J., Wu, M., Ventre, J., Doebber, T., Fujii, N., Musi, N., Hirshman, M. F., Goodyear, L. J., and Moller, D. E. (2001). Role of AMP-activated protein kinase in mechanism of metformin action. Journal of Clinical Investigation, 108(8), 1167–1174.

Zhou, Y., Li, H., Zhang, Y., Zhang, L., Liu, J., and Liu, J. (2019a). Association of Maternal Obesity in Early Pregnancy with Adverse Pregnancy Outcomes: A Chinese Prospective Cohort Analysis. Obesity, 27(6), 1030–1036.

Zhou, Y., Li, W., Zhou, J., Chen, J., Wang, X., Cai, M., Li, F., Xu, W., Carlsson, P. O., and Sun, Z. (2019b). Lipotoxicity reduces β cell survival through islet stellate cell activation regulated by lipid metabolism-related molecules. Experimental cell research, 380(1), 1–8.

Zhou, Y. T., Grayburn, P., Karim, A., Shimabukuro, M., Higa, M., Baetens, D., Orci, L., and Unger, R. H. (2000). Lipotoxic heart disease in obese rats: Implications for human obesity.

Proceedings of the National Academy of Sciences of the United States of America, 97(4), 1784–1789.

Zhu, Q., Glazier, B. J., Hinkel, B. C., Cao, J., Liu, L., Liang, C., and Shi, H. (2019). Neuroendocrine regulation of energy metabolism involving different types of adipose tissues. International Journal of Molecular Sciences, 20(11), 1–22.

Ziccardi, P., Nappo, F., Giugliano, G., Esposito, K., Marfella, R., Cioffi, M., D'Andrea, F., Molinari, A. M., and Giugliano, D. (2002). Reduction of inflammatory cytokine concentrations and improvement of endothelial functions in obese women after weight loss over one year. Circulation, 105(7), 804–809.

Zuriaga, M. A., Fuster, J. J., Gokce, N., and Walsh, K. (2017). Humans and Mice Display Opposing Patterns of "Browning" Gene Expression in Visceral and Subcutaneous White Adipose Tissue Depots. Frontiers in Cardiovascular Medicine, 4(May), 1–5.

APPENDICES

APPENDIX 1: BIOCHEMICAL AND METABOLIC PARAMETERS

Appendix Table 1.1. Maternal diet and offspring diet effects of biochemical and metabolic parameters in from 30-week-old offspring mice fed a chow and HF-diet from chow and HF-fed dams

	Maternal Diet	Offspring Diet	Interaction Effect
IpGTT AUC	p = 0.0166*	p < 0.0001****	ns
Total fat mass	p < 0.0001****	ns	ns
Total adiposity	p < 0.0001****	ns	ns
Fasting blood glucose	p = 0.0004***	p < 0.0001****	p = 0.0019**
Triglyceride	ns	p = 0.0008***	ns
FFAs	p = 0.033*	p = 0.0007***	ns
Total Cholesterol	p < 0.0001****	ns	p = 0.0415*
HDL	ns	p < 0.0001****	ns
LDL	ns	p < 0.0001****	ns
PAT depot weight	ns	p = 0.0011**	p = 0.0164*
TG content	ns	p = 0.0492*	ns

APPENDIX 2: TRANSCRIPTIONAL ANALYSIS

Groups were analysed by two-way ANOVA and Tukey's post-test for multiple comparisons. The interaction between the two variables denotes that the effect of one variable is dependent on the other. ns detonates no statistical significance.

Appendix Table 2.1. Maternal diet and offspring diet in adipose and heart tissue gene expression differences in 30-week-old offspring mice fed a chow and HF-diet from chow and HF-fed dams

	Maternal Diet	Offspring Diet	Interaction Effect
	gWAT		
FABP4	p = 0.0312*	p = 0.0029**	0.0107*
PPARγ	p = 0.0069**	p < 0.0001****	ns
C/EBPα	ns	p = 0.0014**	ns
IL6	ns	p < 0.0001****	ns
TNFα	ns	p < 0.0001****	ns
Leptin	ns	p = 0.0254*	ns
AdipoQ	ns	p < 0.0001****	ns
	iWAT		
UCP1	ns	ns	ns
ADRβ3	ns	p < 0.0001****	ns
DIO2	ns	ns	ns
PGC1α	ns	ns	ns
COX7A1	ns	ns	ns
COX8B	ns	ns	ns
	iBAT		
UCP1	p = 0.0143*	p = 0.0005***	p = 0.0346*
ADRβ3	ns	ns	p = 0.0009***
DIO2	ns	ns	ns
PGC1α	p = 0.0040**	p = 0.0179*	ns
COX7A1	ns	p = 0.0020**	ns
COX8B	p = 0.0179*	p = 0.0360*	ns
	PAT		
FABP4	ns	p = 0.0148*	ns
PPARγ	ns	p = 0.0129*	ns
C/EBPα	ns	p = 0.0304*	ns
IL6	p < 0.0001****	p = 0.0063**	p = 0.0157*

	Treatment	Diet	Interaction Effect
TNFα	$p < 0.0001$****	$p = 0.0485$*	ns
Leptin	ns	$p = 0.0006$***	ns

Heart			
MYH7	ns	ns	ns
MYH6	ns	ns	ns
NPPA	ns	ns	ns
ACTA1	ns	$p < 0.0001$****	ns
NOX4	ns	ns	ns
PLIN1	ns	ns	ns
PGC1α	ns	ns	ns
IL6	ns	ns	ns
TNFα	ns	ns	ns

Appendix Table 2.2. Treatment and diet effect in gonadal white adipose tissue gene expression differences from cells of the stromal vascular fraction in chow-fed and HF-fed 10-week-old mice treated with Vehicle or Cpd14

	Treatment	Diet	Interaction Effect
FABP4	$p = 0.0044$**	$p = 0.0018$**	$p = 0.0009$***
PPARγ	ns	$p = 0.0166$*	ns
C/EBPα	ns	ns	ns

Appendix Table 2.3. Treatment and diet effect in adipose tissue gene expression differences in chow-fed and HF-fed 10-week-old mice treated with Vehicle or Cpd14

	Treatment	Diet	Interaction Effect
gWAT			
FABP4	ns	ns	p = 0.0488*
PPARγ	ns	ns	p = 0.0027**
C/EBPα	ns	p = 0.0030**	p = 0.0024**
IL6	ns	p = 0.0495*	ns
TNFα	ns	ns	ns
Leptin	p = 0.0277*	p = 0.0068**	p = 0.0177*
AdipoQ	ns	ns	ns
iWAT			
UCP1	p = 0.0006***	p < 0.0001****	p = 0.0013**
ADRβ3	ns	ns	p = 0.0007***
DIO2	ns	ns	ns
PGC1α	ns	ns	ns
COX7A1	ns	p = 0.0040**	p = 0.0115*
COX8B	ns	p = 0.0011**	ns
iBAT			
UCP1	ns	p = 0.0005***	ns
ADRβ3	p = 0.0373*	p = 0.0002***	ns
DIO2	p = 0.0009***	ns	ns
PGC1α	p = 0.0118*	ns	ns
COX7A1	ns	p = 0.0035**	ns
COX8B	p = 0.0019**	p < 0.0001****	ns
PAT			
FABP4	ns	ns	p = 0.0436*
PPARγ	ns	ns	ns
C/EBPα	ns	ns	ns
IL6	ns	ns	ns
TNFα	ns	ns	ns
UCP1	ns	ns	ns
PGC1α	ns	ns	p = 0.0444*

APPENDIX 3: HISTOLOGICAL ANALYSIS

Groups were analysed by two-way ANOVA and Tukey's post-test for multiple comparisons. The interaction between the two variables denotes that the effect of one variable is dependent on the other. ns detonates no statistical significance.

Appendix Table 3.1. Statistical analysis of cell volume distribution of chow-fed or HF-fed 10-week-old male mice

	0 to 5×10^5	5×10^5 to 1×10^6	1×10^6 to 5×10^6	5×10^6 to 1×10^7	$> 1 \times 10^7$
chow					
gWAT vs iWAT	ns	ns	ns	p = 0.0162*	p = 0.0428*
gWAT vs C-PAT	p = 0.0007***	ns	p = 0.0005***	p = 0.0024**	p = 0.0302*
iWAT vs PAT	p = 0.0059**	ns	p = 0.0005***	ns	ns
HF					
gWAT vs iWAT	ns	ns	ns	ns	ns
gWAT vs C-PAT	p = 0.0067**	p = 0.0107*	ns	ns	p = 0.0002***
iWAT vs PAT	p = 0.0118*	ns	ns	p = 0.0017**	p = 0.0283*

Appendix Table 3.2. Statistical analysis of cell volume distribution of chow-fed and HF-fed 10-week-old male mice

	0 to 5×10^5	5×10^5 to 1×10^6	1×10^6 to 5×10^6	5×10^6 to 1×10^7	$> 1 \times 10^7$
c-gWAT vs HF-gWAT	ns	ns	p = 0.02*	ns	p < 0.0001****
c-gWAT vs c-iWAT	ns	ns	ns	p = 0.0231*	ns
c-gWAT vs HF-iWAT	ns	ns	ns	ns	p = 0.0006***
c-gWAT vs C-PAT	p = 0.0004***	ns	p = 0.0007***	p = 0.0018**	ns
c-gWAT vs HF-PAT	ns	ns	ns	ns	ns
HF-gWAT vs c-iWAT	ns	p = 0.0102*	p = 0.021*	p = 0.0063**	p < 0.0001****
HF-gWAT vs HF-iWAT	ns	ns	ns	ns	p = 0.0232*
HF-gWAT vs C-PAT	p < 0.0001****	p = 0.0009***	ns	p = 0.0005***	p < 0.0001****
HF-gWAT vs HF-PAT	p = 0.022*	ns	ns	ns	p < 0.0001****
c-iWAT vs HF-iWAT	ns	p = 0.0402*	ns	p < 0.0001****	p < 0.0001****

	0 to 5 x 10⁵	5 x 10⁵ to 1 x 10⁶	1 x 10⁶ to 5 x 10⁶	5 x 10⁶ to 1 x 10⁷	> 1 x 10⁷
c-iWAT vs HF-PAT	ns	ns	ns	ns	ns
HF-iWAT vs C-PAT	p < 0.0001****	p = 0.0039**	ns	p < 0.0001****	p < 0.0001****
HF-iWAT vs HF-PAT	p = 0.041*	ns	ns	p = 0.0062**	p = 0.0038**
C-PAT vs HF-PAT	ns	ns	ns	ns	ns

Appendix Table 3.3. Statistical analysis of cell volume distribution of chow-fed or HF-fed 30-week-old male mice

	0 to 5 x 10⁵	5 x 10⁵ to 1 x 10⁶	1 x 10⁶ to 5 x 10⁶	5 x 10⁶ to 1 x 10⁷	> 1 x 10⁷
chow					
gWAT vs iWAT	ns	ns	ns	ns	ns
gWAT vs C-PAT	ns	ns	ns	ns	ns
iWAT vs PAT	ns	p = 0.093**	ns	p = 0.406*	ns
HF					
gWAT vs iWAT	ns	ns	ns	ns	ns

	0 to 5 x 10⁵	5 x 10⁵ to 1 x 10⁶	1 x 10⁶ to 5 x 10⁶	5 x 10⁶ to 1 x 10⁷	> 1 x 10⁷
gWAT vs C-PAT	ns	ns	ns	ns	ns
iWAT vs PAT	ns	ns	ns	ns	ns

Appendix Table 3.4. Statistical analysis of cell volume distribution of chow-fed and HF-fed 30-week-old male mice

	0 to 5×10^5	5×10^5 to 1×10^6	1×10^6 to 5×10^6	5×10^6 to 1×10^7	$> 1 \times 10^7$
c-gWAT vs HF-gWAT	ns	ns	ns	ns	ns
c-gWAT vs c-iWAT	ns	ns	ns	ns	ns
c-gWAT vs HF-iWAT	ns	ns	ns	ns	ns
c-gWAT vs C-PAT	ns	ns	ns	ns	ns
c-gWAT vs HF-PAT	ns	ns	ns	ns	ns
HF-gWAT vs c-iWAT	ns	ns	ns	ns	p = 0.0264*
HF-gWAT vs	ns	ns	ns	ns	ns

HF-iWAT

HF-gWAT vs C-PAT	ns	p = 0.0011**	ns	ns	p = 0.0006***
HF-gWAT vs HF-PAT	ns	ns	ns	ns	ns
c-iWAT vs HF-iWAT	ns	ns	ns	ns	ns
c-iWAT vs C-PAT	ns	p = 0.0067**	ns	ns	ns
c-iWAT vs HF-PAT	ns	ns	ns	ns	ns
HF-iWAT vs C-PAT	ns	ns	ns	ns	p = 0.0032**
HF-iWAT vs HF-PAT	ns	ns	ns	ns	ns
C-PAT vs HF-PAT	ns	ns	ns	ns	ns

Appendix Table 3.5. Maternal diet and offspring diet effect in the percentage change in cell volume in 30-week-old offspring mice fed a chow and HF-diet from chow and HF-fed dams

	Maternal Diet	Offspring Diet	Interaction Effect
gWAT	$p = 0.0021$**	$p < 0.0001$****	ns
iWAT	ns	$p < 0.0001$****	ns
PAT	$p = 0.0154$*	$p < 0.0001$****	$p = 0.0291$*

Appendix Table 3.6. Maternal diet and offspring diet effect in PAT cell number in 30-week-old offspring mice fed a chow and HF-diet from chow and HF-fed dams

	Maternal Diet	Offspring Diet	Interaction Effect
PAT	ns	$p = 0.0309$*	ns

Appendix Table 3.7. Statistical analysis of cell volume distribution in 30-week-old offspring mice fed a chow and HF-diet from chow and HF-fed dams

	0 to 5×10^5	5×10^5 to 1×10^6	1×10^6 to 5×10^6	5×10^6 to 1×10^7	$> 1 \times 10^7$
gWAT					
C/C vs C/HF	ns	ns	ns	ns	$p = 0.0056$**
C/C vs HF/C	ns	ns	$p = 0.0374$*	ns	$p = 0.0044$**
C/C vs HF/HF	ns	$p = 0.0376$*	$p = 0.0034$**	ns	$p < 0.0001$****
C/HF vs HF/C	ns	ns	ns	ns	ns
C/HF vs HF/HF	ns	ns	ns	ns	$p = 0.011$*

HF/C vs HF/HF	ns	ns	ns	p = 0.0008***	p = 0.0463*
iWAT					
C/C vs C/HF	ns	ns	ns	ns	ns
C/C vs HF/C	ns	ns	ns	ns	ns
C/C vs HF/HF	ns	ns	p = 0.0039**	ns	p = 0.0002***
C/HF vs HF/C	ns	ns	ns	ns	ns
C/HF vs HF/HF	ns	ns	ns	ns	ns
HF/C vs HF/HF	ns	ns	p = 0.0337*	ns	p = 0.004**
PAT					
C/C vs C/HF	ns	ns	ns	ns	p = 0.001***
C/C vs HF/C	ns	ns	ns	ns	ns
C/C vs HF/HF	ns	p = 0.009**	ns	ns	p < 0.0001****
C/HF vs HF/C	ns	ns	p = 0.046*	ns	p = 0.003**
C/HF vs HF/HF	ns	ns	ns	ns	ns

HF/C vs HF/HF	ns	ns	$p = 0.023^*$	ns	$p < 0.0001^{****}$

Appendix Table 3.8. Maternal diet and offspring diet effect in cell volume distribution in 30-week-old offspring mice fed a chow and HF-diet from chow and HF-fed dams

	Maternal Diet	Offspring Diet	Interaction Effect
gWAT			
0 to 5 x 10^5	ns	ns	ns
5 x 10^5 to 1 x 10^6	$p = 0.0244^*$	ns	ns
1 x 10^6 to 5 x 10^6	$p = 0.0018^{**}$	ns	ns
5 x 10^6 to 1 x 10^7	ns	$p = 0.0012^{**}$	$p = 0.0074^{**}$
> 1 x 10^7	$p < 0.0001^{****}$	$p = 0.0001^{***}$	ns
iWAT			
0 to 5 x 10^5	ns	ns	ns
5 x 10^5 to 1 x 10^6	$p = 0.0495^*$	ns	ns
1 x 10^6 to 5 x 10^6	ns	$p = 0037^{**}$	ns
5 x 10^6 to 1 x 10^7	ns	$p = 0.0170^*$	ns
> 1 x 10^7	$p = 0.0134^*$	$p = 0.0001^{***}$	ns
PAT			
0 to 5 x 10^5	ns	ns	ns
5 x 10^5 to 1 x 10^6	$p = 0.0281^*$	$p = 0.0253^*$	ns
1 x 10^6 to 5 x 10^6	ns	$p = 0.0012^{**}$	ns
5 x 10^6 to 1 x 10^7	ns	ns	$p = 0.0393^*$
> 1 x 10^7	ns	$p < 0.0001^{****}$	ns

Appendix Table 3.9. Treatment and diet effect in the percentage change in cell volume in chow-fed and HF-fed 10-week-old mice treated with Vehicle or Cpd14

	Treatment	Diet	Interaction Effect
gWAT	$p = 0.0237^*$	$p < 0.0001^{****}$	$p = 0.0446^*$
iWAT	$p = 0.0002^{***}$	$p < 0.0001^{****}$	$p = 0.0010^{**}$
PAT	$p = 0.0137^*$	$p = 0.0061^{**}$	$p = 0.0301^*$

Appendix Table 3.10. Statistical analysis of cell volume distribution in chow-fed and HF-fed 10-week-old mice treated with Vehicle or Cpd14

	0 to 5×10^5	5×10^5 to 1×10^6	1×10^6 to 5×10^6	5×10^6 to 1×10^7	$> 1 \times 10^7$
gWAT					
C-V vs C-Cpd14	ns	ns	ns	ns	ns
C-V vs HF-V	ns	ns	p = 0.0089**	ns	p < 0.0001****
C-V vs HF-Cpd14	ns	ns	ns	ns	p = 0.0006***
C-Cpd14 vs HF-V	ns	p = 0.0148*	p = 0.0008***	ns	p < 0.0001****
C-Cpd14 vs HF-Cpd14	ns	p = 0.0136*	p = 0.0257*	ns	p = 0.0003***

HF-V vs HF-Cpd14	**ns**	**ns**	**ns**	**ns**	**ns**

iWAT					
C-V vs C-Cpd14	ns	ns	ns	ns	ns
C-V vs HF-V	p = 0.0451*	p = 0.0014**	ns	p < 0.0001****	p < 0.0001****
C-V vs HF-Cpd14	ns	ns	ns	ns	ns
C-Cpd14 vs HF-V	p = 0.0031**	p = 0.0001***	ns	p < 0.0001****	p < 0.0001****
C-Cpd14 vs HF-Cpd14	ns	ns	ns	ns	ns
HF-V vs HF-Cpd14	ns	ns	ns	p = 0.0002***	p = 0.0001****

PAT					
C-V vs C-Cpd14	ns	ns	ns	ns	ns
C-V vs HF-V	ns	ns	p = 0.013*	p = 0.0004***	ns

C-Cpd14 vs HF-V	p = 0.004**	ns	p = 0.001**	p = 0.0002***	p = 0.04*
C-Cpd14 vs HF-Cpd14	ns	ns	ns	ns	ns
HF-V vs HF-Cpd14	ns	ns	ns	p = 0.0004***	ns

Appendix Table 3.11. Treatment and diet effect in the cell volume distribution in chow-fed and HF-fed 10-week-old mice treated with Vehicle or Cpd14

	Treatment	Diet	Interaction Effect
gWAT			
0 to 5×10^5	ns	p = 0.0063**	ns
5×10^5 to 1×10^6	ns	p = 0.0003***	ns
1×10^6 to 5×10^6	ns	p < 0.0001****	ns
5×10^6 to 1×10^7	ns	p = 0.0352*	ns
> 1×10^7	ns	p < 0.0001****	ns
iWAT			
0 to 5×10^5	ns	p = 0.0014**	ns
5×10^5 to 1×10^6	p = 0.0194*	p = 0.0001***	ns
1×10^6 to 5×10^6	ns	ns	p = 0.0134*
5×10^6 to 1×10^7	p = 0.0001***	p < 0.0001****	p = 0.0049**
> 1×10^7	p = 0.0005***	p < 0.0001****	p = 0.0006***
PAT			
0 to 5×10^5	p = 0.0210*	p = 0.0081**	ns
5×10^5 to 1×10^6	ns	ns	p = 0.0129*
1×10^6 to 5×10^6	p = 0.0471*	p = 0.0008***	ns
5×10^6 to 1×10^7	p = 0.0023**	p = 0.0011**	p = 0023**
> 1×10^7	ns	ns	ns

APPENDIX 4: CORRELATION ANALYSIS
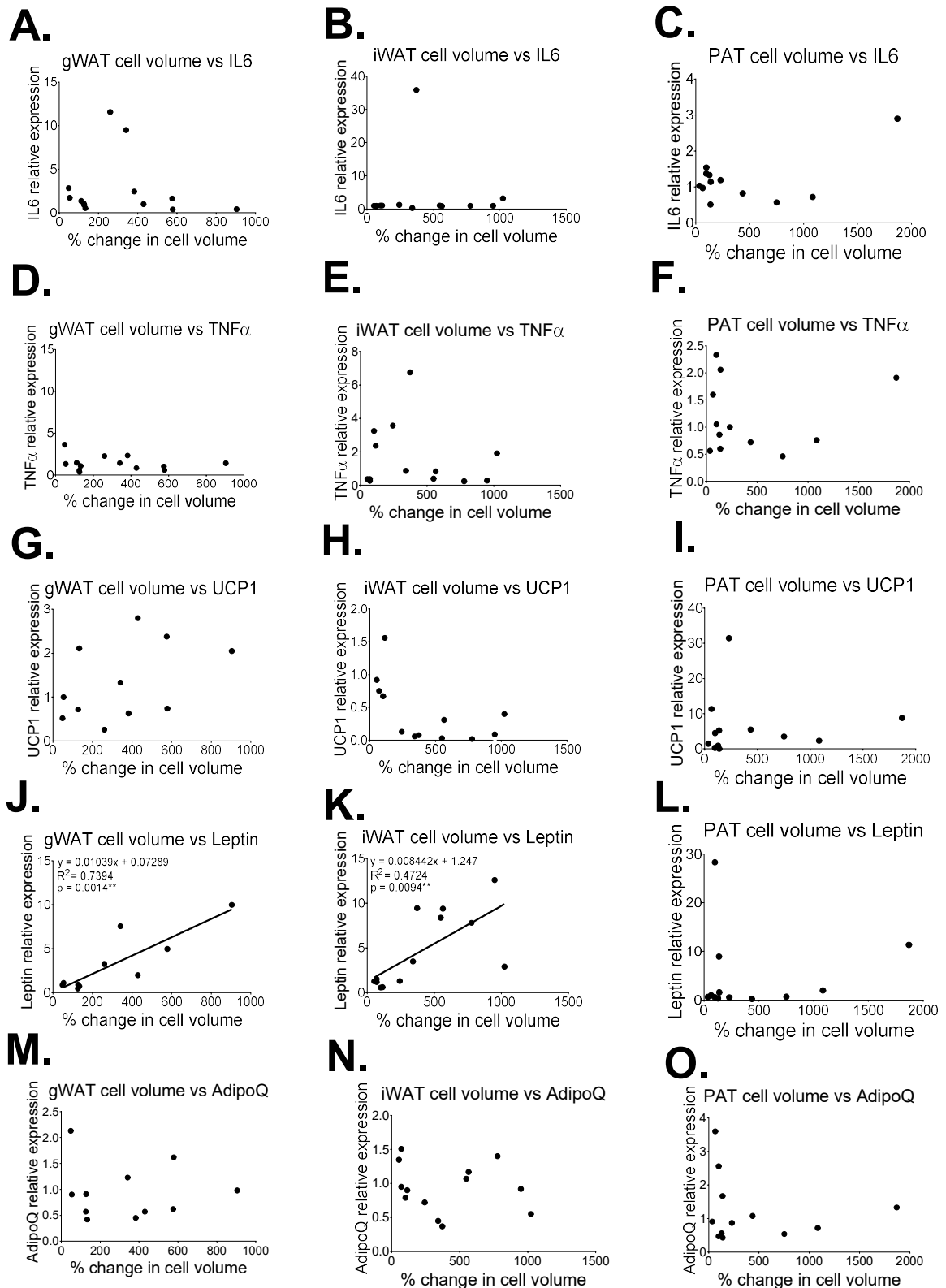
Appendix Figure 4.1. The relationship between the percentage change in cell volume of **gWAT (A,D,G,J,M)**, **iWAT (B,E,H,K,N)** and **PAT (C,F,I,L,O)** compared to the fold change in mRNA expression of IL6, TNFα, UCP1, Leptin and AdipoQ of chow (C) and high-fat (HF)-fed 10-weeks-old male mice. Individual data points plotted, with the line of best fit as determined by simple linear regression. Data analysed by Pearson's correlation coefficient. N = 6-7. * $p<0.05$, ** $p<0.01$, *** $p<0.001$ and **** $p<0.0001$.

A.

gWAT depot weight vs Cell volume

$y = -1535x + 688.6$
$R^2 = 0.3072$
$p = 0.0494*$

B.

gWAT depot weight vs IL6

C.

gWAT depot weight vs TNFα

D.

gWAT depot weight vs UCP1

E.

gWAT depot weight vs AdipoQ

F.

gWAT depot weight vs Leptin
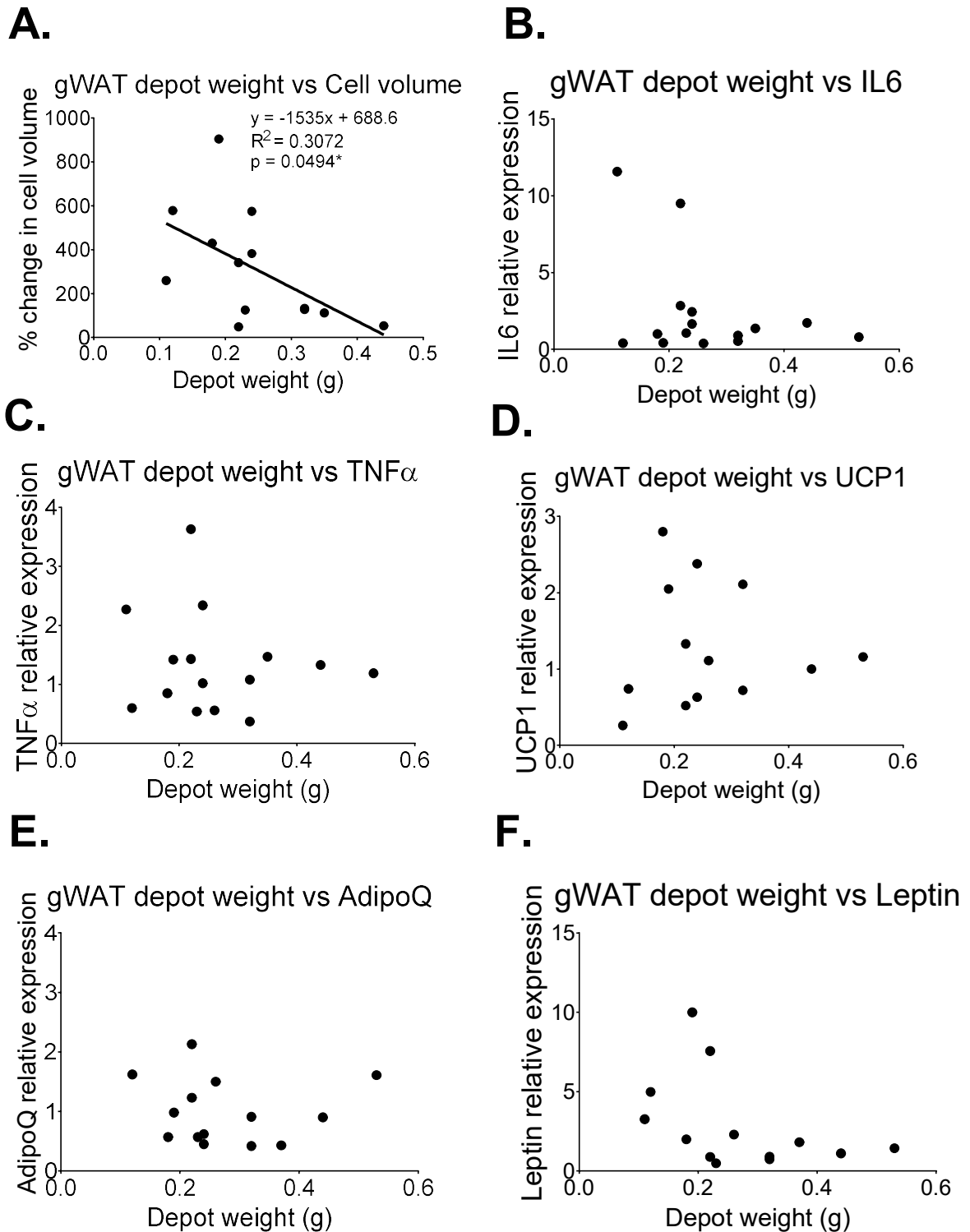
Appendix Figure 4.2. The relationship between the depot weight of **gWAT** compared to the percentage change in cell volume **(A)** and fold change in mRNA expression of IL6 **(B)**, TNFα **(C)**, UCP1 **(D)**, Leptin **(E)** and AdipoQ **(F)** of chow (C) and high-fat (HF)-fed 10-week-old male mice. Individual data points plotted, with the line of best fit as determined by simple linear regression. Data analysed by Pearson's correlation coefficient. N = 6-8. * $p<0.05$, ** $p<0.01$, *** $p<0.001$ and **** $p<0.0001$.
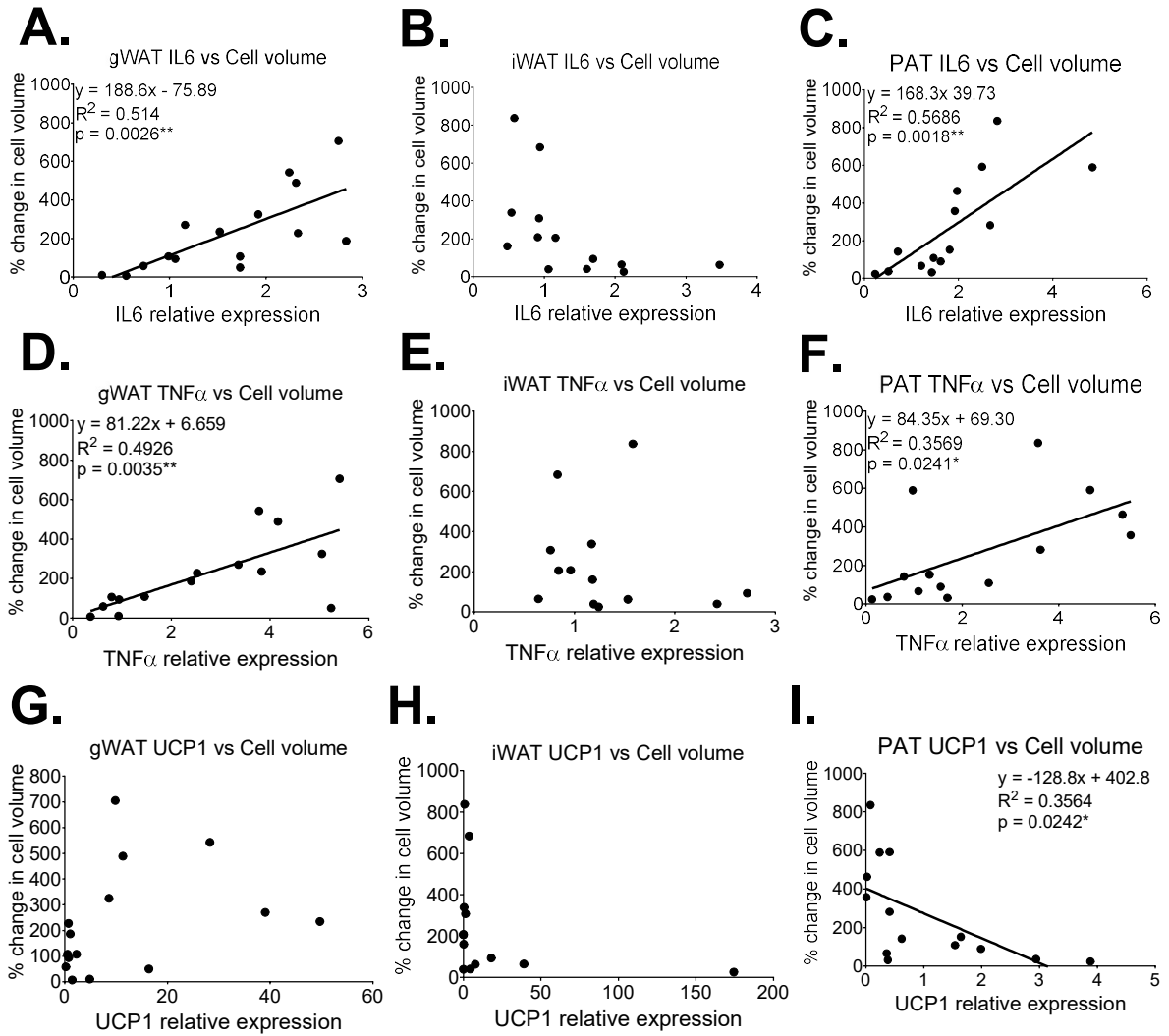
Appendix Figure 4.3. The relationship between the fold change in mRNA expression of IL6, TNFα and UCP1 of **gWAT (A,D,G)**, **iWAT (B,E,H)** and **PAT (C,F,I)** compared to the percentage change in cell volume from chow (C) and high-fat (HF)-fed 30-week-old male mice. Individual data points plotted, with the line of best fit as determined by simple linear regression. Data analysed by Pearson's correlation coefficient. N = 6-11. * p<0.05, ** p<0.01, *** p<0.001 and **** p<0.0001.

A.

gWAT IL6 vs Serum Total Cholesterol

y = 1.492x + 2.615
R^2 = 0.3111
p = 0.0248*

Serum Total Cholesterol (mmol/l)

IL6 relative expression

B.

iWAT IL6 vs Serum Total Cholesterol

y = -1.205x + 5.883
R^2 = 0.3002
p = 0.0186*

Serum Total Cholesterol (mmol/l)

IL6 relative expression

C.

iBAT IL6 vs Serum Total Cholesterol

Serum Total Cholesterol (mmol/l)

IL6 relative expression

D.

PAT IL6 vs Serum Total Cholesterol

Serum Total Cholesterol (mmol/l)

IL6 relative expression

E.

gWAT IL6 vs Serum HDL

y = 0.8635x + 1.533
R^2 = 0.3582
p = 0.0143*

Serum HDL (mmol/l)

IL6 relative expression

F.

iWAT IL6 vs Serum HDL

y = -0.7533x + 3.541
R^2 = 0.3797
p = 0.0065**

Serum HDL (mmol/l)

IL6 relative expression

G.

iBAT IL6 vs Serum HDL

Serum HDL (mmol/l)

IL6 relative expression

H.

PAT IL6 vs Serum HDL

Serum HDL (mmol/l)

IL6 relative expression

I.

gWAT IL6 vs Serum LDL

y = 0.4005x + 0.8136
R^2 = 0.284
p = 0.0336*

Serum LDL (mmol/l)

IL6 relative expression

J.

iWAT IL6 vs Serum LDL

Serum LDL (mmol/l)

IL6 relative expression

K.

iBAT IL6 vs Serum LDL

Serum LDL (mmol/l)

IL6 relative expression

L.

PAT IL6 vs Serum LDL

Serum LDL (mmol/l)

IL6 relative expression

M.

gWAT IL6 vs Serum Triglycerides

Serum Triglycerides (mmol/l)

IL6 relative expression

N.

iWAT IL6 vs Serum Triglycerides

Serum Triglycerides (mmol/l)

IL6 relative expression

O.

iBAT IL6 vs Serum Triglycerides

Serum Triglycerides (mmol/l)

IL6 relative expression

P.

PAT IL6 vs Serum Triglycerides

Serum Triglycerides (mmol/l)

IL6 relative expression

Q.

gWAT IL6 vs Serum Free Fatty Acids

Serum Free Fatty Acids (mmol/l)

IL6 relative expression

R.

iWAT IL6 vs Serum Free Fatty Acids

Serum Free Fatty Acids (mmol/l)

IL6 relative expression

S.

iBAT IL6 vs Serum Free Fatty Acids

Serum Free Fatty Acids (mmol/l)

IL6 relative expression

T.

PAT IL6 vs Serum Free Fatty Acids

Serum Free Fatty Acids (mmol/l)

IL6 relative expression

Appendix Figure 4.4. The relationship between the fold change in mRNA expression of IL6 of **gWAT (A,E,I,M,Q,), iWAT (B,F,J,N,R), iBAT (C,G,K,O,S)** and **PAT (D,H,L,P,T)** compared to serum total cholesterol, HDL, LDL, Triglycerides and Free Fatty Acids levels from chow (C) and high-fat (HF)-fed 30-week-old male mice. Individual data points plotted, with the line of best fit as determined by simple linear regression. Data analysed by Pearson's correlation coefficient. N = 6-12. * p<0.05, ** p<0.01, *** p<0.001 and **** p<0.0001.
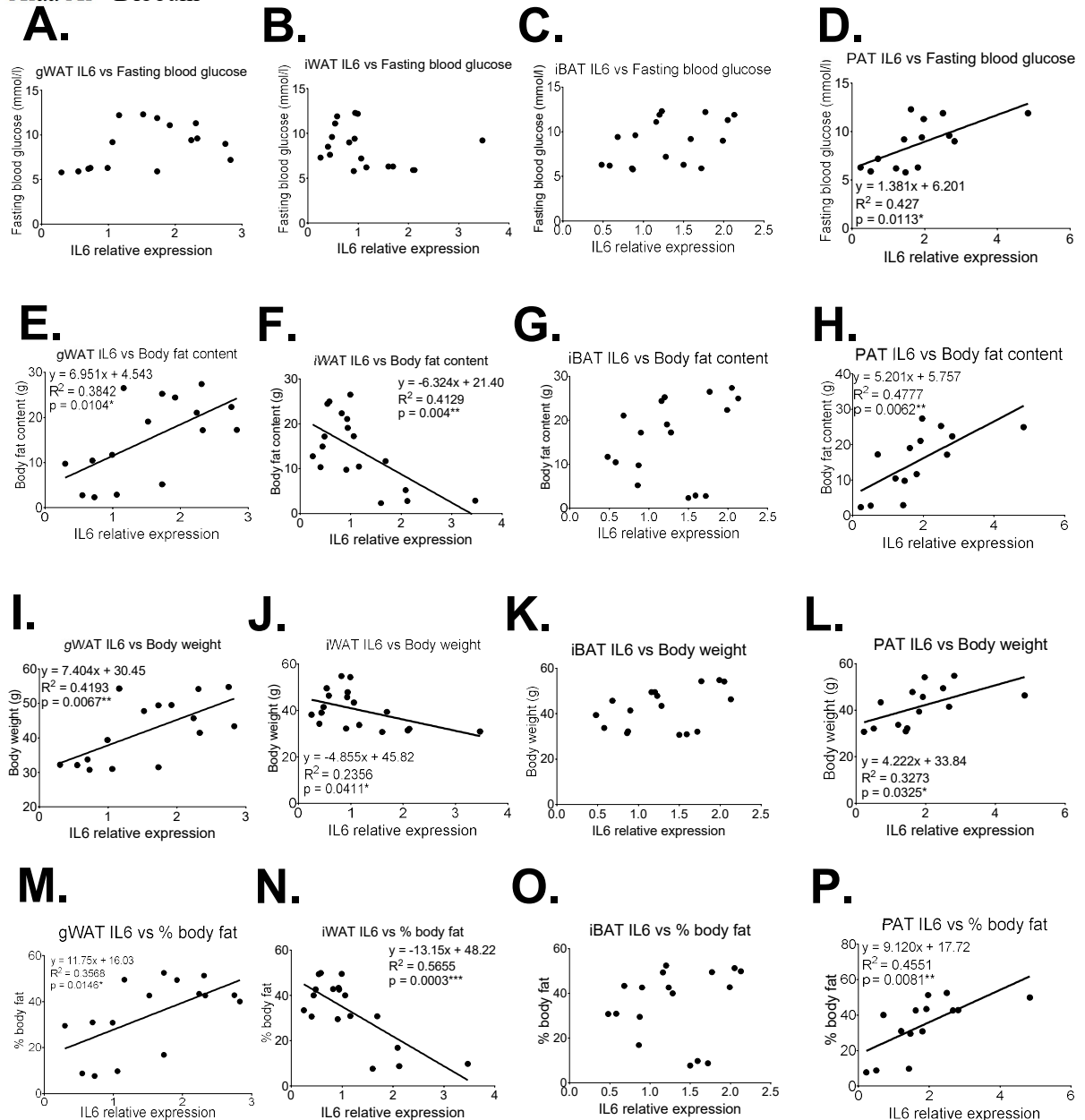
Appendix Figure 4.5. The relationship between the fold change of IL6 in **gWAT (A,E,I,M)**, **iWAT (B,F,J,N)**, **iBAT (C,G,K,O)** and **PAT (D,H,L,P)** compared to compared to fasting blood glucose levels, body fat content, body weight and % body fat from chow (C) and high-fat (HF)-fed 30-week-old male mice. Individual data points plotted, with the line of best fit as determined by simple linear regression. Data analysed by Pearson's correlation coefficient. N = 6-12. * p<0.05, ** p<0.01, *** p<0.001 and **** p<0.0001.

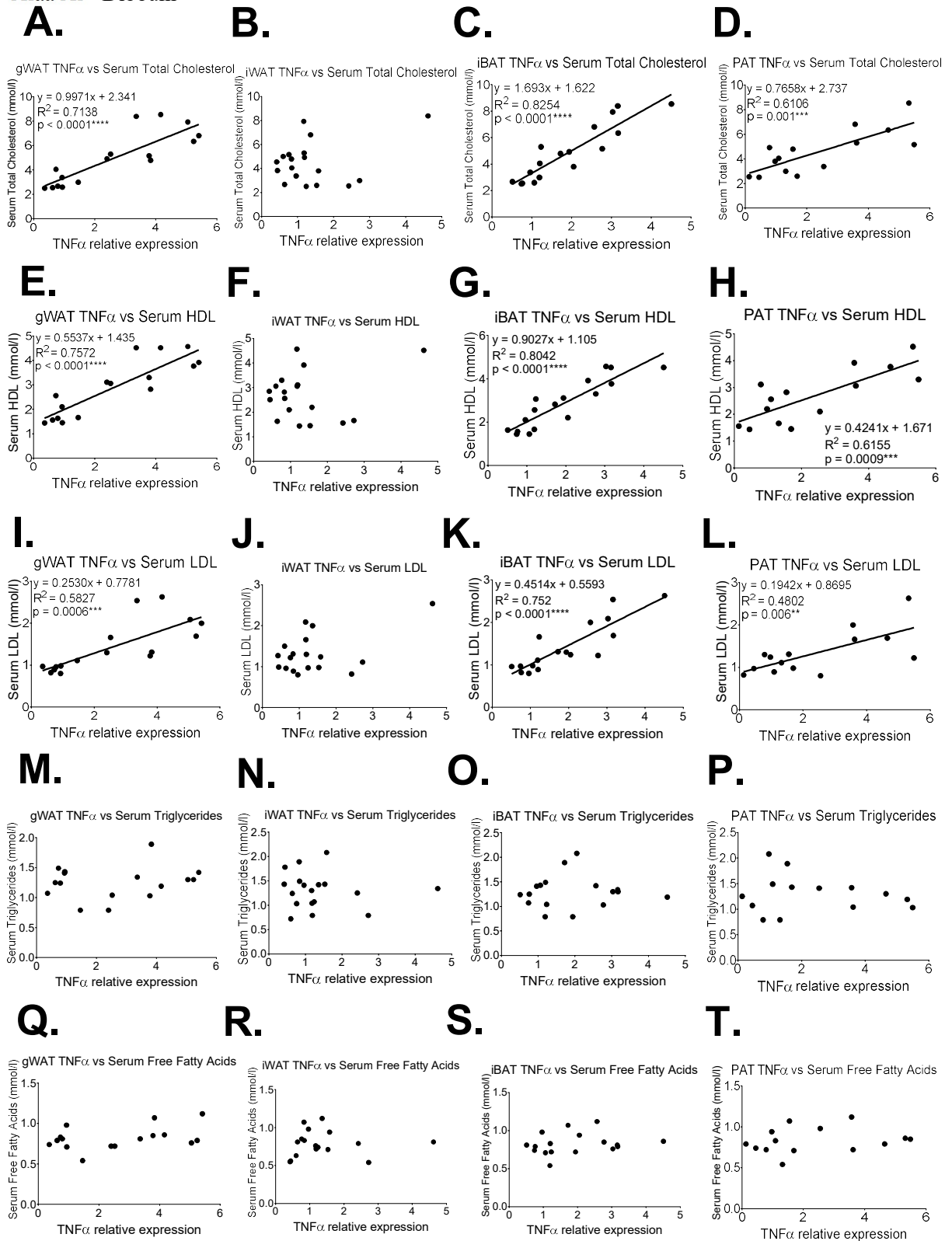**Appendix Figure 4.6.** The relationship between the fold change in mRNA expression of TNFα of **gWAT (A,E,I,M,Q,), iWAT (B,F,J,N,R), iBAT (C,G,K,O,S)** and **PAT (D,H,L,P,T)** compared to serum total cholesterol, HDL, LDL, Triglycerides and Free Fatty Acids levels from chow (C) and high-fat (HF)-fed 30-week-old male mice. Individual data points plotted, with the line of best fit as determined by simple linear regression. Data analysed by Pearson's correlation coefficient. N = 6-12. * p<0.05, ** p<0.01, *** p<0.001 and **** p<0.0001.
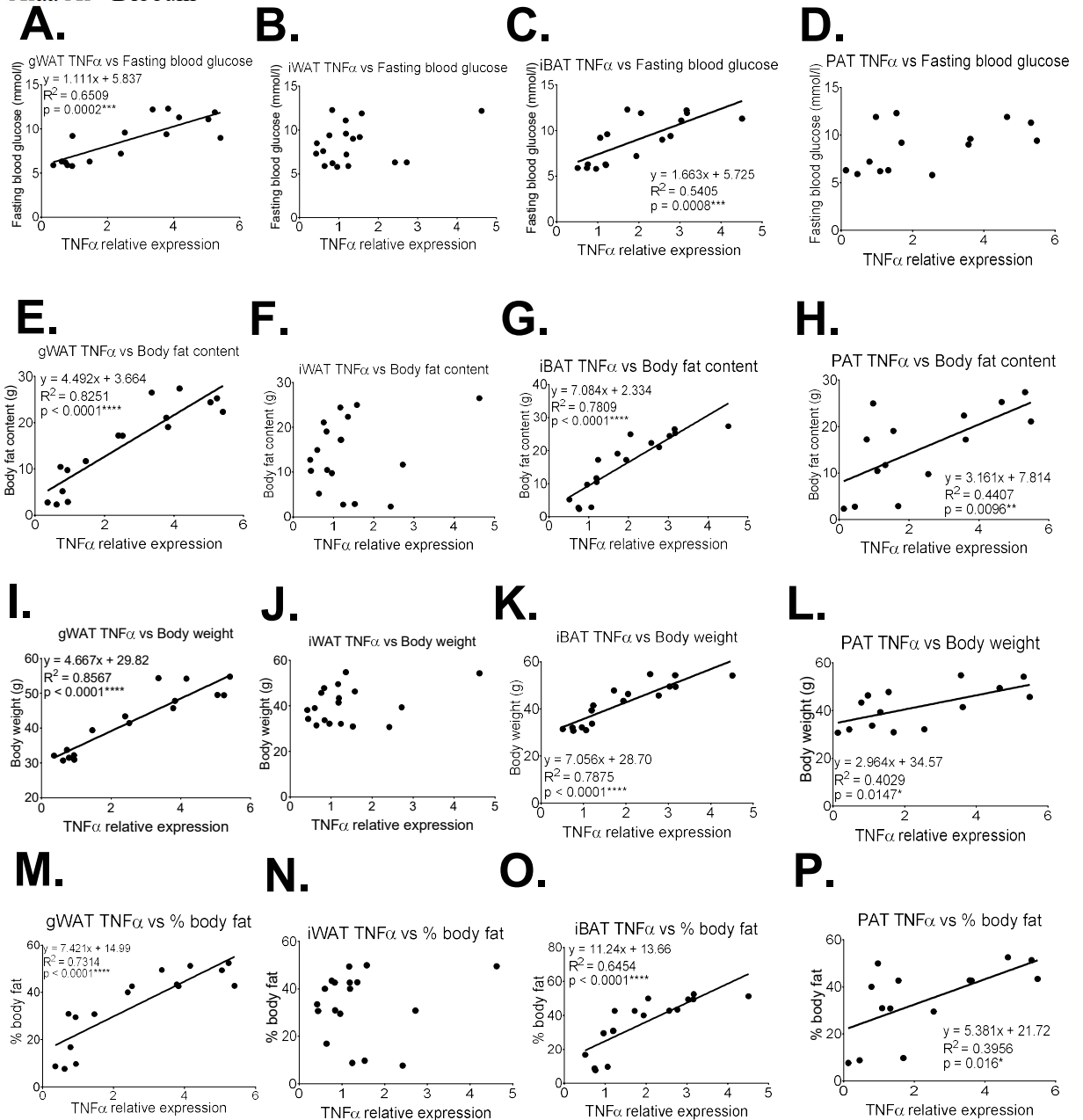
Appendix Figure 4.7. The relationship between the fold change in mRNA expression of TNFα of **gWAT (A,E,I,M)**, **iWAT (B,F,J,N)**, **iBAT (C,G,K,O)** and **PAT (D,H,L,P)** compared to fasting blood glucose levels, body fat content, body weight and % body fat from (C) and high-fat (HF)-fed 30-week-old male mice. Individual data points plotted, with the line of best fit as determined by simple linear regression. Data analysed by Pearson's correlation coefficient. N = 6-12. * p<0.05, ** p<0.01, *** p<0.001 and **** p<0.0001.

Appendix Figure 4.8. The relationship between the fold change in mRNA expression of UCP1 of **gWAT (A,E,I,M,Q,)** , **iWAT (B,F,J,N,R), iBAT (C,G,K,O,S)** and **PAT (D,H,L,P,T)** compared to serum total cholesterol, HDL, LDL, Triglycerides and Free Fatty Acids levels from chow (C) and high-fat (HF)-fed 30-week-old male mice. Individual data points plotted, with the line of best fit as determined by simple linear regression. Data analysed by Pearson's correlation coefficient. N = 6-12. * $p<0.05$, ** $p<0.01$, *** $p<0.001$ and **** $p<0.0001$.
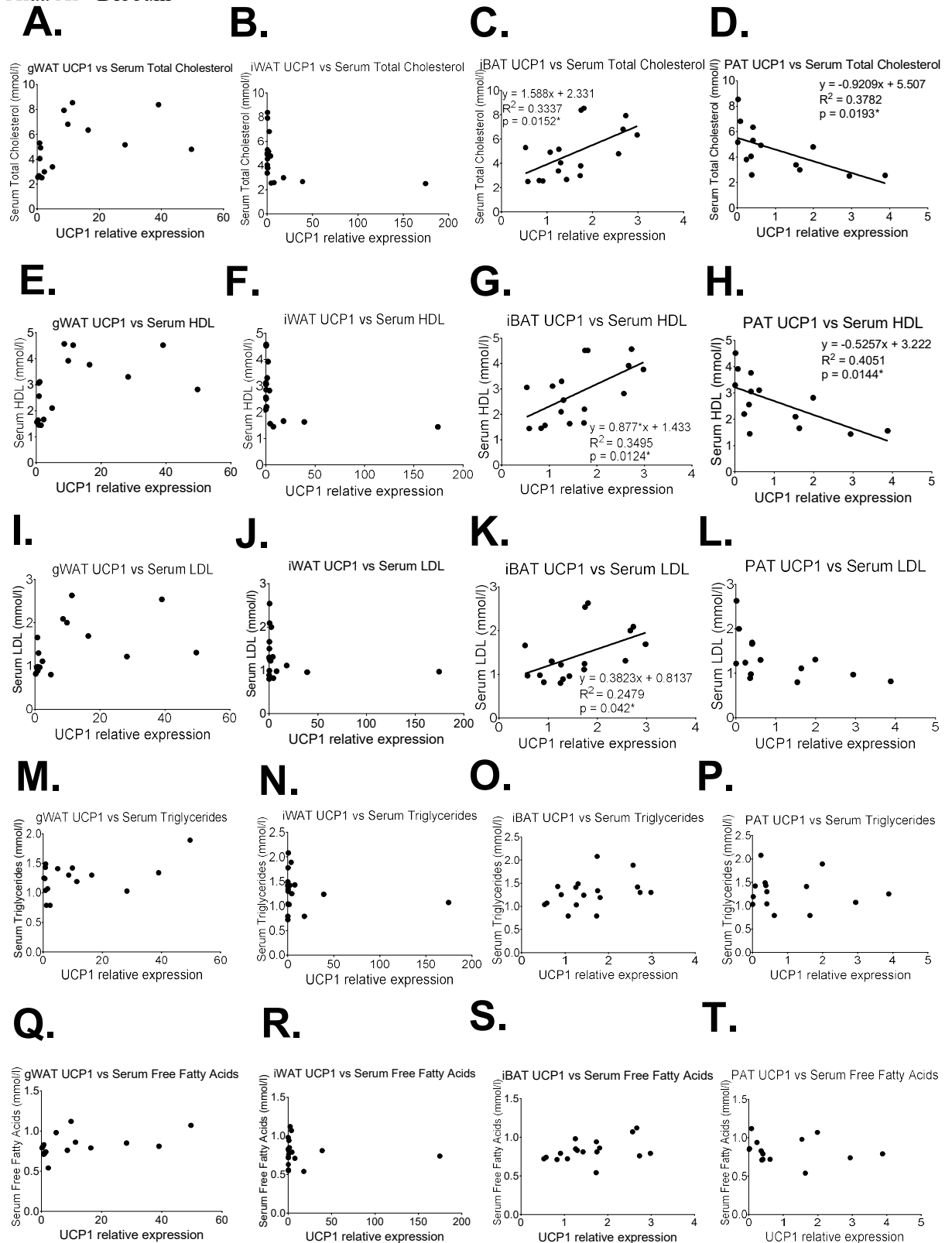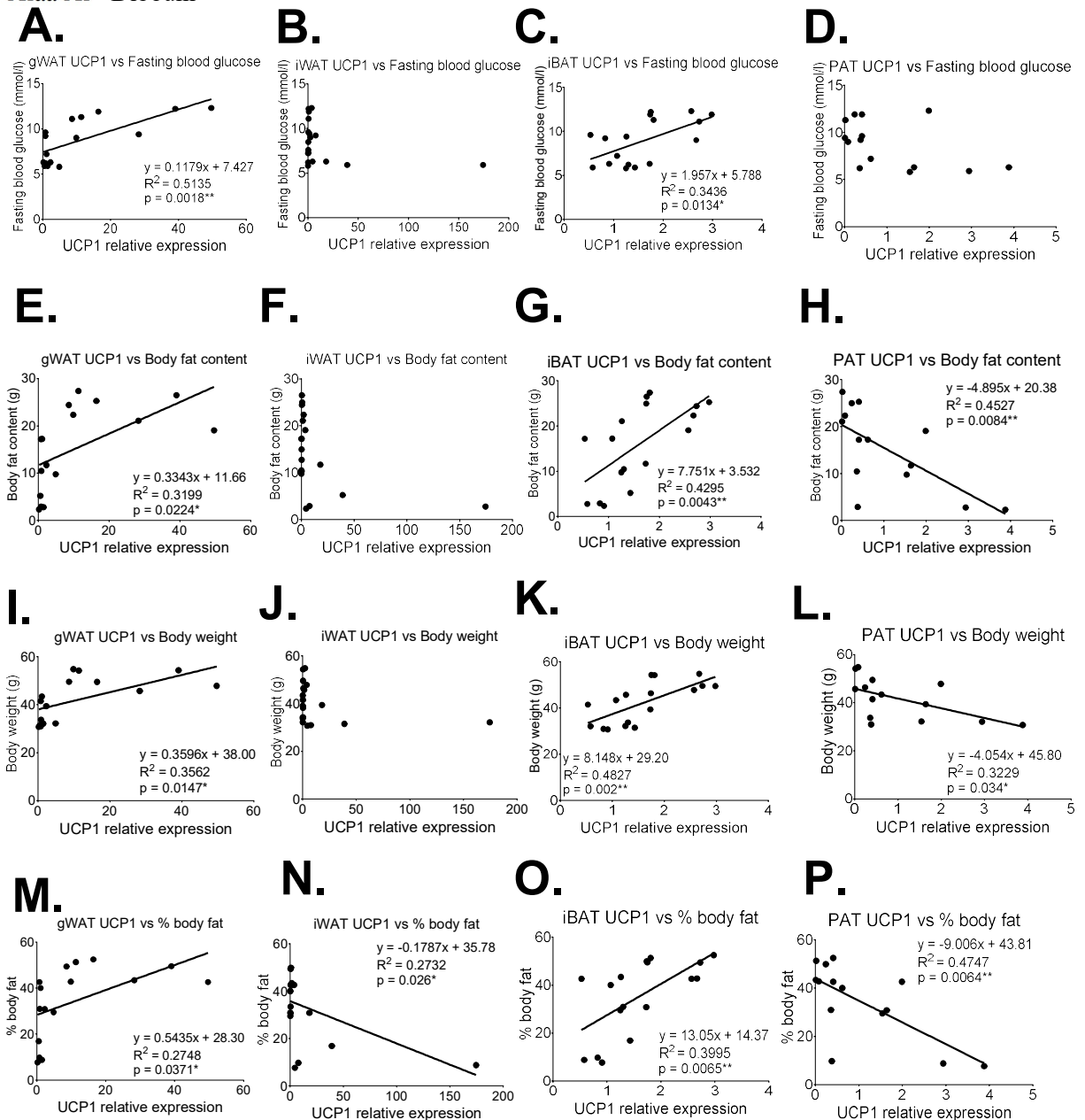
Appendix Figure 4.9. The relationship between the fold change in mRNA expression of UCP1 of **gWAT (A,E,I,M)**, **iWAT (B,F,J,N)**, **iBAT (C,G,K,O)** and **PAT (D,H,L,P)** compared to fasting blood glucose levels, body fat content, body weight and % body fat from (C) and high-fat (HF)-fed 30-week-old male mice. Individual data points plotted, with the line of best fit as determined by simple linear regression. Data analysed by Pearson's correlation coefficient. N = 6-12. * p<0.05, ** p<0.01, *** p<0.001 and **** p<0.0001.
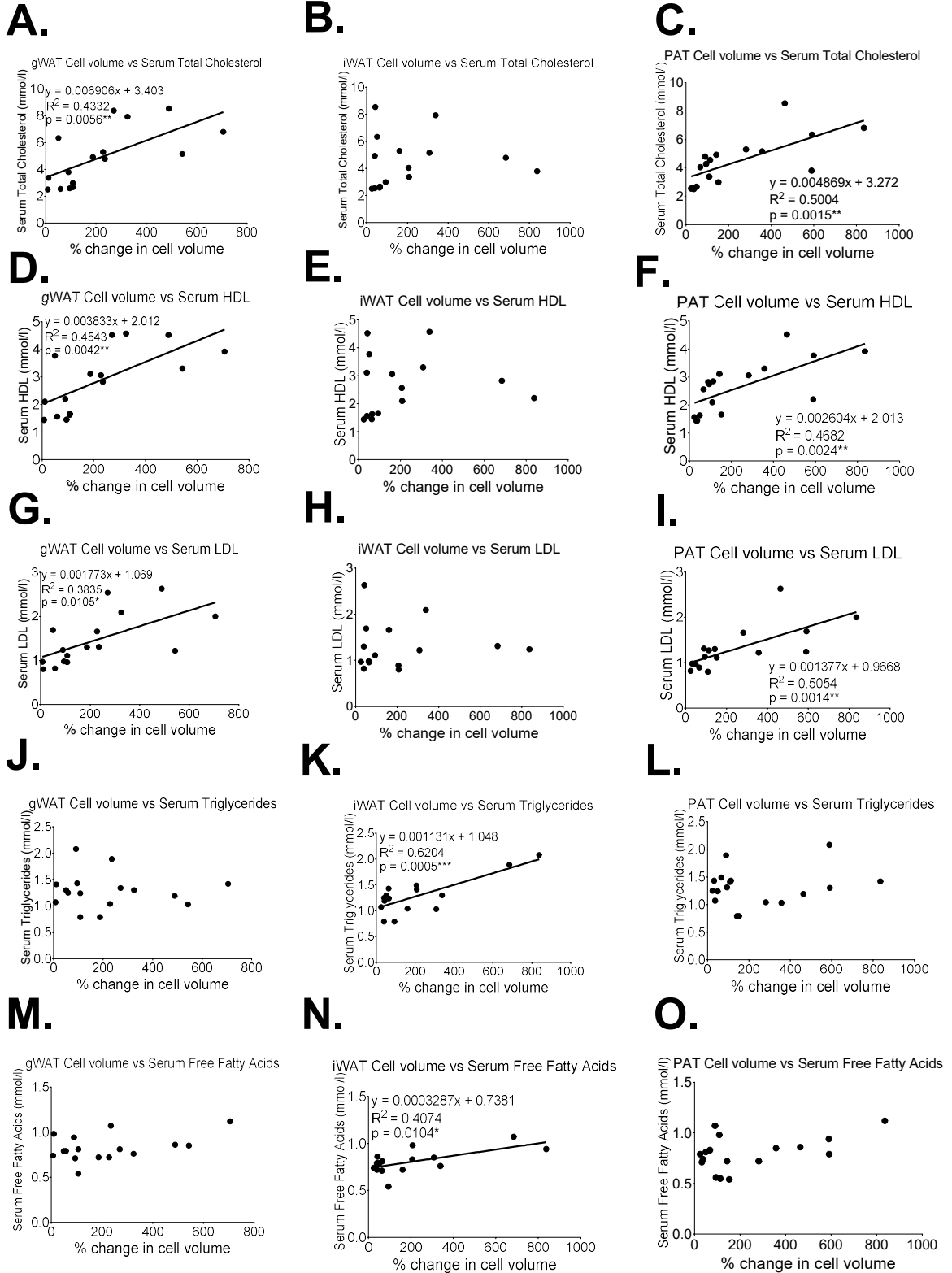
Appendix Figure 4.10. The relationship between the percentage change in cell volume of **gWAT (A,D,G,J,M,)**, **iWAT (B,E,H,K,N)** and **PAT (C,F,I,J,O)** compared to serum total cholesterol, HDL, LDL, Triglycerides and Free Fatty Acids levels from chow (C) and high-fat (HF)-fed 30-week-old male mice. Individual data points plotted, with the line of best fit as determined by simple linear regression. Data analysed by Pearson's correlation coefficient. N = 6-12. * p<0.05, ** p<0.01, *** p<0.001 and **** p<0.0001.

A. gWAT Cell volume vs Fasting blood glucose

B. iWAT Cell volume vs Fasting blood glucose
y = 0.005788x + 7.467
R^2 = 0.3103
p = 0.031*

C. PAT Cell volume vs Fasting blood glucose
y = 0.005783x + 7.072
R^2 = 0.3668
p = 0.01**

D. gWAT Cell volume vs Body fat content
y = 0.02567x + 10.62
R^2 = 0.3282
p = 0.0204*

E. iWAT Cell volume vs Body fat content

F. PAT Cell volume vs Body fat content
y = 0.02798x + 7.536
R^2 = 0.6671
p < 0.0001****

G. gWAT Cell volume vs Body weight
y = 0.03046x + 36.07
R^2 = 0.4873
p = 0.0026**

H. iWAT Cell volume vs Body weight

I. PAT Cell volume vs Body weight
y = 0.02872x + 33.42
R^2 = 0.6973
p < 0.0001****

J. gWAT Cell volume vs % body fat
y = 0.03978x + 26.75
R^2 = 0.2534
p = 0.0469*

K. iWAT Cell volume vs % body fat

L. PAT Cell volume vs % body fat
y = 0.04411x + 22.52
R^2 = 0.5289
p = 0.0009***

Appendix Figure 4.11. The relationship between the percentage change in cell volume of **gWAT (A,D,G,J)**, **iWAT (B,E,H,K)** and **PAT (C,F,I,L)** compared to fasting blood glucose levels, body fat content, body weight and % body fat from (C) and high-fat (HF)-fed 30-week-old male mice. Individual data points plotted, with the line of best fit as determined by simple linear regression. Data analysed by Pearson's correlation coefficient. N = 6-12. * p<0.05, ** p<0.01, *** p<0.001 and **** p<0.0001.
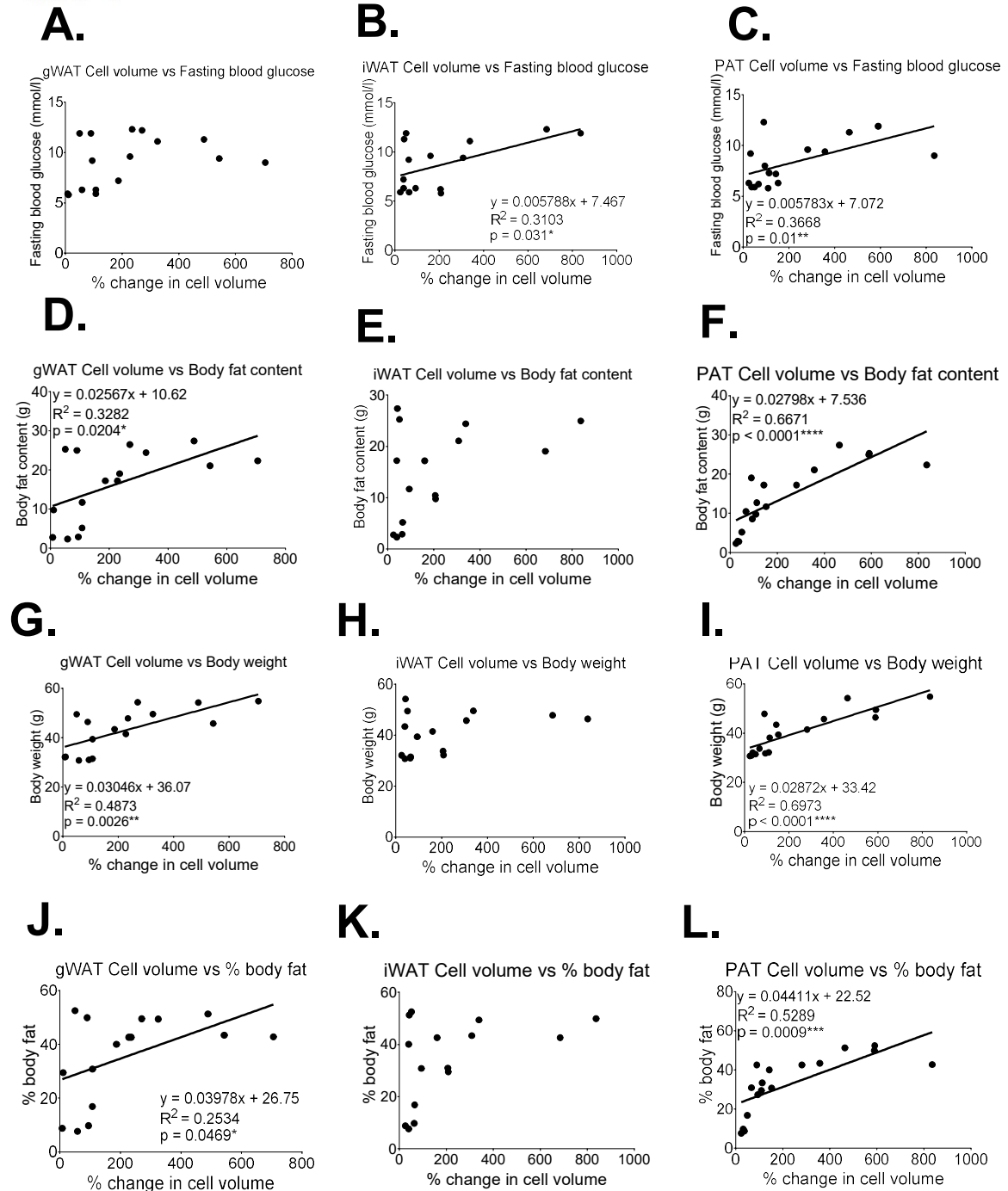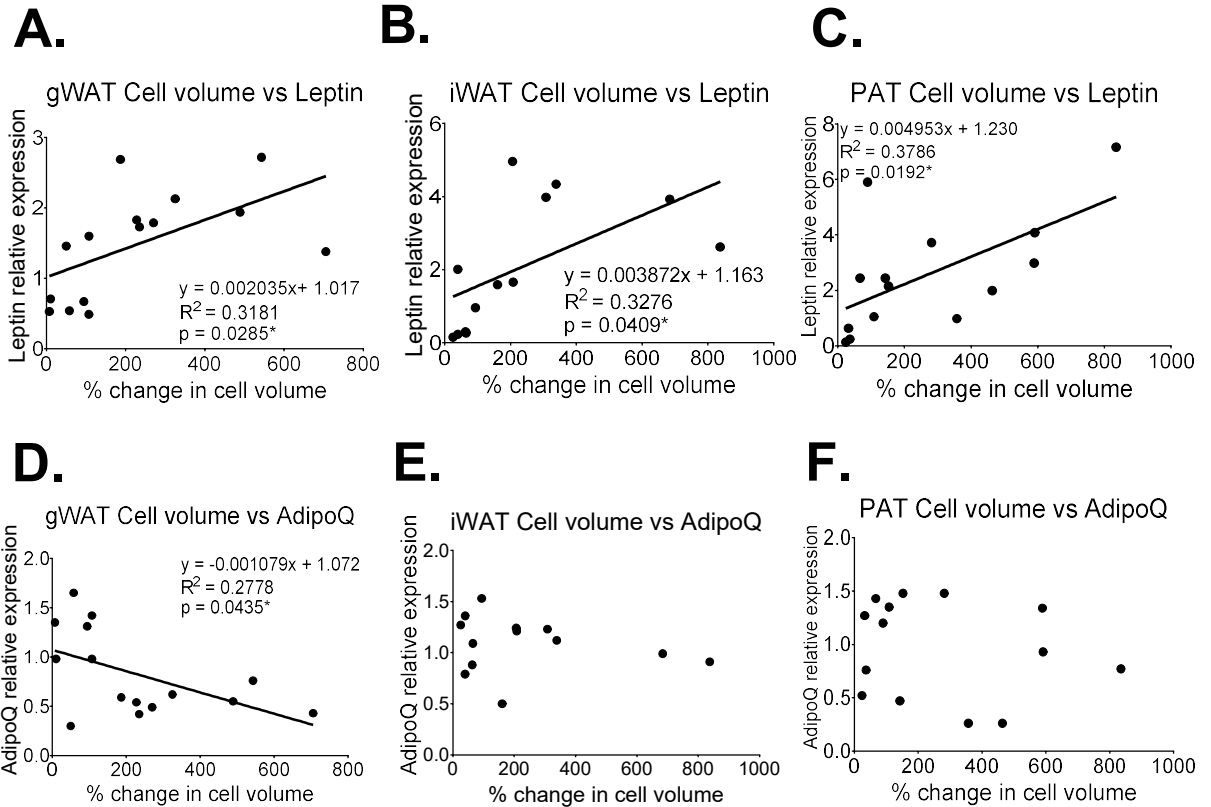
A.

B.

C.

D.

E.

F.

Appendix Figure 4.12. The relationship between the percentage change in cell volume of **gWAT (A,D)**, **iWAT (B,E)** and **PAT (C,F)** compared to fold change in Leptin and AdipoQ expression from chow (C) and high-fat (HF)-fed 30-week-old male mice. Individual data points plotted, with the line of best fit as determined by simple linear regression. Data analysed by Pearson's correlation coefficient. N = 6-12.   * p<0.05, ** p<0.01, *** p<0.001 and **** p<0.0001.

A.

gWAT Leptin vs Body weight
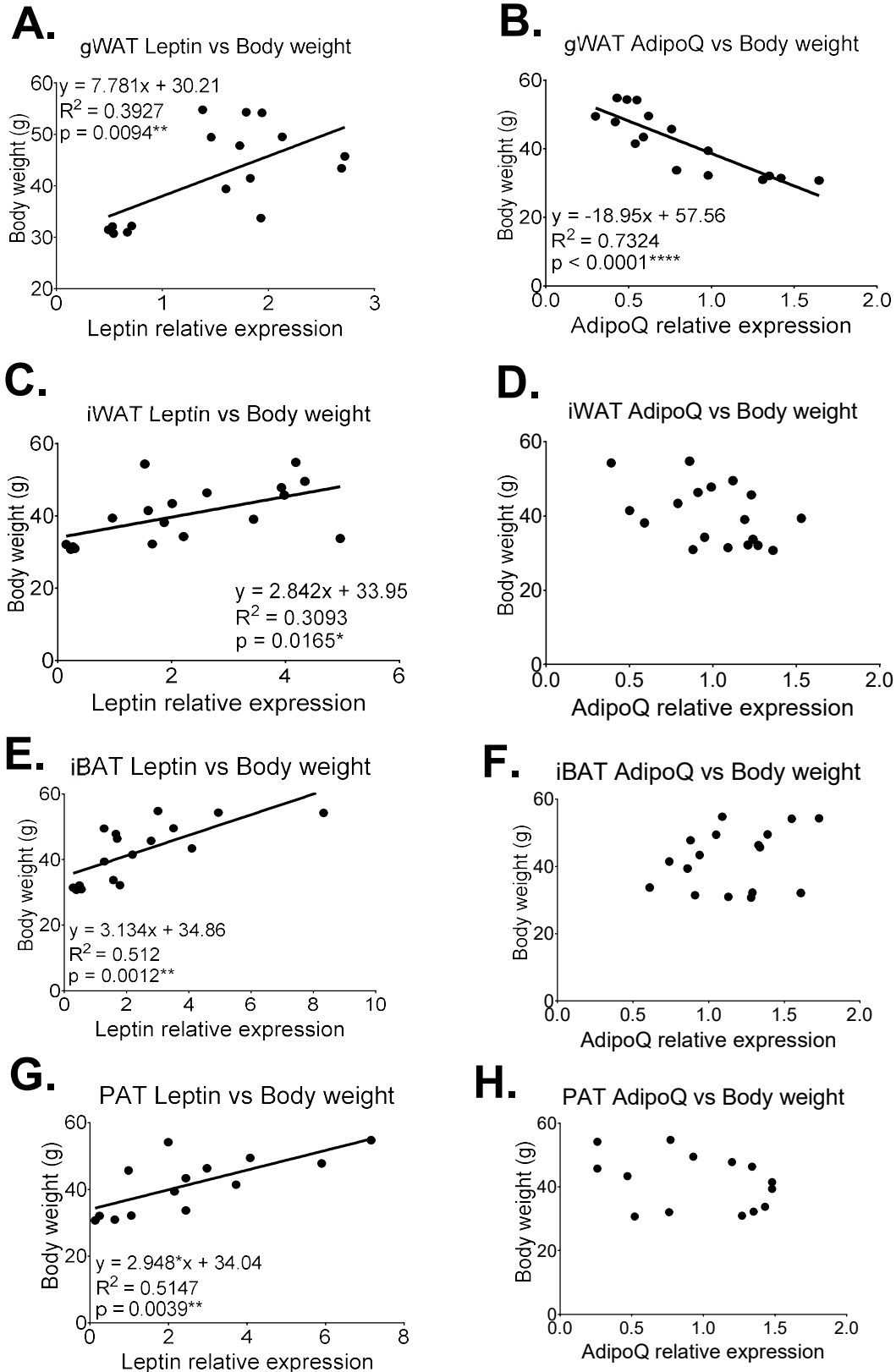
$y = 7.781x + 30.21$
$R^2 = 0.3927$
$p = 0.0094**$

Body weight (g)

Leptin relative expression

B.

gWAT AdipoQ vs Body weight

$y = -18.95x + 57.56$
$R^2 = 0.7324$
$p < 0.0001****$

Body weight (g)

AdipoQ relative expression

C.

iWAT Leptin vs Body weight

$y = 2.842x + 33.95$
$R^2 = 0.3093$
$p = 0.0165*$

Body weight (g)

Leptin relative expression

D.

iWAT AdipoQ vs Body weight

Body weight (g)

AdipoQ relative expression

E.

iBAT Leptin vs Body weight

$y = 3.134x + 34.86$
$R^2 = 0.512$
$p = 0.0012**$

Body weight (g)

Leptin relative expression

F.

iBAT AdipoQ vs Body weight

Body weight (g)

AdipoQ relative expression

G.

PAT Leptin vs Body weight

$y = 2.948*x + 34.04$
$R^2 = 0.5147$
$p = 0.0039**$

Body weight (g)

Leptin relative expression

H.

PAT AdipoQ vs Body weight

Body weight (g)

AdipoQ relative expression

Appendix Figure 4.13. The relationship between the fold change mRNA expression of Leptin and AdipoQ in **gWAT (A,B)**, **iWAT (C,D)**, **iBAT (E,F)** and **PAT (G,H)**, compared to body weight of chow (C) and high-fat (HF)-fed 30-week-old male mice. Individual data points plotted, with the line of best fit as determined by simple linear regression. Data analysed by Pearson's correlation coefficient. N = 6-12. * $p<0.05$, ** $p<0.01$, *** $p<0.001$ and **** $p<0.0001$.

A.

B.

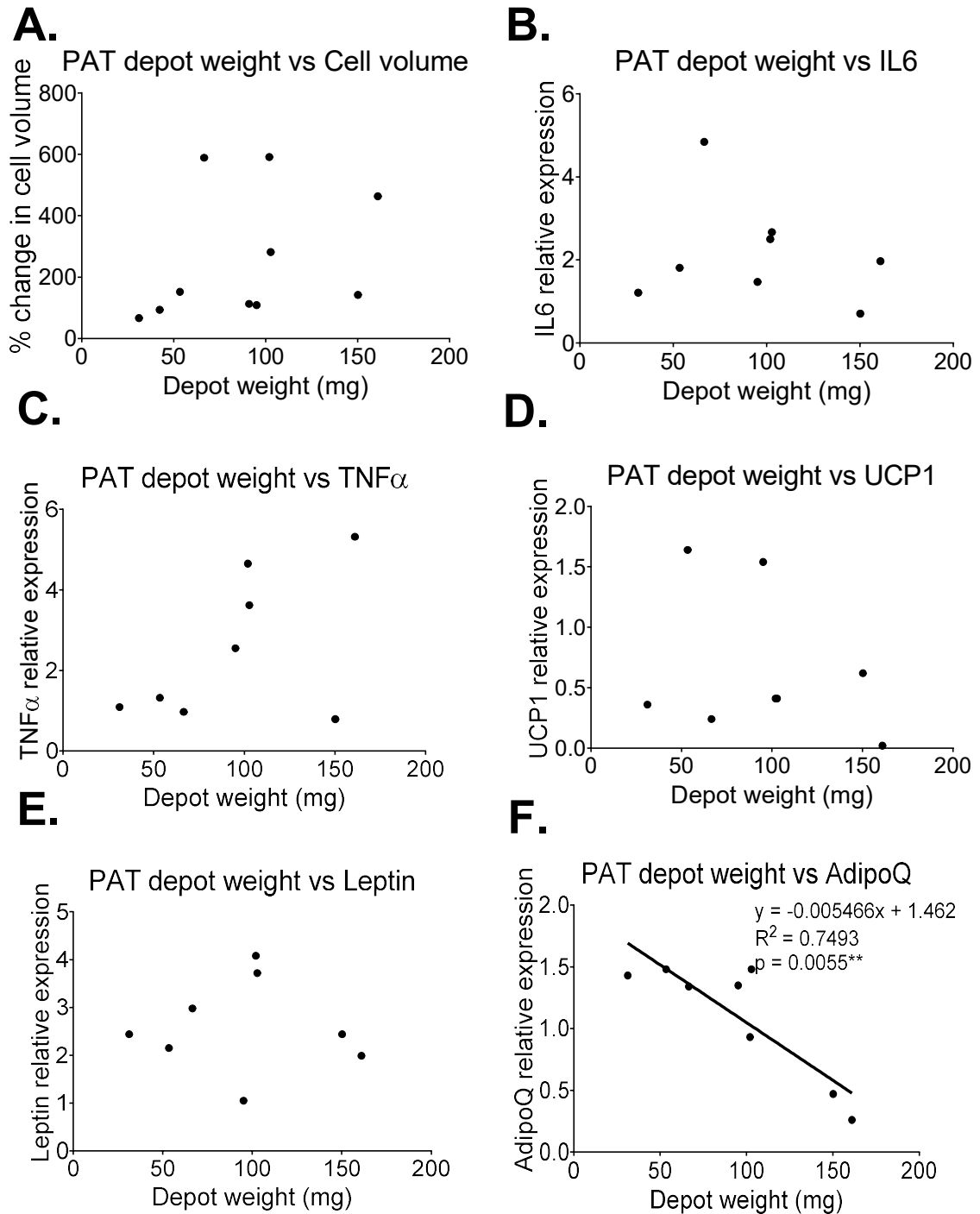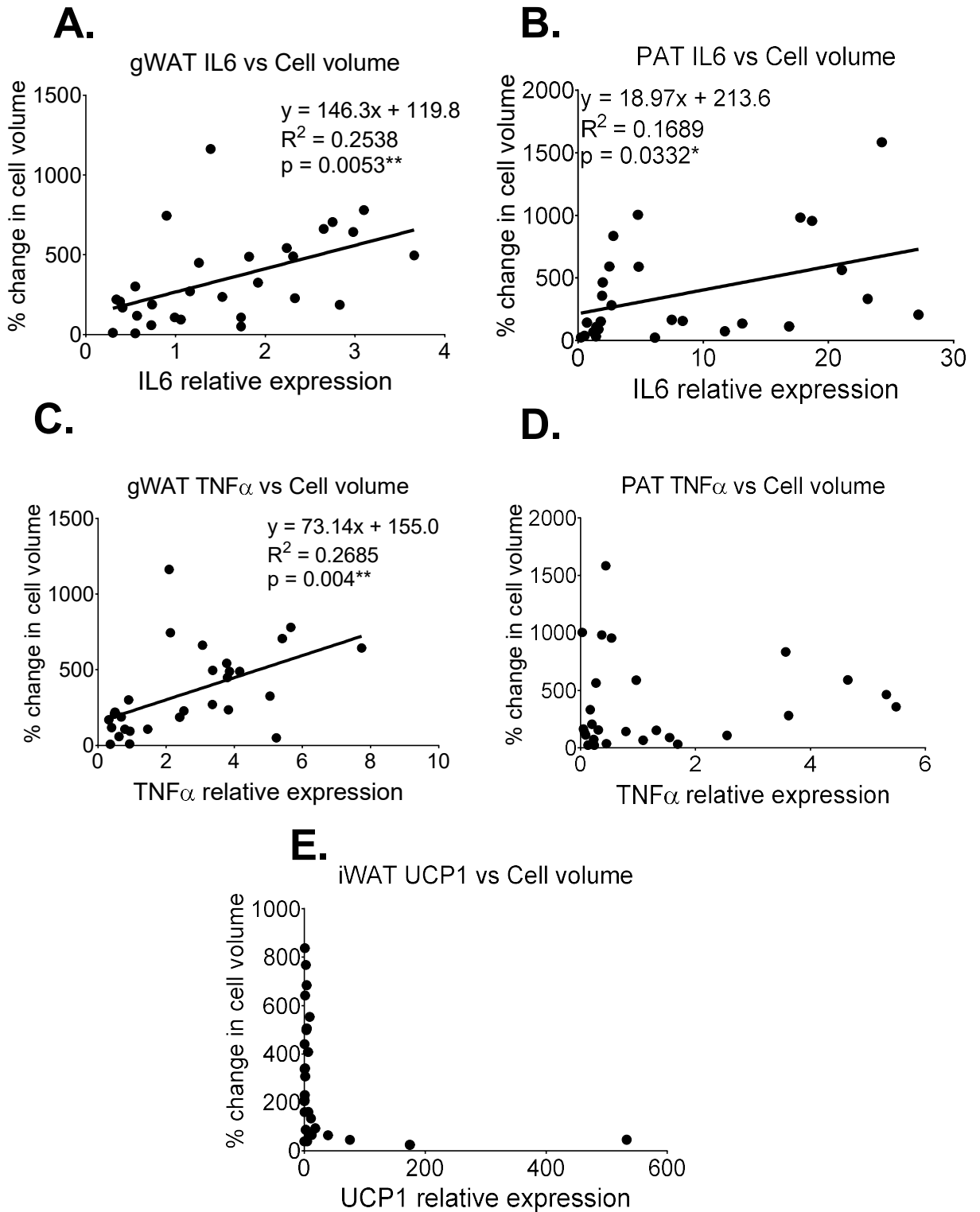**C.**

D.

E.

F.

Appendix Figure 4.14. The relationship between the depot weight of PAT compared to percentage change in cell volume **(A)** and fold change in mRNA expression of IL6 **(B)**, TNFα **(C)**, UCP1 **(D)**, Leptin **(E)** and AdipoQ **(F)** from chow (C) and high-fat (HF)-fed 30-week-old male mice. Individual data points plotted, with the line of best fit as determined by simple linear regression. Data analysed by Pearson's correlation coefficient. N = 6-12. * p<0.05, ** p<0.01, *** p<0.001 and **** p<0.0001.

A.

gWAT IL6 vs Cell volume

$y = 146.3x + 119.8$
$R^2 = 0.2538$
$p = 0.0053**$

B.

PAT IL6 vs Cell volume

$y = 18.97x + 213.6$
$R^2 = 0.1689$
$p = 0.0332*$

C.

gWAT TNFα vs Cell volume

$y = 73.14x + 155.0$
$R^2 = 0.2685$
$p = 0.004**$

D.

PAT TNFα vs Cell volume

E.

iWAT UCP1 vs Cell volume

Appendix Figure 4.15. The relationship between the fold change in mRNA expression of IL6, TNFα and UCP1 of **gWAT (A,C)**, **PAT (B,D)** and **iWAT (E)** compared to percentage change in cell volume of chow (C) or high-fat (HF)-fed 30-week-old male offspring mice from dams fed a chow (C) or (HF)-diet. Individual data points plotted, with the line of best fit as determined by simple linear regression. Data analysed by Pearson's correlation coefficient. N = 6-12. * p<0.05, ** p<0.01, *** p<0.001 and **** p<0.0001.
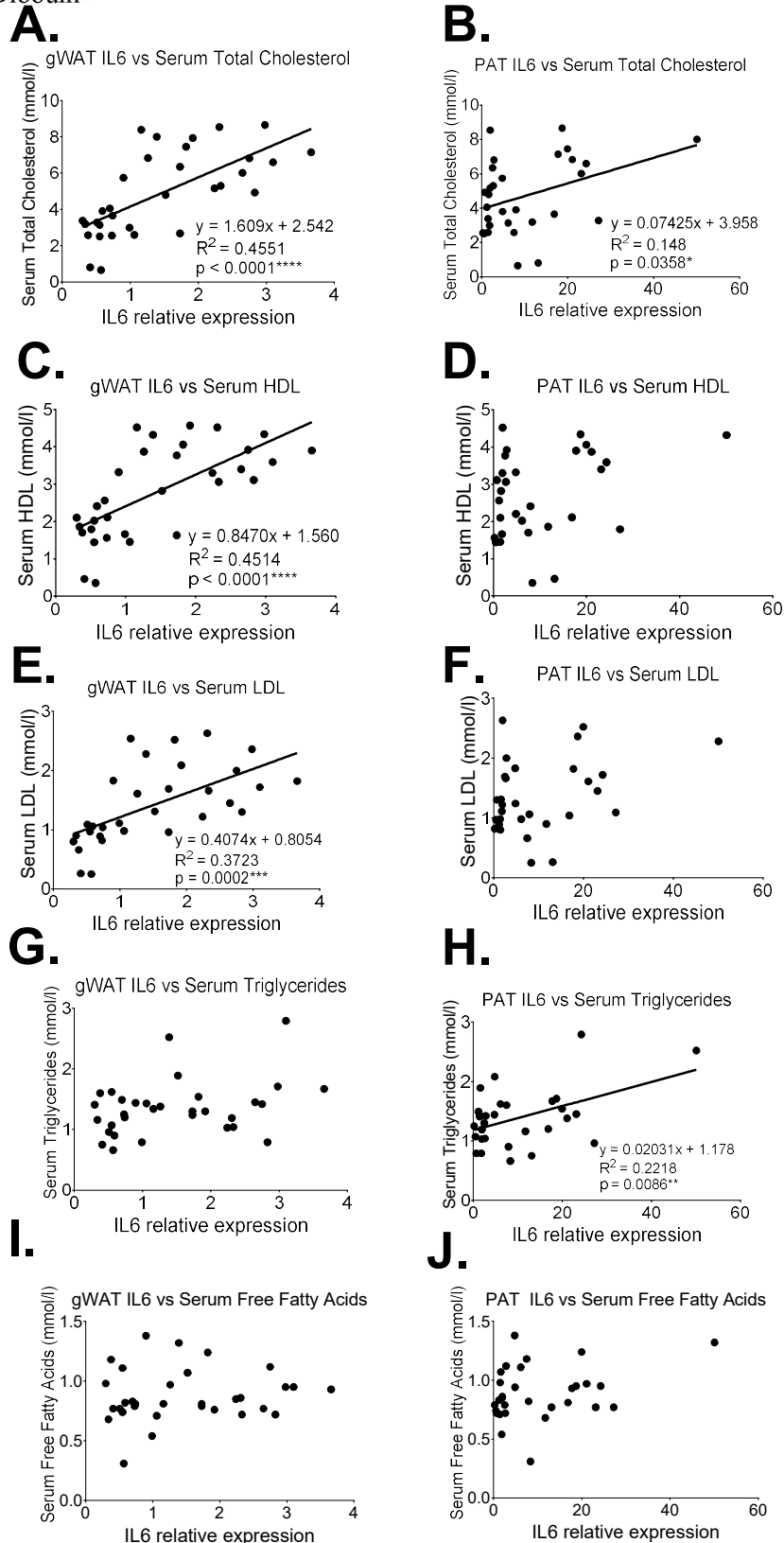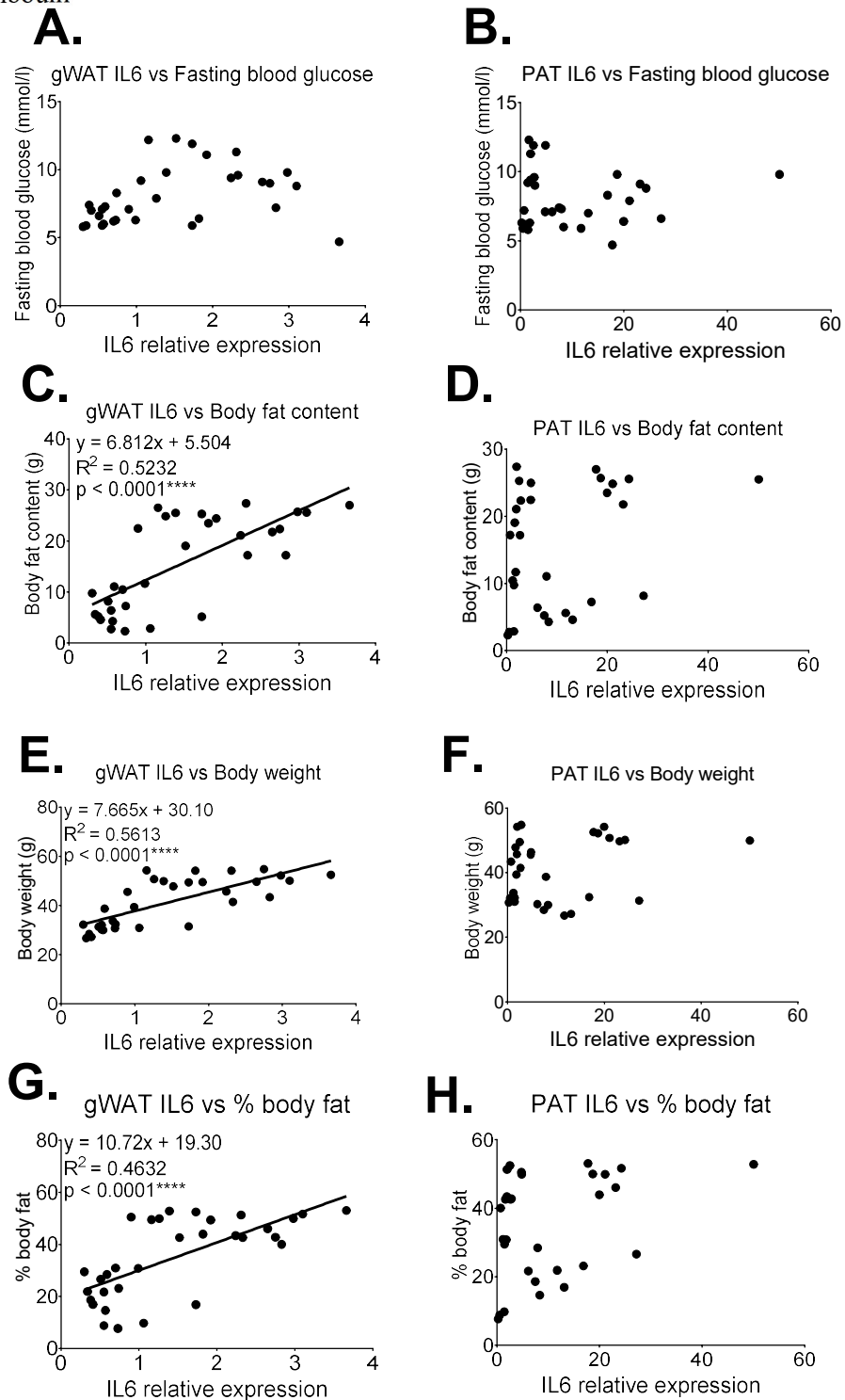
Appendix Figure 4.16. The relationship between the fold change in mRNA expression of IL6 of **gWAT (A,C,E,G,I)** and **PAT (B,D,F,H,J)** compared to serum total cholesterol, HDL, LDL, Triglycerides and Free Fatty Acids levels of chow (C) or high-fat (HF)-fed 30-week-old male offspring mice from dams fed a chow (C) or (HF)-diet. Individual data points plotted, with the line of best fit as determined by simple linear regression. Data analysed by Pearson's correlation coefficient. N = 6-12. * p<0.05, ** p<0.01, *** p<0.001 and **** p<0.0001.
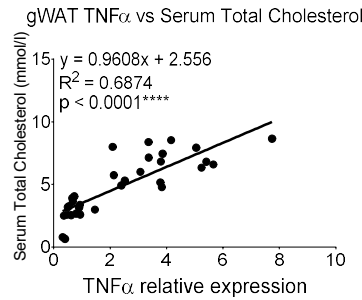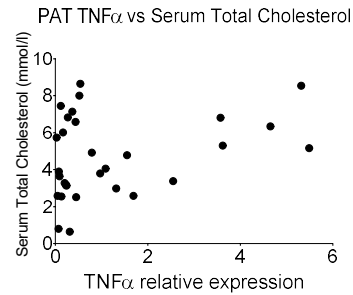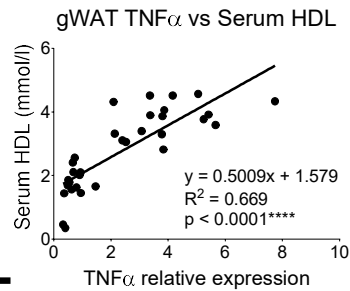
A.

gWAT IL6 vs Fasting blood glucose

B.

PAT IL6 vs Fasting blood glucose

C.

gWAT IL6 vs Body fat content

y = 6.812x + 5.504
R^2 = 0.5232
p < 0.0001****

D.

PAT IL6 vs Body fat content

E.

gWAT IL6 vs Body weight

y = 7.665x + 30.10
R^2 = 0.5613
p < 0.0001****

F.

PAT IL6 vs Body weight

G.

gWAT IL6 vs % body fat

y = 10.72x + 19.30
R^2 = 0.4632
p < 0.0001****

H.

PAT IL6 vs % body fat

Appendix Figure 4.17. The relationship between the fold change in mRNA expression of IL6 of **gWAT (A,C,E,G)** and **PAT (B,D,F,H)** compared to fasting blood glucose levels, body fat content, body wei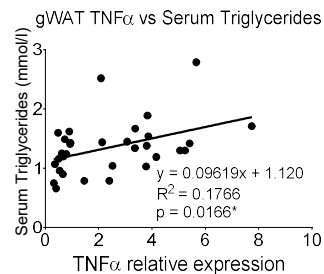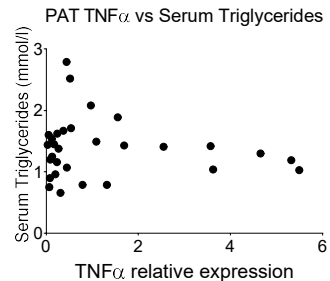ght and % body fat of chow (C) or high-fat (HF)-fed 30-week-old male offspring mice from dams fed a chow (C) or (HF)-diet. Individual data points plotted, with the line of best fit as determined by simple linear regression. Data analysed by Pearson's correlation coefficient. N = 6-12. * p<0.05, ** p<0.01, *** p<0.001 and **** p<0.0001.

A.

gWAT TNFα vs Serum Total Cholesterol

y = 0.9608x + 2.556
$R^2 = 0.6874$
p < 0.0001****

B.

PAT TNFα vs Serum Total Cholesterol

C.

gWAT TNFα vs Serum HDL

y = 0.5009x + 1.579
$R^2 = 0.669$
p < 0.0001****

D.

PAT TNFα vs Serum HDL

E.

gWAT TNFα vs Serum LDL

y = 0.2475x + 0.7984
$R^2 = 0.5823$
p < 0.0001****

F.

PAT TNFα vs Serum LDL

G.

gWAT TNFα vs Serum Triglycerides

y = 0.09619x + 1.120
$R^2 = 0.1766$
p = 0.0166*

H.

PAT TNFα vs Serum Triglycerides

I.

gWAT TNFα vs Serum Free Fatty Acids

J.

PAT TNFα vs Serum Free Fatty Acids
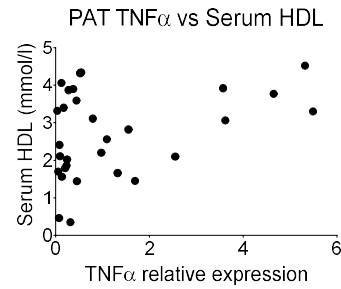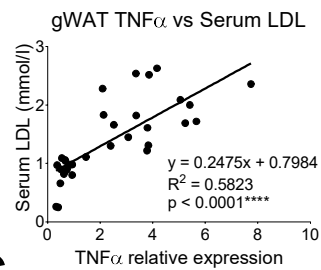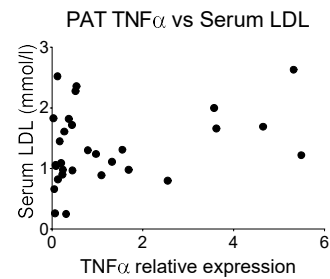
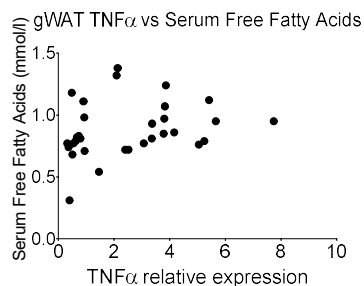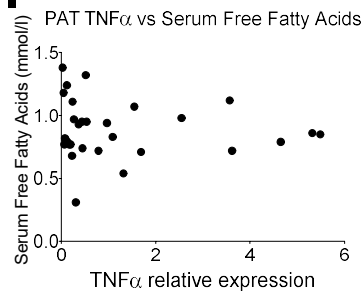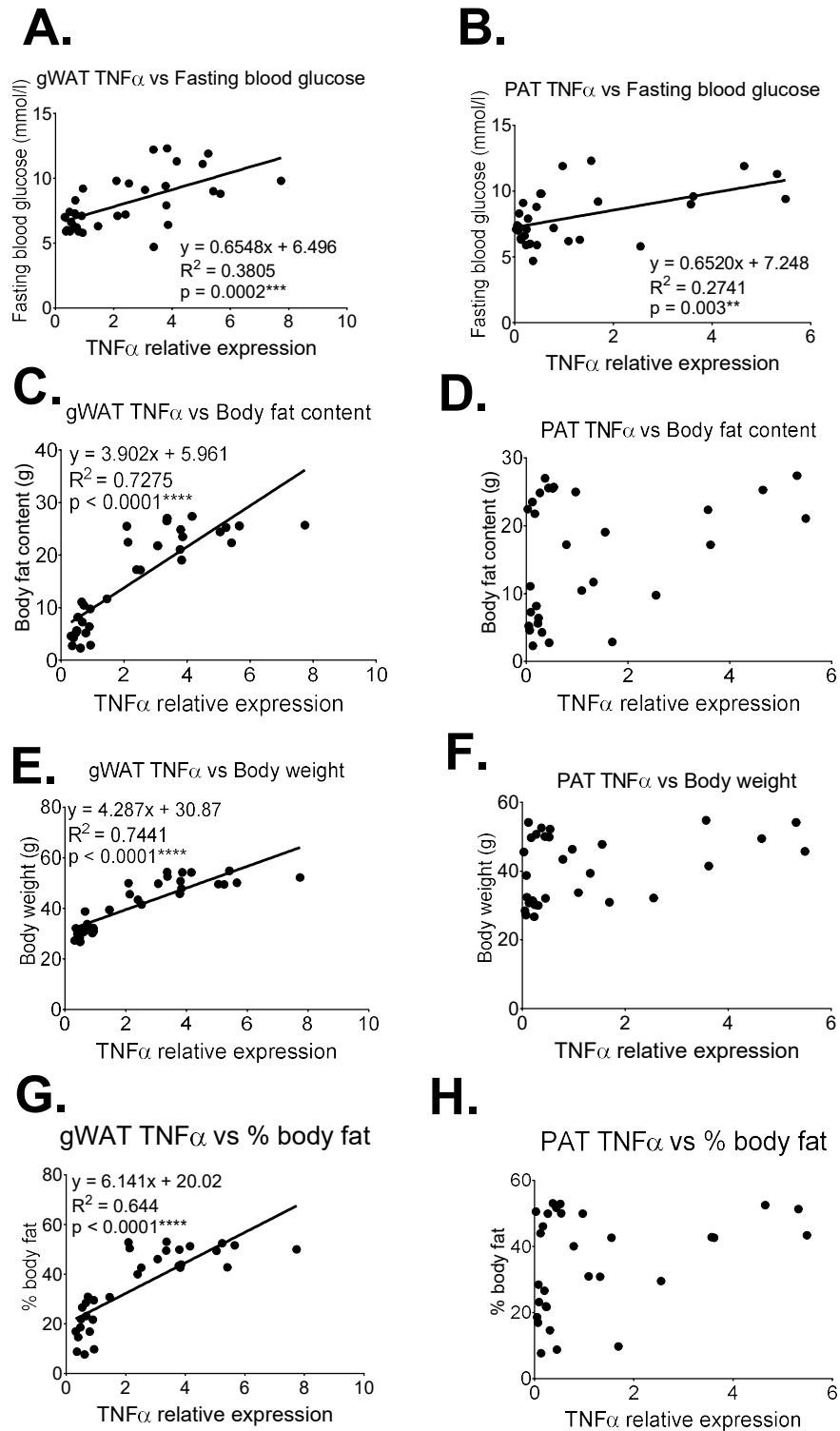**Appendix Figure 4.18.** The relationship between the fold change in mRNA expression of TNFα of **gWAT (A,C,E,G,I)** and **PAT (B,D,F,H,J)** compared to serum total cholesterol, HDL, LDL, Triglycerides and Free Fatty Acids levels of chow (C) or high-fat (HF)-fed 30-week-old male offspring mice from dams fed a chow (C) or (HF)-diet. Individual data points plotted, with the line of best fit as determined by simple linear regression. Data analysed by Pearson's correlation coefficient. N = 6-12. * p<0.05, ** p<0.01, *** p<0.001 and **** p<0.0001.

A. gWAT TNFα vs Fasting blood glucose

$y = 0.6548x + 6.496$
$R^2 = 0.3805$
$p = 0.0002***$

B. PAT TNFα vs Fasting blood glucose

$y = 0.6520x + 7.248$
$R^2 = 0.2741$
$p = 0.003**$

C. gWAT TNFα vs Body fat content

$y = 3.902x + 5.961$
$R^2 = 0.7275$
$p < 0.0001****$

D. PAT TNFα vs Body fat content

E. gWAT TNFα vs Body weight

$y = 4.287x + 30.87$
$R^2 = 0.7441$
$p < 0.0001****$

F. PAT TNFα vs Body weight

G. gWAT TNFα vs % body fat

$y = 6.141x + 20.02$
$R^2 = 0.644$
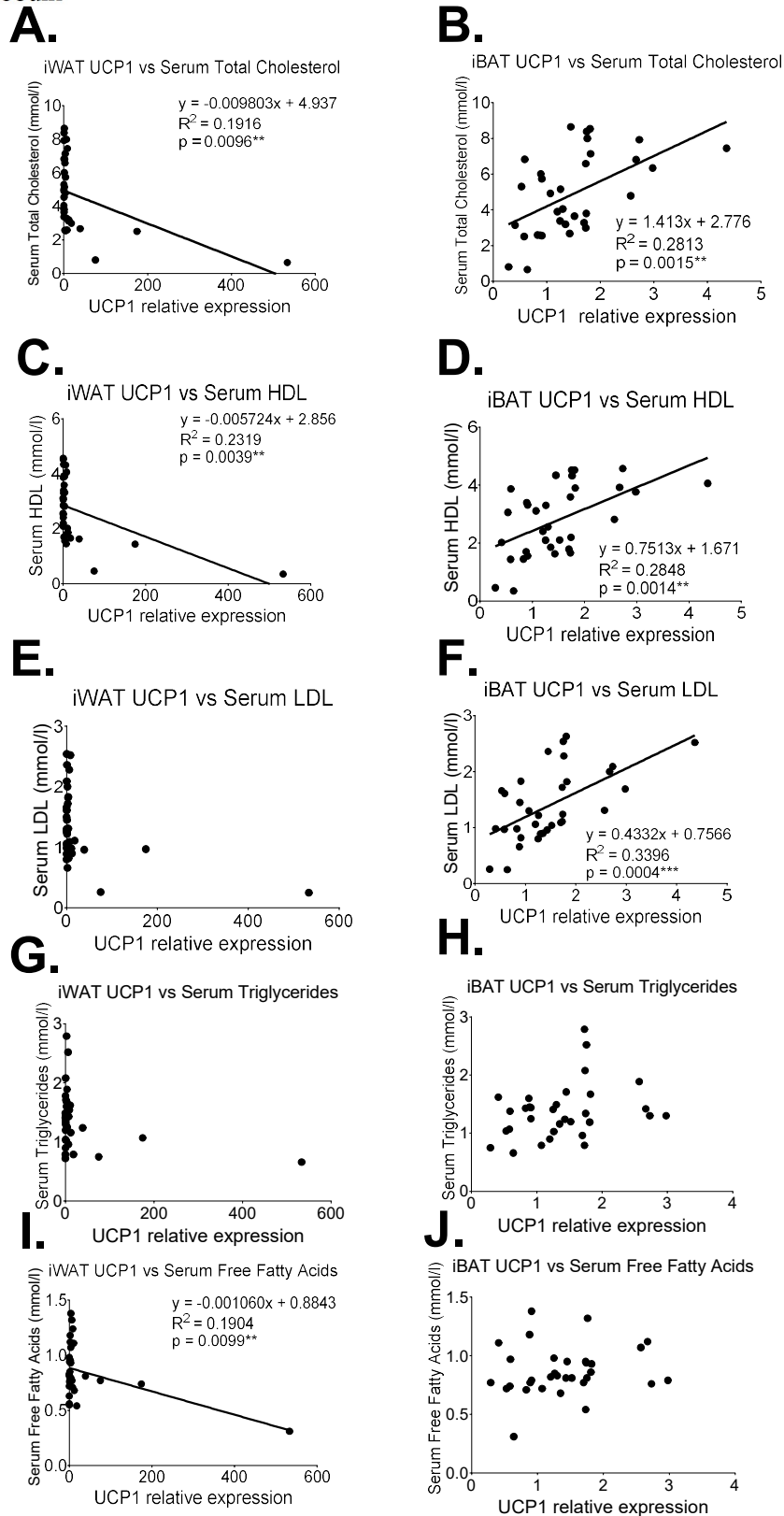$p < 0.0001****$

H. PAT TNFα vs % body fat

Appendix Figure 4.19. The relationship between the fold change in mRNA expression of TNFα of **gWAT (A,C,E,G)** and **PAT (B,D,F,H)** compared to fasting blood glucose levels, body fat content, body weight and % body fat of chow (C) or high-fat (HF)-fed 30-week-old male offspring mice from dams fed a chow (C) or (HF)-diet. Individual data points plotted, with the line of best fit as determined by simple linear regression. Data analysed by Pearson's correlation coefficient. N = 6-12. * $p<0.05$, ** $p<0.01$, *** $p<0.001$ and **** $p<0.0001$.

A.

iWAT UCP1 vs Serum Total Cholesterol

y = -0.009803x + 4.937
R^2 = 0.1916
p = 0.0096**

B.

iBAT UCP1 vs Serum Total Cholesterol

y = 1.413x + 2.776
R^2 = 0.2813
p = 0.0015**

C.

iWAT UCP1 vs Serum HDL

y = -0.005724x + 2.856
R^2 = 0.2319
p = 0.0039**

D.

iBAT UCP1 vs Serum HDL

y = 0.7513x + 1.671
R^2 = 0.2848
p = 0.0014**

E.

iWAT UCP1 vs Serum LDL

F.

iBAT UCP1 vs Serum LDL

y = 0.4332x + 0.7566
R^2 = 0.3396
p = 0.0004***

G.

iWAT UCP1 vs Serum Triglycerides

H.

iBAT UCP1 vs Serum Triglycerides

I.

iWAT UCP1 vs Serum Free Fatty Acids

y = -0.001060x + 0.8843
R^2 = 0.1904
p = 0.0099**
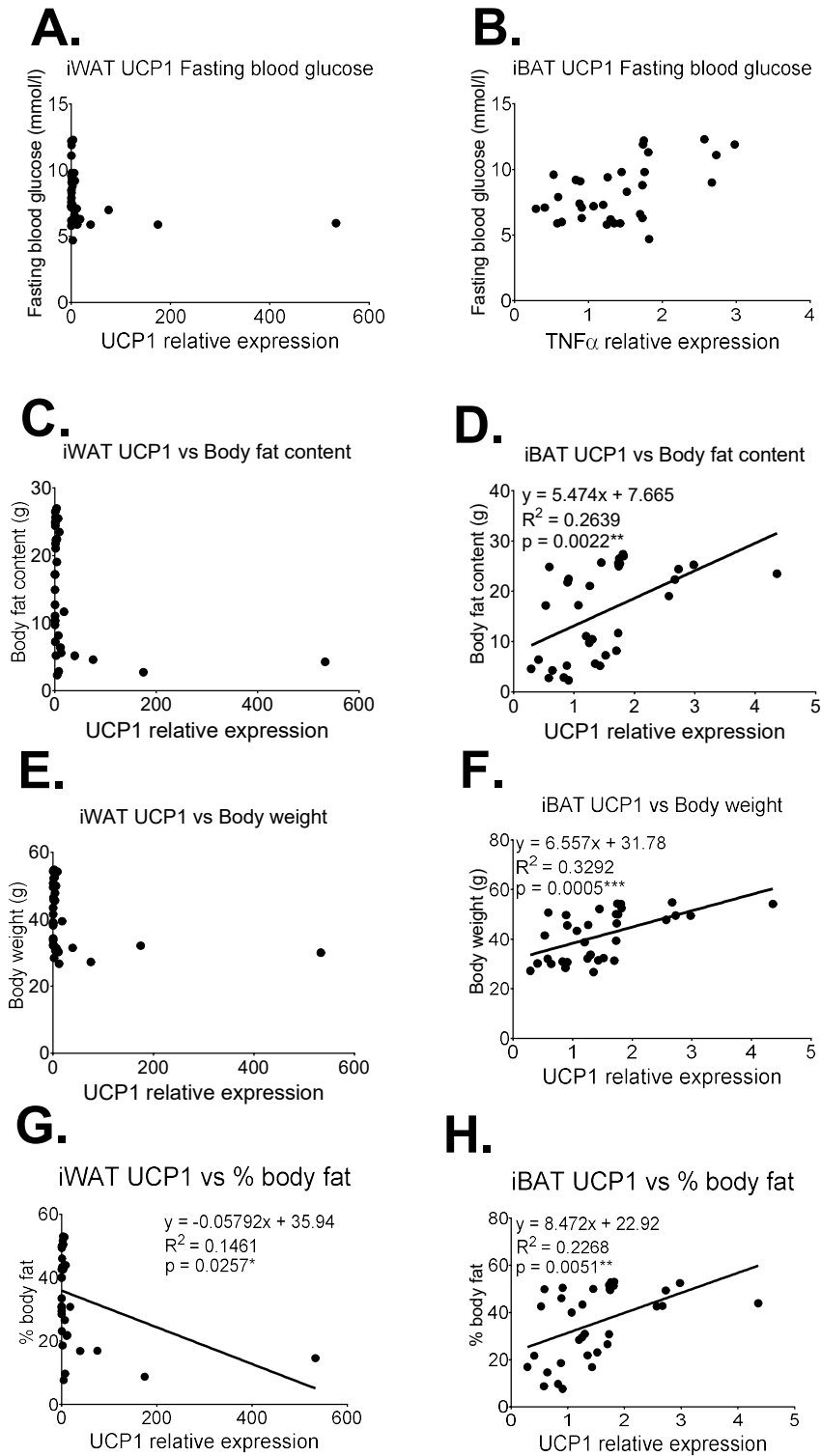
J.

iBAT UCP1 vs Serum Free Fatty Acids

Appendix Figure 4.20. The relationship between the fold change in mRNA expression of UCP1 of **iWAT (A,C,E,G,I)** and **iBAT (B,D,F,H,J)** compared to serum total cholesterol, HDL, LDL, Triglycerides and Free Fatty Acids levels of chow (C) or high-fat (HF)-fed 30-week-old male offspring mice from dams fed a chow (C) or (HF)-diet. Individual data points plotted, with the line of best fit as determined by simple linear regression. Data analysed by Pearson's correlation coefficient. N = 6-12. * p<0.05, ** p<0.01, *** p<0.001 and **** p<0.0001.
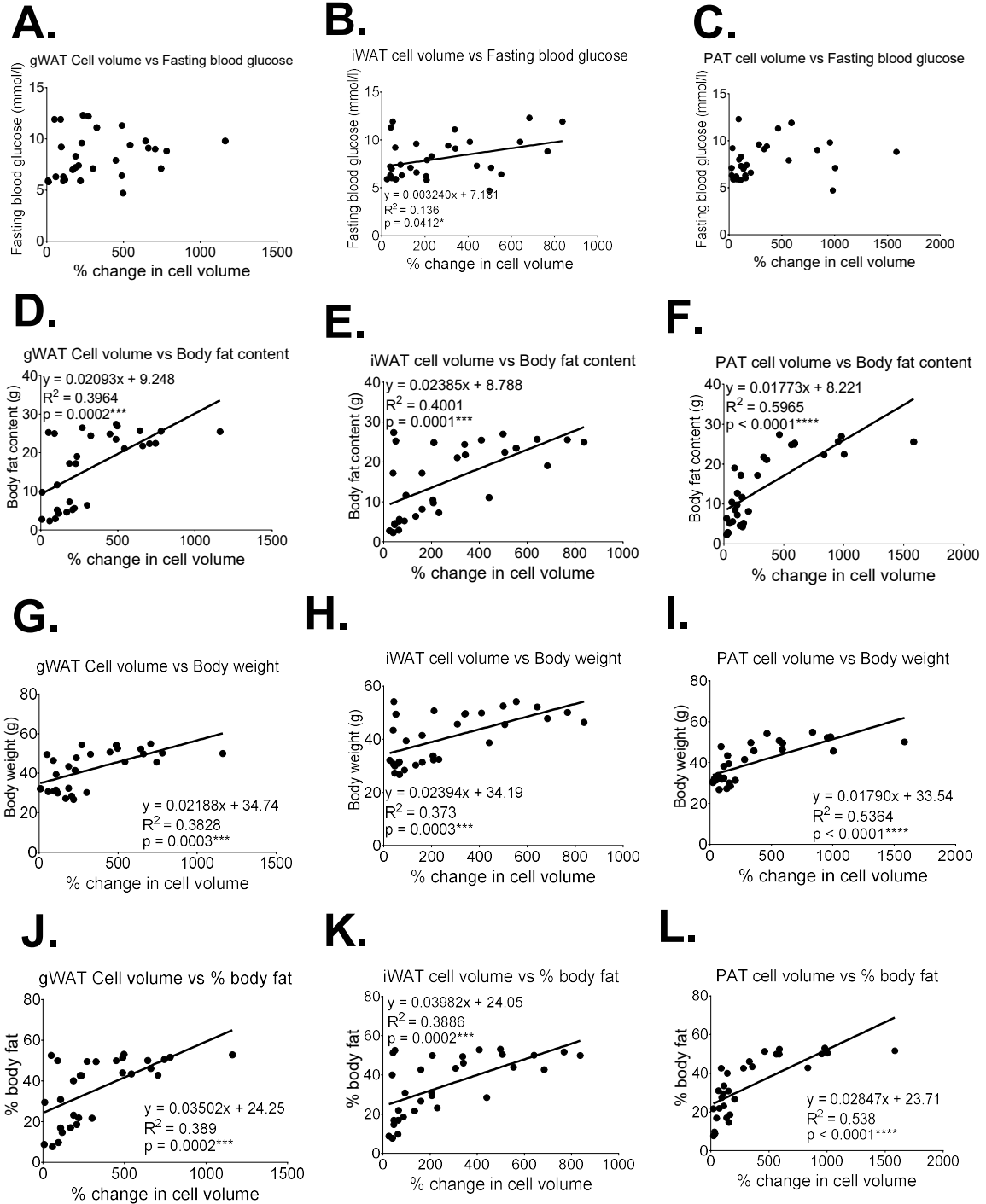
Appendix Figure 4.21. The relationship between the fold change in mRNA expression of UCP1 of **iWAT (A,C,E,G)** and **iBAT (B,D,F,H)** compared to fasting blood glucose levels, body fat content, body weight and % body fat of chow (C) or high-fat (HF)-fed 30-week-old male offspring mice from dams fed a chow (C) or (HF)-diet. Individual data points plotted, with the line of best fit as determined by simple linear regression. Data analysed by Pearson's correlation coefficient. N = 6-12. * p<0.05, ** p<0.01, *** p<0.001 and **** p<0.0001.
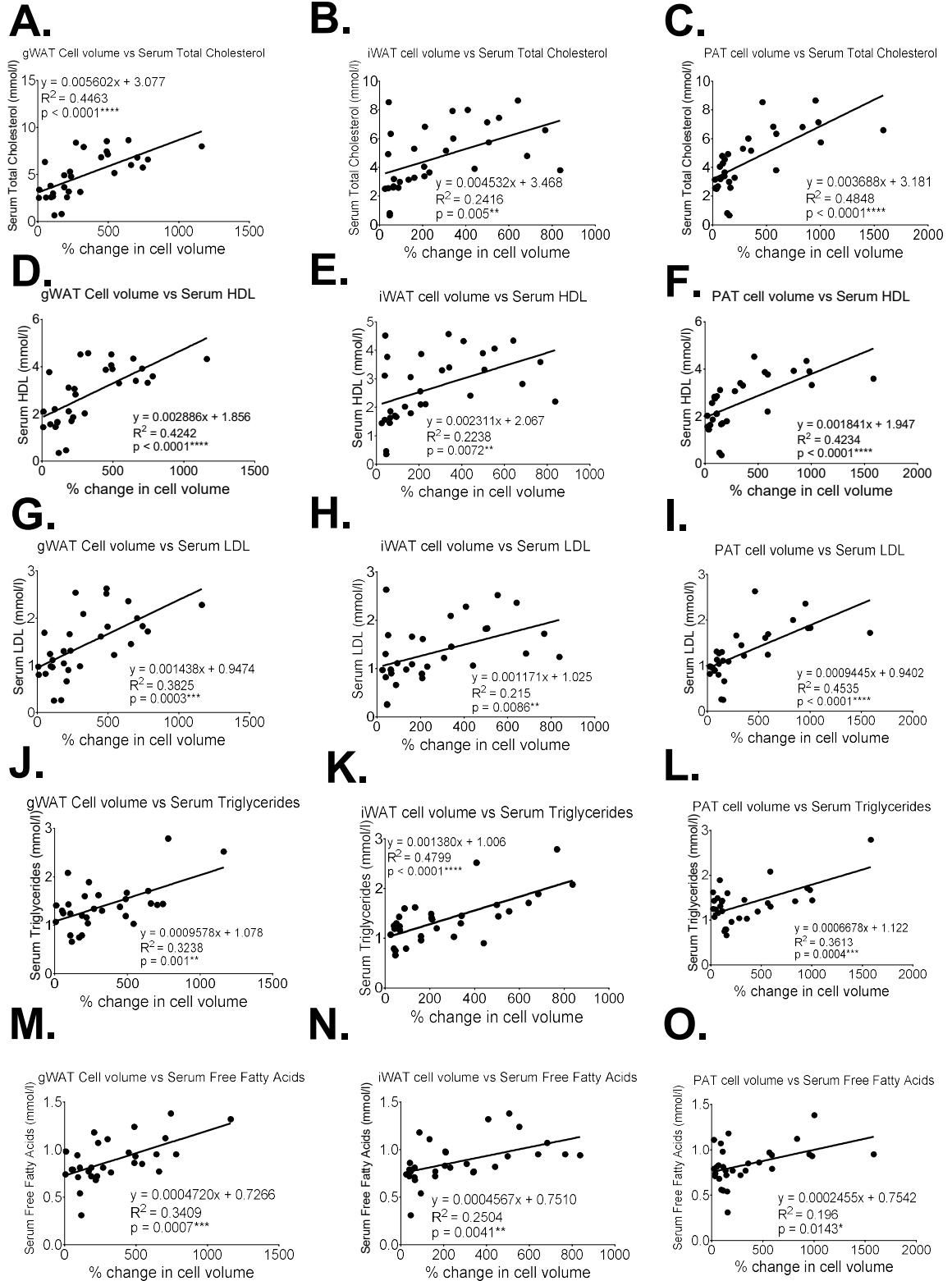
Appendix Figure 4.22. The relationship between the percentage change in cell volume of **gWAT (A,D,G,J,M)**, **iWAT (B,E,H,K,N)** and **PAT (C,F,I,L,O)** compared to serum total cholesterol, HDL, LDL, Triglycerides and Free Fatty Acids levels of chow (C) or high-fat (HF)-fed 30-week-old male offspring mice from dams fed a chow (C) or (HF)-diet. Individual data points plotted, with the line of best fit as determined by simple linear regression. Data analysed by Pearson's correlation coefficient. N = 6-12. * p<0.05, ** p<0.01, *** p<0.001 and **** p<0.0001.

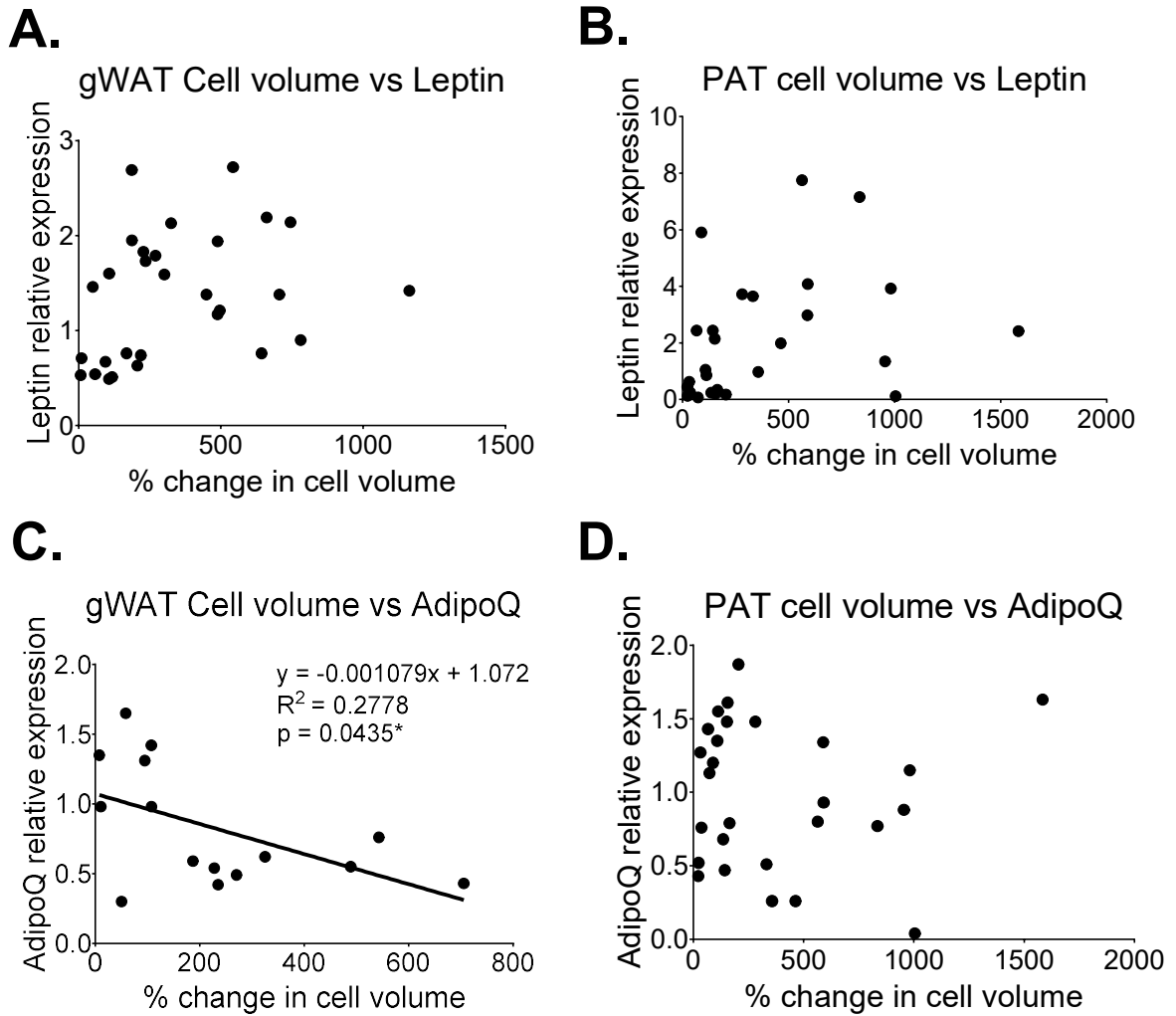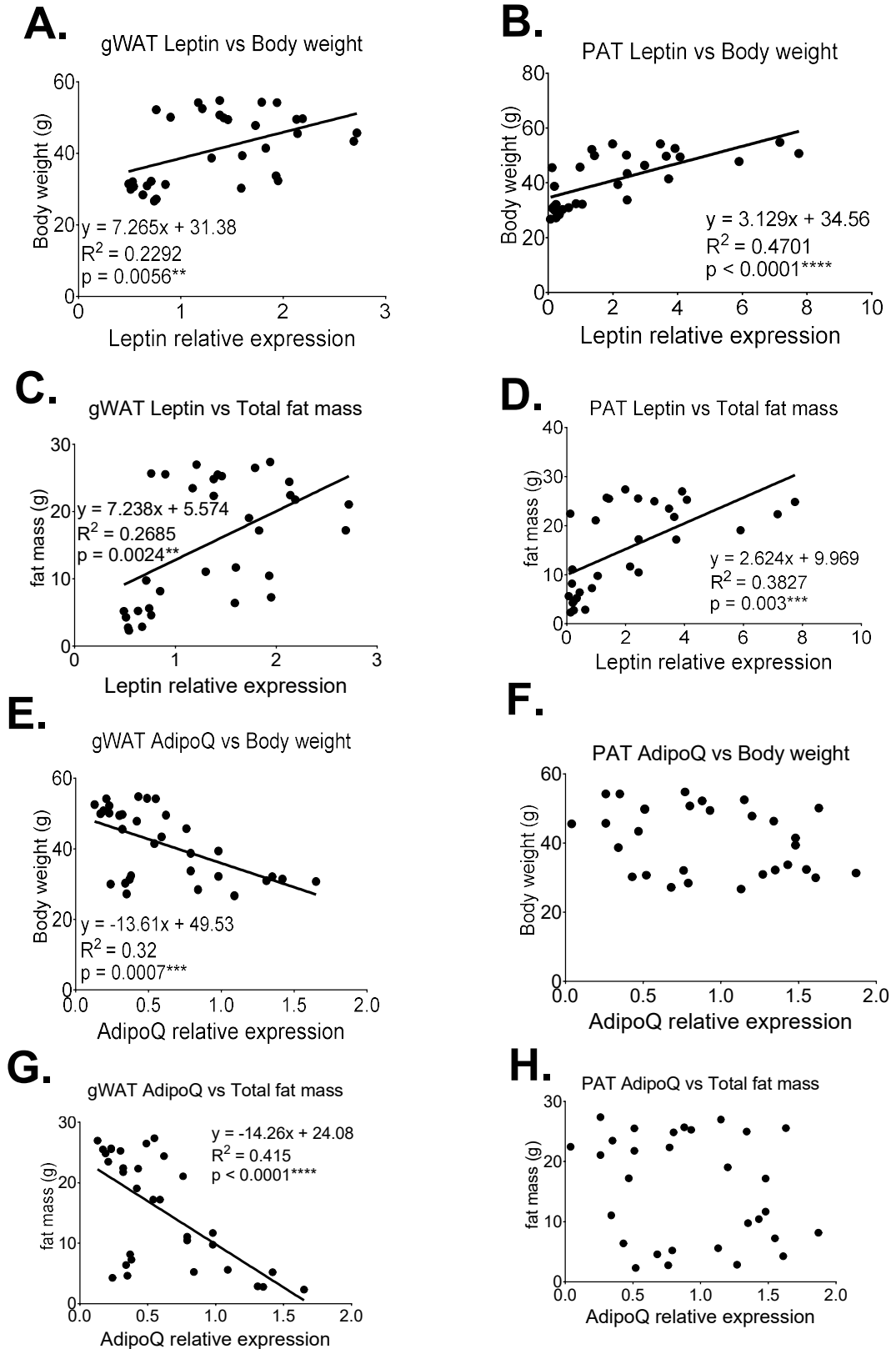**Appendix Figure 4.23.** The relationship between the percentage change in cell volume of **gWAT (A,D,G,J)**, **iWAT (B,E,H,K)** and **PAT (C,F,I,L)** compared to fasting blood glucose levels, body fat content, body weight and % body fat of chow (C) or high-fat (HF)-fed 30-week-old male offspring mice from dams fed a chow (C) or (HF)-diet. Individual data points plotted, with the line of best fit as determined by simple linear regression. Data analysed by Pearson's correlation coefficient. N = 6-12. * p<0.05, ** p<0.01, *** p<0.001 and **** p<0.0001.

A.

B.

C.

D.

Appendix Figure 4.24. The relationship between the percentage change in cell volume of **gWAT (A,C)** and **PAT (B,D)** compared to the fold change in mRNA expression of Leptin and AdipoQ of chow (C) and high-fat (HF)-fed 30-week-old male offspring mice from dams fed a chow (C) or (HF)-diet. Individual data points plotted, with the line of best fit as determined by simple linear regression. Data analysed by Pearson's correlation coefficient. N = 6-12. * p<0.05, ** p<0.01, *** p<0.001 and **** p<0.0001.

Appendix Figure 4.25. The relationship between the fold change in mRNA expression of Leptin and AdipoQ of **gWAT (A,C, E,G)** and **PAT (B,D,F, H)** compared to body weight and total fat mass of chow (C) and high-fat (HF)-fed 30-week-old male offspring mice from dams fed a chow (C) or (HF)-diet. Individual data points plotted, with the line of best fit as determined by simple linear regression. Data analysed by Pearson's correlation coefficient. N = 6-12. * p<0.05, ** p<0.01, *** p<0.001 and **** p<0.0001.

A. PAT depot weight vs Cell volume
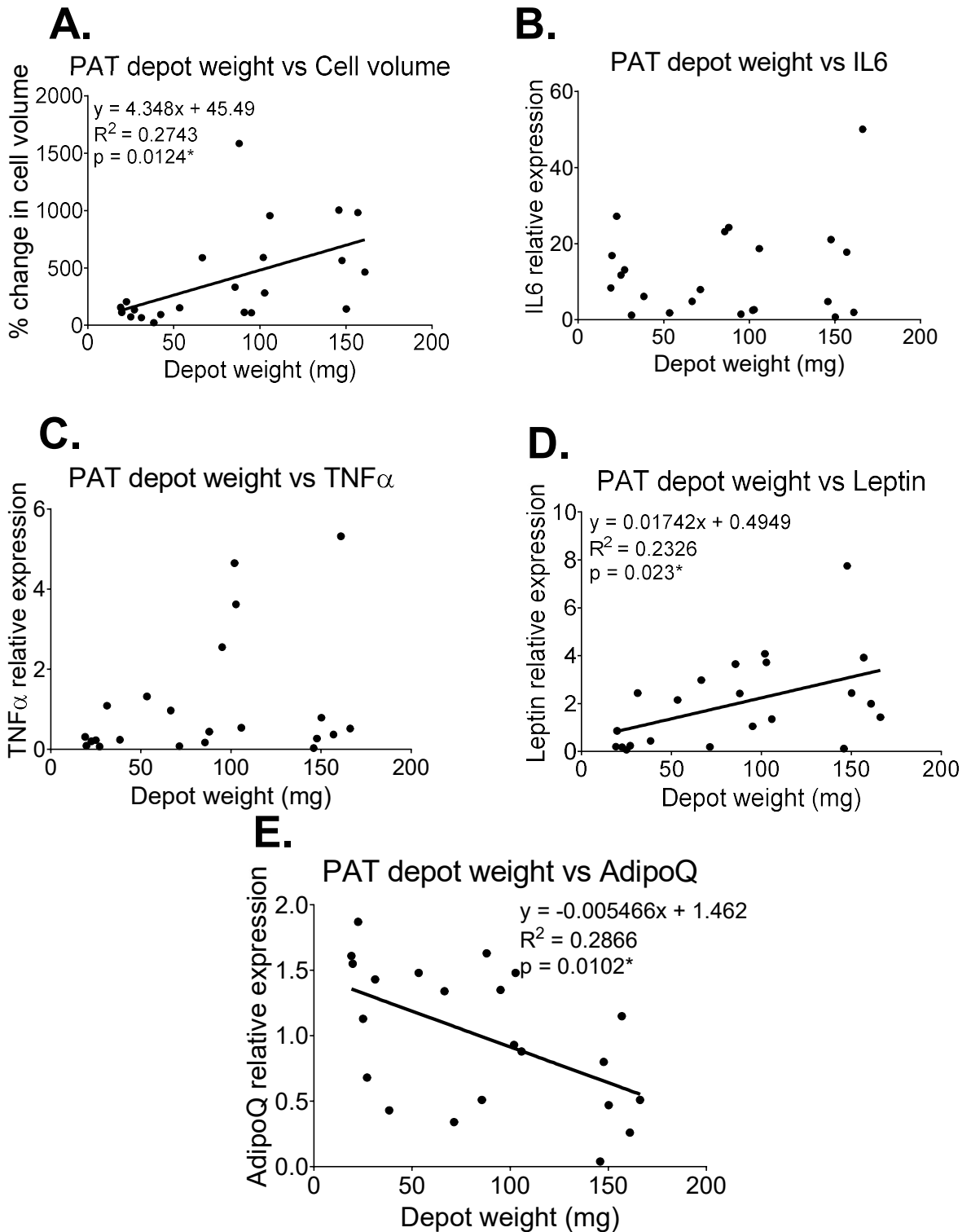
y = 4.348x + 45.49
R^2 = 0.2743
p = 0.0124*

B. PAT depot weight vs IL6

C. PAT depot weight vs TNFα

D. PAT depot weight vs Leptin

y = 0.01742x + 0.4949
R^2 = 0.2326
p = 0.023*

E. PAT depot weight vs AdipoQ

y = -0.005466x + 1.462
R^2 = 0.2866
p = 0.0102*

Appendix Figure 4.26. The relationship between the depot weight of **PAT** compared to the percentage change in cell volume **(A)** and the fold change in mRNA expression of IL6 **(B)**, TNFα **(C)**, Leptin **(D)** and AdipoQ **(E)** of chow (C) and high-fat (HF)-fed 30-week-old male offspring mice from dams fed a chow (C) or (HF)-diet. Individual data points plotted, with the line of best fit as determined by simple linear regression. Data analysed by Pearson's correlation coefficient. N = 6-12. * p<0.05, ** p<0.01, *** p<0.001 and **** p<0.0001.
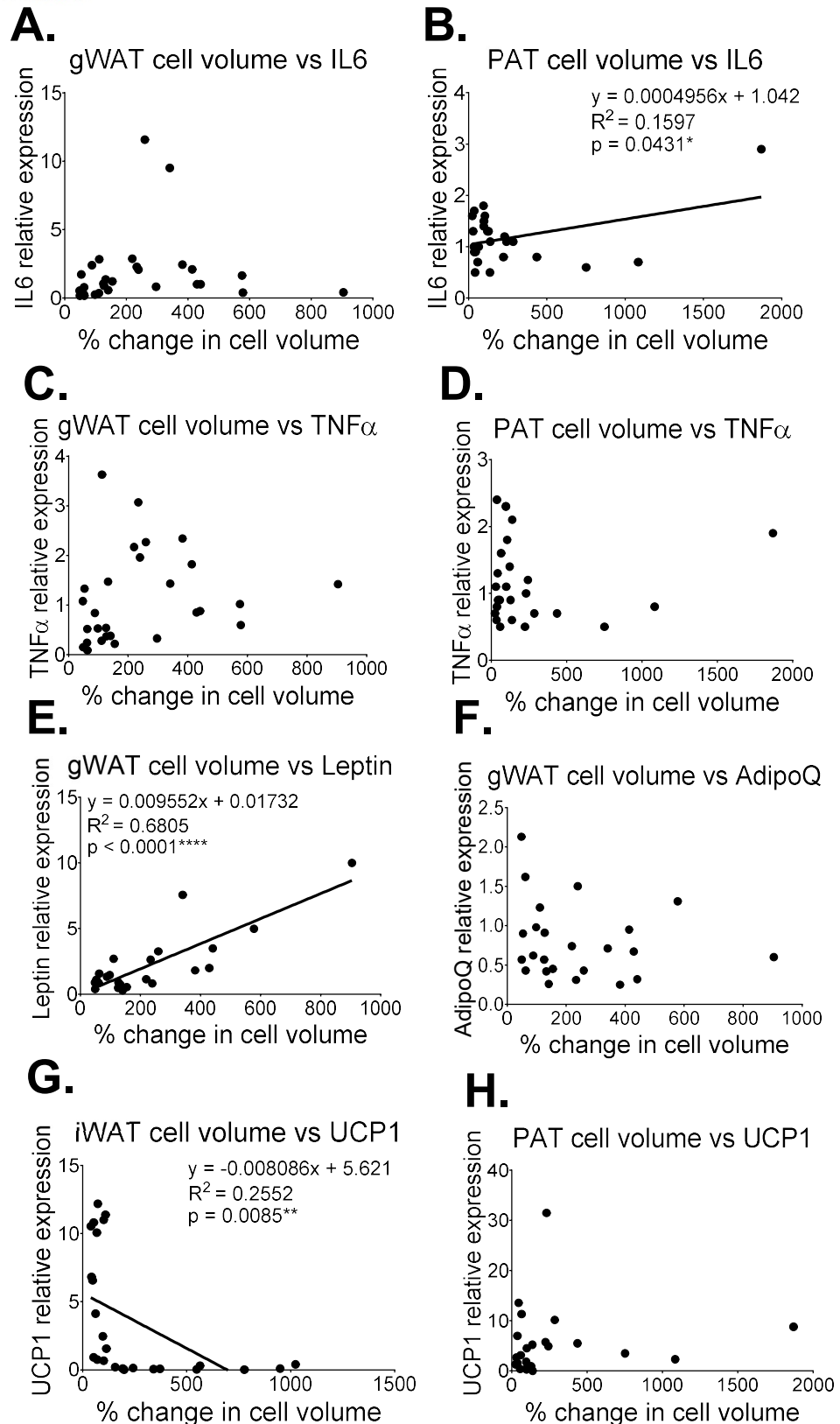
A.
gWAT cell volume vs IL6

B.
PAT cell volume vs IL6

y = 0.0004956x + 1.042
R^2 = 0.1597
p = 0.0431*

C.
gWAT cell volume vs TNFα

D.
PAT cell volume vs TNFα

E.
gWAT cell volume vs Leptin

y = 0.009552x + 0.01732
R^2 = 0.6805
p < 0.0001****

F.
gWAT cell volume vs AdipoQ

G.
iWAT cell volume vs UCP1

y = -0.008086x + 5.621
R^2 = 0.2552
p = 0.0085**

H.
PAT cell volume vs UCP1

Appendix Figure 4.27. The relationship between the percentage change of cell volume of **gWAT (A,C,E)**, **iWAT (G)** and **PAT (B,D,F,H)** compared to the fold change in mRNA expression of IL6, TNFα, Leptin, AdipoQ and UCP1 of chow (C) and high-fat (HF)-fed male mice treated orally with Vehicle (V) or Cpd14 for 10 days. Individual data points plotted, with the line of best fit as determined by simple linear regression. Data analysed by Pearson's correlation coefficient. N = 5-8. * p<0.05, ** p<0.01, *** p<0.001 and **** p<0.0001.
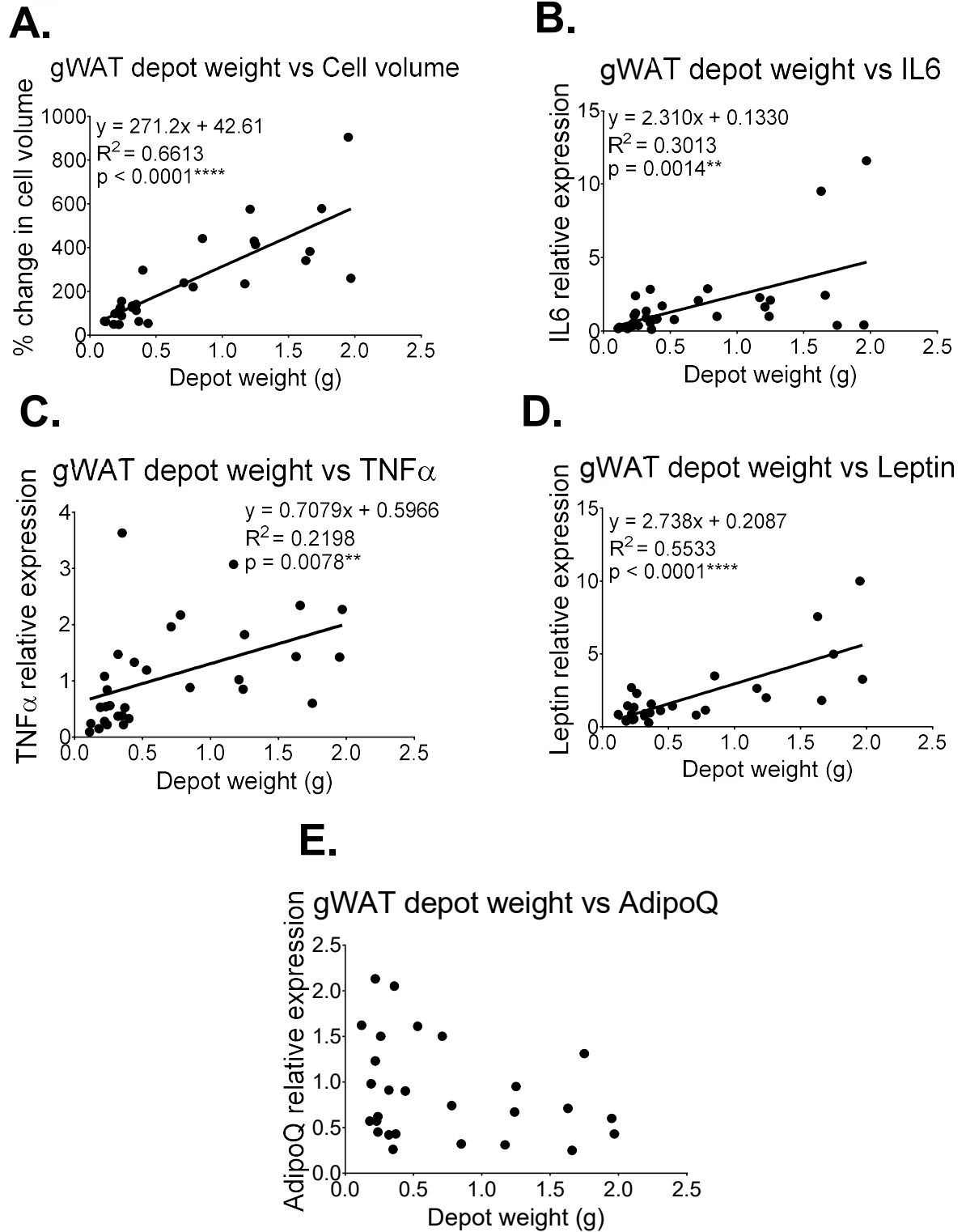
A.

gWAT depot weight vs Cell volume

$y = 271.2x + 42.61$
$R^2 = 0.6613$
$p < 0.0001****$

% change in cell volume — Depot weight (g)

B.

gWAT depot weight vs IL6

$y = 2.310x + 0.1330$
$R^2 = 0.3013$
$p = 0.0014**$

IL6 relative expression — Depot weight (g)

C.

gWAT depot weight vs TNFα

$y = 0.7079x + 0.5966$
$R^2 = 0.2198$
$p = 0.0078**$

TNFα relative expression — Depot weight (g)

D.

gWAT depot weight vs Leptin

$y = 2.738x + 0.2087$
$R^2 = 0.5533$
$p < 0.0001****$

Leptin relative expression — Depot weight (g)

E.

gWAT depot weight vs AdipoQ

AdipoQ relative expression — Depot weight (g)

Appendix Figure 4.28. The relationship between the depot weight of **gWAT** compared to the percentage change in cell volume **(A)** and the fold change in mRNA expression of IL6 **(B)**, TNFα **(C)**, Leptin **(D)** and AdipoQ **(E)** of chow (C) and high-fat (HF)-fed male mice treated orally with Vehicle (V) or Cpd14 for 10 days. Individual data points plotted, with the line of best fit as determined by simple linear regression. Data analysed by Pearson's correlation coefficient. N = 6-8. * $p<0.05$, ** $p<0.01$, *** $p<0.001$ and **** $p<0.0001$.